# Photoresponsive Metallo-Cages and Metallo-Supramolecular Assemblies

**Edward Britton**

Submitted in accordance with the requirements for the degree of Doctor of Philosophy

The University of Leeds

School of Chemistry

March 2020

The candidate confirms that the work submitted is his own and that appropriate credit has been given where reference has been made to the work of others.

## Acknowledgements

I would like to start by thanking Professor Michaele Hardie for giving me the opportunity to undertake this PhD. The last three and a half years have been an incredibly rewarding, worthwhile and often challenging experience. I am very grateful for all the help and guidance that I have received.

I must thank a number of people without whom the work presented in this thesis would not have been possible. Special thanks must go to Sam, whose work formed the solid foundation that this thesis is built upon. You have been an excellent companion to share the load of CTG chemistry with. I would also like to thank Chris for his Herculean efforts in attempting to collect the X-ray data of some truly awfully diffracting crystals. I feel that I must also apologise to Mark for relentlessly uttering the five words that keep him up at night, 'could I get a DOSY?' Thank you for your efforts and perseverance.

Sincere thanks must go to the past members of the Hardie group; Jonny, Hayder and Flo for guiding me through the turbulent waters of supramolecular chemistry. And to our most recent addition Matt (John), your cartography skills are wasted on a chemistry PhD.

In addition to the Hardie group, there have been several relevant others who have made the lab such an enjoyable place to work. I would like to thank the Willans group; Frances, Chrissi, Tom, James, Big Gail and Hamish. Frances, it has been great to have someone to share my love of alpacas with in carborane corner. Chrissi, for someone who appreciates order and cleanliness you are a true whirlwind of destruction in the lab. May Schlenk lines tremble in fear whenever you are near. And finally I'd like to thank Big Gail, for always being large and in charge.

Thanks must also go to my best mates from home; James, Sarah, Harriet and Al. Without you guys I wouldn't have had nearly such a whale of a time outside of work, which has definitely helped to get me through my PhD.

Of course, I have to thank my girlfriend Jess, who has done a most admirable job of sticking with me in Leeds for the past eight years. It would not have been the same experience without our shared love of great food, the most random hobbies and craft classes and the constant laughs! Thank you for everything you have done for me and for the best times I have had in Leeds.

Most importantly, I would like to thank my parents who bought me up to have an appreciation and love for science. Without your guidance and support

growing up there is no way I would have been in a position to do a PhD so thank you!

Last and certainly not least, I would like to thank McVitie's for producing the sublime writing snack that is a chocolate Hobnob. Without the constant supply of oaty goodness, it is debatable whether this thesis would ever have been completed.

## Abstract

This thesis is concerned with the design and study of supramolecular architectures bearing photoresponsive groups, enabling specific properties and functions to be controlled with the use of light. Such systems have many potential applications in sensing, molecular recognition and stimuli responsive materials.

All of the systems presented in this thesis are cage compounds containing a tripodal ligand scaffold based upon cyclotriveratrylene. The cyclotriveratrylene based ligands were functionalised with photo-responsive azobenzene groups. Self-assembly with rationally designed metal complexes furnished a library of $M_3L_2$ metallo-cryptophanes. The self-assembly behaviour of iridium(III), rhodium(III), palladium(II) and platinum (II) complexes with the ligands has been investigated using a range of solution-state techniques.

The photoresponsive properties of the palladium cages have been investigated. The system can be switched between a *trans*/*cis* conformation by irradiation with an appropriate wavelength of light. The structural transformation results in a change in the volume of the internal cavity, enabling applications requiring modulation of the host-guest properties of the cage through the use of light.

The host-guest properties of the palladium cages have also been assessed and found to bind a substituted napthalamide derivative as well as sodium alkyl sulphates. A detailed analysis of the binding of the sodium alkyl sulphates has been performed and association constants have been calculated.

A discussion detailing the possible formation of a large coordination cage bearing the general formula $M_6L_8$ is also included. Spectroscopic and crystallographic data supporting this hypothesis is presented herein.

# Table of Contents

**Acknowledgements** ..... **iii**
**Abstract** ..... **v**
**Table of Contents** ..... **vi**
**List of Figures** ..... **xi**
**List of Schemes** ..... **xxi**
**List of Tables** ..... **xxiii**
**List of Equations** ..... **xxiii**
**List of Abbreviations** ..... **xxiv**

**Chapter 1**
**Introduction** ..... **1**
1.1 Overview ..... 1
1.2 The Origins of Supramolecular Chemistry ..... 1
1.3 Metallo-Supramolecular Chemistry ..... 4
1.4 Applications of Coordination-Cages ..... 10
1.6 Photoswitchable Supramolecular Architectures ..... 18
1.7 Cyclotriveratrylene in Supramolecular Systems ..... 25
1.8 Project Aims ..... 31
References ..... 33

**Chapter 2**
**Component design: Synthesis of ligands and metal tectons** ..... **39**
2.1. Introduction ..... 39
2.2. Self-Assembly Design Principles ..... 39
2.2 Synthesis of Cyclotriguaiacylene ..... 41
2.3 Initial Progress Towards Azobenzene Functionalised $M_3L_2$ Metallo-Cryptophanes ..... 44
2.4 Functionalisation of Azobenzene Appended CTG ..... 52
2.5 Expansion of the Metal Tecton Toolkit ..... 67
2.7 Conclusion ..... 80
2.8 Future Work ..... 80
2.9 Experimental ..... 82
General Remarks ..... 82

Instrumentation ..... 82

3-Methoxy-4-propenyloxybenzyl alcohol[7] (2.1) ..... 82

(±)-2,7,12-Trimethoxy-3,8,13-tris(propenyloxy)-10,15-dihydro-5H-tribenzo[a,d,g] cyclononatriene[51] (2.2)..... 83

(±)-2,7,12-Trimethoxy-3,8,13-tris(hydroxy)-10,15-dihydro-*5H*-tribenzo[*a,d,g*] cyclononatriene[51] (CTG) (2.3) ..... 84

3-Ethoxy- 4-hydroxybenzyl alcohol (2.4) ..... 84

3-Ethoxy-4-(propenyloxy) benzyl alcohol[30] (2.5) ..... 85

(±)-2,7,12-Triethoxy-3,8,13-tris(propenyloxy)-10,15-dihydro-5H-tribenzo[a,d,g] cyclononatriene[30] (2.6)..... 86

(±)-2,7,12-Triethoxy-3,8,13-trihydroxy-10,15-dihydro-5H-tribenzo[a,d,g] cyclononatriene (eCTG) (2.7) ..... 86

3-Methoxy-4-propoxy benzyl alcohol (2.8) ..... 87

(±)-2,7,12-Tripropoxy-3,8,13-trihydroxy-10,15-dihydro-5H-tribenzo[a,d,g] cyclononatriene (2.9) ..... 88

(±)-2,7,12-Tripropoxy-3,8,13-trimethoxy-10,15-dihydro-5H-tribenzo[a,d,g] cyclononatriene[31] (pCTG) (2.10)..... 88

Methyl-4-nitrosobenzoate[22] (2.11)..... 89

3-(4-Sodiumbenzoateazo)pyridine[22] (2.12) ..... 90

3-(4-Benzoyl chlorideazo)pyridine (2.13)..... 90

(±)-2,7,12-Trimethoxy-3,8,13-*tris*(3-pyridyl-4-azophenylcarboxy)-10,15-dihydro-5H-tribenzo[a,d,g] cyclononatriene[22] (L1)..... 91

(±)-2,7,12-Triethoxy-3,8,13-*tris*(3-pyridyl-4-azophenylcarboxy)-10,15-dihydro-5H-tribenzo[a,d,g] cyclononatriene (L2)..... 92

(±)-2,7,12-Tripropoxy-3,8,13-*tris*(3-pyridyl-4-azophenylcarboxy)-10,15-dihydro-5H-tribenzo[a,d,g] cyclononatriene (L3)..... 93

2-(2-4-Difluorophenyl)-5-trifluoromethylpyridine[44] (2.14) ..... 94

Bis(2-phenylpyridine)iridium-µ-chloro dimer[52] (2.15)..... 94

Bis(2-phenylpyridine))bis(acetonitrile)iridium(III) hexafluorophosphate (M1) ..... 95

Bis(2-(2,4-difluorophenyl)-5-trifluoromethylpyridine)iridium-µ-chloro dimer (2.16)..... 96

Bis(2-(2,4-difluorophenyl)-5-trifluoromethylpyridine))bis(acetonitrile) iridium(III) hexafluorophosphate (M2) ..... 96

Bis(2-phenylpyridine)rhodium-µ-chloro dimer[48] (2.17)..... 97

Bis(2-phenylpyridine))bis(acetonitrile)rhodium(III) hexafluorophosphate (M3) ..... 98

Bis(2-(2,4-difluorophenyl)-5-trifluoromethylpyridine)rhodium-μ-chloro dimer (2.18) ..... 98

Bis(2-(2,4-difluorophenyl)-5-trifluoromethylpyridine))bis(acetonitrile)rhodium(III) hexafluorophosphate (M4) ..... 99

2-Phenylpyridine platinum(II)-μ-chloro dimer[54] (2.19) ..... 100

2-Phenylpyridinebis(acetonitrile)platinum(II) hexafluorophosphate (M5) ..... 100

(2-(2,4-difluorophenyl)5-trifluoromethylpyridine) platinum(II)-μ-chloro dimer (2.20) ..... 101

(2-(2,4-difluorophenyl)5-trifluoromethylpyridine)bis(acetonitrile) platinum(II) hexafluorophosphate (M6) ..... 102

References ..... 103

**Chapter 3**

**Self-assembly and characterisation of photoresponsive $M_3L_2$ metallo-cryptophanes ..... 106**

3.1 Introduction ..... 106

3.2 Expansion of the Ir(III) metallo-cryptophane library ..... 108

3.3 Synthesis of azobenzene appended Rh(III) metallo-cryptophanes ..... 124

3.4 Synthesis of azobenzene appended Pt(II) metallo-cryptophanes ..... 139

3.5 Synthesis of azobenzene appended Pd(II) metallo-cryptophanes ..... 143

3.6 Conclusions ..... 151

3.7 Future Work ..... 152

3.8 Experimental ..... 153

General Remarks ..... 153

Instrumentation ..... 153

$[(M1)_3(L1)_2]^{3+}\bullet 3PF_6^-$ (C1)[33] ..... 154

$[(M2)_3(L1)_2]^{3+}\bullet 3PF_6^-$ (C2) ..... 155

$[(M1)_3(L2)_2]^{3+}\bullet 3PF_6^-$ (C3) ..... 156

$[(M2)_3(L2)_2]^{3+}\bullet 3PF_6^-$ (C4) ..... 157

$[(M1)_3(L3)_2]^{3+}\bullet 3PF_6^-$ (C5) ..... 158

$[(M2)_3(L3)_2]^{3+}\bullet 3PF_6^-$ (C6) ..... 159

$[(M3)_3(L1)_2]^{3+}\bullet 3PF_6^-$ (C7) ..... 160

$[(M4)_3(L1)_2]^{3+}\bullet 3PF_6^-$ (C8) ..... 161

$[(M3)_3(L2)_2]^{3+}\bullet 3PF_6^-$ (C9) ..... 162
$[(M4)_3(L2)_2]^{3+}\bullet 3PF_6^-$ (C10) ..... 163
$[(M3)_3(L3)_2]^{3+}\bullet 3PF_6^-$ (C11) ..... 164
$[(M4)_3(L3)_2]^{3+}\bullet 3PF_6^-$ (C12) ..... 165
$[(M5)_3(L1)_2]^{3+}\bullet 3PF_6^-$ (C13) ..... 166
$[(Pd(en))_3(L1)_2]^{6+}\bullet 6NO_3^-$ (C19) ..... 167
$[(Pd(en))_3(L2)_2]^{6+}\bullet 6NO_3^-$ (C20) ..... 168
$[(Pd(en))_3(L3)_2]^{6+}\bullet 6NO_3^-$ (C21) ..... 169
References ..... 170

**Chapter 4**

**Photoisomerisation of CTG based Pd(II) metallo-cryptophanes ..... 173**

4.1 Introduction ..... 173
4.1.1 Photophysical behaviour of azobenzenes ..... 173
4.1.2 Azobenzenes in supramolecular architectures ..... 176
4.2 Photoisomerisation studies of azobenzene appended CTG based ligands ..... 181
4.3 Photoisomerisation studies of Pd(II) metallo-cryptophanes ..... 186
4.4 Conclusions ..... 194
4.5 Future work ..... 195
4.6 Experimental ..... 196
General Remarks ..... 196
Instrumentation ..... 196
4.6.1 UV studies of free ligands ..... 197
4.6.2 $^1$H-NMR studies of C19 ..... 197
References ..... 198

**Chapter 5**

**Host-Guest Behaviour of Photoswitchable Metallo-Cryptophanes .... 201**

5.1 Introduction ..... 201
5.1.1 Guest Encapsulation by CTV Derivatives ..... 201
5.1.2 Photoswitchable Host-Guest Systems ..... 206
5.2 Palladium Azobenzene Cryptophanes as Host Molecules ..... 209
5.2.1 Interactions Between Palladium Cryptophanes and Napthalamide Derivatives ..... 210

5.2.2. Encapsulation of Sodium Alkyl Sulfates in Palladium Metallo-Cryptophanes ..... 221
5.3 Conclusion ..... 233
5.4 Future Work ..... 234
5.5 Experimental ..... 236
General Remarks ..... 236
Instrumentation ..... 236
Preparation of compounds ..... 236
$^{1}$H-NMR titration procedure ..... 237
References ..... 238

**Chapter 6**

**Larger Supramolecular Assemblies of Azobenzene CTG Ligands ..... 241**

6.1 Introduction ..... 241
6.1.1 Expansion of the metallo-cage library ..... 241
6.2 Synthesis of stella octangula azobenzene cage ..... 247
6.3 Photoisomerisation studies of stella octangula azo-cage ..... 258
6.3.1 Photoisomerisation of the free ligand ..... 258
6.4.2 Photoisomerisation of the cage assembly ..... 260
6.4 Conclusion ..... 264
6.5 Future work ..... 265
6.6 Experimental ..... 266
General Remarks ..... 266
Instrumentation ..... 266
Preparation of compounds ..... 267
4-(4-sodiumbenzoateazo)pyridine (6.1) ..... 267
4-(4-benzoyl chlorideazo)pyridine (6.2) ..... 267
(±)-2,7,12-Trimethoxy-3,8,13-*tris*(4-pyridyl-4-azophenylcarboxy)-10,15-dihydro-5H-tribenzo[a,d,g] cyclononatriene (L4) ..... 268
$[Pd_6(L4)_8]$•12$BF_4$ (C22) ..... 269
6.7.1 $^{1}$H-NMR photoswitching studies of C22 ..... 269
References ..... 270

# List of Figures

Figure 1.1. SCXRD structure of human haemoglobin, each individual protein strand is highlighted in a different colour. Taken from PDB, identification 1A3N.[4] ..... 2

Figure 1.2. Structure of dibenzo-18-crown-6 capable of binding group one metal cations through electrostatic interactions (blue). Reported by Pedersen.[8] ..... 3

Figure 1.3. Cryptand reported by Lehn displaying selectivity for $Cd^{2+}$ cations due to N-Cd interactions and good cavity size match.[11] ..... 3

Figure 1.4. Lehn's Cu(I) helicate self-assembled from oligobipyridine ligands.[23] ..... 5

Figure 1.5. Schematic representation of Sauvage's synthetic route to form the first example of a molecular trefoil knot.[33] ..... 7

Figure 1.6. SCXRD structure of Leigh's pentafoil knot, displaying the bound chloride ion in the centre of the assembly. Each individual strand pre-joining is shown in a different colour.[34] Reproduced with permission from reference 34. ..... 8

Figure 1.7. Li's four component one pot synthesis of a molecular wheel formed in a quantitative yield.[36] Adapted with permission from reference [36]. ..... 9

Figure 1.8. a) UHV-LT-STM image of Li's supramolecular wheel on an Ag(111) surface, b) zoomed in UHV-LT-STM image of a single molecule of Li's supramolecular wheel on an Ag(111) surface.[36] Adapted with permission from reference.[36] ..... 10

Figure 1.9. General structure of Nitschke's tetrahedral $Fe_4L_6$ coordination cages.[47] ..... 11

Figure 1.10. SCXRD structure of $Fe_4L_6$ coordination cage, containing $P_4$ within the internal cavity.[48] Reproduced with permission from reference.[48] ..... 12

Figure 1.11. a) Structure of Raymond's $Ga_4L_6$ cage capable of catalysing the hydrolysis of orthoformate, b) The proposed mechanism of hydrolysis within the cage.[65] ..... 14

Figure 1.12. Fujita's $Pd_nL_{2n}$ polyhedral cages.[42] Adapted with permission from reference.[42] ..... 15

Figure 1.13. 'Gate opening' process of the stellated cuboctahedron, modulated by the presence of free TMEDA or $Pd^{2+}$ cations.[76] Adapted with permission from reference.[76] ..... 16

Figure 1.14. Structural rearrangement of a cuboctahedron to a pair of octahedra followed by a pair of superposed *bis*triangles following sequential dilution of the sample.[82] Adapted with permission from reference.[82] ..... 17

Figure 1.15. Lee's heterometallic photoresponsive macrocycle undergoing reversible light promoted splitting into two smaller subunits.[89] ..... 19

Figure 1.16. Yang and Zhu's photoswitchable macrocycle ring containing DTE subunits.[90] Adapted with permission from reference [90]. ..... 19

Figure 1.17. Yang's photoswitchable Pt(II)/ Ir(III) metallo-cycle showing switchable on/off phosphorescence due to FRET.[91] ..... 20

Figure 1.18. a) Individual subunits that comprise Xu's hexagonal metallo-cycle, b) Schematic representation of the metallo-cycle displaying rare switch-on luminescence following photoswitching of the DTE subunits into the closed state.[92] ..... 21

Figure 1.19. Nishihara's Cu(I) helicate, stabilising π-π interactions (blue) are disrupted by photoswitching and enable ligand substitution by 2,2'-bipy.[93] ..... 22

Figure 1.20. a) Azobenzene functionalised isophthalate ligand displaying photoswitching behaviour, b) $Cu_{24}L_{24}$ metal-organic polyhedral bearing exohedral azobenzene groups. Guest uptake and release of methylene blue could be modulated in the solid state by photoswitching of the azobenzene groups.[94] Reproduced with permission from reference.[94] ..... 23

Figure 1.21. $Pd_{12}L_{24}$ bearing endohedral azobenzene groups capable of photoswitching and modulating binding affinity of a 1-pyrenecarboxaldehyde guest.[95] Adapted with permission from reference.[95] ..... 24

Figure 1.22. $Pd_2L_4$ photoswitchable cage containing DTE groups described by Clever *et al*. Modulation of guest binding affinities was achieved by photoswitching of the DTEs.[97] ..... 25

Figure 1.23. Structure of CTV adopting the crown conformation. ..... 26

Figure 1.24. a) Structure of CTV derivative CTC, b) Structure of CTV derivative CTG and mechanism of chiral inversion proceeding through the saddle conformer. ..... 26

Figure 1.25. Nature of common CTV intramolecular interactions a) Bowl in bowl columnar stacking b) Dimeric handshake motif, each CTV unit is simultaneously acting as both a host and guest between neighbouring molecules.[102] Reproduced with permission from reference.[102] ..... 27

Figure 1.26. a) Structure of Brotin's cryptophane capable of binding xenon gas,[103] b) SCXRD structure of Hardie's disulphide linked cryptophane capable of binding methane gas.[113] Reproduced with permission from reference.[113] ..... 28

Figure 1.27. Structure of Jarosz's sucrose based hemicryptophane, displaying excellent water solubility.[115] ..... 29

Figure 1.28. a) SCXRD of $Ir_3L_2$ metallo-cryptophane,[118] b) SCXRD of $Pd_6L_8$ stella octangula cage,[117] c) SCXRD of infinite chainmail array of $Cu_6L_6$ Borromean Rings.[119] Importantly all of the above structures were obtained using the same 4-pyridyl ligand. Reproduced with permission from references [117, 118] and [119] respectively. ..... 30

Figure 1.29. Molecular model of $Ir_3L_2$ metallo-cryptophane bearing azobenzene groups. Photoswitching occurred upon irradiation at 355 nm.[96] Reproduced with permission from reference.[96] ..... 31

Figure 2.1. Synthesis of Fujita's molecular square.[1] ..... 40

Figure 2.2. Structure of cyclotriguaiacylene. ..... 41

Figure 2.3. $^1$H-NMR (300 MHz, $d_6$-DMSO) of CTG showing characteristic *endo* and *exo* doublets. ..... 44

Figure 2.4. Photoswitching of stilbene between *trans* and *cis* isomers. ..... 45

Figure 2.5. 6π electrocyclisation of stilbene followed by oxidation and deactivation of photoswitching properties. ..... 45

Figure 2.6. Photoisomerisation of DTEs upon irradiation with light. ..... 45

Figure 2.7. General structure of azobenzene moiety. ..... 46

Figure 2.8. Photo-induced switching of azobenzene displaying the distorted *cis* isomer.[15] ..... 46

Figure 2.9. $^{1}$H-NMR (300 MHz, $d_6$-DMSO) of L1 showing characteristic *endo* and *exo* CTG proton environments. ..... 49

Figure 2.10. SCXRD structure of Pritchard's cage showing ideal octahedral bond angles at the iridium(III) centres (yellow).[25] ..... 50

Figure 2.11. Examples of solubilised ligand and metal tectons. ..... 52

Figure 2.12. Diagram highlighting the efforts made to functionalise the hydroxyl positions of CTG whilst neglecting potential substitution at the methoxy position. ..... 53

Figure 2.13. $^{1}$H-NMR (300 MHz, $CDCl_3$) of eCTG showing characteristic *endo* and *exo* doublets of CTG core. ..... 56

Figure 2.14. $^{1}$H-NMR (300 MHz, $CDCl_3$) of pCTG showing characteristic *endo* and *exo* doublets of CTG core. ..... 59

Figure 2.15. $^{1}$H-NMR (300 MHz, $CDCl_3$) of azobenzene derivatives of CTG (L1, red), eCTG (L2, green) and pCTG(L3, blue) showing the expected similarity between the spectra. ..... 61

Figure 2.16. HRMS spectrum of L2. ..... 61

Figure 2.17. HRMS spectrum of L3. ..... 62

Figure 2.18. From the crystal structure of L1 showing the large channels formed in the crystal due to π-π stacking between the azobenzene arms[22] ..... 63

Figure 2.19. SCXRD structure of L2, a) Asymmetric unit, ellipsoids are shown at 50% probability, hydrogen atoms omitted for clarity, b) Bowl in bowl stacking arrangement of L2, different ligand enantiomers are shown in red and blue. ..... 64

Figure 2.20. SCXRD structure of L3•$CHCl_3$, a) Asymmetric unit, ellipsoids are shown at 50% probability, hydrogen atoms omitted for clarity, b) π-π stacking interactions between adjacent azobenzene arms of L3•$CHCl_3$, hydrogen atoms and solvents of crystallisation have been omitted for clarity. ..... 65

Figure 2.21. SCXRD structures of L3•$CHCl_3$; a) six membered ring formed by π-π stacking interactions between ligands, b) interpenetration of seven π-π stacked lattices, c) stick representation of the grid of seven interpenetrated networks, d) Borromean rings formed between the individual π-π stacked networks. ..... 66

Figure 2.22. $M_8L_{12}$ metallo-cube reported by the Thomas group, bearing rationally designed ruthenium tectons acting as the verticies.[38] ..... 67

Figure 2.23. The structure of the iridium ppy tecton showing protection of coordination sites by phenylpyridine groups and the 90° bond angle between available coordination sites occupied by acetonitrile. ..... 68

Figure 2.24. $^{1}$H-NMR (300 MHz, $d_3$-MeCN) of M2, confirming the formation of only one species in the reaction. ..... 70

Figure 2.25. HRMS of M2 showing the $[M2\text{-}MeCN\text{-}PF_6]^+$ as the major species detected. ..... 71

Figure 2.26. Two possible enantiomers of iridium phenylpyridine tectons Δ and Λ. ..... 71

Figure 2.27. Simplified Jablonski diagram showing excitation by light (blue) to the excited singlet state, non-radiative relaxation by internal conversion (black). Radiative relaxation pathways are fluorescence (red), and phosphorescence (green). ..... 72

Figure 2.28. Comparison of the $^{1}$H-NMR spectra (300 MHz, $d_3$-$MeNO_2$) of the iridium phenylpyridine tecton (M1, blue) and rhodium phenylpyridine tecton (M3, black), showing the expected similarities between the analogues. ..... 73

Figure 2.29. Comparison of the $^{1}$H-NMR spectra (300 MHz, $d_3$-$MeNO_2$) of the iridium phenylpyridine tecton (M2, blue) and rhodium phenylpyridine tecton (M4, black), showing the expected similarities between the analogues. ..... 74

Figure 2.30. a) HRMS spectrum of M3, b) HRMS spectrum and M4. ..... 75

Figure 2.31. a) $^{1}$H-NMR (500 MHz, $d_3$-$MeNO_2$) of M5, b) $^{1}$H-NMR (500 MHz, $d_3$-$MeNO_2$) of M6 ..... 78

Figure 2.32. a) HRMS spectrum of M5, b) HRMS spectrum of M6. ..... 79

Figure 2.33. Possible hydrogen bonded dimer of L2 detected in the mass spectra. ..... 81

Figure 3.1. An example of a $Pd_6L_4$ coordination cage catalysing a Diels-Alder reaction with unusual regioselectivity. ..... 106

Figure 3.2. The first example of an $M_3L_2$ metallo-cryptophane reported by Shinkai and co-workers.[26] ..... 107

Figure 3.3. Possible *syn* and *anti* diastereomers of cryptophanes. ..... 108

Figure 3.4. Time-course $^{1}$H-NMR (500 MHz, $d_3$-$MeNO_2$) showing the NMR spectra of L3 and M1 as unmixed solutions and immediately upon mixing. ..... 112

Figure 3.5. Fully assigned $^{1}$H-NMR (500 MHz, $d_3$-$MeNO_2$) of C3. ..... 112

Figure 3.6. ESI-MS of C3 acquired in $MeNO_2$ (M1 = M1 – 2MeCN – $PF_6$) ..... 113

Figure 3.7. ESI-MS of C5 acquired in $MeNO_2$ (M1 = M1 – 2MeCN – $PF_6$) ..... 113

Figure 3.8. Comparison of $^{1}$H-NMR (500 MHz, $d_3$-$MeNO_2$) spectra of C1 (black), C3 (green) and C5 (red) revealing the striking similarity between the spectra. ..... 115

Figure 3.9. Timecourse $^{1}$H-NMR (500MHz, $d_3$-$MeNO_2$) of the self-assembled product (C4) of L2 and M2. C4 peaks are highlighted in red and an minor self-assembly product in blue. ..... 116

Figure 3.10. $^{19}$F-NMR (471 MHz, $d_3$-$MeNO_2$) of cage C4 showing the presence of two species in the sample, C4 (red) and a minor (blue) product. .....117

Figure 3.11. Structure of the proposed $M_3L$ minor product. .....119

Figure 3.12. Fully assigned $^1$H-NMR (500 MHz, $d_3$-$MeNO_2$) of cage C4. Both C2 and C6 produced almost identical spectra. .....119

Figure 3.13. Molecular model of C1 calculated by Professor Colin Fishwick. The *meta* position on the pyridine of the phenylpyridine group (pink) points towards L1. Substitution of this position by a $CF_3$ group could feasibly result in steric clashes with a phenyl ring of the azobenzene (green). .....120

Figure 3.14. $^1$H-NMR (500 MHz, $d_3$-$MeNO_2$) of the self-assembly reaction between L3 and M2 in nitromethane (black) and tetrachloroethane (red). Diagnostic $M_3L$ peaks highlighted in blue. .....122

Figure 3.15. Example of a Rh(I) complex that switches between an open and closed form dependent upon the solvent polarity and electron withdrawing nature of the ligand.[36] .....123

Figure 3.16. HRMS of C4 acquired in $MeNO_2$ (M2 = M2 – 2MeCN – $PF_6$). .....123

Figure 3.17. Rhodium metal tectons bearing *cis* protecting phenylpyridine moieties. .....124

Figure 3.18. (Blue) $^1$H-NMR (300 MHz, $d_3$-$MeNO_2$) of M3. (Red) $^1$H-NMR (300 MHz, $d_3$-$MeNO_2$) of L1. (Green) $^1$H-NMR (300 MHz, $d_3$-$MeNO_2$) of C7 obtained immediately after mixing of components. .....125

Figure 3.19. $^1$H-NMR (300 MHz, $d_3$-$MeNO_2$) of C7 displaying simplified molecular structure and assignments of all proton signals. .....127

Figure 3.20. Mass spectrum of C7 acquired in $MeNO_2$, showing the desired $[M_3L_2]^{3+}$ as well as a range of fragmentation species. (M3 = M3 – 2MeCN – $PF_6$) .....128

Figure 3.21. DOSY NMR of C7 showing metal tecton and ligand diffusing at the same rate and the presence of a single large species in solution. .....129

Figure 3.22. $^1$H-$^1$H ROESY (600 MHz, $d_3$-$MeNO_2$) spectrum of C7 showing the cross-coupling between h and l indicative of metallo-cryptophane formation. .....130

Figure 3.23. The self-assembly of pyridyl appended CTG with palladium(II) nitrate, illustrating the subtle effects that can influence chiral self-sorting.[42] .....132

Figure 3.24. $^1$H-NMR (500 MHz, $d_3$-$MeNO_2$) of C7, C9 and C11 showing distinctly similar spectra .....135

Figure 3.25. ESI-MS of C9 acquired in $MeNO_2$ (M3 = M3 - 2MeCN - $PF_6$). .....135

Figure 3.26. ESI-MS of C11 acquired in $MeNO_2$ (M3 = M3 - 2MeCN - $PF_6$). .....136

Figure 3.27. $^1$H-NMR (500 MHz, $d_3$-$MeNO_2$) of fluorinated rhodium cages C8, C10 and C12 .....137

Figure 3.28. Representative HRMS acquired in $MeNO_2$ of fluorinated rhodium phenylpyridine cages, example shown is of C10. C8 and C12 both showed similar spectra. (M4 = M4 – 2MeCN – $PF_6$) .....137

Figure 3.29. $^{1}$H-NMR (500 MHz, $d_2$-tetrachloroethane) of fluorinated rhodium C12 displaying the formation of the $M_3L$ product. Diagnostic $M_3L$ peaks highlighted in blue. ....138

Figure 3.30. $^{1}$H-NMR (500 MHz, $d_2$-tetrachloroethane) of fluorinated rhodium C12 with increasing quantities of nitromethane added. Formation of the $M_3L_2$ species is observed upon each subsequent addition of the nitromethane. 0 Drops (red), 5 drops (green), 15 drops (blue). $M_3L$ peaks highlighted in blue. ....139

Figure 3.31. $^{1}$H-NMR (300 MHz, $d_3$-$MeNO_2$) of M5, L1 and the formation of C13. ....142

Figure 3.32. ESI-MS of C13 acquired in $MeNO_2$, (M5 = M5 – 2MeCN – $PF_6$). ....142

Figure 3.33. $^{1}$H-NMR (500 MHz, $d_6$-DMSO) spectrum of reaction of L1 and $Pd(en)(NO_3)_2$ obtained immediately after mixing, revealing a surprising simplicity to the spectrum. ....147

Figure 3.34. $^{1}$H-$^{1}$H NOESY (500 MHz, $d_6$-DMSO) spectrum of C20 displaying through space cross-couplings between metal tecton and ligand highlighted in green. ....148

Figure 3.35. $^{1}$H-NMR DOSY (600 MHz, $d_6$-DMSO) spectrum of C19 showing a single large species in solution. ....148

Figure 3.36. ESI-MS of metallo-cryptophane C19, acquired in DMSO. ....149

Figure 3.37. $^{1}$H-NMR (500 MHz, $d_6$-DMSO) of palladium cryptophane C19 displaying the peaks corresponding to metallo-cryptophane (red) and 'free' ligand (blue). ....150

Figure 3.38. Sugar appended NHC tecton to enhance the water solubility of metallo-cryptophanes. ....152

Figure 4.1. Structure of an azobenzene group and the general conditions under which switching between the *trans* and *cis* rich state can be promoted. ....174

Figure 4.2. The three main classes of azobenzenes; a) azobenzene type, b) aminoazobenzene, c) pseudo-stilbene. ....175

Figure 4.3. Two of the proposed mechanisms for the photoisomerisation of *trans* azobenzene to *cis* azobenzene. ....176

Figure 4.4. Azobenzene (green) and cyclodextrin (blue) appended polymers capable or switching undergoing a reversible sol-gel transition upon azobenzene *cis-trans* isomerisation.[33] ....177

Figure 4.5. Nabeshima's tris azobenzene containing titanium metallocycle capable of completely inhibiting the photoswitching behaviour.[36] ....178

Figure 4.6. $Pd_2L_4$ cage reported by Liu and co-workers containing azobenzene groups embedded with the structural framework.[37] ....179

Figure 4.7. Clever's $Pd_2L_4$ DTE functionalised cage, able to photoisomerise between an open and closed form.[23] ....180

Figure 4.8. Molecular model of the azobenzene appended iridium-cryptophane reported by the Hardie group. The metallo-cage is capable of reversible *trans* to *cis* photoisomerisation. ....181

Figure 4.9. UV/visible spectra of L1, L2 and L3 showing the π-π* and n-π* azobenzene absorption bands. ....182

Figure 4.10. UV/visible spectrum of L1 (30 μM, $CHCl_3$) upon irradiation with 365 nm light. ....183

Figure 4.11. UV/visible spectrum of L2 (30 μM, $CHCl_3$) upon irradiation with 365 nm light. ....183

Figure 4.12. UV/visible spectrum of L3 (30 μM, $CHCl_3$) upon irradiation with 365 nm light. ....184

Figure 4.13. UV/visible spectra (30 μM, DMSO) of the thermal relaxation of *cis* L1 to *trans* L1 at 298 K. ....186

Figure 4.14. UV/visible spectrum (30 μM, DMSO) of C19 upon irradiation with a 365 nm 30 W lamp for specified amounts of time. ....187

Figure 4.15. $^1$H-NMR (500 MHz, $d_6$-DMSO) of cage C19 following dilution, compared to $^1$H-NMR (300 MHz, $d_6$-DMSO) of the free ligand L1. ....188

Figure 4.16. a) $^1$H-NMR (500 MHz, $d_6$-DMSO) of cage C19; b) upon illumination with a 355 nm Nd:YAG laser (20 mJ, 10 Hz, 1200 s); c) Re-irradiation with 450 nm Xe lamp (1 hour). L1 (red) and $Pd(en)_2(NO_3)_2$ (blue) peaks are shown. ....190

Figure 4.17. Drift plot of cage C19 in *trans* rich state (top) and *cis* rich state (bottom). Peak highlighted in red corresponds to the $[M_3L_2]^{6+}$ peak. ....193

Figure 4.18. Drift time of $[M_3L_2]^{6+}$ peak for *trans* rich state (left) and *cis* rich state (right). ....194

Figure 4.19. Structure of proposed NHC protected palladium tecton designed to resist photodegradation. ....195

Figure 5.1. Pedersen discovered that crown ethers are capable of binding alkali metal cations *via* electrostatic interactions (red).[2] ....201

Figure 5.2. Structure of exTTF functionalised CTG receptor designed to bind to fullerene guests.[19] ....202

Figure 5.3. Structure of organic soluble cryptophane (A)[21] and water soluble cryptophane (B)[22] hosts capable of xenon binding. ....203

Figure 5.4. $[(\eta^5\text{-}Cp^*)Ru]^+$ coordinated to the arene faces of the CTV bowl improve aqueous solubility of fullerene cryptophane host.[28] ....204

Figure 5.5. Structure of disulfide linked cryptophane (left) capable of binding methane in solution. SCXRD structure (right) highlights the small size of the internal cavity.[29] ....204

Figure 5.6. SCXRD structure of $Pd_3L_2$ cryptophane displaying the uptake of $I_2$ in the solid state.[30] ....205

Figure 5.7. Molecular model of palladium stella-octangula cage with two surfactant guest molecules residing inside. ....206

Figure 5.8. Example of a photoswitchable host system reported by Rebek and co-workers where an adamantane guest is ejected following the *trans* to *cis* photoswitching of an azobenzene group.[36] ....207

Figure 5.9. Structure of Houk's gated container molecule, capable of uptake and release of 1,4-dimethoxybenzene in solution.[39] .....208

Figure 5.10. $Pd_2L_4$ Metallo-cage reported by Clever *et al*. photoswitching of the dithienylethene group results in uptake or release of a $B_{12}F_{12}^{2-}$ guest.[40] .....209

Figure 5.11. $^1$H-NMR (500 MHz, $d_6$-DMSO) of G1, the molecule contains a number of desirable features, beneficial for its use as a guest molecule for CTV based hosts. .....211

Figure 5.12. Stacked $^1$H-NMR (500 MHz, $d_6$-DMSO) of G1 and C19 titration experiment where [G1] is constant at 0.24 mM and [H] is decreasing from 1.4 – 0.06 mM (black). Degradation of host at low concentrations is evident when compared to fully formed host (blue) and L1 (red). .....212

Figure 5.13. Self-titration of G1 monitored by $^1$H-NMR, subtle shifts of the proton environments are observed. .....213

Figure 5.14. $^1$H-NMR (500 MHz, $d_6$-DMSO) titration of G1 and C19 where host concentration is constant (2.75 mM) and guest concentration is varied. .....215

Figure 5.15. $^1$H-NMR (500 MHz, $d_6$-DMSO) titration of G1 and C20 where host concentration is constant (2.75 mM) and guest concentration is varied. .....216

Figure 5.16. $^1$H-NMR (500 MHz, $d_6$-DMSO) titration of G1 and C21 where host concentration is constant (2.75 mM) and guest concentration is varied. .....217

Figure 5.17. Comparison between the interaction of G1 (1.0 M) and cages C19, C20 and C21 (2.75 M) displaying the faster interaction between C19 than C20 and C21. .....218

Figure 5.18. Plots of the chemical shift of Hb on G1 vs the concentration of G1 in the presence of $Pd_3Lx_2$ cages (Lx = L1, L2 or L3) ([H] = 2.75 mM). .....220

Figure 5.19. $^1$H DOSY-NMR (600 MHz, $d_6$-DMSO) of C19 (blue) and G1 (red) showing the similar diffusion constant. .....220

Figure 5.20. $^1$H-NMR (500 MHz, $d_6$-DMSO) of SOS at 298 K. .....221

Figure 5.21. $^1$H-NMR (500 Hz, $d_6$-DMSO) of SOS over a concentration range of 1.0 mM – 40 mM. .....222

Figure 5.22. $^1$H-NMR (500 MHz, $d_6$-DMSO) of C19 (3.85 mM) in the presence of varying concentrations of SOS. .....223

Figure 5.23. $^1$H-NMR (500 MHz, $d_6$-DMSO) of C20 (3.85 mM) in the presence of varying concentrations of SOS. .....224

Figure 5.24. $^1$H-NMR (500 MHz, $d_6$-DMSO) of C21 (3.85 mM) in the presence of varying concentrations of SOS. .....225

Figure 5.25. $^1$H-$^1$H NOESY spectrum (500 MHz, $d_6$-DMSO) of C21 displaying couplings between host and guest circled in green. .....227

Figure 5.26. Binding isotherms derived from the chemical shift proton environment Hd on SOS plotted against the [SOS] for cages C19, C20 and C21. .....228

Figure 5.27. Fitting of the binding isotherms using HypNMR for a 1:1 HG ratio of C19 and SOS with no guest self-association factor. .....229

Figure 5.28. Fitting of the binding isotherms using HypNMR for a 1:1 HG ratio of C19 and SOS, including a SOS dimerisation factor. ..... 230

Figure 5.29. Fitting of the binding isotherms using HypNMR for a 1:1 HG ratio of C20 and SOS, including a SOS dimerisation factor. ..... 231

Figure 5.30. Fitting of the binding isotherms using HypNMR for a 1:1 HG ratio of C21 and SOS, including a SOS dimerisation factor. ..... 231

Figure 5.31. Gold napthalamide complex shown to possess anticancer properties.[51, 52] ..... 234

Figure 5.32. Palladium NHC appended azobenzene metallo-cryptophane. The extra stability afforded by the *bis*-NHC may be sufficient to increase the photo-fatigue resistance of this class of cages. ..... 235

Figure 6.1. X-ray crystal structure of $Pd_4L_4$ topologically complex Solomon's cube, each ligand is represented by a different colour.[9] ..... 242

Figure 6.2. Regioselective control of the photochemical radical reaction between *ortho*-quinone and a substituted toluene leading to a single isomer in the presence of a $Pd_6L_4$ cage.[25] ..... 243

Figure 6.3. Synthesis of $Pd_{12}L_{24}$ cage (blue) capable of templating the formation of monodisperse silica nanoparticles (green).[26] ..... 244

Figure 6.4. X-ray structure $Pd_3L_4$ cage synthesised by Hardie and co-workers displaying host-guest interactions with DMSO molecules.[6] ..... 245

Figure 6.5. X-ray crystal structure of $Pd_6L_8$ stella octangula structure synthesised by Hardie and co-workers shown in ball and stick (left) and space filling (right) representations.[5] ..... 246

Figure 6.6. Structure of extended ligands capable of forming stella octangula structure with naked palladium.[6] ..... 246

Figure 6.7. $^1$H-NMR (500 MHz, $d_6$-DMSO) of L1 and $Pd(MeCN)_4.2BF_4$ in a 2:3 stoichiometry ..... 247

Figure 6.8. Molecular panelling of ligands L1 – L3 tessellated onto an octahedron showing the ligands are not sufficiently preorganised to form stella-octangula structure. ..... 248

Figure 6.9. $^1$H-NMR (500 MHz, $d_6$-DMSO) of L4. ..... 250

Figure 6.10. Molecular panelling of ligands L4 tessellated onto an octahedron showing that a stella octangula structure is accessible from this ligand. ..... 251

Figure 6.11. $^1$H-NMR (500 MHz, $d_6$-DMSO) of L4 (red) and after immediately after addition of 0.75 equivalents of $[Pd(MeCN)_4]2BF_4$ (blue). ..... 252

Figure 6.12. $^1$H-$^1$H COSY NMR (600 MHz, $d_6$-DMSO) of C22 at room temperature (top) and 60 °C (bottom). Cross coupling peak highlighted in green only visible at elevated temperatures. ..... 254

Figure 6.13. DOSY-NMR (500 MHz, $d_6$-DMSO) of $[Pd_6L4_8]12BF_4$ cage showing a single large species in solution ..... 255

Figure 6.14. ESI-MS of $Pd_6L4_8$ showing a multitude of different species detected. ..... 256

Figure 6.15. Zoomed in section of Figure 6.14 showing 12+ peaks of possible $[Pd_6L_8]^{12+}$ detected with varying amounts of solvent molecules. .....257

Figure 6.16. Appearance of the crystals of $[Pd_6L_8]12BF_4$ displaying the distinctive shape of an octahedron. .....258

Figure 6.17. UV/visible spectrum (30 μM, $CHCl_3$) of L4. .....259

Figure 6.18. Timecourse UV/visible spectrum (30 μM, DMSO) of L4 upon irradiation with a 30 W 306 nm lamp. .....259

Figure 6.19. $^1$H-NMR (500 MHz, $d_6$-DMSO) of a) C22 before photoswitching, b) after irradiation with 355 nm laser light for 15 mins, c) after heating to 80 °C for 24 hours.....261

Figure 6.20. Drift plot of C22 in resting *trans* state (top) and *cis* rich state (bottom). Peaks highlighted correspond to $[Pd_6L4_8]^x$, where x is the charge labelled on the peak. .....263

Figure 6.21. Drift times of $[Pd_6L4_8]^{12+}$ (left), $[Pd_6L4_8]^{11+}$ (middle) and $[Pd_6L4_8]^{10+}$ (right) in a *trans* and *cis* rich state. .....263

# List of Schemes

Scheme 2.1. Isomerisation of crown enantiomers through the saddle intermediate. ..... 42

Scheme 2.2. Synthesis of CTG. ..... 43

Scheme 2.3. Proposed mechanism of the modified Mills reaction used to synthesise azobenzene arm.[22] ..... 47

Scheme 2.4. Synthesis of azobenzene appended CTG (L1). ..... 48

Scheme 2.5. Synthesis of $M_3L_2$ metallo-cryptophane reported by Pritchard *et al*.[25] ..... 50

Scheme 2.6. Synthesis of the first example of an azobenzene linked $M_3L_2$ metallo-cryptophane synthesised by Oldknow *et al*.[22, 26] ..... 51

Scheme 2.7. Synthesis of eCTG monomer 2.5. ..... 54

Scheme 2.8. Successful synthesis of allyl protected CTG (top) and unsuccessful synthesis of allyl protected eCTG (bottom). ..... 54

Scheme 2.9. Successful synthesis of allyl protected eCTG using $Sc(OTf)_3$ as a Lewis acid catalyst.[30] ..... 55

Scheme 2.10. Palladium catalysed deprotection of allyl eCTG to furnish eCTG. ..... 56

Scheme 2.11. First and second step towards the synthesis of pCTG. ..... 57

Scheme 2.12. Successful synthesis of pCTG utilising lithium diphenylphosphide and unsuccessful attempts using other dealkylating reagents. ..... 58

Scheme 2.13. Synthesis of solubilised azobenzene appended ligands L2 and L3. ..... 60

Scheme 2.14. Synthesis of fluorinated ppy iridium tecton M2. ..... 69

Scheme 2.15. Synthesis of rhodium metal tectons M3 and M4.[48] ..... 73

Scheme 2.16. Synthesis of platinum phenylpyridine tectons. ..... 77

Scheme 3.1. Synthesis of azobenzene containing Ir(III) metallo-cryptophane.[33] ..... 109

Scheme 3.2. Synthetic methodology to expand the iridium(III) metallo-cryptophane library. ..... 110

Scheme 3.3. Synthesis of an $M_3L_2$ metallo-cryptophane from M3 and L1 to form C7. ..... 126

Scheme 3.4. Synthesis of $Ir_3L_2$ cage displaying chiral self-sorting of coordination cage.[41] ..... 131

Scheme 3.5. Scheme showing synthesis of all possible permutations of rhodium cryptophanes. ..... 133

Scheme 3.6. Synthesis of platinum(II) containing metallo-cryptophanes. ..... 140

Scheme 3.7. Synthesis of palladium containing metallo-cryptophanes C19, C20 and C21. ..... 146

Scheme 4.1. Decomposition of palladium tecton, promoted by the photoswitching of cage C19 into the *cis* rich state. .....191

Scheme 6.1. Synthesis of ligand L4 first reported by Dr Samuel Oldknow.[31] .....249

Scheme 6.2. Synthesis of $Pd_6L4_8$ stella octangula structure. .....251

# List of Tables

Table 3.1. Reaction codes of iridium-cryptophanes resulting from the reaction of azobenzene ligand with metal tecton. .....110

Table 3.2. Reaction codes of rhodium-cryptophanes resulting from the reaction of azobenzene ligand with metal tecton. .....134

Table 3.3. Reaction codes of platinum-cryptophanes resulting from the reaction of azobenzene ligand with metal tecton .....141

Table 4.1. Percentage conversion of azobenzene groups in ligands L1, L2 and L3 upon irradiation with 365 nm light. .....185

Table 5.1. Table containing the predicted chemical shifts of the species present in a system containing C19 and SOS. .....230

Table 5.2. Binding constants calculated for host guests systems containing palladium cryptophanes and SOS. .....232

# List of Equations

Equation 4.1. Calculation to determine the conversion of *trans* isomer to *cis* isomer. $A_0$ and $A_{PSS}$ are measured at the maxima of the π-π* transition.....184

Equation 6.1. Stokes-Einstein equation to estimate hydrodynamic radius of particle in solution from diffusion constant. D = diffusion constant, R = ideal gas constant, T = temperature, $N_A$ = Avogadro constant, η = solvent viscosity, r = hydrodynamic radius. .....255

## List of Abbreviations

**Ar** - Aryl

**AZB** - Azobenzene

**COSY** - Correlation spectroscopy

**CTC** - Cyclotricatechylene

**CTG** - Cyclotriguaiacylene

**CTV** - Cyclotriveratrylene

**DCM** - Dichloromethane

**DMF** - Dimethylformamide

**DMSO** - Dimethyl sulfoxide

**DOSY** - Diffusion ordered spectroscopy

**DTE** - Dithienylethene

**eCTG** - Ethyl cyclotriguaiacylene

**en** - 1,2-ethylenediamine

***et al*** - And others

**IM-MS** - Ion mobility mass spectrometry

**HMBC** - Heteronuclear multiple bond coherence

**HPLC** - High performance liquid chromatography

**HSQC** - Heteronuclear multiple bond coherence

**ESI-MS** - Electrospray ionisation mass spectrometry

**IR** - Infrared

**M** - Metal tecton

**L** - Ligand

**MLCT** - Metal to ligand charge transfer

**MOF** - Metal organic framework

**Nd:YAG** - Neodymium: Yttrium aluminium garnet

**NHC** - N-Heterocyclic carbene

**NMR** - Nuclear magnetic resonance

**NOESY** - Nuclear Overhauser effect spectroscopy

**pCTG** - Propyl cyclotriguaiacylene

**ppy** - 2-Phenylpyridine

**ROESY** - Rotating frame Overhauser effect

**RT** - Room temperature

**SAXS** - Small angle X-ray scattering

**SCXRD** - Single crystal X-ray diffraction

**TOCSY** - Total correlation spectroscopy

**UV** - Ultraviolet

**VT NMR** - Variable temperature nuclear magnetic resonance

# Chapter 1

# Introduction

## 1.1 Overview

The work discussed herein draws its inspiration from the field of supramolecular chemistry. As an interdisciplinary subject in nature, elements of organic, inorganic and physical chemistry are explored. This thesis is principally concerned with the design, synthesis and characterisation of a range of metallo-supramolecular architectures that change shape in response to light. This chapter is intended to introduce the basic principles governing supramolecular systems and provides several examples of noteworthy research originating from the field. For each component of this work, a more focussed introduction can be found at the beginning of every chapter.

## 1.2 The Origins of Supramolecular Chemistry

The basic building blocks of chemistry are atoms. The linking of atoms through covalent bonds to form molecules has been the fundamental aim of chemists since the field's inception. Supramolecular chemistry however, is a relatively new discipline, concerned with chemistry 'beyond the molecule'.[1] Instead of atoms, a supramolecular chemist uses molecules as their fundamental building blocks, assembling them together through weak intermolecular forces to form a supramolecule. Nature utilises the principles of supramolecular chemistry when building biomolecules, be it the innumerable hydrogen bonds that lead to the double helical structure of DNA, or the complex quaternary structure of haemoglobin. Each molecule of haemoglobin is comprised of four non-covalently bound haem groups, held together by intramolecular forces.[2] Moreover, the tertiary structure of each subunit is also held in a very specific shape by weak hydrogen bonds and hydrophobic interactions (Figure 1.1).[3] Without the interplay between the intra and intermolecular forces the complex structure and function would be impossible to achieve. Further research into supramolecular chemistry could allow us to mimic such structures, developing functional materials that are not accessible through traditional chemistry.

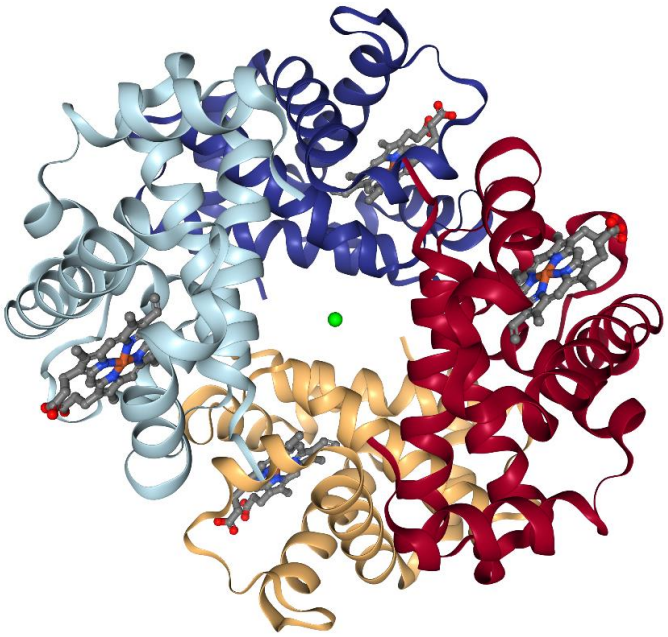

**Figure 1.1.** SCXRD structure of human haemoglobin, each individual protein strand is highlighted in a different colour. Taken from PDB, identification 1A3N.[4]

The origins of supramolecular chemistry can be traced back to 1961 and the discovery by Pedersen that crown ethers are capable of binding group one metal cations.[5] Crown ethers are cyclic ethers possessing a small internal cavity. In Pedersen's first example he discovered that sodium cations were bound within the cavity of dibenzo-18-crown-6. The sodium ions resided inside the cavity where electrostatic interactions between the positively charged cation and the negative dipoles on the oxygen atoms stabilised the complex (Figure 1.2).[5] Further study revealed that although capable of binding sodium ions, dibenzo-18-crown-6 has a preference to bind potassium ions due to improved size matching between the cavity and cation, resulting in stronger electrostatic forces.[6, 7] Not only had Pedersen discovered the first example of a host-guest system, but had also shown that crown ethers are capable of molecular recognition between different alkali metal cations. He published a breakthrough paper in 1967 detailing the synthesis of approximately 50 crown ethers and their ability to bind a range of metal cations.[8]

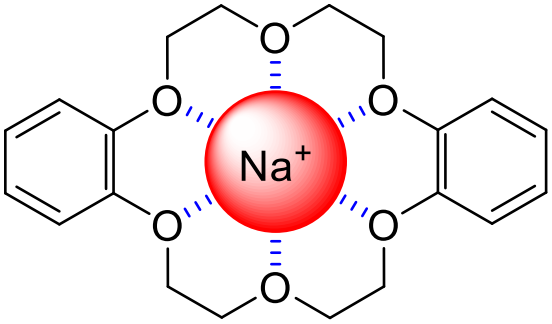


**Figure 1.2.** Structure of dibenzo-18-crown-6 capable of binding group one metal cations through electrostatic interactions (blue). Reported by Pedersen.[8]

The work of Pedersen led to a rapid expansion of the field of supramolecular chemistry, of particular note was the work of Cram and Lehn.[9, 10] Lehn developed a new class of macrocycles known as cryptands.[11] Although similar to crown ethers, cryptands possess the important property of existing in three dimensions. Crown ethers exist in a 2D conformation which somewhat limits their ability to recognise molecules. Lehn showed that cryptands were able to bind metal cations with an even higher affinity than crown ethers as the metal can be completely encapsulated by the ligand, resulting in a greater number of stabilising interactions.[11] In contrast to crown ethers, cryptands have a well-documented ability to bind transition metal cations, in addition to alkali metal cations, lanthanides and main group metals. The addition of nitrogen or sulphur containing groups into the cryptand host has been shown to improve the ability of cryptands to bind transition metals through the formation of coordination bonds.[12, 13] This property allows molecular recognition to occur that is not solely dictated by the degree of cavity size matching but also by strength of the N-M bond. An elegant example was shown for the cryptand shown in Figure 1.3, where a selectivity of approximately $10^6$ was observed for $Cd^{2+}$ ions over $Zn^{2+}$ and $Ca^{2+}$.[11] The $Cd^{2+}$ and $Ca^{2+}$ both have a good match to the cavity size unlike the $Zn^{2+}$ which is too small for efficient binding. The nitrogen centres can form strong bonds between the $Cd^{2+}$ and $Zn^{2+}$ but form weaker bonds to the $Ca^{2+}$ ions. The interplay between these two variables introduces a double parameter method of discriminating between guests, allowing even greater selectivity to be achieved.[11]

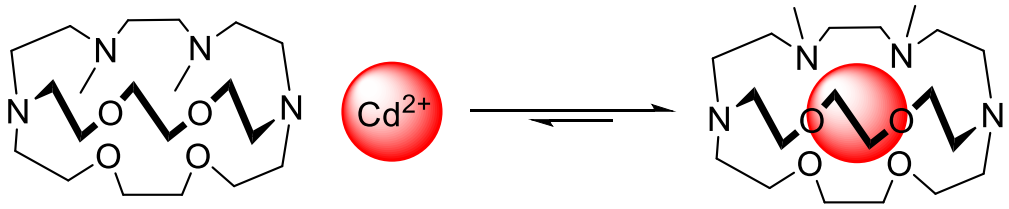


**Figure 1.3.** Cryptand reported by Lehn displaying selectivity for $Cd^{2+}$ cations due to N-Cd interactions and good cavity size match.[11]

Cram developed the field of supramolecular chemistry even further by developing host molecules with ever increasing complexity and in particular by pioneering computational chemistry as a method of predicting host-guest interactions.[14] An important observation that Cram noticed was that host molecules that do not undergo structural change to accommodate a guest tend to have more favourable binding interactions.[15] This phenomena is known as pre-organisation. A host which is preorganised to accommodate a guest will not have an enthalpy penalty associated with binding as no structural rearrangement is required. The entropy penalty is also lessened as in order to be preorganised the host must be relatively rigid and as such, when a guest is bound the loss in degrees of freedom is reduced. Cram used this trend, along with computational studies to design intricate host molecules capable of binding a wide range of guests.[16]

For their work in establishing supramolecular chemistry Pedersen, Lehn and Cram were awarded the 1987 Nobel Prize in chemistry and since then the field has continued to grow, with the notion of host-guest chemistry remaining an integral and important part of it.

### 1.3 Metallo-Supramolecular Chemistry

Although the field of supramolecular chemistry began with organic based hosts, the science has since expanded to encompass systems containing metallic elements, known as metallo-supramolecular systems. The coordination bond possesses a number of beneficial characteristics that make it a good candidate for use in supramolecular chemistry.[17] The strength of an average coordination bond lies between the strong, irreversible covalent bond and weak, reversible intermolecular forces such as hydrogen bonds. This property means that depending on the choice of metal, a coordination bond can be relatively labile under standard room temperature conditions.[17] This can lead to self-assembly occurring in such systems; any kinetic products that form during the course of the reaction can undergo the reverse reaction due to the labile coordination bonds. The intermediate then has a chance to react again where it may form the thermodynamic product.[17] This process is known as error correction and is very rare in organic systems, with a notable exception being imine bond formation,[18] as the covalent bond is too strong and therefore non-labile. Any kinetic side products that form during a reaction are irreversibly trapped in this state. Self-assembly provides a synthetic route to highly complex systems that would be impossible to synthesise using traditional synthetic techniques.

Moreover, metal centres adopt well defined and predictable geometries, for example palladium(II) is almost invariably square planar, whereas iridium(III) adopts a predictable octahedral geometry. Not only would these shapes be impossible to achieve using traditional organic chemistry, but can simplify the design of supramolecular architectures. By acting as the vertices of geometric shapes the metal ions template components into highly specific shapes, an approach known as directional bonding.[17] Inclusion of a metal into the framework of a cage can introduce additional functionality to the system. Redox,[19] luminescent,[20] biomedical[21] and catalytic functions[22] have all been reported for metallo-supramolecular architectures and can be attributed to the inclusion of a metal within the framework of the structure.

One of the first examples of a metallo-supramolecular system was reported by Lehn in 1987. It was discovered that in the presence of Cu(I) ions, oligobipyridine ligands assembled to form a double stranded helical structure in a quantitative yield (Figure 1.4).[23] The two ligands wrapped around each other to form a chiral structure held together by tetrahedral Cu(I) cations between the strands. The helical structure was stabilised by π-π stacking interactions between the bipyridine derivatives on each strand, such interactions could not occur in a non-helical structure. Obtaining a quantitative yield this reaction is remarkable, such a reaction would be expected to yield a multitude of oligomeric side products. The Cu-N bond facilities the formation of the helical product exclusively, as the associated lability places the system under thermodynamic control and allows self-assembly to occur.

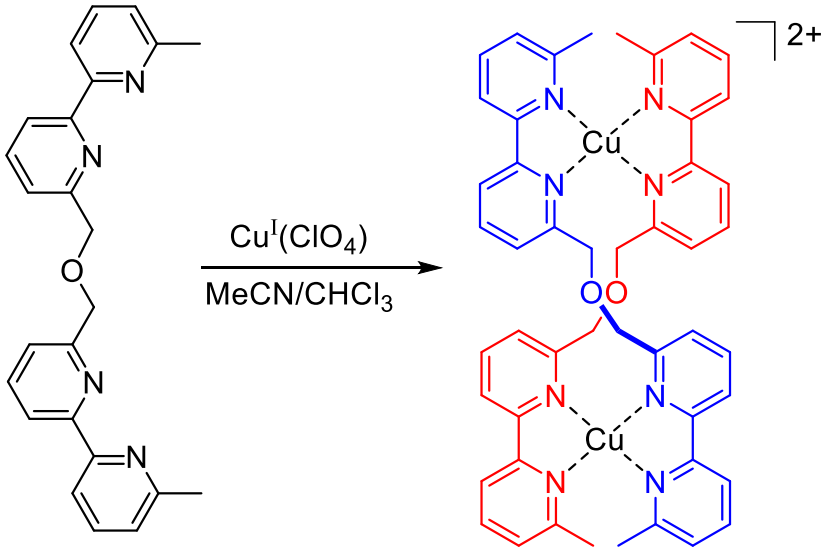


**Figure 1.4.** Lehn's Cu(I) helicate self-assembled from oligobipyridine ligands.[23]

The ligands were designed so that they contained a linker between the bipyridine linkers that was flexible enough to allow for strain free formation of

a helix. The ligands were constrained however so that they were unable to wrap around and coordinate twice to the same copper centre. The -$CH_2OCH_2$- linker proved suitable, and altering this group or changing its position on the pyridyl rings prevented the helicate formation.[23] This highlights the subtle interplay between flexibility and rigidity that is required for a system to self-assemble into a desired product. The length of the helix could be extended by simply appending more bipyridine groups onto the ligand with dinuclear $Cu_2L_2$ up to pentanuclear $Cu_5L_2$ double helicates reported.[24] The system was eventually shown to display analogous behaviour with tetrahedral Ag(I) cations in the place of Cu(I) centres.[25] More recent studies have shown that each sequential addition of a metal ion in the helicate becomes more favourable as the double strands become more preorganised. This effect is so strong that even in system containing a very low metal: ligand ratio only two species are observed, the free ligand and the double helix.[26] The propensity for such systems to form double helices presents potentially exciting biomedical applications, as such systems are likely to interact with DNA, which famously also adopts a double helical structure.[27-29]

Lehn's work highlighted the versatility of metal ions in supramolecular systems. Since then, the labile coordination bond has been utilised to provide access to synthetically challenging and topologically complex species.[30-32] Sauvage has demonstrated this principle by expanding upon Lehn's work by using a linear metal helicate to template the formation of a trefoil knot, the first example of a molecular knot.[33] The helix held the two strands in such a fashion that linking the strands at position a-c and b-d (Figure 1.5), followed by demetallation resulted in the isolation of the trefoil knot in a 3% yield.

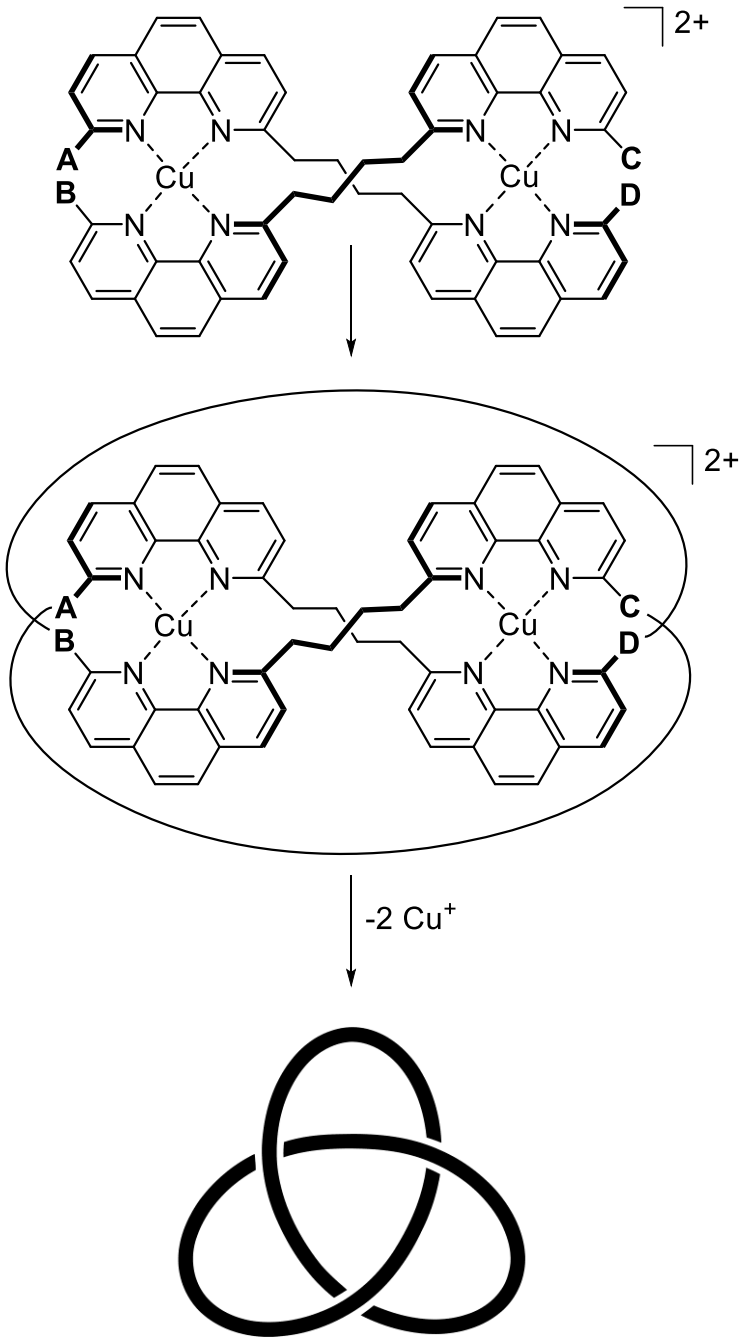


**Figure 1.5.** Schematic representation of Sauvage's synthetic route to form the first example of a molecular trefoil knot.[33]

The science of molecular knots has seen a rapid expansion, thanks in part to the rise of metallo-supramolecular chemistry and self-assembly, making highly challenging syntheses trivial. One of the most topologically complex architectures synthesised to date is the pentafoil knot reported by the Leigh group.[34] Remarkably such an intricate structure was obtained in a single step synthesis. Taking inspiration from the work of Sauvage and Lehn, Leigh reacted oligopyridine ligands with iron(II) chloride (Figure 1.6). Crucially the individual strands were 'tied together' through reversible imine bond formation

ensuring error correction could occur, resulting in a 44% yield of the pentafoil knot, an astonishingly high yield for such a topologically complex architecture. The pentafoil knot proved to be an effective host molecule for chloride anions. The internal cavity at the centre of the assembly was found to selectively bind chloride anions. A combination of C-H---$Cl^-$ hydrogen bonds and an efficient cavity size match held the bound anion strongly in place, requiring a 90 equivalent excess of the halide abstracting reagent $AgPF_6$ in order to completely remove it.[34] Since this initial discovery the pentafoil knot has been prepared in even greater yields by Leigh and co-workers. The ligands were templated around five iron centres as before, yet the joining of the strands was achieved through ring closing metathesis (RCM). The reversibility of the RCM reaction enabled yields of 98% to be achieved using this procedure.[35]

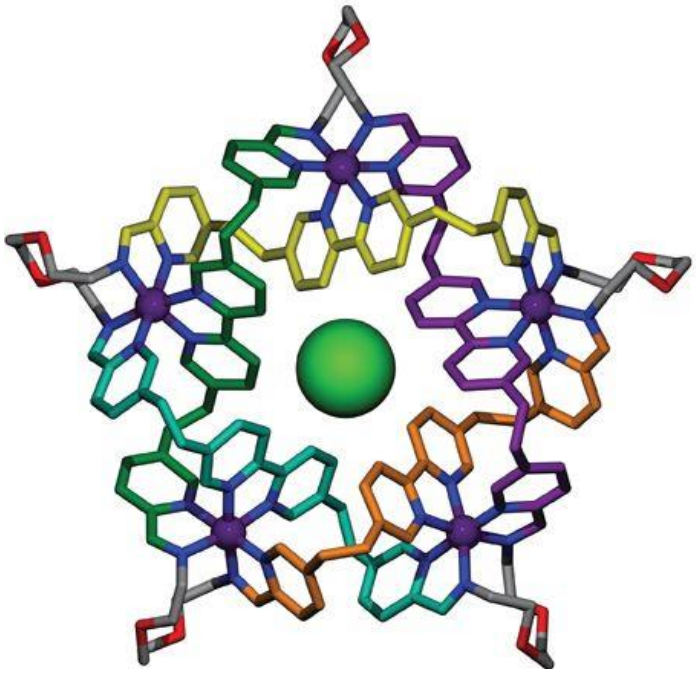

**Figure 1.6.** SCXRD structure of Leigh's pentafoil knot, displaying the bound chloride ion in the centre of the assembly. Each individual strand pre-joining is shown in a different colour.[34] Reproduced with permission from reference 34.

Some of the largest structures assembled to date utilising the coordination bond as a building block has been reported by the Li group.[36-38] In a recent example a total of three different terpyridine ligands were combined in DMSO and heated in the presence of zinc(II) cations.[36] Remarkably, after only 24 hours all of the reactants had completely self-assembled into just one product (Figure 1.7). The product resembled a series of concentric rings linked by reversible Zn-terpyridine bonds forming a wheel like structure. The individual rings are linked to one another through the irreversible condensation of a pyrylium salt and a primary amine, resembling the spokes of a wheel. Where A/B/C are the different ligands used in the reaction, the final product has a

composition of $Zn_{18}A_6B_6C_1$ and a calculated diameter of approximately 8 nm. The supramolecular species was large enough to image under an ultrahigh vacuum, low temperature, scanning tunnelling microscope (UHV-LT-STM) (Figure 1.8). This example shows that irreversible and reversible bond formation can occur orthogonally in certain circumstances and can be used to build large, sophisticated supramolecular structures in a simple one step synthesis.[36]

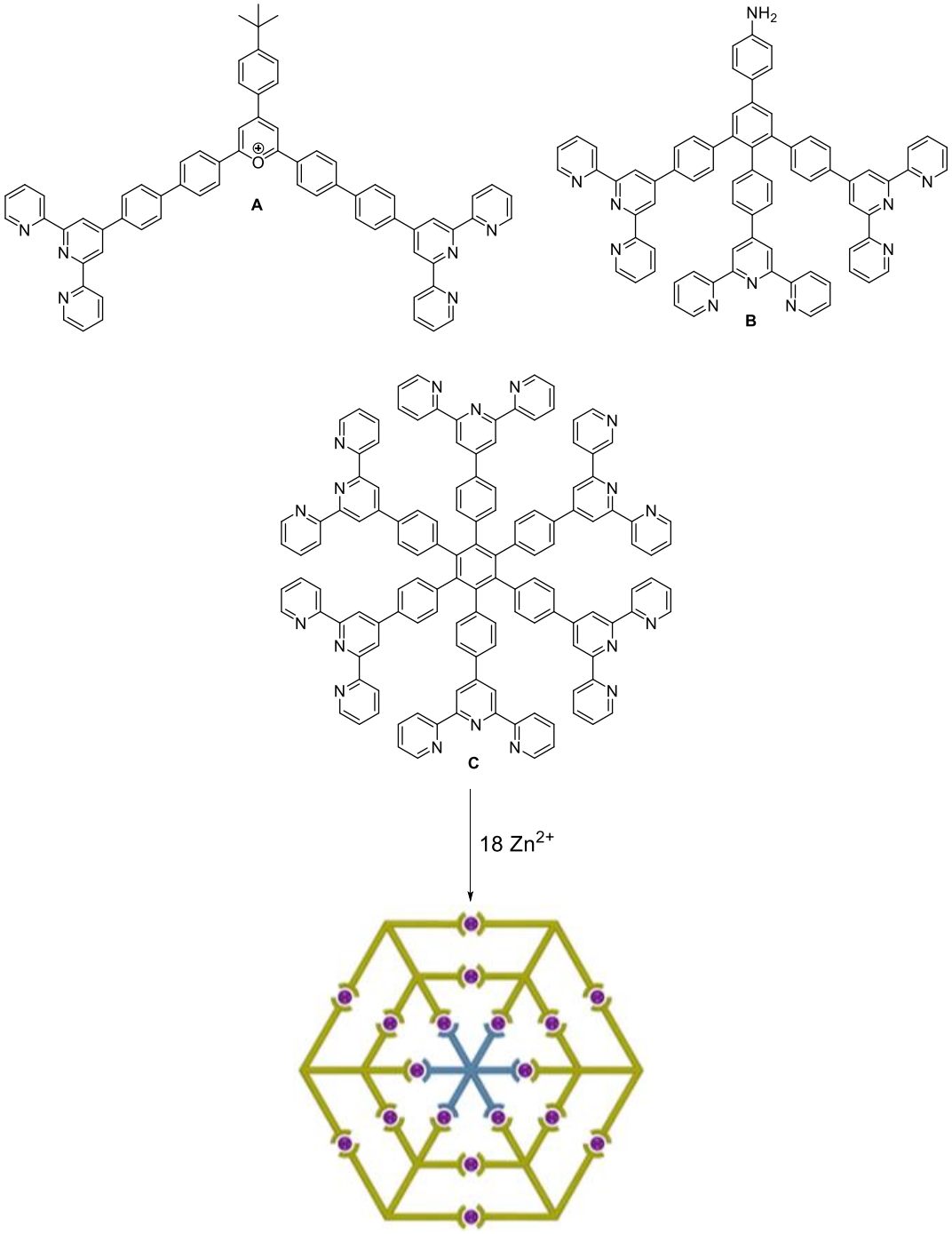


**Figure 1.7.** Li's four component one pot synthesis of a molecular wheel formed in a quantitative yield.[36] Adapted with permission from reference 36.

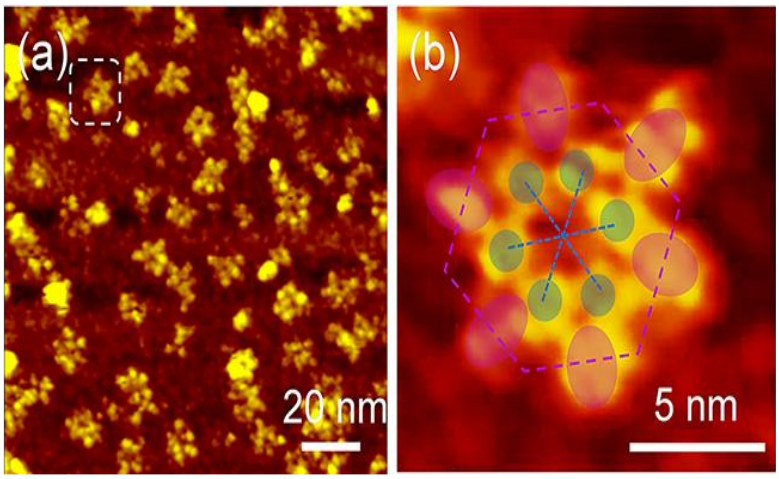


**Figure 1.8.** a) UHV-LT-STM image of Li's supramolecular wheel on an Ag(111) surface, b) zoomed in UHV-LT-STM image of a single molecule of Li's supramolecular wheel on an Ag(111) surface.[36] Adapted with permission from reference 36.

This section has highlighted the potential of using the lability of coordination bonds to synthesise highly intricate structures with relative ease. The next section will continue to examine the use of the coordination bond to synthesise 3D assemblies possessing an internal cavity, a class of compounds known as coordination cages.

### 1.4 Applications of Coordination-Cages

Coordination-cages form a hugely important sub-class of metallo-supramolecular structures. The ease at which complex 3D structures can be formed in high yields from simple starting materials is a major reason why they have been intensely studied. Modification of these systems is often trivial, and can be achieved by simply altering the structure of the initial ligands or metal tectons. The origins of these advantages is due to the labile nature of the coordination bond, allowing error correction and placing the system under thermodynamic control. Conversely, organic cages regularly suffer from complex synthetic procedures and poor yields due to irreversible bond formation resulting in unwanted oligomeric side products, a common problem associated with macrocycle formation. The most important property of coordination cages however is that they contain an internal cavity suitable for binding guests and as such the host-guest chemistry of these systems has been extensively studied. A number of excellent reviews have been written concerning recent advances in the synthesis and applications of metallo-cages.[39-42]

A number of highlights from the chemistry of coordination cages have been reported from the Nitschke group.[43-46] As a general approach, metals which adopt a rigid octahedral geometry such as iron(II), are used to form the corners of a tetrahedron. The metal centres are held in place with bidentate pyridyl-imine bridging ligands aligning along the edges of the tetrahedron to form an $Fe_4L_6$ assembly (Figure 1.9).[47]

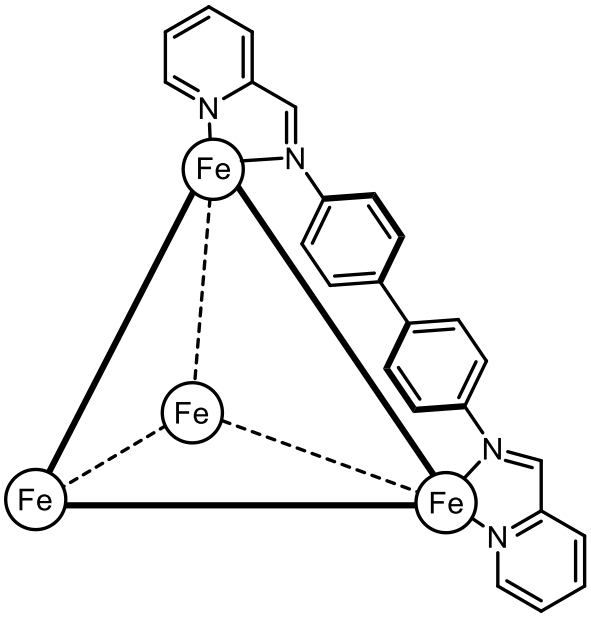


**Figure 1.9.** General structure of Nitschke's tetrahedral $Fe_4L_6$ coordination cages.[47]

It is possible to form an $Fe_4L_6$ cage using an array of different ligands, making the system highly reproducible.[47] Nitschke has shown that functionalisation of such a cage with sulfate groups makes the cage water soluble. Moreover the cage is also capable of uptaking white phosphorus when dissolved in an aqueous environment.[48] $P_4$ is a highly pyrophoric element which reacts spontaneously with oxygen in the atmosphere (Figure 1.10). This property has led to safety concerns associated with the storage and handling of white phosphorus. However, encapsulation of white phosphorus by the coordination cage stabilises $P_4$ against oxidation. No evidence of oxidation of the bound guest was observed even after four months in solution. The phosphorus could be released in a controlled manner by addition of benzene, which acted as a competing guest. This resulted in the complete oxidation of the phosphorus which became too large to re-enter the coordination cage. The phosphorus was stabilised against oxidation due to the constrictive effect of the surrounding cage. Although the cage was large enough to allow dioxygen through the portals, the oxygen could not react with the phosphorus. Any reaction would result in the formation of a P=O bond during the transition state which could not be accommodated by the cage without causing significant

distortion. It is therefore the constriction applied by the cage to the $P_4$ that prevents oxidation and not the exclusion of dioxygen.[48]

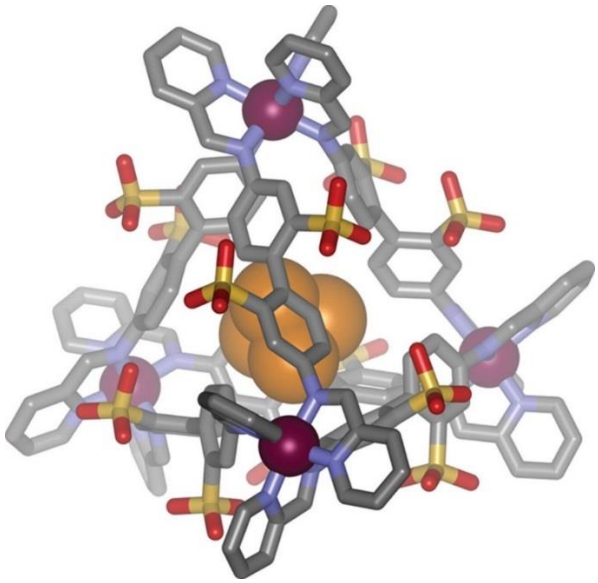

**Figure 1.10.** SCXRD structure of $Fe_4L_6$ coordination cage, containing $P_4$ within the internal cavity.[48] Reproduced with permission from reference 48.

The class of tetrahedral cages bearing the general formula $M_4L_6$ has been extensively studied by the Nitschke and Raymond groups, amongst others. Aside from iron they have been shown to form using Zn(II),[49, 50] Ni(II),[49] Co(II),[50] Ga(III)[51] and Al(III)[51] to name but a few examples, highlighting the general reproducibility of the system.

In addition to stabilising reactive species, coordination cages have the ability to act as catalysts. Whilst the catalytic behaviour of some cages originates from the presence of transition metal cations, their catalytic ability often results from their complex 3D structures. In particular the internal cavities can interact with the substrates in a variety of ways to catalyse the reaction.[52] Coordination cages can confine the substrates, increasing the effective concentration of them, promoting reaction.[53, 54] Additionally the cages can hold the substrates in a preorganised fashion which results in efficient overlap of the reactive orbitals.[55-57] As mentioned earlier they can even stabilise reactive intermediates which would otherwise degrade back into the unreacted starting materials.[58-60] In this way they can be considered to be the synthetic equivalent of naturally occurring enzymes, both behaving in a similar fashion. The list of reactions known to be catalysed by coordination cages is large, and includes but is not limited to Diels-Alder reactions,[55-57] Knoevenagel condensations,[61] Photo-hydrogen evolution[62] and even C-H activation.[51, 63, 64]

Raymond has reported a $Ga_4L_6$ coordination cage that is capable of catalysing the hydrolysis of orthoformate (Figure 1.11).[65] Orthoformate hydrolysis is traditionally performed in an acidic environment. What is remarkable is that in the presence of the cage hydrolysis of orthoformate occurs even in basic solution. Rate accelerations of up to 890 fold are observed under these typically unfavourable conditions. The rate is increased in such a dramatic fashion due to the electrostatic interactions between host and guest. The cage has an overall 12- charge due to the tetra-anionic ligands in combination with the tri-cationic gallium centres. Upon encapsulation, a neutral guest experiences a large increase in its p$K_{a,}$ as evidenced by the guest *N,N,N',N'*-tetramethyl-1,2-diaminoethane which experienced an increase to its p$K_a$ upon encapsulation of 14.3. A substantial increase compared to the p$K_a$ of the free species in solution at 10.8. A protonated guest is favoured in the cavity as favourable electrostatic interactions can occur between the cationic guest and the overall negatively charged host.[65] It is due to this effect that the cage can catalyse the hydrolysis of orthoformate under basic conditions. The host acts as a nanoscale reaction vessel containing a microenvironment which can form protonated intermediates in an otherwise basic media.

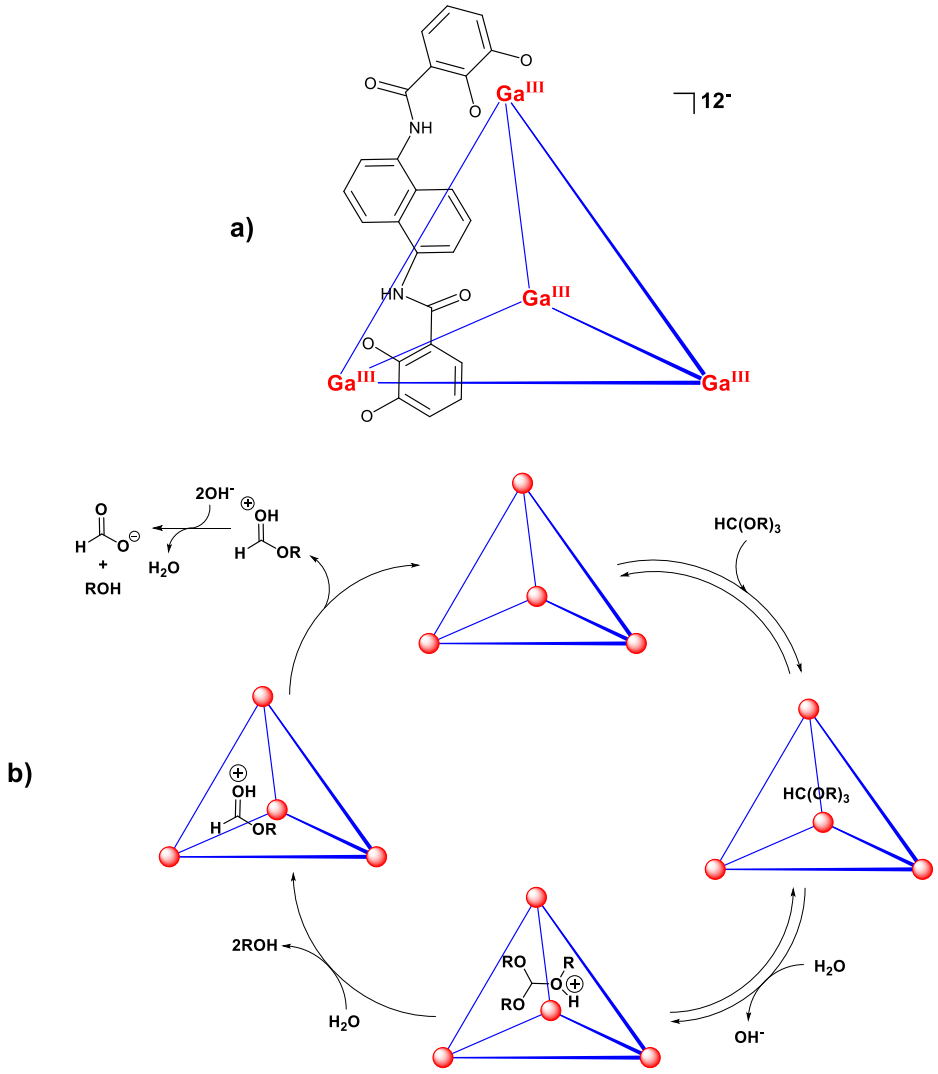


**Figure 1.11.** a) Structure of Raymond's $Ga_4L_6$ cage capable of catalysing the hydrolysis of orthoformate, b) The proposed mechanism of hydrolysis within the cage.[65]

The ability of these cages to catalyse hydrolysis reactions is not limited to orthoformate as a substrate. Raymond has shown that the same cage can catalytically hydrolyse a range of small acetals, even under basic conditions.[66] It was observed that when the acetals went above a certain size no hydrolysis was observed as the large acetals were an unsuitable size to fit within the cavity.[67] This emphasised the importance of the internal cavity and that the substrates were not simply reacting on the exterior of the cage. Nitschke has reported a cationic tetrahedral cage which is capable of catalytically hydrolysing the neurotoxin and insecticide dichlorvos.[43] It achieves this by polarising the P-O bond through interactions with the highly positively charged cage, increasing its susceptibility to nucleophilic attack and subsequent decomposition of the organophosphorus species. Such cages may have potential applications in the safe disposal of chemical weapons, which often contain similar organophosphorus moieties.[43]

In addition to the tetrahedral coordination cages discussed previously there exist a multitude of classes of coordination-cages, limited only by the imagination of the chemists designing them. The Fujita group was one of the first groups to pursue research into coordination cages and have published a plethora of high impact papers.[68-70] A particular research focus has been the predictable construction of large polyhedral molecules. Work began to synthesise a series of roughly spherical polyhedral species with the general formula $M_nL_{2n}$. To do this palladium(II) cations were self-assembled with bent, rigid, *bis*-pyridyl ligands. Using simple geometric constraints it was possible to determine that n is limited to 6, 12, 24, 30 or 60 if the system is to be entropically favourable and a regular polyhedral species is desired (Figure 1.12).[42] The first spherical polyhedral to be discovered was the $Pd_{12}L_{24}$ assembly.[71] The architecture was assembled from palladium(II) cations and 1,3-dipyridylbenzene ligands to form the cuboctahedra. The angle between the two pyridyl groups was very close to the ideal value of 120°. Fujita realised that by modifying the angle between the two pyridyl moieties it should be possible to assemble the remainder of the series. Work began on synthesising ligands that possessed the appropriate bond angles and the remainder of the series excluding n = 60 have been synthesised to date, including an unexpected structure where n = 48.[72-75] This work highlights the subtle steric factors that can dictate what species are obtained from a self-assembly reaction and how, with rational design of the building blocks, specific assemblies may be targeted.

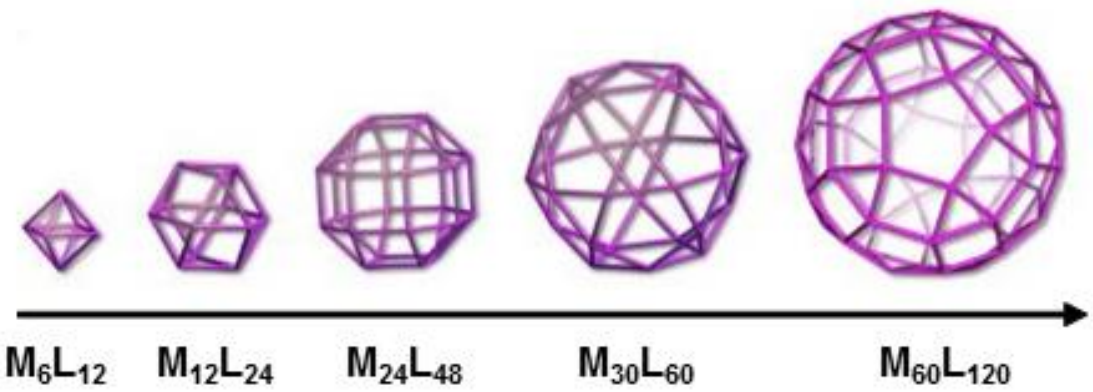


**Figure 1.12.** Fujita's $Pd_nL_{2n}$ polyhedral cages.[42] Adapted with permission from reference 42.

Fujita expanded upon this work even further and developed a functional metallo-cage by stellation of the $Pd_{12}L_{24}$ cuboctahedron to form the $Pd_{18}L_{24}$ stellated cuboctahedron.[76] A stellated cuboctahedron is formed by extending the square faces of a cuboctahedron until they meet at a point. This was achieved by appending pendant metal binding pyridyl groups to the ligands so

that post-assembly they would lie *exo* to the cage framework. Addition of 12 equivalents of palladium to 24 of the ligand formed the cuboctahedron exclusively. However, upon addition of a further 6 equivalents the stellated cuboctahedron was synthesised. It was possible to modulate the stellation by addition of *N,N,N',N'*-tetramethylethylenediamine (TMEDA) which selectively sequestered the palladiums residing on the stellated vertices, yet had no effect on the remaining palladium cations (Figure 1.13). This process was reversible and upon addition of further palladium cations the stellated structure was reformed. This system could potentially lead to selective release and uptake of guests by switching between the stellated and un-stellated forms. Potential applications for such a 'gate opening' process may include targeted drug release or isolation of valuable substances from a complex mixture.[76] Nature uses similar metal mediated gate opening processes, for example viruses use the presence of $Ca^{2+}$ ions to open channels in their protein shell, subsequent escape of viral RNA initiates protein transcription.[77]

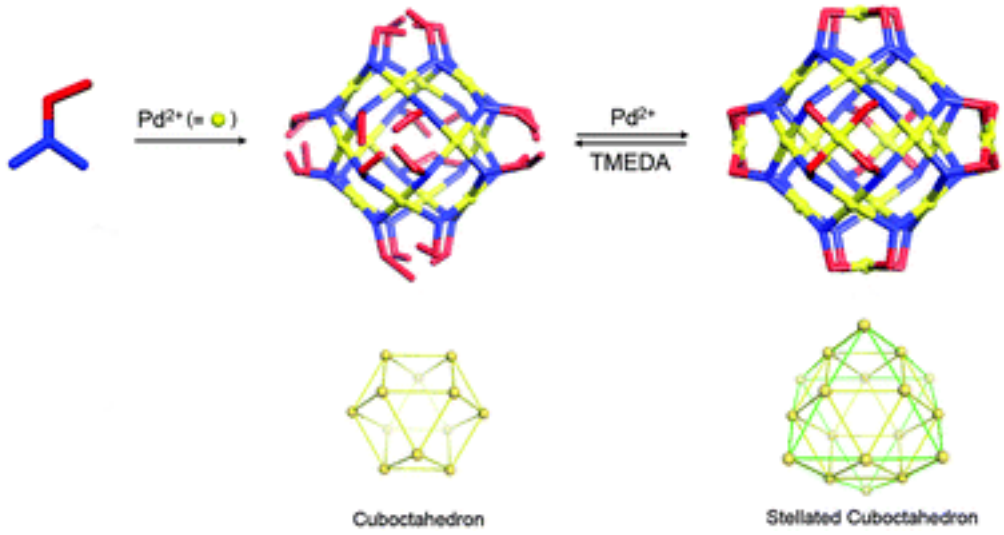


**Figure 1.13.** 'Gate opening' process of the stellated cuboctahedron, modulated by the presence of free TMEDA or $Pd^{2+}$ cations.[76] Adapted with permission from reference 76.

Coordination cages which can undergo structural transformations in response to a stimulus are a growing area of research within the community.[78, 79] The use of such systems in catalytic or host-guest applications may allow the modulation of parameters such as regioselectivity, turnover number and binding affinity over the course of a reaction. Coordination cages are, by their nature, dynamic structures and can therefore be affected by parameters which do not affect covalently bound systems. Concentration is one such example, and there are several reports in the literature of concentration dependant

supramolecular systems.[80, 81] A particularly elegant example was reported by Newkome who described a zinc based metallo-cage which underwent a series of drastic structural changes in response to the concentration.[82] Self-assembly of a tetrakisterpyridine ligand bearing a flexible crown ether core with zinc(II) cations resulted in the formation of a $Zn_{24}L_{12}$ cuboctahedron. Upon dilution of the cage framework however, a spontaneous rearrangement occurred where each cuboctahedron split into two $Zn_{12}L_6$ octahedra. Further dilution resulted in the formation of two $Zn_6L_3$ superposed *bis*triangles (Figure 1.14). The latter transformation could also be induced by exchange of the counterion by $PF_6^-$ or $BPh_4^-$. The process was fully reversible and the cages could be cycled between architectures by simple dilution or concentration. The structural transformations are likely driven by Le Chatelier's principle. Notably, no evidence of any intermediates were detected during cage transformations, showing the process to be both rapid and highly selective for the three variants of coordination cage.

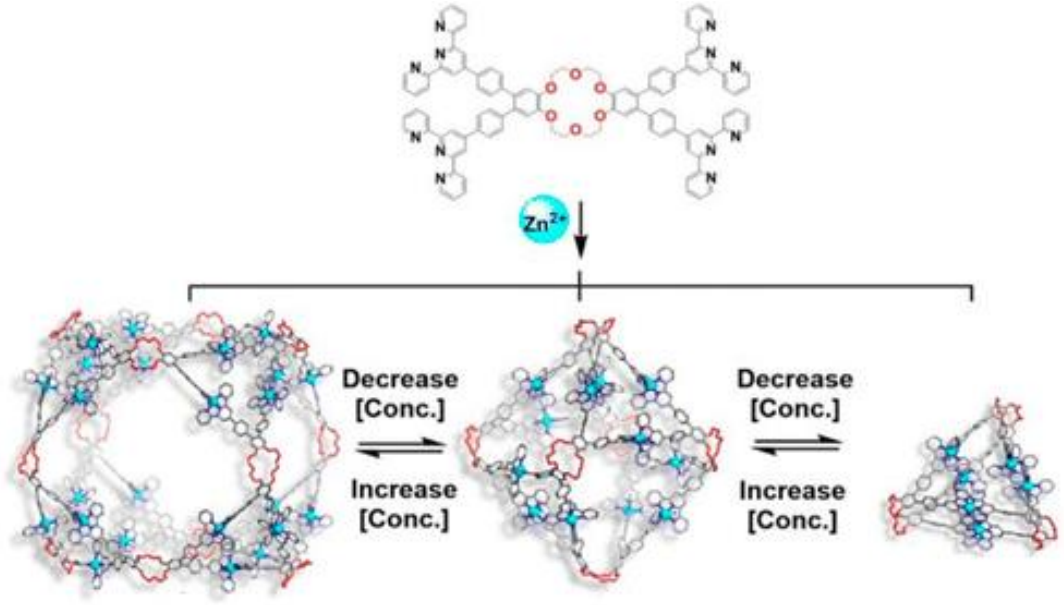


**Figure 1.14.** Structural rearrangement of a cuboctahedron to a pair of octahedra followed by a pair of superposed *bis*triangles following sequential dilution of the sample.[82] Adapted with permission from reference 82.

Functional metallo-supramolecular systems which respond in a controlled and predictable manner to stimuli form an exciting new class of materials, with many potential applications. The next section will focus specifically upon stimuli responsive supramolecular architectures which respond to the most benign of stimuli, light.

### 1.6 Photoswitchable Supramolecular Architectures

Supramolecular systems have been designed that respond to a wide array of stimuli, with concentration,[80-82] temperature,[83, 84] pH[85, 86] and chemical[87, 88] being just a few of the examples. By incorporating photoswitches, molecules which undergo a structural transformation upon irradiation with light, within the supramolecular components it is possible to design a system which changes in response to light. Light as a stimulus has a number of advantages over other stimuli. It is easily applied as an external source and importantly, no side-products or unwanted materials are introduced to the system making it a very clean method of facilitating a response. Irradiation is also tolerated by a wide range of functional groups, decreasing the likelihood of structural degradation occurring. All of these advantages mean that photoresponsive metallo-supramolecular architectures have the potential to be cycled between states multiple times without any loss in efficiency due to side-product accumulation or decomposition.

In light of these advantages a significant amount of effort has been spent on trying to design photoresponsive host-guest systems. An early example was reported by Lees *et al*. who described a heterometallic molecular square containing photoswitchable azobenzene ligands (Figure 1.15).[89] Irradiation of the azobenzene groups with light of 366 or 313 nm causes a structural isomerisation to occur, whereby the C-N=N-C bond switches from a *trans* to *cis* arrangement. In this example this rearrangement triggered a total structural rearrangement of the molecular square, which disassembled into two smaller heterometallic subunits. The system could be cycled between states by heating the *cis* isomer which reverted it back to the resting *trans* state, reforming the larger square.

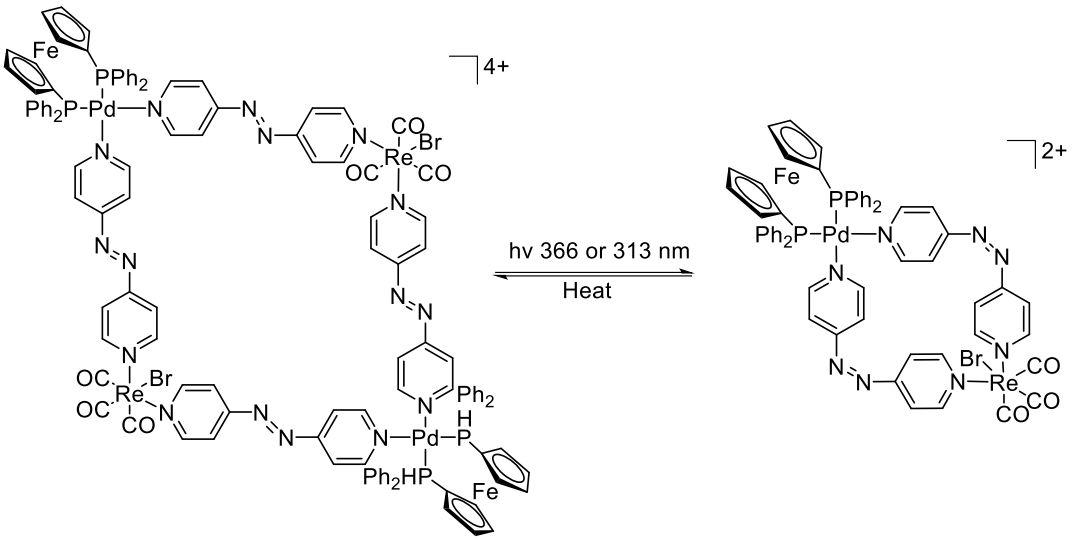


**Figure 1.15.** Lee's heterometallic photoresponsive macrocycle undergoing reversible light promoted splitting into two smaller subunits.[89]

Yang and Zhu have also reported a photoresponsive macrocycle constructed with a different photoswitch, dithienylethenes (DTEs).[90] Pyridyl appended DTEs self-assembled with linear or bent di-platinum species to produce relatively flexible flat macrocycles (Figure 1.16). Irradiation of the sample with UV light causes the DTEs to undergo a ring closing reaction, inhibiting rotation and increasing the rigidity of the macrocycle. The back reaction could be promoted by irradiation with light at a visible wavelength.

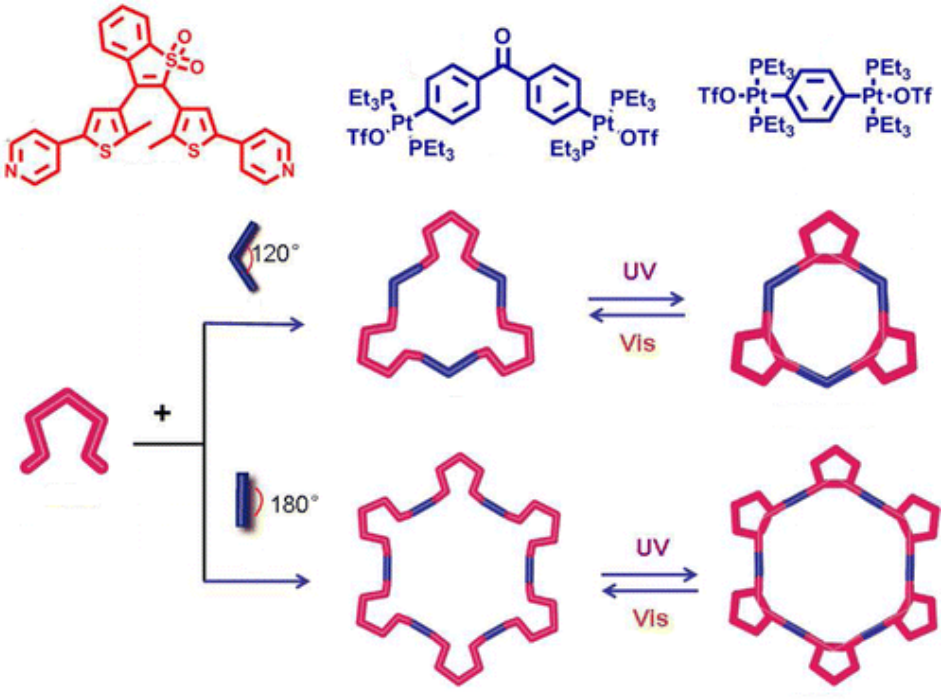


**Figure 1.16.** Yang and Zhu's photoswitchable macrocycle ring containing DTE subunits.[90] Adapted with permission from reference 90.

More recently Yang has reported another photoswitchable heterometallic macrocycle which exhibits switch on or off luminescence controlled by the open or closed form of a DTE group.[91] The architecture was synthesised through coordination bond mediated self-assembly at the platinum centres. The iridium groups were incorporated to act as chromophores. The iridium chromophores emits light due to phosphorescence from the $T_1$ state which has an energy of 2.06 eV. The luminescence can be switched off by Förster resonance energy transfer (FRET) from the triplet excited state of the iridium centre to the lowest singlet state of the DTE group. In the open form of the DTE the $S_1$ has an energy of 2.77 eV, higher than that of the $T_1$ state so FRET cannot occur and luminescence is switched on in the open state. Whereas in the closed state the energy of the $S_1$ state is reduced to 2.00 eV, lower than the $T_1$ state. FRET can now occur and luminescence is switched off in the closed state as energy is rapidly removed from the excited triplet state responsible for emission.[91]

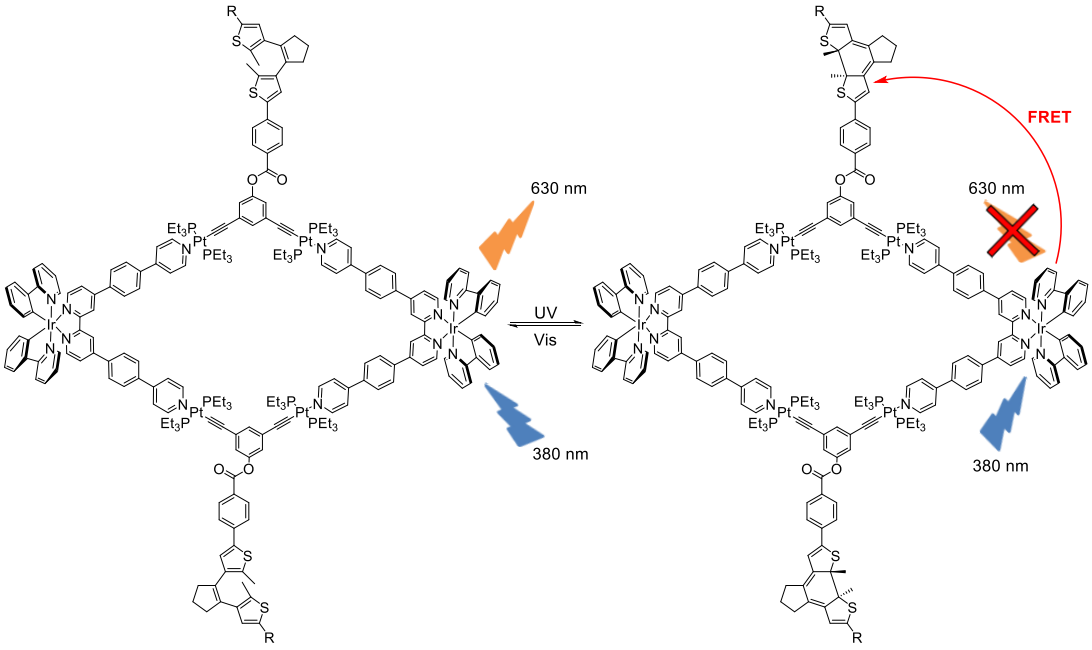


**Figure 1.17.** Yang's photoswitchable Pt(II)/ Ir(III) metallo-cycle showing switchable on/off phosphorescence due to FRET.[91]

The preceding example describes a system which exhibits turn off luminescence when exposed to UV light. It is possible, although rarer, to design a system which responds to UV light by switching on the luminescence. A recent example by Xu describes a DTE containing platinum metallocycle existing in a hexagonal arrangement.[92] The metallocycle in the resting open state showed no luminescent behaviour. However, upon transformation by light from the open to the closed form the species became fluorescent, with maximal emittance at 536 nm. DFT calculations for the closed and open form

of the metallo-cycle show that the closed form is more stable as the angle between the pyridyls on the DTE groups are closer to 120°. This is the ideal angle to form a molecular hexagon as no strain will be imparted to the system through non-ideal bond angles. Switch on fluorescent metallocycles may find applications in super-resolution fluorescence imaging, a bio-imaging technique requiring switch on fluorescent species.[92]

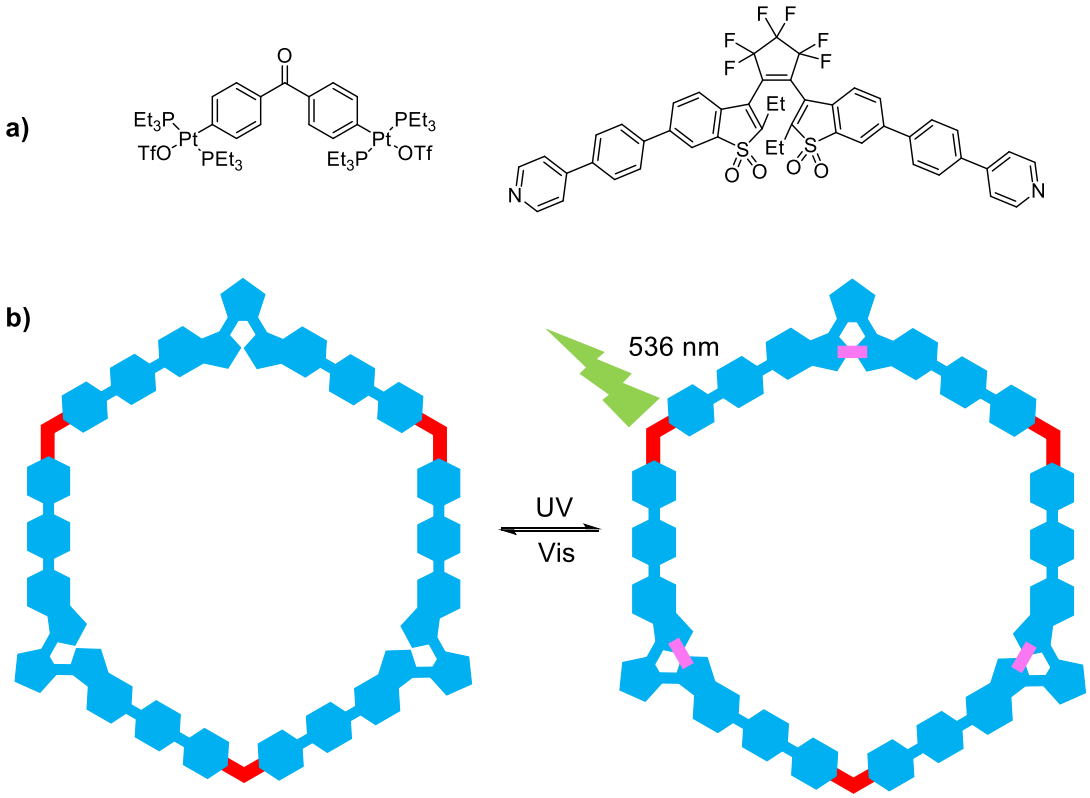


**Figure 1.18.** a) Individual subunits that comprise Xu's hexagonal metallo-cycle, b) Schematic representation of the metallo-cycle displaying rare switch-on luminescence following photoswitching of the DTE subunits into the closed state.[92]

The previous examples describe photoswitches which exist in a relatively planar arrangement. However, photoswitchable coordination cages and other 3D architectures have also been reported. A Cu(I) helicate complex was reported by the Nishihara group which consisted of two 2,2'-bipyridine ligands functionalised to contain azobenzene groups at the 6,6' positions (Figure 1.19).[93] In the all *trans* resting state the azobenzene groups were stabilised by π-π stacking interactions between the individual ligand strands. When two equivalents of the *trans* azobenzene ligand were added to a solution of $[Cu(bpy)_2]^+$ the azobenzene ligand was capable of replacing 32% of the bpy ligand to form $[Cu(\textit{trans}\text{-azo})_2]^+$. Following photoswitching to the *cis* isomer the π-π stacking interactions were lost and as such formation of the helicate became less favourable, with the *cis* isomer completely unable to substitute

the bpy ligands in the same experiment. The two copper complexes had different redox potentials due to the different ligand environments surrounding them. It was therefore possible to modulate the redox potentials of the copper by controlling ligand exchange with the appropriate wavelengths of light.[93]

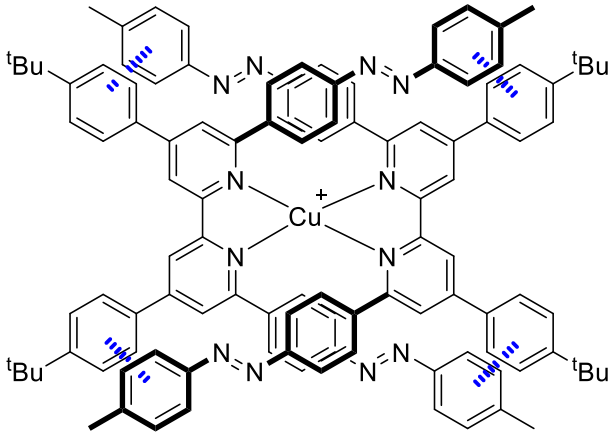


**Figure 1.19.** Nishihara's Cu(I) helicate, stabilising π-π interactions (blue) are disrupted by photoswitching and enable ligand substitution by 2,2'-bipy.[93]

The isomerisation of photoswitches can induce desirable changes even when the photoswitches are not directly embedded within the framework of a cage. Zhou *et al*. have reported a $Cu_{24}L_{24}$ paddlewheel like metal-organic polyhedra where L is an azobenzene functionalised isophthalate (Figure 1.20).[94] When assembled the azobenzene groups reside on the outside of the cage. UV/vis spectroscopy was used to determine that methylene blue was taken up from solution by crystals of the *trans* cage acting as a molecular sponge. The methylene blue resided within the interstitial sites between the cages, no evidence was obtained for direct encapsulation of the guest by the cage. Residing in the interstitial sites made the methylene blue susceptible to ejection from the crystal by photoswitching of the exohedral azobenzene groups as they resided in direct contact. Photoswitching of the azobenzenes to the *cis* isomer resulted in ejection of the methylene blue guest back into solution. Zhou suggested that the *cis* isomer of the cages cannot form intermolecular interactions of sufficient strength to form persistent interstitial pockets large enough to bind the guest, resulting in release of the guest.[94]

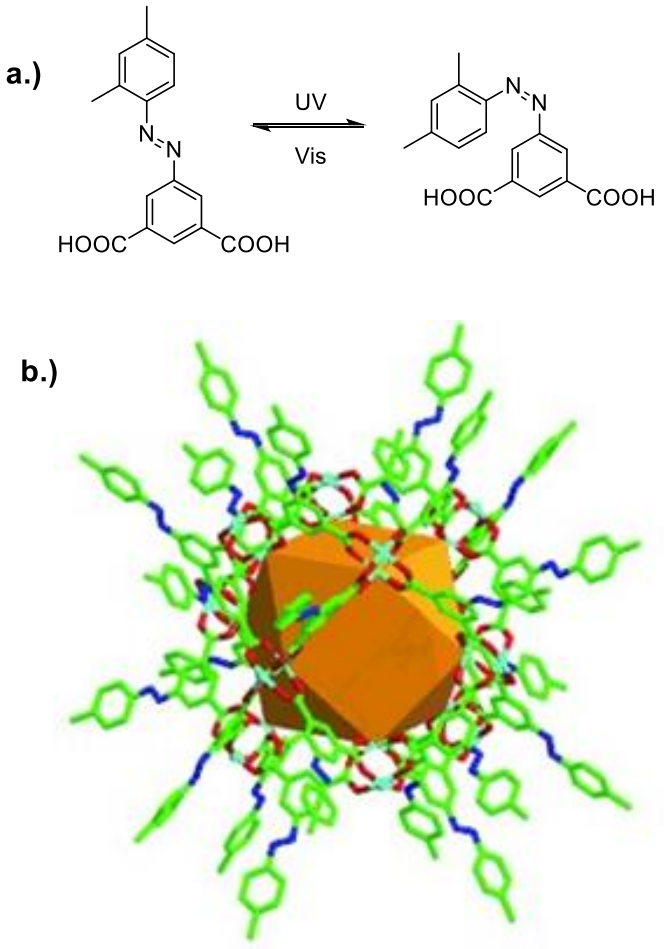


**Figure 1.20.** a) Azobenzene functionalised isophthalate ligand displaying photoswitching behaviour, b) $Cu_{24}L_{24}$ metal-organic polyhedral bearing exohedral azobenzene groups. Guest uptake and release of methylene blue could be modulated in the solid state by photoswitching of the azobenzene groups.[94] Reproduced with permission from reference 94.

Fujita has demonstrated variations of the previous example could also modulate guest uptake and release. This was achieved by designing a $Pd_{12}L_{24}$ spherical complex bearing endohedral azobenzene moieties residing within the cavity of the cage (Figure 1.21).[42, 95] The terminal phenyl rings of the azobenzene groups were pointed directly towards the centre of the cage in the *trans* state making the cavity highly hydrophobic. Switching on the azobenzenes to the *cis* isomer moves the phenyl groups away from the centre and exposes more of the polar N=N group, decreasing the hydrophobicity. To probe whether this change in hydrophobicity could be utilised to control guest binding a hydrophobic guest 1-pyrenecarboxaldehyde was used as a probe. It was found that the when the guest was bound within the *trans* cage the $^1$H-NMR signal for the guest protons shifted upfield due to the shielding provided by the cage. Switching of the cage to the *cis* isomer resulted in the signal for the protons on the guest moving back downfield, a clear indication of weaker shielding by the cage because of a smaller binding affinity. The azobenzenes

could be switched between *cis* and *trans* multiple times meaning the guest could be taken-up and ejected from the cage using light as the trigger.[95]

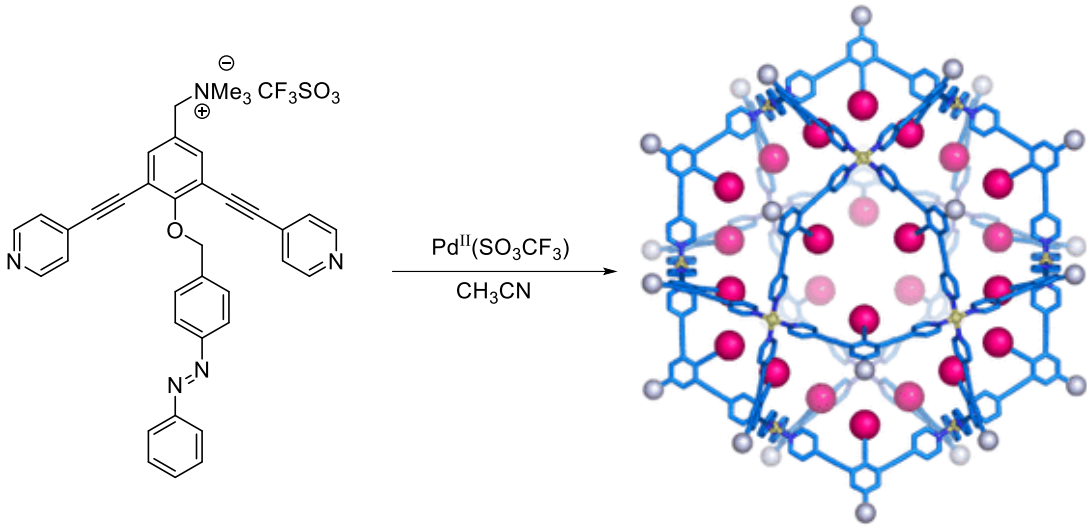


**Figure 1.21.** $Pd_{12}L_{24}$ bearing endohedral azobenzene groups capable of photoswitching and modulating binding affinity of a 1-pyrenecarboxaldehyde guest.[95] Adapted with permission from reference 95.

Despite the numerous examples of photoswitchable coordination cages reported in the literature there remain a surprising lack of examples where the photoswitchable group is embedded directly into the structural framework of the cage. The reasons for this are discussed further in Chapter 4, but one of the key reasons is that photoswitching of a cage is often followed by a structural rearrangement to a species of a different composition compared to the original.[96] There do exist however a small number of examples where such a system has been successfully designed and shown to retain its photoswitching properties without resulting in cage decomposition.[96, 97] The benefits of designing a system containing the photoswitchable groups embedded in the structure is that any isomerisation should result in a large structural change of the cage, desirable if modulation of the guest binding potential is being targeted.

The Clever group have reported possibly the most advanced photoactive cage described in the literature.[97] A ligand was designed containing two pyridyl groups connected *via* a dithienylethene group. When in the presence of palladium(II) cations spontaneous self-assembly occurred to yield a $Pd_2L_4$ cage (Figure 1.22). Remarkably the coordination cage retained its ability to photoswitch. Presumably the small structural change associated with photo-isomerisation with the DTE groups helps to facilitate this. Clever *et al.* successfully demonstrated that the binding affinity of a $B_{12}F_{12}^{2-}$ could be changed by photoswitching between the open form and the closed form of the

DTEs.[97] This remains the most sophisticated example of guest uptake and release by a coordination cage bearing structurally integral photoswitches in the literature.

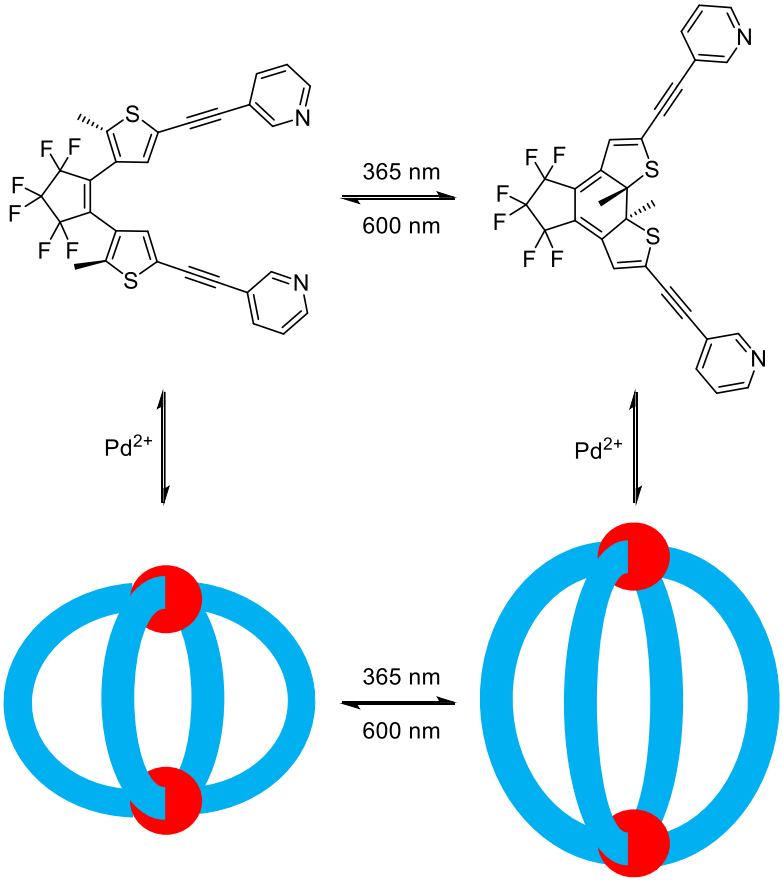


**Figure 1.22.** $Pd_2L_4$ photoswitchable cage containing DTE groups described by Clever *et al*. Modulation of guest binding affinities was achieved by photoswitching of the DTEs.[97]

## 1.7 Cyclotriveratrylene in Supramolecular Systems

There exist many classes of molecular host available to a supramolecular chemist. The body of work presented within this thesis is primarily concerned with the use of cyclotriveratrylene (CTV) analogues as host molecules. Related to the calixarene class of molecular hosts, CTV is a rigid, bowl shaped molecule which possesses a shallow hydrophobic cavity (Figure 1.23). The non-polar nature of the cavity makes CTV and its derivatives excellent candidates for the encapsulation of large, spherical hydrophobic guests such as fullerenes or carboranes.[98, 99]

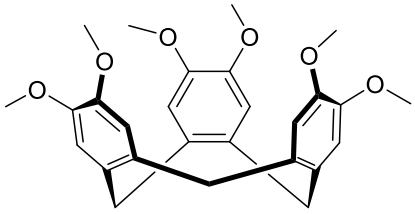

**Figure 1.23.** Structure of CTV adopting the crown conformation.

In order to expand the scope of systems containing CTV the ether groups on the upper rim can be substituted for hydroxyl groups. These act as synthetic handles, allowing the upper rim of the bowl to be easily functionalised with electrophilic substrates. Depending upon the number of hydroxyl groups on the upper rim of the bowl two distinct species can be generated. Complete demethylation and removal of all six methoxy groups results in the formation of cyclotricatechylene (CTC). Whereas the presence of three methoxy groups and three hydroxyl groups yields the *C*$_3$ symmetric, cyclotriguaiacylene (CTG) (Figure 1.24). CTG is the main scaffold used to create ligands in the Hardie group, however other CTV variants containing amino[100] and thiol groups[101] have previously been reported in the literature.

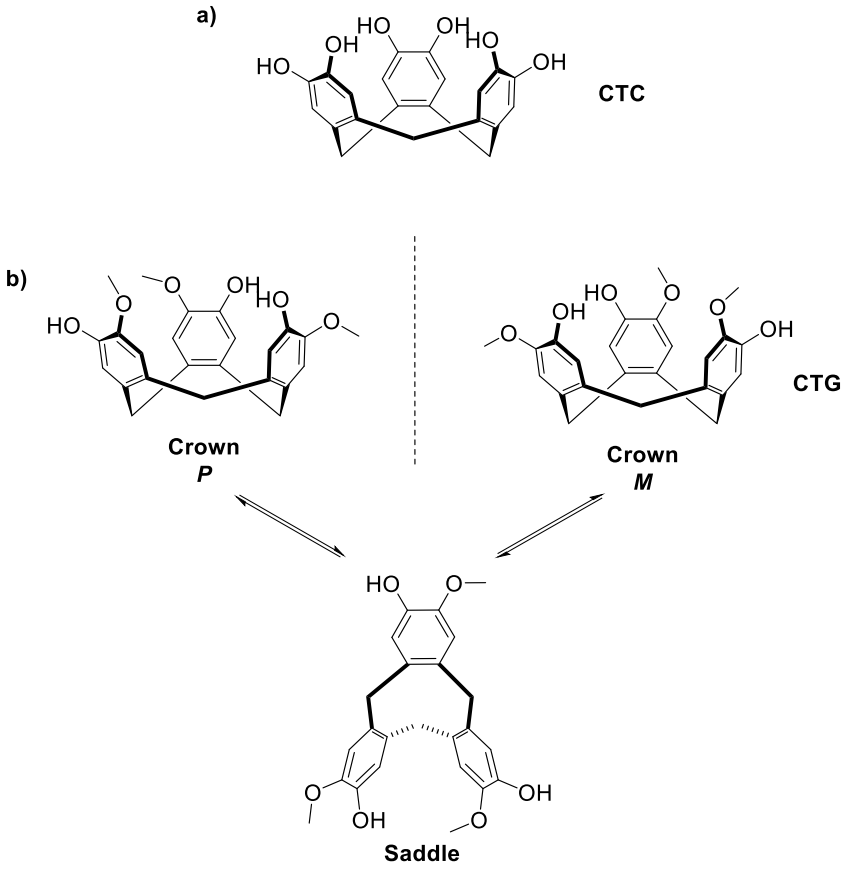


**Figure 1.24.** a) Structure of CTV derivative CTC, b) Structure of CTV derivative CTG and mechanism of chiral inversion proceeding through the saddle conformer.

CTG exhibits helical chirality and can exist in an *M* or *P* type conformation. This property enables CTG based molecular hosts to distinguish between different enantiomeric forms of guest molecules. CTG is able to interchange between the two thermodynamically stable enantiomeric 'crown' conformers by passing through an unstable conformation known as a 'saddle' intermediate. CTV derivatives often self-associate in the solid state through hydrophobic bowl in bowl stacking interactions to form columnar arrangements. Alternatively a dimeric handshake motif may form where each bowl simultaneously acts as both a host and as a guest for each neighbouring CTV unit (Figure 1.25).[102]

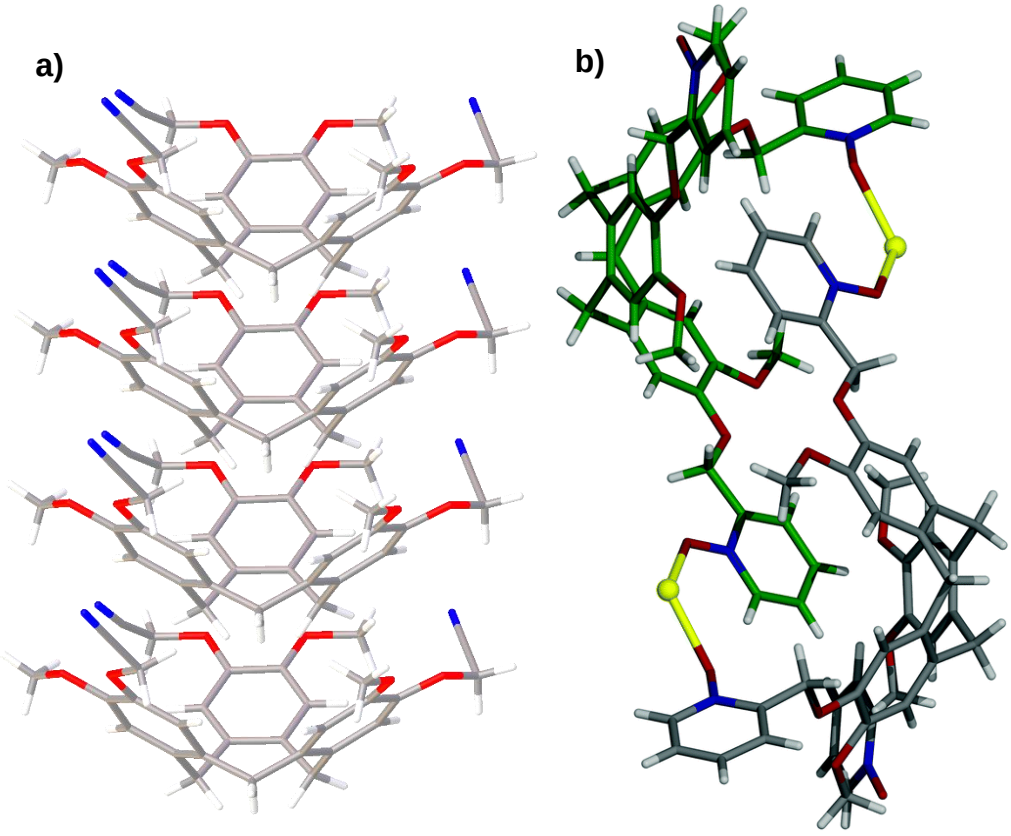


**Figure 1.25.** Nature of common CTV intramolecular interactions a) Bowl in bowl columnar stacking b) Dimeric handshake motif, each CTV unit is simultaneously acting as both a host and guest between neighbouring molecules.[102] Reproduced with permission from reference 102.

The host-guest chemistry of CTV derivatives can be enriched by joining two CTV units together in a head to head fashion to form a molecular capsule known as a cryptophane. A cryptophane possesses a well-defined internal cavity as a result of efficient shielding from the bulk environment by the surrounding cage. The presence of the two CTV bowls situated within the cavity further enhances the host potential of a cryptophane which can therefore partake in extremely rich host-guest chemistry. Cryptophanes have been shown to bind neutral, cationic and even anionic guests within the

internal cavity.[103-105] As a result of their intriguing host properties, cryptophanes have been studied for many potential uses including molecular recognition, sensing and biomedical applications.[105-107]

A popular method of synthesising cryptophanes is to link two CTV motifs with organic linkers.[108, 109] However, such an approach invariably results in the poor yields often associated with macrocycle formation. Despite this, there are numerous examples in the literature of organic cryptophanes synthesised in this way. The groups of Collett,[110] Dutasta[109] and Brotin[109] have been leading proponents of the field, having written any detailed reviews on the subject. Brotin[103, 106, 111] and Dutasta have both reported organic cryptophanes which are capable of encapsulating xenon has in solution (Figure 1.26.a).[103] This is significant as $^{129}Xe$ is used in hyperpolarised magnetic resonance imaging (MRI) to improve the signal to noise ratio of the technique. Further studies have revealed that the strength of the binding of xenon gas can be improved by functionalisation of the cryptophane host which also further enhances the water solubility of the complex.[106, 112] Work within the Hardie group has revealed that a cryptophane derived from thiol substituted CTG derivatives linked through disulphide bridges is even capable of binding methane gas (Figure 1.26.b).[113] This has been conjectured to occur due to favourable size matching of the methane guest and the cryptophane cavity.

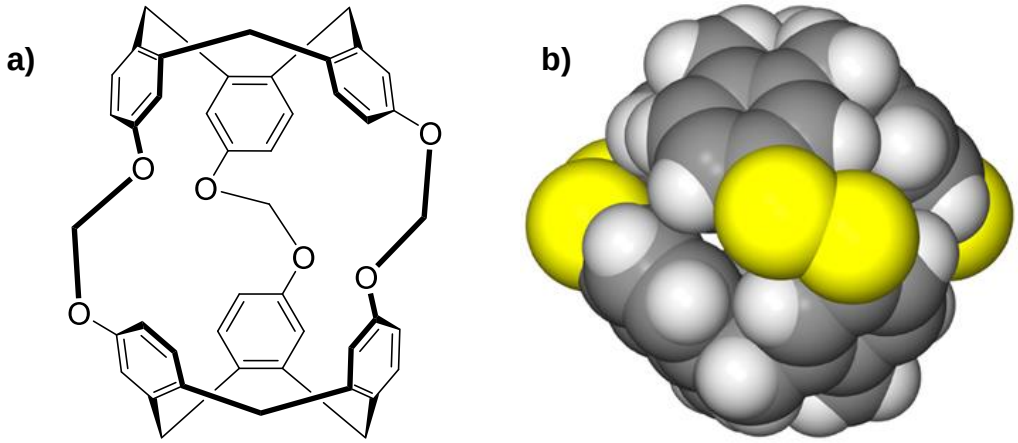


**Figure 1.26.** a) Structure of Brotin's cryptophane capable of binding xenon gas,[103] b) SCXRD structure of Hardie's disulphide linked cryptophane capable of binding methane gas.[113] Reproduced with permission from reference 113.

CTV can also be capped by units other than another CTV unit. This class of molecular hosts are known as hemicryptophanes and share many of the same properties of the structurally related cryptophanes.[114] Jarosz and co-workers have reported a sucrose capped CTG capsule (Figure 1.27).[115] The hemicryptophane displayed excellent solubility in aqueous media which is rare for a molecule containing the non-polar CTG core.

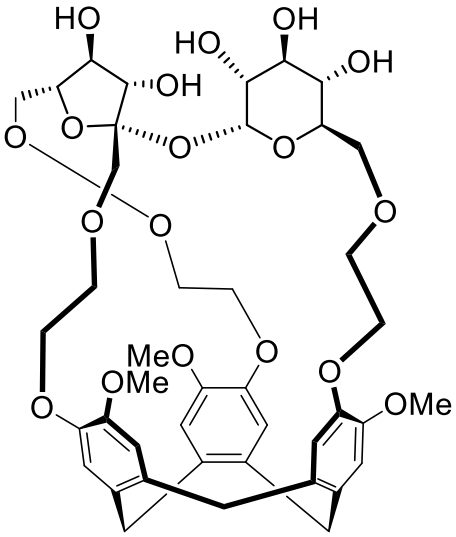


**Figure 1.27.** Structure of Jarosz's sucrose based hemicryptophane, displaying excellent water solubility.[115]

An approach to synthesise cryptophanes favoured by the Hardie group takes inspiration from the metallo-supramolecular systems described in the previous sections and utilises the labile coordination bond to form metallo-cryptophanes. In order to achieve this the CTG core is first functionalised with a metal binding group which have included carboxylate,[116] pyridyl,[117-122] bipyridine,[123, 124] N-oxide,[125] thiazole[126] and benzimidazole,[127] amongst others.[128, 129] Self-assembly of these ligands with metal cations can result in the formation of an $M_3L_2$ metallo-cryptophane. Using this method a huge array of different architectures can be targeted, the smallest being the $M_3L_2$ metallo-cryptophanes,[118, 121] increasing in size to the larger $M_6L_8$ stella octangula[117] and once again up to an infinite coordination polymer.[119, 120, 125, 128] Often small changes in the conditions or the metal used can result in the formation of a wholly different architecture. This has not been better illustrated than with one of the most simple ligands used in the Hardie group, a 4-pyridyl appended CTG ligand. Self-assembly with a rationally designed metal complex known as a metal tecton, in this case, an iridium(III)phenylpyridine tecton results in the isolation of a $M_3L_2$ metallo-cryptophane (Figure 1.28.a).[118] Taking this same ligand and reacting it with palladium(II) nitrate results in the formation of an $M_6L_8$ stella-octangula structure (Figure 1.28.b),[117] whereas reaction with copper(II) bromide leads to the formation of an 'infinite chainmail' array of topologically complex $M_6L_6$ Borromean rings (Figure 1.28.c).[119] Remarkably, this wide array of supramolecular architectures were all obtained using the same simple ligand, highlighting the richness of CTV based supramolecular chemistry. Other examples of topologically complex architectures have been

reported using different ligands, including an $[Ag_3L_2]_2$ [2]catenane[122] and a $Pd_4L_4$ Solomon cube.[130]

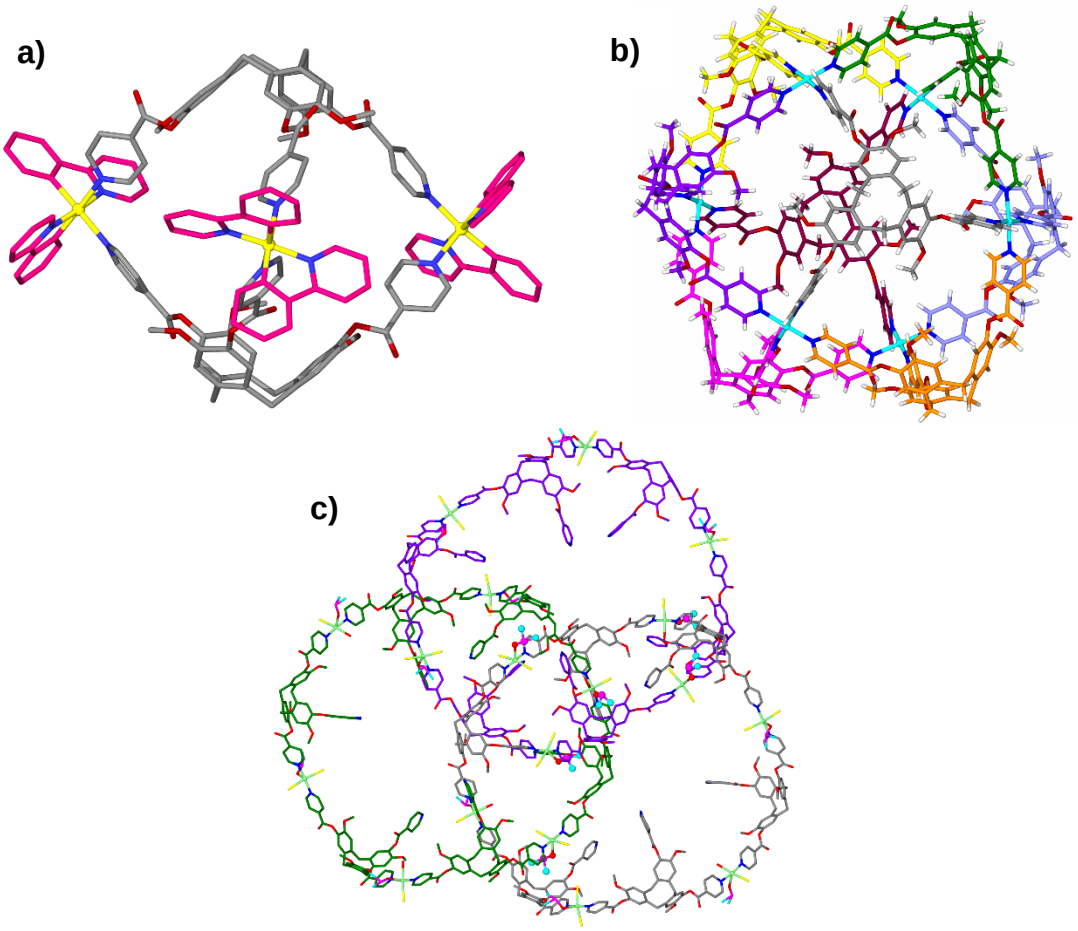


**Figure 1.28.** a) SCXRD of $Ir_3L_2$ metallo-cryptophane,[118] b) SCXRD of $Pd_6L_8$ stella octangula cage,[117] c) SCXRD of infinite chainmail array of $Cu_6L_6$ Borromean Rings.[119] Importantly all of the above structures were obtained using the same 4-pyridyl ligand. Reproduced with permission from references [117, 118] and [119] respectively.

As with organic cryptophanes, one of the benefits of creating extended arrays of CTV based ligands is that the host potential of such systems is vastly increased by the presence of well-defined internal cavities. CTV containing supramolecular architectures have been shown to bind a range of substrates in both solution and the solid phase. These have included sodium alkyl sulphates,[107] iodine[121] and carboranes.[131] Solvent molecules are frequently observed crystallographically to interact with the CTV bowls through intramolecular forces such as hydrophobic and CH-π interactions.[132]

Despite the wealth of examples where CTV derivatives form complex supramolecular architectures, there is only a small subset of examples where CTV based systems respond in a controlled and predictable manner to a stimulus. One such example was reported by the Hardie group and describes the controlled disassembly and reassembly of a $Pd_6L_8$ cage.[133] Addition of 24

equivalents of *N,N*-dimethylaminopyridine (DMAP) to a solution of the $Pd_6L_8$ resulted in the complete disassembly of the cage as the palladium cations were sequestered by the DMAP. Addition of 24 equivalents of tosyl alcohol (TsOH) protonates the DMAP making it non-coordinating, releasing the palladium cations and allowing the cage to reform in a quantitative yield.[133]

A more recent example, also reported from the Hardie group, describes the photoswitching behaviour of an azobenzene appended CTG based iridium metallo-cryptophane (Figure 1.29).[96] Irradiation of the cage with 355 nm light resulted in switching of the azobenzene groups from a *trans* to a *cis* conformation. The cage remained intact throughout the process. Molecular modelling suggests that this change is also associated with a change in the size of the internal cavity, making modulation of the host-guest properties of the cage an exciting possibility.[96] This remains the most sophisticated example of a dynamic metallo-cryptophane system that can undergo structural transformations in a controlled manner.

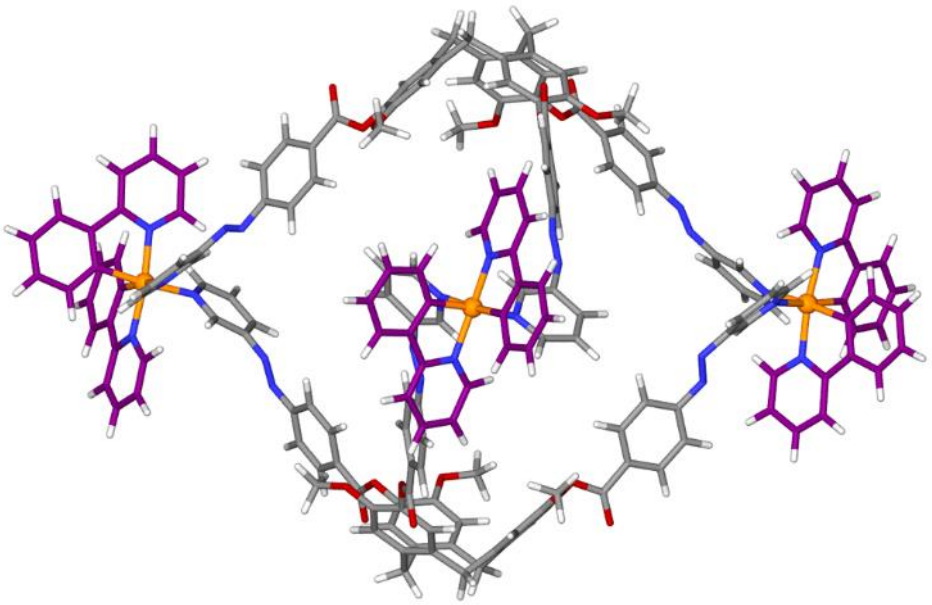

**Figure 1.29.** Molecular model of $Ir_3L_2$ metallo-cryptophane bearing azobenzene groups. Photoswitching occurred upon irradiation at 355 nm.[96] Reproduced with permission from reference 96.

## 1.8 Project Aims

The aim of this project is synthesise and characterise a range of photoresponsive metallo-supramolecular architectures. The ligands will based upon the CTV motif but will be functionalised with photoswitchable groups such as azobenzenes. It is hoped that the use of a cavitand containing ligand will encourage binding of guests; in particular fullerenes and carboranes. In

order to create a more distinct internal environment to encourage guest binding the ligands will be assembled with *cis* protected metallo-tectons to target $M_3L_2$ metallo-cryptophanes. A range of metals will be targeted for this role including palladium, platinum, rhodium and iridium to determine whether the choice of metal can promote or inhibit efficient photoswitching. Upon photoswitching it is envisioned that the cages will undergo a structural change. The properties of the internal cavity should vary between the switched and unswitched form. As a result it may be possible to modulate guest uptake and release from the cages using only light as an external stimulus. Such a system would have numerous advantages over other systems utilising methods such as temperature, pH or competing guests to eject guests from the internal cavity as they are fundamentally less benign than light, and could lead to cage degradation. The ultimate aim of this project therefore is to develop a novel photoswitchable host molecule and demonstrate its ability to take up and release guests using only light as the stimulus.

## References


1. J. W. Steed and J. L. Atwood, *Supramolecular Chemistry*, John Wiley & Sons, Ltd, 2000.
2. M. F. Perutz, M. G. Rossmann, A. F. Cullis, H. Muirhead, G. Will and A. C. T. North, *Nature*, 1960, **185**, 416-422.
3. M. Bringas, A. A. Petruk, D. A. Estrin, L. Capece and M. A. Martí, *Sci. Rep.*, 2017, **7**, 10926.
4. J. R. Tame and B. Vallone, *Acta Cryst. D.*, 2000, **56**, 805-811.
5. C. J. Pedersen, *J. Am. Chem. Soc.*, 1967, **89**, 2495-2496.
6. H. K. Frensdorff, *J. Am. Chem. Soc.*, 1971, **93**, 600-606.
7. C. J. Pedersen and H. K. Frensdorff, *Angew. Chem. Int. Ed.*, 1972, **11**, 16-25.
8. C. J. Pedersen, *J. Am. Chem. Soc.*, 1967, **89**, 7017-7036.
9. J.-M. Lehn, *Science*, 2002, **295**, 2400-2403.
10. D. J. Cram, *Nature*, 1992, **356**, 29-36.
11. J. M. Lehn, *Acc. Chem. Res.*, 1978, **11**, 49-57.
12. B. Dietrich, J. M. Lehn and J. P. Sauvage, *J. Chem. Soc., Chem. Commun.*, 1970, 1055-1056.
13. J.-M. Lehn and F. Montavon, *Helv. Chim. Acta.*, 1976, **59**, 1566-1583.
14. D. J. Cram, *Angew. Chem. Int. Ed.*, 1988, **27**, 1009-1020.
15. D. J. Cram, T. Kaneda, R. C. Helgeson and G. M. Lein, *J. Am. Chem. Soc.*, 1979, **101**, 6752-6754.
16. D. J. Cram, *Science*, 1983, **219**, 1177-1183.
17. B. J. Holliday and C. A. Mirkin, *Angew. Chem. Int. Ed.*, 2001, **40**, 2022-2043.
18. S. Fischmann and U. Lüning, *Isr. J. Chem.*, 2013, **53**, 87-96.
19. S. Tanaka, H. Tsurugi and K. Mashima, *Coord. Chem. Rev.*, 2014, **265**, 38-51.
20. D. Rota Martir and E. Zysman-Colman, *Chem. Commun.*, 2019, **55**, 139-158.
21. N. Falcone and H.-B. Kraatz, *Chem. Eur. J.*, 2018, **24**, 14316-14328.
22. M. Yoshizawa, J. K. Klosterman and M. Fujita, *Angew. Chem. Int. Ed.*, 2009, **48**, 3418-3438.
23. J. M. Lehn, A. Rigault, J. Siegel, J. Harrowfield, B. Chevrier and D. Moras, *Proc. Natl. Acad. Sci. USA*, 1987, **84**, 2565-2569.
24. J.-M. Lehn and A. Rigault, *Angew. Chem. Int. Ed.*, 1988, **27**, 1095-1097.
25. T. M. Garrett, U. Koert and J.-M. Lehn, *J. Phys. Org. Chem.*, 1992, **5**, 529-532.
26. A. Pfeil and J.-M. Lehn, *J. Chem. Soc., Chem. Commun.*, 1992, DOI: 10.1039/C39920000838, 838-840.
27. I. Meistermann, V. Moreno, M. J. Prieto, E. Moldrheim, E. Sletten, S. Khalid, P. M. Rodger, J. C. Peberdy, C. J. Isaac, A. Rodger and M. J. Hannon, *Proc. Natl. Acad. Sci. USA*, 2002, **99**, 5069-5074.
28. L. Cardo, I. Nawroth, P. J. Cail, J. A. McKeating and M. J. Hannon, *Sci. Rep.*, 2018, **8**, 13342.

29. U. Rana, C. Chakraborty, R. K. Pandey, M. D. Hossain, R. Nagano, H. Morita, S. Hattori, T. Minowa and M. Higuchi, *Bioconjugate Chem.*, 2016, **27**, 2307-2314.
30. Q. Chen, F. Jiang, D. Yuan, G. Lyu, L. Chen and M. Hong, *Chem. Sci.*, 2014, **5**, 483-488.
31. J. J. Danon, A. Krüger, D. A. Leigh, J.-F. Lemonnier, A. J. Stephens, I. J. Vitorica-Yrezabal and S. L. Woltering, *Science*, 2017, **355**, 159-162.
32. G. F. Swiegers and T. J. Malefetse, *Chem. Rev.*, 2000, **100**, 3483-3538.
33. C. O. Dietrich-Buchecker and J.-P. Sauvage, *Angew. Chem. Int. Ed.*, 1989, **28**, 189-192.
34. J.-F. Ayme, J. E. Beves, D. A. Leigh, R. T. McBurney, K. Rissanen and D. Schultz, *Nature Chem.*, 2012, **4**, 15-20.
35. V. Marcos, A. J. Stephens, J. Jaramillo-Garcia, A. L. Nussbaumer, S. L. Woltering, A. Valero, J.-F. Lemonnier, I. J. Vitorica-Yrezabal and D. A. Leigh, *Science*, 2016, **352**, 1555-1559.
36. H. Wang, Y. Li, H. Yu, B. Song, S. Lu, X.-Q. Hao, Y. Zhang, M. Wang, S.-W. Hla and X. Li, *J. Am. Chem. Soc.*, 2019, **141**, 13187-13195.
37. M. Wang, K. Wang, C. Wang, M. Huang, X.-Q. Hao, M.-Z. Shen, G.-Q. Shi, Z. Zhang, B. Song, A. Cisneros, M.-P. Song, B. Xu and X. Li, *J. Am. Chem. Soc.*, 2016, **138**, 9258-9268.
38. L. Wang, Z. Zhang, X. Jiang, J. A. Irvin, C. Liu, M. Wang and X. Li, *Inorg. Chem.*, 2018, **57**, 3548-3558.
39. R. A. S. Vasdev, D. Preston and J. D. Crowley, *Chem. Asian J.*, 2017, **12**, 2513-2523.
40. H. Amouri, C. Desmarets and J. Moussa, *Chem. Rev.*, 2012, **112**, 2015-2041.
41. A. J. McConnell, C. S. Wood, P. P. Neelakandan and J. R. Nitschke, *Chem. Rev.*, 2015, **115**, 7729-7793.
42. K. Harris, D. Fujita and M. Fujita, *Chem. Commun.*, 2013, **49**, 6703-6712.
43. J. L. Bolliger, A. M. Belenguer and J. R. Nitschke, *Angew. Chem. Int. Ed.*, 2013, **52**, 7958-7962.
44. W. Meng, B. Breiner, K. Rissanen, J. D. Thoburn, J. K. Clegg and J. R. Nitschke, *Angew. Chem. Int. Ed.*, 2011, **50**, 3479-3483.
45. R. A. Bilbeisi, J. K. Clegg, N. Elgrishi, X. d. Hatten, M. Devillard, B. Breiner, P. Mal and J. R. Nitschke, *J. Am. Chem. Soc.*, 2012, **134**, 5110-5119.
46. P. Mal, D. Schultz, K. Beyeh, K. Rissanen and J. R. Nitschke, *Angew. Chem. Int. Ed.*, 2008, **47**, 8297-8301.
47. S. M. Jansze, G. Cecot, M. D. Wise, K. O. Zhurov, T. K. Ronson, A. M. Castilla, A. Finelli, P. Pattison, E. Solari, R. Scopelliti, G. E. Zelinskii, A. V. Vologzhanina, Y. Z. Voloshin, J. R. Nitschke and K. Severin, *J. Am. Chem. Soc.*, 2016, **138**, 2046-2054.
48. P. Mal, B. Breiner, K. Rissanen and J. R. Nitschke, *Science*, 2009, **324**, 1697-1699.
49. R. Custelcean, P. V. Bonnesen, N. C. Duncan, X. Zhang, L. A. Watson, G. Van Berkel, W. B. Parson and B. P. Hay, *J. Am. Chem. Soc.*, 2012, **134**, 8525-8534.
50. I. A. Riddell, T. K. Ronson and J. R. Nitschke, *Chem. Sci.*, 2015, **6**, 3533-3537.

51. D. H. Leung, D. Fiedler, R. G. Bergman and K. N. Raymond, *Angew. Chem. Int. Ed.*, 2004, **43**, 963-966.
52. Y. Fang, J. A. Powell, E. Li, Q. Wang, Z. Perry, A. Kirchon, X. Yang, Z. Xiao, C. Zhu, L. Zhang, F. Huang and H.-C. Zhou, *Chem. Soc. Rev.*, 2019, **48**, 4707-4730.
53. F. Yu, D. Poole III, S. Mathew, N. Yan, J. Hessels, N. Orth, I. Ivanović-Burmazović and J. N. H. Reek, *Angew. Chem. Int. Ed.*, 2018, **57**, 11247-11251.
54. S. Gonell, X. Caumes, N. Orth, I. Ivanović-Burmazović and J. N. H. Reek, *Chem. Sci.*, 2019, **10**, 1316-1321.
55. K. Takahiro, N. Tatsuya, O. Takashi and F. Makoto, *Chem. Lett.*, 2003, **32**, 284-285.
56. M. Yoshizawa, M. Tamura and M. Fujita, *Science*, 2006, **312**, 251-254.
57. T. Murase, S. Horiuchi and M. Fujita, *J. Am. Chem. Soc.*, 2010, **132**, 2866-2867.
58. W. M. Hart-Cooper, K. N. Clary, F. D. Toste, R. G. Bergman and K. N. Raymond, *J. Am. Chem. Soc.*, 2012, **134**, 17873-17876.
59. W. Cullen, M. C. Misuraca, C. A. Hunter, N. H. Williams and M. D. Ward, *Nature Chem.*, 2016, **8**, 231-236.
60. J. Jiao, Z. Li, Z. Qiao, X. Li, Y. Liu, J. Dong, J. Jiang and Y. Cui, *Nat. Commun.*, 2018, **9**, 4423.
61. T. Murase, Y. Nishijima and M. Fujita, *J. Am. Chem. Soc.*, 2012, **134**, 162-164.
62. J. Guo, Y.-W. Xu, K. Li, L.-M. Xiao, S. Chen, K. Wu, X.-D. Chen, Y.-Z. Fan, J.-M. Liu and C.-Y. Su, *Angew. Chem. Int. Ed.*, 2017, **56**, 3852-3856.
63. D. H. Leung, R. G. Bergman and K. N. Raymond, *J. Am. Chem. Soc.*, 2006, **128**, 9781-9797.
64. D. Fiedler, D. H. Leung, R. G. Bergman and K. N. Raymond, *Acc. Chem. Res.*, 2005, **38**, 349-358.
65. M. D. Pluth, R. G. Bergman and K. N. Raymond, *Science*, 2007, **316**, 85-88.
66. M. D. Pluth, R. G. Bergman and K. N. Raymond, *Angew. Chem.*, 2007, **119**, 8741-8743.
67. M. D. Pluth, R. G. Bergman and K. N. Raymond, *J. Org. Chem.*, 2009, **74**, 58-63.
68. M. Fujita, M. Tominaga, A. Hori and B. Therrien, *Acc. Chem. Res.*, 2005, **38**, 369-378.
69. F. Makoto, J. Yakazi and K. Ogura, *J. Am. Chem. Soc.*, 1990, **112**, 5645-5647.
70. M. Fujita, S.-Y. Yu, T. Kusukawa, H. Funaki, K. Ogura and K. Yamaguchi, *Angew. Chem. Int. Ed.*, 1998, **37**, 2082-2085.
71. M. Tominaga, K. Suzuki, M. Kawano, T. Kusukawa, T. Ozeki, S. Sakamoto, K. Yamaguchi and M. Fujita, *Angew. Chem. Int. Ed.*, 2004, **43**, 5621-5625.
72. D. Fujita, Y. Ueda, S. Sato, N. Mizuno, T. Kumasaka and M. Fujita, *Nature*, 2016, **540**, 563-566.
73. K. Suzuki, M. Tominaga, M. Kawano and M. Fujita, *Chem. Commun.*, 2009, DOI: 10.1039/B822311D, 1638-1640.
74. Q.-F. Sun, J. Iwasa, D. Ogawa, Y. Ishido, S. Sato, T. Ozeki, Y. Sei, K. Yamaguchi and M. Fujita, *Science*, 2010, **328**, 1144-1147.

75. D. Fujita, Y. Ueda, S. Sato, H. Yokoyama, N. Mizuno, T. Kumasaka and M. Fujita, *Chem*, 2016, **1**, 91-101.
76. Q.-F. Sun, S. Sato and M. Fujita, *Nature Chem.*, 2012, **4**, 330-333.
77. J. A. Speir, S. Munshi, G. Wang, T. S. Baker and J. E. Johnson, *Structure*, 1995, **3**, 63-78.
78. W. Wang, Y.-X. Wang and H.-B. Yang, *Chem. Soc. Rev.*, 2016, **45**, 2656-2693.
79. D. B. Amabilino, D. K. Smith and J. W. Steed, *Chem. Soc. Rev.*, 2017, **46**, 2404-2420.
80. S. Chakraborty, K. J. Endres, R. Bera, L. Wojtas, C. N. Moorefield, M. J. Saunders, N. Das, C. Wesdemiotis and G. R. Newkome, *Dalton Trans.*, 2018, **47**, 14189-14194.
81. M. Fujita, F. Ibukuro, H. Hagihara and K. Ogura, *Nature*, 1994, **367**, 720-723.
82. T.-Z. Xie, K. J. Endres, Z. Guo, J. M. Ludlow, C. N. Moorefield, M. J. Saunders, C. Wesdemiotis and G. R. Newkome, *J. Am. Chem. Soc.*, 2016, **138**, 12344-12347.
83. M. Fujita, F. Ibukuro, K. Yamaguchi and K. Ogura, *J. Am. Chem. Soc.*, 1995, **117**, 4175-4176.
84. T. Weilandt, R. W. Troff, H. Saxell, K. Rissanen and C. A. Schalley, *Inorg. Chem.*, 2008, **47**, 7588-7598.
85. S. Hiraoka, Y. Sakata and M. Shionoya, *J. Am. Chem. Soc.*, 2008, **130**, 10058-10059.
86. P. J. Lusby, P. Müller, S. J. Pike and A. M. Z. Slawin, *J. Am. Chem. Soc.*, 2009, **131**, 16398-16400.
87. S. Freye, R. Michel, D. Stalke, M. Pawliczek, H. Frauendorf and G. H. Clever, *J. Am. Chem. Soc.*, 2013, **135**, 8476-8479.
88. R. Sekiya, M. Fukuda and R. Kuroda, *J. Am. Chem. Soc.*, 2012, **134**, 10987-10997.
89. S.-S. Sun, J. A. Anspach and A. J. Lees, *Inorg. Chem.*, 2002, **41**, 1862-1869.
90. S. Chen, L.-J. Chen, H.-B. Yang, H. Tian and W. Zhu, *J. Am. Chem. Soc.*, 2012, **134**, 13596-13599.
91. Y. Qin, L.-J. Chen, Y. Zhang, Y.-X. Hu, W.-L. Jiang, G.-Q. Yin, H. Tan, X. Li, L. Xu and H.-B. Yang, *Chem. Commun.*, 2019, **55**, 11119-11122.
92. Y. Qin, Y. Zhang, G. Yin, Y. Wang, C. Zhang, L. Chen, H. Tan, X. Li, L. Xu and H. Yang, *Chin. J. Chem.*, 2019, **37**, 323-329.
93. S. Kume, M. Murata, T. Ozeki and H. Nishihara, *J. Am. Chem. Soc.*, 2005, **127**, 490-491.
94. J. Park, L.-B. Sun, Y.-P. Chen, Z. Perry and H.-C. Zhou, *Angew. Chem. Int. Ed.*, 2014, **53**, 5842-5846.
95. T. Murase, S. Sato and M. Fujita, *Angew. Chem. Int. Ed.*, 2007, **46**, 5133-5136.
96. S. Oldknow, D. R. Martir, V. E. Pritchard, M. A. Blitz, Colin W. G. Fishwick, E. Zysman-Colman and M. J. Hardie, *Chem. Sci.*, 2018, **9**, 8150-8159.
97. M. Han, R. Michel, B. He, Y.-S. Chen, D. Stalke, M. John and G. H. Clever, *Angew. Chem. Int. Ed.*, 2013, **52**, 1319-1323.
98. R. Ahmad and M. J. Hardie, *CrystEngComm*, 2002, **4**, 227-231.
99. J. W. Steed, P. C. Junk, J. L. Atwood, M. J. Barnes, C. L. Raston and R. S. Burkhalter, *J. Am. Chem. Soc.*, 1994, **116**, 10346-10347.

100. D. S. Bohle and D. J. Stasko, *Inorg. Chem.*, 2000, **39**, 5768-5770.
101. J. Sanseverino, J.-C. Chambron, E. Aubert and E. Espinosa, *J. Org. Chem.*, 2011, **76**, 1914-1917.
102. C. Carruthers, T. K. Ronson, C. J. Sumby, A. Westcott, L. P. Harding, T. J. Prior, P. Rizkallah and M. J. Hardie, *Chem. Eur. J.*, 2008, **14**, 10286-10296.
103. H. A. Fogarty, P. Berthault, T. Brotin, G. Huber, H. Desvaux and J.-P. Dutasta, *J. Am. Chem. Soc.*, 2007, **129**, 10332-10333.
104. L.-L. Chapellet, J.-P. Dognon, M. Jean, N. Vanthuyne, P. Berthault, T. Buffeteau and T. Brotin, *ChemistrySelect*, 2017, **2**, 5292-5300.
105. K. T. Holman, S. D. Drake, J. W. Steed, G. W. Orr and J. L. Atwood, *Supramol. Chem.*, 2010, **22**, 870-890.
106. G. Huber, T. Brotin, L. Dubois, H. Desvaux, J.-P. Dutasta and P. Berthault, *J. Am. Chem. Soc.*, 2006, **128**, 6239-6246.
107. N. J. Cookson, J. J. Henkelis, R. J. Ansell, C. W. G. Fishwick, M. J. Hardie and J. Fisher, *Dalton Trans.*, 2014, **43**, 5657-5661.
108. T. Brotin, V. Roy and J.-P. Dutasta, *J. Org. Chem.*, 2005, **70**, 6187-6195.
109. T. Brotin and J.-P. Dutasta, *Chem. Rev.*, 2009, **109**, 88-130.
110. A. Collet, *Tetrahedron*, 1987, **43**, 5725-5759.
111. O. Baydoun, N. De Rycke, E. Léonce, C. Boutin, P. Berthault, E. Jeanneau and T. Brotin, *J. Org. Chem.*, 2019, **84**, 9127-9137.
112. R. M. Fairchild, A. I. Joseph, K. T. Holman, H. A. Fogarty, T. Brotin, J.-P. Dutasta, C. Boutin, G. Huber and P. Berthault, *J. Am. Chem. Soc.*, 2010, **132**, 15505-15507.
113. M. A. Little, J. Donkin, J. Fisher, M. A. Halcrow, J. Loder and M. J. Hardie, *Angew. Chem. Int. Ed.*, 2012, **51**, 764-766.
114. D. Zhang, A. Martinez and J.-P. Dutasta, *Chem. Rev.*, 2017, **117**, 4900-4942.
115. Ł. Szyszka, P. Cmoch, A. Butkiewicz, M. A. Potopnyk and S. Jarosz, *Org. Lett*, 2019, **21**, 6523-6528.
116. T. K. Ronson, H. Nowell, A. Westcott and M. J. Hardie, *Chem. Commun.*, 2011, **47**, 176-178.
117. T. K. Ronson, J. Fisher, L. P. Harding and M. J. Hardie, *Angew. Chem. Int. Ed.*, 2007, **46**, 9086-9088.
118. V. E. Pritchard, D. Rota Martir, S. Oldknow, S. Kai, S. Hiraoka, N. J. Cookson, E. Zysman-Colman and M. J. Hardie, *Chem. Eur. J.*, 2017, **23**, 6290-6294.
119. F. L. Thorp-Greenwood, A. N. Kulak and M. J. Hardie, *Nature Chem.*, 2015, **7**, 526-531.
120. F. L. Thorp-Greenwood, T. K. Ronson and M. J. Hardie, *Chem. Sci.*, 2015, **6**, 5779-5792.
121. J. J. Henkelis, C. J. Carruthers, S. E. Chambers, R. Clowes, A. I. Cooper, J. Fisher and M. J. Hardie, *J. Am. Chem. Soc.*, 2014, **136**, 14393-14396.
122. J. J. Henkelis, T. K. Ronson, L. P. Harding and M. J. Hardie, *Chem. Commun.*, 2011, **47**, 6560-6562.
123. A. Westcott, J. Fisher, L. P. Harding, P. Rizkallah and M. J. Hardie, *J. Am. Chem. Soc.*, 2008, **130**, 2950-2951.
124. V. E. Pritchard, D. Rota Martir, E. Zysman-Colman and M. J. Hardie, *Chem. Eur. J.*, 2017, **23**, 8839-8849.

125. J. J. Henkelis, S. A. Barnett, L. P. Harding and M. J. Hardie, *Inorg. Chem.*, 2012, **51**, 10657-10674.
126. J. M. Fowler, F. L. Thorp-Greenwood, S. L. Warriner, C. E. Willans and M. J. Hardie, *Chem. Commun.*, 2016, **52**, 8699-8702.
127. J. M. Fowler, E. Britton, C. M. Pask, C. E. Willans and M. J. Hardie, *Dalton Trans.*, 2019, **48**, 14687-14695.
128. M. A. Little, T. K. Ronson and M. J. Hardie, *Dalton Trans.*, 2011, **40**, 12217-12227.
129. M. A. Little, M. A. Halcrow, L. P. Harding and M. J. Hardie, *Inorg. Chem.*, 2010, **49**, 9486-9496.
130. T. K. Ronson, J. Fisher, L. P. Harding, P. J. Rizkallah, J. E. Warren and M. J. Hardie, *Nature Chem.*, 2009, **1**, 212-216.
131. M. J. Hardie and C. J. Sumby, *Inorg. Chem.*, 2004, **43**, 6872-6874.
132. T. K. Ronson, C. Carruthers, J. Fisher, T. Brotin, L. P. Harding, P. J. Rizkallah and M. J. Hardie, *Inorg. Chem.*, 2010, **49**, 675-685.
133. J. J. Henkelis, J. Fisher, S. L. Warriner and M. J. Hardie, *Chem. Eur. J.*, 2014, **20**, 4117-4125.

# Chapter 2
# Component design: Synthesis of ligands and metal tectons

## 2.1. Introduction

In order to target a specific supramolecular architecture, the individual building blocks that make up the assembly must be designed so that self-assembly processes will furnish the desired outcome. In this chapter the rational design of both the ligand and metal precursors will be discussed to reveal how the $M_3L_2$ metallo-cryptophane architecture can be specifically targeted. In addition, a range of functions and physical properties have been engineered into the metallo-cryptophanes through design of the sub-components. A discussion of the strategies and methods used in order to achieve this follows.

## 2.2. Self-Assembly Design Principles

Self-assembly processes allow access to structures that would be very difficult or even impossible to synthesise utilising traditional synthetic methods. In order to achieve this, the components used in self-assembly need to be designed so that the thermodynamic minimum lies with the desired product. In general, ligands used in self-assembly are rich in $sp^2$ and *sp* hybridised centres, which limits the number of ways in which they can react due to their decreased flexibility. Incorporating certain transition metals into this process can make it easier to predict where this minimum will occur and enable a greater degree of control over which species will be favoured by the system. This is due in part to the predictable geometries that some metals adopt, palladium and platinum are rigidly square planar in all but the most sterically demanding situations. This, coupled with the use of strongly chelating ligands used to block unwanted coordination sites, results in a highly rigid and predictable component for use in self-assembly.

This approach for designing supramolecular architectures was first reported by Fujita in 1990 when he demonstrated that the mixing of bis(ethylenediamine)palladium(II)nitrate with 4,4'-bipyridine in a 1:1 ratio resulted in the quantitative formation of a molecular square (Figure 2.1).[1]

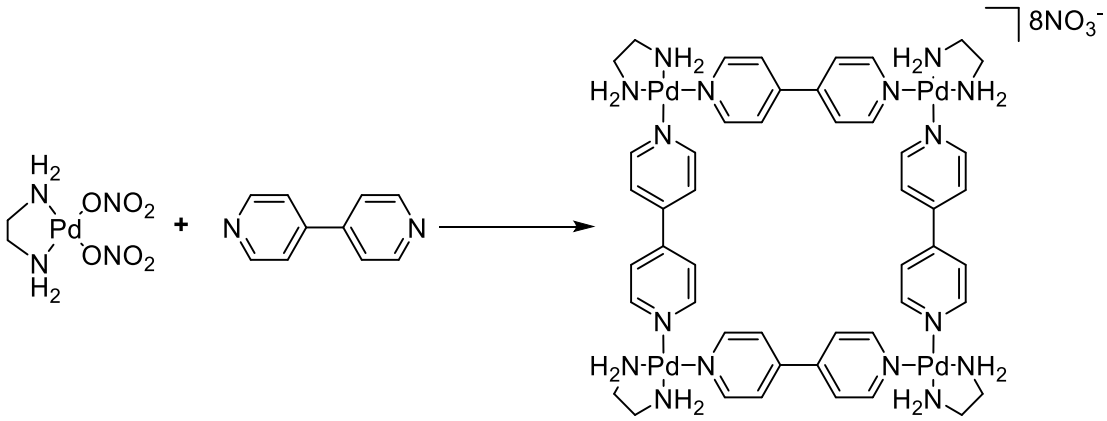


**Figure 2.1.** Synthesis of Fujita's molecular square.[1]

The result was surprising as formation of macrocycles is usually accompanied by formation of unwanted oligomers.[2] The reason that this reaction proceeds with a quantitative yield is that it is in fact a self-assembly process. The labile nature of the palladium-pyridine bonds enable error correction to take place so any undesired species that initially form will, in time, convert to the thermodynamic product.[2] To rationalise why this is the thermodynamic product both enthalpic and entropic contributions need to be taken into consideration. The *cis*-protected square planar palladium has 90$^{o}$ bond angles between the available coordination sites whereas the bipyridine has 180$^{\circ}$ between binding sites. When assembled into the square shape shown in Figure 2.1 the palladium and bipyridine are at the ideal bond angle resulting in no enthalpic penalty to square formation. In fact the loss of the weakly bound nitrate anions make the formation of the square an enthalpically favourable process. The molecular square is also the smallest molecule that can be made where all coordination sites are occupied by strongly bound ligands and where there are no strained bond angles. Therefore, entropically the formation of the molecular square is a relatively favourable process.

By rationalising the enthalpic and entropic contributions in this way it is possible to predict how a system will self-assemble. Since Fujita's initial discovery of the metallo-square many more metallo-supramolecular systems have been discovered to self-assemble into ever more complex architectures. Fujita currently holds the record of the largest metallo-supramolecular assembly ever synthesised with a $Pd_{46}L_{98}$ cage.[3] Despite the apparent complexity of the system, the basic design principles remain constant. In this chapter the rational design of both ligand and metal tectons will be discussed to reveal how the targeted approach of $M_3L_2$ metallo-cryptophanes can be achieved.

## 2.2 Synthesis of Cyclotriguaiacylene

CTG is a bowl shaped cavitand related to calixarenes, differing mainly in that the arene rings are linked in an *ortho* fashion as opposed to a *meta* arrangement (Figure 2.2). The result is that the molecule is far more rigid than calixarenes, adopting a bowl shape containing a shallow hydrophobic cavity. These properties make it an excellent host molecule with well documented host-guest behaviour with large, spherical non-polar molecules such as fullerenes and carboranes.[4-6] This is due to the propensity to form strong hydrophobic and π-π interactions with these guests.

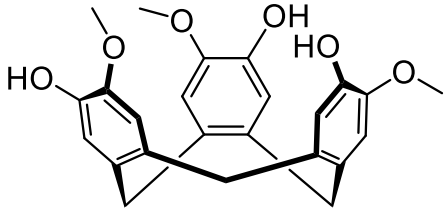


**Figure 2.2.** Structure of cyclotriguaiacylene.

CTG exhibits helical chirality due to the alternate hydroxy-methoxy substitution pattern on the upper rim and can exist as the *M* or *P* isomer. It can however slowly interconvert in solution, usually with a $t_{1/2}$ in the range of a few days depending upon the substitution on the upper rim. It does so by passing over a considerable energy barrier of 110-115 KJ $mol^{-1}$ to an unfavourable 'saddle' conformation before relaxing back to its thermodynamic resting 'crown' conformation (Scheme 2.1).[7] Isolation of enantiopure CTG is possible using chiral HPLC however over time it would interconvert back into a racemic mixture. For this reason all the work carried out in this chapter was carried out using a racemic mixture of CTG based ligands.

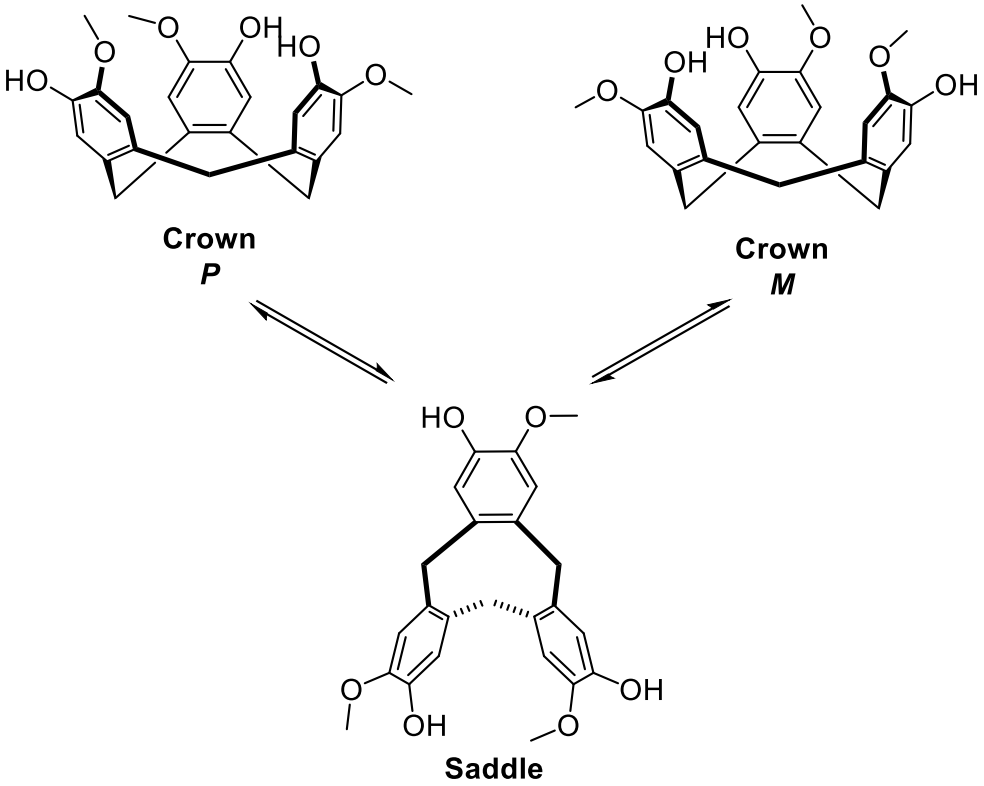


**Scheme 2.1.** Isomerisation of crown enantiomers through the saddle intermediate.

CTG was synthesised according to a reported three step process (Scheme 2.2) starting with the protection of 3-methoxy-4-hydroxybenzyl alcohol with allyl bromide. This yielded the allyl protected product **2.1** in an excellent yield of 98%. **2.1** is then heated to 100 °C causing it to melt, in the presence of super phosphoric acid. A dehydration reaction occurs where the benzylic alcohol becomes protonated, facilitating nucleophilic attack of the adjoining carbon by the phenyl ring of another molecule of **2.1**. The protection of the phenolic hydroxyl group in the previous step is critical as it renders the group non-nucleophilic and as a result cannot react to form unwanted side products in the second step. The reaction is performed without any solvent as the desired trimeric product **2.2** immediately precipitates from molten **2.1**, preventing further reaction and subsequently improving the yield. Despite these precautions, a significant proportion of unwanted oligomers and polymer still form during the reaction, reducing the yield to 31%. Pure **2.2** was obtained by triturating the crude mixture in methanol, followed by filtration. The allyl groups on the trimer are removed *via* a palladium catalysed deprotection to yield CTG (**2.3**) in a good yield of 80%.

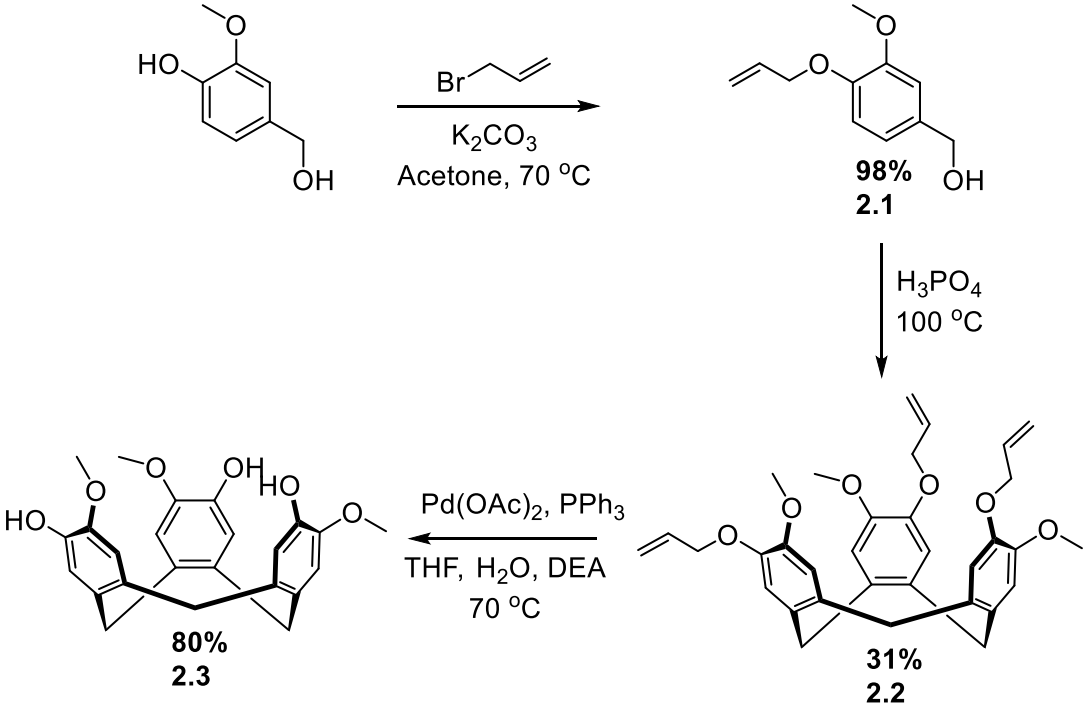


**Scheme 2.2.** Synthesis of CTG.

The $^{1}$H-NMR spectrum of CTG contains a number of diagnostic peaks, the most important being the *endo* and *exo* protons on the methylene linkers between arene rings (Figure 2.3). The crown conformation of CTG is rigid and as such the protons on the methylene bridge are held in different chemical environments and therefore split into two distinct doublets. The presence of these doublets shows that the final product from Scheme 2.2 exhibits $C_3$ symmetry. Any lower symmetry would result of splitting of the well-resolved doublets into a broad singlet. This factor can be used to determine whether exhaustive deprotection of the hydroxyl groups has been achieved. The $^{1}$H-NMR of CTG shows well resolved peaks and a relatively simple spectrum, confirming that exhaustive removal of the allyl groups has occurred.

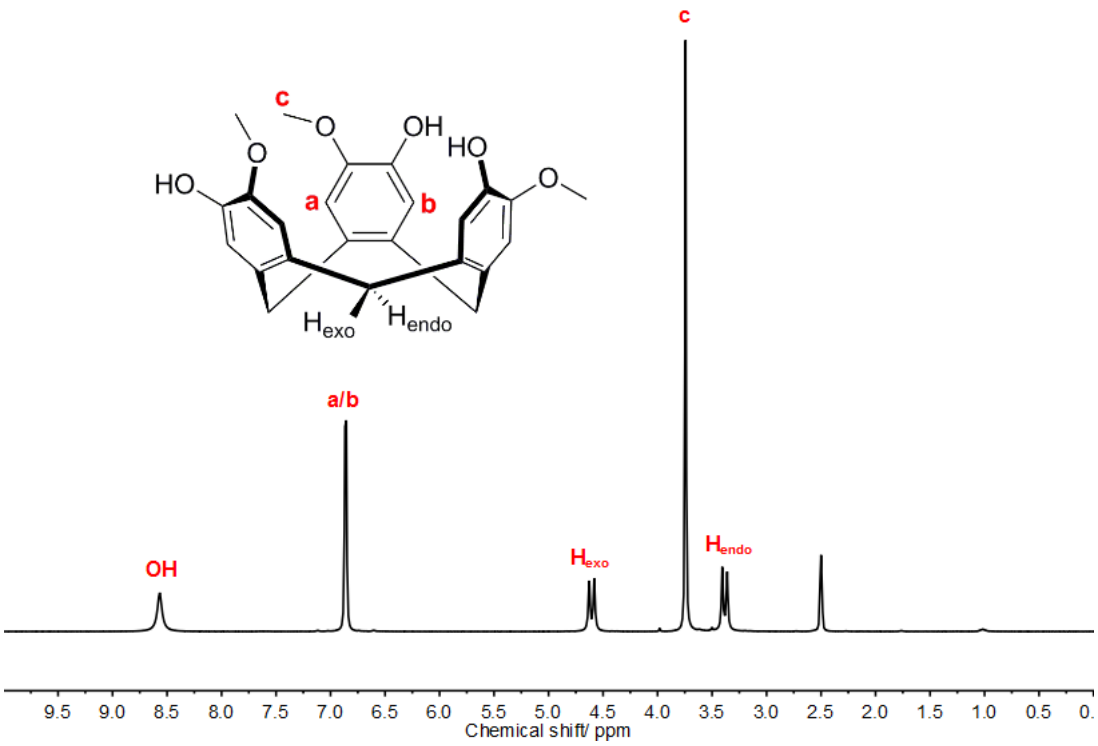


**Figure 2.3.** $^{1}$H-NMR (300 MHz, $d_6$-DMSO) of CTG showing characteristic *endo* and *exo* doublets.

## 2.3 Initial Progress Towards Azobenzene Functionalised $M_3L_2$ Metallo-Cryptophanes

As discussed in the previous Chapter the ultimate goal of this research project is to develop photoresponsive metallo-cryptophanes. Photo-isomerisation of the cage could potentially lead to modulation of its host-guest properties, a desirable property that could be applied to the separation of useful chemicals. In order to achieve this two elements need to be combined into the ligand, firstly a photoswitch and secondly a molecular host.

When considering what photoswitch to incorporate into the cage framework there are several classes of photoswitchable groups to choose from. For this work there were a number of desirable features. Upon photoisomerisation a large change in conformational shape is beneficial as the larger the change in shape of the host, the more likely it will be that the binding affinity of guests will change as a result. Diarylthenes such as stilbene undergo a reversible *trans* to *cis* photoisomerisation upon irradiation with an appropriate wavelength of light (Figure 2.4).

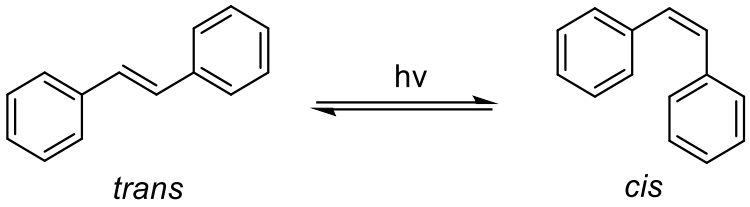


**Figure 2.4.** Photoswitching of stilbene between *trans* and *cis* isomers.

The conformational change associated with this isomerisation is large. However, diarylethenes often suffer from poor photostability making them unsuitable for use in chemical separation as the cage would ideally be reusable.[8, 9] The reason for the poor fatigue diarylethenes exhibit is that the *Z* isomer can undergo an intramolecular 6π electrocyclisation. Oxidation of this species results in the irreversible formation of phenanthrene (Figure 2.5).[9]

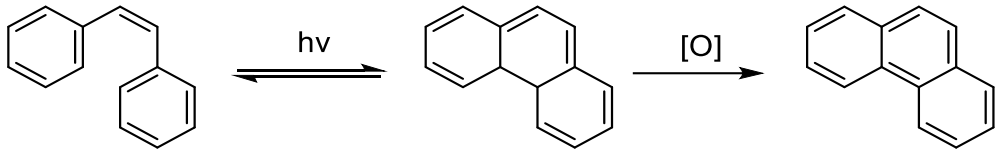


**Figure 2.5.** 6π electrocyclisation of stilbene followed by oxidation and deactivation of photoswitching properties.

Dithienylethenes (DTEs) are a specific class of diarylethenes that exhibit remarkable photostability due to *ortho* substitution of the aromatic rings, preventing oxidation and subsequent deactivation.[10] Unlike stilbenes the 6π electrocyclisation reaction is responsible for the photoisomerisable behaviour of DTEs as the addition of a fused ring onto the C-C double bond prevents *trans* to *cis* isomerisation (Figure 2.6).[10]

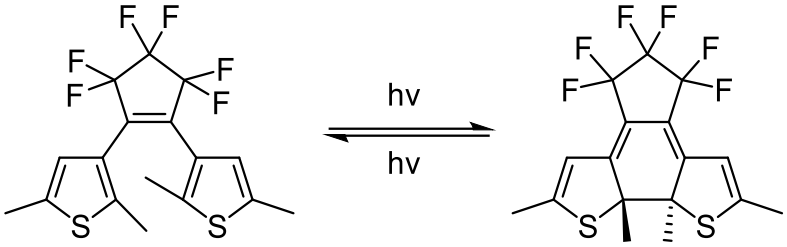


**Figure 2.6.** Photoisomerisation of DTEs upon irradiation with light.

Clever has reported the use of DTE units to produce a photoswitchable $Pd_2L_4$ coordination cage utilising rigid *bis* pyridyl ligands. It was shown that the photoisomerisation of the cage could be used to modulate guest uptake and release of a $B_{12}F_{12}^{2-}$ guest.[11] Whilst the problems regarding photostability would be improved by incorporating DTEs into a CTG based coordination cage, another potential issue has arisen due to the small change in conformation upon isomerisation. The subtle change in shape that occurs

during photoswitching may not be enough to effectively modulate host-guest dynamics.

Azobenzenes (Figure 2.7) are a class of photoswitch that exhibit excellent photostability and also undergo a large conformational change upon photoswitching. This makes them a suitable class of photoswitch for use in this project.

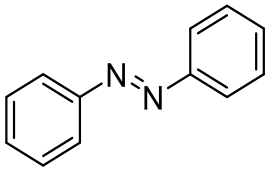


**Figure 2.7.** General structure of azobenzene moiety.

Azobenzenes usually exist in a thermodynamically stable planar *trans* conformation.[12, 13] Irradiation with an appropriate wavelength of light, usually in the region of 300-360 nm will switch the azobenzene from a *trans* to *cis* conformation.[12, 14] The change to the *cis* isomer results in a slight twisting of the phenyl rings which results in the molecule adopting a non-planar conformation (Figure 2.8).[15] The *cis* to *trans* isomerisation occurs spontaneously due to the greater thermodynamic stability of the *trans* isomer. The rate can be increased however by irradiating at a longer wavelength (~450 nm) or by heating the sample to promote the thermal back reaction.

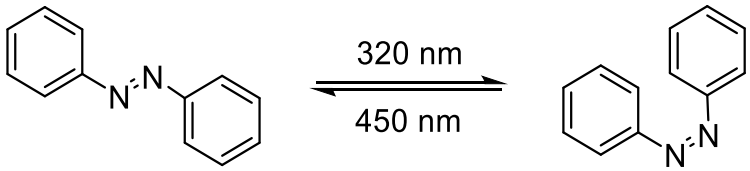


**Figure 2.8.** Photo-induced switching of azobenzene displaying the distorted *cis* isomer.[15]

The mechanism of photoisomerisation of azobenzene is still a hotly debated process with four mechanisms proposed as possible pathways; rotation, inversion, concerted inversion and inversion assisted rotation.[12, 16-18] Azobenzenes exhibit two characteristic absorbance bands in the UV-vis region. A strong π-π*band at 350 nm and a weak n-π* absorbance at ~450 nm, exciting the molecule at these wavelengths promotes it into a $S_2$ and $S_1$ excited state respectively.[19] These excited states can relax through isomerisation, amongst other means, into the *cis* or *trans* isomer. Curiously the quantum yield of the process is dependent on the wavelength used to excite the molecule, as exciting the molecule into the $S_2$ state first rather than the $S_1$ state can lead to different quantum yields of isomerisation.[20] This appears to violate Kasha's rule which states that the $S_2$ state should relax into

the $S_1$ state before any appreciable relaxation by other means could occur, so the quantum yield should be independent of excitation wavelength.[20]

Previous PhD student Dr Samuel Oldknow successfully synthesised a photoresponsive CTG based ligand by appending azobenzene moieties onto the CTG scaffold. The formation of the azobenzene was achieved by coupling 3-aminopyridine with methyl-(4-nitroso)-benzoate. The nitroso arene was synthesised in a biphasic system of water and DCM using Oxone™ as the oxidant.[21] Biphasic conditions were essential as the insolubility of the nitroso compound in water prevented over oxidation to the nitro compound by separating the desired product from the oxidising agent. A modified Mills reaction was used to synthesise the azobenzene arms used in this thesis as shown in Scheme 2.3.[22]

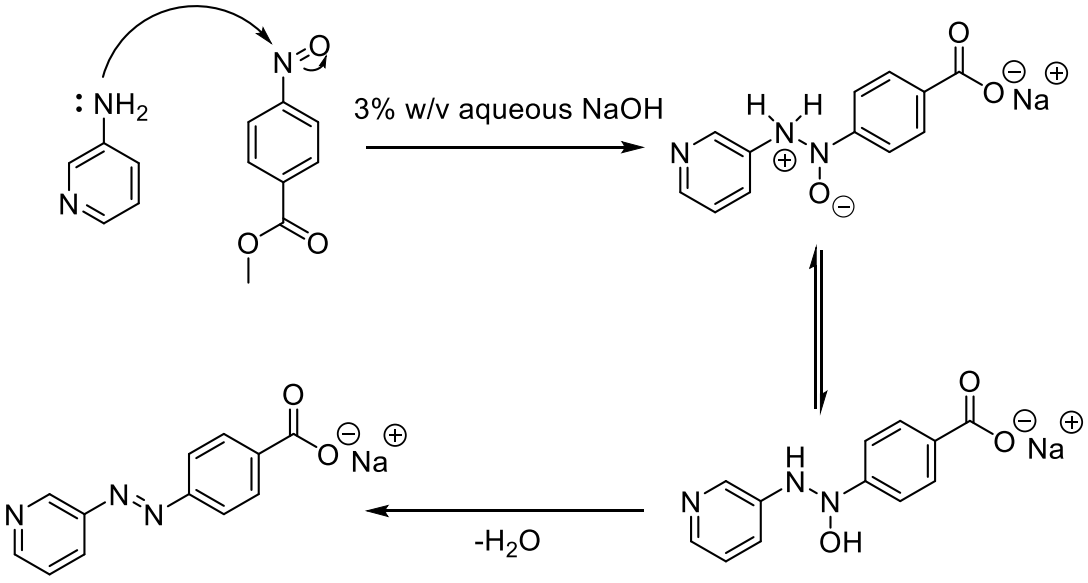


**Scheme 2.3.** Proposed mechanism of the modified Mills reaction used to synthesise azobenzene arm.[22]

The synthesis of the azobenzene shown in Scheme 2.3 is atypical for a Mills reaction, which are normally performed under mildly acidic conditions.[23] However, under acidic conditions the reaction fails. This is likely due to the formation of the pyridine to form a pyridinium cation. The positive charge formed withdraws electron density from the amine lone pair, decreasing the nucleophilicty of the nitrogen. The result is that the amine is sufficiently deactivated to prevent the reaction occurring with the nitroso group and subsequent azobenzene formation.

The azobenzene linker contains two important features, firstly a metal binding group in the form of the pyridyl moiety at one end of the azobenzene to allow binding to metal cations. It also contained a carboxylate group which could be used as a handle to couple the molecule to CTG *via* an esterification reaction.

In order to react CTG and the azobenzene in such a way the carboxylate group was first converted into an acid chloride using thionyl chloride. This enabled coupling with the hydroxyl groups on CTG under mildly basic conditions using trimethylamine as a scavenger base (Scheme 2.4). Purification of the ligand was performed by triturating the crude product in methanol and collection by filtration, by-passing the need for a complicated purification step. The resultant 3-pyridyl ester linked azobenzene CTG was obtained in a reasonable yield of 81% (**L1**).

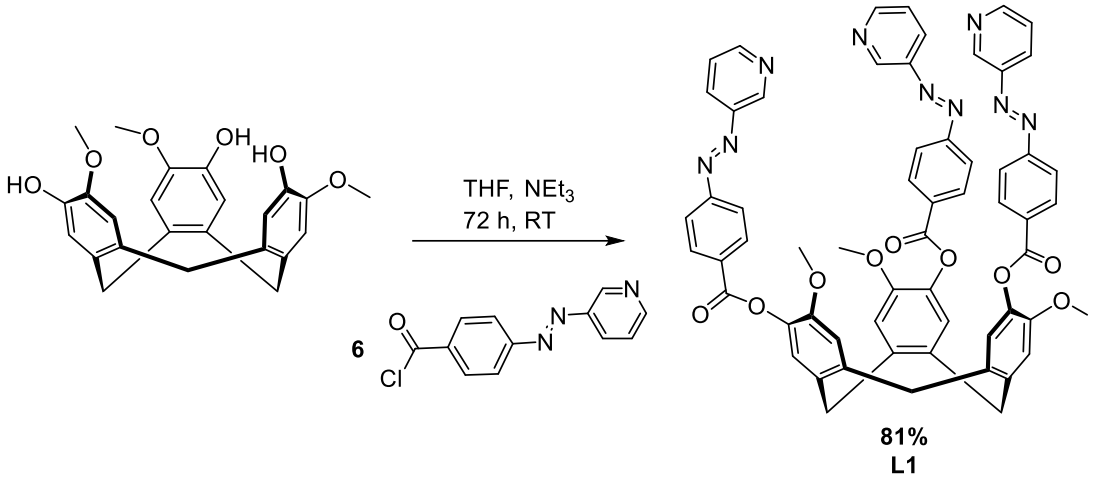


**Scheme 2.4.** Synthesis of azobenzene appended CTG (**L1**).

The ligand was characterised using $^{1}$H-NMR (Figure 2.9) which showed the presence of the characteristic CTG doublets and a relatively simple spectrum. This confirms that total substitution of the hydroxyl groups has occurred and *C*$_3$ symmetry has been retained. If this was not the case the spectrum would be far more complicated and considerably broader.

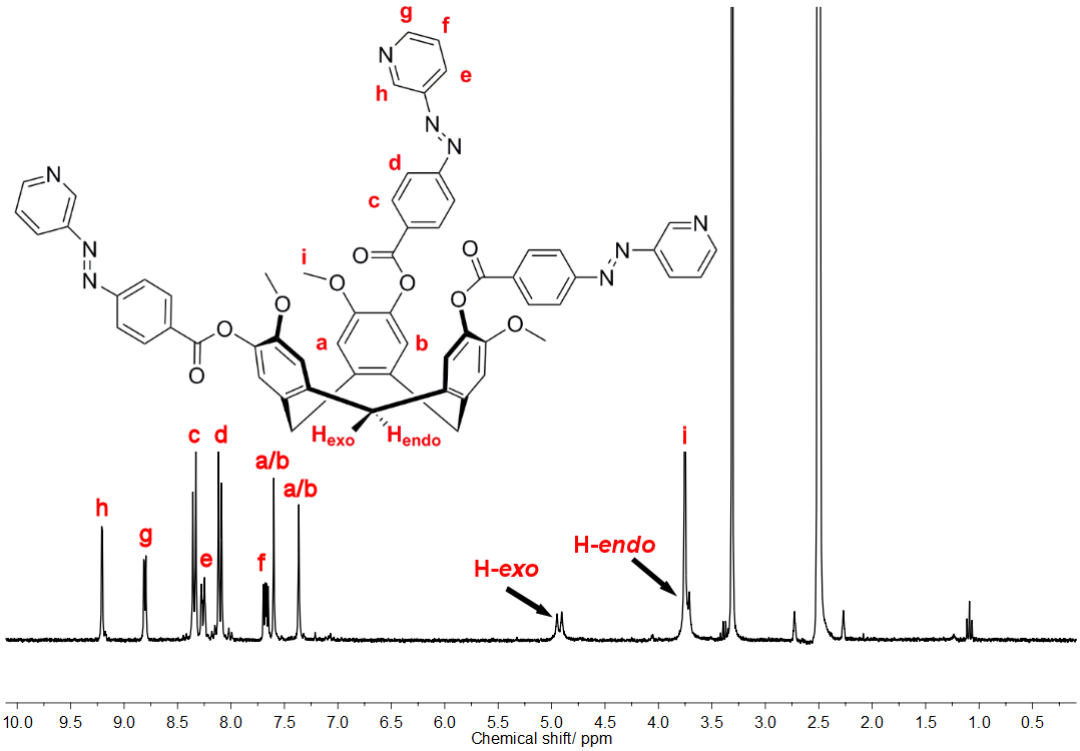


**Figure 2.9.** $^{1}$H-NMR (300 MHz, $d_6$-DMSO) of **L1** showing characteristic *endo* and *exo* CTG proton environments.

The synthesis of a tripodal photoswitchable ligand was a significant step towards achieving the aims of this project. The reaction of the ligand with appropriately designed metal tectons would allow access to $M_3L_2$ metallo-cryptophanes. Previous work within the Hardie group has shown that the self-assembly of *cis* protected metal tectons with tripodal CTG ligands can lead to the isolation of $M_3L_2$ cages.[24] A good example of this is the work carried out by previous PhD student Dr Vikki Pritchard who showed that the reaction of pyridyl functionalised CTG with iridum(III) *bis*(2-phenylpyridine) *bis*(acetonitrile) hexafluorophosphate in a 2:3 ratio resulted in the formation of the desired cage complex (Scheme 2.5).[25]

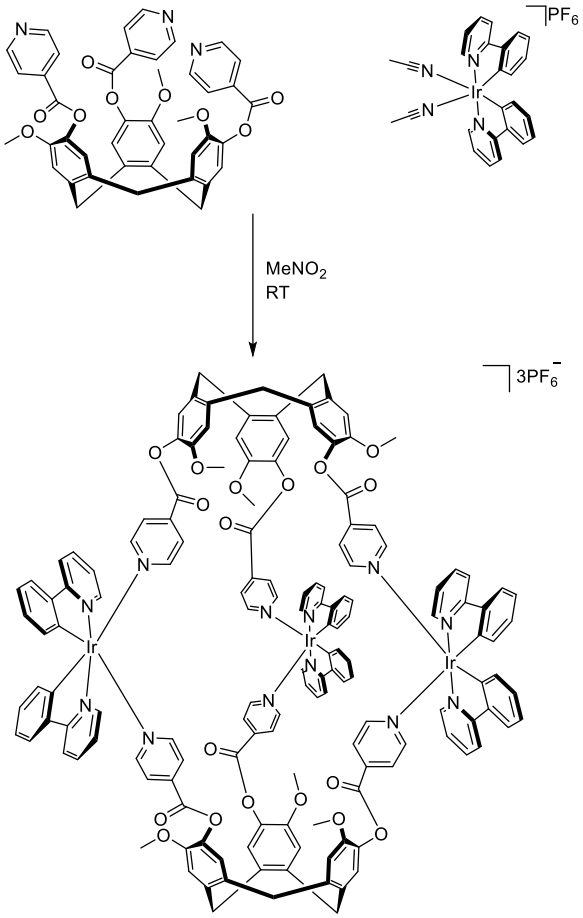


**Scheme 2.5.** Synthesis of $M_3L_2$ metallo-cryptophane reported by Pritchard *et al*.[25]

The phenylpyridine units protect the iridium centre from substitution; reaction can only occur by displacement of the weakly bound acetonitrile units, preventing formation of oligomeric products or coordination polymers. Analysis of the crystal structure reveals that the 90° bond angle between the available coordination sites facilitates the formation of the $M_3L_2$ complex (Figure 2.10). The bond angles in this species are not bent significantly away from ideality, increasing the thermodynamic favourability of cryptophane formation.

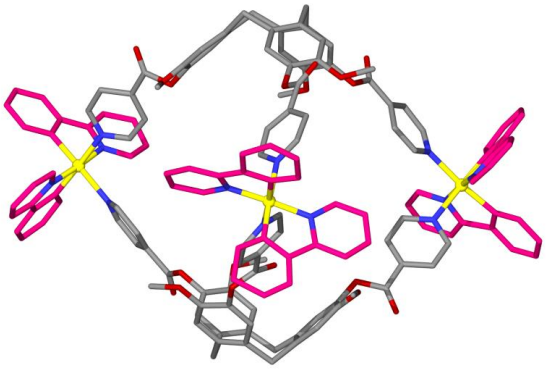

**Figure 2.10.** SCXRD structure of Pritchard's cage showing ideal octahedral bond angles at the iridium(III) centres (yellow).[25]

Modification of this process by substituting the pyridyl appended CTG with **L1** provided access to the first example of a photoswitchable $M_3L_2$ metallo-cryptophane where azobenzenes were incorporated into the cage framework (Scheme 2.6).

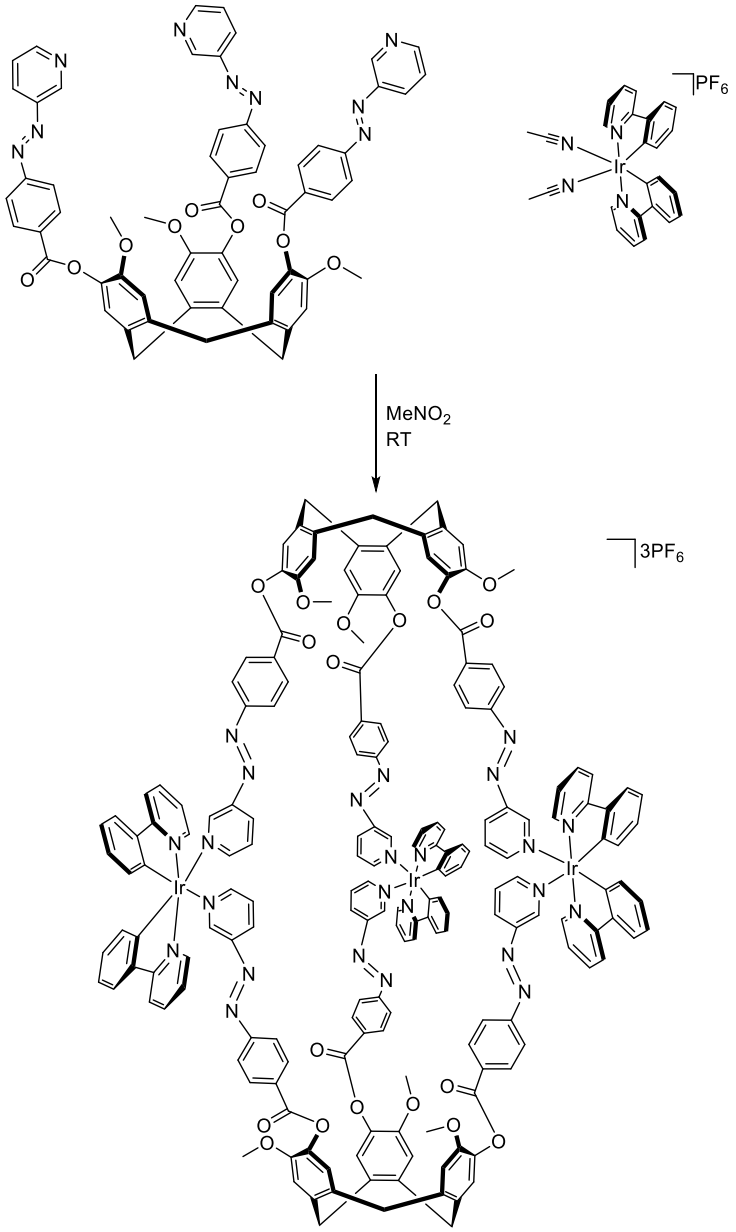


**Scheme 2.6.** Synthesis of the first example of an azobenzene linked $M_3L_2$ metallo-cryptophane synthesised by Oldknow *et al*.[22, 26]

Subsequent Chapters will discuss the characterisation and photoswitching of these complex species. The solubility of the cage was unfortunately very poor in all solvents apart from nitromethane. This limited the usefulness of the cage due to safety concerns regarding the use of UV light with the solvent nitromethane which could potentially form an explosive mixture. Efforts to solubilise the cage by modifying the ligand and metal tecton (Figure 2.11) were partially successful. The increased solubility came at a price however as

the use of the more soluble ligand resulted in a cage with larger windows due to the increased length of the ligand ‘arms’. As the size of the window increases, the internal environment becomes more similar to the bulk. Therefore, it is desirable to minimise this property as much as possible if efficient guest binding is desired.

**Solubilised metal tectons**

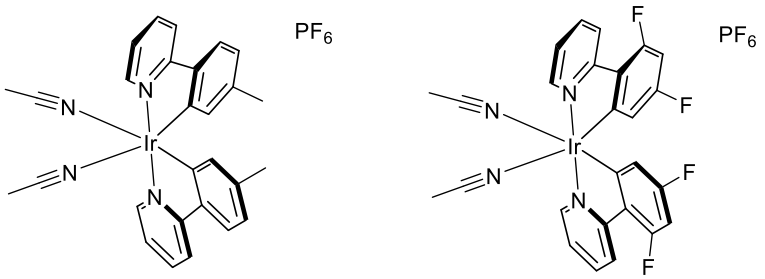


**Solubilised ligand**

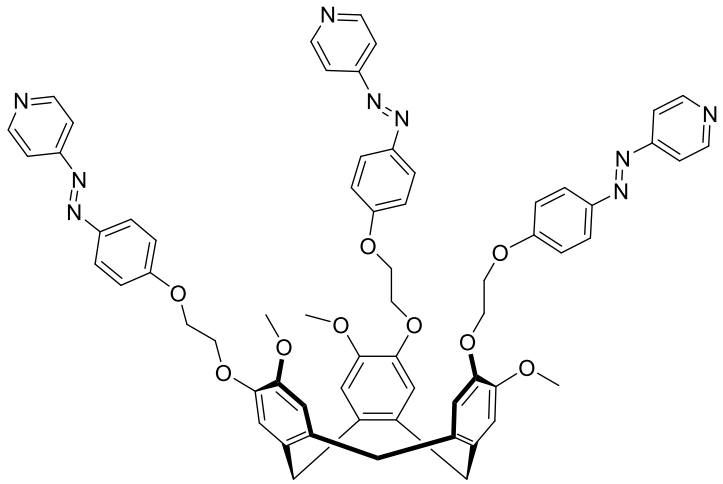


**Figure 2.11.** Examples of solubilised ligand and metal tectons.

There were also concerns that due to the proximity of the azobenzene to the iridium centre energy transfer pathways, such as Förster resonance electron transfer (FRET) or photoinduced electron transfer (PET), could reduce the switching efficiency of the azobenzene groups by deactivating the excited state before the switch from *trans* to *cis* could occur.[27] The efforts made to address these problems are discussed in the remainder of this Chapter.

## 2.4 Functionalisation of Azobenzene Appended CTG

CTG and its derivatives are often rigid molecules with a propensity to form strong bowl-in-bowl stacking interactions in the solid phase. This leads to poor solubility due to the large enthalpic cost associated with breaking these

interactions. Increasing the solubility of CTG is therefore a worthwhile but synthetically challenging goal. A method to increase the solubility of compounds is to functionalise with long flexible groups. This has the effect of increasing the entropy released upon dissolution, thus making dissolution a more thermodynamically favourable process. The increasing chain length of upper rim substituents can also interfere with the strong hydrophobic bowl in bowl stacking arrangements commonly observed with the CTG scaffold. This has the effect of decreasing the enthalpic cost of solvation, once again making dissolution a more thermodynamically favourable process.

There are two sites on CTG which are targets for variation, the hydroxyl group and the methoxy groups on the upper rim of the bowl (Figure 2.12). The hydroxyl group is readily functionalised and vast amounts of effort have been undertaken to synthesise CTG derivatives which have been functionalised at this position.[28] However, there has been considerably less effort in attempting to vary the methoxy group on the upper rim of the bowl. This is presumably a result of the more synthetically challenging procedures required to do so. There are a number of benefits associated with modification of this position. First and foremost, alterations at this position are far less likely to interfere with the self-assembly of the ligand. This is because the position is situated a large distance from where the metal binding site resides in a functionalised CTG type ligand. Considerable efforts were made to increase the length of the alkyl chain at this position in an attempt to increase the solubility.

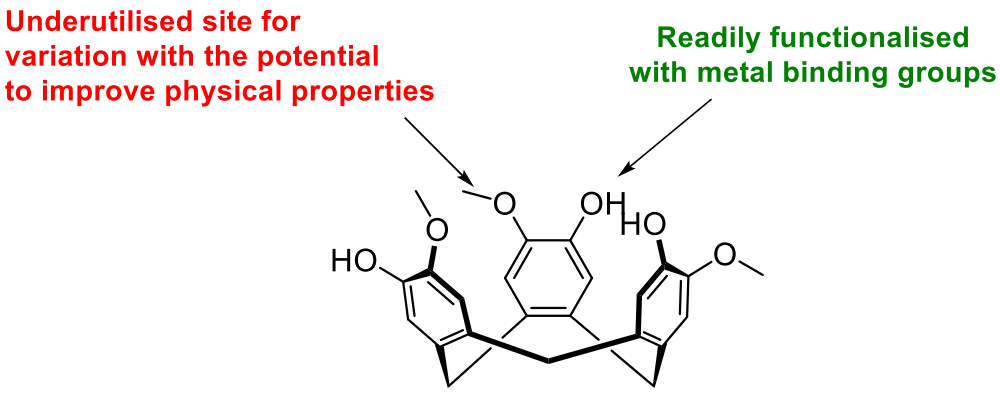


**Figure 2.12.** Diagram highlighting the efforts made to functionalise the hydroxyl positions of CTG whilst neglecting potential substitution at the methoxy position.

Ethoxy and propoxy variants were chosen as synthetic targets. Unfortunately the required starting materials, 3-ethoxy/propoxy-4-hydroxybenzyl alcohol were not commercially available so new synthetic methods had to be developed. Synthesis of ethyl CTG (eCTG) began with the borohydride reduction of commercially available ethyl vanillin to produce **2.4** (Scheme 2.7).

The hydroxyl group was then protected with an allyl group by reaction with allyl bromide in the presence of a weak base to produce **2.5**.

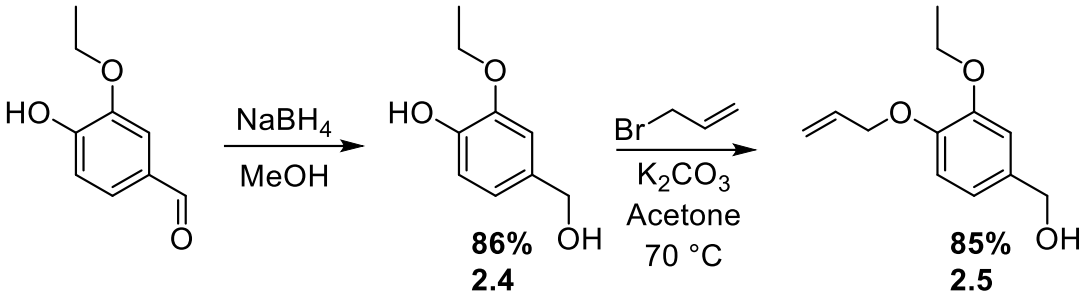


**Scheme 2.7.** Synthesis of eCTG monomer **2.5**.

Trimerisation to produce allyl protected CTG is conducted using superphosphoric acid and, due to the similarity between starting materials, it was envisioned that this method would also work to produce eCTG. Upon attempting the reaction however, an inseparable mixture of polymers and oligomers was obtained with no evidence of the desired product detected (Scheme 2.8).

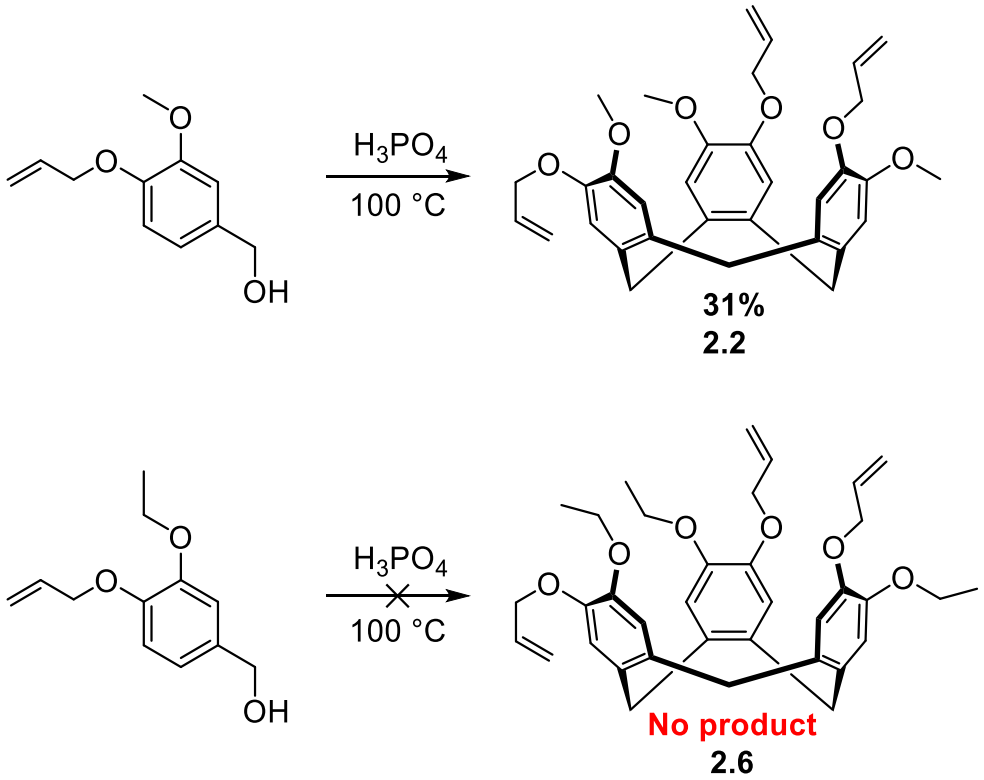


**Scheme 2.8.** Successful synthesis of allyl protected CTG (top) and unsuccessful synthesis of allyl protected eCTG (bottom).

It was unexpected that the substitution of the methoxy group for an ethoxy group would have such a drastic effect on the reaction. It has been hypothesised by Collet *et al*. that the increased solubility of the product may be the reason for the poor yield. Allyl protected CTG (**2.2**) precipitates out of

the solvent during the reaction which protects it from reacting further. The increased solubility due to the ethoxy group of allyl protected eCTG (**2.6**) means that it does not precipitate out of the solution as readily during the course of the reaction. This allows it to undergo further acid catalysed side reactions which invariably result in oligomeric side products.[29] An alternative synthesis was therefore required. Brotin *et al.* have previously reported the use of scandium(III) triflate as a Lewis acid that is capable of catalytically generating the desired compound.[30] The monomer was reacted with $Sc(OTf)_3$ under anhydrous conditions at 60 °C for 48 hours to yield the crude product (Scheme 2.9). The pure product was isolated by a simple trituration in ethanol to yield **2.6** as a pale cream powder in a good yield of 34%, even surpassing the yield obtained in traditional CTG synthesis. Presumably the milder reaction conditions employed when using scandium triflate as a Lewis acid promote formation of the desired product as opposed to oligomer formation.

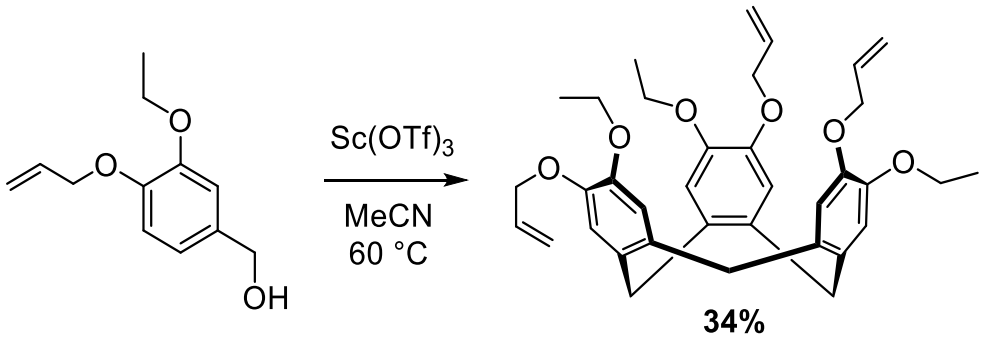


**Scheme 2.9.** Successful synthesis of allyl protected eCTG using $Sc(OTf)_3$ as a Lewis acid catalyst.[30]

Removal of the allyl protecting groups *via* a palladium catalysed deprotection yielded eCTG in a 68% yield (Scheme 2.10). $^1$H-NMR analysis of the product revealed a relatively simple spectrum almost identical to CTG in the aromatic regions. Small differences in the aliphatic region were due to the substitution of the methoxy group for an ethoxy group. The simple spectrum and well resolved methylene bridge doublets shows that the product exhibited the expected $C_3$ symmetry and confirms that pure eCTG had been obtained (Figure 2.13).

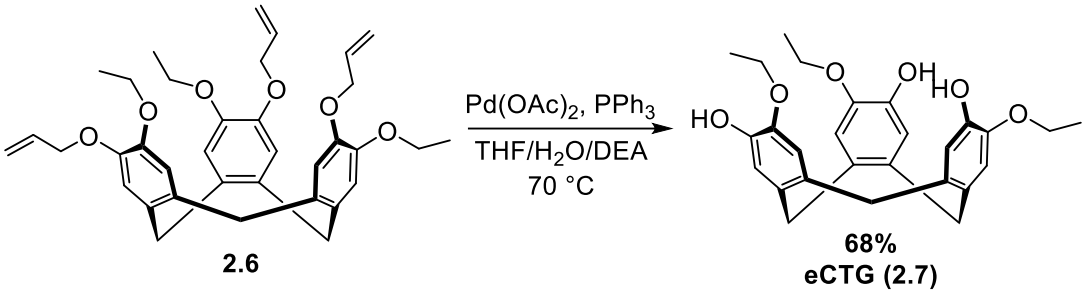


**Scheme 2.10.** Palladium catalysed deprotection of allyl eCTG to furnish eCTG.

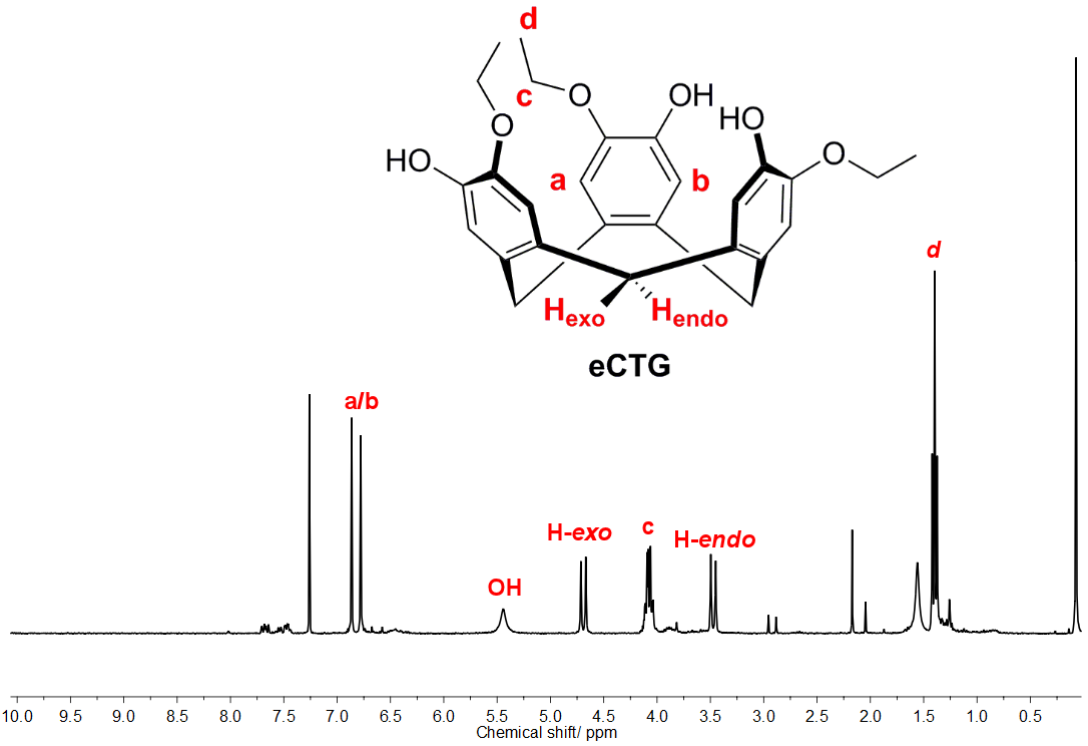


**Figure 2.13.** $^{1}$H-NMR (300 MHz, $CDCl_3$) of eCTG showing characteristic *endo* and *exo* doublets of CTG core.

After the successful synthesis of eCTG the synthesis of a propylated analogue was then pursued. It has been shown by previous PhD student Dr James Henkelis that the solubility of CTG ligands can be improved by substituting the methoxy group for a propoxy group.[31] Unfortunately the reported synthesis of propyl CTG (pCTG) proved to be inconsistent with unrepeatable results. Therefore a reliable method for the synthesis of propyl CTG was developed. The first two steps of the synthesis were performed according to the literature procedure.[31] The hydroxy group on 3-methoxy-4-hydroxybenzyl alcohol was first converted into a propoxy group by reaction with 1-bromopropane. The product then underwent an acid catalysed trimerisation similar to the second step of CTG (Scheme 2.11). Unfortunately, a poor yield of 13% was obtained from this step, presumably due to the excessive formation of polymers and

oligomers once again due to the increased solubility encouraging side product formation.[29]

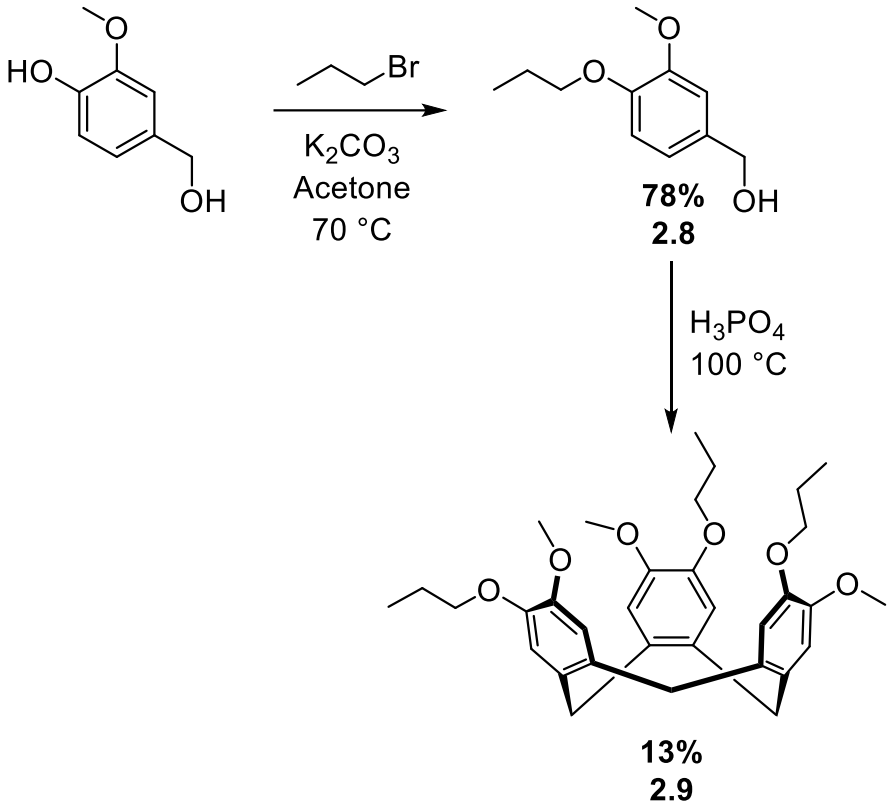


**Scheme 2.11.** First and second step towards the synthesis of pCTG.

The next step required selective conversion of the methoxy groups to hydroxyl groups. Strong Lewis acids such as boron tribromide are regularly used as dealkylating reagents. However the use of boron tribromide on **2.9** results in a statistical mix of inseparable products as no selectivity was observed for methoxy over propoxy groups.[32] The stronger inductive effect of the propyl group compared to the methyl group results in an increase of the electron density of the lone pair situated on the ether oxygen. The increased nucelophilicity promotes reaction at the propoxy group preferentially (Scheme 2.12).[32] The use of boron tribromide is therefore unsuitable for this reaction. Lithium diphenylphosphide is known to selectively remove methoxy groups over propoxy groups, provided that careful monitoring of the stoichiometry and reaction conditions are observed.[33] In order to understand why this is the case the mechanisms of dealkylation must be considered. Unlike conventional dealkylating reagents which are usually strong Lewis acids, lithium diphenylphosphide is a very strong nucleophile. The inductive effect of the extra carbons on the propyl group results in a relatively electropositive α-carbon. The methyl group in comparison remains more electrophilic. This makes the methyl group more susceptible to nucleophilic attack by the lithium

diphenylphosphide, ultimately resulting in the preferential abstraction of the methyl group over the propyl moiety.

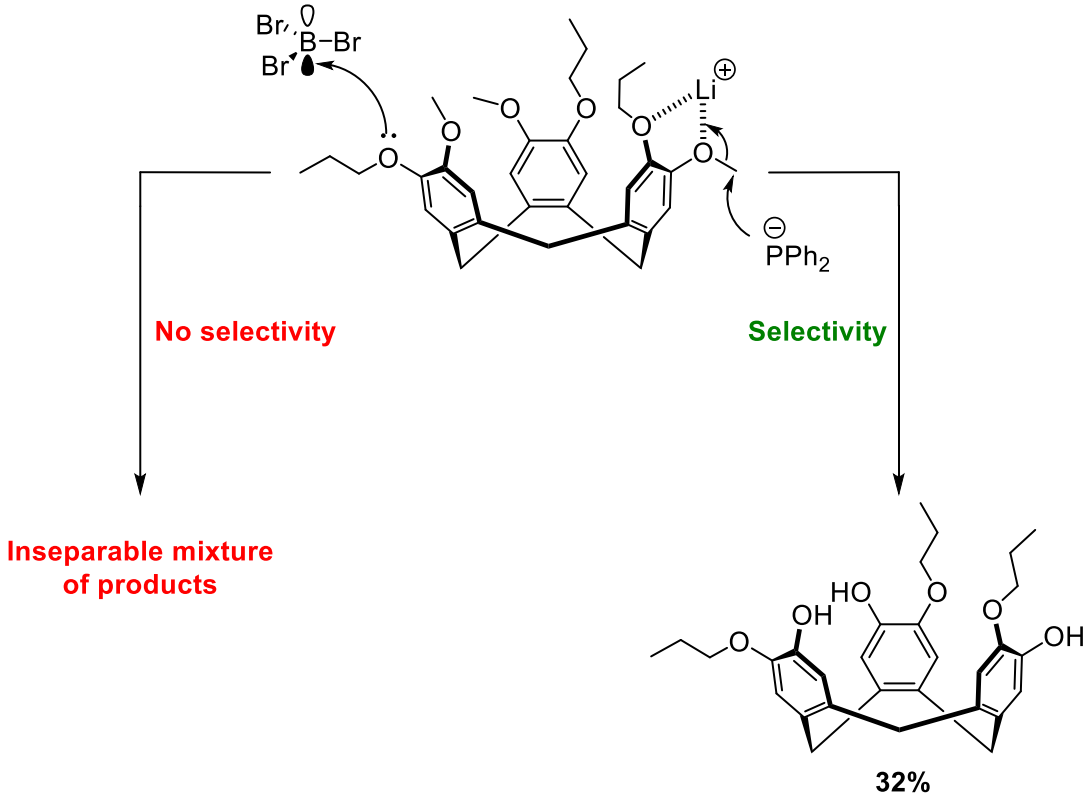


**Scheme 2.12.** Successful synthesis of pCTG utilising lithium diphenylphosphide and unsuccessful attempts using other dealkylating reagents.

*In situ* generation of lithium diphenylphosphide was performed by deprotonating diphenylphosphine with $^{n}$BuLi at -78 °C which was then warmed to room temperature and added slowly to a solution of **2.9** which was stirred overnight.[32] The mixture solidified as the desired product precipitated out of solution. In order to isolate the product a modified work up procedure was employed. Purification of the crude product was achieved by column chromatography on silica using a gradient solvent system of DCM up to 5% methanol in DCM. The pure pCTG was obtained in a reasonable yield of 32%. The $^{1}$H-NMR of pCTG revealed a relatively simple spectrum which was predictably similar to the spectra obtained for both CTG and eCTG. As expected, the aromatic region was almost identical to the previous examples, with small differences in the aliphatic region due to the presence of the propoxy groups. The characteristic methylene CTG doublets were present and well resolved indicating a $C_3$ symmetric product and confirming complete removal of the methyl groups and no reaction of the desired propyl groups (Figure 2.14).

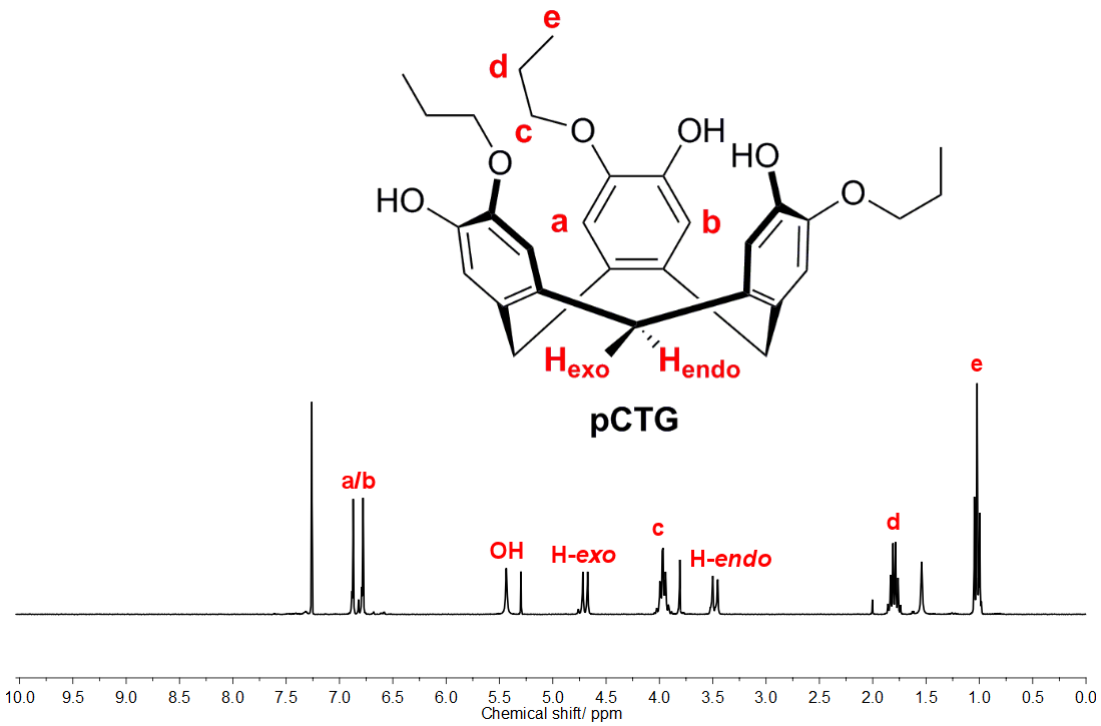


**Figure 2.14.** $^{1}$H-NMR (300 MHz, $CDCl_3$) of pCTG showing characteristic *endo* and *exo* doublets of CTG core.

The successful synthesis of longer alkyl chain derivatives of CTG was a significant step towards solubilisation of CTG based metallo-cryptophanes. In order to furnish the desired ligand, the ethoxy and propoxy modified CTG scaffolds were appended with 3-pyridyl-4'-carboxyazobenzene (Scheme 2.13). This was achieved by reacting modified CTG scaffolds with the acid chloride of the azobenzene 'arm' in the presence of trimethylamine as a scavenger base. The reactions were monitored by mass spectrometry which revealed complete substitution of the upper rim hydroxyl groups occurred after three days. A large excess of the azobenzene arm was required to push the reaction fully to completion. The resultant crude products were triturated in methanol and filtered to yield the products **L2** and **L3** in 61% and 57% yields respectively.

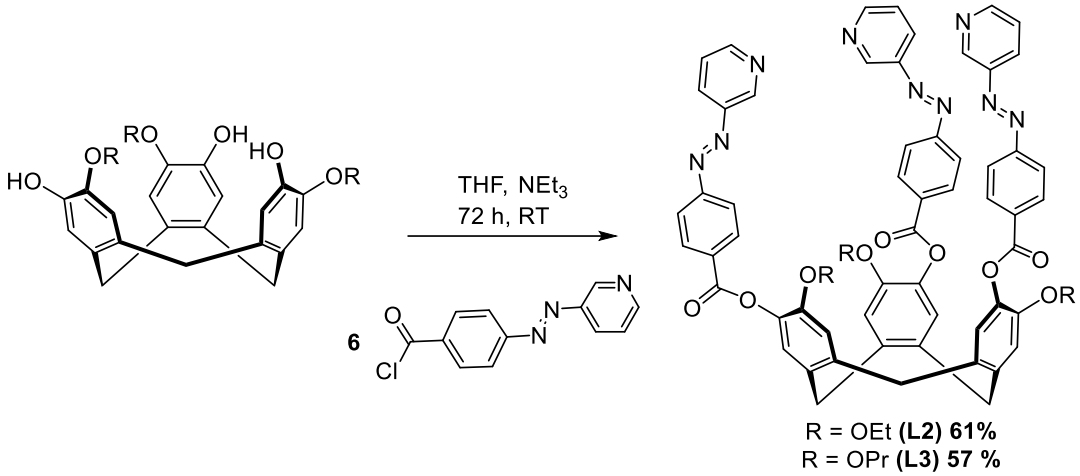


**Scheme 2.13.** Synthesis of solubilised azobenzene appended ligands **L2** and **L3**.

Comparison of the $^{1}$H-NMR of **L1**, **L2**, and **L3** revealed, as expected, very similar spectra, only differing substantially in the aliphatic region due to the differing lengths of alkyl chain (Figure 2.15). The resonances of **L2** are subtly broader than for **L1** and **L3**, likely due to the presence of small amounts of mono and di substituted eCTG cores. The simple spectra and clean doublets of the *endo* and *exo* protons on the CTG bowl provided evidence that total substitution of the upper rim hydroxyl groups has occurred as the $C_3$ symmetry has been retained. The complete loss of the hydroxyl peak in the 5-6 ppm region provides further evidence that this has occurred. The ESI-MS provides unequivocal evidence for the formation of **L2** with peaks corresponding to an m/z of $[539.6991]^{2+}$ and $[1078.3892]^{+}$ for **L2** (Figure 2.16). These peaks agree well with the calculated values for an [**L2**+2H]$^{2+}$ and a [**L2**+H]$^{+}$ species of 539.6978 and 1078.3883 respectively. The ESI-MS data obtained for **L3** also provided strong evidence for its formation with m/z peaks of $[560.7228]^{2+}$ and $[1120.4371]^{+}$ observed. These correlate well with the calculated peaks for [**L3**+2H]$^{2+}$ and [**L3**+H]$^{+}$ of 560.7212 and 1120.4352 respectively .

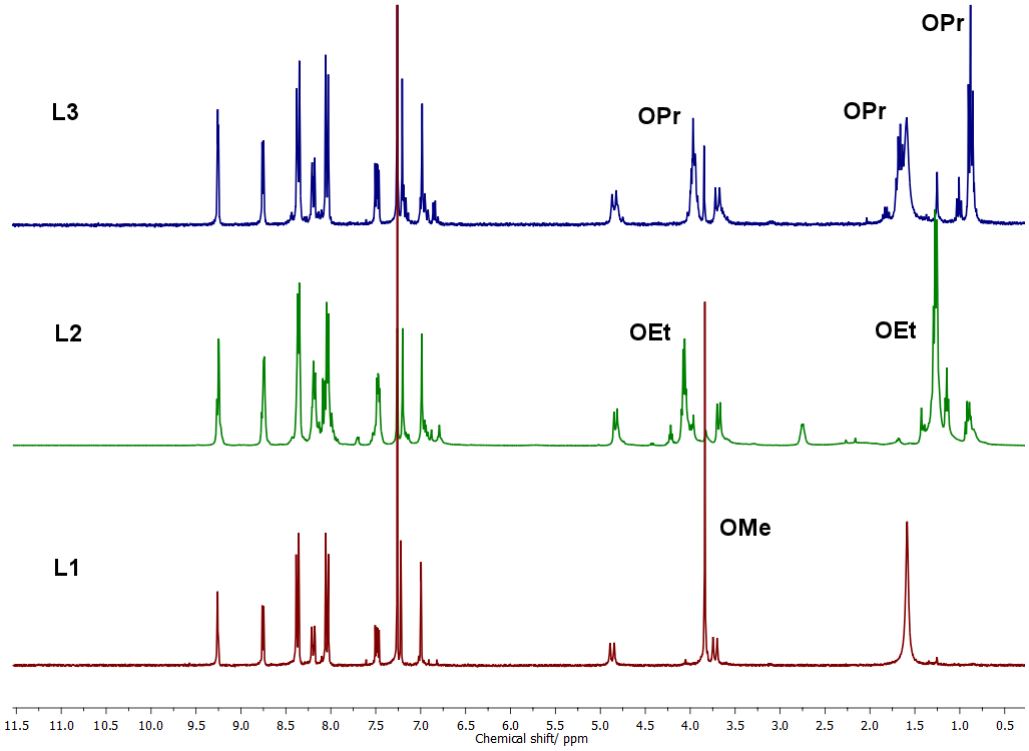


**Figure 2.15.** $^{1}$H-NMR (300 MHz, $CDCl_3$) of azobenzene derivatives of CTG (**L1**, **red**), eCTG (**L2**, **green**) and pCTG(**L3**, **blue**) showing the expected similarity between the spectra.

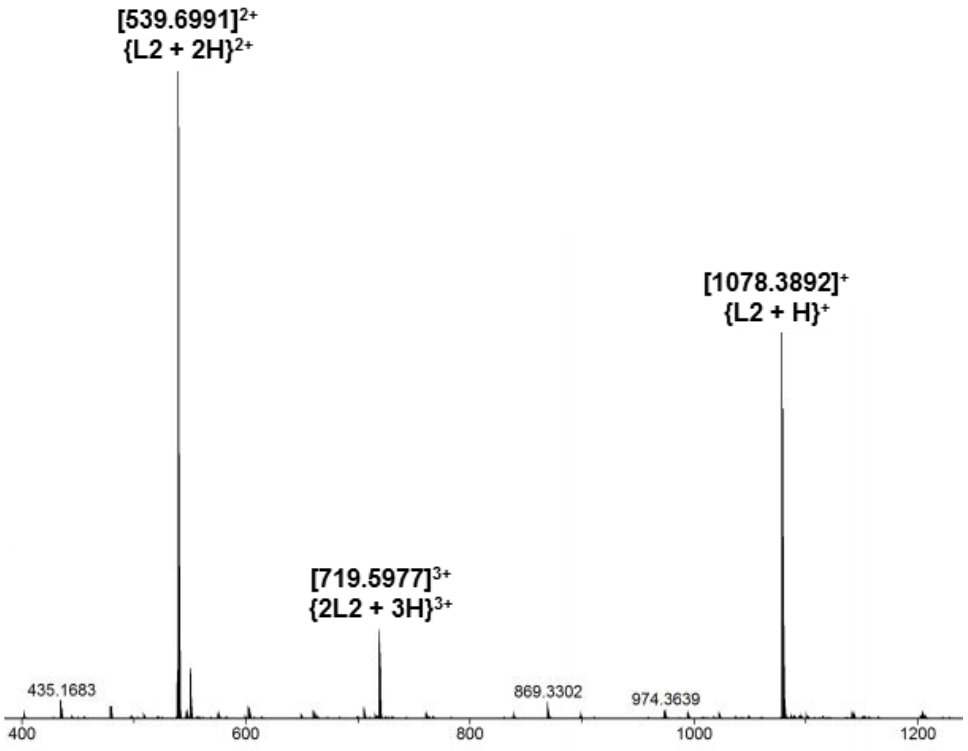


**Figure 2.16.** HRMS spectrum of **L2**.

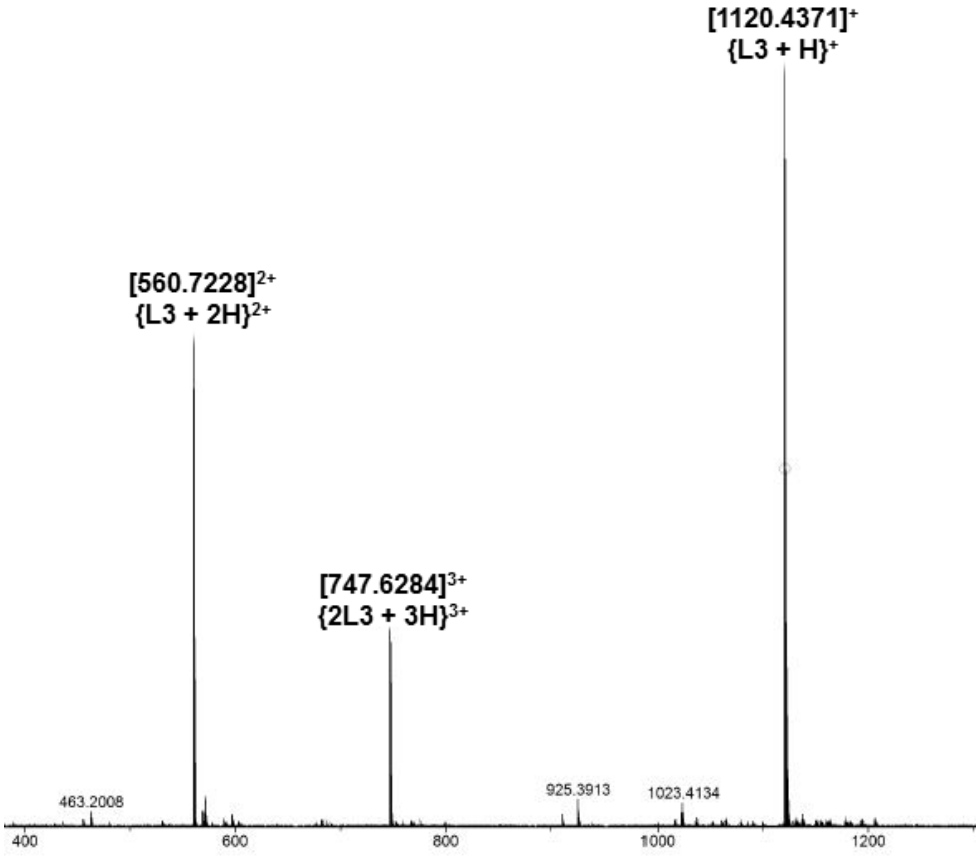


**Figure 2.17.** HRMS spectrum of **L3**.

An interesting feature that was noted in the ESI-MS of **L2** was the peak present at 719.5977 which corresponded to a [2**L2** + 3H]$^{3+}$ species with a calculated m/z of 719.5957. A similar peak at 747.6284 was observed for **L3**, this agreed well with a [2**L3** + 3H]$^{3+}$ species bearing a calculated m/z of 747.6270. The presence of such peaks suggests that hydrogen bonded dimeric capsules may be forming during the ionisation process. Hydrogen bonded capsules of CTV derivatives have been reported in the literature.[34, 35] Purohit and co-workers have studied a pyridyl appended CTC derivative that was found to form water mediated dimeric hydrogen bonded capsules in the solid state.[35] It is feasible the azobenzene appended ligands may be capable of partaking in such interactions to form proton mediated dimeric capsules.

Both compounds gave fully assignable $^{13}$C-NMR spectra as well as IR spectra which revealed the presence of the expected functional groups. Particularly diagnostic was the presence of the C=O carbonyl stretching frequency at approximately 1750 cm$^{-1}$ for both ligands, consistent with the expected peak for an ester moiety. The existence of this peak confirms the reaction between the CTG substituents and the azobenzene arm was a success.

The structures of both **L2** and **L3** were confirmed by X-ray crystallography. In both cases single crystals suitable for X-ray diffraction were grown from the diffusion of diethyl ether into a saturated solution of the ligand in chloroform. The crystals exhibited considerably better diffraction than crystals of **L1**, however the data was still collected using synchrotron radiation at Diamond Light Source to improve the resolution. Despite the only structural difference between ligands being the length of the alkoxy chain, the ligands all packed in vastly different ways in the crystalline state.

Oldknow *et al*. has reported the crystal structure of **L1** previously[22] and found that the ligands packed in such a way such that the ligand arms on adjacent molecules π-π stacked. The result was the formation of channels with diameters as large as 2 nm across (Figure 2.18).[22] The large amount of disordered solvent in the channels within the crystal were attributed to the poor resolution obtained during SCXRD experiments.

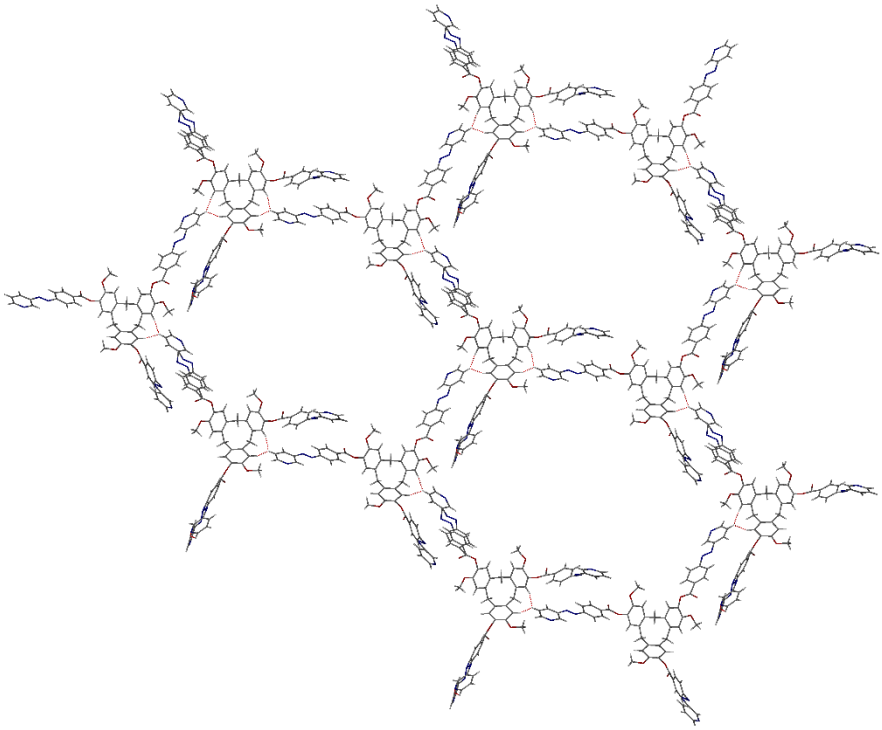

**Figure 2.18.** From the crystal structure of **L1** showing the large channels formed in the crystal due to π-π stacking between the azobenzene arms[22]

The crystal structure of **L2** was solved using SHELXT and refined using least squares SHELXL. The crystals were of very poor quality as evidenced by a high R(int) for a triclinic cell of 30%. Large voids were present within the crystal lattice and as such, a solvent mask was applied. All non-hydrogen atoms were refined anisotropically. The crystal structure of **L2** reveals that the substitution of the methoxy group for an ethoxy completely changes the packing (Figure

2.19). The ligands form columns of the same enantiomer through bowl in bowl stacking interactions displaying an average distance of 4.692 Å. The *M* enantiomer stacks in a parallel yet opposite direction to the *P* enantiomer. As well as the bowl-in-bowl stacking interaction, π-π interactions are observed between the azobenzene groups. Each azo group interacts with the phenyl ring of the azobenzene group above it and the pyridyl ring of the azobenzene group below it with an average distance of 3.622 Å, consistent with π-π stacking interactions. Unlike **L1**, interactions between the individual molecules are limited to interactions within the same stack and for this reason no large void spaces are observed within the crystal lattice, explaining why the data was somewhat easier to collect.

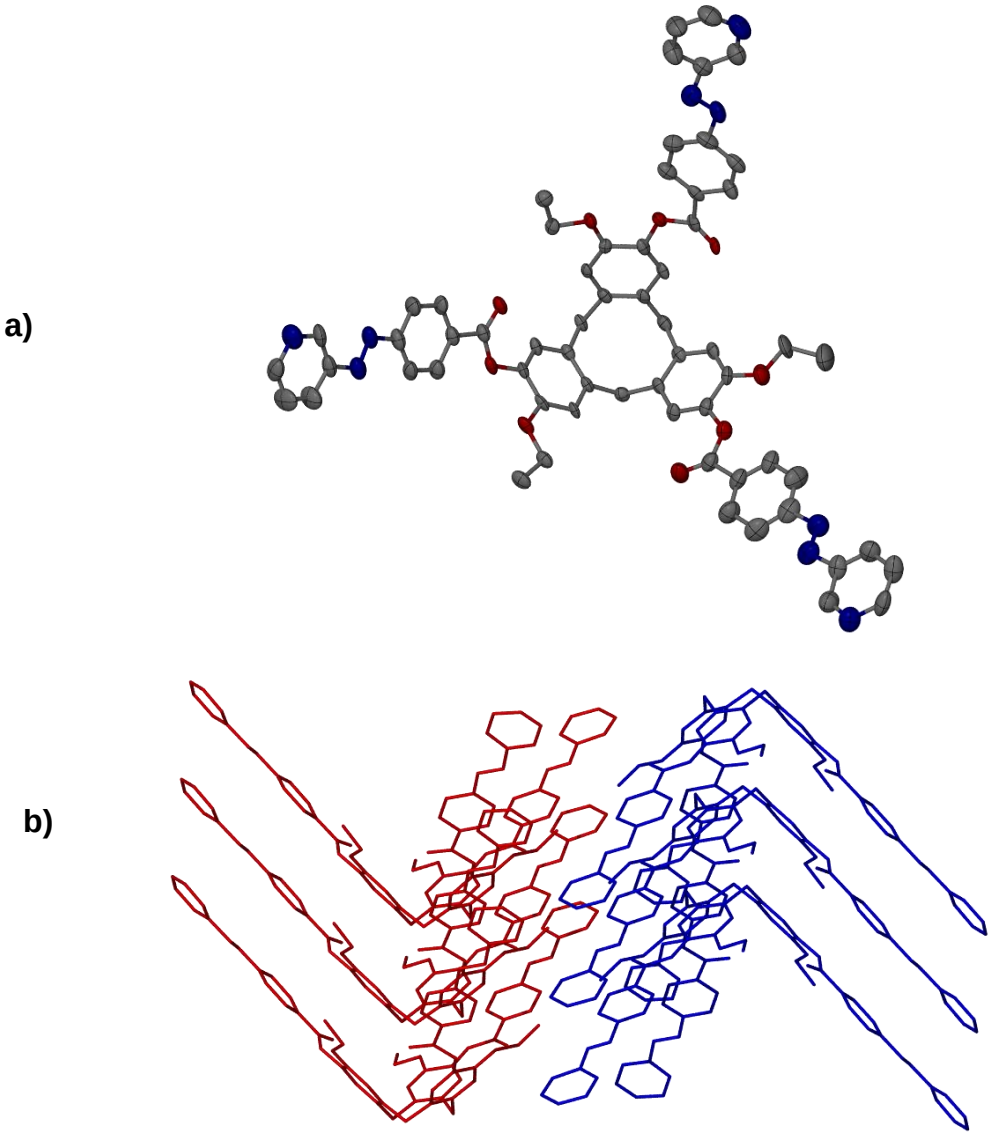


**Figure 2.19.** SCXRD structure of **L2**, **a)** Asymmetric unit, ellipsoids are shown at 50% probability, hydrogen atoms omitted for clarity, **b)** Bowl in bowl stacking arrangement of **L2**, different ligand enantiomers are shown in red and blue.

The crystal structure of **L3**•$CHCl_3$ was solved using SHELXT and refined using least squares SHELXL. All non-hydrogen atoms were refined anisotropically. Analysis of the disagreeable reflections indicates that the crystals used were not single and may be twinned. The crystal structure of **L3**•$CHCl_3$ is unlike the structures of both **L1** and **L2**. The crystal itself is racemic and contains equal quantities of *M* and *P* enantiomers. Unusually for a CTG containing compound there are no bowl-in-bowl stacking interactions present in the solid state. Instead, the crystal is dominated by a vast array of π-π stacking interactions between adjacent molecules. Each pyridyl group located at the terminus of the azobenzene motif forms a π-π interaction with a neighbouring pyridyl group on a different ligand. The average centroid to centroid distance between these rings is 3.983 Å, small enough to facilitate the π-π interaction. The result is a 2D sheet of ligands engaged in π-π interactions which stack to give the packing arrangement shown in Figure 2.20.

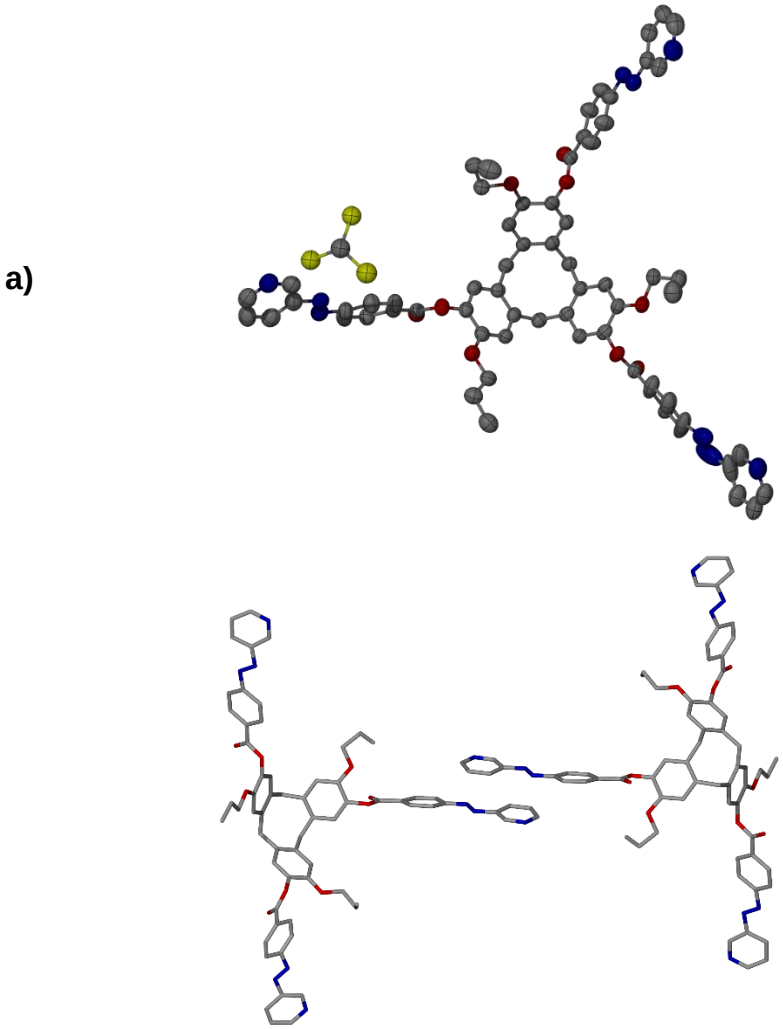


**Figure 2.20.** SCXRD structure of **L3**•$CHCl_3$, **a)** Asymmetric unit, ellipsoids are shown at 50% probability, hydrogen atoms omitted for clarity, **b)** π-π stacking interactions between adjacent azobenzene arms of **L3**•$CHCl_3$, hydrogen atoms and solvents of crystallisation have been omitted for clarity.

The π-π stacking interactions between neighbouring ligands form a grid composing of an infinite array of six membered rings. The crystal lattice is composed of seven independent networks which do not engage in π-π stacking interactions with one another. Each of these grids is interpenetrated by six independent π-π stacked networks. The networks are arranged in such a way such that they form a Borromean entanglement where any networks that are selected will be composed of an infinite series of Borromean rings.

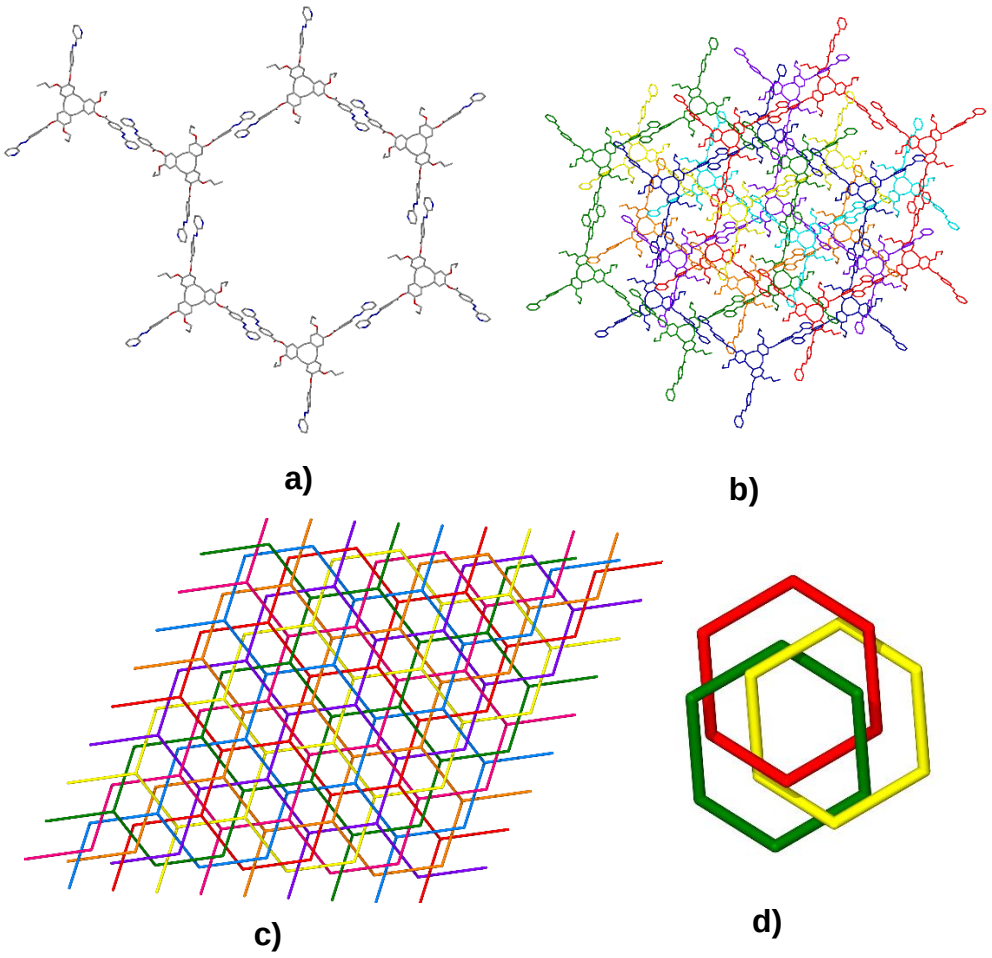


**Figure 2.21.** SCXRD structures of **L3**•$CHCl_3$; **a)** six membered ring formed by π-π stacking interactions between ligands, **b)** interpenetration of seven π-π stacked lattices, **c)** stick representation of the grid of seven interpenetrated networks, **d)** Borromean rings formed between the individual π-π stacked networks.

The synthesis of the ligands **L2** and **L3** provided access to solubilised $M_3L_2$ metallo-cryptophanes. In order to achieve this, appropriately designed metal tectons were required to facilitate the self-assembly of these complex species.

## 2.5 Expansion of the Metal Tecton Toolkit

When designing a metallo-tecton intended to self-assemble into a discrete metallo-cage there are a number of approaches available to the supramolecular chemist. One such strategy that can be employed is to block specific coordination sites with chelating ligands so as to limit the number of sites that the ligand can react at, driving the formation of discrete species.[36, 37] An excellent example of this was described by the Thomas group with their rational design of an $M_8L_{12}$ metallo-cube.[38] The ruthenium tecton was designed so that three of the coordination sites were blocked by a 1,4,7-trithiacyclononane group. The remaining sites were occupied by easily displaced DMSO groups and chloride anions. The available sites were arranged in a *fac* arrangement with a 90° angle between them. This arrangement effectively made the ruthenium centres templates for the vertices of a cube. When reacted with the linear coordinating group 4,4'-bipyridine, a $M_8L_{12}$ metallo-cube self-assembled, highlighting the synthetic potential of a rationally designed metallo-tecton.

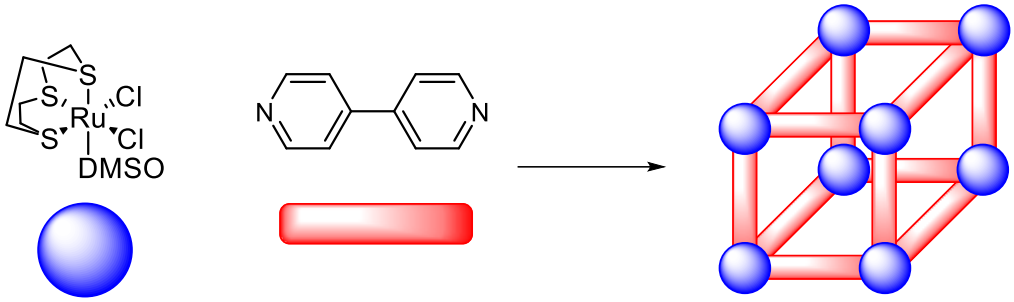


**Figure 2.22.** $M_8L_{12}$ metallo-cube reported by the Thomas group, bearing rationally designed ruthenium tectons acting as the verticies.[38]

In the case of metallo-cryptophanes, this usually means blocking coordination sites so that the only available coordination sites remain at a 90° angle to each other.[22, 24, 39, 40] Formation of discrete species such as metalllo-cryptophanes is encouraged by preventing formation of oligomers or coordination polymers due to the absence of available coordination sites.[41] These tectons can go on to form a species known as a *cis* linked $M_3L_2$ cryptophane. Although rarer, there are a number of examples where a metallo-tecton bearing available coordination sites at 180° to each other have produced *trans* linked $M_3L_2$ metallo-cryptophanes. Often these involve using linear metal ions such as Ag(I) or Cu(II) to direct the assembly.[41, 42] These examples are rarer and typically require a greater degree of flexibility in the ligand system.

Several classes of metallo-cryptophanes have been synthesised in the Hardie group utilising iridium phenylpyridine (ppy) tectons.[22, 25] Most notably for this

project is the reported self-assembly of the iridium phenylpyridine tectons with the azobenzene appended CTG ligand **L1**.[22] The strongly bound, chelating phenylpyridine moieties afford protection to all but two of the coordination sites. The remaining two sites are held 90° apart by the rigid octahedral geometry of the iridium centre and are occupied by weakly bound acetonitrile ligands. These are easily displaced by an incoming ligand and help to promote reaction at these sites (Figure 2.23). These two features help to drive the thermodynamic minimum towards metallo-cryptophane formation.

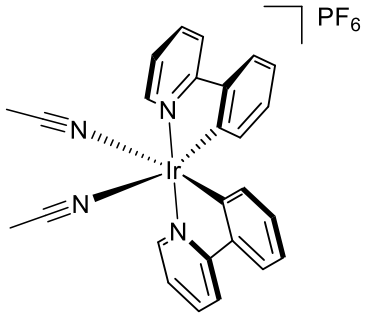


**M1**

**Figure 2.23.** The structure of the iridium ppy tecton showing protection of coordination sites by phenylpyridine groups and the 90° bond angle between available coordination sites occupied by acetonitrile.

The metallo-cryptophanes made using **L1** and the metal tecton above (**M1**) was only sparingly soluble in nitromethane. The use of polar aprotic solvents such as DMSO and DMF resulted in complete dissolution of the cage. $^{1}$H-NMR and electrospray mass spectrometry revealed that the solvent had displaced the **L1** from the metal centre, resulting in the complete destruction of the cage in the process. The same result was observed when acetonitrile was used. The cage was nearly completely insoluble in all other solvents tested. In order to photoisomerise the azobenzene groups UV light of approximately 350 nm is required. This made the use of nitromethane as a solvent unsuitable due to a high UV/vis solvent cut-off value of 380 nm. Moreover, safety issues associated with the potentially explosive decomposition of nitromethane under UV light further complicated matters. Fortunately, the phenylpyridine groups bound to the iridium centre provide an easily modifiable site from which to increase the solubility of the metallo-cryptophane.

The addition of fluorine atoms onto the phenylpyridine groups increases the lipophilicity and therefore the solubility of the complexes in organic solvents. This approach has been used by the Hardie group previously.[41, 43] A heavily fluorinated ppy was synthesised according to the literature by a palladium

catalysed Suzuki-Miyaura cross coupling.[44] In order to obtain the desired 90° bond angle between vacant coordination sites a two-step procedure was used. The first step was to react the fluorinated ppy with iridium trichloride in a 2:1 ratio to form the chloride bridged iridium dimer (Scheme 2.14). The reaction with the fluorinated derivative took 48 hours, double that required for the non-fluorinated ppy. This is likely due to the addition of several fluorine atoms which withdraws electron density from the ppy, making the bonding orbitals less accessible to the iridium and decreasing the reactivity. This effect also plays an important part in metallo-cryptophane assembly discussed later. The formation of the dimer is important in controlling the stereochemistry and it ensures that when the dimer is split in the second step the accessible coordination site will be always be found *cis* to one another. The splitting of the dimer was performed in acetonitrile which replaced the chloride ions that were abstracted using silver hexafluorophosphate as a halide abstracting reagent (Scheme 2.14).

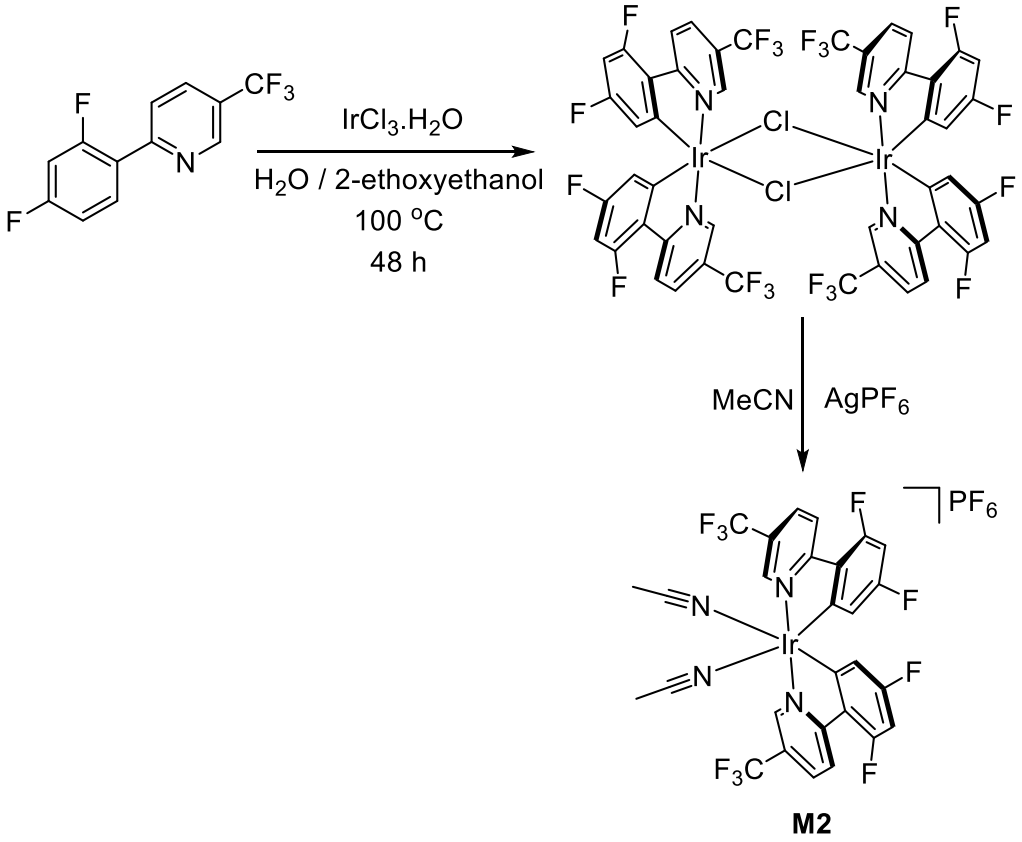


**Scheme 2.14.** Synthesis of fluorinated ppy iridium tecton **M2**.

The composition of the resultant metal tecton was confirmed by $^{1}$H-NMR spectroscopy. A large downfield shift of the signal associated with $H_a$ is consistent with complexation of the pyridyl ring to a metal centre. An upfield shift of the signal arising from $H_e$ was also observed and once again can be

rationalised by considering the effect of cyclometallation on the phenyl ring. The formation of the C-Ir bond pushes electron density into the phenyl ring, shielding the proton $H_e$ in the process resulting in a upfield shift of the proton signal. Despite the possibility of the formation of isomers in the reaction, the lack of peaks in the spectrum is indicative of the formation of only one species (Figure 2.24). According to the literature precedent the species that exclusively forms consists of the pyridyl groups in a *trans* arrangement to one another with the cyclometallated phenyl rings residing *cis* to one another. Due to the positive charge residing on the complex good quality ESI-MS spectra could be obtained (Figure 2.25). The species was detected having lost the hexafluorophosphate anion and between zero and two acetonitrile adducts. Peaks at m/z 709.0307 (**M2** – 2MeCN – $PF_6$)$^+$, 750.0570 (**M2** – MeCN – $PF_6$)$^+$ and 791.0835 (**M2** – $PF_6$)$^+$ correlated well with calculated values of 709.0308, 750.0574 and 791.0839 respectively. $^{13}$C-NMR data was also consistent with the proposed structure.

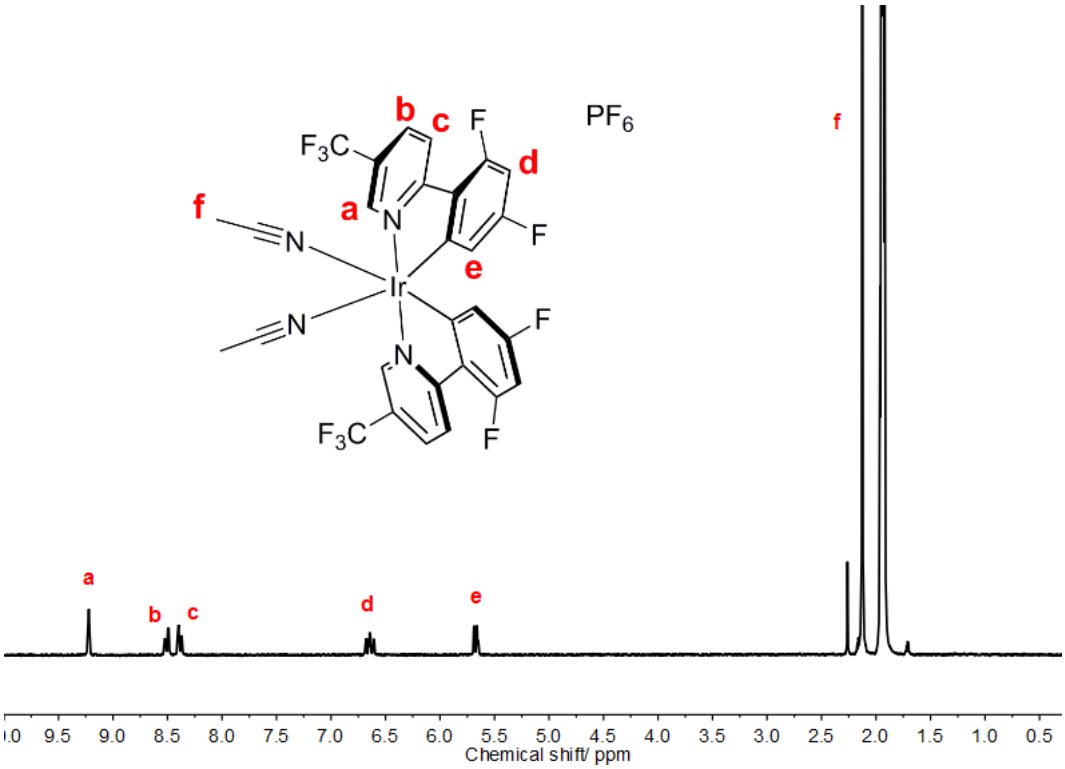


**Figure 2.24.** $^1$H-NMR (300 MHz, $d_3$-MeCN) of **M2**, confirming the formation of only one species in the reaction.

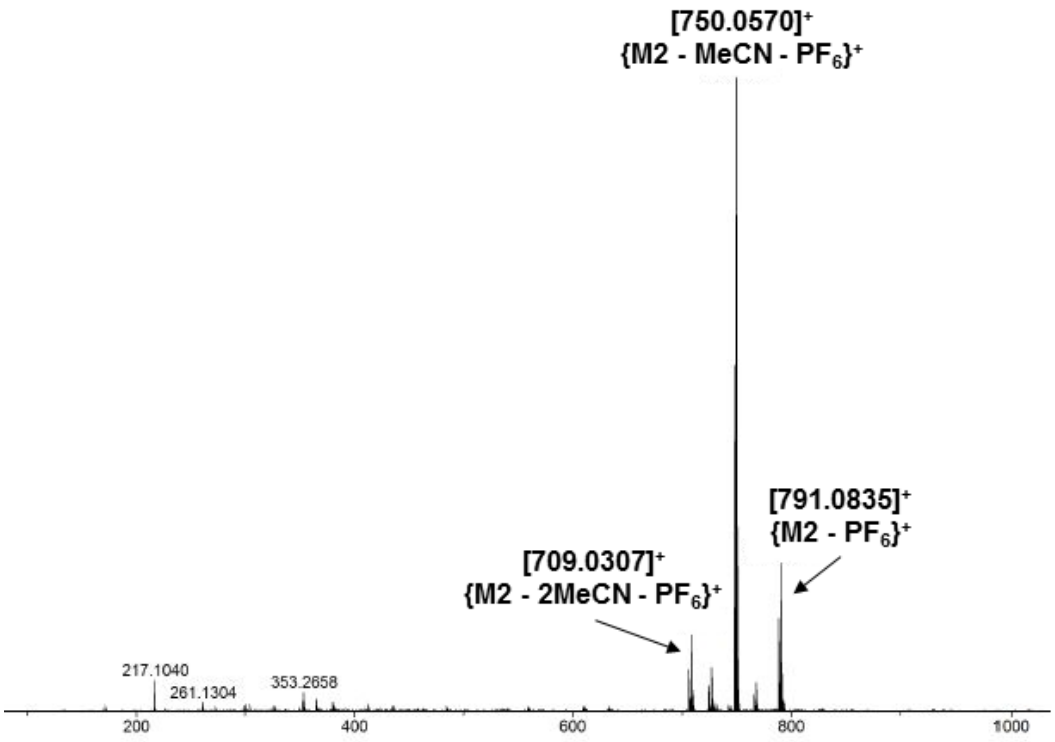


**Figure 2.25.** HRMS of **M2** showing the [**M2**-MeCN-$PF_6$]$^+$ as the major species detected.

The metal tecton existed as a 50:50 racemic mixture of Δ and Λ enantiomers (Figure 2.26). For the purpose of this work it was not necessary to separate the enantiomers, the system would self-assemble regardless if a racemic mixture was used or not.

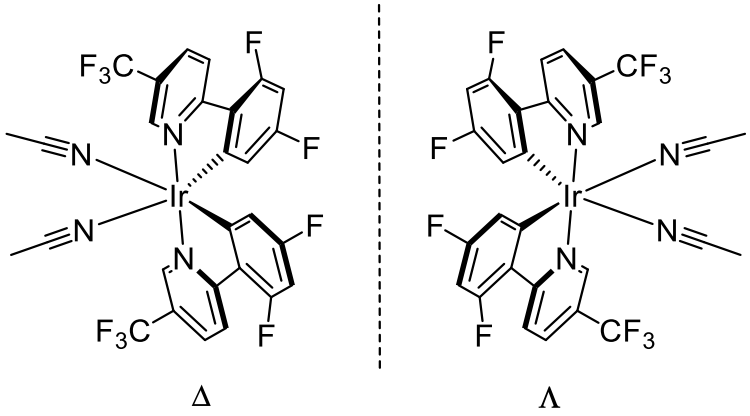


**Figure 2.26.** Two possible enantiomers of iridium phenylpyridine tectons Δ and Λ.

In addition to solubilising the metal tecton it would be desirable to introduce a metal centre that would be less likely to partake in FRET interactions, which could potentially reduce the switching efficiency of the ligand. The luminescent nature of iridium complexes is a result of spin-orbit coupling which facilitates the spin forbidden intersystem crossing between the excited singlet state to an excited triplet state (Figure 2.27). Subsequent electronic relaxation of the

molecule back to the singlet ground state releases a photon in the process, making the luminescence of the iridium phenylpyridine complexes phosphorescent in nature.[45, 46]

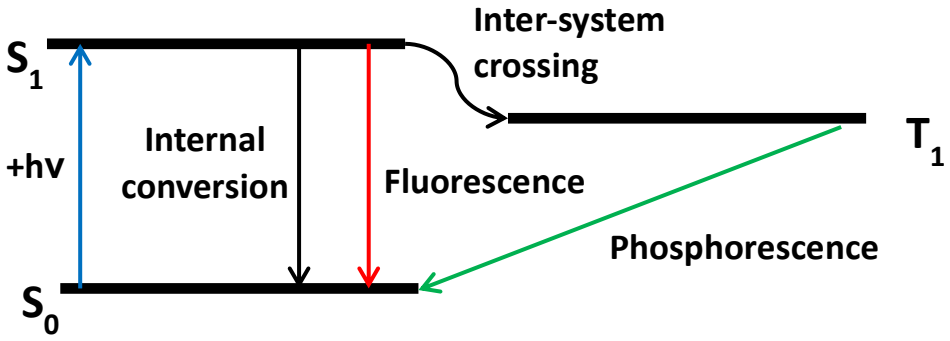


**Figure 2.27.** Simplified Jablonski diagram showing excitation by light (**blue**) to the excited singlet state, non-radiative relaxation by internal conversion (**black**). Radiative relaxation pathways are fluorescence (**red**), and phosphorescence (**green**).

Rhodium, being in the same group as iridium would likely react in the same way, providing access to a novel series of rhodium metallo-cryptophanes. Rhodium is in the row above iridium and as a result of being lighter it cannot spin-orbit couple as effectively as iridium, this is due to spin orbit coupling being a relativistic phenomenon which only affects the heavier elements.[47] The outcome of this effect is a reduction in the photophysical activity of rhodium phenylpyridine complexes. They show much weaker luminescence as well as slightly blue-shifted absorption profiles when compared to iridium phenylpyridines. The result is a metal tecton which would be less likely to quench the switching of the azobenzene through an energy transfer deactivation pathway such as FRET or PET.

Isostructural analogues of the iridium tectons were synthesised containing rhodium in place of iridium as the metal centre. Due to the similar nature of the two metals the syntheses of the tectons followed identical procedures (Scheme 2.15).[48] This was to ensure that the rhodium tectons exhibited the required *cis* protection.

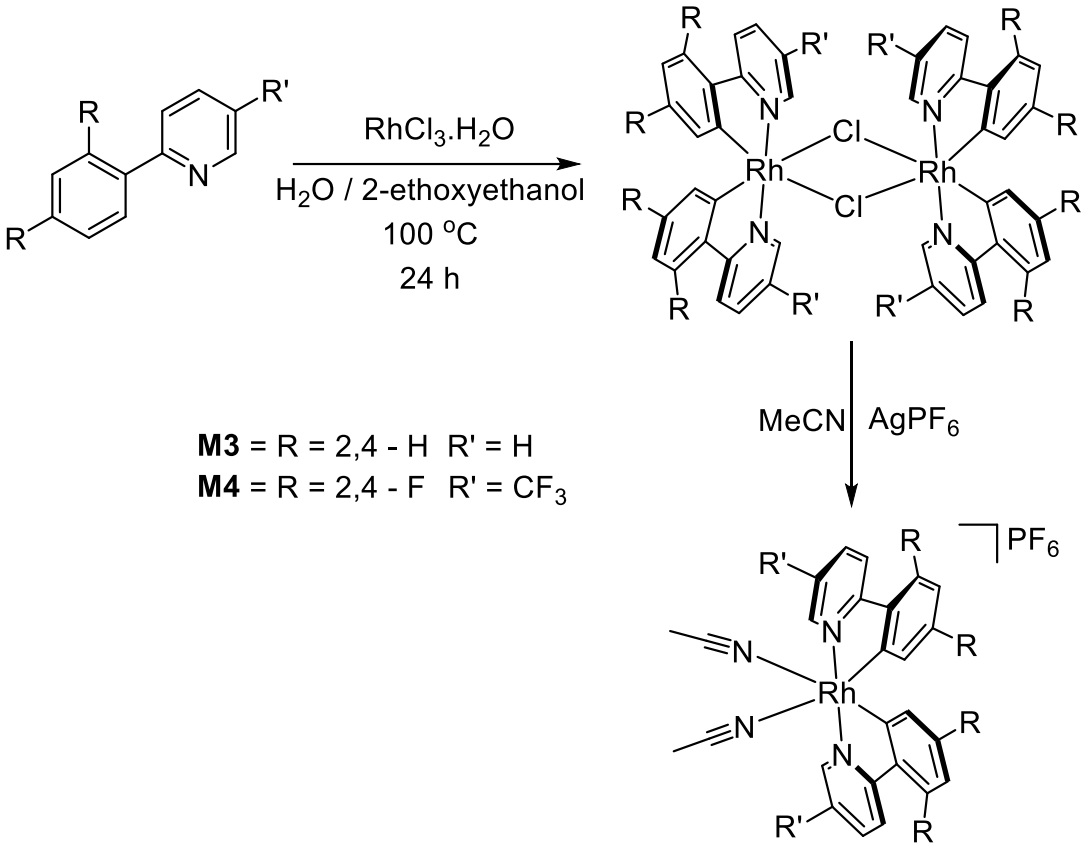


**Scheme 2.15.** Synthesis of rhodium metal tectons **M3** and **M4**.[48]

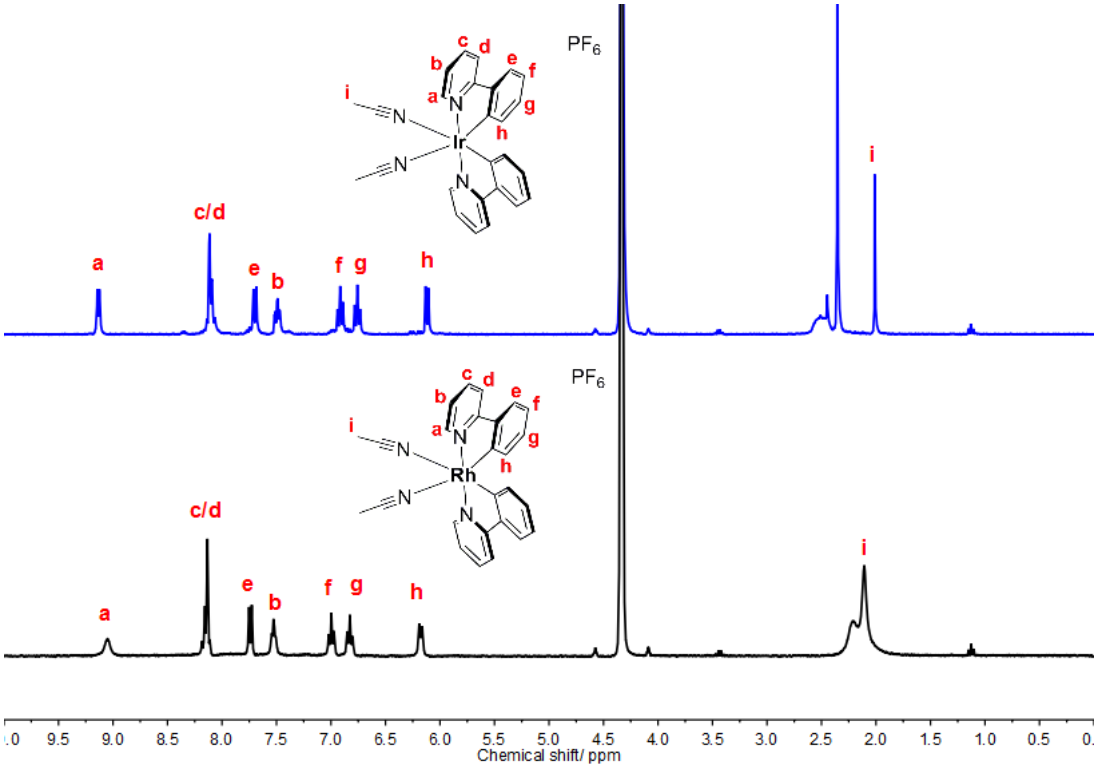


**Figure 2.28.** Comparison of the $^{1}$H-NMR spectra (300 MHz, $d_3$-$MeNO_2$) of the iridium phenylpyridine tecton (**M1, blue**) and rhodium phenylpyridine tecton (**M3, black**), showing the expected similarities between the analogues.

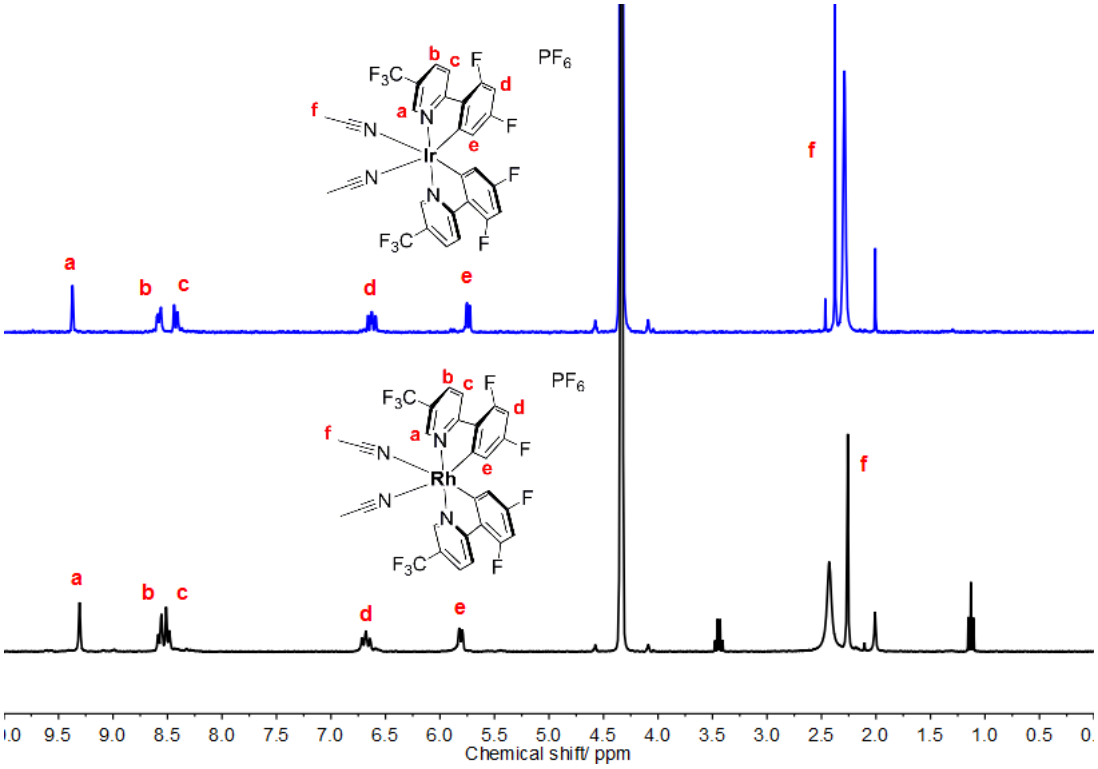


**Figure 2.29.** Comparison of the $^{1}$H-NMR spectra (300 MHz, $d_3$-$MeNO_2$) of the iridium phenylpyridine tecton (**M2, blue**) and rhodium phenylpyridine tecton (**M4, black**), showing the expected similarities between the analogues.

The rhodium metallo-tectons were analysed by $^{1}$H-NMR spectroscopy which revealed striking similarities between spectra of the iridium and rhodium analogues (Figure 2.28 and Figure 2.29). This was expected as iridium and rhodium are isoelectronic and chemically similar to one another. This similarity helped to confirm the identity of the new complexes. ESI-MS spectra of the complexes provided unequivocal evidence of their formation. An experimental peak m/z at 411.0381 (**M3** – 2MeCN – $PF_6$)$^+$ and 848.0742 (2**M3** + CN)$^+$ correlated well with a calculated m/z of 411.0363 and 848.0762 for **M3** (Figure 2.30.a). Similarly, an experimental m/z peak at 618.9760 (**M4** – 2MeCN – $PF_6$)$^+$ and 660.0015 (**M4** – MeCN – $PF_6$)$^+$ agree well with calculated values of 618.9734 and 659.9999 (Figure 2.30.b).

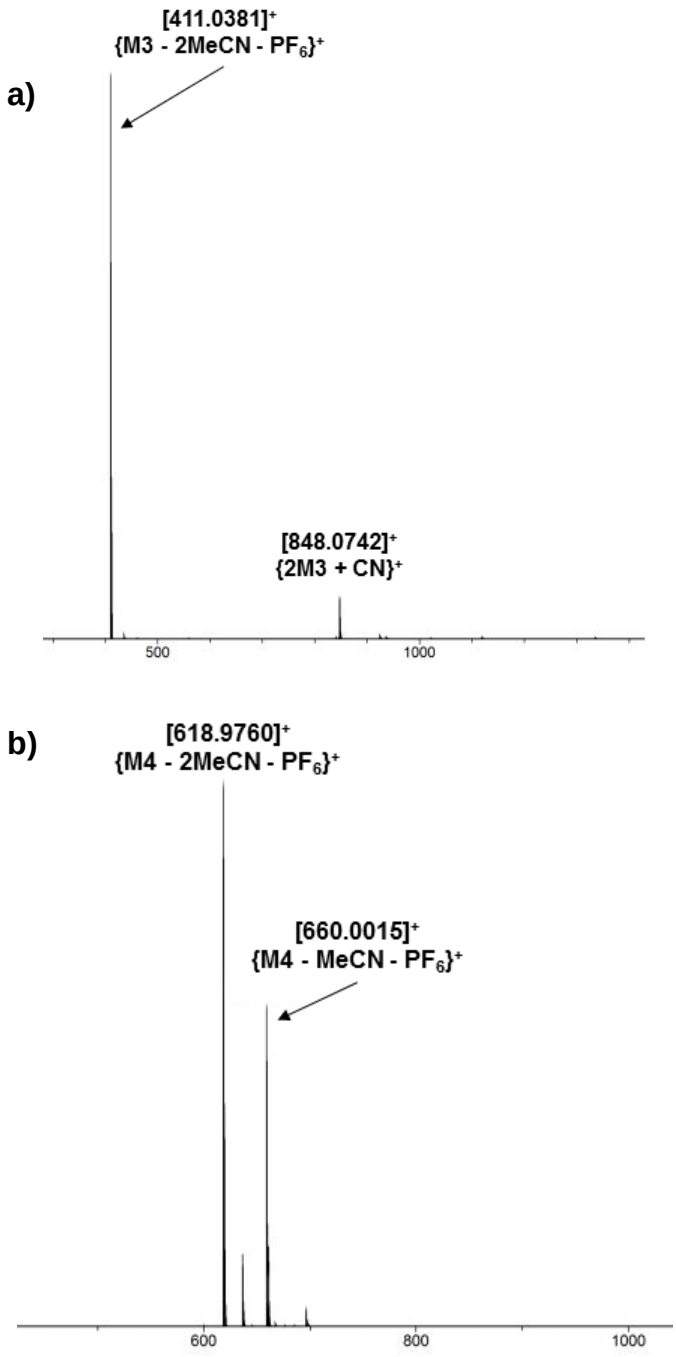


**Figure 2.30. a)** HRMS spectrum of **M3**, **b)** HRMS spectrum and **M4**.

The differences between the iridium and the rhodium complexes were immediately obvious. Both were low spin $d^6$ octahedral complexes which are kinetically inert due to the associated strong crystal field stabilisation energies. The rhodium complexes however were significantly more labile due to a smaller value of $\Delta_{oct}$ as a result of being in a higher row on the periodic table. Shorter reaction times were required which also has implications that the rhodium metallo-cryptophanes may be more dynamic in solution and have the ability to correct errors faster than the iridium counterparts. The solid and solution states of the rhodium tectons were colourless, unlike the iridium

analogues which exhibited a brilliant yellow colour. Moreover, they did not visibly luminesce under UV irradiation unlike the iridium tectons which upon illumination by UV light displayed intense cyan phosphorescence. These differences can be attributed to the poorer ability of rhodium to spin-orbit couple compared to iridium.

In addition to the rhodium tectons, platinum phenylpyridine tectons were also synthesised. The reason for this was twofold. Firstly the emission of platinum phenylpyridine tectons is significantly red shifted compared to the emission from iridium phenylpyridine tectons, often appearing in the red part of the spectrum.[49] This may improve the switching efficiency by reducing accessible deactivation pathways to the azobenzene group by removing overlapping absorption and emission bands from the approximately 350 nm centred azobenzene absorption. Moreover it was desirable to gain more understanding of the self-assembly processes governing cage formation. In particular if the azobenzene functionalised metallo-cryptophanes could self-assemble with metals other than group 9 octahedral metals. The platinum tectons developed adopted a square planar geometry with the phenylpyridine group acting as a *cis* protecting group and the vacant coordination sites at a 90° angle to each other. As discussed earlier the *cis* protection of the metal helps to prevent polymer forming side-reactions to occur.[2, 24, 25]

The platinum tectons were synthesised in a two-step procedure analogous to that used to furnish the iridium and rhodium tectons (Scheme 2.16). Potassium tetrachloroplatinate(II) reacted with 2-phenylpyridine derivatives to form a dichloro-bridged cyclometalated dimer. The dimer was split in the presence of acetonitrile which occupied the vacant coordination sites. The use of silver hexafluorophosphate as a halide abstracting reagent yielded the *cis* protected platinum tectons in good yields.

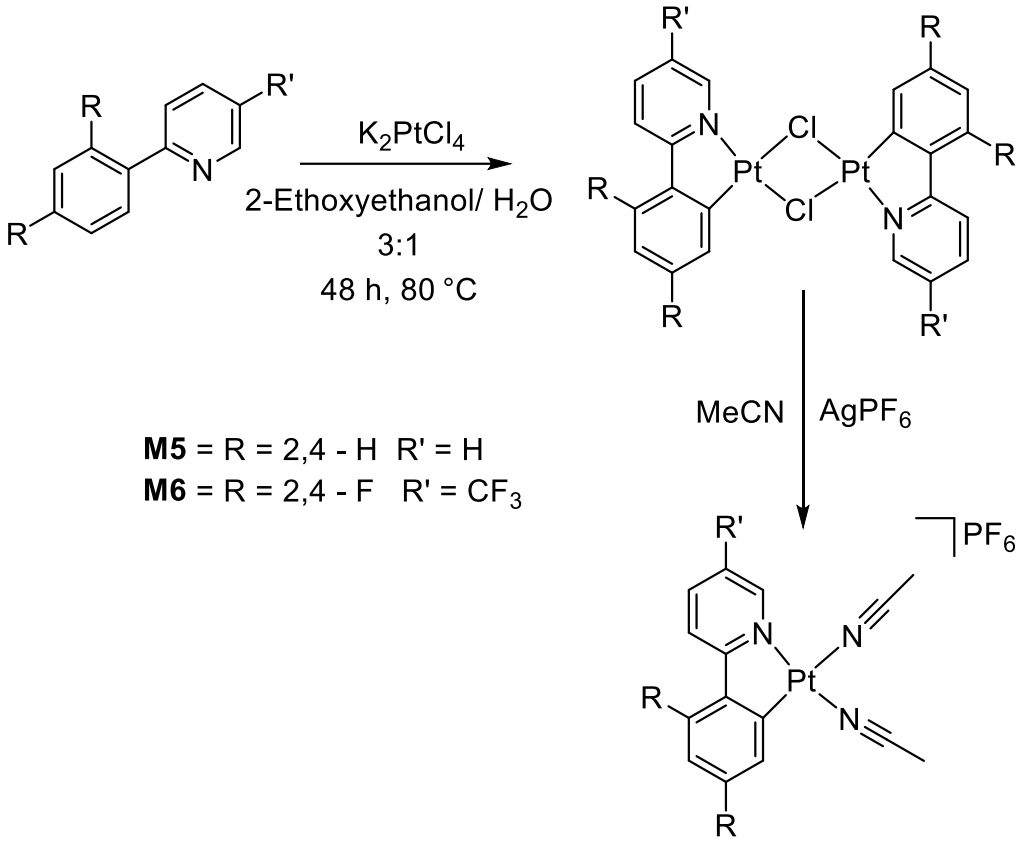


**Scheme 2.16.** Synthesis of platinum phenylpyridine tectons.

The formation of the desired complexes was confirmed using a combination of HRMS and $^{1}$H-NMR. The $^{1}$H-NMR spectra of **M5** and **M6** both featured characteristic $^{3}$J splitting of the signal arising from the proton *ortho* to the pyridyl nitrogen, arising from coupling to the $^{195}$Pt centre. This observation, along with a downfield shift of the same signal is consistent with successful platinum complexation. An upfield shift was also observed for the protons on the cyclometalated phenyl ring. Both iridium and rhodium phenylpyridine tectons displayed the same trend due to the metal centre donating electrons into the phenyl ring, leading to an increase in the shielding experienced by the adjoining proton environments.

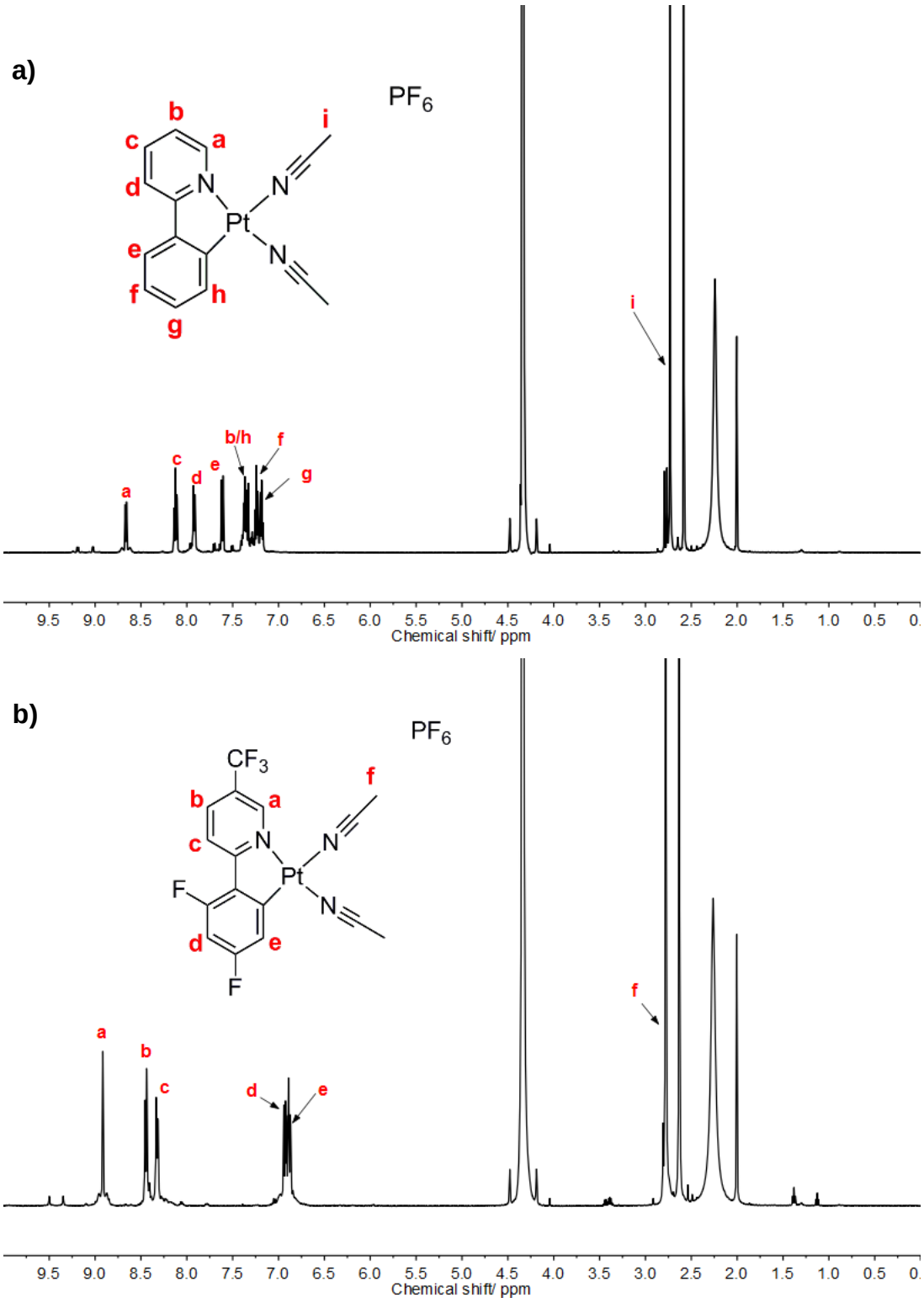


**Figure 2.31. a)** $^{1}$H-NMR (500 MHz, $d_3$-$MeNO_2$) of **M5**, **b)** $^{1}$H-NMR (500 MHz, $d_3$-$MeNO_2$) of **M6**.

Further evidence to corroborate the proposed structure was obtained from the ESI-MS spectra of **M5** and **M6**. An experimental peak of m/z 390.0558 (**M5** - MeCN - $PF_6$)$^+$ correlated well with a calculated m/z of 390.0570 for **M5** (Figure 2.32.a). In the HRMS obtained for **M6** contained three main peaks at 535.0512 (**M6** - $PF_6$)$^+$, 512.0358 (**M6** - MeCN - $PF_6$ + $H_2O$)$^+$ and 494.0254 (**M6** - MeCN

- $PF_6)^+$, all three peaks agree remarkably well with calculated values for these species of 535.0515, 512.0356 and 494.0250 (Figure 2.32.b). $^{13}$C-NMR spectra were consistent with the formation of the proposed structure.

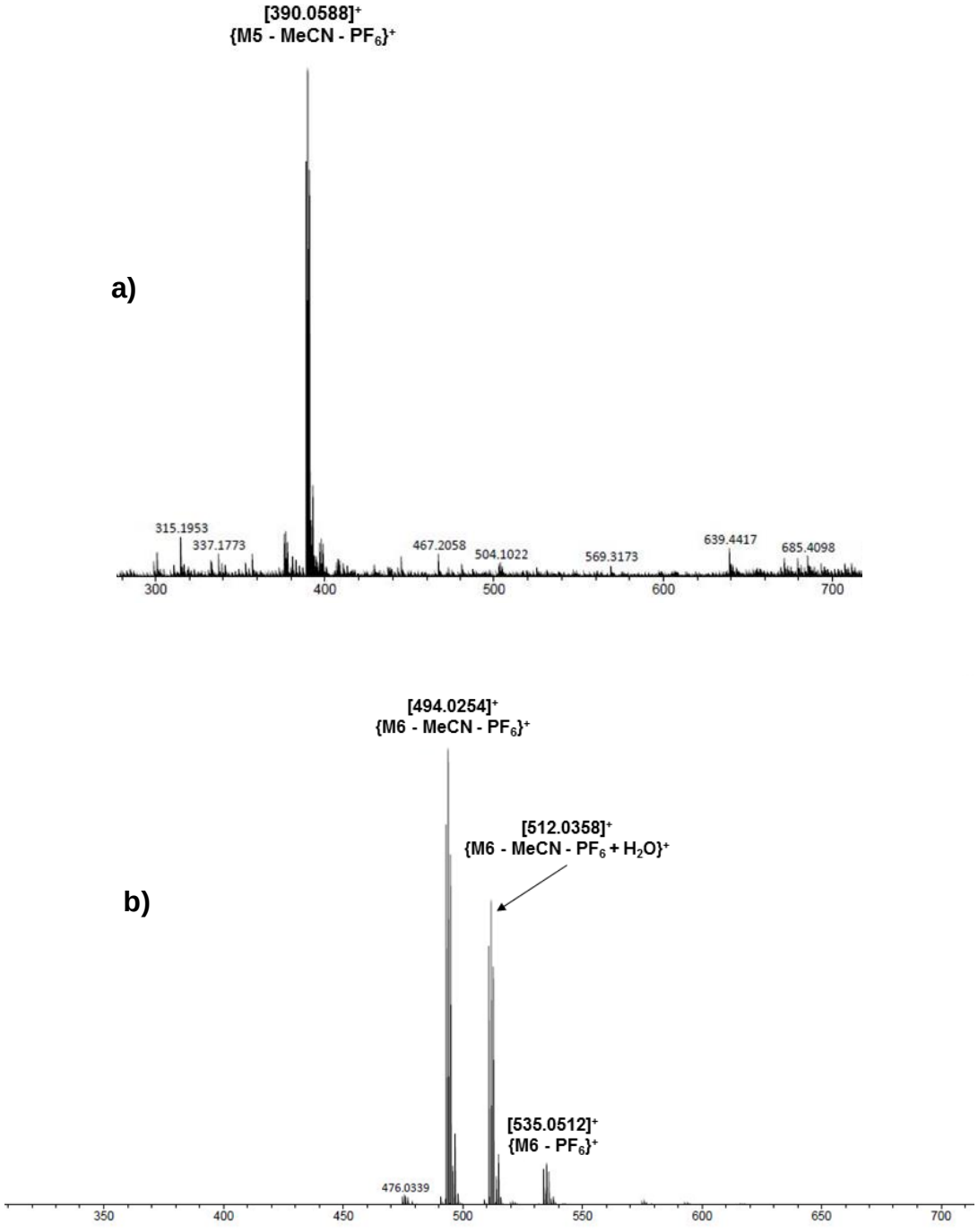


**Figure 2.32. a)** HRMS spectrum of **M5**, **b)** HRMS spectrum of **M6**.

## 2.7 Conclusion

Two CTG derivatives with increased upper rim alkoxy chain lengths have been successfully synthesised and appended with azobenzene groups. It is envisioned that incorporation of these ligands into an $M_3L_2$ metallo-cryptophane framework will increase the solubility of these complexes. The coordination chemistry of these novel ligands will be discussed in Chapter 3.

In addition to the attempts to solubilise the ligands in these assemblies, the metal tecton itself has also been targeted. Fluorinated iridium, rhodium and platinum phenylpyridine tectons have been synthesised which are envisioned to display increased solubility in organic solvents. All were synthesised using a similar methodology whereby a dichloro-bridged dimer was first synthesised and subsequently split in the presence of acetonitrile using silver hexafluorophosphate as a halide abstracting reagent. This ensured that the available coordination sites were *cis* to one another, designed to promote metallo-cryptophane formation. The use of these tectons to produce solubilised metallo-cryptophanes is discussed in Chapter 3.

The photoswitching behaviour of the ligands and metallo-cryptophanes will be discussed in Chapter 4. In particular, the photoswitching behaviour of the rhodium cryptophanes will be compared to the iridium cryptophanes. The switching potential of both will be determined to ascertain whether the use of a lighter metal in the assembly increases the switching ability of the assembly due to the decrease in azobenzene deactivation pathways.

## 2.8 Future Work

There remains enormous scope for functionalisation and variation of the photoresponsive CTG based ligands discussed in this chapter. In this work azobenzene groups have been employed as the photoswitchable component in the ligand. There exist a multitude of photoswitchable groups such as spiropyrans, fulgides and dithienylethenes that have not been investigated. Although synthetically challenging, appending these groups to CTG would create whole new classes of photoswitchable CTG based ligands. From these a library of photoresponsive metallo-cages could be produced that each possess different photophysical properties. This modular approach may allow desirable functions and properties to be introduced into a system by the simple selection of a different ligand.

In this work ethoxy and propoxy variants of CTG have been synthesised. In addition to these groups it would be desirable to synthesise CTG ligand variants with alternative upper rim substituents such as benzyl or napthyl groups. When assembled into a metallo-cage, these substituents would more effectively shield the internal environment from the bulk solution which could lead to improved host-guest properties.

In addition, the ligands **L2** and **L3** were both detected in the mass spectrometer as triply protonated dimers (Figure 2.33). This suggests that these ligands may be capable of forming hydrogen bonded dimers in an acidic non-aqueous environment. Similar hydrogen bonded CTV capsules have been reported in the literature.[34, 50] The photoswitching potential of hydrogen bonded capsules may be improved due to the lack of metal centres. These metal centres could feasibly provide deactivation pathways for the azobenzene groups.

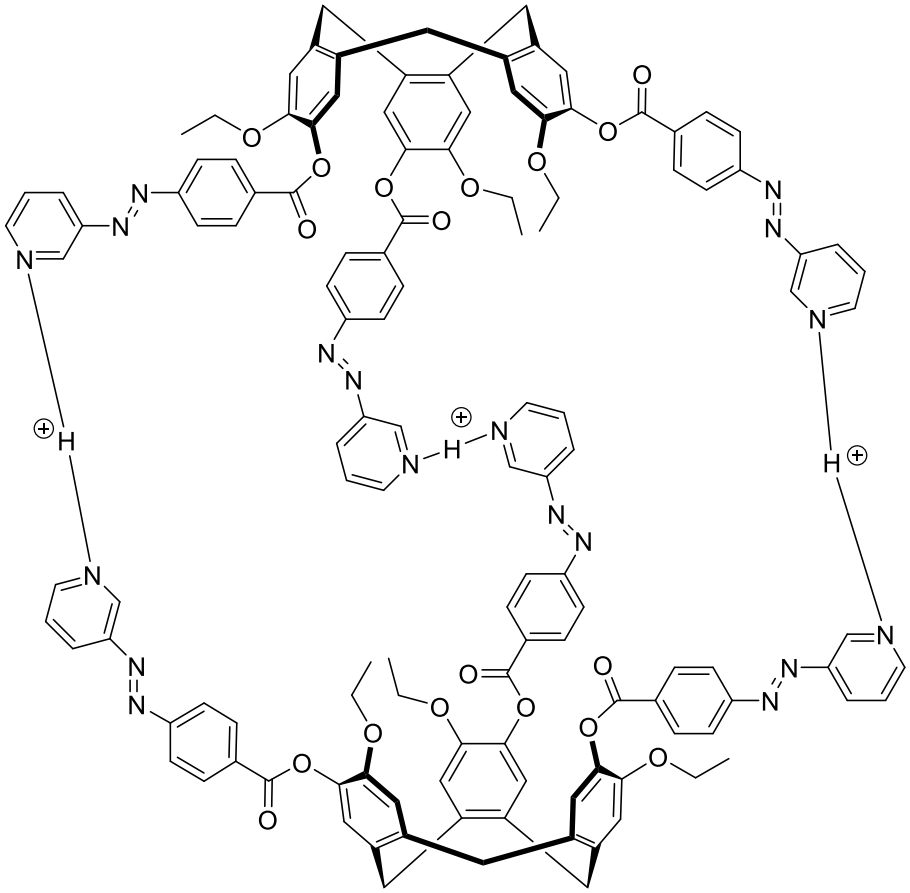

**Figure 2.33.** Possible hydrogen bonded dimer of **L2** detected in the mass spectra.

## 2.9 Experimental

### General Remarks

All reagents were purchased from commercial suppliers and without further purification. Where stated reactions were carried out under an inert atmosphere of nitrogen using a dual vacuum/ nitrogen manifold and standard Schlenk techniques. Dry solvent was obtained by passing through a column of activated alumina.

### Instrumentation

$^{1}H$ and $^{13}C$ NMR were performed on either a Bruker Avance III 300 MHz, Bruker Avance III HD 400 MHz or a Bruker AV4 NEO 11.75 T 500 MHz CP spectrometer. All $^{1}H$ and $^{13}C\{^{1}H\}$ NMR spectra were referenced to residual solvent peaks. Where appropriate NMR assignments were confirmed using 2-D NMR techniques including COSY, TOCSY, HSQC, HMBC, NOESY, ROESY and DOSY. Electrospray mass spectra were performed on a Bruker micro-TOFQ mass spectrometer in either positive or negative mode. Infra-red spectra were recorded as solid or liquid samples using a Perkin Elmer Spectrum One spectrometer. Melting points were recorded on a Stuart melting point apparatus SMP3.

Crystals were mounted under an inert oil and on a MiTeGen tip and flash frozen (100 K) using an Oxford Cryostreams cryostream low temperature device. X-ray diffraction data was collected using synchrotron radiation (λ = 0.6889 Å) on beamline I19 at Diamond Light Source. Crystal structures were solved using SHELXT and refined using least squares SHELXL.

### 3-Methoxy-4-propenyloxybenzyl alcohol[7] (2.1)

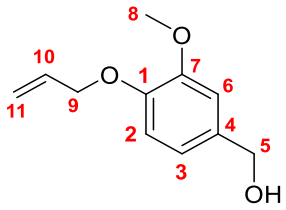


3-Methoxy-4-hydroxybenzyl alcohol (25.0 g, 158 mmol) was dissolved in acetone (125 mL). Potassium carbonate (21.8 g, 176 mmol) and allyl bromide (15.1 mL, 158 mmol) were added to the solution and heated at reflux overnight. The solvent was removed *in vacuo.* The residue was dissolved in water (100 mL) and DCM (150 mL). The product was extracted with DCM (3

x 200 mL) and the combined organics washed with water (2 x 200 mL). The organic layer was dried with $MgSO_4$ and the solvent was removed *in vacuo* to yield the product (30.21 g, 155 mmol, 98%) as a cream solid. Data is consistent with the literature values.[7]

**$^1$H-NMR** (300 MHz, $CDCl_3$): 6.85 (s, 1H, **$H^6$**); 6.77 (s, 2H, **$H^2$** + **$H^3$**); 6.09 - 5.96 (m, 1H, **$H^{10}$**); 5.35 (dd, 1H, *J* = 1.5, 17.4 Hz, **$H^{11\text{-Trans}}$**); 5.22 (dd, 1H, *J* = 1.5, 10.5 Hz, **$H^{11\text{-Cis}}$**); 4.53 (d, 2H, *J* = 5.4 Hz, **$H^9$**); 4.50 (s, 2H, **$H^5$**); 3.78 (s, 3H, **$H^8$**); 2.88 (bs, 1H, **OH**). **$^{13}$C-NMR** (75 MHz, $CDCl_3$): 149.4, 147.3, 134.1, 133.3, 119.2, 117.9, 113.4, 110.8, 69.9, 64.8, 55.8. **ESI-MS** (+ve) $[M+Na]^+$ m/z = 217.0831 calcd 217.0835.

**(±)-2,7,12-Trimethoxy-3,8,13-tris(propenyloxy)-10,15-dihydro-5H-tribenzo[a,d,g] cyclononatriene[51] (2.2)**

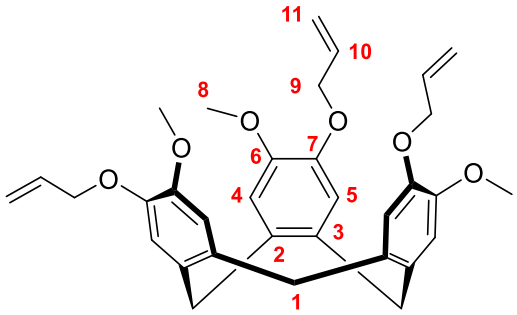


3-Methoxy-4-propenyloxybenzyl alcohol (30.0 g, 155 mmol) was heated at 100 $^o$C until all the solid had melted. Super phosphoric acid (spatula tip) was added with vigorous stirring and the solution was left to react overnight, forming a brown solid. The solid was triturated in methanol (150 mL), sonicated and then filtered to produce a fine white powder. The solid was washed with methanol followed by diethyl ether and then dried *in vacuo* to yield the product (8.02 g, 15.2 mmol, 31%) as a cream solid. Data is consistent with literature values.[51]

**$^1$H-NMR** (300 MHz, $CDCl_3$): 6.86 (s, 3H, **$H^{4/5}$**), 6.80 (s, 3H, **$H^{4/5}$**), 6.13 - 6.00 (m, 3H, **$H^{10}$**), 5.38 (d, 3H, *J* = 17.4 Hz, **$H^{11\text{-Trans}}$**), 5.25 (d, 3H, *J* = 10.5 Hz, **$H^{11\text{-cis}}$**), 4.74 (d, 3H, *J* = 13.5 Hz, **$H^{1\text{-exo}}$**), 4.60 (m, 6H, **$H^9$**), 3.84 (s, 9H, **$H^8$**), 3.51 (d, 3H, *J* = 13.8 Hz, **$H^{1\text{-endo}}$**). **$^{13}$C-NMR** (75 MHz, $CDCl_3$): 148.2, 146.8, 133.8, 132.3, 131.8, 117.5, 115.6, 113.6, 70.2, 56.1, 36.5. **ESI-MS** (+ve) $[M+Na]^+$ m/z = 551.2409 calcd 551.2404.

**(±)-2,7,12-Trimethoxy-3,8,13-tris(hydroxy)-10,15-dihydro-*5H*-tribenzo[*a,d,g*] cyclononatriene[51] (CTG) (2.3)**

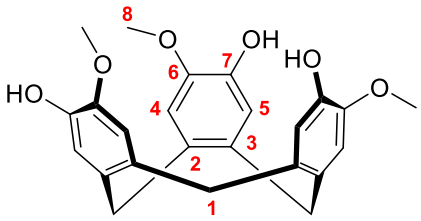


(±)-2,7,12-Trimethoxy-3,8,13-tris(propenyloxy)-10,15-dihydro-5H-tribenzo[a,d,g] cyclononatriene (3.00 g, 5.67 mmol) and triphenylphosphine (0.28 g, 1.07 mmol) was dissolved in a mixture of dry THF (150 mL), water (30 mL) and diethylamine (27 mL) under an atmosphere of $N_2$. The yellow solution was heated to reflux and $Pd(OAc)_2$ (0.09 g, 0.39 mmol) was added. The solution was refluxed overnight and then filtered through Celite. The solvent was removed *in vacuo* to give a brown residue which was triturated in methanol (100 mL) and then filtered to yield the product (1.84 g, 2.64 mmol, 80%) as a grey/ white powder. Data is consistent with literature values.[51]

**$^1$H-NMR** (300 MHz, $d_6$-DMSO): 8.61 (bs, 1H, **OH**), 6.91 (s, 3H, **$H^{4/5}$**), 6.89 (s, 3H, **$H^{4/5}$**), 4.64 (d, 3H, *J* = 13.5 Hz, **$H^{1\text{-exo}}$**), 3.86 (s, 9H, **$H^{8}$**), 3.50 (d, 3H, *J* = 13.5 Hz, **$H^{1\text{-endo}}$**). **$^{13}$C-NMR** (75 MHz, $d_6$-DMSO): 146.0, 144.9, 132.6, 130.4, 116.8, 114.0, 56.0, 35.0. **ESI-MS** (+ve) $[M+NH_4]^+$, $[2M+Na]^+$ m/z = 426.1915, 839.3038 calcd 426.1917, 839.3038.

**3-Ethoxy- 4-hydroxybenzyl alcohol (2.4)**

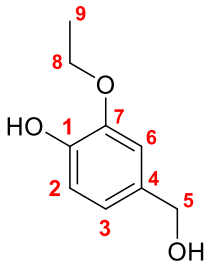


Ethyl vanillin (30 g, 180 mmol) was dissolved in dry ethanol (200 mL) under an atmosphere of $N_2$. The flask was cooled to 0 $^o$C and sodium borohydride (10.2 g, 270 mmol) was added in small portions. The flask was stirred overnight. The solvent was removed *in vacuo* and the residue dissolved in ethyl acetate (200 mL) and water (200 mL). The aqueous phase was extracted with ethyl acetate (3 x 200 mL) and the combined organics were washed with brine (100 mL) and dried with $MgSO_4$. Removal of solvent yielded the product

as a colourless oil which solidified on standing into white crystals (26.3 g, 156 mmol, 86%).

**$^{1}$H-NMR** (300 MHz, $CDCl_3$): 6.88 (s, 1H, **H$^{6}$**), 6.87 (d, 1H, *J* = 6.0 Hz, **H$^{2}$**), 6.80 (dd, 1H, *J* = 6.0, 1.2 Hz, **H$^{3}$**), 5.81 (s, 1H, **OH**-phenol), 4.56 (s, 2H, **H$^{5}$**), 4.10 (q, 2H, *J* = 7.0 Hz, **H$^{8}$**), 1.99 (s, 1H, **OH**-benzylic), 1.43 (t, 3H, *J* = 7.0 Hz, **H$^{9}$**). **$^{13}$C-NMR** (75 MHz, $CDCl_3$): 145.9, 145.4, 132.9, 120.1 114.2, 110.9, 65.4, 64.5, 14.9.

**3-Ethoxy-4-(propenyloxy) benzyl alcohol[30] (2.5)**

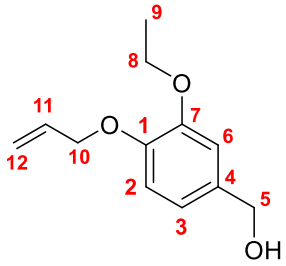


3-Ethoxy-4-hydroxy benzyl alcohol (23.4 g, 139 mmol) was dissolved in acetone (200 mL). Potassium carbonate (21.1 g, 153 mmol) and allyl bromide (12.1 mL, 139mmol) were added and the solution was heated to reflux overnight. The solvent was removed *in vacuo* and the residue was dissolved in DCM (200 mL) and water (150 mL). The aqueous layer was extracted with DCM (3 x 150 mL) and the combined organics were washed with water (2 x 150 mL) and dried with $MgSO_4$. Removal of solvent yielded the product as a pale yellow oil (24.46 g, 117 mmol, 85%). Data is consistent with literature values.[30]

**$^{1}$H-NMR** (300 MHz, $CDCl_3$): 6.87 (s, 1H, **H$^{6}$**), 6.80 (m, 2H, **H$^{2}$** + **H$^{3}$**), 6.05 (m, 1H, **H$^{11}$**), 5.37 (dd, 1H, *J* = 17.3, 1.6 Hz, **H$^{12\text{-Trans}}$**), 5.23 (dd, 1H, *J* = 10.5, 1.4 Hz, **H$^{12\text{-cis}}$**), 4.55 (m, 4H, **H$^{5/10}$**), 4.04 (q, 2H, *J* = 7.0 Hz, **H$^{8}$**), 2.51 (t, 1H, **OH**), 1.41 (t, 3H, *J* = 7.0 Hz, **H$^{9}$**). **$^{13}$C-NMR** (75 MHz, $CDCl_3$): 149.0, 147.8, 134.3, 133.6, 119.4, 117.6, 114.2, 112.7, 70.1, 65.1, 64.5, 14.9. **ESI-MS** (+ve) $[M+Na]^+$ m/z = 231.0987 calcd 231.0992.

**(±)-2,7,12-Triethoxy-3,8,13-tris(propenyloxy)-10,15-dihydro-5H-tribenzo[a,d,g] cyclononatriene[30] (2.6)**

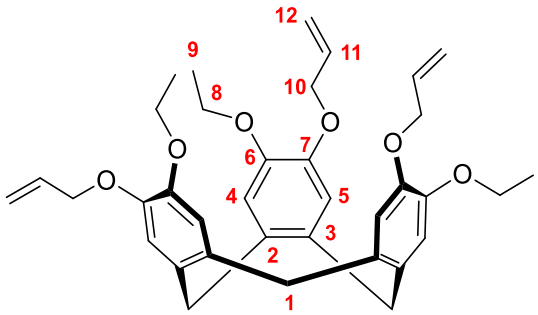


3-Ethoxy-4-(Propenyloxy)benzyl alcohol (6.64 g, 25.9 mmol) and scandium(III) triflate (0.32 g, 0.52 mmol) were dissolved in dry acetonitrile (40 mL) under an atmosphere of $N_2$. The solution was heated to 60 °C for two days. The reaction was then cooled to room temperature and the solvent was removed *in vacuo*. The residue was triturated in ethanol (50 mL), filtered and washed with water and minimum volumes of ethanol to yield the product as an off white powder (1.66 g, 2.90 mmol, 34%). All data is consistent with literature values.[30]

**$^1$H-NMR** (300 MHz, $CDCl_3$): 6.85 (s, 3H, **H$^{4/5}$**), 6.81 (s, 3H, **H$^{4/5}$**), 6.06 (m, 3H, **H$^{11}$**), 5.37 (dd, 3H, *J* = 17.3, 1.6 Hz, **H$^{12\text{-trans}}$**), 5.23 (dd, 3H, *J* = 10.5, 1.4 Hz, **H$^{12\text{-cis}}$**), 4.71 (d, 3H, *J* = 13.8 Hz, **H$^{1\text{-exo}}$**), 4.56 (d, 6H, *J* = 5.4 Hz, **H$^{10}$**), 4.06 (q, 6H, *J* = 7.0 Hz, **H$^{8}$**), 3.49 (d, 3H, *J* = 13.8 Hz, **H$^{1\text{-endo}}$**), 1.40 (t, 9H, *J* = 7.0 Hz. **H$^{9}$**). **$^{13}$C-NMR** (75 MHz, $CDCl_3$): 147.6, 147.3, 134.0, 132.6, 132.1, 117.2, 116.4, 115.8, 70.5, 64.8, 36.5, 15.0. **ESI-MS** (+ve) $[M+Na]^+$ : m/z = 593.2869 calcd 593.2879. **Infrared analysis** (FT-IR, cm $^{-1}$): 3073, 2978, 2927, 1684, 1604, 1507, 1475, 1441, 1424, 1392, 1341, 1254, 1213, 1192, 1143, 1107, 1083, 1040, 1012. **M.P** 113 °C.

**(±)-2,7,12-Triethoxy-3,8,13-trihydroxy-10,15-dihydro-5H-tribenzo[a,d,g] cyclononatriene (eCTG) (2.7)**

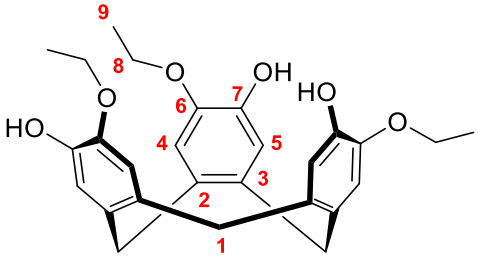


**1.10** (1.90 g, 3.36 mmol) and triphenylphosphine (0.26 g, 1.01 mmol) were dissolved in a mixture of diethylamine (15 mL), water (15 mL) and anhydrous

THF (80 mL) under an atmosphere of $N_2$. The solution was heated to reflux and palladium(II) acetate (0.04 g, 0.17 mmol) was added in one portion. The solution was heated overnight and the resultant black suspension was filtered through Celite to yield an orange solution. The solvent was removed and the residue was triturated in ethanol. The product was filtered and washed with ethanol then diethyl ether to yield the product as an off white powder. (1.03 g, 2.29 mmol, 68%).

**$^1$H-NMR** (300 MHz, $CDCl_3$): 6.86 (s, 3H, **$H^{4/5}$**), 6.78 (s, 3H, **$H^{4/5}$**), 5.44 (bs, 3H, **OH**), 4.69 (d, 3H, *J* = 13.7 Hz, **$H^{1\text{-exo}}$**), 4.08 (q, 6H, *J* = 7.0 Hz, **$H^8$**), 3.47 (d, 3H, *J* = 13.8 Hz, **$H^{1\text{-endo}}$**), 1.40 (t, 9H, *J* = 7.0 Hz, **$H^9$**). **$^{13}$C-NMR** (75 MHz, $CDCl_3$): 143.5, 143.2, 131.4, 130.2, 114.3, 112.2, 63.6, 35.2, 13.8. **ESI-MS** (+ve) $[M+Na]^+$: m/z = 473.1936 calcd 473.1940. **Infrared analysis** (FT-IR, $cm^{-1}$): 3535, 3359, 3032, 2963, 2918, 1621, 1591, 1507, 1473, 1437, 1392, 1370, 1355, 1263, 1218, 1175, 1136, 1113, 1079, 1031. **M.P** 166 $^o$C (decomposes).

**3-Methoxy-4-propoxy benzyl alcohol (2.8)**

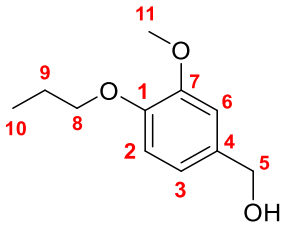


3-Methoxy-4-hydroxybenzylalcohol (20.0 g, 129 mmol) and potassium carbonate (19.7 g, 143 mmol) were added to acetone (150 mL) to form a white suspension. 1-Bromopropane (13.0 mL, 143 mmol) was added and heated to reflux overnight. The reaction was cooled to room temperature and the solvent was removed. The residue was taken up in water (150 mL) and DCM (200 mL). The layers were separated and the aqueous layer was extracted with DCM (3 x 200 mL). The combined organics were washed with water (100 mL) and brine (100 mL), dried with $MgSO_4$ and filtered. The solvent was removed to yield the product as a yellow oil (19.8 g, 101 mmol, 78%).

**$^1$H-NMR** (300 MHz, $CDCl_3$): 6.92 (s, 1H, **$H^6$**), 6.86 (bs, 2H, **$H^2$** + **$H^3$**), 4.62 (s, 2H, **$H^5$**), 3.97 (t, 2H, *J* = 6.9 Hz, **$H^8$**), 3.88 (s, 3H, **$H^{11}$**), 2.17 (s, 1H, **OH**), 1.86 (hextet, 2H, *J* = 7.2 Hz, **$H^9$**), 1.03 (t, 3H, *J* = 7.5 Hz, **$H^{10}$**). **$^{13}$C-NMR** (75 MHz, $CDCl_3$): 149.7, 148.3, 133.6, 119.59, 113.0, 111.1, 70.8, 65.5, 56.1, 22.6, 10.5.

**(±)-2,7,12-Tripropoxy-3,8,13-trihydroxy-10,15-dihydro-5H-tribenzo[a,d,g] cyclononatriene (2.9)**

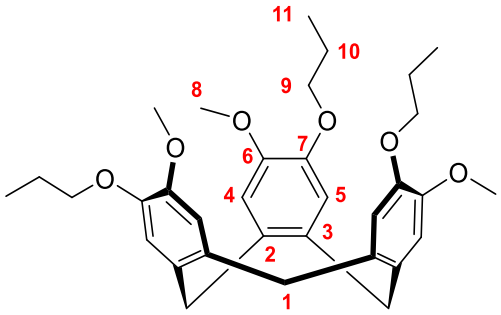


3-Methoxy-4-propoxybenzyl alcohol (19.8 g, 101 mmol) was heated at 100 °C with vigorous stirring. Super phosphoric acid (spatula tip) was added and the liquid immediately turned brown. The liquid was stirred overnight over which time it solidified into a brown solid. The solid was triturated in methanol (150 mL), filtered and washed with methanol and diethyl ether to yield the product as an off white solid (2.31 g, 4.32 mmol, 13%).

**$^{1}$H-NMR** (400 MHz, $CDCl_3$): 6.84 (s, 3H, **$H^{4/5}$**), 6.82 (s, 3H, **$H^{4/5}$**), 4.75 (d, 3H, *J* = 14.0 Hz, **$H^{1\text{-exo}}$**), 3.95 (m, 6H, **$H^{9}$**), 3.82 (s, 9H, **$H^{8}$**), 3.53 (d, 3H, *J* = 14.0 Hz, **$H^{1\text{-endo}}$**), 1.81 (hextet, 6H, *J* = 7.2 Hz, **$H^{10}$**), 1.02 (t, 9H, *J* = 7.6 Hz, **$H^{11}$**). **$^{13}$C-NMR** (75 MHz, $CDCl_3$): 148.3, 147.3, 132.1, 115.2, 113.9, 70.9, 56.3, 36.6, 22.6, 10.6. **ESI-MS** (+ve) $[M+Na]^+$ m/z = 557.2878 calcd 557.2874.

**(±)-2,7,12-Tripropoxy-3,8,13-trimethoxy-10,15-dihydro-5H-tribenzo[a,d,g] cyclononatriene[31] (pCTG) (2.10)**

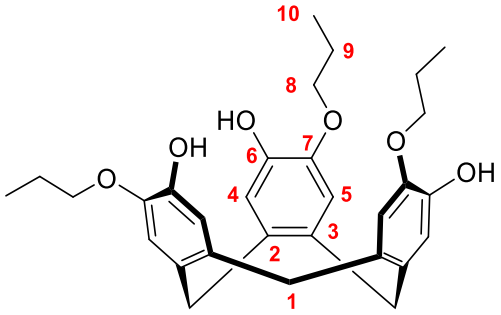


(±)-2,7,12-Tripropoxy-3,8,13-trihydroxy-10,15-dihydro-5H-tribenzo[a,d,g] cyclononatriene(1.0 g, 1.87 mmol) was dissolved in dry THF (30 mL) under $N_2$. In a separate flask diphenylphosphine (1.01 mL, 5.81 mmol) was dissolved in dry THF (10 mL) under $N_2$ and cooled to -78 °C. 2.5 M $^{n}$BuLi in hexanes (2.32 mL, 5.81 mmol) was added dropwise to form a deep red solution, stirred for 30 minutes at -78 °C and then at room temperature for one hour. The

solution was then transferred to the flask containing **2.9** dropwise forming an orange solution. The reaction was stirred overnight over which time a white precipitate formed. The reaction was quenched by the addition of HCl (1M, 10 mL). The solvent was removed and the residue dissolved in water (50 mL) and DCM (100 mL). The aqueous layer was extracted with DCM (3 x 100 mL) and washed with 1M HCl (3 x 50 mL). The solvent was removed and the residue was purified by column chromatography on silica gel using a gradient solvent system of DCM to DCM/ MeOH 5% to obtain the product as an off white powder (0.30 g, 0.60 mmol, 32 %). Data is consistent with the literature.[31]

**$^1$H-NMR** (300 MHz, $CDCl_3$): 6.87 (s, 3H, **H$^{4/5}$**), 6.78 (s, 3H, **H$^{4/5}$**), 5.44 (bs, 3H, **OH**), 4.70 (d, 3H, *J* = 13.8 Hz, **H$^{1\text{-exo}}$**), 3.97 (dt, 6H, *J* = 2.7, 6.6 Hz, **H$^{8}$**), 3.47 (d, 3H, *J* = 14.1 Hz, **H$^{1\text{-endo}}$**), 1.80 (hextet, 6H, *J* = 7.2 Hz, **H$^{9}$**), 1.02 (t, 9H, *J* = 7.2 Hz, **H$^{10}$**). **$^{13}$C-NMR** (75 MHz, $CDCl_3$): 144.59, 144.25, 132.38, 131.19, 115.30, 113.20, 70.55, 36.31, 22.56, 10.48. **ESI-MS** (+ve) $[M+Na]^+$ m/z = 515.2406 calcd 515.2404.

**Methyl-4-nitrosobenzoate[22] (2.11)**

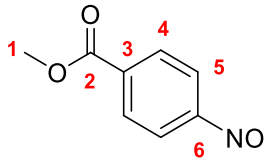


Methyl-4-aminobenzoate (2.5 g, 16.6 mmol) was dissolved in DCM (100 mL). A solution of Oxone™ (20.3 g, 66.0 mmol) in water (200 mL) was added and the solution was stirred vigorously for two hours forming a green solution. The layers were separated and the aqueous layer was further extracted with DCM (3 x 150 mL). The combined organics were washed successively with HCl (1M, 50 mL), aqueous $NaHCO_3$ (saturated, 50 mL), water (50 mL) and brine (50 mL). The solution was dried with $MgSO_4$ and filtered. The solvent was removed to yield the product as a yellow powder (2.54 g, 15.4 mmol, 93%). All data is consistent with literature values.[22]

**$^1$H-NMR** (300 MHz, $CDCl_3$): 8.30 (d, 2H, *J* = 8.7 Hz, **H$^{5}$**), 7.94 (d, 2H, *J* = 8.4 Hz, **H$^{4}$**), 3.98 (s, 3H, **H$^{1}$**). **$^{13}$C-NMR** (75 MHz, $CDCl_3$): 165.9, 164.5, 135.4, 131.2, 120.5, 52.9.

**3-(4-Sodiumbenzoateazo)pyridine[22] (2.12)**

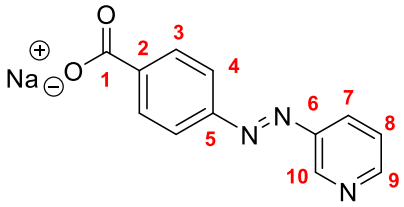


Methyl-4-nitrosobenzoate (2.78 g, 16.6 mmol) and 3-aminopyridine (2.92 g, 31.0 mmol) were dissolved in an aqueous NaOH solution (3% w/v, 300 mL) and heated to reflux overnight during which the solution turned a deep red colour. The solution was then cooled in an ice bath resulting the formation of an orange precipitate. The solid was filtered and washed with acetone then ether to yield the product as an orange microcrystalline powder (3.54 g, 15.6 mmol, 94%). All data is consistent with literature values.[22]

**$^{1}$H-NMR** (300 MHz, $CD_3OD$): 9.14 (d, 1H, *J* = 2.4 Hz, **H$^{10}$**), 8.69 (dd, 1H, *J* = 1.8, 4.8 Hz, **H$^{9}$**) 8.31 (ddd, 1H, *J* = 1.5, 2.1, 8.1 Hz, **H$^{7}$**) 8.13 (d, 2H, *J* = 8.7 Hz, **H$^{3}$**), 7.96 (d, 2H, *J* = 8.7 Hz, **H$^{4}$**), 7.64 (ddd, 1H, *J* = 0.6, 4.8, 8.1 Hz, **H$^{8}$**). **$^{13}$C-NMR** (75 MHz, $CD_3OD$): 174.20, 154.74, 152.36, 149.72, 147.32, 131.25, 129.19, 126.00, 123.51. **ESI-MS** (-ve) [$M^-$]: m/z = 226.0608 calcd 226.0622.

**3-(4-Benzoyl chlorideazo)pyridine (2.13)**

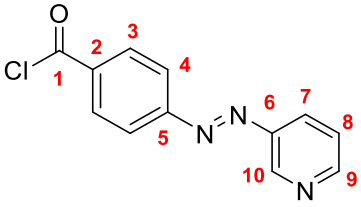


3-(4-Benzoic acidazo)pyridine (369 mg, 1.48 mmol) was dissolved in thionyl chloride (5 mL) under $N_2$ and heated at 70 $^{o}$C overnight forming a red solution. The thionyl chloride was removed under high vacuum leaving an orange residue which was used without further purification (quantitative).

**(±)-2,7,12-Trimethoxy-3,8,13-*tris*(3-pyridyl-4-azophenylcarboxy)-10,15-dihydro-5H-tribenzo[a,d,g] cyclononatriene[22] (L1)**

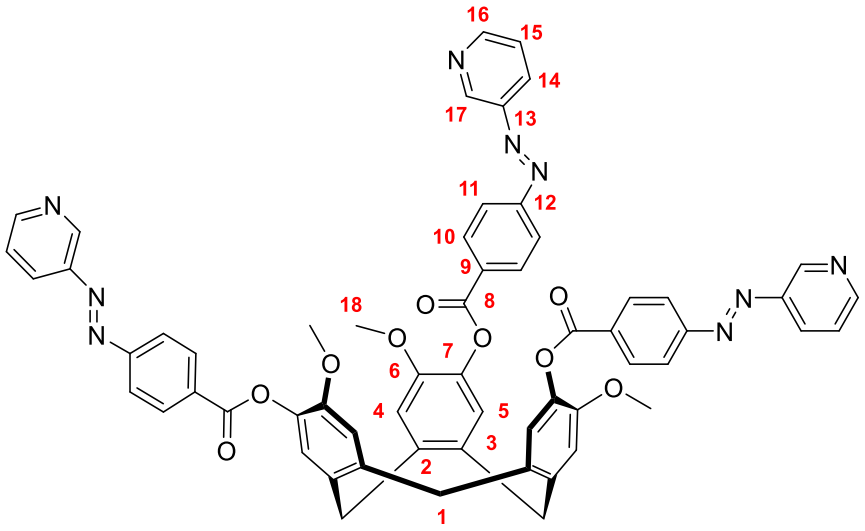


CTG (100 mg, 0.24 mmol) was dissolved in anhydrous THF (30 mL) under $N_2$, anhydrous triethylamine (3 mL) was added and stirred for 30 minutes. The solution was transferred to a flask containing **2.13** (363 mg, 1.48 mmol) and stirred at room temperature for three days. The suspension was filtered and the eluent was collected. The solvent was removed to yield an orange residue which was triturated in methanol (150 mL), filtered and washed with methanol and diethyl ether to yield the product as a bright orange powder (201 mg, 0.19 mmol, 81%). All data is consistent with literature values.[22]

**$^1$H-NMR** (300 MHz, $CDCl_3$): 9.25 (d, 3H, *J* = 2.4 Hz, **$H^{17}$**), 8.76 (dd, 3H, *J* = 1.8, 4.5 Hz, **$H^{16}$**), 8.38 (d, 6H, *J* = 8.7 Hz, **$H^{10}$**), 8.20 (dt, 3H, *J* = 1.8, 8.4 Hz, **$H^{14}$**), 8.05 (d, 6H, *J* = 8.7 Hz, **$H^{11}$**), 7.48 (dd, 3H, *J* = 4.8, 8.1 Hz, **$H^{15}$**), 7.22 (s, 3H, **$H^{5}$**), 7.00 (s, 3H, **$H^{4}$**), 4.88 (d, 3H, *J* = 13.5 Hz, **$H^{1\text{-exo}}$**), 3.84 (s, 9H, **$H^{18}$**), 3.73 (d, 3H, *J* = 13.8 Hz, **$H^{1\text{-endo}}$**). **$^{13}$C-NMR** (75 MHz, $CDCl_3$): 164.2, 155.3, 152.6, 150.0, 148.1, 147.9, 138.7, 138.3, 131.9, 131.6, 127.2, 124.2, 123.1, 114.4, 106.0, 56.4, 36.71. **ESI-MS** (+ve) $[M+H]^+$: m/z = 1036.3228 calcd 1036.3413.

**(±)-2,7,12-Triethoxy-3,8,13-*tris*(3-pyridyl-4-azophenylcarboxy)-10,15-dihydro-5H-tribenzo[a,d,g] cyclononatriene (L2)**

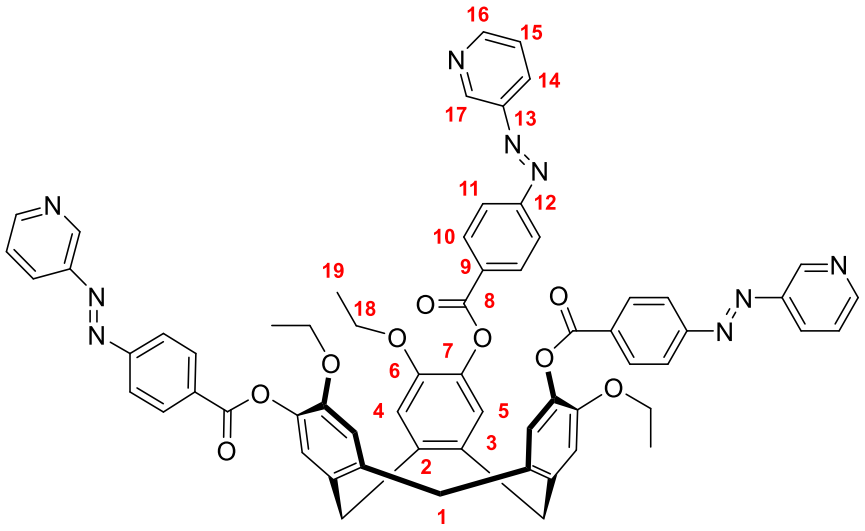


Ethyl CTG (219 mg, 0.49 mmol) was dissolved in anhydrous THF (60 mL) under $N_2$, anhydrous triethylamine (6 mL) was added and stirred for 30 minutes. The solution was transferred to a flask containing **2.13** (738 mg, 2.96 mmol) and stirred at room temperature for three days. The suspension was filtered and the eluent was collected. The solvent was removed to yield an orange residue which was triturated in methanol (200 mL), filtered and washed with methanol and diethyl ether to yield the product as a bright orange powder (323 mg, 0.30 mmol, 61%).

**$^1$H-NMR** (500 MHz, $CDCl_3$): 9.25 (s, 3H, **H$^{17}$**), 8.75 (d, 3H, *J* = 4.4 Hz, **H$^{16}$**), 8.36 (d, 6H, *J* = 6.8 Hz, **H$^{10}$**), 8.18 (d, 3H, *J* = 8.0 Hz, **H$^{14}$**), 8.04 (d, 6H, *J* = 8.0 Hz, **H$^{11}$**), 7.47 (m, 3H, **H$^{15}$**), 7.20 (s, 3H, **H$^{5}$**), 6.99 (s, 3H, **H$^{4}$**), 4.83 (d, 3H, *J* = 13.6 Hz, **H$^{1\text{-exo}}$**), 4.07 (q, 6H, *J* = 6.8 Hz, **H$^{18}$**), 3.68 (d, 3H, *J* = 13.6 Hz, **H$^{1\text{-endo}}$**), 1.26 (t, 9H, *J* = 6.8 Hz, **H$^{19}$**). **$^{13}$C-NMR** (125 MHz, $CDCl_3$): 164.2 (**C$^{8}$**), 155.2 (**C$^{9}$**), 152.5 (**C$^{16}$**), 149.3 (**C$^{3}$**), 147.9 (**C$^{13}$**), 147.8 (**C$^{17}$**), 139.2 (**C$^{7}$**), 138.2 (**C$^{2}$**), 132.1 (**C$^{12}$**), 131.8 (**C$^{10}$**), 131.5 (**C$^{6}$**), 127.2 (**C$^{14}$**), 124.2 (**C$^{15}$**), 124.1 (**C$^{5}$**), 123.1 (**C$^{11}$**), 115.8 (**C$^{4}$**), 65.0 (**C$^{18}$**), 36.7 (**C$^{1}$**), 14.9 (**C$^{19}$**). **ESI-MS** (+ve) $[M+H]^+$: m/z = 1078.3662  calcd 1078.3883.

**(±)-2,7,12-Tripropoxy-3,8,13-*tris*(3-pyridyl-4-azophenylcarboxy)-10,15-dihydro-5H-tribenzo[a,d,g] cyclononatriene (L3)**

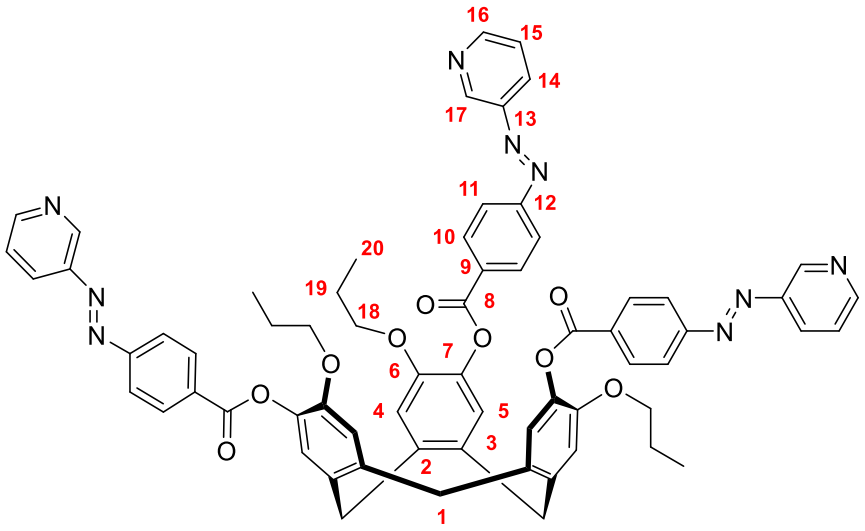


Propyl CTG (118 mg, 0.24 mmol) was dissolved in anhydrous THF (30 mL) under $N_2$, anhydrous triethylamine (3 mL) was added and stirred for 30 minutes. The solution was transferred to a flask containing **2.13** (363 mg, 1.48 mmol) and stirred at room temperature for three days. The suspension was filtered and the eluent was collected. The solvent was removed to yield an orange residue which was triturated in methanol (100 mL), filtered and washed with methanol and diethyl ether to yield the product as a bright orange powder (154 mg, 0.14 mmol, 57%).

**$^1$H-NMR** (500 MHz, $CDCl_3$): 9.25 (s, 3H, **H$^{17}$**), 8.75 (d, 3H, *J* = 1.5, 4.8 Hz, **H$^{16}$**), 8.36 (d, 6H, *J* = 9.0 Hz, **H$^{10}$**), 8.19 (dt, 3H, *J* = 1.5, 8.1 Hz, **H$^{14}$**), 8.04 (d, 6H, *J* = 8.7 Hz, **H$^{11}$**), 7.48 (dd, 3H, *J* = 4.8, 8.1 Hz, **H$^{15}$**), 7.21 (s, 3H, **H$^{5}$**), 6.98 (s, 3H, **H$^{4}$**), 4.85 (d, 3H, *J* = 15.0 Hz, **H$^{1\text{-exo}}$**), 3.97 (m, 6H, **H$^{18}$**), 3.69 (d, 3H, *J* = 13.8 Hz, **H$^{1\text{-endo}}$**), 1.68 (sextet, 6H, *J* = 7.2 Hz, **H$^{19}$**), 0.88 (t, 9H, *J* = 7.2 Hz, **H$^{20}$**). **$^{13}$C-NMR** (126 MHz, $CDCl_3$): 164.2 (**C$^{8}$**), 155.2 (**C$^{9}$**), 152.6 (**C$^{16}$**), 149.4 (**C$^{3}$**), 147.9 (**C$^{13}$**), 147.7 (**C$^{17}$**), 139.1 (**C$^{7}$**), 138.2 (**C$^{2}$**), 132.1 (**C$^{12}$**), 131.6 (**C$^{10}$**), 131.5 (**C$^{6}$**), 127.1 (**C$^{14}$**), 124.2 (**C$^{15}$**), 124.0 (**C$^{5}$**), 123.1 (**C$^{11}$**), 115.6 (**C$^{4}$**), 70.7 (**C$^{18}$**), 36.7 (**C$^{1}$**), 22.6 (**C$^{19}$**), 10.5 (**C$^{20}$**). **ESI-MS** (+ve) $[M+H]^+$: m/z = 1120.4137 calcd 1120.4352.

**2-(2-4-Difluorophenyl)-5-trifluoromethylpyridine[44] (2.14)**

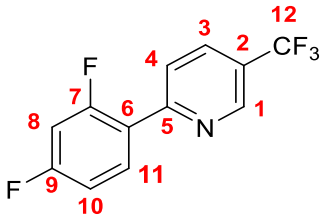


2, 4-Difluorophenyl boronic acid (1.58 g, 10 mmol), 2-bromo-5-trifluoromethylpyridine (1.88 g, 8.3 mmol) and potassium carbonate (5.52 g, 40 mmol) were dissolved in anhydrous THF (40 mL) and water (30 mL) under a $N_2$ atmosphere. The solution was heated to reflux and tetrakis(triphenylphosphine)palladium(0) (0.12 g, 0.1 mmol) was added in one portion forming a yellow solution. The flask was heated overnight resulting in the formation of an orange solution. The solvents were removed *in vacuo* to yield a black residue that was triturated in DCM (100 mL) and filtered through Celite. The eluent was washed with water (3 x 30 mL) and brine (30 mL), dried with $MgSO_4$ and filtered. The solvent was removed and the product dissolved in a minimal amount of EtOAc and passed through a silica plug with petrol (40-60 $^oC$) as the eluent. The solvent was removed to yield the product as pale yellow crystals (1.00 g, 3.86 mmol, 47%). All data is consistent with literature values.[44]

**$^1$H-NMR** (300 MHz, $CDCl_3$): 8.96 (s, 1H, **H$^1$**), 8.11 (q, 1H, *J* = 8.9 Hz, **H$^{10}$**), 7.99 (d, 1H, *J* = 8.4 Hz, **H$^3$**), 7.91 (d, 1H, *J* = 8.4 Hz, **H$^4$**), 7.04 (t, 1H, *J* = 8.7 Hz, **H$^{11}$**), 6.95 (t, 1H, *J* = 8.7 Hz, **H$^8$**). **$^{13}$C-NMR** (75 MHz, $CDCl_3$): 165.7, 162.8, 162.3, 159.4, 155.9, 146.7, 133.9, 132.6, 125.5, 123.8, 112.4, 104.9. **ESI-MS** (+ve) $[M+Na]^+$: m/z = 260.0493 calcd 260.0493.

**Bis(2-phenylpyridine)iridium-μ-chloro dimer[52] (2.15)**

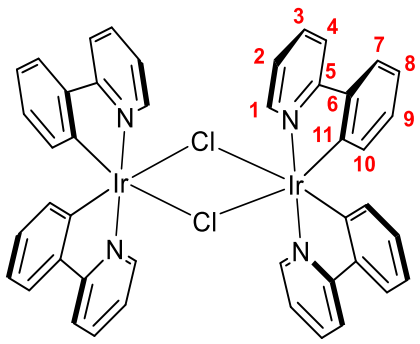


Iridium trichloride hydrate (100 mg, 0.33 mmol) was dissolved in a mix of 2-ethoxyethanol (3 mL) and water (1 mL). 2-Phenylpyridine (0.094 mL, 0.66 mmol) was added and the mixture was heated to reflux overnight. The mixture

was then filtered and washed with water then diethyl ether to yield the product as a yellow powder (125 mg, 0.12 mmol, 70%).Data is consistent with the literature.[52]

**$^1$H-NMR** (300 MHz, $CDCl_3$): 9.24 (d, 1H, *J* = 5.1 Hz, $H^1$), 7.87 (d, 1H, *J* = 7.9 Hz, $H^4$), 7.74 (t, 1H, *J* = 8.1 Hz, $H^3$), 7.48 (d, 1H, *J* = 7.0 Hz, $H^7$), 6.76 (m, 2H, $H^2$/ $H^9$), 6.56 (t, 1H, *J* = 6.9 Hz, $H^8$), 5.93 (d, 1H, *J* = 7.1 Hz, $H^{10}$). **$^{13}$C-NMR:** Too insoluble to collect.

**Bis(2-phenylpyridine))bis(acetonitrile)iridium(III) hexafluorophosphate (M1)**

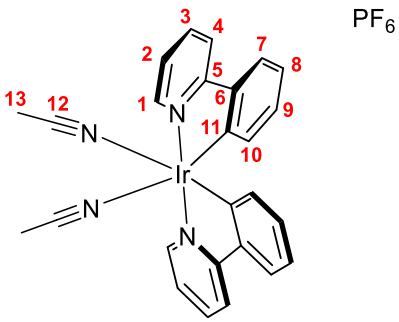


**2.15** (230 mg, 0.21 mmol) and silver(I) hexafluorophosphate (160 mg, 0.63 mmol) were dissolved in acetonitrile (30 mL) in the dark and under an atmosphere of $N_2$. The mixture was heated to reflux overnight. The solution was cooled to room temperature and the suspension was filtered through Celite to yield a yellow solution. The volume was reduced down to 1 mL and diethyl ether was added dropwise until the product crashed out as bright yellow crystals which were collected by filtration to yield the pure product (266 mg, 0.37 mmol, 87%). All data is consistent with the literature.[53]

**$^1$H-NMR** (300 MHz, $CD_3CN$): 8.91 (s, 1H, **$H^1$**), 7.88 (m, 2H, **$H^3$** + **$H^4$**), 7.47 (d, 1H, *J* = 7.7 Hz, **$H^7$**), 7.27 (t, 1H, *J* = 6.1 Hz, **$H^2$**), 6.69 (t, 1H, *J* = 7.5 Hz, **$H^8$**), 6.53 (t, 1H, *J* = 7.4 Hz, **$H^9$**), 5.89 (d, 1H, *J* = 7.6 Hz, **$H^{10}$**). **$^{13}$C-NMR** (75 MHz, $CD_3CN$): 168.0, 151.9, 145.5, 144.6, 139.9, 132.1, 130.6, 125.5, 124.5, 123.6, 120.7, 118.3, 1.37. **ESI-MS** (+ve) $[M\text{-}2MeCN\text{-}PF_6]^+$: m/z = 501.098, calcd 501.0943.

**Bis(2-(2,4-difluorophenyl)-5-trifluoromethylpyridine)iridium-μ-chloro dimer (2.16)**

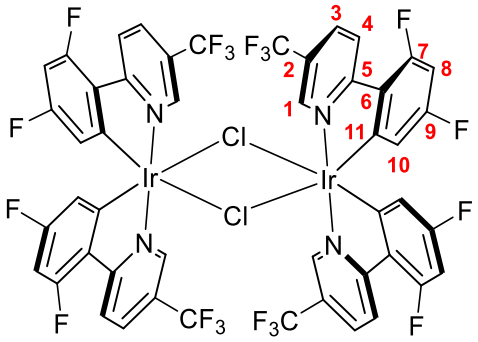

2-(2-4-Difluorophenyl)-5-trifluoromethylpyridine (170 mg, 0.67 mmol) and iridium(III) trichloride hydrate (100 mg, 0.34 mmol) were dissolved in a mixture of water (1 mL) and 2-ethoxyethanol (3 mL) and heated to 100 °C for 48 hours. The yellow suspension was filtered and the solid washed with water and diethyl ether to yield the product as a yellow powder (78 mg, 0.05 mmol, 31%).

**$^1$H-NMR** (300 MHz, $CDCl_3$): 9.51 (d, 1H, *J* = 1.5 Hz, **H$^1$**), 8.46 (dd, 1H, *J* = 2.7, 8.4 Hz, **H$^4$**), 8.04 (dd, 1H, *J* = 1.5, 8.4 Hz, **H$^3$**), 6.47–6.39 (m, 1H, **H$^8$**), 5.07 (dd, 1H, *J* = 2.1, 8.7 Hz, **H$^{10}$**). **$^{13}$C-NMR:** Too insoluble to collect.

**Bis(2-(2,4-difluorophenyl)-5-trifluoromethylpyridine))bis(acetonitrile) iridium(III) hexafluorophosphate (M2)**

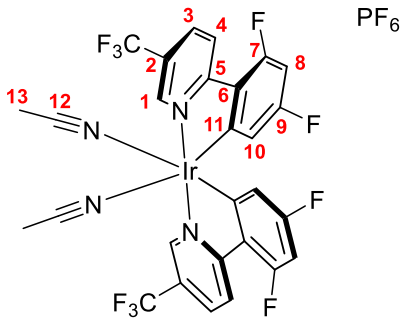

**2.16** (78.0 mg, 0.05 mmol) and silver(I) hexafluorophosphate (25.2 mg, 0.10 mmol) were dissolved in acetonitrile (20 mL) and heated to reflux overnight in the absence of light. The resultant suspension was filtered through a pad of Celite, the solvent was collected and reduced in volume to 1 mL. Diethyl ether was added dropwise until the product precipitated as a yellow powder. The product was filtered and washed with diethyl ether to yield the product as a bright yellow microcrystalline powder (76.7 mg, 0.08 mmol, 82%).

**$^1$H-NMR** (300 MHz, $CD_3NO_2$): 9.39 (s, 1H, **H$^1$**) 8.60 (d, 1H, *J* = 8.7 Hz, **H$^3$**), 8.45 (d, 1H, *J* = 8.7 Hz, **H$^4$**), 6.65 (m, 1H, **H$^8$**), 5.76 (dd, 1H, *J* = 2.4, 9.0 Hz,

**H**[10]). **$^{13}$C-NMR** (126 MHz, $CD_3NO_2$): 168.6, 166.0, 164.0, 162.0, 149.5, 138.6, 128.8, 127.1, 125.1, 123.2, 122.9, 115.3, 100.8, 3.4. **ESI-MS** (+ve): [M-MeCN-$PF_6$]$^+$: m/z =750.0600, calcd 750.0579.

**Bis(2-phenylpyridine)rhodium-μ-chloro dimer[48] (2.17)**

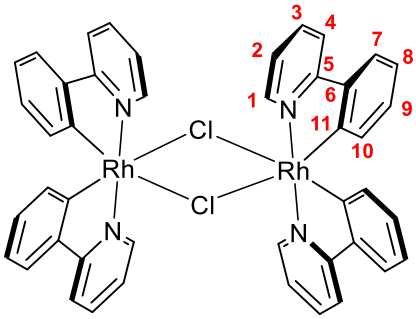


Rhodium trichloride hydrate (100 mg, 0.38 mmol) was dissolved in a mix of 2-ethoxyethanol (6 mL) and water (2 mL). 2-Phenylpyridine (0.14 mL, 0.95 mmol) was added and the mixture was heated to reflux overnight. The mixture was then filtered and washed with water then diethyl ether to yield the product as a yellow powder (112 mg, 0.12 mmol, 66%). All data is consistent with the literature.[48]

**$^1$H-NMR** (300 MHz, $d_6$-DMSO): 9.51 (d, 1H, *J* = 5.4 Hz, **H**[1]), 8.20 (d, 1H, *J* = 7.8 Hz, **H**[4]), 8.12 (t, 1H, *J* = 7.2 Hz, **H**[3]), 7.78 (d, 1H, *J* = 7.5 Hz, **H**[7]), 7.52 (t, 1H, *J* = 6.0 Hz, **H**[2]), 6.89 (t, 1H, *J* = 7.5 Hz, **H**[8]), 6.77 (t, 1H, *J* = 7.5 Hz, **H**[9]), 5.99 (d, 1H, *J* = 7.5 Hz, **H**[10]) **$^{13}$C-NMR** (75 MHz, $d_6$-DMSO): 166.0, 164.5, 151.0, 143.6, 138.4, 131.8, 129.0, 124.0, 122.9, 122.4, 119.6.

**Bis(2-phenylpyridine))bis(acetonitrile)rhodium(III) hexafluorophosphate (M3)**

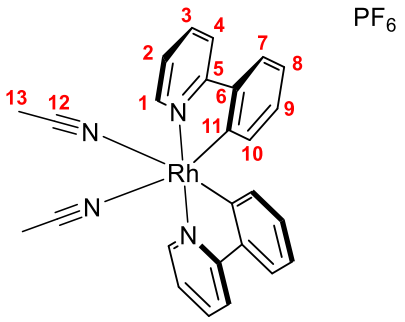


**2.17** (95 mg, 0.11 mmol) and silver(I) hexafluorophosphate (67 mg, 0.27 mmol) were dissolved in acetonitrile (20 mL) in the dark and under an atmosphere of $N_2$. The mixture was heated to reflux overnight. The solution was cooled to room temperature and the suspension was filtered through Celite to yield a pale yellow solution. The volume was reduced down to 1 mL and diethyl ether was added dropwise until the product precipitated. The solid was collected by filtration to yield the pure product as a colourless powder (114 mg, 0.18 mmol, 81%).

**$^1$H-NMR** (300 MHz, $CD_3NO_2$): 9.07 (s, 1H, **H$^1$**), 8.18 (m, 2H, **H$^3$** + **H$^4$**), 7.76 (d, 1H, *J* = 7.8 Hz, **H$^7$**), 7.55 (t, 1H, *J* = 6.0 Hz, **H$^2$**), 7.02 (t, 1H, *J* = 7.8 Hz Hz, **H$^8$**), 6.85 (t, 1H, *J* = 7.8 Hz, **H$^9$**), 6.19 (d, 1H, *J* = 7.2 Hz, **H$^{10}$**). **$^{13}$C-NMR** (75 MHz, $CD_3NO_2$): 150.4, 144.4, 138.9, 132.3, 129.5, 125.3, 124.8, 124.1, 123.4, 119.8, 93.5, 3.1. **ESI-MS** (+ve): $[M\text{-}2MeCN\text{-}PF_6]^+$: m/z = 411.0358, calcd 411.0369.

**Bis(2-(2,4-difluorophenyl)-5-trifluoromethylpyridine)rhodium-μ-chloro dimer (2.18)**

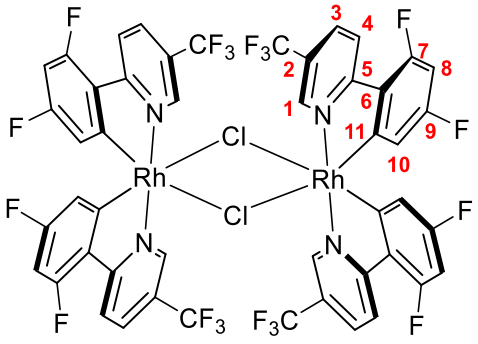


2-(2-4-Difluorophenyl)-5-trifluoromethylpyridine (192 mg, 0.76 mmol) and rhodium (III) trichloride hydrate (100 mg, 0.38 mmol) and were dissolved in a mix of 2-ethoxyethanol (6 mL) and water (2 mL) and heated to reflux overnight.

The mixture was then filtered and washed with water then diethyl ether to yield the product as a yellow powder (171 mg, 0.12 mmol, 68%).

**$^1$H-NMR** (300 MHz, $CDCl_3$): 9.53 (s, 1H, **H$^1$**), 8.44 (d, 1H, *J* = 8.7 Hz, **H$^4$**), 8.13 (d, 1H, *J* = 9.0 Hz, **H$^3$**), 6.50–6.43 (m, 1H, **H$^8$**), 5.12 (d, 1H, *J* = 9.0 Hz, **H$^{10}$**). **$^{13}$C-NMR:** Too insoluble to collect.

**Bis(2-(2,4-difluorophenyl)-5-trifluoromethylpyridine))bis(acetonitrile)rhodium(III) hexafluorophosphate (M4)**

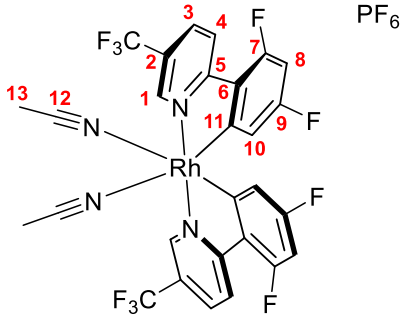


**2.18** (150 mg, 0.11 mmol) and silver(I) hexafluorophosphate (72 mg, 0.29 mmol) were dissolved in acetonitrile (20 mL) in the dark and under an atmosphere of $N_2$. The mixture was heated to reflux overnight. The solution was cooled to room temperature and the suspension was filtered through Celite to yield a pale yellow solution. The volume was reduced down to 1 mL and diethyl ether was added dropwise until the product precipitated. The solid was collected by filtration to yield the pure product as a colourless powder (114 mg, 0.16 mmol, 71%).

**$^1$H-NMR** (300 MHz, $CD_3NO_2$): 9.33 (s, 1H, **H$^1$**) 8.60 (d, 1H, *J* = 8.7 Hz, **H$^3$**), 8.51 (d, 1H, *J* = 8.7 Hz, **H$^4$**), 6.70 (m, 1H, **H$^8$**), 5.83 (dd, 1H, *J* = 2.4, 8.1 Hz, **H$^{10}$**). **$^{13}$C-NMR** (126 MHz, $CD_3NO_2$): 167.8, 167.5, 165.7, 165.0, 163.3, 163.0, 161.2, 148.9, 138.6, 125.3, 123.0, 116.2, 101.6, 3.0. **ESI-MS** (+ve) [M-2MeCN-$PF_6$]: m/z = 618.9476 calcd 698.9739.

**2-Phenylpyridine platinum(II)-μ-chloro dimer[54] (2.19)**

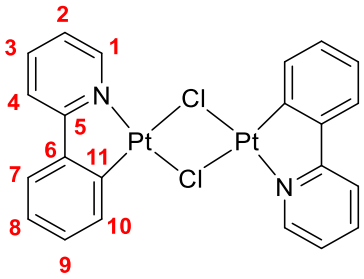


Potassium tetrachloroplatinate(II) (100 mg, 0.24 mmol) was dissolved in a degassed mixture of 2-ethoxyethanol (3 mL) and water (1 mL) under an atmosphere of $N_2$. 2-Phenylpyridine (34 μL, 0.24 mmol) was added and the solution was heated to 80 °C for two days during which time a yellow precipitate formed. The reaction was then cooled in an ice bath and water was added resulting in further precipitation. The solid was collected by filtration and washed with water then diethyl ether to yield the product as a yellow powder (79 mg, 0.10 mmol, 86%). The product was used in the next step without purification due to insolubility in organic solvents.

**2-Phenylpyridinebis(acetonitrile)platinum(II) hexafluorophosphate (M5)**

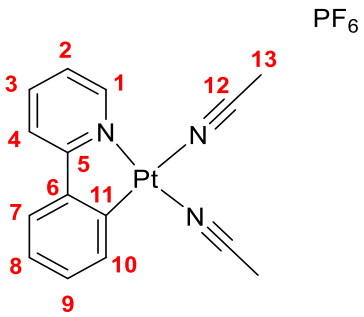


**2.19** (79 mg, 0.10 mmol) and silver(I) hexafluorophosphate (51 mg, 0.20 mmol) were dissolved in acetonitrile (50 mL) and stirred at room temperature for four hours in the absence of light. The resulting suspension was filtered through a pad of Celite. The solvent was collected and reduced to a volume of 1 mL. Diethyl ether was added and the product precipitated. The solid was collected by filtration and washed with ether to yield the product as a green/ yellow powder (65 mg, 0.11 mmol, 56%).

**$^1$H-NMR** (500 MHz, $d_3$-$MeNO_2$): 8.66 (dd, 1H, $J$ = 5.9, 45.1 Hz, **H$^1$**) 8.12 (t, 1H, $J$ = 8.0 Hz, **H$^3$**), 7.92 (d, 1H, $J$ = 7.8 Hz, **H$^4$**), 7.61 (d, 1H, $J$ = 7.8 Hz, **H$^7$**), 7.38–7.33 (m, 2H, **H$^2$/H$^{10}$**), 7.24 (t, 1H, $J$ = 7.5 Hz, **H$^8$**), 7.18 (t, 1H, $J$ = 7.5 Hz, **H$^9$**), 2.73 (s, 3H, **H$^{13}$**). **$^{13}$C-NMR** (125 MHz, $d_3$-$MeNO_2$): 168.0 (**C$^5$**), 151.6 (**C$^1$**), 146.5 (**C$^6$**), 142.6 (**C$^3$**), 135.9 (**C$^{11}$**), 134.4 (**C$^{10}$**), 131.6 (**C$^9$**), 127.2 (**C$^8$**), 125.4

(**C**[7]), 124.9 (**C**[2]), 123.1 (**C**[12]), 121.0 (**C**[4]), 3.9 (**C**[13]). **ESI-MS** (+ve) [M-MeCN-$PF_6$]: m/z = 390.0002 calcd 390.0570.

**(2-(2,4-difluorophenyl)5-trifluoromethylpyridine) platinum(II)-μ-chloro dimer (2.20)**

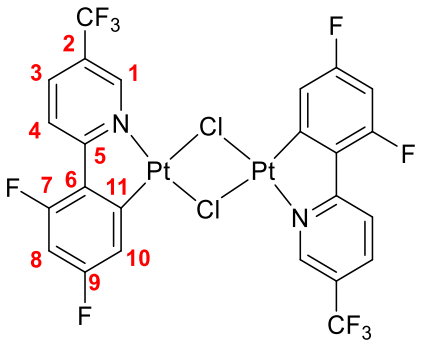


2-(2-4-Difluorophenyl)-5-trifluoromethylpyridine (61 mg, 0.24 mmol) potassium tetrachloroplatinate(II) (100 mg, 0.24 mmol) was dissolved in a degassed mixture of 2-ethoxyethanol (3 mL) and water (1 mL) under an atmosphere of $N_2$. The solution was heated to 80 $^oC$ for two days during which time a yellow precipitate formed. The reaction was then cooled in an ice bath and water was added resulting in further precipitation. The solid was collected by filtration and washed with water then diethyl ether to yield the product as a yellow powder (75 mg, 0.08 mmol, 64%).

**$^1$H-NMR** (300 MHz, $CDCl_3$): 10.00 (s, 1H, **H**[1]), 8.26 (d, 1H, *J* = 8.4 Hz, **H**[3]), 7.88 (d, 1H, *J* = 8.7 Hz, **H**[4]), 6.84–6.77 (m, 1H, **H**[8]), 6.60–6.52 (m, 1H, **H**[10]). **$^{13}$C-NMR**: Too insoluble to collect.

**(2-(2,4-difluorophenyl)5-trifluoromethylpyridine)bis(acetonitrile) platinum(II) hexafluorophosphate (M6)**

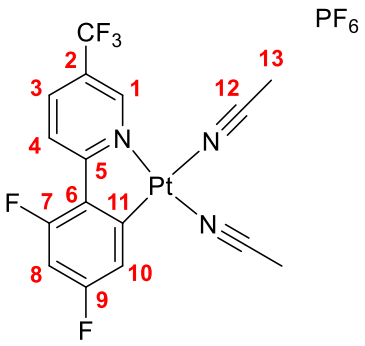


**2.20** (75 mg, 0.08 mmol) and silver(I) hexafluorophosphate (40 mg, 0.16 mmol) were dissolved in acetonitrile (50 mL) and stirred at room temperature overnight in the absence of light. The resulting suspension was filtered through a pad of Celite. The solvent was collected and reduced to a volume of 1 mL. Diethyl ether was added and the product precipitated. The solid was collected by filtration and washed with ether to yield the product as a yellow powder (69 mg, 0.10 mmol, 63%).

**$^{1}$H-NMR** (500 MHz, $d_3$-$MeNO_2$): 8.91 (t, 1H, *J* = 45.2 Hz, **$H^{1}$**), 8.45 (d, 1H, *J* = 8.7 Hz, **$H^{3}$**), 8.33 (d, 1H, *J* = 8.4 Hz, **$H^{4}$**), 6.94 (ddd, 1H, *J* = 2.4, 8.6 Hz, **$H^{8}$**) 6.88 (dd, 1H, *J* = 2.2, 9.4 Hz, **$H^{10}$**), 2.77 (s, 1H, **$H^{13}$**).**$^{13}$C-NMR** (125 MHz, $d_3$-$MeNO_2$): 168.0 (**$C^{5}$**), 164.1 (**$C^{10}$**), 163.1 (**$C^{11}$**), 160.0 (**$C^{6}$**) 148.8 (**$C^{1}$**), 140.4 (**$C^{3}$**), 129.1 (**$C^{7}$**), 126.6 (**$CF_3$**) 124.5 (**$C^{4}$**), 124.1 (**$C^{2}$**), 121.7 (**$C^{12}$**) 117.5 (**$C^{8}$**), 103.1 (**$C^{10}$**), 2.6 (**$C^{13}$**). **ESI-MS** (+ve) [M-MeCN-$PF_6$+$H_2O$]: m/z = 512.0012 calcd 512.0361.

## References


1. M. Fujita, J. Yazaki and K. Ogura, *J. Am. Chem. Soc.*, 1990, **112**, 5645-5647.
2. M. Fujita, M. Tominaga, A. Hori and B. Therrien, *J. Am. Chem. Soc.*, 2005, **38**, 369-378.
3. D. Fujita, Y. Ueda, S. Sato, N. Mizuno, T. Kumasaka and M. Fujita, *Nature.*, 2016, **540**, 563.
4. D. Canevet, E. M. Pérez and N. Martín, *Angew. Chem.*, 2011, **50**, 9248-9259.
5. R. J. Blanch, M. Williams, G. D. Fallon, M. G. Gardiner, R. Kaddour and C. L. Raston, *Angew. Chem.*, 1997, **36**, 504-506.
6. D. Felder, B. Heinrich, D. Guillon, J.-F. Nicoud and J.-F. Nierengarten, *Chem. Eur. J.*, 2000, **6**, 3501-3507.
7. J. Canceill, A. Collet and G. Gottarelli, *J. Am. Chem. Soc.*, 1984, **106**, 5997-6003.
8. M. Irie, *Chem. Rev*, 2000, **100**, 1685-1716.
9. D. H. Waldeck, *Chem. Rev.*, 1991, **91**, 415-436.
10. M. Irie, T. Lifka, K. Uchida, S. Kobatake and Y. Shindo, *Chem. Commun*, 1999, 747-750.
11. M. Han, R. Michel, B. He, Y.-S. Chen, D. Stalke, M. John and G. H. Clever, *Angew. Chem. Int. Ed.*, 2013, **52**, 1319-1323.
12. C. R. Crecca and A. E. Roitberg, *J. Phys. Chem. A*, 2006, **110**, 8188-8203.
13. C. J. Brown, *Acta Cryst.*, 1966, **21**, 146-152.
14. T. Schultz, J. Quenneville, B. Levine, A. Toniolo, T. J. Martínez, S. Lochbrunner, M. Schmitt, J. P. Shaffer, M. Z. Zgierski and A. Stolow, *J. Am. Chem. Soc*, 2003, **125**, 8098-8099.
15. L. Gagliardi, G. Orlandi, F. Bernardi, A. Cembran and M. Garavelli, *Theor. Chem. Acc.*, 2004, **111**, 363-372.
16. H. Rau and E. Lueddecke, *J. Am. Chem. Soc*, 1982, **104**, 1616-1620.
17. J. L. Magee, W. Shand and H. Eyring, *J. Am. Chem. Soc*, 1941, **63**, 677-688.
18. D. Y. Curtin, E. J. Grubbs and C. G. McCarty, *J. Am. Chem. Soc*, 1966, **88**, 2775-2786.
19. I. K. Lednev, T. Q. Ye, P. Matousek, M. Towrie, P. Foggi, F. V. R. Neuwahl, S. Umapathy, R. E. Hester and J. N. Moore, *Chem. Phys. Lett*, 1998, **290**, 68-74.
20. P. Bortolus and S. Monti, *J. Phys. Chem.*, 1979, **83**, 648-652.
21. B. Priewisch and K. Rück-Braun, *J. Org. Chem.*, 2005, **70**, 2350-2352.
22. S. Oldknow, D. R. Martir, V. E. Pritchard, M. A. Blitz, Colin W. G. Fishwick, E. Zysman-Colman and M. J. Hardie, *Chem. Sci.*, 2018, **9**, 8150-8159.
23. K. Ueno and S. Akiyoshi, *J. Am. Chem. Soc*, 1954, **76**, 3670-3672.
24. J. J. Henkelis, C. J. Carruthers, S. E. Chambers, R. Clowes, A. I. Cooper, J. Fisher and M. J. Hardie, *J. Am. Chem. Soc*, 2014, **136**, 14393-14396.

25. V. E. Pritchard, D. Rota Martir, S. Oldknow, S. Kai, S. Hiraoka, N. J. Cookson, E. Zysman-Colman and M. J. Hardie, *Chem. Eur. J.*, 2017, **23**, 6290-6294.
26. S. Oldknow, PhD Thesis, University of Leeds, 2018.
27. A. Raman, G. Augustine, N. Ayyadurai and S. Easwaramoorthi, *New J. Chem*, 2018, **42**, 9300-9305.
28. M. J. Hardie, *Chem. Soc. Rev.*, 2010, **39**, 516-527.
29. J. Canceill, A. Collet, J. Gabard, G. Gottarelli and G. P. Spada, *J. Am. Chem. Soc*, 1985, **107**, 1299-1308.
30. T. Brotin, V. Roy and J.-P. Dutasta, *J. Org. Chem.*, 2005, **70**, 6187-6195.
31. J. J. Henkelis, J. Fisher, S. L. Warriner and M. J. Hardie, *Chem. Eur. J*, 2014, **20**, 4117-4125.
32. J. Henkelis, PhD Thesis, University of Leeds, 2014.
33. J. Canceill, L. Lacombe and A. Collet, *J. Chem. Soc. Chem. Commun.*, 1987, 219-221.
34. E. Huerta, S. A. Serapian, E. Santos, E. Cequier, C. Bo and J. de Mendoza, *Chem. Eur. J*.
35. G. T. Illa, S. Hazra, P. Satha and C. S. Purohit, *CrystEngComm.*, 2017, **19**, 4759-4765.
36. L. Chen, Q. Chen, M. Wu, F. Jiang and M. Hong, *Acc. Chem. Res.*, 2015, **48**, 201-210.
37. B. J. Holliday and C. A. Mirkin, *Angew. Chem. Int. Ed.*, 2001, **40**, 2022-2043.
38. S. Roche, C. Haslam, S. L. Heath and J. A. Thomas, *Chem. Commun.*, 1998, 1681-1682.
39. A. Schaly, Y. Rousselin, J.-C. Chambron, E. Aubert and E. Espinosa, *Eur. J. Inorg. Chem.*, 2016, **2016**, 832-843.
40. Z. Zhong, A. Ikeda, S. Shinkai, S. Sakamoto and K. Yamaguchi, *Org. Lett.*, 2001, **3**, 1085-1087.
41. N. J. Cookson, J. M. Fowler, D. P. Martin, J. Fisher, J. J. Henkelis, T. K. Ronson, F. L. Thorp-Greenwood, C. E. Willans and M. J. Hardie, *Supramol. Chem.*, 2018, **30**, 255-266.
42. J. J. Henkelis, T. K. Ronson, L. P. Harding and M. J. Hardie, *Chem. Commun.*, 2011, **47**, 6560-6562.
43. N. J. Cookson, PhD Thesis, University of Leeds, 2016.
44. M. S. Lowry, J. I. Goldsmith, J. D. Slinker, R. Rohl, R. A. Pascal, G. G. Malliaras and S. Bernhard, *Chem. Mater*, 2005, **17**, 5712-5719.
45. S. Lamansky, P. Djurovich, D. Murphy, F. Abdel-Razzaq, R. Kwong, I. Tsyba, M. Bortz, B. Mui, R. Bau and M. E. Thompson, *Inorg. Chem.*, 2001, **40**, 1704-1711.
46. K. A. King, P. J. Spellane and R. J. Watts, *J. Am. Chem. Soc*, 1985, **107**, 1431-1432.
47. M. G. Colombo, T. C. Brunold, T. Riedener, H. U. Guedel, M. Fortsch and H.-B. Buergi, *Inorg. Chem.*, 1994, **33**, 545-550.
48. H. Liang, T. Hao, C. Yin, X. Yang, H. Fu, X. Zheng, R. Li, D. Xiao and H. Chen, *Eur. J. Inorg. Chem.*, 2017, **2017**, 4149-4157.
49. H. Geng, K. Luo, G. Zou, H. Wang, H. Ni, W. Yu, Q. Li and Y. Wang, *New J. Chem*, 2016, **40**, 10371-10377.
50. L. Wang, G.-T. Wang, X. Zhao, X.-K. Jiang and Z.-T. Li, *J. Org. Chem.*, 2011, **76**, 3531-3535.

51. J. M. Fowler, F. L. Thorp-Greenwood, S. L. Warriner, C. E. Willans and M. J. Hardie, *Chem. Commun*, 2016, **52**, 8699-8702.
52. N. Matsuo, *Bull. Chem. Soc. Jpn.*, 1974, **47**, 767-768.
53. K. A. McGee and K. R. Mann, *Inorg. Chem.*, 2007, **46**, 7800-7809.
54. N. Godbert, T. Pugliese, I. Aiello, A. Bellusci, A. Crispini and M. Ghedini, *Eur. J. Inorg. Chem.*, 2007, **2007**, 5105-5111.

# Chapter 3

# Self-assembly and characterisation of photoresponsive $M_3L_2$ metallo-cryptophanes

## 3.1 Introduction

Coordination cages have been the subject of extensive research in recent years, mainly due to their willingness to form host-guest inclusion complexes.[1-4] The propensity to form these complexes lends coordination cages to applications such as catalysis where they can act as nanoscale reaction vessels[5-7] or molecular separation where the host-guest properties can be used to extract otherwise difficult to obtain chemicals from a mixture.[8, 9] A major reason why coordination cages receive such interest is due to the ease at which structural variability can be achieved through rational design of ligand and metal tectons. Several design strategies exist for the construction of these cages with excellent examples originating from the groups of Nitschke,[10-12] Fujita,[13-15] Stang[16, 17] and Ward.[2, 18-20]

An early example highlighting the synthetic value of these systems was reported by Fujita where a $Pd_6L_4$ octahedral cage was used to catalyse a Diels-Alder reaction between 9-hydroxymethylanthracene and N-cyclohexylpthalimide (Figure 3.1).[5]

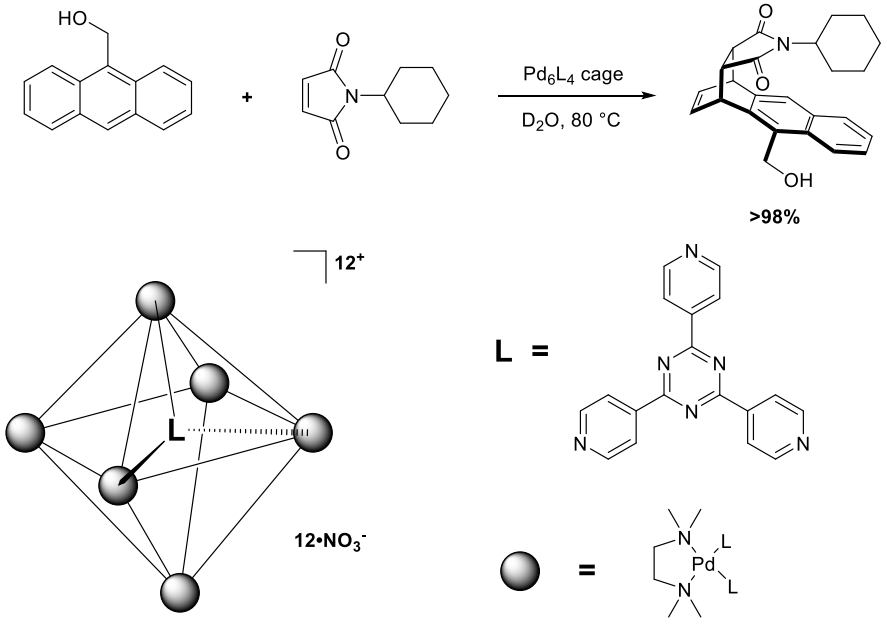


**Figure 3.1.** An example of a $Pd_6L_4$ coordination cage catalysing a Diels-Alder reaction with unusual regioselectivity.

The reactants and cage were mixed in $D_2O$ for 5 minutes at room temperature to form the inclusion complex prior to heating at 80 °C for 5 hours. The product was isolated in over a 98% yield; which greatly surpassed the yield of 44% obtained when no cage was present.[5] Moreover, when the reaction was performed in the coordination cage only one product was isolated, the 1,4-*syn* isomer shown in Figure 3.1. In the absence of cage only the 9,10-Diels-Alder product was isolated.[5] This example highlights the synthetic power of coordination cages as not only has the yield been vastly improved but it is possible to impart unusual regioselectivity on a chemical reaction due to the effects of confinement.

$M_3L_2$ metallo-cryptophanes represent one of the most fundamental architectures accessible using CTV based ligands. However, specifically targeting this motif can be challenging.[21] Metallo-cryptophanes are usually targeted through self-assembly, due to the tripodal nature of CTV ligands a plethora of alternative architectures are accessible including coordination polymers, larger cage-like structures and topologically complex species.[22-24] The first organically linked cryptophane was reported in 1981 by Collett[25] and it wasn't until 2001 that the first metallo-cryptophane was reported by Shinkai, Yamaguchi and co-workers. They discovered that three *cis* protected palladium cations self-assembled with two 4-pyridyl appended CTG molecules in a head to head fashion to yield the first example of an $M_3L_2$ metallo-cryptophane.[26] The field has since expanded, with notable examples reported from the group of Chambron and coworkers.[27]

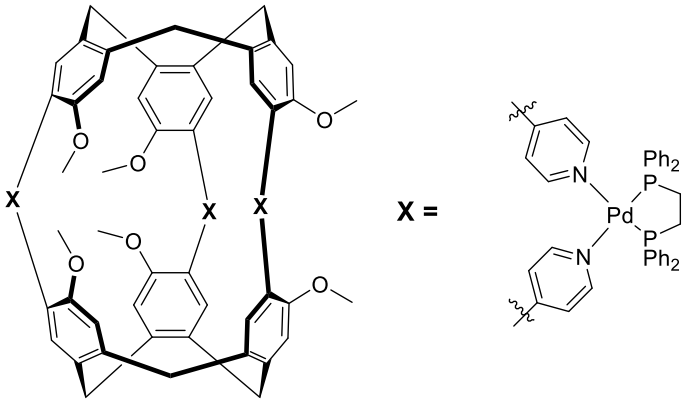


**Figure 3.2.** The first example of an $M_3L_2$ metallo-cryptophane reported by Shinkai and co-workers.[26]

By virtue of its electron rich and hydrophobic cavity, CTG displays inherent host properties that are often amplified upon incorporation into the hollow interior of a metallo-cryptophane.[21, 28] It is for this reason, that targeting these structures is an incredibly worthwhile endeavour. The improved host

properties can result in numerous secondary applications for these cages such as nanoscale reaction vessels or in enzyme-like catalysis.[29, 30] In addition, the inclusion of two chiral CTG units within the cryptophane means that the resultant cage can exist as diastereomers. Cryptophanes can exist in two diastereomeric forms, *syn* or *anti* (Figure 3.3). A *syn* isomer contains two CTG units of opposite chirality, displaying $C_{3h}$ symmetry. Conversely, an *anti* isomer consists of two CTG units of the same chirality and displays $D_3$ symmetry. The chirality of the hosts enables molecular recognition of chiral guests to occur.[31, 32]

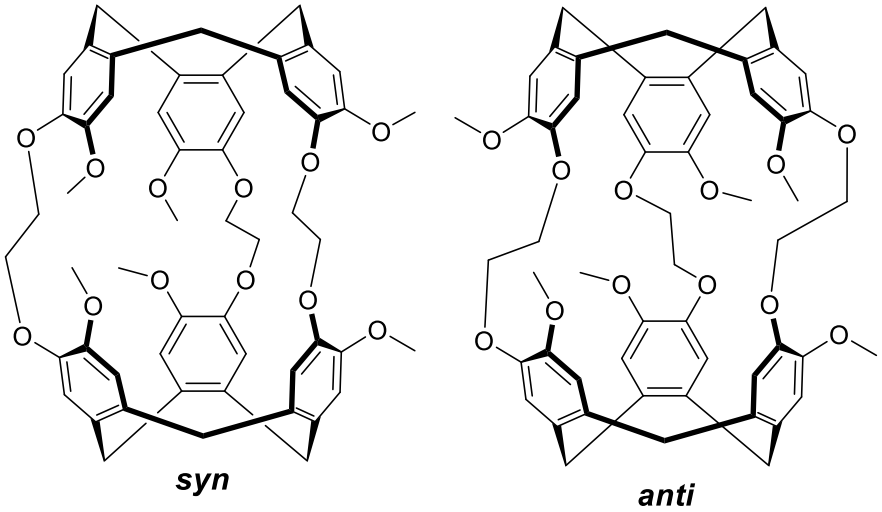


**Figure 3.3.** Possible *syn* and *anti* diastereomers of cryptophanes.

## 3.2 Expansion of the Ir(III) metallo-cryptophane library

The synthesis of iridium(III) metallo-cryptophanes bearing photoresponsive azobenzene linkers was first reported by previous PhD student Samuel Oldknow.[33] It was found that when an azobenzene appended CTG ligand was mixed with an Ir(III) tecton bearing *cis* protecting phenylpyridine ligands in a 2:3 ratio an $M_3L_2$ metallo-cryptophane was obtained in quantitative yields (Scheme 3.1).

The structure of these cryptophanes were able to be unequivocally assigned through a combination of high resolution mass spectrometry which in all cases showed a peak for the $[M_3L_2]^{3+}$ cation, DOSY NMR confirmed the presence of only one species in solution and a variety of 2D NMR techniques such as COSY, TOCSY, HSQC and NOESY were used to confirm the connectivity of the components.

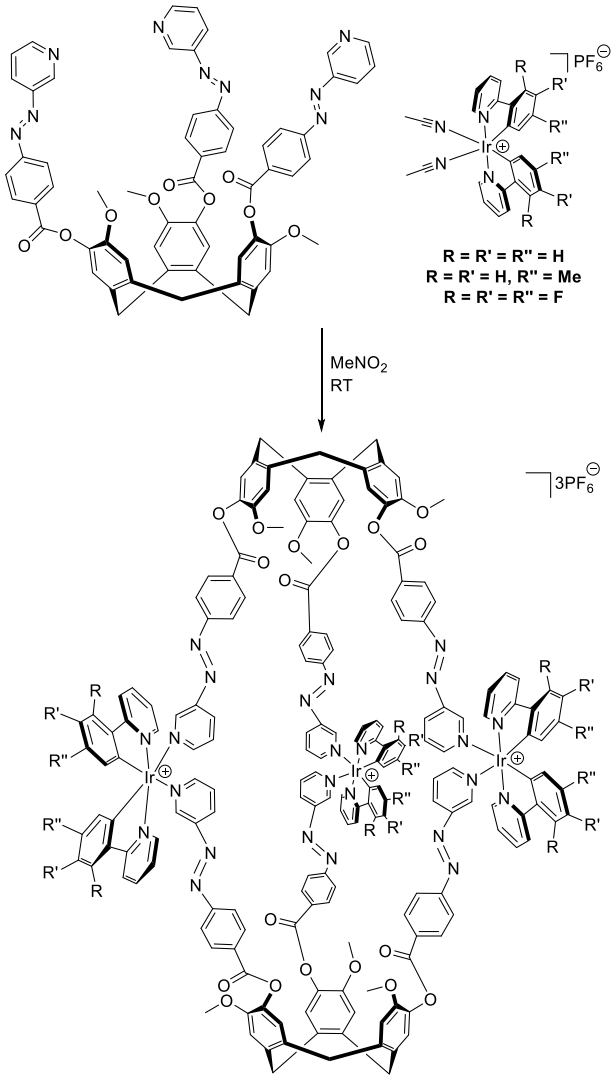


**Scheme 3.1.** Synthesis of azobenzene containing Ir(III) metallo-cryptophane.[33]

As mentioned in Chapter 2 poor solubility of the iridium metallo-cryptophanes in solvents other than nitromethane has proven to be a hindrance towards developing further applications for these complexes. The fluorination of components has been shown to be a viable strategy to increase the solubility of metallo-cages in organic solvents.[33, 34] Therefore, attempts were made to expand the library of iridium metallo-cryptophanes to include polyfluorinated phenylpyridine tectons in order to increase the solubility further. Whilst functionalisation of the metal tecton has already been shown to be effective in increasing its solubility, it is unknown whether functionalisation of the ligand will also have an effect. To investigate this, azobenzene ligands bearing ethoxy and propoxy groups, as discussed in the previous Chapter were also used to form complexes in an attempt to solubilise the metallo-cryptophanes in solvents other than nitromethane (Scheme 3.2).

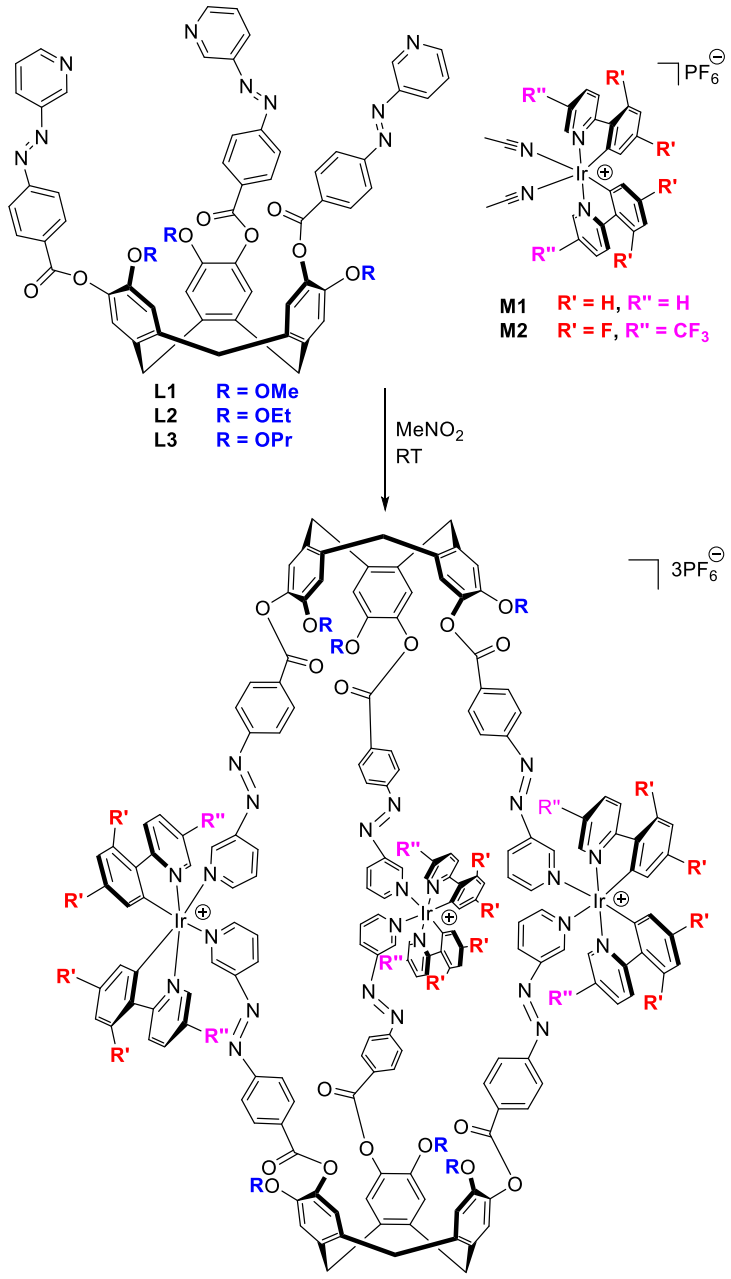


**Scheme 3.2.** Synthetic methodology to expand the iridium(III) metallo-cryptophane library.

**Table 3.1.** Reaction codes of iridium-cryptophanes resulting from the reaction of azobenzene ligand with metal tecton.

| Ligand | Metal tecton | Metallo-cryptophane |
|---|---|---|
| L1 | M1 | C1 |
| L1 | M2 | C2 |
| L2 | M1 | C3 |
| L2 | M2 | C4 |
| L3 | M1 | C5 |
| L3 | M2 | C6 |

Synthesis of the metallo-cryptophanes was carried out in an analogous manner to that reported by Dr Samuel Oldknow, where **M1** and **L1** were used to synthesise the first example of an azobenzene containing metallo-cryptophane.[33] As seen in Table 3.1 the ligands and metal tectons could be mixed in a total of six possible permutations and therefore, it was theoretically possible to synthesise six different metallo-cryptophanes. Three equivalents of the metal tecton were dissolved in deuterated nitromethane and added dropwise to two equivalents of the ligand also dissolved in deuterated nitromethane and the progress of the reaction was monitored by $^{1}$H-NMR spectroscopy.[33]

Initial investigations focused upon the self-assembly of the solubilised ligands **L2** and **L3** with the unsubstituted iridium phenylpyridine tecton **M1**. These were designed to yield metallo-cryptophanes **C3** and **C5**. Upon mixing of the reagents, the $^{1}$H-NMR resonances immediately underwent significant broadening (Figure 3.4). Resonances arising from the pyridyl group on the ligand and the phenyl ring of the phenylpyridine tecton were shifted downfield. Whereas the signals for the pyridyl on the metal tecton were shifted upfield. This pattern is consistent with substitution of the acetonitrile ligands at the iridium centre by **L2** or **L3.** In total it took approximately five minutes for the metallo-cryptophanes to fully assemble. The progress of the reaction could also be monitored by mass spectrometry. As the reaction progressed, increasing quantities of the $M_3L_2$ species were detected in the mass spectrometer as $[M_3L_2]^{3+}$ species alongside fragments originating from this complex such as $[M_2L]^{2+}$ (Figure 3.6 and Figure 3.7). 2-D NMR techniques allowed complete assignment of every proton environment on the metallo-cryptophane (Figure 3.5). The values obtained are consistent with the literature values for similar complexes.[33]

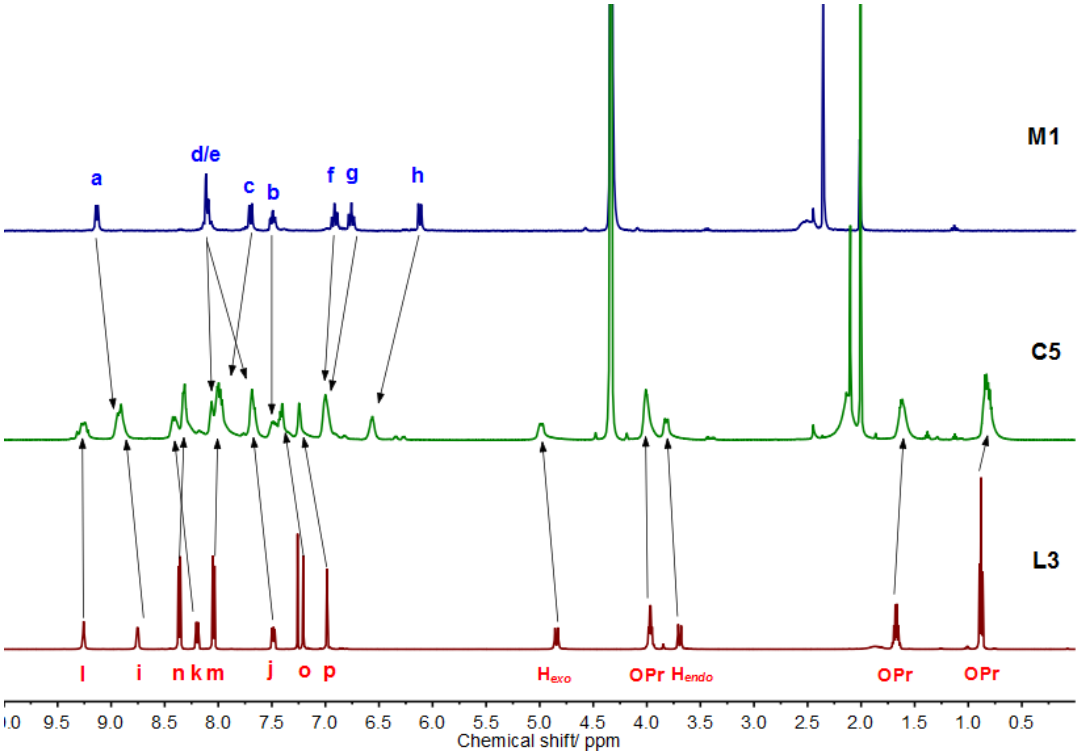


**Figure 3.4.** Time-course $^{1}$H-NMR (500 MHz, $d_3$-$MeNO_2$) showing the NMR spectra of **L3** and **M1** as unmixed solutions and immediately upon mixing.

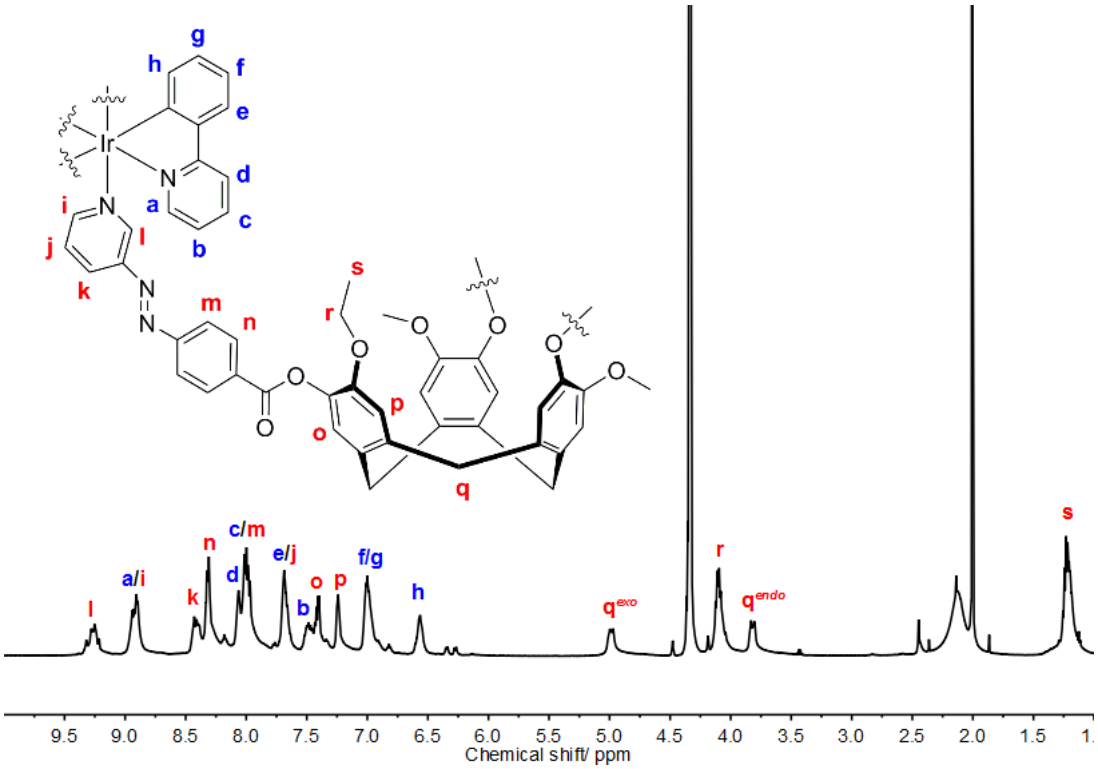


**Figure 3.5.** Fully assigned $^{1}$H-NMR (500 MHz, $d_3$-$MeNO_2$) of **C3**.

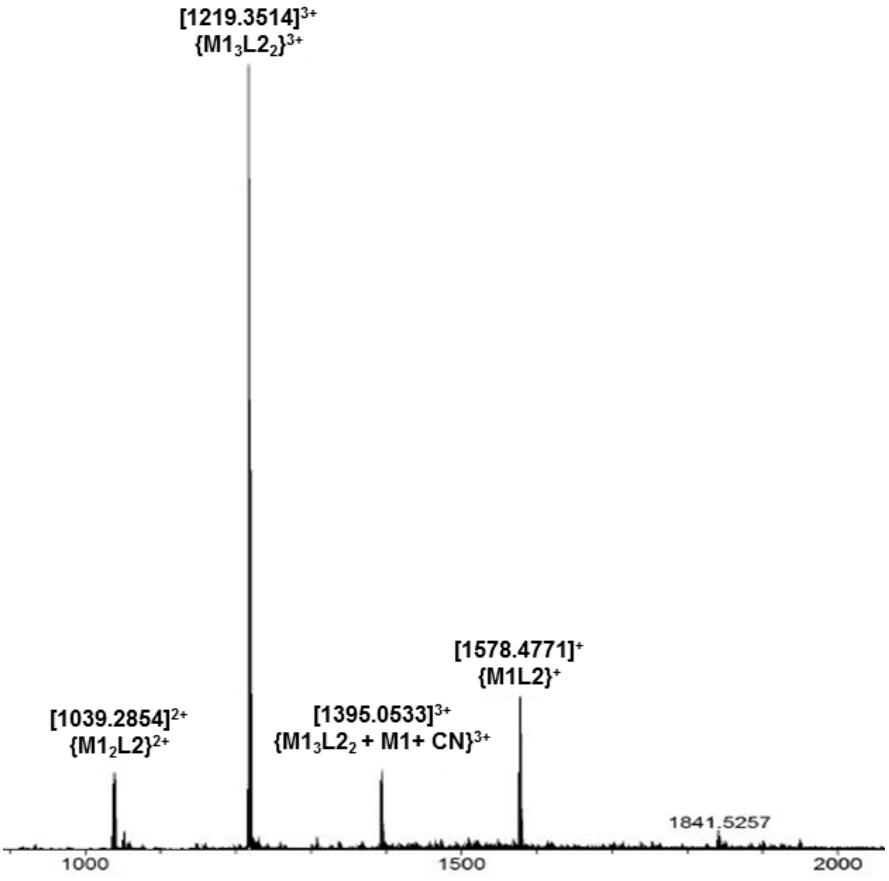


**Figure 3.6.** ESI-MS of **C3** acquired in $MeNO_2$ (**M1 = M1 – 2MeCN – $PF_6$**).

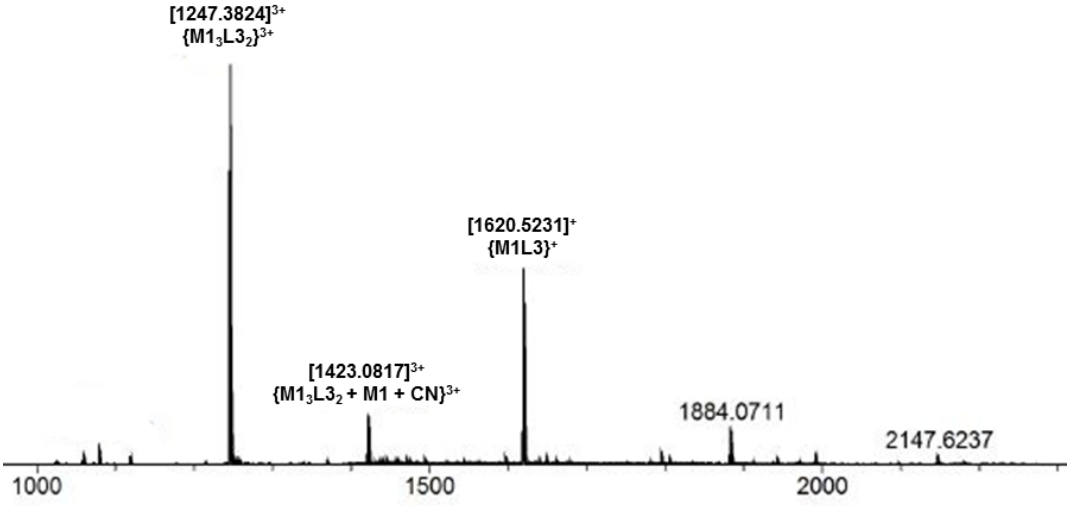


**Figure 3.7.** ESI-MS of **C5** acquired in $MeNO_2$ (**M1 = M1 – 2MeCN – $PF_6$**).

The NMR spectra of **C3** and **C5** were remarkably similar to the spectrum reported in the literature for the known metallo-cryptophane **C1** (Figure 3.8). Importantly, a downfield shift was observed for the signals arising from the

*ortho* pyridyl position on the ligand (9.18 – 9.25 ppm, $H_l$) and the position closest to the iridium on the cyclometallated phenyl ring, (6.11 – 6.56 ppm, $H_h$). The shifts in these peaks are indicative of complexation to the iridium centre. The predicted metallo-cryptophane species differ only by the upper rim alkoxy substituent in each case and as expected the NMR spectra only differed significantly in the aliphatic region, with the aromatic region proving almost identical. The similarity between the spectra, and detection of the $M_3L_2$ species in the mass spectra provides very strong evidence for the formation of **C3** and **C5**. In all cases a very small quantity of a minor product was observed in the NMR spectra at approximately 6.30 ppm. Whilst not present in significant quantities, this minor product will be discussed further later in this Chapter.

It was envisioned that the use of the solubilised ligands would facilitate dissolution of the resulting metallo-cryptophanes in solvents other than nitromethane. However, attempts to self-assemble **C3** and **C5** in solvents other than nitromethane ultimately failed. Upon mixing, the product immediately precipitated from chloroform, dichloromethane and tetrachloroethane solutions as an unassignable powder. The metallo-cryptophanes were not sufficiently solubilised using just the solubilised ligands. Therefore, a combination approach using both solubilised ligands and metal tectons was required.

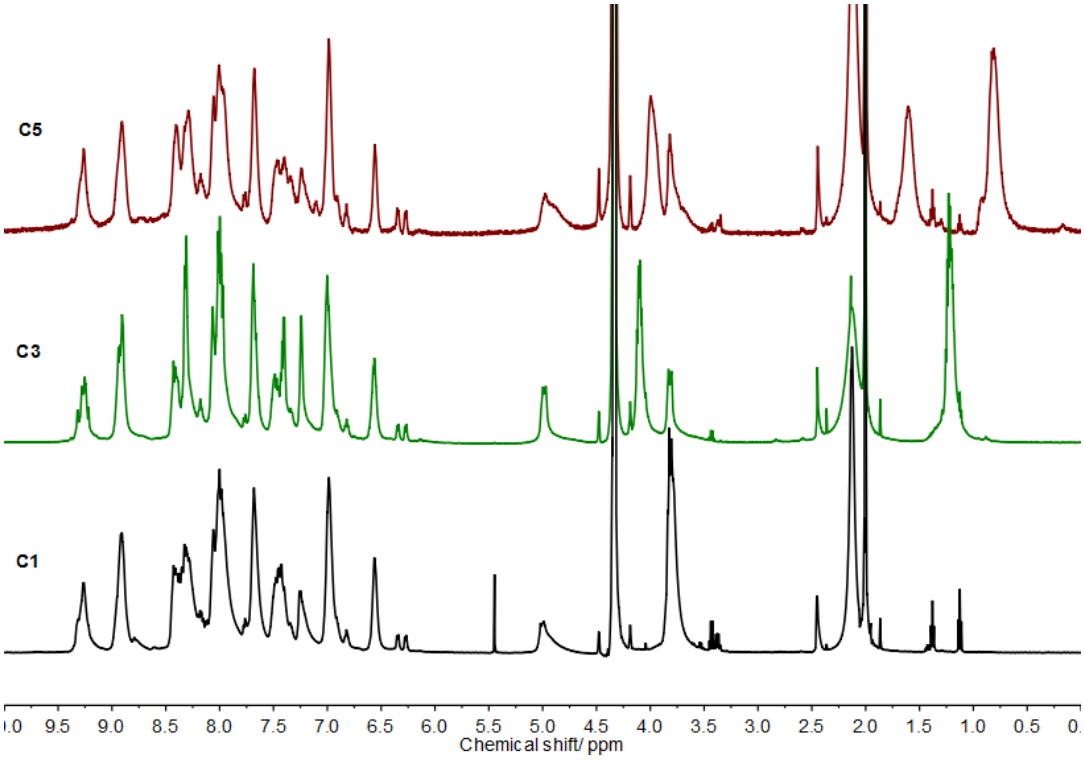


**Figure 3.8.** Comparison of $^{1}$H-NMR (500 MHz, $d_3$-$MeNO_2$) spectra of **C1** (black), **C3** (green) and **C5** (red) revealing the striking similarity between the spectra.

The fluorinated iridium phenylpyridine tecton **M2** was combined with the three azobenzene appended ligands **L1** – **L3**. The metal and ligand were both dissolved in deuterated nitromethane and mixed together in a 3:2 ratio. The progress of the reaction was monitored by $^{1}$H-NMR until no further changes were observed in the spectra (Figure 3.9). It was found that the fluorination of the phenylpyridine tecton has a dramatic effect on the kinetics of the reaction. The time taken to self-assemble was substantially increased for the fluorinated tecton compared to the un-fluorinated tecton. The time required to reach equilibrium was increased from under five minutes to over 24 hours, approximately a 300 fold increase. This same effect has been observed for iridium metallo-cryptophanes reported previously within the group,[33] the rationale behind this observation is that the fluorine groups withdraw electron density from the ring, thereby weakening the C-Ir bond. A weaker C-Ir bond then leads to a reduction in the strength of the *trans* effect. This is important as in order to form a metallo-cryptophane it is required that the bonds *trans* to the phenyl ring are sufficiently labile so that self-assembly can occur and the thermodynamic minimum can be reached. With the reduction of lability the system takes longer to reach the thermodynamic minimum as the reaction intermediates are more kinetically inert. Methylated analogues of the metal tectons have been shown to self-assemble at a similar rate to unsubstituted

tectons, ruling out the possibility that steric clashes are responsible for the decrease in reaction rate and confirming that the phenomenon must be due to the electronics of the system.[33] The simplicity of the spectrum and relative sharpness of the peaks confirms that the main product is not of a lower symmetry than the original $C_3$ symmetry of the ligand. The expected downfield shift of the resonances *ortho* to the pyridyl on the ligand and the protons on the phenyl ring of the phenylpyridine moiety provide further evidence that complexation with the ligand has occurred to form the metallo-cryptophane.

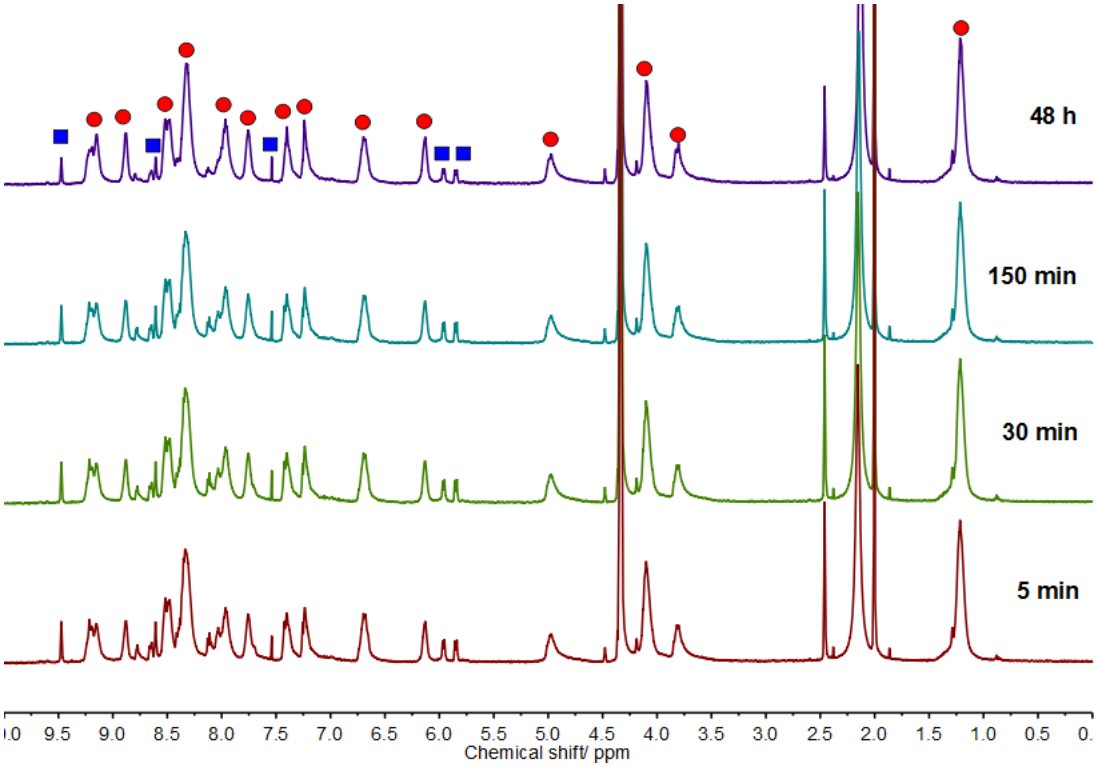


**Figure 3.9.** Timecourse $^1$H-NMR (500MHz, $d_3$-$MeNO_2$) of the self-assembled product (**C4**) of **L2** and **M2**. **C4** peaks are highlighted in red and an minor self-assembly product in blue.

An unexpected product of self-assembly was detected in all cases where **M2** was used as the metal tecton. As the reaction proceeds towards the thermodynamic minimum intermediate species could be detected in the $^1$H-NMR spectra which initially increased in intensity before decreasing. These peaks were assigned as originating from an intermediate cage species such as $[ML]^+$, $[M_2L]^{2+}$, $[M_2L_2]^{2+}$ or $[M_3L]^{3+}$ which must transiently exist during cage formation. After 24 hours, the equilibrium of the system had been reached, yet signals originating from at least one of the cage intermediates persisted. These signals did not disappear upon heating the reaction or leaving it to stand for over three months. Despite the complexity of the $^1$H-NMR spectrum, it was possible to determine that only two species, a major and a minor product, were present in solution using $^{19}$F-NMR (Figure 3.10).

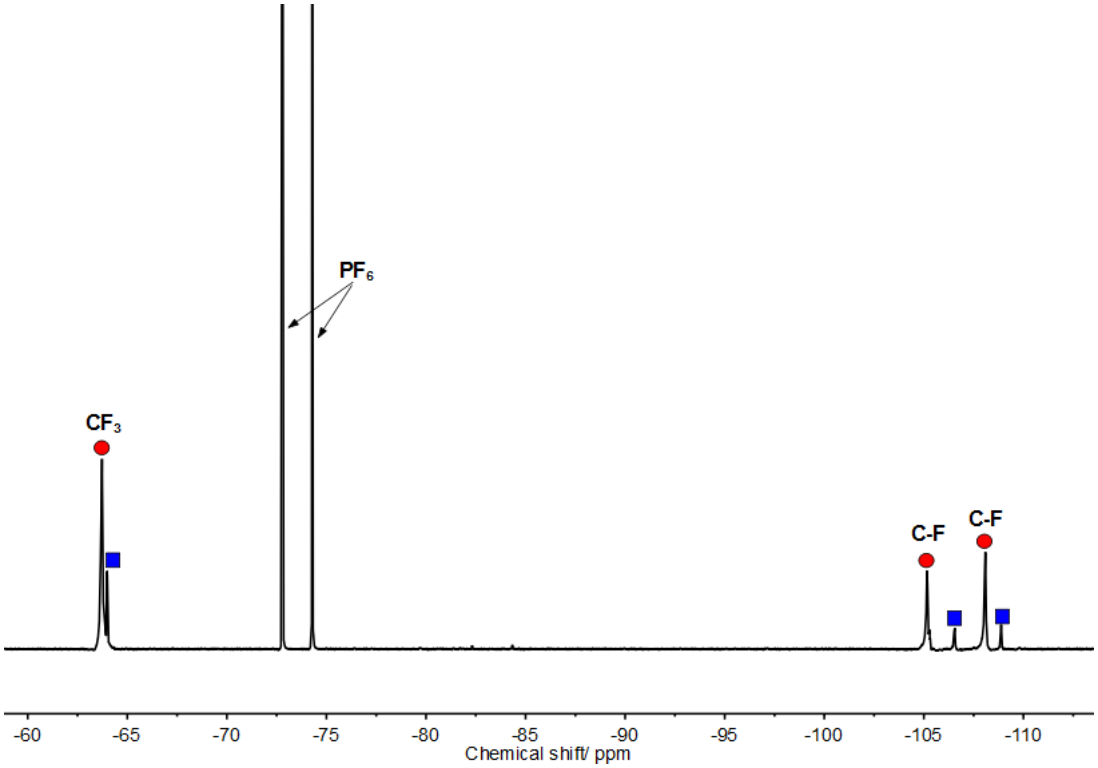


**Figure 3.10.** $^{19}$F-NMR (471 MHz, $d_3$-$MeNO_2$) of cage **C4** showing the presence of two species in the sample, **C4** (red) and a minor (blue) product.

An NMR titration experiment was performed where the equivalents of the metal tecton was varied between an $M_2L_2$ ratio up to an $M_4L_2$ ratio. At the lower concentrations the spectrum contains a large number of peaks resulting from the mismatch in stoichiometries promoting intermediate cage formation. Despite this, the peaks for the intact cage species were able to be clearly assigned, in addition to a small amount of the persistent cage intermediate seen previously. As the ratio of metal to ligand was increased up to 3:2 the number of intermediate species detected decreased as more intact cage was formed, not including the persistent intermediate which was observed to increase in intensity. As the ratio of metal was increased even further peaks corresponding to unbound metal tecton appeared accompanied by an increase in intensity of the undesired cage intermediate and a decrease in the intact $M_3L_2$ cage. Importantly, despite the careful control of reaction stoichiometry the minor product could not be eliminated from the reaction mixture.

It is difficult to ascertain exactly what processes are occurring but a reasonable explanation can be proposed that fits with the observed trends. Increasing the metal ratio above a 2:3 ligand: metal ratio does not push the equilibrium further towards the $M_3L_2$ species. The equilibrium in fact shifts towards the undesired cage intermediate. This implies that the intermediate

has a ligand: metal ratio greater than 2:3. The $M_3L$ is the only intermediate species that fits this criteria (Figure 3.11). Moreover, the intermediate peaks that are observed in the NMR spectrum are indicative of an $M_3L$ species. A diagnostic peak of **M2** is the proton *ortho* to the cyclometalated position which displays an usually upfield shift for an aromatic proton of approximately 6 ppm. Complexation of the two ligands during cage assembly results in a downfield shift of this signal yet it remains easily identifiable as the most upfield aromatic peak. If only a single molecule of **L1** is bound to the metal centre as in $M_3L$ a peak would be expected equidistant between the signal for the free **M2** and the cage. A set of peaks can be found in this position that also increase in intensity with increasing **M2** concentration. The signal also broadens in the intact cage assembly, in part due to the large size of the cage species. It would be expected that the signal from the same proton in the $M_3L$ intermediate would be less broad as the assembly is considerably smaller in size. Analysis of the peak in question confirms this is indeed the case. Perhaps the most tantalising evidence that the identity of the persistent intermediate is $M_3L$ can be attained by considering the symmetry of the $M_3L$ and $M_3L_2$ species. Of all the possible cage intermediates, the only one that retains the high symmetry of the starting materials is $M_3L$, which would be expected to possess $C_3$ symmetry. The sharp nature of the peaks attributed to the $M_3L$ intermediate support that this is the case. In an $M_3L_2$ species both phenylpyridine rings on the iridium experience the same chemical environment so are equivalent in the NMR spectrum. In an $M_3L$ species the symmetry is broken at the iridium centre and both phenylpyridine rings would be in subtly different environments. This is perhaps the most indicative evidence that an $M_3L$ species exists in equilibrium with the intact cage species. Proving this theory conclusively would be challenging, yet the data obtained does provide convincing evidence to support this hypothesis. The acquisition of a DOSY $^1$H-NMR spectrum would conclusively determine the number of species in solution and a $^1$H-$^1$H NOESY spectrum would potentially allow determination of the connectivity of the species. These two techniques may help to conclusively prove the above hypothesis Despite the presence of the minor product complete assignment of all of the proton environments was possible using 2D NMR techniques (Figure 3.12).

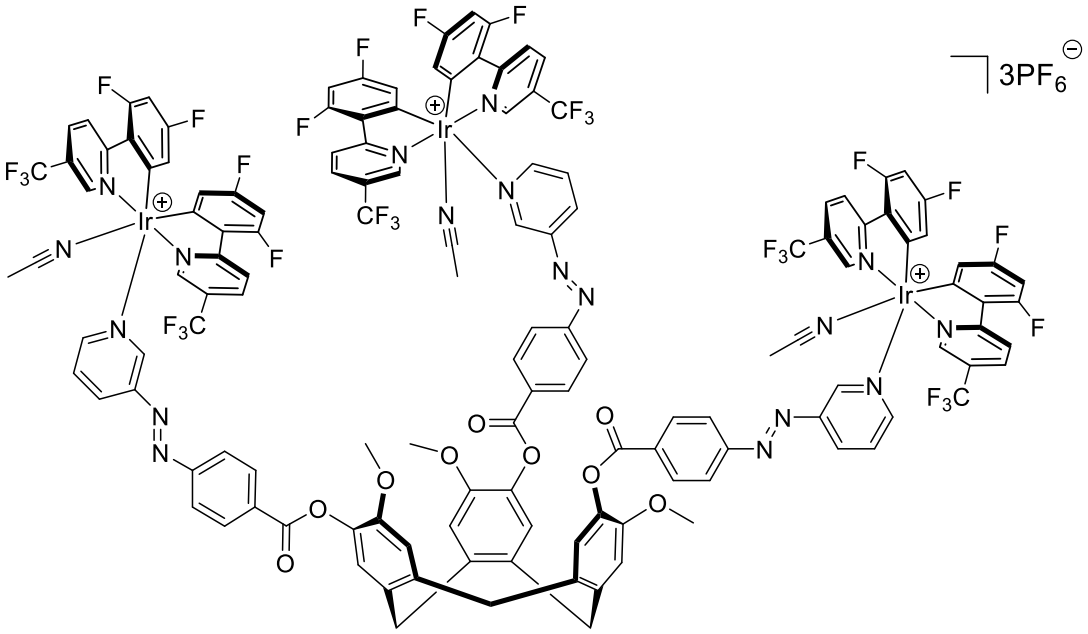


**Figure 3.11.** Structure of the proposed $M_3L$ minor product.

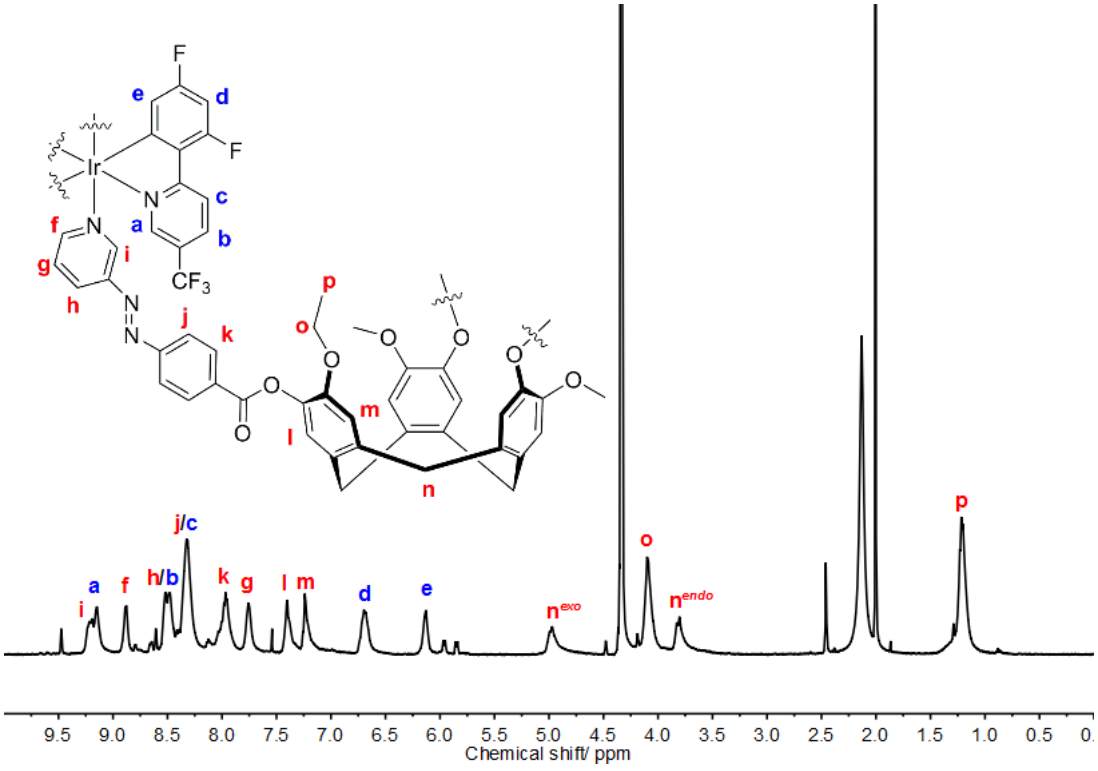


**Figure 3.12.** Fully assigned $^1$H-NMR (500 MHz, $d_3$-$MeNO_2$) of cage **C4**. Both **C2** and **C6** produced almost identical spectra.

The mechanism by which these iridium cages self-assemble can be inferred from the data described above. It appears most steps in the assembly of these cages are quite rapid as peaks that are due to these products are only present fleetingly in the NMR spectra. However, the persistence of the $M_3L$ species suggests that each ligand reacts with three iridium tectons initially before another ligand reacts to form the capsule in a rate determining step. The

reason why **M2** does not completely self-assemble in a single product may be due to a number of reasons. The deactivating effect that fluorination has upon the **M2** may sufficiently decrease the lability of the iridium tecton so as to hinder error correction during the reaction. This potentially results in a small amount of the product becoming kinetically trapped in the $M_3L$ state. Alternatively, the observation can be explained by considering the steric effects of incorporating **M2** into the metallo-cryptophane framework. The addition of fluorine atoms, particularly the $CF_3$ group has increased the steric bulk of the tecton. The capping of the $M_3L$ state by another ligand hinders the ability of the **M2** tectons to rotate and enforces a highly rigid geometry upon them. This could result in significant steric clashes between the fluorinated positions and the azobenzene arms of the ligand. Scrutiny of the molecular models of cage **C1** produced by Professor Colin Fishwick provide further evidence that the fluorinated phenylpyridines are capable of sterically clashing with the azobenzene arms (Figure 3.13). The result of these unfavourable interactions may be to destabilise the $M_3L_2$ state and in doing so push the equilibrium further towards the $M_3L$ state.

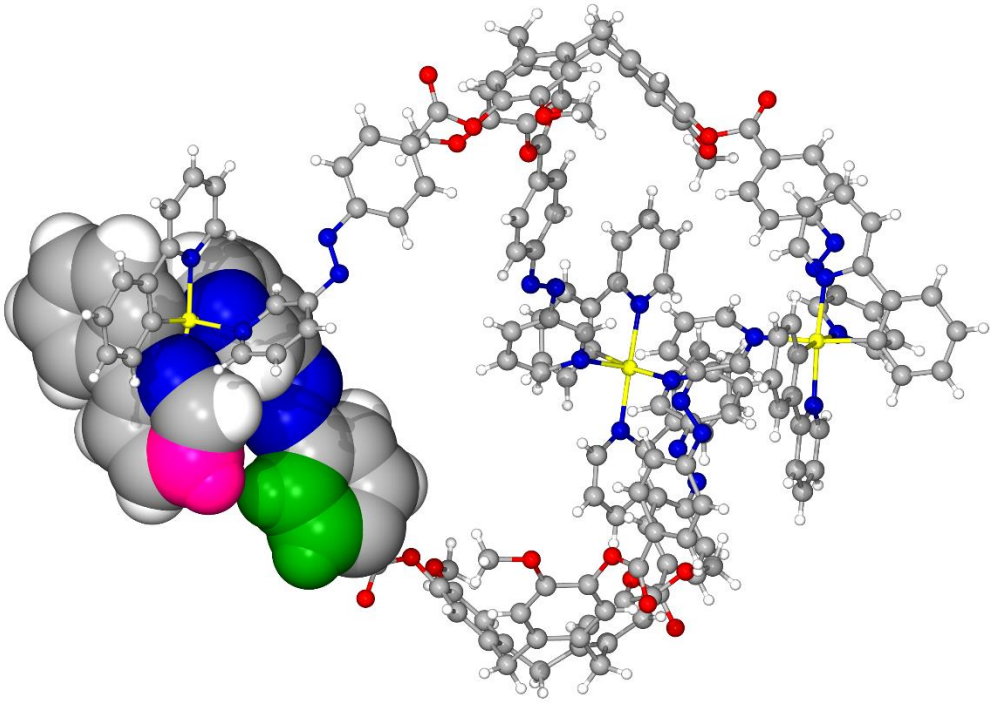

**Figure 3.13.** Molecular model of **C1** calculated by Professor Colin Fishwick. The *meta* position on the pyridine of the phenylpyridine group (pink) points towards **L1**. Substitution of this position by a $CF_3$ group could feasibly result in steric clashes with a phenyl ring of the azobenzene (green).

Unfortunately, the metallo-cryptophanes incorporating **M2** do not fully self-assemble in nitromethane. The purpose of using **M2** was to solubilise the

metallo-cryptophane assembly and as a result, the assembly of this metal tecton with ligands **L1**, **L2** and **L3** was conducted in the relatively non-polar solvent $d_2$-tetrachloroethane. It was immediately apparent that the use of **M2** had a marked effect on solubility with significantly less precipitate appearing when **L1** and **L2** were used. To our delight, the use of the most soluble ligand **L3** provided sufficient solubility to the system to facilitate complete dissolution of approximately 10 mg of sample in 0.6 mL of tetrachloroethane, a significant improvement. $^1$H-NMR spectroscopy revealed that the system initially behaved similarly in tetrachloroethane to samples in nitromethane. All of the peaks that appeared transiently in the nitromethane also disappeared in tetrachloroethane at approximately the same rate. The major effect that the different solvents had upon the system became obvious when the reaction had reached equilibrium (Figure 3.14). Much greater quantities of the $M_3L$ state were detected when using tetrachloroethane as the solvent. The use of tetrachloroethane drives the equilibrium further towards the $M_3L$ state and disfavours the $M_3L_2$ cryptophane. This observation implies that the formation of the metallo-cryptophanes may be thermodynamically driven by the creation of the large hydrophobic cavity of the cage. This would allow the hydrophobic bowls of the CTG ligands to exist in a relatively non-polar environment with respect to the bulk solvent. The use of a non-polar solvent would negate this effect as favourable interactions already exist between the solvent and the ligand. Without this driving force the equilibrium between $M_3L_2$ and $M_3L$ would be pushed further towards the $M_3L$ side. This may account for the smaller quantities of intact $M_3L_2$ metallo-cryptophanes detected in non-polar solvents.

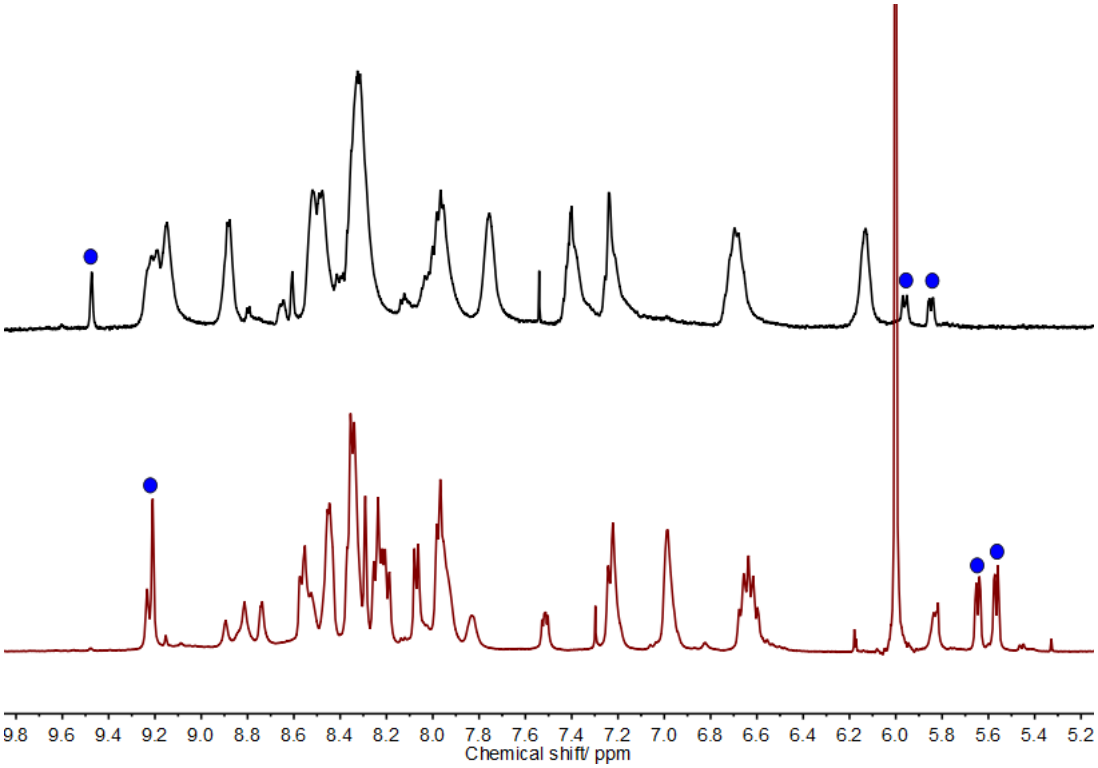


**Figure 3.14.** $^{1}$H-NMR (500 MHz, $d_3$-$MeNO_2$) of the self-assembly reaction between **L3** and **M2** in nitromethane (black) and tetrachloroethane (red). Diagnostic $M_3L$ peaks highlighted in blue.

Examples of supramolecular systems that switch between different states dependent upon the solvent are comparatively rare. Mirkin has reported a discrete triangular copper macrocycle that forms in methanol.[35-38] However, attempting the same reaction using pyridine as the solvent causes polymerisation of the discrete macrocycles into a coordination polymer. A sample of either the macrocycle or polymer can be reversibly cycled between these states by addition or removal of the appropriate solvent.[35] In another example, Mirkin found that a rhodium complex could switch between its open and closed form depending upon the solvent polarity and the electron withdrawing nature of the ligand substituents (Figure 3.15).[36] A non-polar solvent coupled with an electron withdrawing ligand resulted in incomplete reaction of the ligand at the rhodium centre. Instead chloride occupied the site usually taken by the ligand. Rhodium and iridium are in the same group and possess similar chemical properties. It is reasonable to conclude that a similar process may be occurring in the case of the iridium metallo-cryptophanes.

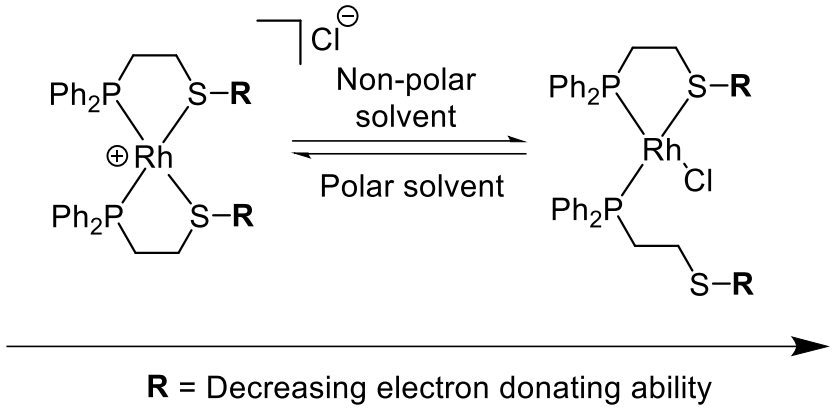


**Figure 3.15.** Example of a Rh(I) complex that switches between an open and closed form dependent upon the solvent polarity and electron withdrawing nature of the ligand.[36]

The progress of the reaction with **M2** and ligand could be monitored with high resolution mass spectrometry. Upon addition of the metal tecton to the ligand a small peak corresponding to the $[M_3L_2]^{3+}$ species is immediately observed. However peaks corresponding to intermediate species such as $[ML]^{+}$, $[M_2L]^{2+}$, and $[M_3L]^{3+}$ are detected in large quantities. Over time however, these peaks decrease in intensity as the metallo-cryptophane peak increases, further corroborating the NMR evidence that metallo-cryptophanes take a significant amount of time to self-assemble. Even when no further change can be detected in the NMR spectra and the reaction has reached equilibrium, fragments of the $M_3L_2$ cages can still be detected (Figure 3.16). This is not unexpected as the use of **M2** results in cage intermediates which are present at equilibrium.

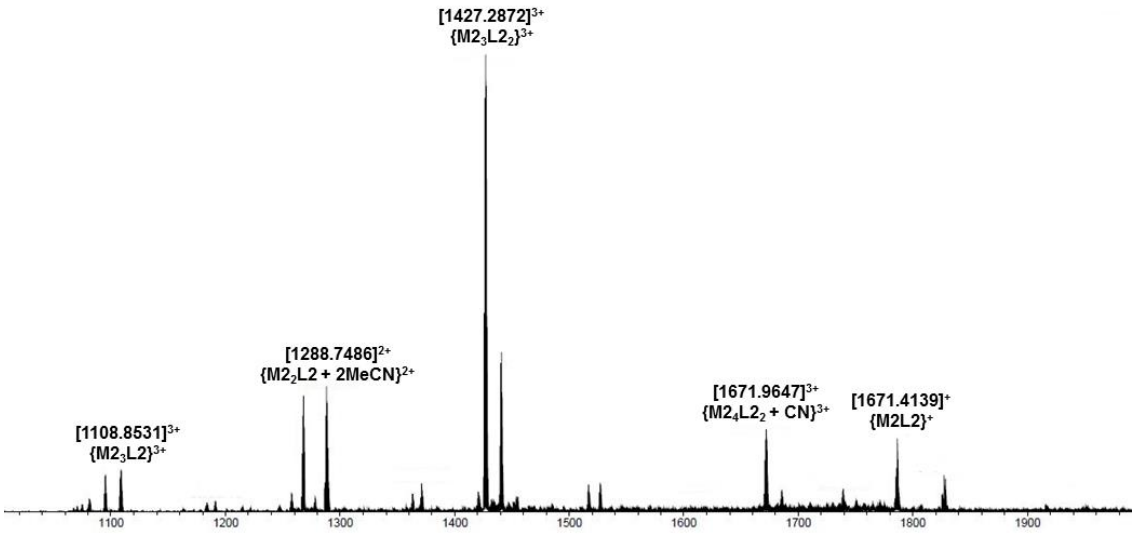


**Figure 3.16.** HRMS of **C4** acquired in $MeNO_2$ (**M2 = M2 – 2MeCN – $PF_6$**).

Infrared-spectra and elemental analysis of these cages were not attempted. In order to obtain these analyses the sample must be isolated in the solid form.

Whilst it was possible to precipitate the cryptophanes from solution, analysis of the redissolved cages showed that the stoichiometry of the reaction had been altered in the process and clean NMR spectra could not reliably be obtained. Moreover, the coordination cages discussed retain high levels of solvation in the solid state within the internal cavities. The presence of solvent makes microanalysis of these compounds challenging and results obtained usually deviate significantly from calculated values. Due to these reasons, infrared and elemental analysis were not obtained for any metallo-cryptophanes in this chapter.

## 3.3 Synthesis of azobenzene appended Rh(III) metallo-cryptophanes

In light of the apparent propensity for systems containing azobenzene functionalised CTG and suitably protected iridium(III) tectons to form metallo-cryptophanes; it was desirable to investigate whether similar systems would self-assemble in the presence of metals other than iridium. An obvious starting point would be to employ the rhodium metal tectons developed in Chapter 2 (Figure 3.17).

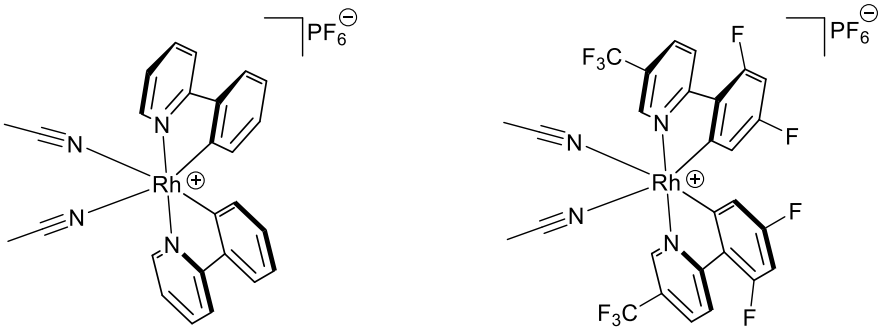


**Figure 3.17.** Rhodium metal tectons bearing *cis* protecting phenylpyridine moieties.

There may be several possible benefits in using rhodium tectons in place of iridium tectons.

The synthesis of the rhodium cryptophanes was approach in an identical way to that used for the synthesis of the iridium cryptophanes. Initially **L1** and unfunctionalised rhodium tecton **M3** in a 2:3 ratio were mixed in deuterated nitromethane and the progress of the reaction monitored by $^{1}$H-NMR (Scheme 3.3) (Figure 3.18).

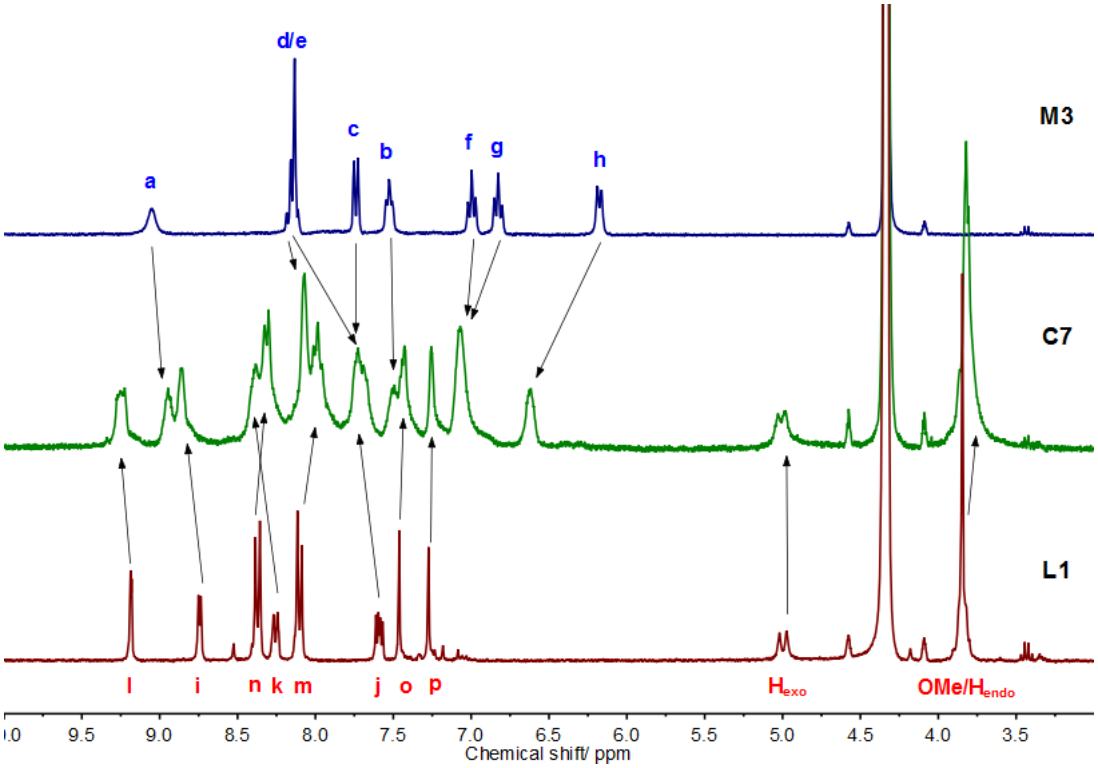


**Figure 3.18.** (Blue) $^{1}$H-NMR (300 MHz, $d_3$-$MeNO_2$) of **M3**. (Red) $^{1}$H-NMR (300 MHz, $d_3$-$MeNO_2$) of **L1**. (Green) $^{1}$H-NMR (300 MHz, $d_3$-$MeNO_2$) of **C7** obtained immediately after mixing of components.

The reaction between metal tecton and ligand occurred remarkably quickly, the time taken to acquire a $^{1}$H-NMR was sufficient for complete reaction after which no further change was observed in the spectrum. Rhodium complexes are generally more labile than iridium complexes due to a smaller crystal field stabilisation energy. This increased lability explains why the rhodium tecton reacts faster than the iridium analogue. A combination of 2D-NMR techniques, namely COSY, TOCSY and NOESY allowed for complete assignment of every proton environment on the molecule (Figure 3.19).

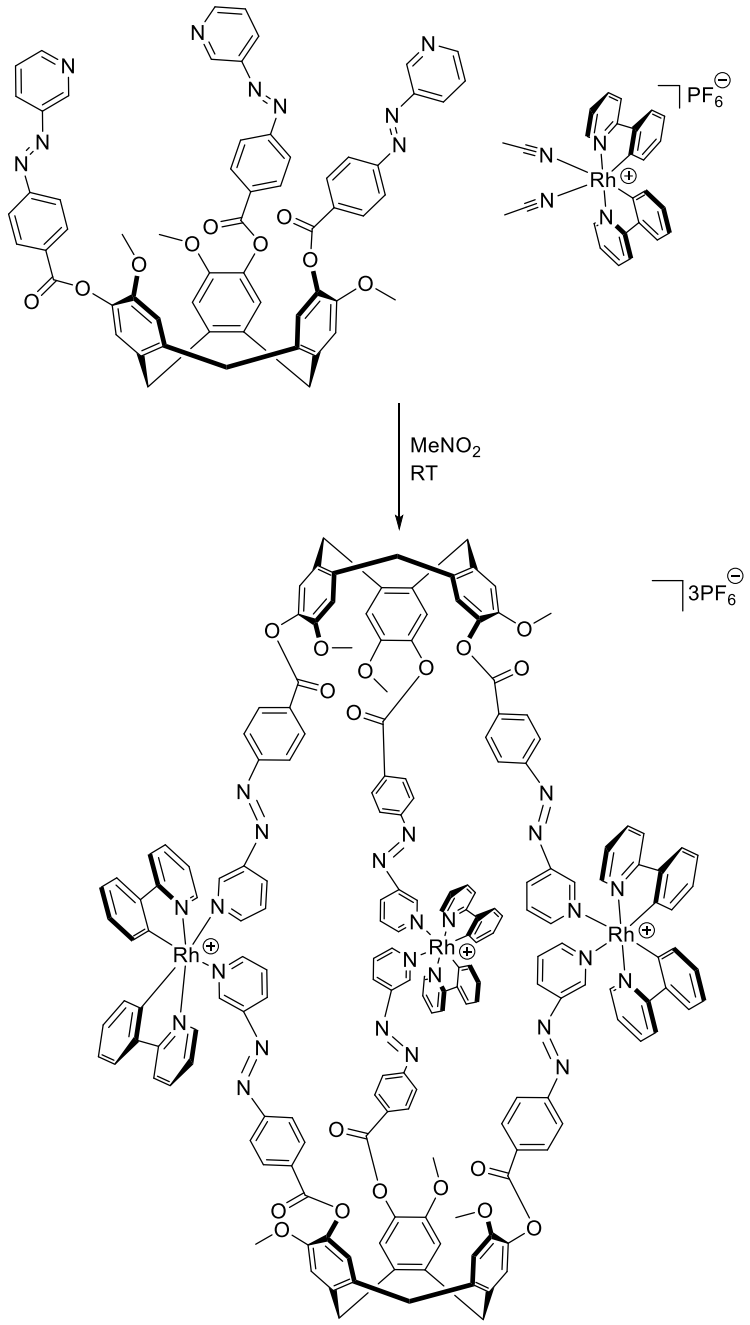


**Scheme 3.3.** Synthesis of an $M_3L_2$ metallo-cryptophane from **M3** and **L1** to form **C7**.

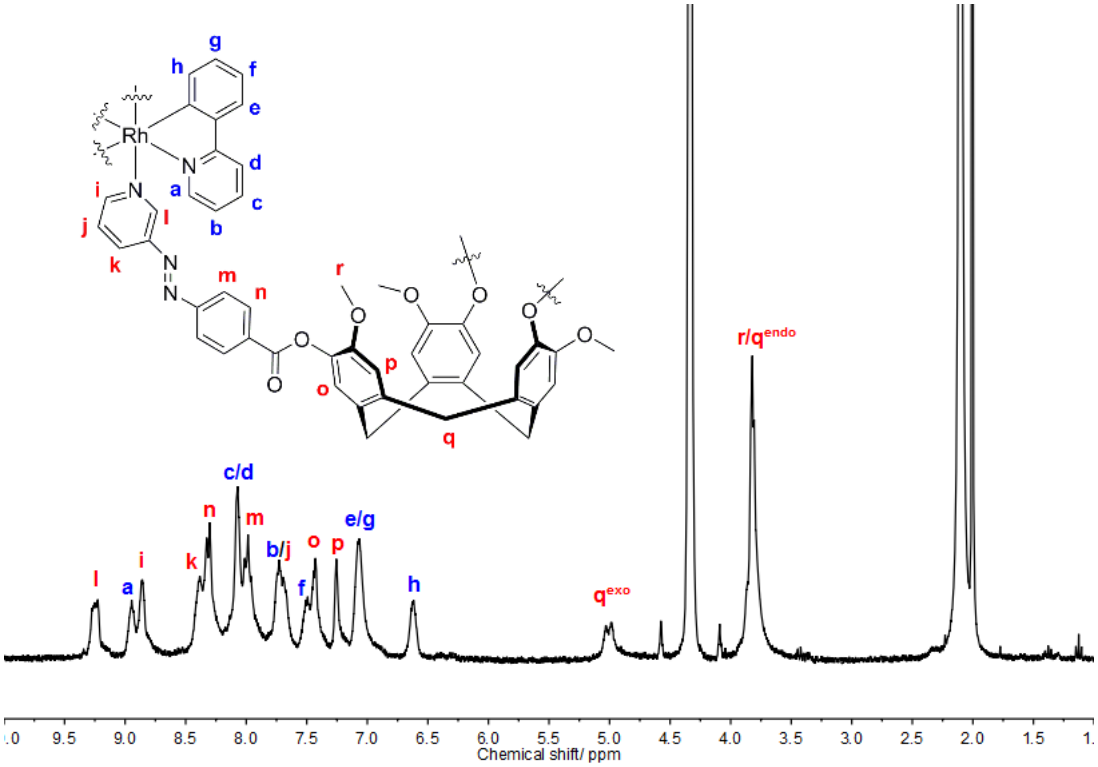


**Figure 3.19.** $^{1}$H-NMR (300 MHz, $d_3$-$MeNO_2$) of **C7** displaying simplified molecular structure and assignments of all proton signals.

The peaks corresponding to proton environments **l** and **i** on the ligand were shifted downfield from 8.76 to 8.89 and 9.20 to 9.27 respectively. A downfield shift of the protons *ortho* to the pyridyl group on the ligand is consistent with complexation to a metal centre. Immediately following mixing of the components the peaks for both metal and ligand tecton became broad, a common consequence of metallo-cryptophane formation. High resolution mass spectra of **C7** were obtained with the help of Dr Stuart Warriner (Figure 3.20). Attempts to collect the data with the same method used for the iridium cryptophanes, where acetonitrile is used as a carrier solvent failed. The resultant spectrum contained only free ligand and metal tecton peaks, likely due to degradation of the cage by acetonitrile in the instrument. The increased lability of the rhodium results in complete cage disassembly by the acetonitrile before the intact cage can be detected. Direct injection in nitromethane was required to observe the $[M_3L_2]^{3+}$ species. In addition to the $[M_3L_2]^{3+}$ species numerous fragments of the cage were observed such as $[M_2L]^{2+}$ and $[ML]^{+}$. Intact cage was also detected with varying amounts of $[M]^{+}[CN]^{-}$ adducts. The cyanide adducts were likely a result of decomposition of the acetonitrile solvent during the ionisation process in the mass spectrometer.

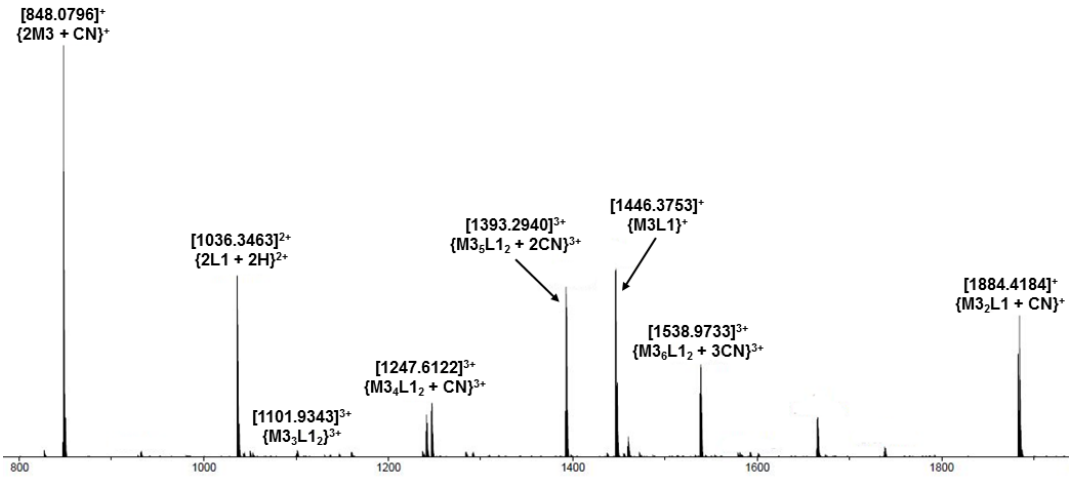


**Figure 3.20.** Mass spectrum of **C7** acquired in $MeNO_2$, showing the desired $[M_3L_2]^{3+}$ as well as a range of fragmentation species. (**M3** = **M3 – 2MeCN – $PF_6$**)

A common technique in supramolecular chemistry is to utilise DOSY NMR to determine the number of species present in solution.[39, 40] In order to ascertain whether the large number of species present in the mass spectrum were a consequence of fragmentation in the gas phase or were indeed present in the solution phase DOSY NMR was employed to determine the number of species in solution. The individual fragments of the intact cage such as $[ML]^+$ or $[M_2L]^{2+}$ would have significantly different hydrodynamic radii to each other and would be expected to possess different diffusion constants. The DOSY spectrum of **C7** revealed that peaks corresponding to both metal tecton and ligand environment were diffusing at the same rate in solution (Figure 3.21). In addition only one diffusion constant was detected, this confirms that the only species present in solution in appreciable concentrations is the desired $M_3L_2$ metallo-cryptophane.

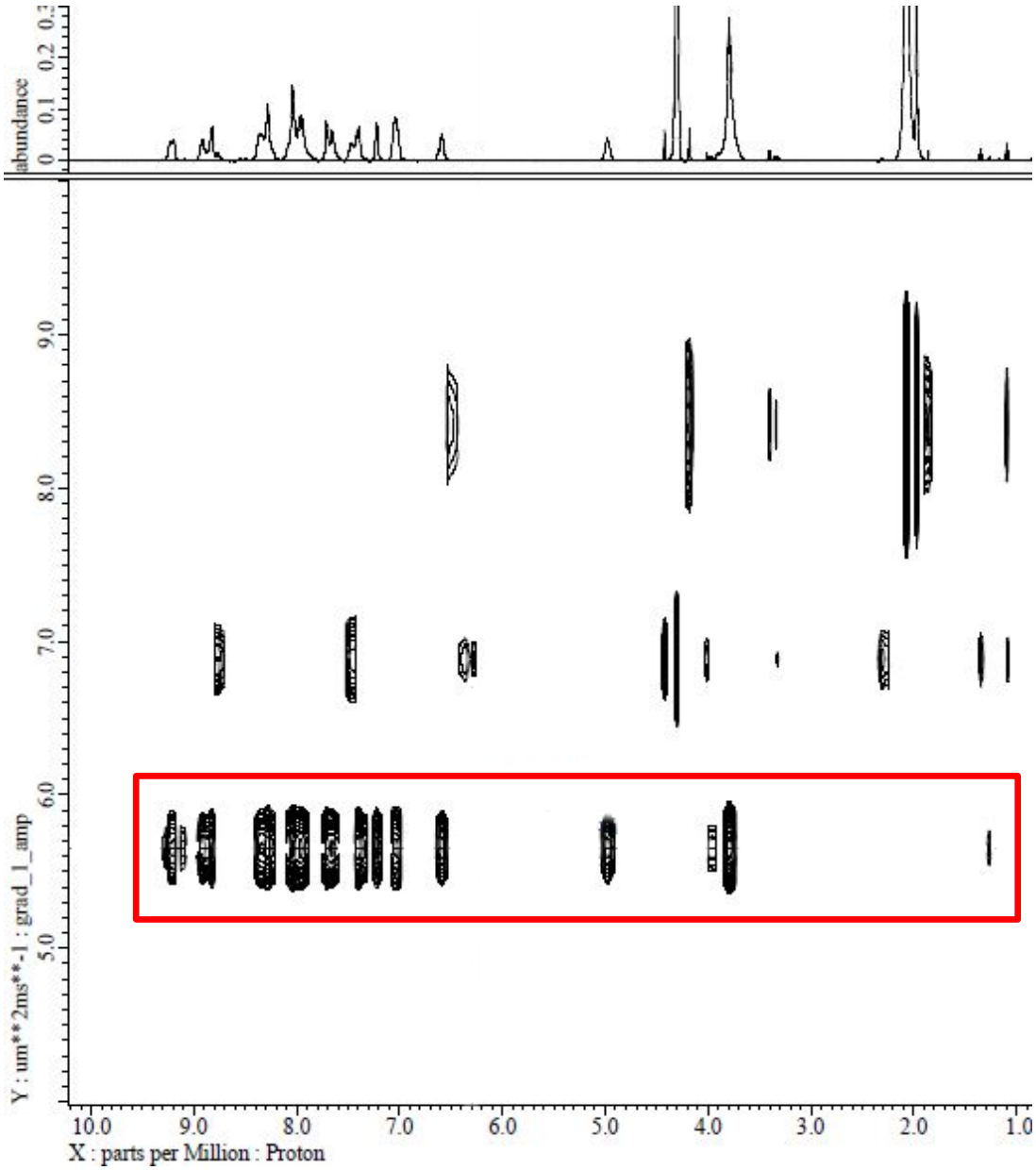


**Figure 3.21.** DOSY NMR of **C7** showing metal tecton and ligand diffusing at the same rate and the presence of a single large species in solution.

Further evidence of metallo-cryptophane formation was obtained by acquiring rotating frame Overhauser effect spectroscopy (ROESY) to probe the through space interactions present in the metallo-cryptophane. The most compelling evidence supporting metallo-cryptophane formation was through-space couplings observed between proton environment **h** found on the metal tecton, and proton environment **I** on the ligand (Figure 3.22). In order for coupling to occur between these protons they have to be within 5-6 Å of one another. The fact that they couple proves that the metal tecton and ligand have reacted as they are found to reside in close proximity to one another, providing further evidence for metallo-cryptophane formation.

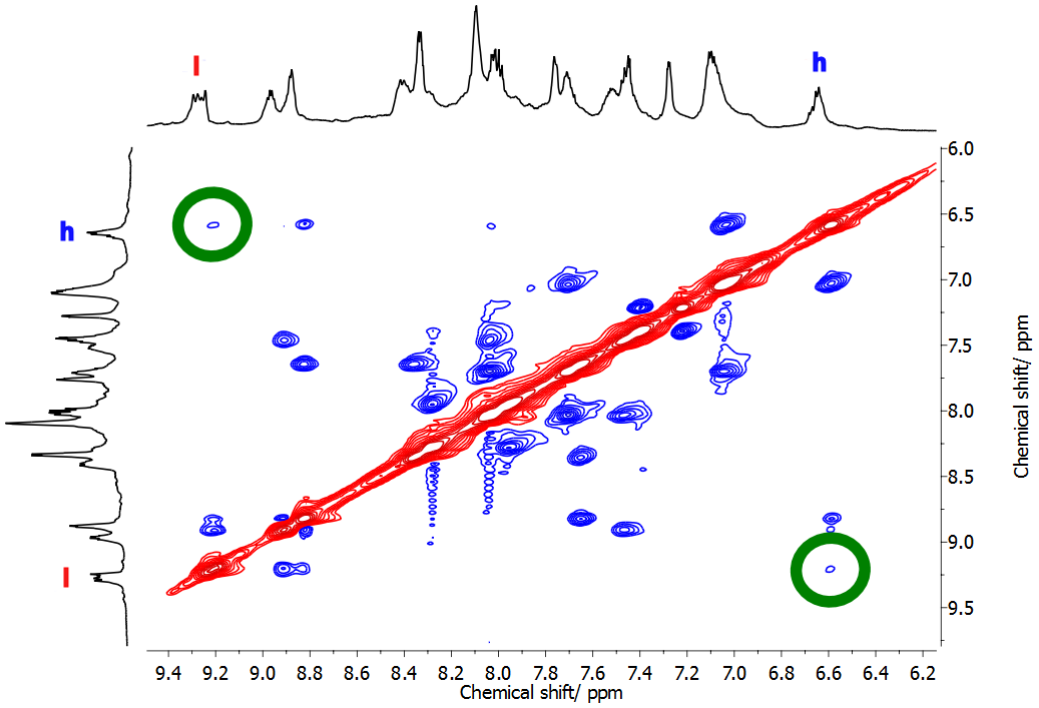


**Figure 3.22.** $^{1}$H-$^{1}$H ROESY (600 MHz, $d_3$-$MeNO_2$) spectrum of **C7** showing the cross-coupling between **h** and **l** indicative of metallo-cryptophane formation.

Systems containing CTV based ligands have been observed to undergo chiral self-sorting in solution.[27, 41, 42] 4-Pyridyl functionalised CTG prepared by PhD student Vikki Pritchard self-assembled with iridium phenylpyridine tecton **M1** to form an $M_3L_2$ cage. Over the course of several months as monitored by $^{1}$H-NMR the peaks corresponding to the cage environment became sharper and more defined. This was attributed to self-sorting of the heterochiral cage complexes bearing mixed *M*/*P* and Δ/Λ substituents into homochiral cages where the system existed as a racemic mixture of *MM*-*ΛΛΛ* and *PP*-*ΔΔΔ* cage isomers (Scheme 3.4).[41]

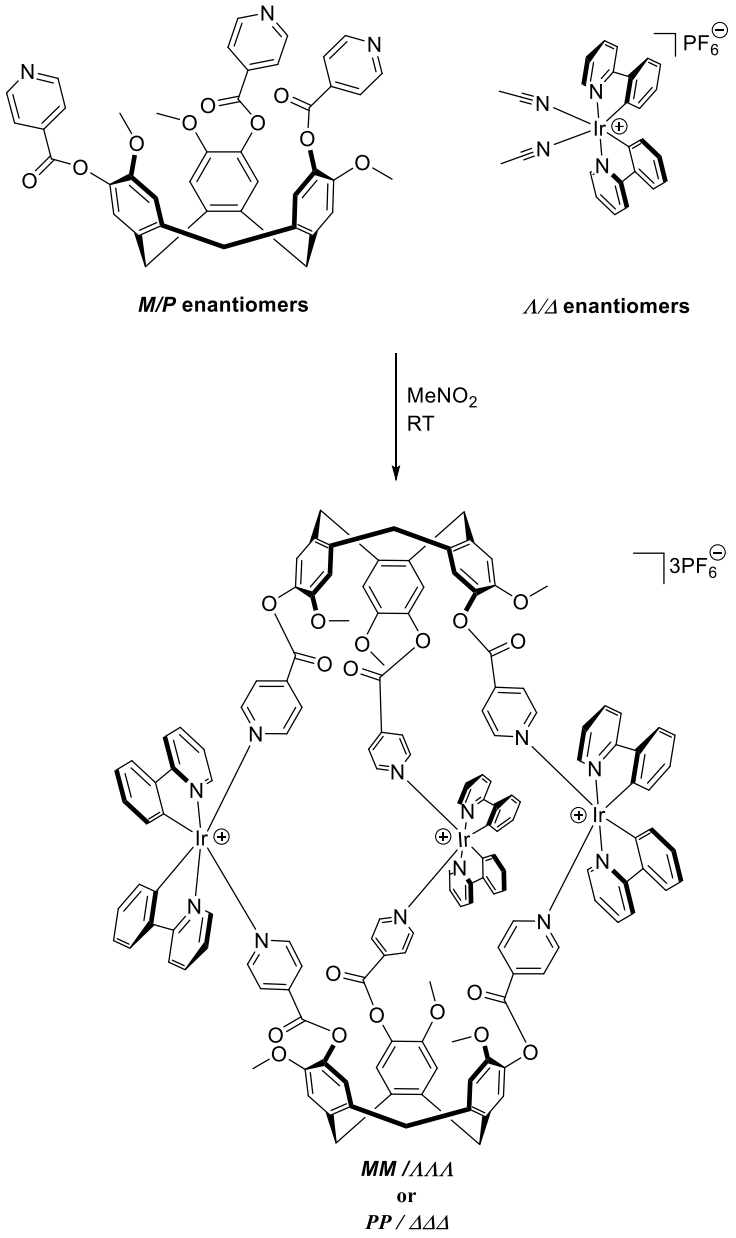


**Scheme 3.4.** Synthesis of $Ir_3L_2$ cage displaying chiral self-sorting of coordination cage.[41]

The $^1$H-NMR of the iridium cryptophane **C1** was reported to sharpen upon standing in nitromethane for several months.[43] This was attributed to chiral self-sorting reducing the amount of diastereomers in solution and in the process reducing the number of subtly different peaks in the NMR spectra.[33] Interestingly the analogous rhodium cryptophane remains unchanged when left in solution for a comparable amount of time. This implies that the rhodium analogue is unable to undergo chiral self-sorting. Small changes to a system such as the choice of solvent, ligand variation and the presence of chiral species have all been shown to inhibit or promote chiral self-sorting.[41, 42] For example a 4-pyridyl appended CTG ligand was shown to chirally self-sort with palladium(II) nitrate in DMSO to form a racemic mixture of $Pd_6L_8$ cages with

each cage possessing only a single ligand enantiomer (Figure 3.23). If the ligand was modified such that the methoxy group was changed to a propoxy group and the same reaction attempted no chiral self-sorting was observed in DMSO, yet chirally pure cages could still be obtained if the reaction was attempted in $MeNO_2$.[42]

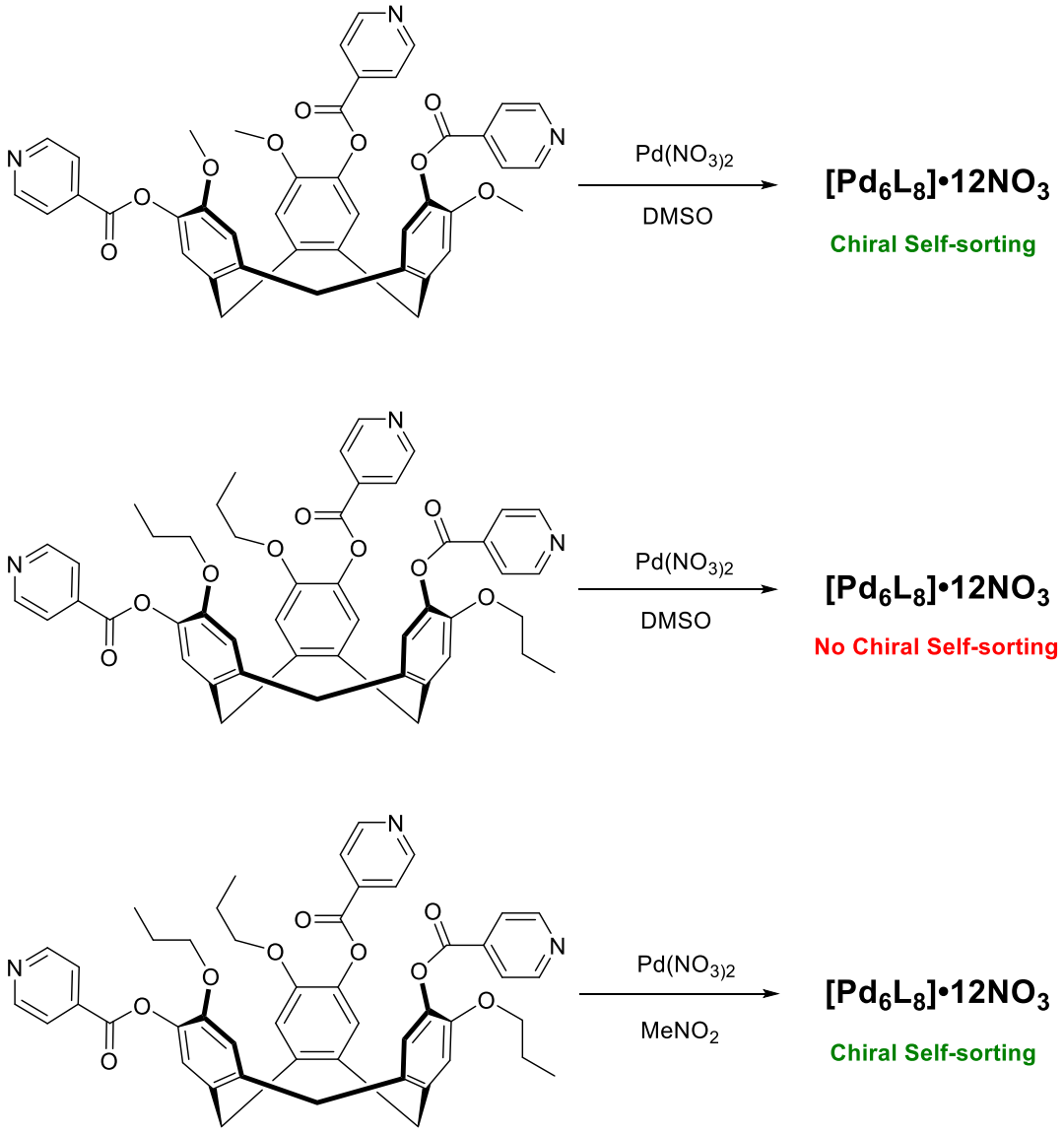


**Figure 3.23.** The self-assembly of pyridyl appended CTG with palladium(II) nitrate, illustrating the subtle effects that can influence chiral self-sorting.[42]

This highlights how a subtle change in the conditions of a reaction can result in vastly different outcomes for a self-assembled system. It is feasible therefore that the change from iridium to rhodium could potentially inhibit or promote chiral self-sorting.

As stated in chapter 2 one of the main objectives of this project was to solubilise azobenzene containing metallo-cryptophanes, hence ligands **L2**

and **L3** as well as rhodium tecton **M4** were developed. As sufficient evidence had been obtained to confirm that the reaction of unsubstituted rhodium tecton **M3** and the simplest azobenzene containing ligand **L1** reacted to form a metallo-cryptophane it was desirable to investigate whether the same species would form with all possible permutations of ligand and metal and whether the use of solubilising ligand and tecton would result in a solubilised cryptophane (Scheme 3.5) (Table 3.1).

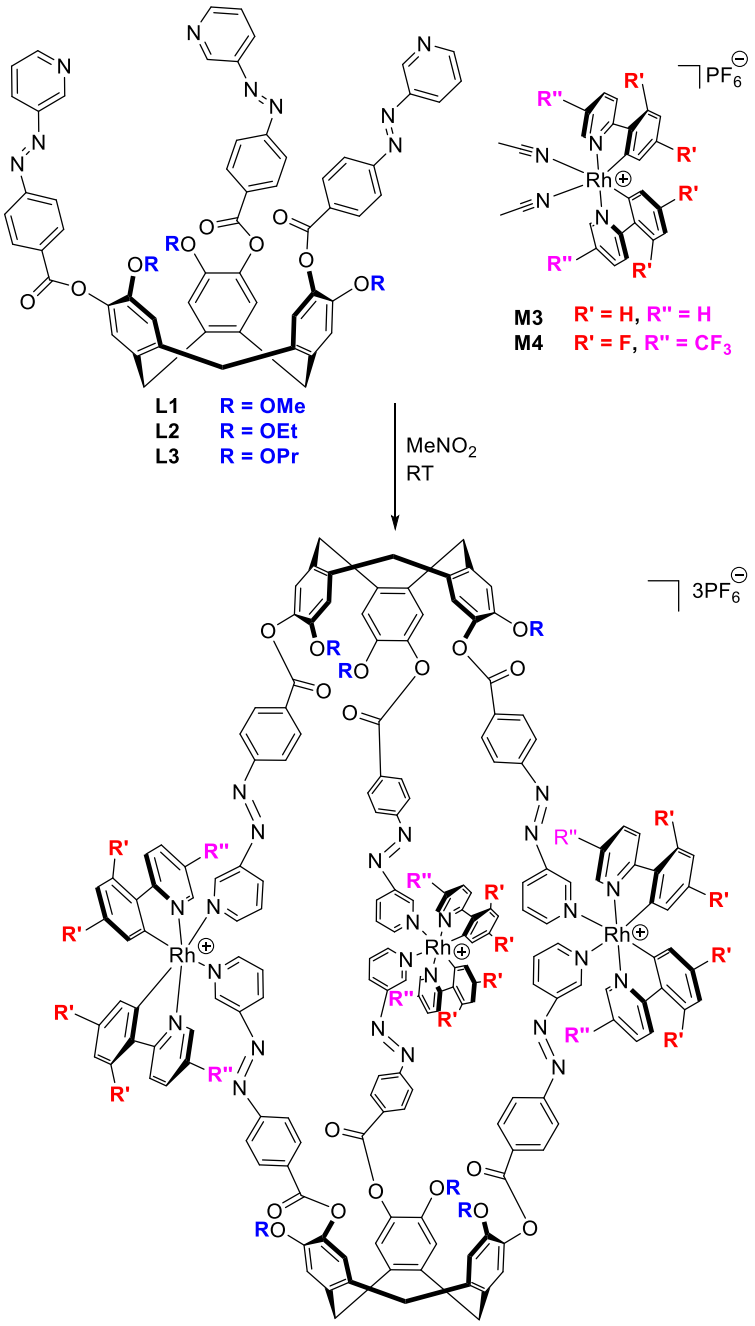


**Scheme 3.5.** Scheme showing synthesis of all possible permutations of rhodium cryptophanes.

**Table 3.2.** Reaction codes of rhodium-cryptophanes resulting from the reaction of azobenzene ligand with metal tecton.

| Ligand | Metal tecton | Metallo-cryptophane |
|---|---|---|
| L1 | M3 | C7 |
| L1 | M4 | C8 |
| L2 | M3 | C9 |
| L2 | M4 | C10 |
| L3 | M3 | C11 |
| L3 | M4 | C12 |

Self-assembly of the metallo-cryptophanes incorporating **M3** and ligands **L2** and **L3** were attempted first. Analysis by $^{1}$H-NMR (Figure 3.24) and ESI-MS (Figure 3.25 and Figure 3.26) showed that these species behaved in much the same way as their iridium analogues. Comparison of the NMR spectra with the rhodium cryptophane **C7** reveals a striking similarity between them and along with the mass spectra, is strong evidence that the metallo-cryptophanes **C9** and **C11** form with the solubilised ligands. The 2D NMR techniques used to confirm the composition of previous samples was employed and provides conclusive evidence of clean metallo-cryptophane formation with no detectable side products. Unfortunately, the addition of the solubilised ligands **L2** or **L3** into the assembly once again did not provide sufficient solubility in non-polar, non-coordinating solvents such as dichloromethane, chloroform or tetrachloroethane to facilitate dissolution of samples at an appropriate concentration to be routinely identified by $^{1}$H-NMR spectroscopy.

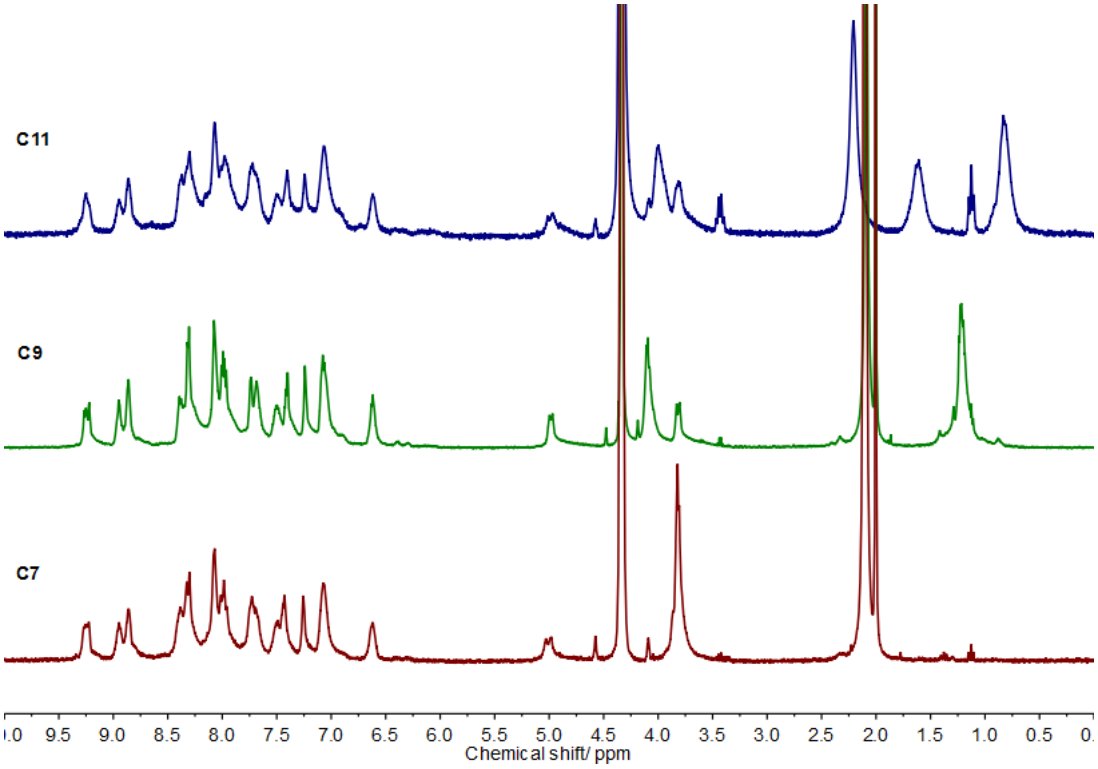


**Figure 3.24.** $^{1}$H-NMR (500 MHz, $d_3$-$MeNO_2$) of **C7**, **C9** and **C11** showing distinctly similar spectra

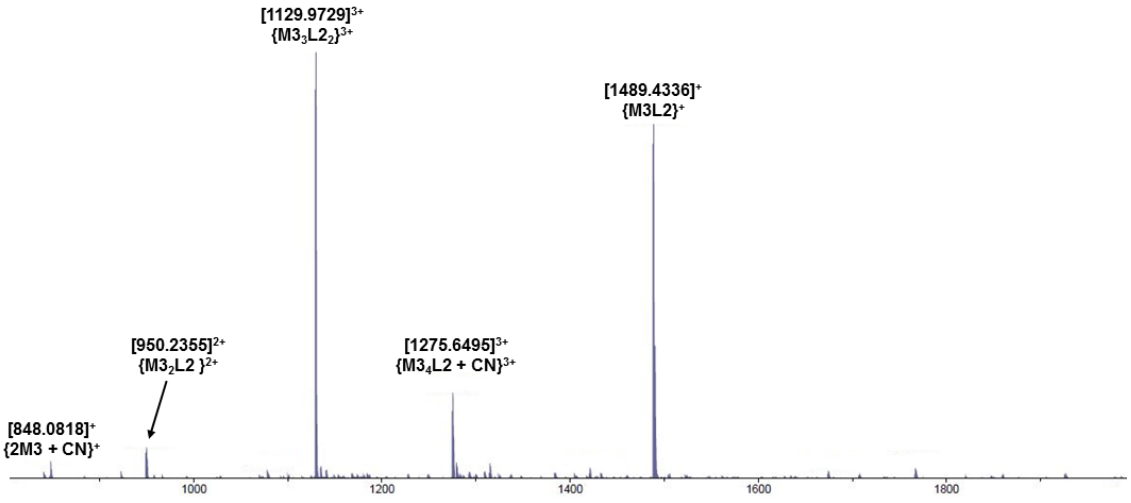


**Figure 3.25.** ESI-MS of **C9** acquired in $MeNO_2$ (**M3** = **M3 - 2MeCN - $PF_6$**).

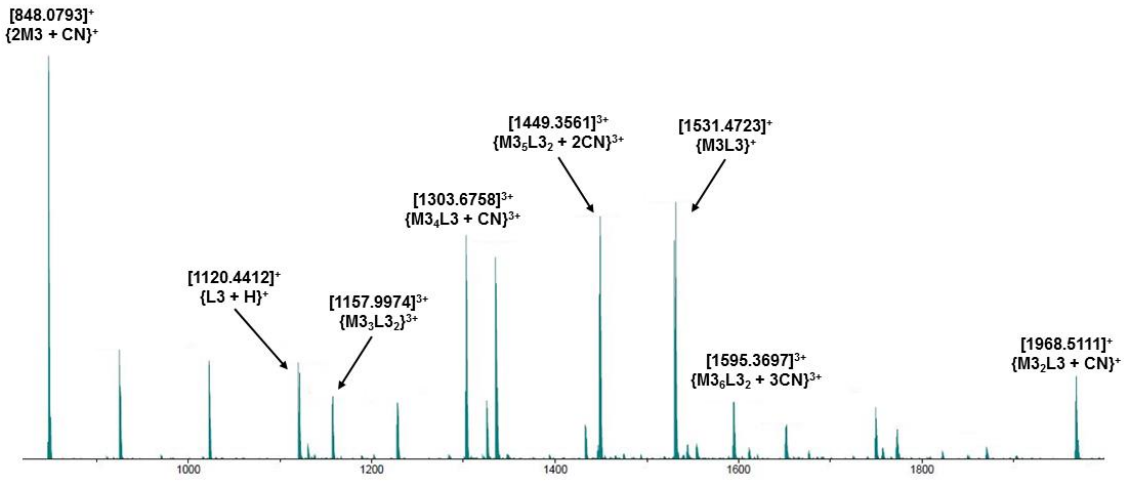


**Figure 3.26.** ESI-MS of **C11** acquired in $MeNO_2$ (**M3** = **M3 - 2MeCN - $PF_6$**).

The self-assembly of the fluorinated rhodium tecton **M4** with the azobenzene appended CTG ligands was then investigated by $^1$H-NMR spectroscopy. The same procedure as before was employed where three equivalents of **M4** were dissolved in $d_3$-nitromethane and added to two equivalents of the ligand dissolved in $d_3$-nitromethane. Interestingly, unlike the iridium metallo-cryptophanes no differences in the rate of self-assembly was observed for fluorinated and non-fluorinated rhodium tectons. The increased kinetic lability of rhodium complexes compared to iridium complexes is likely to be the reason, facilitating vastly increased rates of reaction due to the faster displacement of the acetonitrile ligands on the metal centre. The ligands **L1**, **L2** and **L3** all self-assembled with **M4** to form mostly the intact $M_3L_2$ cage, with $^1$H-NMR and ESI-MS studies to support this (Figure 3.27 and Figure 3.28). However, it was found that the fluorinated rhodium phenylpyridine tecton was incapable of reacting to fully form the desired $M_3L_2$ cage, much like the iridium analogue. Once again a persistent cage intermediate was detected that was likely to be an $M_3L$ species as it exhibited almost identical spectra properties as in the cases described earlier for iridium. The fact that this intermediate is also observed in examples containing the much more kinetically labile rhodium as well as iridium, confirms that the deactivating effect of the fluorinated phenylpyridine rings is not the main reason why this reaction does not go to completion. Instead the steric repulsion afforded by the $CF_3$ moiety is likely to drive equilibrium of the reaction towards the $M_3L$ product. Further evidence supporting this hypothesis is the fact that the proportion of $M_3L$ detected in the NMR is proportional to the length of alkoxy chain. A longer alkoxy chain would increase the steric clash with the metal tecton and force the equilibrium further away from the $M_3L_2$ species.

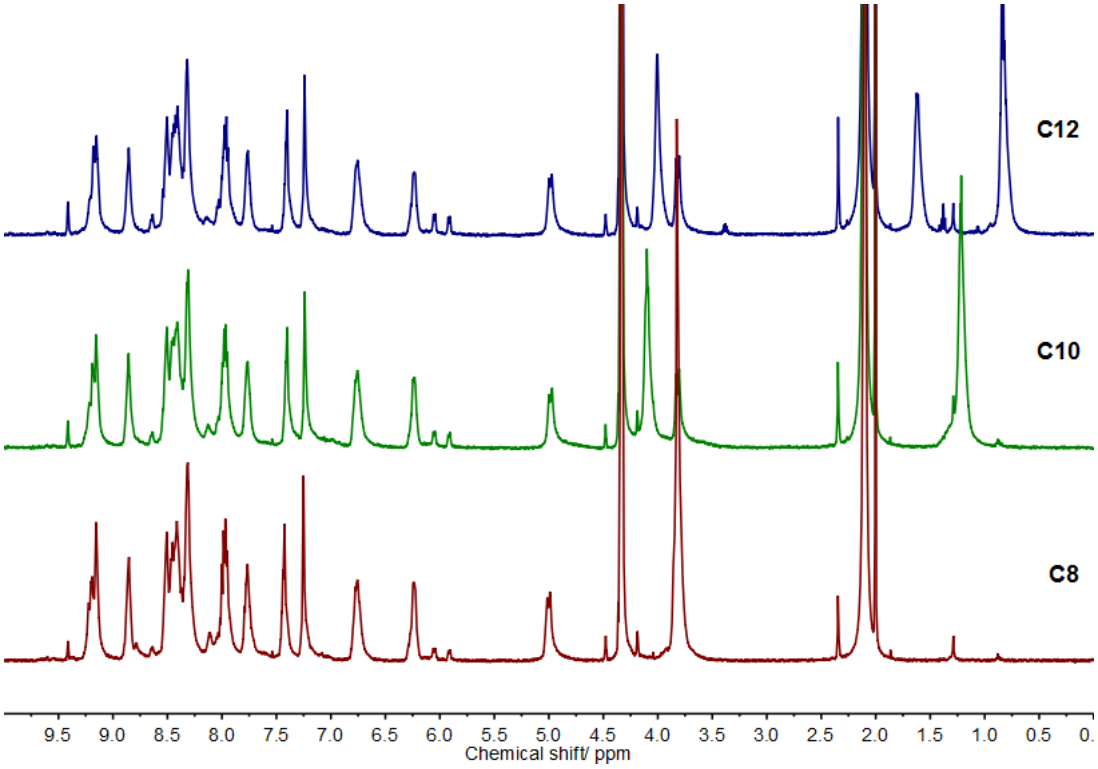


**Figure 3.27.** $^{1}$H-NMR (500 MHz, $d_3$-$MeNO_2$) of fluorinated rhodium cages **C8**, **C10** and **C12**.

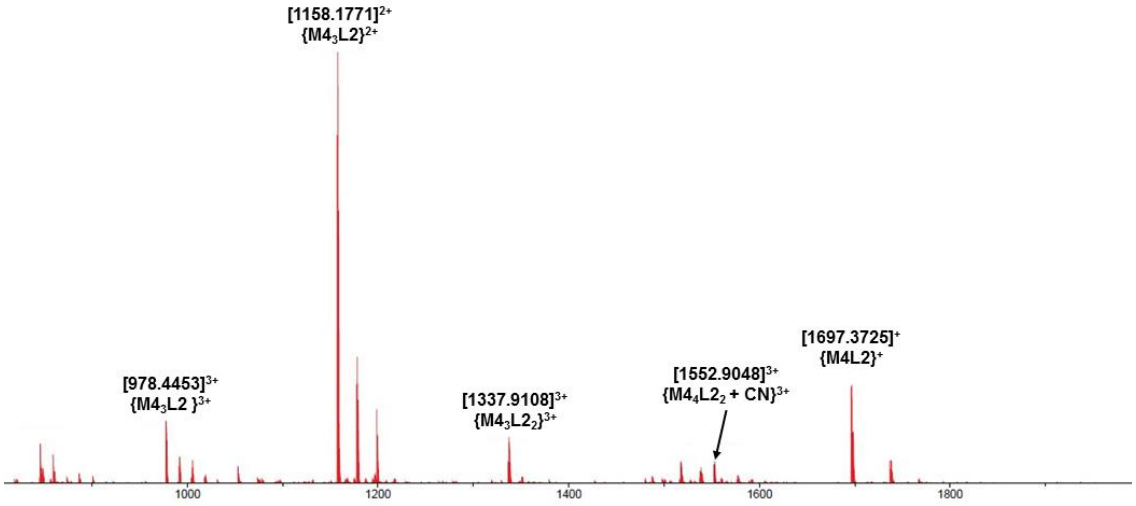


**Figure 3.28.** Representative HRMS acquired in $MeNO_2$ of fluorinated rhodium phenylpyridine cages, example shown is of **C10**. **C8** and **C12** both showed similar spectra. (**M4** = **M4 – 2MeCN – $PF_6$**)

Confirmation that the rhodium cryptophanes were able to self-assemble in nitromethane allowed the investigation of the assembly in other non-polar solvents. Exactly the same reaction procedure was employed, the only difference being the self-assembly was conducted in $d_2$-tetrachloroethane. The dual approach of solubilising both ligand and rhodium tecton was a success. The rhodium-cryptophanes incorporating the **M4** tecton were considerably more soluble than their **M3** counterparts. Increasing the length

of the alkoxy chain on the ligand had a similar effect with the combination of **M4** and **L3** producing the most solubilised cryptophane **C12**. The rate of assembly was the same irrespective of the solvent used. However, analysis of the rhodium cryptophane **C12** by $^{1}$H-NMR spectroscopy revealed that the rhodium cryptophane displayed the same behaviour as the iridium analogue **C6**, whereby the equilibrium of the reaction was shifted to favour the $M_3L$ intermediate in non-polar solvents (Figure 3.29).

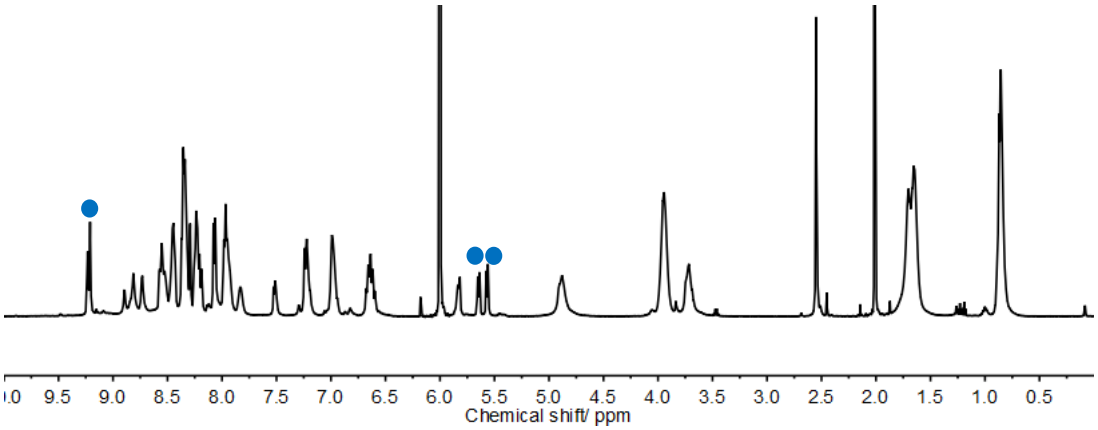


**Figure 3.29.** $^{1}$H-NMR (500 MHz, $d_2$-tetrachloroethane) of fluorinated rhodium **C12** displaying the formation of the $M_3L$ product. Diagnostic $M_3L$ peaks highlighted in blue.

As discussed earlier, the difference between the hydrophobic interior of the cage and the bulk solvent is less in a non-polar solvent than a polar solvent such as nitromethane. The shift in the equilibrium suggests that the formation of the hydrophobic cavity is a significant driving force as it allows the non-polar hydrophobic CTG cores to exist isolated from the polar bulk solvent. In non-polar solvents this manifests as a weaker driving force for metallo-cryptophane formation. To test this theory the polarity of the solvent was increased by adding a few drops of nitromethane to the sample and monitoring the effect on cage formation by $^{1}$H-NMR spectroscopy. Upon addition of the nitromethane, changes are immediately observed in the spectrum where the $M_3L$ peaks decrease in intensity as the $M_3L_2$ peaks grow. The broadening of the resonances suggest the formation of the larger $M_3L_2$ species is occurring as the polarity of the solvent is increased. This approach could not be used to drive the reaction fully to the $M_3L_2$ complex but instead shifted the equilibrium in favour of this species.

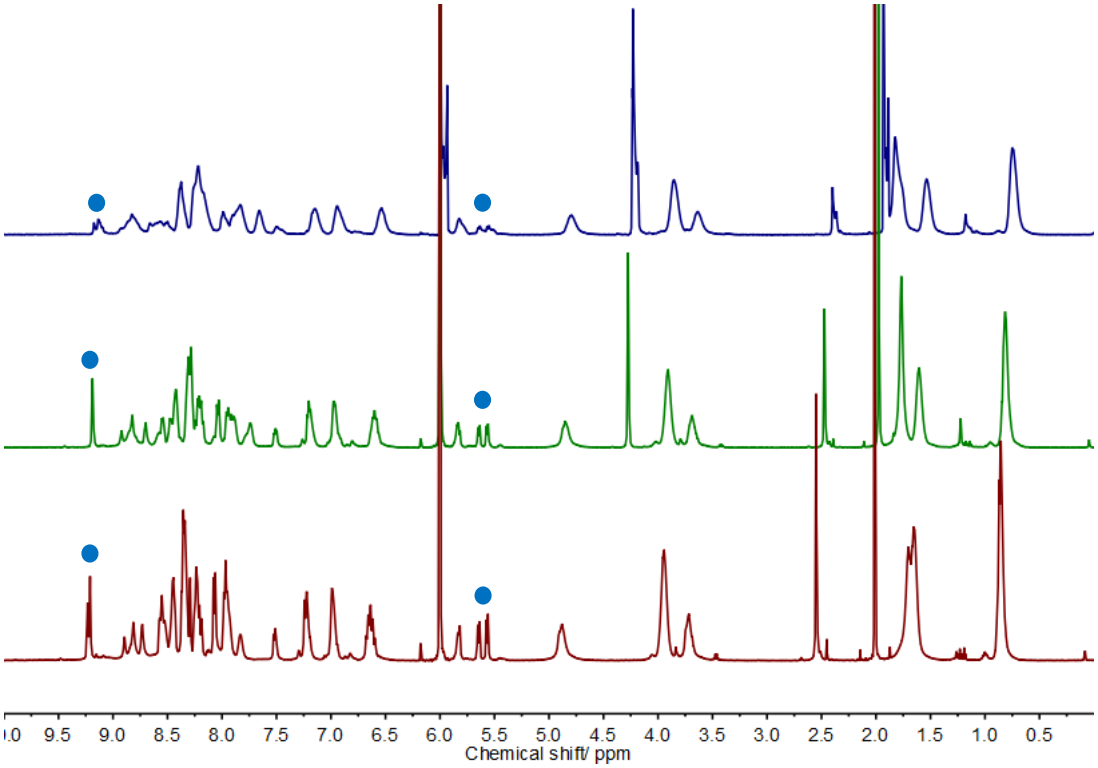


**Figure 3.30.** $^{1}$H-NMR (500 MHz, $d_2$-tetrachloroethane) of fluorinated rhodium **C12** with increasing quantities of nitromethane added. Formation of the $M_3L_2$ species is observed upon each subsequent addition of the nitromethane. 0 Drops (red), 5 drops (green), 15 drops (blue). $M_3L$ peaks highlighted in blue.

## 3.4 Synthesis of azobenzene appended Pt(II) metallo-cryptophanes

Group 9 metals have already been shown to facilitate the self-assembly of azobenzene containing CTG based ligands into a library of $M_3L_2$ metallo-cryptophanes. The use of group 9 metals is uncommon in self-assembly,[44] with much of the research focused on palladium instead.[45, 46] These metals are typically kinetically inert when in an octahedral $d_6$ environment and therefore do not display the necessary lability required to facilitate error correction in a given system, a fundamental requisite of self-assembly. For this reason palladium is more routinely used in self-assembly owing to its increased lability whilst also acting as a predictable square planar metal centre. Despite being similar to palladium, platinum is less commonly used in self-assembly. The reason for this is a result of its position on the periodic table. Platinum lies in the row below palladium and like palladium, platinum(II) almost always exists in a square planar geometry. The consequence of existing in a lower row on the periodic table means that the gap between

energy levels in significantly increased which makes platinum a kinetically inert metal. However previous work with iridium metallo-cryptophanes has shown that the azobenzene type ligands are capable of self-assembling with such metals, albeit more slowly. The kinetic inertness does have a beneficial consequence in that the metallo-cryptophanes made with 3rd row metals appear to be more stable at lower concentrations than their 2nd row analogues. The assembly of the platinum phenylpyridine tectons **M5** and **M6** with the ligands **L1**, **L2** and **L3** was investigated (Scheme 3.6).

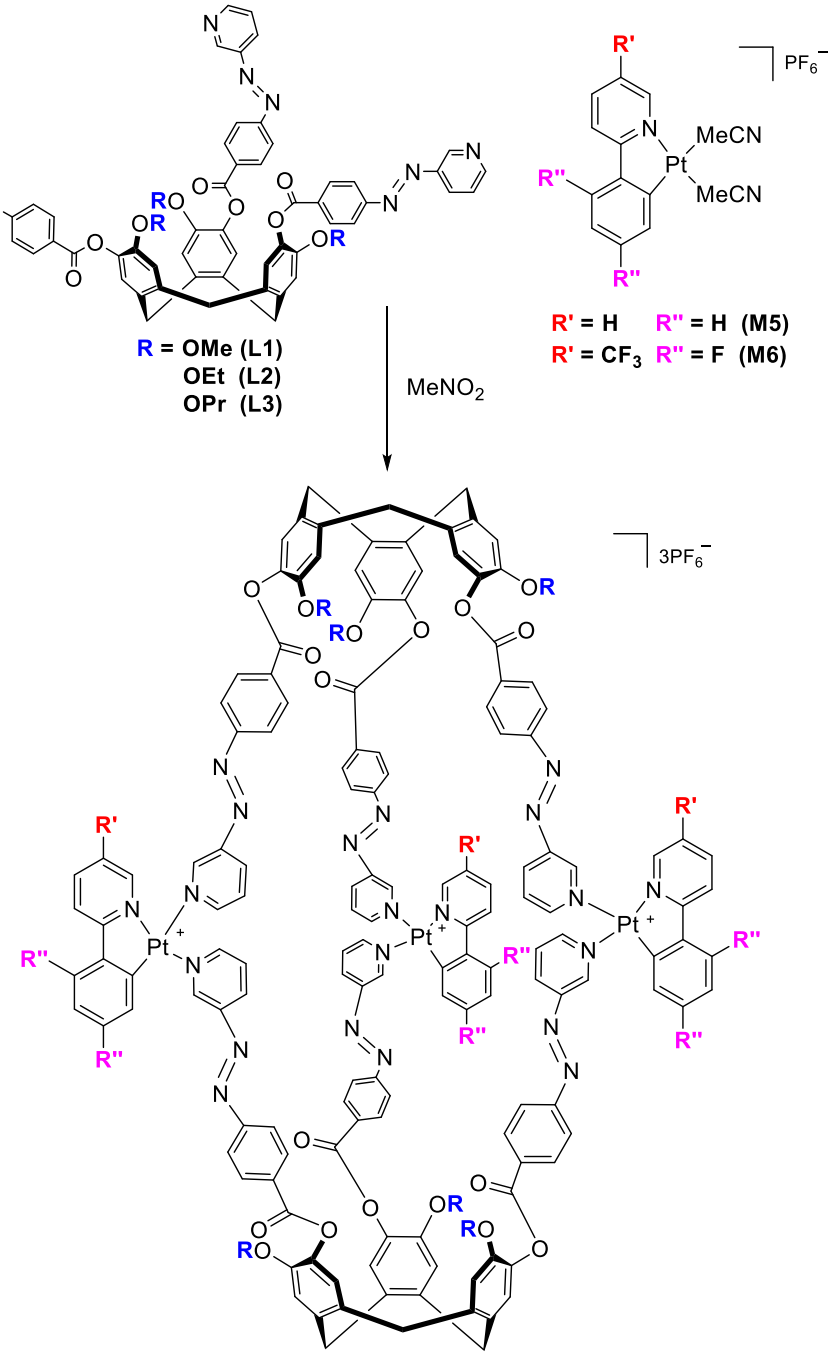


**Scheme 3.6.** Synthesis of platinum(II) containing metallo-cryptophanes.

**Table 3.3.** Reaction codes of platinum-cryptophanes resulting from the reaction of azobenzene ligand with metal tecton

| Ligand | Metal tecton | Metallo-cryptophane |
|---|---|---|
| L1 | M5 | C13 |
| L1 | M6 | C14 |
| L2 | M5 | C15 |
| L2 | M6 | C16 |
| L3 | M5 | C17 |
| L3 | M6 | C18 |

In preliminary experiments, two equivalents of **L1** were dissolved in a solution of deuterated nitromethane. This was added dropwise to a solution containing three equivalents of **M5** in deuterated nitromethane. The progress of the reaction was monitored by $^{1}$H-NMR spectroscopy and mass spectrometry (Figure 3.31 and Figure 3.32). The spectrum initially appeared as a summation of the free ligand and metal tecton peaks, with small broad peaks in the baseline. When monitored over the course of several days the small broad peaks increased in intensity whilst the intensity of the free ligand and metal peaks decreased. Eventually after 2 days the spectrum ceased changing and remained constant, showing the system had reached thermodynamic equilibrium. The length of time required to reach equilibrium is not unusual amongst platinum containing supramolecular systems, with some examples requiring months or elevated temperatures to achieve equilibrium.[47, 48] No evidence of the initial sharp well-resolved peaks remained, instead all that persisted were a series of extremely broad peaks.

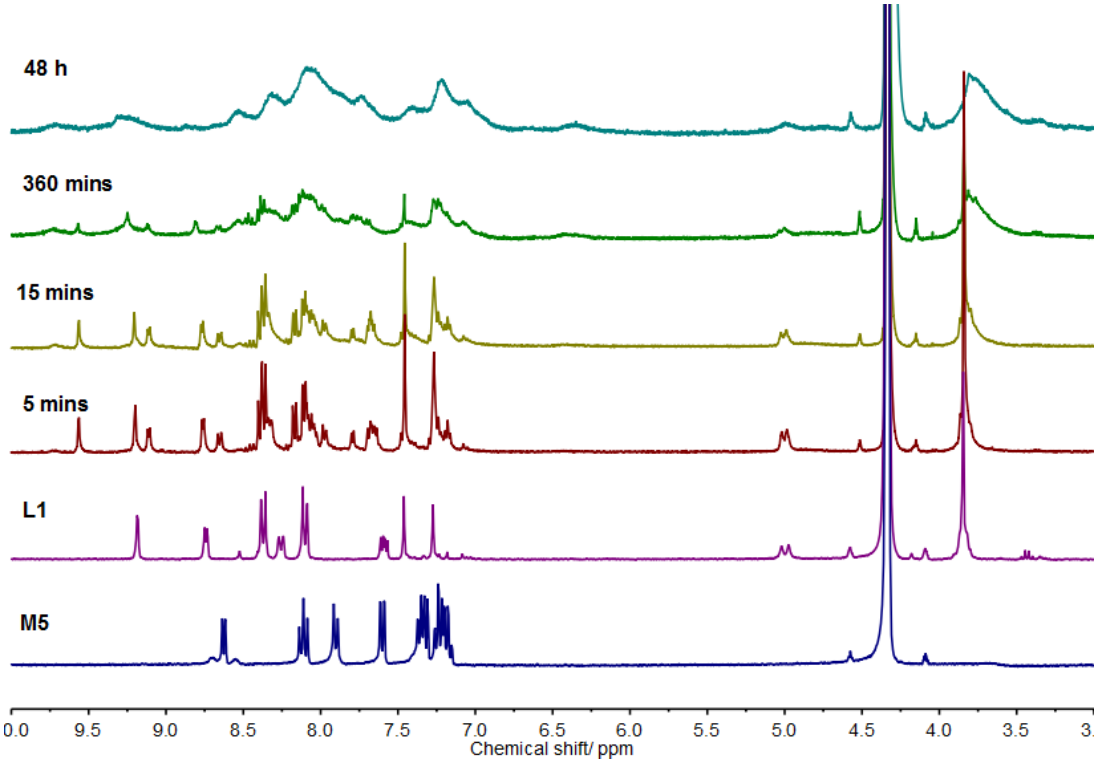


**Figure 3.31.** $^{1}$H-NMR (300 MHz, $d_3$-$MeNO_2$) of **M5**, **L1** and the formation of **C13**.

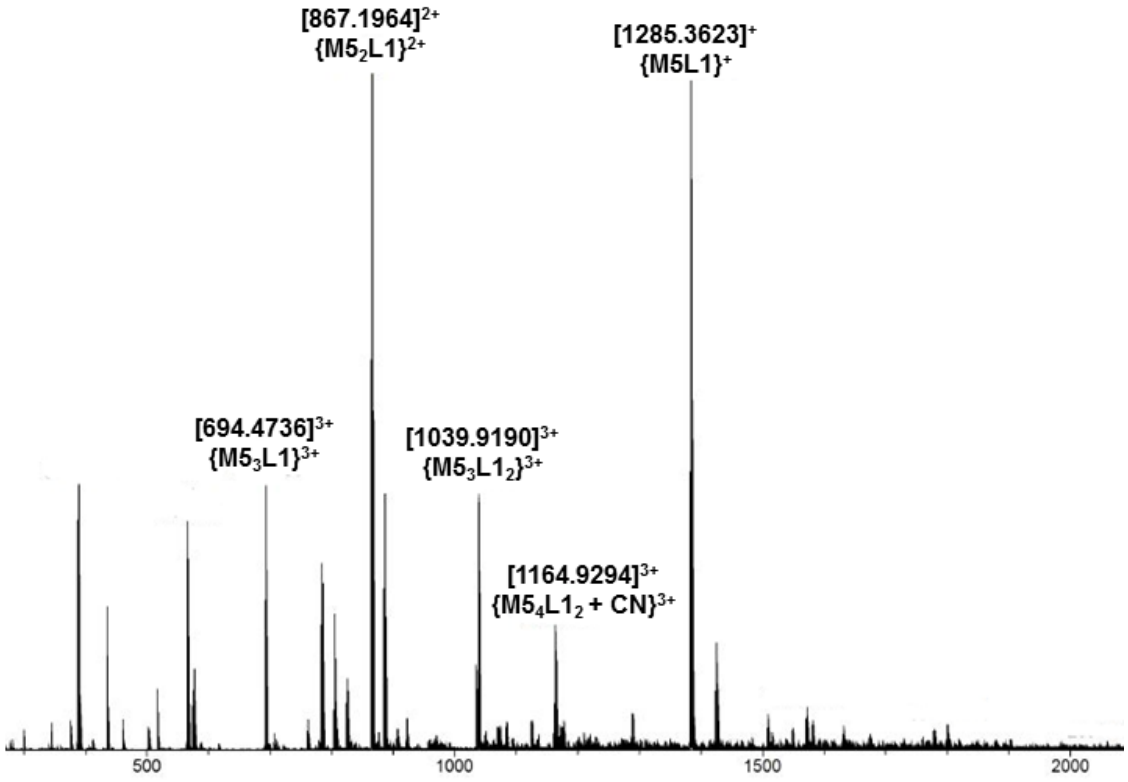


**Figure 3.32.** ESI-MS of **C13** acquired in $MeNO_2$, (**M5** = **M5 – 2MeCN – $PF_6$**).

The broad overlapping nature of the peaks made assignment to specific proton environments incredibly challenging. The broadening of the peaks

does suggest that a cage-like architecture has been formed as this phenomenon usually accompanies the formation of large species. ESI-MS proved useful in elucidating the structure of the species. As expected, initial spectra detected significant quantities of **L1** and **M5** with small quantities of cage intermediates detected. As time progressed, the broadening of the $^{1}$H-NMR spectra was accompanied by the detection of more of the desired $Pt_3\mathbf{L1}_2$ species in the mass spectrum. These observations combined imply that the platinum cryptophane is forming at a very slow rate, considerably slower even than the iridium phenylpyridine cryptophanes. The substantial broadening of the peaks in the $^{1}$H-NMR is further evidence that this process is occurring and moreover, agrees well with the previous observations that the slower the rate of assembly, the more broad the NMR signals become. This is possibly due to the ligands in the iridium and platinum examples exchanging at an intermediate rate on the NMR time scale, resulting in significant broadening. In addition, the platinum metallo-cryptophane may exist as several different isomers depending upon whether an *M* or *P* ligand enantiomer is included in the assembly. Alternatively, the relative orientation of the phenylpyridine groups in the cage assembly may also result in the formation of several isomers, potentially contributing to the broadness of the $^{1}$H-NMR spectrum.

Upon standing in solution for a number of days the sample began to degrade and a black/blue precipitate began to form. Platinum can exist in a +2 or +4 oxidation state. The metal tectons used existed in a +2 oxidation state, making them susceptible to oxidation unless stored under an inert atmosphere. The oxidation of platinum phenylpyridine complexes from the +2 to the +4 oxidation state has been reported.[49] The investigation of the host-guest and photoswitching properties of these complexes involves considerable manipulations of the solutions which would be unfeasible to perform under an inert atmosphere. For this reason focus shifted towards the lighter group ten element, palladium. Synthesis of platinum complexes **C14**, **C15**, **C16**, **C17** and **C18** were not attempted. Palladium routinely exists in a +2 oxidation state and would therefore not have the issues associated with oxidation and subsequent decomposition experienced by the platinum tectons.

## 3.5 Synthesis of azobenzene appended Pd(II) metallo-cryptophanes

The vast majority of metallo-supramolecular architectures reported in the literature utilise palladium(II) cations as a metal source. The reasons for this are two-fold. Firstly palladium(II) almost always adopts a rigid square planar

structure; making it a highly predictable and versatile building block. Unlike platinum, palladium(IV) compounds are comparatively rare and oxidation from +2 to +4 is less of a potential source of interference. Secondly palladium is far less kinetically inert than many other 2$^{nd}$ and 3$^{rd}$ row late transition metals. The ease at which ligand exchange can occur enables error correction processes to occur and subsequently increase the reliability of self-assembly reactions. Fujita's molecular square and Shinkai's first example of a metallo-cryptophane both utilised palladium cations as metal building blocks.[26, 50] In order to target discrete assemblies a *cis* protecting strategy is employed where the two coordination sites are blocked by a chelating ligand. Frequently ethylenediamine (en) and 1,3-bis(diphenylphosphino)propane are used to fulfil this role.[51, 52] Weakly coordinating nitrate anions are used to occupy the available coordination sites which can be easily displaced by coordinating groups such as a pyridyl or carboxylate.

The previous examples of metallo-cryptophanes in this thesis have employed iridium, rhodium and platinum as their metal source. An important caveat when using these metals is that a non-coordinating solvent such as nitromethane must be used. Coordinating solvents such as DMSO or even acetonitrile act to completely disassemble the cage by outcompeting the ligand for available coordination sites on the metal. Attempts to synthesise $Pd_3L_2$ metallo-cryptophanes in such solvents, using palladium(ethylenediamine)dinitrate as the metal source resulted in the immediate precipitation of an unassignable species. The formation of such a precipitate was encouraging as it confirmed that ligand and metal were reacting and warranted further investigation. There are numerous examples in the literature where palladium supramolecular architectures have successfully been synthesised in DMSO.[13, 14, 42] This observation implies that palladium metallo-cryptophanes may tolerate DMSO as a solvent more effectively than cryptophanes synthesised with other metals. This potentially could be a result of weaker palladium solvent interactions, or stronger palladium ligand interactions. The former may be more likely as palladium(II) complexes where DMSO binds through either the oxygen or the sulphur atom are well documented. A soft metal will preferentially bind to sulphur whereas a hard metal will bind to the oxygen. The fact that palladium is known to form complexes with both suggests it usually exhibits an intermediate hardness and is therefore cannot form strong hard-hard or soft-soft interactions in either case.

Owing to the precedent of palladium complexes forming in DMSO, attempts were made to synthesise palladium metallo-cryptophanes utilising the ligand **L1**, **L2** and **L3** (Scheme 3.7). In the first instance, ligand **L1** was dissolved in $d_6$-DMSO and added to a solution of palladium(ethylenediamine)dinitrate in $d_6$-DMSO. Analysis by $^1$H-NMR revealed that an immediate reaction had occurred (Figure 3.33). The signals for the protons situated *ortho* to the pyridyl nitrogen ($H^e$) exhibited a downfield shift from 9.20 – 9.62 ppm, consistent with binding of the pyridyl nitrogen to the palladium centre. All resonances were broadened slightly, which again suggested the formation of a larger species such as metallo-cryptophane. Importantly, the $^1$H-NMR spectra remained very simple and no additional peaks were observed. This means that the $C_3$ symmetry of the ligand has not been reduced during complex formation. This is highly suggestive of metallo-cryptophane formation which display $C_3$ or $D_3$ symmetry depending on whether the *syn* or *anti* diastereomer is formed respectively. Although broadened, the splitting of the methylene *exo* and *endo* protons on the CTG backbone into a clean doublet is still evident; further reinforcing that the symmetry of the complex retains that of the unbound ligand.

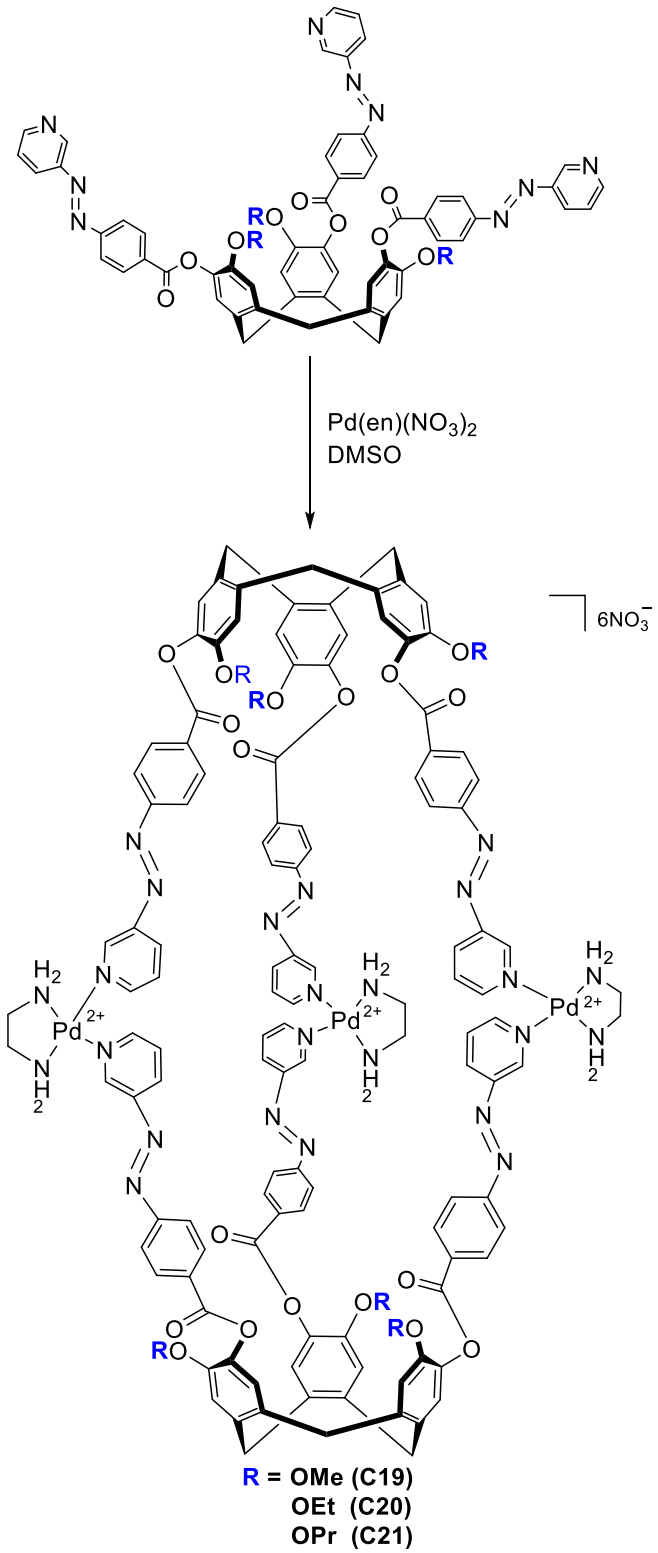


**Scheme 3.7.** Synthesis of palladium containing metallo-cryptophanes **C19**, **C20** and **C21**.

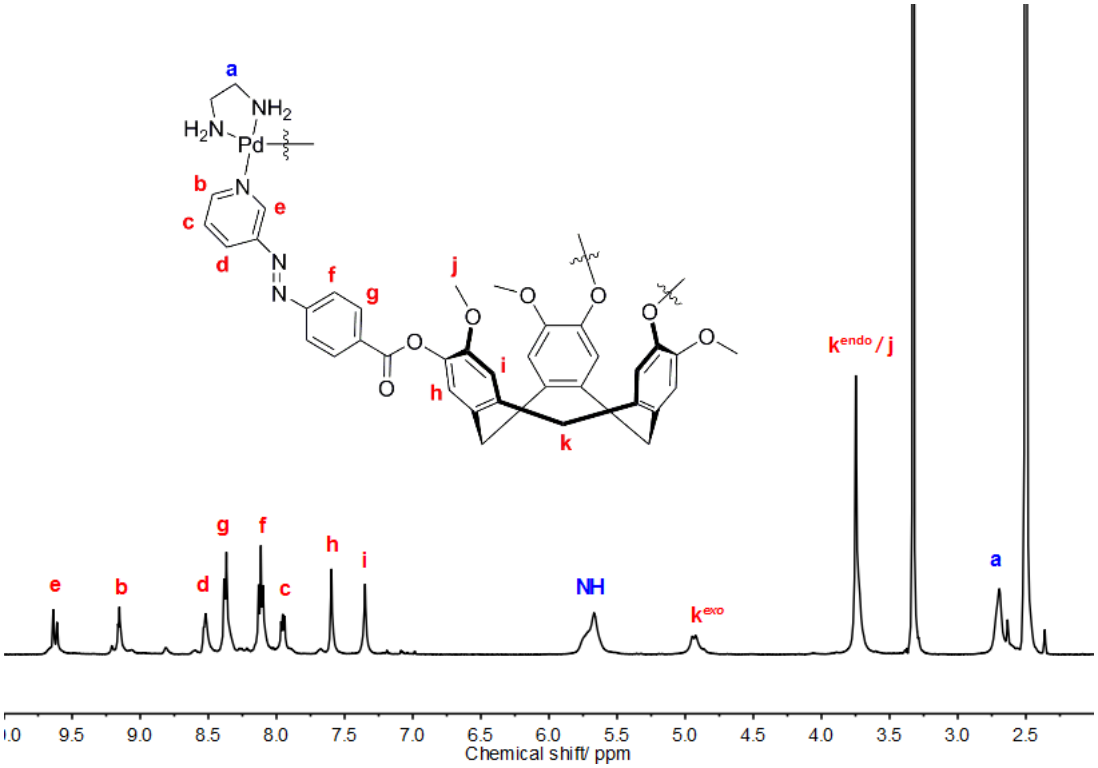


**Figure 3.33.** $^{1}$H-NMR (500 MHz, $d_6$-DMSO) spectrum of reaction of **L1** and Pd(en)$(NO_3)_2$ obtained immediately after mixing, revealing a surprising simplicity to the spectrum.

A $^{1}$H-$^{1}$H NOESY spectrum of the reaction was obtained which displayed a characteristic cross-coupling between the amine protons on the palladium ethylenediamine complex and the *ortho* pyridyl protons on the ligand **L1** (Figure 3.34). This cross-coupling reveals that the metal tecton and ligand are held together close in space and along with the other NMR evidence obtained so far, suggests that a novel palladium metallo-cryptophane (**C19**) has been successfully synthesised. The $^{13}$C-NMR spetrum of the sample reveals a consistent number of peaks with the proposed structure and rigorous analysis by 2-D NMR techniques COSY, HSQC and HMBC allow for complete assignment of all proton environments. As with previous metallo-cryptophane examples, a DOSY NMR spectrum was obtained of the sample and confirmed that the signals arising from the metal tecton and ligand were diffusing at the same rate in solution, confirming that all of the metal and ligand had reacted in a 2:3 ratio to form a single discrete species (Figure 3.35). DOSY NMR confirmed that ligands **L2** and **L3** also reacted with palladium ethylenediamine nitrate in DMSO to form a single large species with a similar diffusion constant to **C19**. These species were assigned as **C20** and **C21** respectively.

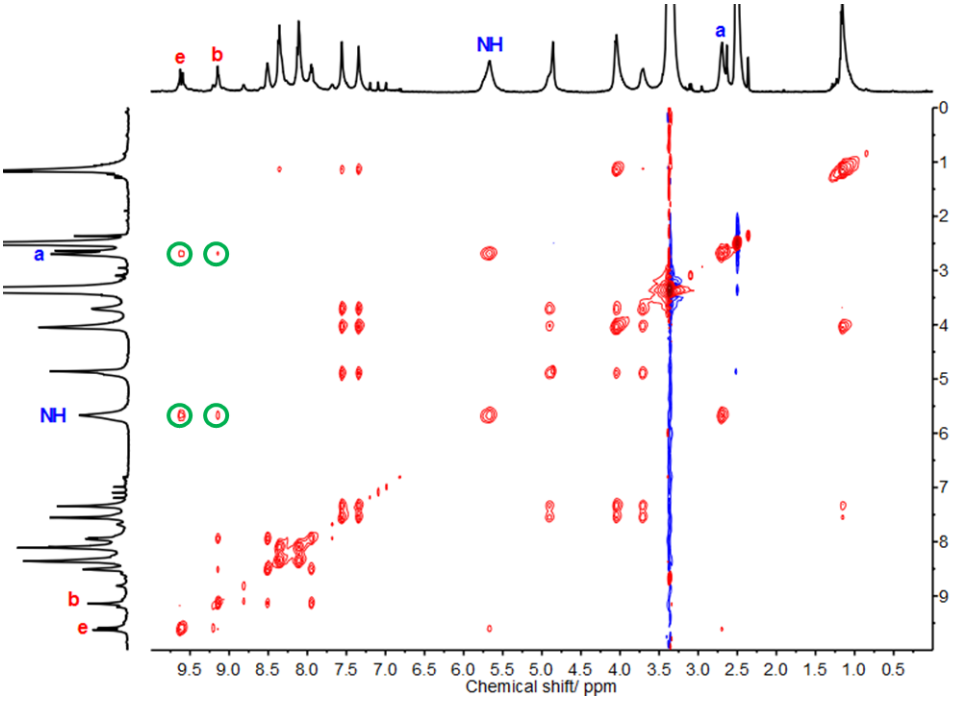


**Figure 3.34.** $^{1}$H-$^{1}$H NOESY (500 MHz, $d_6$-DMSO) spectrum of **C20** displaying through space cross-couplings between metal tecton and ligand highlighted in green.

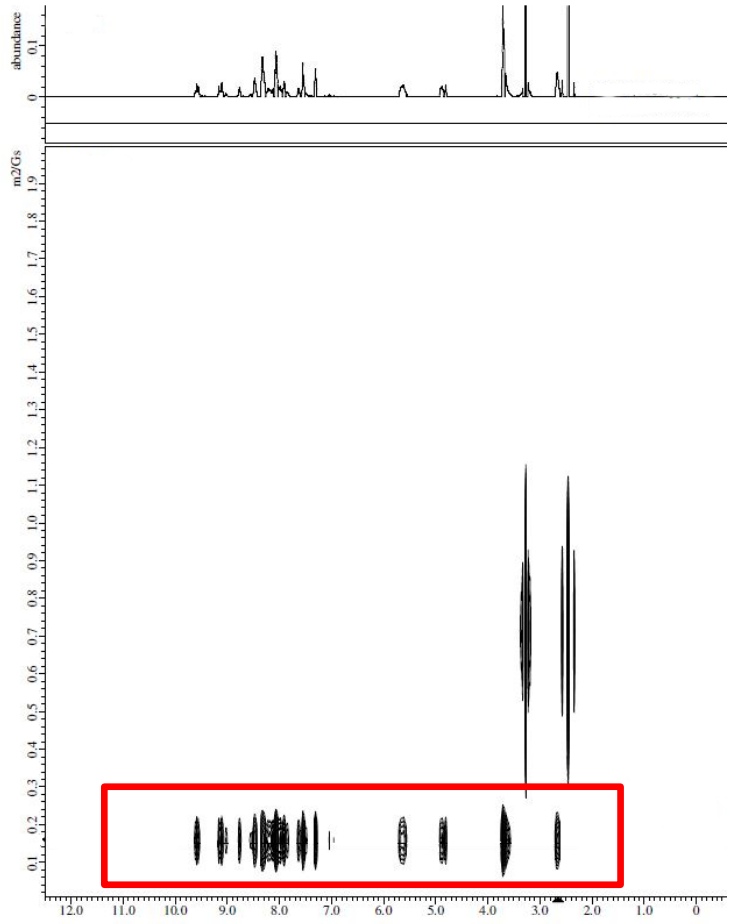


**Figure 3.35.** $^{1}$H-NMR DOSY (600 MHz, $d_6$-DMSO) spectrum of **C19** showing a single large species in solution.

In order to unambiguously confirm the formation of the new metallo-cryptophane **C19** a mass spectrum was required. Unfortunately, all attempts to characterise the species using automated ESI-MS procedures ultimately failed. This observation is consistent with the trend that more kinetically labile metallo-cryptophanes such as the rhodium examples rapidly disassemble under the conditions in the mass spectrometer. Either due to dilution, competition from the acetonitrile carrier solvent or simply because the ESI source imposed conditions too harsh for the metallo-cryptophane to withstand. In order to obtain quality mass spectra the samples were directly injected into the mass spectrometer in collaboration with the Liverpool Materials Innovation Factory. Under these conditions a m/z of $[428.1710]^{6+}$ was detected (Figure 3.36). This is in good agreement with the calculated value for a $[Pd(en)_3\mathbf{L1}_2]^{6+}$ species which possesses a m/z of 428.4311.

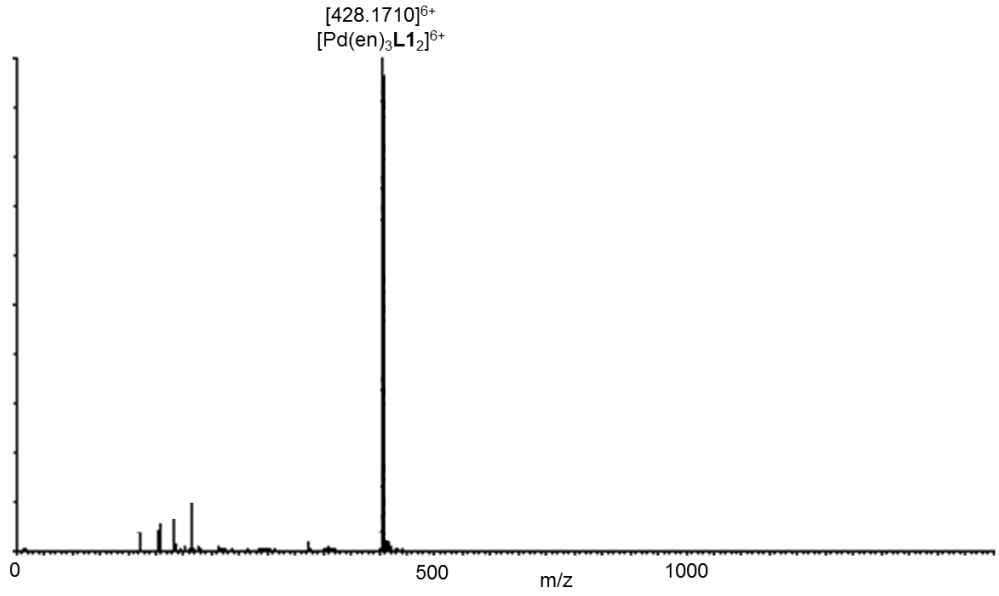


**Figure 3.36.** ESI-MS of metallo-cryptophane **C19**, acquired in DMSO.

Reaction of palladium(ethylenediamine)dinitrate and the other azobenzene appended CTG ligands **L2** and **L3** was also attempted in an analogous procedure to **L1**. $^1$H-NMR spectra taken immediately after mixing revealed almost identical spectra to that obtained for **C19**. The only noticeable difference between the spectra is the appearance of the aliphatic region. This can be attributed to the different alkoxy substituents on the upper rim of the CTG bowl, the reactions with **L2** and **L3** both display the expected splitting, integration and number of peaks in the aliphatic region. NOESY spectra once again confirmed the close proximity of metal tecton and ligand in solution and DOSY NMR was used to identify the presence of a single large species in solution. MALDI MS provided the final piece of evidence corroborating the

formation of two novel palladium complexes with **L2** and **L3**, forming **C20** and **C21** respectively.

Closer analysis of the $^{1}$H-NMR spectra of the palladium metallo-cryptophanes revealed a feature which was not present in any of the previously reported examples. Alongside the major peaks which can be attributed to the metallo-cryptophane were a number of much smaller which align perfectly with the peaks of the free ligands (Figure 3.37). Unlike the peaks for the free ligand however they were significantly broadened which suggests that the ligand is in rapid exchange with the metallo-cryptophane. Interestingly no peaks were present in the spectra which could be attributed to any intermediate species such as $[M_2L_2]^{4+}$. This implies that whilst the cryptophane species is in rapid exchange with its constituent parts, the process of metallo-cryptophane formation becomes progressively more energetically favourable once formation has started with an $[ML]^{+}$ species. This behaviour has been observed for self-assembled systems previously, with Lehn's helicates serving as a good example.[53] The rationale for this phenomenon is that as the reaction progresses towards the $M_3L_2$ metallo-cryptophane, the intermediates become successively more pre-organised towards this species which makes the following steps more energetically favourable. This is in contrast to rhodium and particularly iridium metallo-cryptophanes which have detectable intermediate states present in the NMR at times. The intermediates of these cages do not possess such a strong pre-organisation effect driving the reaction towards the $M_3L_2$ cage.

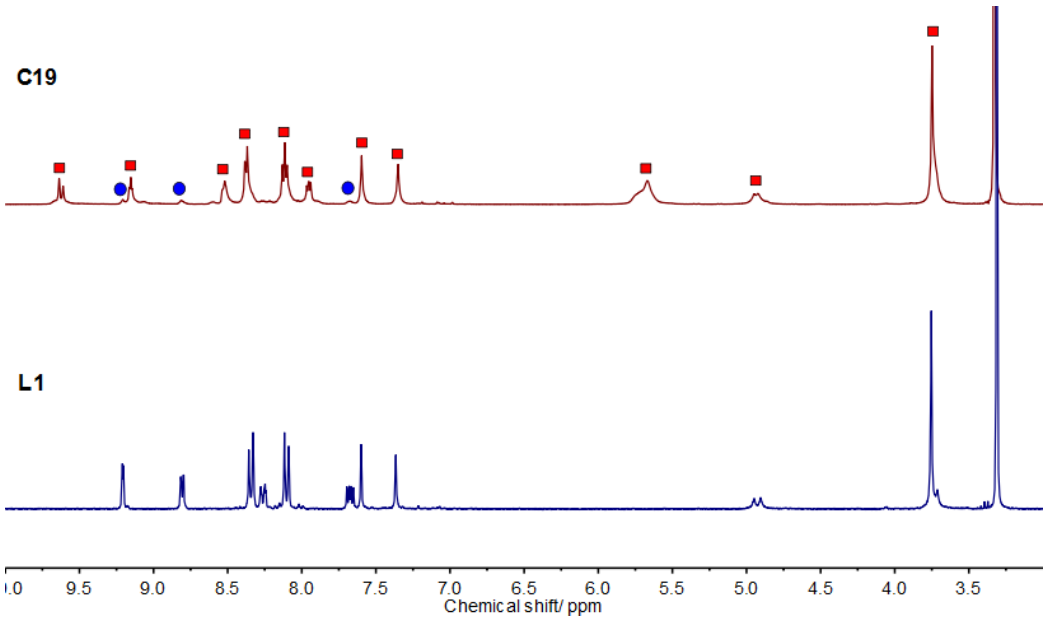


**Figure 3.37.** $^{1}$H-NMR (500 MHz, $d_6$-DMSO) of palladium cryptophane **C19** displaying the peaks corresponding to metallo-cryptophane (red) and 'free' ligand (blue).

## 3.6 Conclusions

A series of novel rhodium, platinum and palladium containing cryptophanes have been synthesised from azobenzene appended CTG ligands. In addition, the library of iridium cryptophanes first reported by the Hardie group has been expanded to contain solubilised derivatives. A total of 15 new metallo-cryptophanes have been reported. The strategy of *cis* protecting a metal tecton results in a highly predictable method of targeting $M_3L_2$ cryptophanes. The ability to form metallo-cryptophanes reliably from four different metals exemplifies the flexibility and specificity of such an approach.

Significant progress has been made towards the solubilisation of the rhodium and iridium azobenzene appended metallo-cryptophanes which can be dissolved in substantial amounts in non-polar solvents such as tetrachloroethane. This expands the scope of these metallo-cryptophanes and may facilitate the use of these complexes in a range solvent dependant host-guest applications. The preferential formation of a suspected $M_3L$ species in tetrachloroethane was unexpected. However, the formation of this species may be used to form heteroleptic metallo-cryptophane. The $M_3L$ species may act as a template, facilitating addition of a different ligand to ‘cap off’ the metallo-cryptophane. The discovery that the palladium metallo-cryptophanes discussed previously are stable in the strongly coordinating solvent DMSO was a surprise and enables a plethora of further applications to be investigated due to the strong solubilising power and biocompatibility of DMSO.

The synthesis of a substantial library of metallo-cryptophanes allows for an investigation into the structure-function relationship of the various components. A discussion of the photoswitching potential of these cages will be discussed in the subsequent chapter, followed by an investigation into the host-guest behaviour in Chapter five.

## 3.7 Future Work

The work described in this chapter confirms that efforts synthesise solubilised ligand and metal tectons, with the ultimate goal to increase solubility of the resultant assemblies were a success. An unintended consequence of the efforts to solubilise the metal tecton with a $CF_3$ group in the 5 position of the pyridine on the phenylpyridine resulted in a steric clash with the tecton and the ligand. This clash resulted in incomplete cage formation. Nevertheless, the $M_3L_2$ cages were predominantly formed and displayed significantly better solubility when a combination of solubilised ligand and tecton were used. This highlights the validity of this approach for solubilising the metallo-cryptophanes. Repositioning the solubilising groups away from the 5 position to the 3 or 4 position should alleviate the steric clash and may allow for complete formation of the desired solubilised metallo-cryptophanes.

The dissolution of CTG containing species in aqueous solvents has always been a challenge due to the hydrophobic nature of the CTG bowl. Utilising the approach described previously to engineer water soluble metal tectons may enable dissolution in a aqueous solvents. The use of water as a solvent is under increasing interest from industry due to its negligible environmental impact. In addition, water solubility is a prerequisite for most biomedical applications. Recent work from Jarosz has shown that appending sucrose to a CTG unit enables dissolution of the species in water.[54] A similar approach could be undertaken where sugars are attached to a metal tecton and upon self-assembly with a CTG ligand would furnish a water soluble metallo-cryptophane. Investigations are currently ongoing within the Hardie group to determine if this is a viable strategy (Figure 3.38).

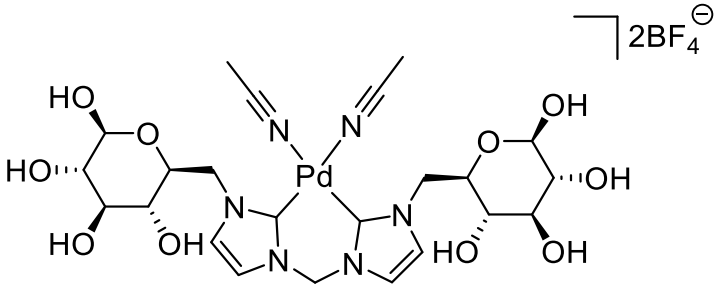


**Figure 3.38.** Sugar appended NHC tecton to enhance the water solubility of metallo-cryptophanes.

## 3.8 Experimental

### General Remarks

All reagents were purchased from commercial suppliers and used without further purification. Where stated reactions were carried out under an inert atmosphere of nitrogen using a dual vacuum/ nitrogen manifold and standard Schlenk techniques. Dry solvent was obtained by passing through a column of activated alumina.

### Instrumentation

$^{1}H$ and $^{13}C$ NMR were performed on either a Bruker Avance III 300 MHz spectrometer, Bruker Avance III HD 400 MHz spectrometer or a Bruker 500-CP 500 MHz spectrometer and referenced to residual solvent peaks. Where appropriate NMR assignments were confirmed using 2-D NMR techniques including COSY, TOCSY, HSQC, HMBC, NOESY, ROESY and DOSY.

Electrospray mass spectra were performed on a Bruker micro-TOFQ mass spectrometer. Direct injection experiments were performed in collaboration with Dr Stuart Warriner in-house or with the assistance of the Liverpool Materials Innovation Factory on a Bruker Synapt G2-Si mass spectrometer.

**$[(M1)_3(L1)_2]^{3+}\bullet 3PF_6^-$ (C1)[33]**

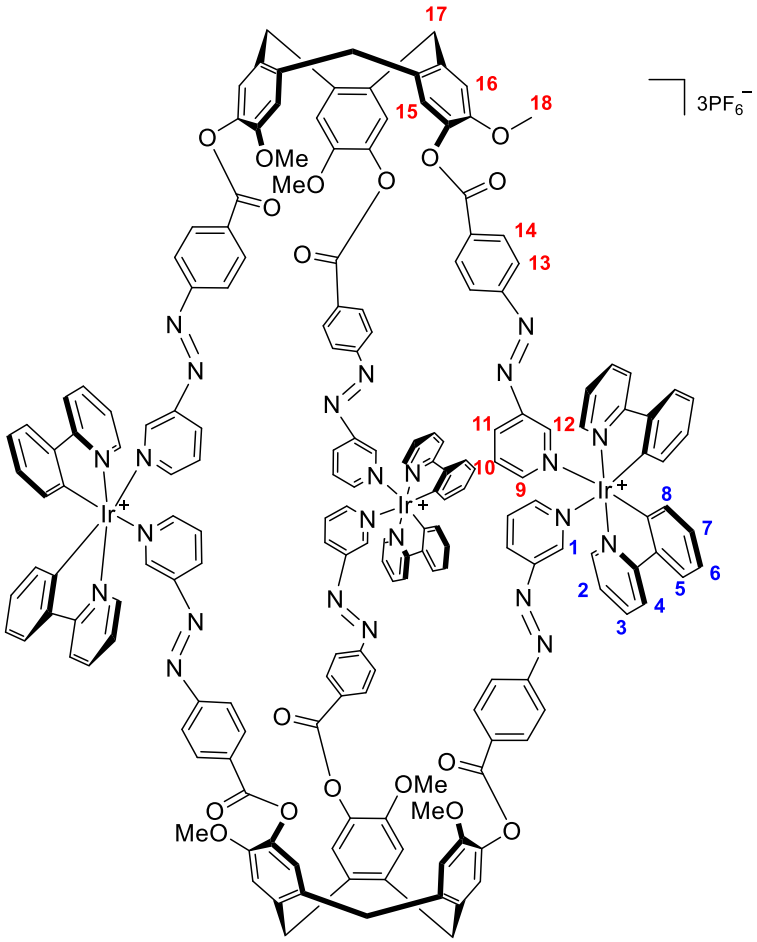


**L1** (4.0 mg, 3.86 µmol) was dissolved in $d_3$-nitromethane (0.3 mL). **M1** (4.2 mg, 5.78 µmol) was dissolved in $d_3$-nitromethane (0.3 mL) and added dropwise to the solution of **L1**. The bright orange solution was left to stand for fifteen minutes after which a $^1$H-NMR was acquired. Complete conversion of the starting materials to cage **C1** had occurred during this time. Data is consistent with literature values.[33]

**$^1$H-NMR** (500 MHz, $d_3$-$MeNO_2$): 9.26 (bs, 6H, $H^{12}$), 8.92 (bs, 12H, $H^9$/ $H^1$), 8.42 (bs, 6H, $H^{11}$), 8.32 (bs, 12H, $H^{14}$), 8.02-7.98 (m, 24H, $H^3$/ $H^4$/ $H^{13}$), 7.68 (bs, 12H, $H^5$/ $H^{10}$), 7.45-7.42 (m, 12H, $H^2$/ $H^{15}$), 7.26 (bs, 6H, $H^{16}$), 7.00 (bs, 12H, $H^6$/ $H^7$), 6.56 (bs, 6H, $H^8$), 5.00 (bs, 6H, $H^{17\text{-}exo}$), 3.83 (bs, 24H, $H^{17\text{-}endo}$/ $H^{18}$).

**ESI-MS** (+ve): $[M_3L_2]^{3+}$: m/z =1191.3209, calcd 1191.3179.

**$[(M2)_3(L1)_2]^{3+}\bullet 3PF_6^-$ (C2)**

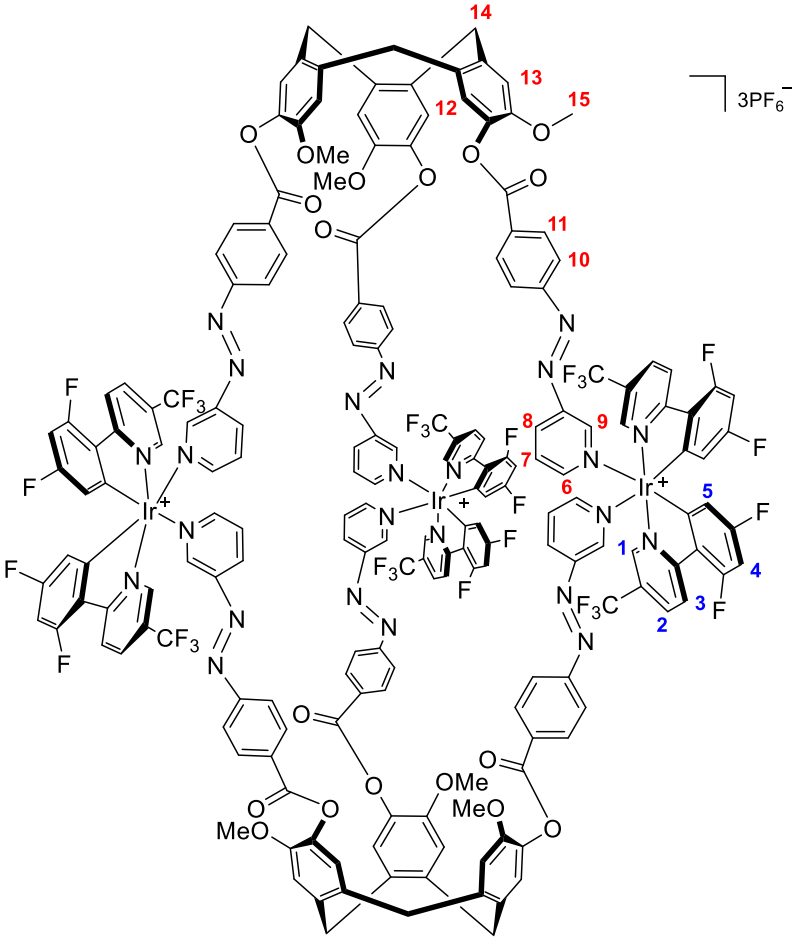


**L1** (4.0 mg, 3.86 µmol) was dissolved in $d_3$-nitromethane (0.3 mL). **M2** (4.2 mg, 5.78 µmol) was dissolved in $d_3$-nitromethane (0.3 mL) and added dropwise to the solution of **L1**. The bright orange solution was left to stand for 24 hours after which time a $^1$H-NMR was acquired. Complete conversion of the starting materials to cage **C2** and a small amount of minor product had occurred in this time.

**$^1$H-NMR** (300 MHz, $d_3$-$MeNO_2$): 9.21 (bs, 6H, **$H^9$**), 9.15 (bs, 6H, **$H^1$**), 8.88 (bs, 6H, **$H^6$**), 8.51 (bs, 12H, **$H^8$/ $H^2$**), 8.33 (bs, 18H, **$H^{11}$/ $H^3$**), 7.97 (bs, 12H, **$H^{10}$**), 7.76 (bs, 6H, **$H^7$**), 7.43 (bs, 6H, **$H^{12}$**), 7.25 (bs, 6H, **$H^{13}$**), 6.69 (bs, 6H, **$H^4$**), 6.13 (bs, 6H, **$H^5$**), 4.99 (bs, 6H, **$H^{14\text{-}exo}$**), 3.82 (bs, 24H, **$H^{14\text{-}endo}$/ $H^{15}$**).

**ESI-MS** (+ve): $[M_3L_2]^{3+}$: m/z = 1399.5904, calcd 1399.2549.

**$[(M1)_3(L2)_2]^{3+}\bullet 3PF_6^-$ (C3)**

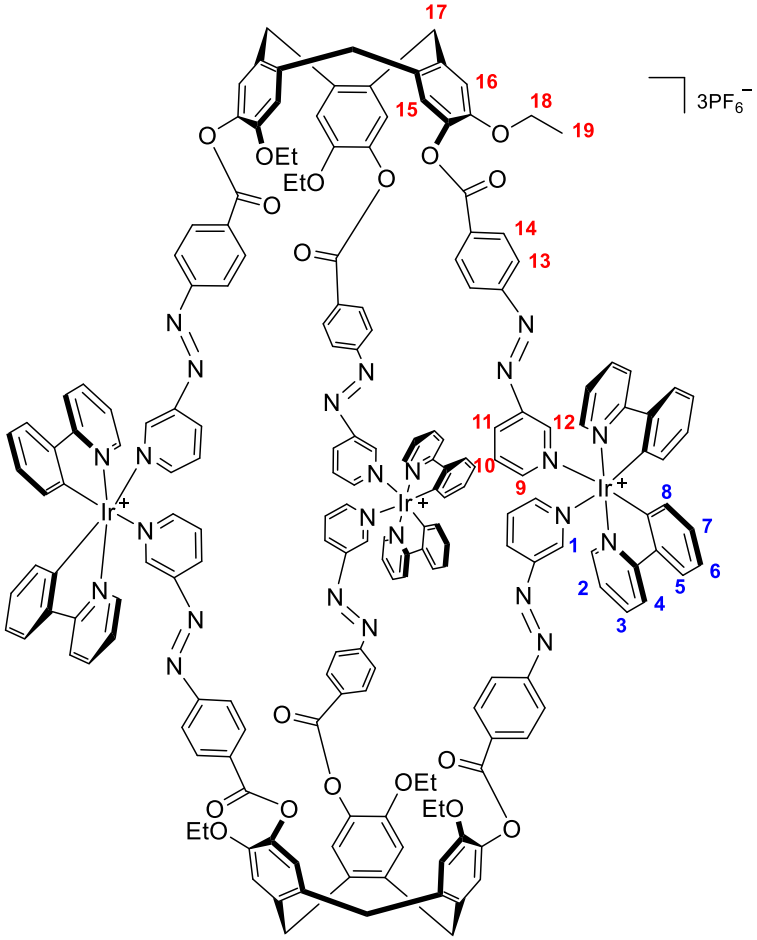


**L2** (4.0 mg, 3.86 µmol) was dissolved in $d_3$-nitromethane (0.3 mL). **M1** (4.2 mg, 5.78 µmol) was dissolved in $d_3$-nitromethane (0.3 mL) and added dropwise to the solution of **L2**. The bright orange solution was left to stand for five minutes after which time a $^1$H-NMR was acquired. Complete conversion of the starting materials to cage **C3** had occurred in this time.

**$^1$H-NMR** (500 MHz, $d_3$-$MeNO_2$): 9.26 (bs, 6H, **$H^{12}$**), 8.92 (bs, 12H, **$H^9$/ $H^1$**), 8.41 (bs, 6H, **$H^{11}$**), 8.32 (bs, 12H, **$H^{14}$**), 8.02-7.98 (m, 24H, **$H^3$/ $H^4$/ $H^{13}$**), 7.68 (bs, 12H, **$H^5$/ $H^{10}$**), 7.45-7.40 (m, 12H, **$H^2$/ $H^{15}$**), 7.26 (bs, 6H, **$H^{16}$**), 7.00 (bs, 12H, **$H^6$/ $H^7$**), 6.56 (bs, 6H, **$H^8$**), 4.98 (d, 6H, *J* = 14.0 Hz, **$H^{17\text{-}exo}$**), 4.12-4.08 (m, 12H, **$H^{18}$**), 3.82 (d, 6H, *J* = 14.0 Hz, **$H^{17\text{-}endo}$**), 1.24-1.20 (m, 18H, **$H^{19}$**).

**ESI-MS** (+ve): $[M_3L_2]^{3+}$: m/z =1219.3514, calcd 1219.3492.

**$[(M2)_3(L2)_2]^{3+}\bullet 3PF_6^-$ (C4)**

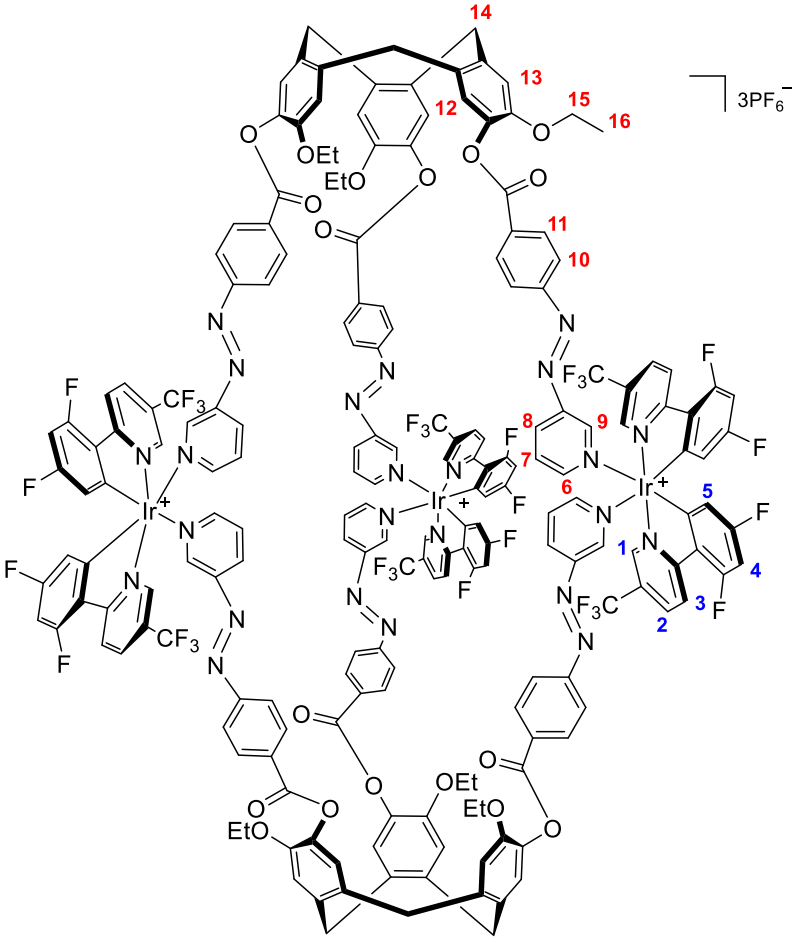


**L2** (4.0 mg, 3.86 µmol) was dissolved in $d_3$-nitromethane (0.3 mL). **M2** (4.2 mg, 5.78 µmol) was dissolved in $d_3$-nitromethane (0.3 mL) and added dropwise to the solution of **L2**. The bright orange solution was left to stand for 24 hours after which time a $^1$H-NMR was acquired. Complete conversion of the starting materials to cage **C4** and a small amount of minor product had occurred in this time.

**$^1$H-NMR** (500 MHz, $d_3$-$MeNO_2$): 9.21 (bs, 6H, **$H^9$**), 9.16 (bs, 6H, **$H^1$**), 8.89 (bs, 6H, **$H^6$**), 8.52 (bs, 12H, **$H^8$/ $H^2$**), 8.34 (bs, 18H, **$H^{11}$/ $H^3$**), 7.98 (bs, 12H, **$H^{10}$**), 7.76 (bs, 6H, **$H^7$**), 7.40 (bs, 6H, **$H^{12}$**), 7.24 (bs, 6H, **$H^{13}$**), 6.69 (bs, 6H, **$H^4$**), 6.13 (bs, 6H, **$H^5$**), 4.98 (bs, 6H, **$H^{14\text{-}exo}$**), 4.15-4.01 (m, 12H, **$H^{15}$**), 3.82 (bs, 6H, **$H^{14\text{-}endo}$**), 1.21 (bs, 18H, **$H^{16}$**).

**ESI-MS** (+ve): $[M_3L_2]^{3+}$: m/z = 1427.2872, calcd 1427.2862.

**$[(M1)_3(L3)_2]^{3+}\bullet 3PF_6^-$ (C5)**

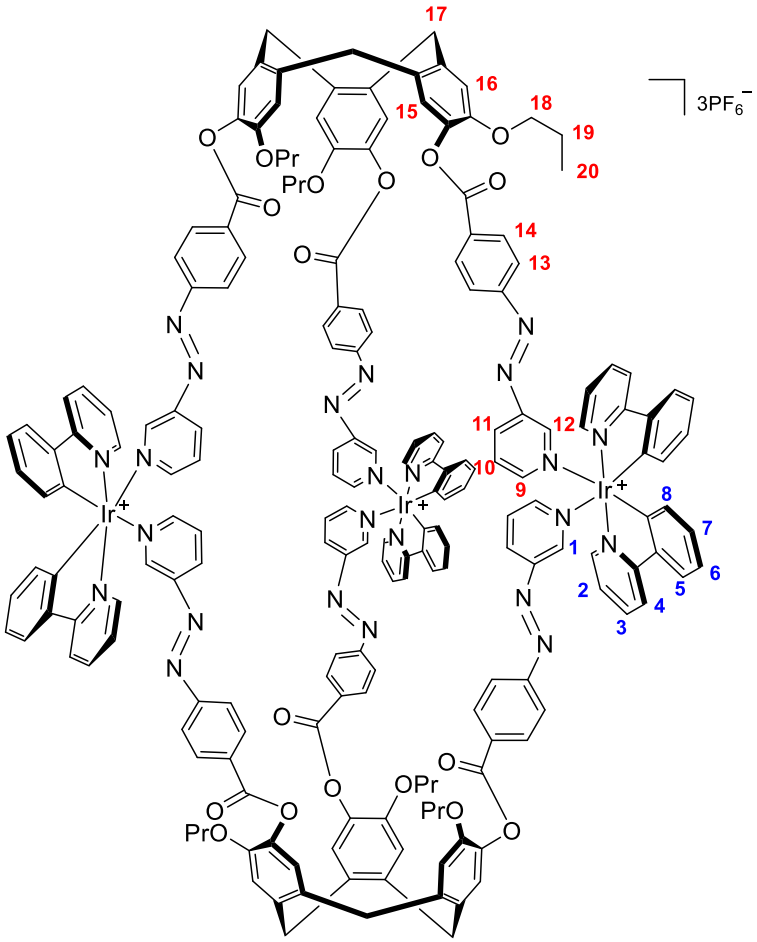


**L3** (4.0 mg, 3.86 µmol) was dissolved in $d_3$-nitromethane (0.3 mL). **M1** (4.2 mg, 5.78 µmol) was dissolved in $d_3$-nitromethane (0.3 mL) and added dropwise to the solution of **L3**. The bright orange solution was left to stand for five minutes after which time a $^1$H-NMR was acquired. Complete conversion of the starting materials to cage **C5** had occurred in this time.

**$^1$H-NMR** (500 MHz, $d_3$-$MeNO_2$): 9.26 (bs, 6H, **$H^{12}$**), 8.92 (bs, 12H, **$H^9$/ $H^1$**), 8.41 (bs, 6H, **$H^{11}$**), 8.32 (bs, 12H, **$H^{14}$**), 8.06-7.97 (m, 24H, **$H^3$/ $H^4$/ $H^{13}$**), 7.69 (bs, 12H, **$H^5$/ $H^{10}$**), 7.50-7.40 (m, 12H, **$H^2$/ $H^{15}$**), 7.24 (bs, 6H, **$H^{16}$**), 7.00 (bs, 12H, **$H^6$/ $H^7$**), 6.56 (bs, 6H, **$H^8$**), 4.98 (d, 6H, *J* = 14.0 Hz, **$H^{17\text{-}exo}$**), 4.02-3.99 (m, 12H, **$H^{18}$**), 3.82 (d, 6H, *J* = 14.0 Hz, **$H^{17\text{-}endo}$**), 1.64-1.60 (m, 12H, **$H^{19}$**), 0.84-0.80 (m, 18H, **$H^{20}$**).

**ESI-MS** (+ve): $[M_3L_2]^{3+}$: m/z =1247.3824, calcd 1247.3805.

**$[(M2)_3(L3)_2]^{3+}\bullet 3PF_6^-$ (C6)**

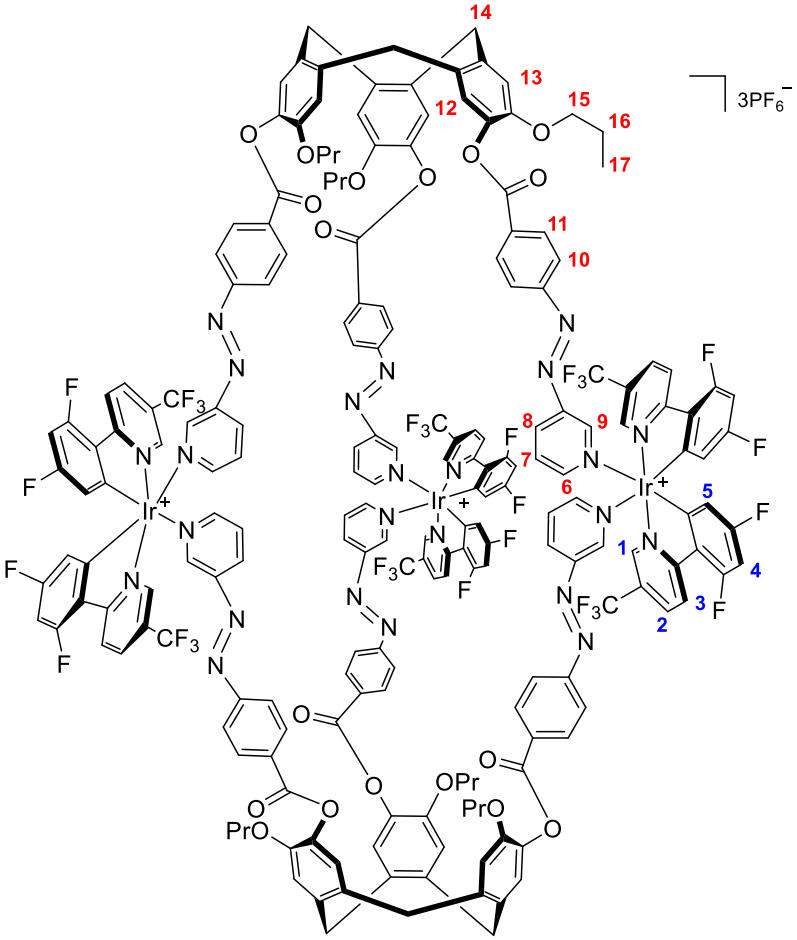


**L3** (4.0 mg, 3.86 µmol) was dissolved in $d_3$-nitromethane (0.3 mL). **M2** (4.2 mg, 5.78 µmol) was dissolved in $d_3$-nitromethane (0.3 mL) and added dropwise to the solution of **L3**. The bright orange solution was left to stand for 24 hours after which time a $^1$H-NMR was acquired. Complete conversion of the starting materials to cage **C6** and a small amount of minor product had occurred in this time.

**$^1$H-NMR** (500 MHz, $d_3$-$MeNO_2$): 9.19 (bs, 6H, **$H^9$**), 9.15 (bs, 6H, **$H^1$**), 8.88z (bs, 6H, **$H^6$**), 8.52 (bs, 12H, **$H^8$/ $H^2$**), 8.34 (bs, 18H, **$H^{11}$/ $H^3$**), 7.98 (bs, 12H, **$H^{10}$**), 7.76 (bs, 6H, **$H^7$**), 7.40 (bs, 6H, **$H^{12}$**), 7.24 (bs, 6H, **$H^{13}$**), 6.71 (bs, 6H, **$H^4$**), 6.13 (bs, 6H, **$H^5$**), 4.98 (bs, 6H, **$H^{14\text{-}exo}$**), 4.02 (bs, 12H, **$H^{15}$**), 3.82 (bs, 6H, **$H^{14\text{-}endo}$**), 1.62 (bs, 18H, **$H^{16}$**), 0.85-0.80 (m, 18H, **$H^{17}$**).

**ESI-MS** (+ve): $[M_3L_2]^{3+}$: m/z =1455.3181, calcd 1455.3175.

**$[(M3)_3(L1)_2]^{3+}\bullet 3PF_6^-$ (C7)**

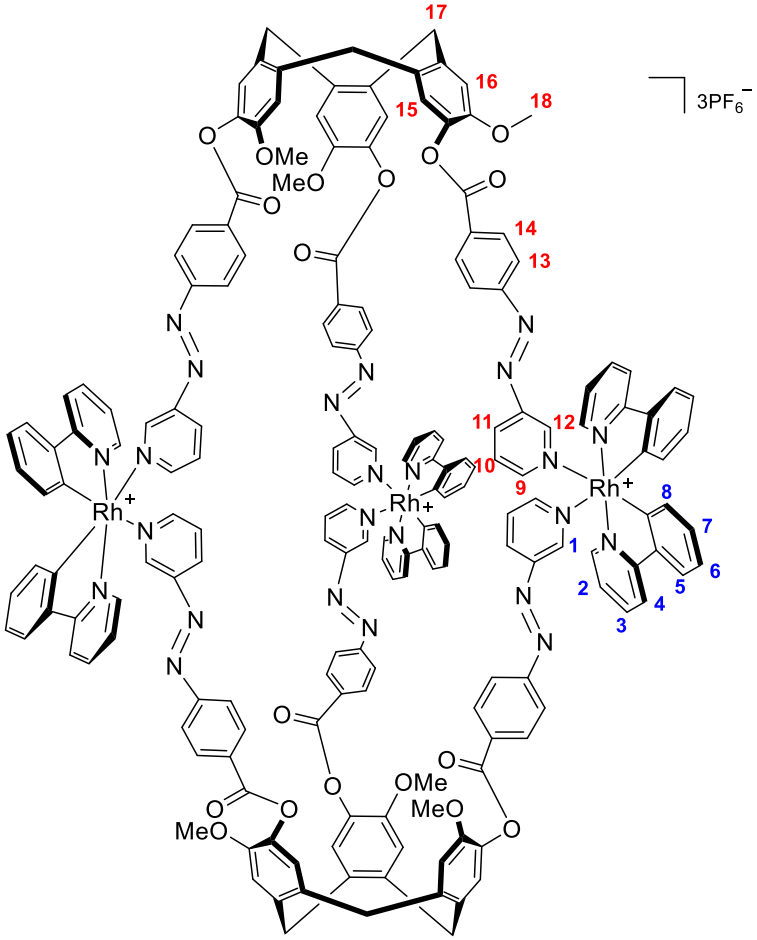


**L1** (4.0 mg, 3.86 µmol) was dissolved in $d_3$-nitromethane (0.3 mL). **M3** (4.2 mg, 5.78 µmol) was dissolved in $d_3$-nitromethane (0.3 mL) and added dropwise to the solution of **L1**. The bright orange solution was left to stand for five minutes after which time a $^1$H-NMR was acquired. Complete conversion of the starting materials to cage **C7** had occurred in this time.

**$^1$H-NMR** (300 MHz, $d_3$-$MeNO_2$): 9.25 (bs, 6H, **$H^{12}$**), 8.95 (bs, 6H, **$H^1$**), 8.86 (bs, 6H, **$H^9$**) 8.39-8.30 (m, 18H, **$H^{11}$/ $H^{14}$**), 8.07 (bs, 12H, **$H^3$/ $H^4$**), 7.99 (bs, 12H, **$H^{13}$**), 7.73 (bs, 12H, **$H^5$/ $H^{10}$**), 7.50-7.43 (m, 12H, **$H^2$/ $H^{15}$**), 7.26 (bs, 6H, **$H^{16}$**), 7.06 (bs, 12H, **$H^6$/ $H^7$**), 6.62 (bs, 6H, **$H^8$**), 5.00 (d, 6H, *J* = 12.9 Hz, **$H^{17\text{-}exo}$**), 3.83 (bs, 24H, **$H^{17\text{-}endo}$/ $H^{18}$**).

**ESI-MS** (+ve): $[M_3L_2]^{3+}$ : m/z = 1101.9343, calcd 1101.9279.

**$[(M4)_3(L1)_2]^{3+}\bullet 3PF_6^-$ (C8)**

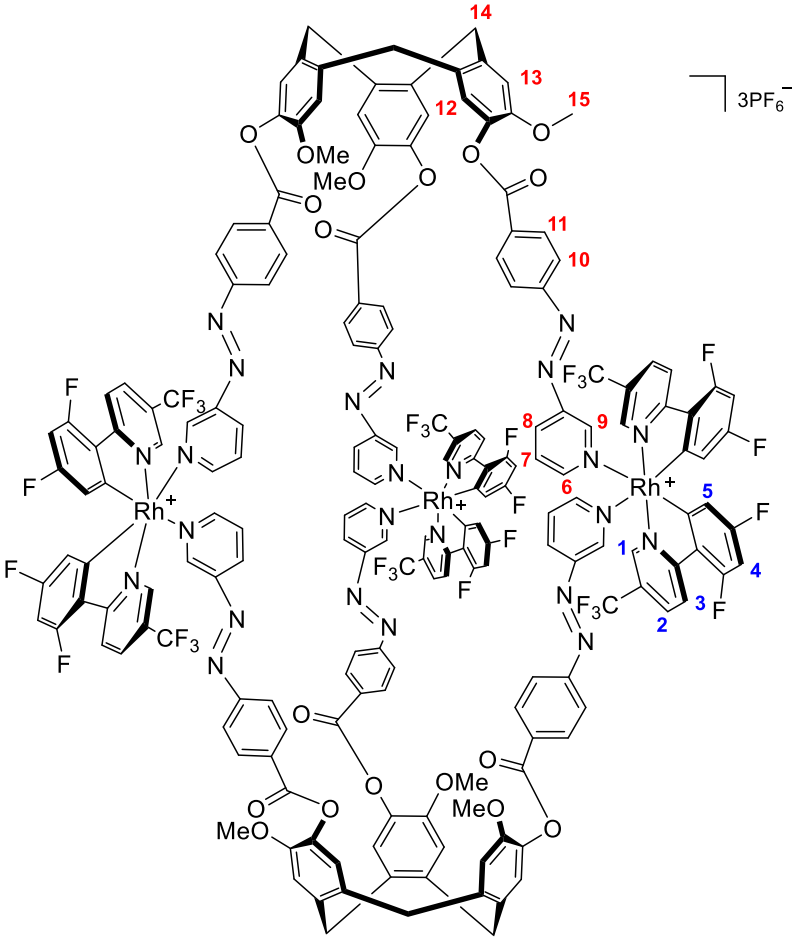


**L1** (4.0 mg, 3.86 µmol) was dissolved in $d_3$-nitromethane (0.4 mL). **M4** (4.2 mg, 5.78 µmol) was dissolved in $d_3$-nitromethane (0.3 mL) and added dropwise to the solution of **L1**. The bright orange solution was left to stand for five minutes after which time a $^1$H-NMR was acquired. Complete conversion of the starting materials to cage **C8** and a small minor product had occurred in this time.

**$^1$H-NMR** (500 MHz, $d_3$-$MeNO_2$): 9.23-9.16 (m, 12H, **$H^9$/ $H^1$**), 8.86 (s, 6H, **$H^6$**), 8.49-8.30 (m, 30H, **$H^2$/ $H^3$/ $H^8$/ $H^{11}$**) 8.14-7.97 (m, 12H, **$H^{10}$**), 7.77 (bs, 6H, **$H^7$**), 7.43 (bs, 6H, **$H^{12}$**), 7.25 (bs, 6H, **$H^{13}$**), 6.75 (bs, 6H, **$H^4$**), 6.24 (bs, 6H, **$H^5$**), 4.98 (bs, 6H, **$H^{14\text{-}exo}$**), 3.82 (bs, 24H, **$H^{14\text{-}endo}$/ $H^{15}$**).

**ESI-MS** (+ve): $[M_3L_2]^{3+}$ + MCN: m/z = 1524.8573, calcd 1524.8613.

**$[(M3)_3(L2)_2]^{3+}\bullet 3PF_6^-$ (C9)**

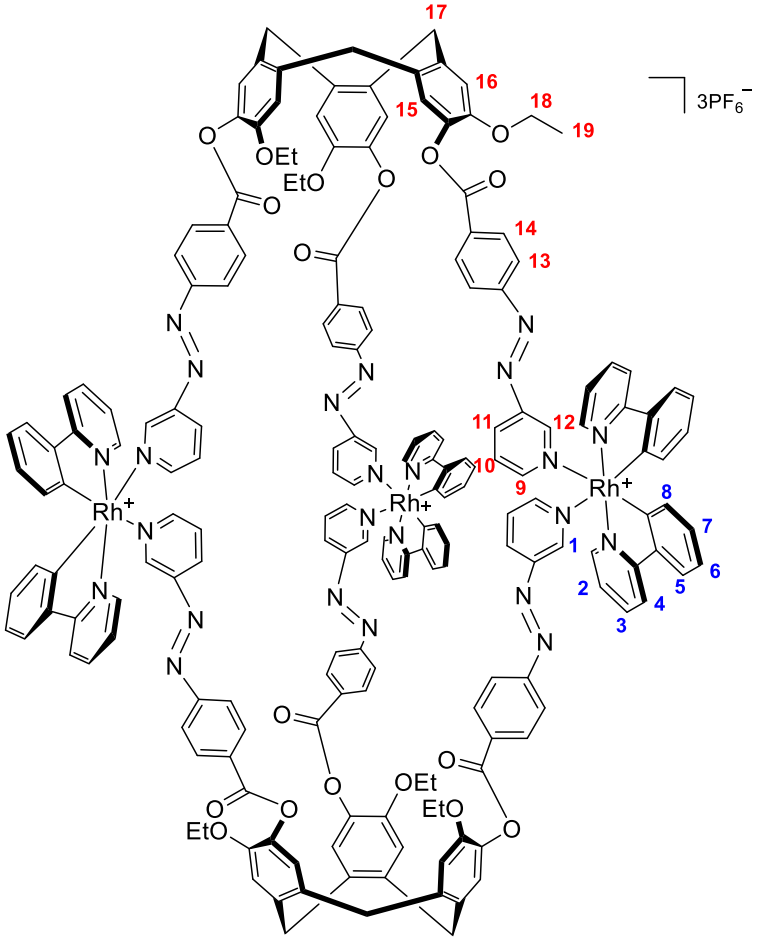


**L2** (4.0 mg, 3.86 µmol) was dissolved in $d_3$-nitromethane (0.4 mL). **M3** (4.2 mg, 5.78 µmol) was dissolved in $d_3$-nitromethane (0.3 mL) and added dropwise to the solution of **L2**. The bright orange solution was left to stand for five minutes after which time a $^1$H-NMR was acquired. Complete conversion of the starting materials to cage **C9** had occurred in this time.

**$^1$H-NMR** (500 MHz, $d_3$-$MeNO_2$): 9.25 (bs, 6H, $H^{12}$), 8.95 (bs, 6H, $H^1$), 8.86 (bs, 6H, $H^9$) 8.39-8.30 (m, 18H, $H^{11}$/ $H^{14}$), 8.08 (bs, 12H, $H^3$/ $H^4$), 7.99 (bs, 12H, $H^{13}$), 7.73-7.69 (bs, 12H, $H^5$/ $H^{10}$), 7.50 (bs, 6H, $H^2$), 7.42 (bs, 6H, $H^{15}$), 7.24 (bs, 6H, $H^{16}$), 7.07 (bs, 12H, $H^6$/ $H^7$), 6.62 (bs, 6H, $H^8$), 5.00 (d, 6H, $J$ = 14.0 Hz, $H^{17\text{-}exo}$), 4.13-4.06 (m, 12H, $H^{18}$), 3.81 (bs, 6H, $J$ = 13.5 Hz, $H^{17\text{-}endo}$), 1.26-1.14 (m, 18H, $H^{19}$).

**ESI-MS** (+ve): $[M_3L_2]^{3+}$: m/z = 1129.9729, calcd 1129.9592.

**$[(M4)_3(L2)_2]^{3+}\bullet 3PF_6^-$ (C10)**

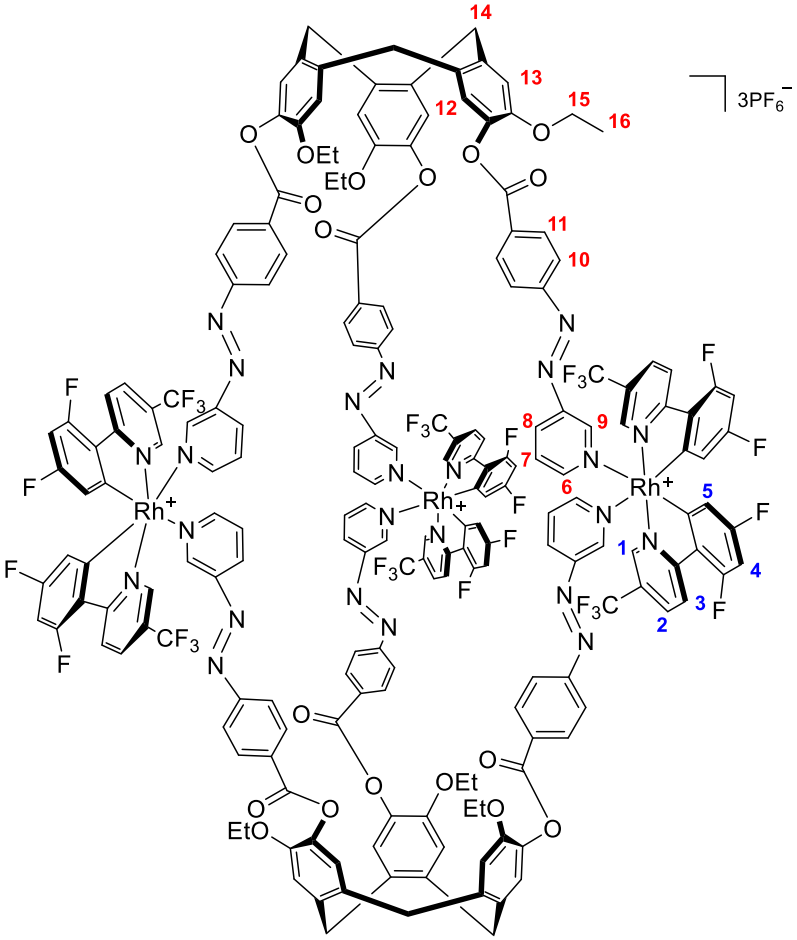


**L2** (4.0 mg, 3.86 µmol) was dissolved in $d_3$-nitromethane (0.3 mL). **M4** (4.2 mg, 5.78 µmol) was dissolved in $d_3$-nitromethane (0.3 mL) and added dropwise to the solution of **L2**. The bright orange solution was left to stand for five minutes after which time a $^1$H-NMR was acquired. Complete conversion of the starting materials to cage **C10** and a small minor product had occurred in this time.

**$^1$H-NMR** (300 MHz, $d_3$-$MeNO_2$): 9.22-9.16 (m, 12H, **$H^9$/ $H^1$**), 8.86 (s, 6H, **$H^6$**), 8.49-8.30 (m, 30H, **$H^2$/ $H^3$/ $H^8$/ $H^{11}$**) 8.14-7.97 (m, 12H, **$H^{10}$**), 7.76 (bs, 6H, **$H^7$**), 7.40 (bs, 6H, **$H^{12}$**), 7.24 (bs, 6H, **$H^{13}$**), 6.75 (bs, 6H, **$H^4$**), 6.23 (bs, 6H, **$H^5$**), 4.98 (d, 6H, *J* = 13.5 Hz, **$H^{14\text{-}exo}$**), 4.09 (bs, 12H, **$H^{15}$**) 3.82 (d, 6H, *J* = 14.0 Hz, **$H^{14\text{-}endo}$**), 1.21 (bs, 18H, **$H^{16}$**).

**ESI-MS** (+ve): m/z = 1337.9108, calcd 1337.8963.

**$[(M3)_3(L3)_2]^{3+}\bullet 3PF_6^-$ (C11)**

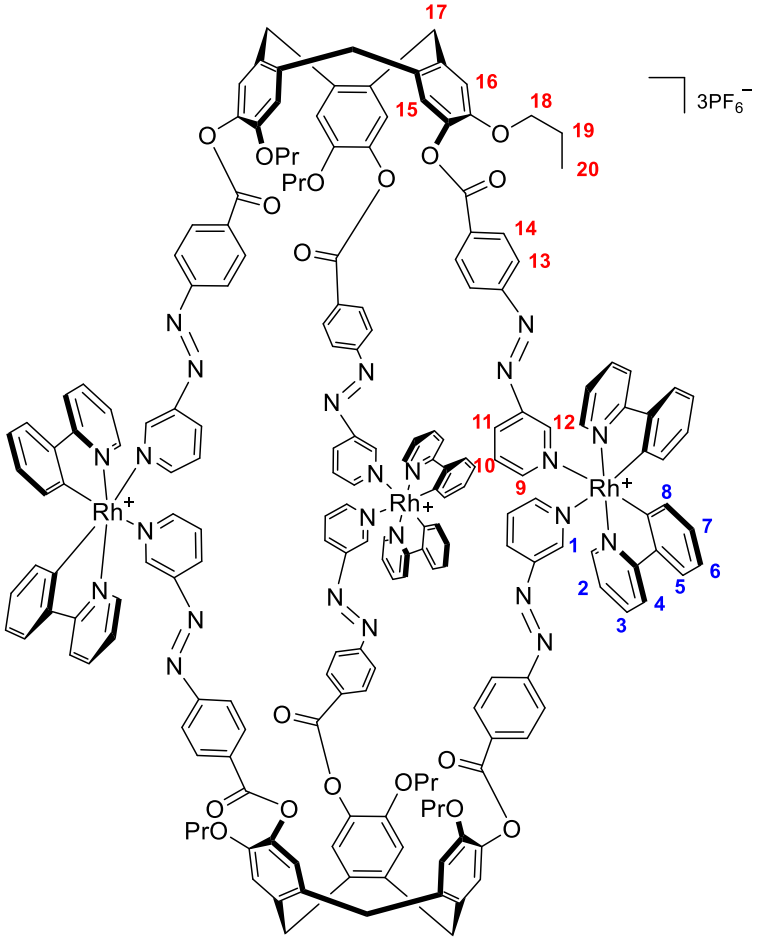


**L3** (4.0 mg, 3.86 µmol) was dissolved in $d_3$-nitromethane (0.3 mL). **M3** (4.2 mg, 5.78 µmol) was dissolved in $d_3$-nitromethane (0.3 mL) and added dropwise to the solution of **L3**. The bright orange solution was left to stand for five minutes after which time a $^1$H-NMR was acquired. Complete conversion of the starting materials to cage **C11** had occurred in this time.

**$^1$H-NMR** (300 MHz, $d_3$-$MeNO_2$): 9.25 (bs, 6H, **$H^{12}$**), 8.95 (bs, 6H, **$H^1$**), 8.86 (bs, 6H, **$H^9$**) 8.39-8.30 (m, 18H, **$H^{11}$/ $H^{14}$**), 8.07 (bs, 12H, **$H^3$/ $H^4$**), 7.98 (bs, 12H, **$H^{13}$**), 7.72 (bs, 12H, **$H^5$/ $H^{10}$**), 7.50-7.41 (m, 12H, **$H^2$/ $H^{15}$**), 7.24 (bs, 6H, **$H^{16}$**), 7.07 (bs, 12H, **$H^6$/ $H^7$**), 6.61 (bs, 6H, **$H^8$**), 5.00 (d, 6H, *J* = 13,2 Hz, **$H^{17\text{-}exo}$**), 4.00 (s, 12H, **$H^{18}$**), 3.82 (bs, 6H, **$H^{17\text{-}endo}$**), 1.61 (bs, 12H, **$H^{19}$**), 0.83 (bs, 18H, **$H^{20}$**).

**ESI-MS** (+ve): $[M_3L_2]^{3+}$: m/z =1157.9974, calcd 1157.9905.

**$[(M4)_3(L3)_2]^{3+}\bullet 3PF_6^-$ (C12)**

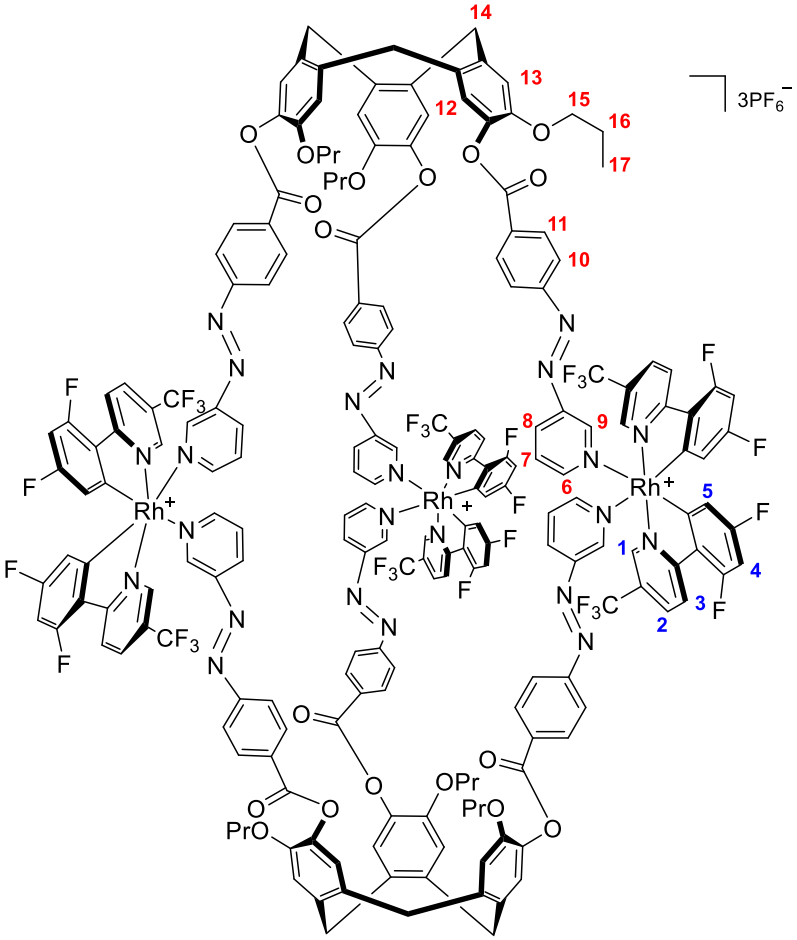


**L3** (4.0 mg, 3.86 µmol) was dissolved in $d_3$-nitromethane (0.3 mL). **M4** (4.2 mg, 5.78 µmol) was dissolved in $d_3$-nitromethane (0.3 mL) and added dropwise to the solution of **L3**. The bright orange solution was left to stand for five minutes after which time a $^1$H-NMR was acquired. Complete conversion of the starting materials to cage **C12** and a small minor product had occurred in this time.

**$^1$H-NMR** (300 MHz, $d_3$-$MeNO_2$): 9.28-9.17 (m, 12H, **$H^9$/ $H^1$**), 8.85 (s, 6H, **$H^6$**), 8.50-8.31 (m, 30H, **$H^2$/ $H^3$/ $H^8$/ $H^{11}$**) 8.14-7.96 (m, 12H, **$H^{10}$**), 7.76 (bs, 6H, **$H^7$**), 7.40 (bs, 6H, **$H^{12}$**), 7.24 (bs, 6H, **$H^{13}$**), 6.74 (bs, 6H, **$H^4$**), 6.23 (bs, 6H, **$H^5$**), 4.96 (bs, 6H, **$H^{14\text{-}exo}$**), 4.00 (bs, 12H, **$H^{15}$**) 3.82 (bs, 6H, **$H^{14\text{-}endo}$**), 1.62 (bs, 12H, **$H^{16}$**), 0.83 (bs, 18H, **$H^{17}$**).

**ESI-MS** (+ve): $[M_3L_2]^{3+}$: m/z = 1365.9361, calcd 1365.9276.

**$[(M5)_3(L1)_2]^{3+}\bullet 3PF_6^-$ (C13)**

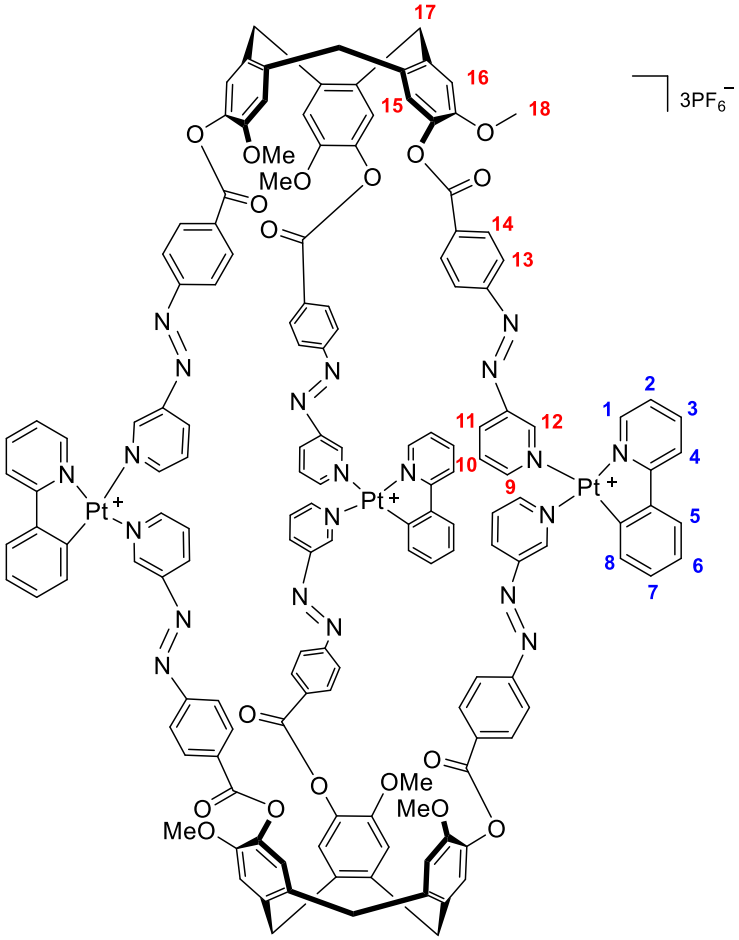


**L1** (4.0 mg, 3.86 µmol) was dissolved in $d_3$-nitromethane (0.3 mL). **M5** (4.2 mg, 5.78 µmol) was dissolved in $d_3$-nitromethane (0.3 mL) and added dropwise to the solution of **L1**. The bright orange solution was left to stand for 48 hours after which time a $^1$H-NMR was acquired. Complete conversion of the starting materials to cage **C13** had occurred in this time.

**$^1$H-NMR:** Spectrum too broad to assign.

**ESI-MS** (+ve): $[M_3L_2]^{3+}$: m/z = 1039.9190, calcd 1039.5864.

**$[(Pd(en))_3(L1)_2]^{6+}\bullet 6NO_3^-$ (C19)**

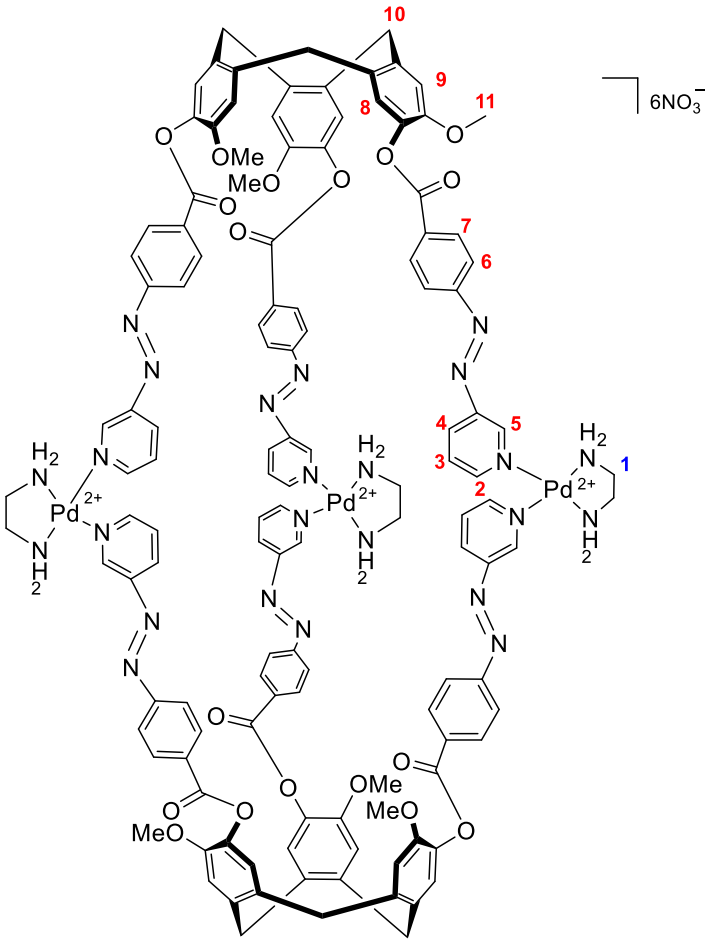


**L1** (4.0 mg, 3.86 µmol) was dissolved in $d_6$-DMSO (0.3 mL). $Pd(en)(NO_3)_2$ (1.6 mg, 5.78 µmol) was dissolved in $d_6$-DMSO (0.3 mL) and added dropwise to the solution of **L1**. The bright orange solution was left to stand for five minutes after which time a $^1$H-NMR was acquired. Complete conversion of the starting materials to cage **C19** had occurred during this time.

**$^1$H-NMR** (500 MHz, $d_6$-DMSO): 9.62 (d, 6H, *J* = 13.3 Hz, **$H^5$**), 9.15 (bs, 6H, **$H^2$**), 8.52 (bs, 6H, **$H^4$**), 8.37 (d, 12H, *J* = 8.5 Hz, **$H^7$**), 8.11 (t, 12H, *J* = 8.3 Hz, **$H^6$**), 7.95 (t, 6H, *J* = 8.1 Hz, **$H^3$**), 7.60 (s, 6H, **$H^8$**), 7.35 (s, 6H, **$H^9$**), 5.67 (bs, 15H, **NH**), 4.93 (d, 6H, *J* = 14.1 Hz, **$H^{10\text{-}exo}$**), 3.75 (s, 24H, **$H^{10\text{-}endo,\ 11}$**), 2.69 (bs, 12H, **$H^1$**).

**ESI-MS** (+ve): $[M_3L_2]^{6+}$: m/z = 428.1710, calcd 428.4311.

**$[(Pd(en))_3(L2)_2]^{6+}\bullet 6NO_3^-$ (C20)**

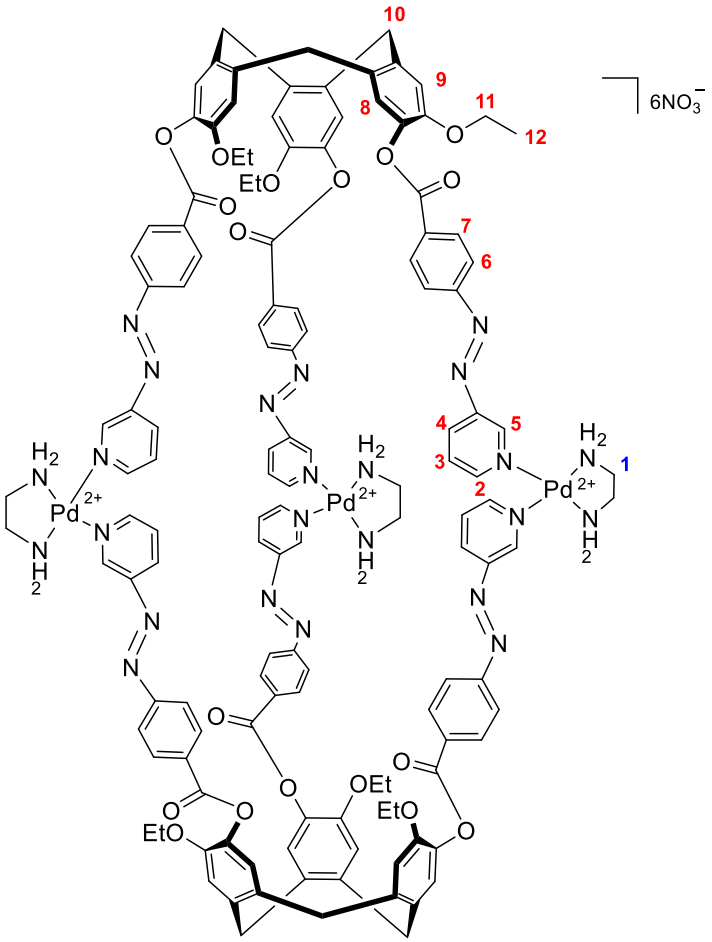


**L2** (4.0 mg, 3.71 µmol) was dissolved in $d_6$-DMSO (0.3 mL). $Pd(en)(NO_3)_2$ (1.5 mg, 5.56 µmol) was dissolved in $d_6$-DMSO (0.3 mL) and added dropwise to the solution of **L2**. The bright orange solution was left to stand for five minutes after which time a $^1$H-NMR was acquired. Complete conversion of the starting materials to cage **C20** had occurred during this time.

**$^1$H-NMR** (500 MHz, $d_6$-DMSO): 9.62 (m, 6H, **$H^5$**), 9.15 (m, 6H, **$H^2$**), 8.51 (bs, 6H, **$H^4$**), 8.37 (t, 12H, *J* = 8.3 Hz, **$H^7$**), 8.10 (t, 12H, *J* = 8.3 Hz, **$H^6$**), 7.94 (t, 6H, *J* = 8.1 Hz, **$H^3$**), 7.56 (bs, 6H, **$H^8$**), 7.34 (bs, 6H, **$H^9$**), 5.67 (bs, 12H, **NH**), 4.87 (bs, 6H, **$H^{10\text{-}exo}$**), 4.04 (bs, 12H, **$H^{11}$**), 3.71 (bs, 6H, **$H^{10\text{-}endo}$**), 2.70 (bs, 12H, **$H^1$**), 1.16 (m, 18H, **$H^{12}$**).

**$[(Pd(en))_3(L3)_2]^{6+}\bullet 6NO_3^-$ (C21)**

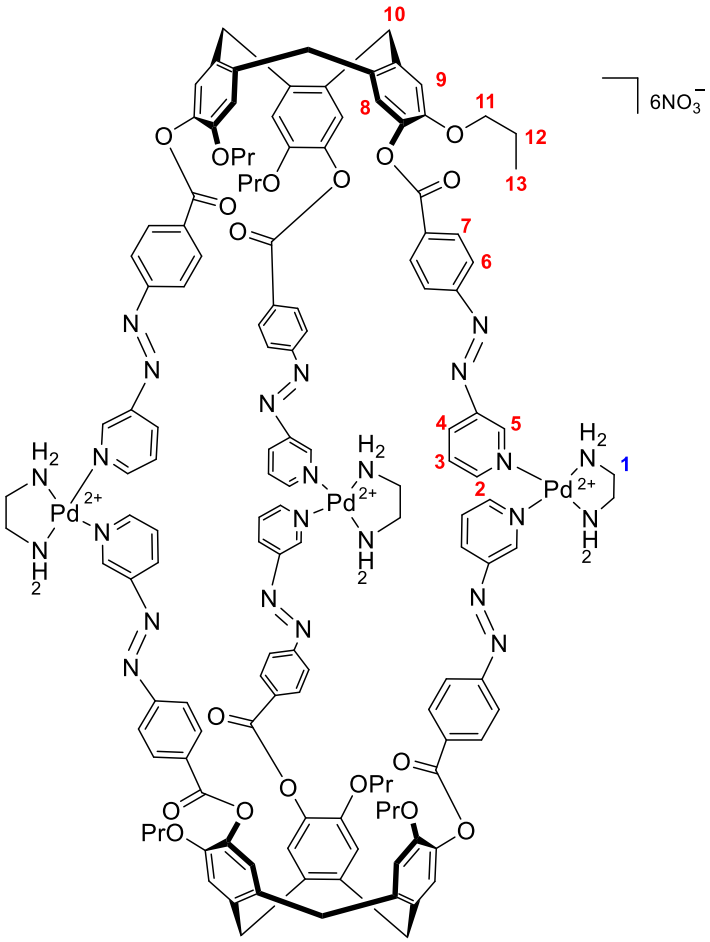


**L3** (4.0 mg, 3.57 µmol) was dissolved in $d_6$-DMSO (0.3 mL). $Pd(en)(NO_3)_2$ (1.5 mg, 5.56 µmol) was dissolved in $d_6$-DMSO (0.3 mL) and added dropwise to the solution of **L3**. The bright orange solution was left to stand for five minutes after which time a $^1$H-NMR was acquired. Complete conversion of the starting materials to cage **C21** had occurred during this time.

**$^1$H-NMR** (500 MHz, $d_6$-DMSO): 9.60 (m, 6H, **$H^5$**), 9.16 (m, 6H, **$H^2$**), 8.50 (bs, 6H, **$H^4$**), 8.35 (t, 12H, *J* = 8.6 Hz, **$H^7$**), 8.11 (t, 12H, *J* = 8.2 Hz, **$H^6$**), 7.95 (t, 6H, *J* = 8.0 Hz, **$H^3$**). 7.56 (bs, 6H, **$H^8$**), 7.35 (bs, 6H, **$H^9$**), 5.67 (bs, 12H, **NH**), 4.90 (bs, 6H, **$H^{10\text{-}exo}$**), 3.95 (bs, 12H, **$H^{11}$**), 3.72 (bs, 6H, **$H^{10\text{-}endo}$**), 2.70 (bs, 12H, **$H^1$**), 1.53 (bs, 12H, **$H^{12}$**), 0.79 (m, 18H, **$H^{13}$**).

## References


1. Y. Fang, J. A. Powell, E. Li, Q. Wang, Z. Perry, A. Kirchon, X. Yang, Z. Xiao, C. Zhu, L. Zhang, F. Huang and H.-C. Zhou, *Chem. Soc. Rev.*, 2019, **48**, 4707-4730.
2. M. D. Ward, C. A. Hunter and N. H. Williams, *Chem. Lett.*, 2017, **46**, 2-9.
3. C. Tan, D. Chu, X. Tang, Y. Liu, W. Xuan and Y. Cui, *Chem. Eur. J.*, 2019, **25**, 662-672.
4. R. Custelcean, *Chem. Soc. Rev.*, 2014, **43**, 1813-1824.
5. M. Yoshizawa, M. Tamura and M. Fujita, *Science.*, 2006, **312**, 251-254.
6. D. Fiedler, R. G. Bergman and K. N. Raymond, *Angew. Chem. Int. Ed.*, 2004, **43**, 6748-6751.
7. M. L. Merlau, M. del Pilar Mejia, S. T. Nguyen and J. T. Hupp, *Angew. Chem. Int. Ed.*, 2001, **40**, 4239-4242.
8. C. García-Simón, M. Garcia-Borràs, L. Gómez, T. Parella, S. Osuna, J. Juanhuix, I. Imaz, D. Maspoch, M. Costas and X. Ribas, *Nat. Commun.*, 2014, **5**, 5557.
9. T.-H. Wong, J.-C. Chang, C.-C. Lai, Y.-H. Liu, S.-M. Peng and S.-H. Chiu, *J. Org. Chem.*, 2014, **79**, 3581-3586.
10. P. Mal, B. Breiner, K. Rissanen and J. R. Nitschke, *Science*, 2009, **324**, 1697-1699.
11. P. Mal, D. Schultz, K. Beyeh, K. Rissanen and J. R. Nitschke, *Angew. Chem. Int. Ed.*, 2008, **47**, 8297-8301.
12. I. A. Riddell, M. M. J. Smulders, J. K. Clegg, Y. R. Hristova, B. Breiner, J. D. Thoburn and J. R. Nitschke, *Nature Chem.*, 2012, **4**, 751-756.
13. D. Fujita, Y. Ueda, S. Sato, H. Yokoyama, N. Mizuno, T. Kumasaka and M. Fujita, *Chem*, 2016, **1**, 91-101.
14. Q.-F. Sun, J. Iwasa, D. Ogawa, Y. Ishido, S. Sato, T. Ozeki, Y. Sei, K. Yamaguchi and M. Fujita, *Science*, 2010, **328**, 1144-1147.
15. M. Fujita, S. Nagao and K. Ogura, *J. Am. Chem. Soc.*, 1995, **117**, 1649-1650.
16. M. Schweiger, T. Yamamoto, P. J. Stang, D. Bläser and R. Boese, *J. Org. Chem.*, 2005, **70**, 4861-4864.
17. C. J. Kuehl, Y. K. Kryschenko, U. Radhakrishnan, S. R. Seidel, S. D. Huang and P. J. Stang, *Proc. Natl. Acad. Sci. U.S.A.*, 2002, **99**, 4932-4936.
18. R. L. Paul, A. J. Amoroso, P. L. Jones, S. M. Couchman, Z. R. Reeves, L. H. Rees, J. C. Jeffery, J. A. McCleverty and M. D. Ward, *J. Chem. Soc., Dalton Trans.*, 1999, DOI: 10.1039/A900805E, 1563-1568.
19. A. J. Amoroso, J. C. Jeffery, P. L. Jones, J. A. McCleverty, P. Thornton and M. D. Ward, *Angew. Chem. Int. Ed.*, 1995, **34**, 1443-1446.
20. S. P. Argent, H. Adams, T. Riis-Johannessen, J. C. Jeffery, L. P. Harding and M. D. Ward, *J. Am. Chem. Soc.*, 2006, **128**, 72-73.
21. J. J. Henkelis and M. J. Hardie, *Chem. Commun.*, 2015, **51**, 11929-11943.
22. F. L. Thorp-Greenwood, A. N. Kulak and M. J. Hardie, *Nature Chem.*, 2015, **7**, 526-531.

23. J. M. Fowler, F. L. Thorp-Greenwood, S. L. Warriner, C. E. Willans and M. J. Hardie, *Chem. Commun.*, 2016, **52**, 8699-8702.
24. T. K. Ronson, J. Fisher, L. P. Harding, P. J. Rizkallah, J. E. Warren and M. J. Hardie, *Nature Chem.*, 2009, **1**, 212-216.
25. J. Gabard and A. Collet, *J. Chem. Soc., Chem. Commun.*, 1981, DOI: 10.1039/C39810001137, 1137-1139.
26. Z. Zhong, A. Ikeda, S. Shinkai, S. Sakamoto and K. Yamaguchi, *Org. Lett.*, 2001, **3**, 1085-1087.
27. A. Schaly, Y. Rousselin, J.-C. Chambron, E. Aubert and E. Espinosa, *Eur. J. Inorg. Chem.*, 2016, **2016**, 832-843.
28. M. J. Hardie, *Isr. J. Chem.*, 2011, **51**, 807-816.
29. D.-W. Kang, X. Han, X.-J. Ma, Y.-Y. Liu and J.-F. Ma, *Dalton Trans.*, 2018, **47**, 16197-16204.
30. Y. Fang, Z. Xiao, A. Kirchon, J. Li, F. Jin, T. Togo, L. Zhang, C. Zhu and H.-C. Zhou, *Chem. Sci.*, 2019, **10**, 3529-3534.
31. A. Bouchet, T. Brotin, M. Linares, H. Ågren, D. Cavagnat and T. Buffeteau, *J. Org. Chem.*, 2011, **76**, 4178-4181.
32. J. Canceill, L. Lacombe and A. Collet, *J. Am. Chem. Soc.*, 1985, **107**, 6993-6996.
33. S. Oldknow, D. R. Martir, V. E. Pritchard, M. A. Blitz, Colin W. G. Fishwick, E. Zysman-Colman and M. J. Hardie, *Chem. Sci.*, 2018, **9**, 8150-8159.
34. N. J. Cookson, PhD Thesis, University of Leeds, 2016.
35. J. Heo, Y.-M. Jeon and C. A. Mirkin, *J. Am. Chem. Soc.*, 2007, **129**, 7712-7713.
36. M. J. Wiester, A. B. Braunschweig, H. Yoo and C. A. Mirkin, *Inorg. Chem.*, 2010, **49**, 7188-7196.
37. D. M. Weekes, C. Diebold, P. Mobian, C. Huguenard, L. Allouche and M. Henry, *Chem. Eur. J.*, 2014, **20**, 5092-5101.
38. M. Fujita, *Acc. Chem. Res.*, 1999, **32**, 53-61.
39. Y. Cohen and S. Slovak, *Org. Chem. Front.*, 2019, **6**, 1705-1718.
40. T. Megyes, H. Jude, T. Grósz, I. Bakó, T. Radnai, G. Tárkányi, G. Pálinkás and P. J. Stang, *J. Am. Chem. Soc.*, 2005, **127**, 10731-10738.
41. V. E. Pritchard, D. Rota Martir, S. Oldknow, S. Kai, S. Hiraoka, N. J. Cookson, E. Zysman-Colman and M. J. Hardie, *Chem. Eur. J.*, 2017, **23**, 6290-6294.
42. J. J. Henkelis, J. Fisher, S. L. Warriner and M. J. Hardie, *Chem. Eur. J.*, 2014, **20**, 4117-4125.
43. S. Oldknow, PhD Thesis, University of Leeds, 2018.
44. D. Rota Martir and E. Zysman-Colman, *Chem. Commun.*, 2019, **55**, 139-158.
45. D. Bardhan and D. K. Chand, *Chem. Eur. J.*, 2019, **25**, 12241-12269.
46. Z. Qin, M. C. Jennings and R. J. Puddephatt, *Inorg. Chem.*, 2003, **42**, 1956-1965.
47. M. Fujita, N. Fujita, K. Ogura and K. Yamaguchi, *Nature*, 1999, **400**, 52-55.
48. X. Yan, T. R. Cook, P. Wang, F. Huang and P. J. Stang, *Nature Chem.*, 2015, **7**, 342-348.
49. C. P. Newman, K. Casey-Green, G. J. Clarkson, G. W. V. Cave, W. Errington and J. P. Rourke, *Dalton Trans.*, 2007, DOI: 10.1039/B705609E, 3170-3182.

50. M. Fujita, M. Tominaga, A. Hori and B. Therrien, *Acc. Chem. Res.*, 2005, **38**, 369-378.
51. M. Ferrer, A. Gutiérrez, M. Mounir, O. Rossell, E. Ruiz, A. Rang and M. Engeser, *Inorg. Chem.*, 2007, **46**, 3395-3406.
52. P. J. Stang and D. H. Cao, *J. Am. Chem. Soc.*, 1994, **116**, 4981-4982.
53. A. Pfeil and J.-M. Lehn, *J. Chem. Soc., Chem. Commun.*, 1992, DOI: 10.1039/C39920000838, 838-840.
54. Ł. Szyszka, P. Cmoch, A. Butkiewicz, M. A. Potopnyk and S. Jarosz, *Org. Lett.*, 2019, **21**, 6523-6528.

# Chapter 4
# Photoisomerisation of CTG based Pd(II) metallo-cryptophanes

## 4.1 Introduction

Photoswitchable azobenzene groups have been embedded within the framework of a series of $M_3L_2$ metallo-cryptophanes. Each cage contains a total of six azobenzene moieties. Photoisomerisation of these groups may be achieved through irradiation of the cage with an appropriate wavelength of light to promote the *trans* to *cis* isomerisation. The back *cis* to *trans* reaction may be promoted through irradiation at a longer wavelength. This chapter begins with a general consideration of the photophysical behaviour of azobenzenes and examples of photoswitchable supramolecular architectures. This is followed by a photoisomerisation study of the azobenzene containing CTG based ligands and the Pd(II) metallo-cryptophanes discussed in chapters two and three respectively.

### 4.1.1 Photophysical behaviour of azobenzenes

Azobenzenes are one of the most widely used class of photoswitchable groups in the literature.[1-4] A combination of high fatigue resistance, simple synthetic methodology and tunability of wavelength at which photoisomerisation occurs accounts for their popularity.[5] In general, irradiation of an azobenzene with UV light results in rotation around the N=N bond and the switching of the species from a *trans* to a *cis* conformation (Figure 4.1).[6] This *cis* isomer can be converted back to a *trans* rich state by irradiation with a longer wavelength of light, usually in the blue region of the visible spectrum. In the case of azobenzene, the *trans* isomer is 42 kJ $mol^{-1}$ more stable than the *cis* isomer which will revert back to the *trans* isomer in the dark.[7, 8] This property is observed for nearly all azobenzenes.[5] In addition to light and heat;[9] electrochemical,[10, 11] and mechanical stimuli[12] have been used to convert azobenzenes between different states. The photoactive properties of azobenzenes have been utilised in a plethora of applications, including in molecular machines, protein probes, nanoparticles and polymers. The light triggered motion is often used as a switch modulate specific functions or change the physical properties of a substance.

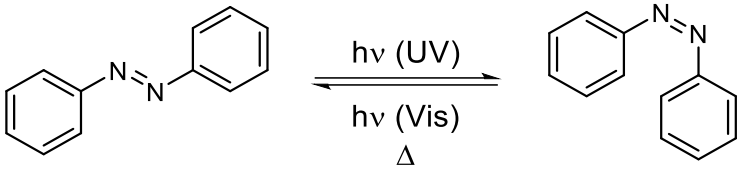


**Figure 4.1.** Structure of an azobenzene group and the general conditions under which switching between the *trans* and *cis* rich state can be promoted.

The photo-induced motion on the azobenzene group is initiated by the excitation of the azo group from the π to the π* orbital. The molecule can be excited to this state from either the π or n molecular orbital leading to the formation of an excited $S_2$(π-π*) or $S_1$(n-π*) state respectively.[13-15] The electronic relaxation from both of these states leads to both *trans* to *cis* and *cis* to *trans* isomerisation.[16] Relaxation from the $S_1$(n-π*) state results in a far higher quantum yield for the *cis* to *trans* isomerisation and can be used to form the *trans* isomer preferentially.[17] The opposite is true for relaxation from the $S_2$(π-π*) state, which promotes the formation of the *cis* isomer.[17] This phenomenon seemingly violates a general rule of photochemistry, which states, that the only appreciable relaxation to the ground state will occur from the $S_1$ -> $S_0$ state.[18] This is due to the faster relaxation that generally occurs from the $S_2$->$S_1$ state than from the $S_1$->$S_0$ state.[5, 18, 19] If this were true for azobenzenes then excitation to either the $S_1$ or $S_2$ state would result in the same quantum yield for *trans* to *cis* isomerisation. This observation suggests that complex relaxation pathways are available for azobenzenes that allow them to seemingly relax directly from the $S_2$ state to the $S_0$ state, bypassing the $S_1$ state.[20-22] Unlike other photoswitchable groups such as dithienylethenes,[23] it is usually not possible to photoswitch a system containing azobenzenes into exclusively a *cis* or *trans* state;[24-26] although it is possible to obtain a fully *trans* state through thermal relaxation of a *cis* rich state.[27] The ratio of *trans* to *cis* azobenzene groups upon irradiation is known as the photo-stationary state (PSS).

Of the myriad of reported azobenzene containing compounds, nearly all can be classified between just three main groups; azobenzene-type, aminoazobenzenes and pseudo-stilbenes (Figure 4.2).[5] The differences between these groups is attributed to the location and spacing of the π-π* and n-π* absorption bands, which has a marked effect upon the photophysical behaviour of these molecules.[5] Azobenzene-type molecules are characterised by benzene groups which have either no substituents, or substitution with electron-withdrawing groups. The most simple azobenzene, diphenyldiazene belongs to this group. A key feature the azobenzene-type class is the wide spacing of the π-π* and n-π* absorption bands. The π-π* is

found in the UV region whereas the weakly absorbing n- π* occurs in the visible region. The wide spacing means that these azobenzenes can be effectively switched between *trans* and *cis* rich states. The second class, aminoazobenzenes, possess electron donating groups *ortho* or *para* to the azo group. This pushes the π-π* and n-π* absorption bands further into the visible region. Suitably designed aminoazobenzene class azobenzenes have absorption bands residing in the red region of the visible spectrum. This class of azobenzenes have found particular use in biomedical applications for this reason, as red light is capable of penetrating biological tissues to a greater depth than shorter wavelengths. The final class as azobenzenes are known as pseudo-stilbenes or push-pull azobenzenes. Substitution of an azobenzene in the 4,4' positions with both an electron withdrawing and donating group produces this class. Pseudo-stilbenes are unique due to the fact that the π-π* and n-π* absorption bands overlap. This means that a single wavelength of light can be used to promote both the *trans* to *cis* isomerisation as well as the reverse.

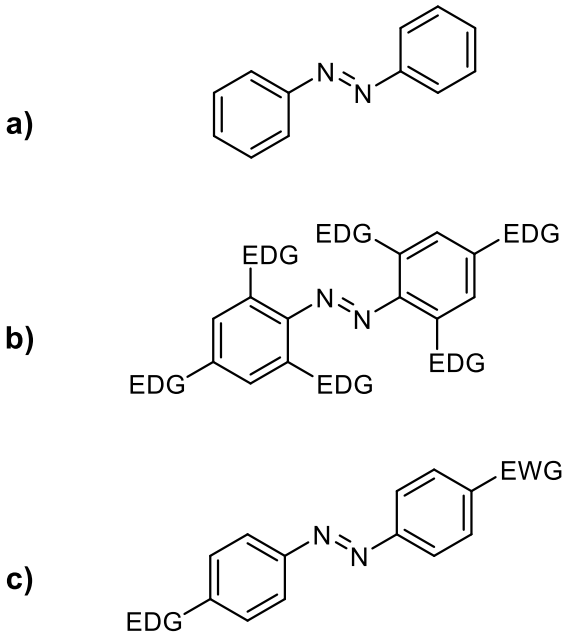


**Figure 4.2.** The three main classes of azobenzenes; a) azobenzene type, b) aminoazobenzene, c) pseudo-stilbene.

Despite the almost ubiquitous appearance of azobenzenes within most fields of chemistry, the exact mechanism through which photoisomerisation occurs is the subject of intense debate.[5] Four main mechanisms have been proposed to explain the mechanism of photoisomerisation; inversion, rotation, concerted inversion and inversion-assisted rotation.[5, 20, 28] Rotation and inversion are likely to be the most relevant mechanisms to this body of work and are detailed in Figure 4.3. Many factors influence which mechanism predominates

including solvent polarity and viscosity as well as temperature.[29] A combination of several different pathways usually occurs during photoisomerisation.[13] The transition states in all of the proposed mechanisms can relax back into a *cis* or *trans* form, explaining why a quantitative yield of either isomer cannot be obtained through irradiation.[5]

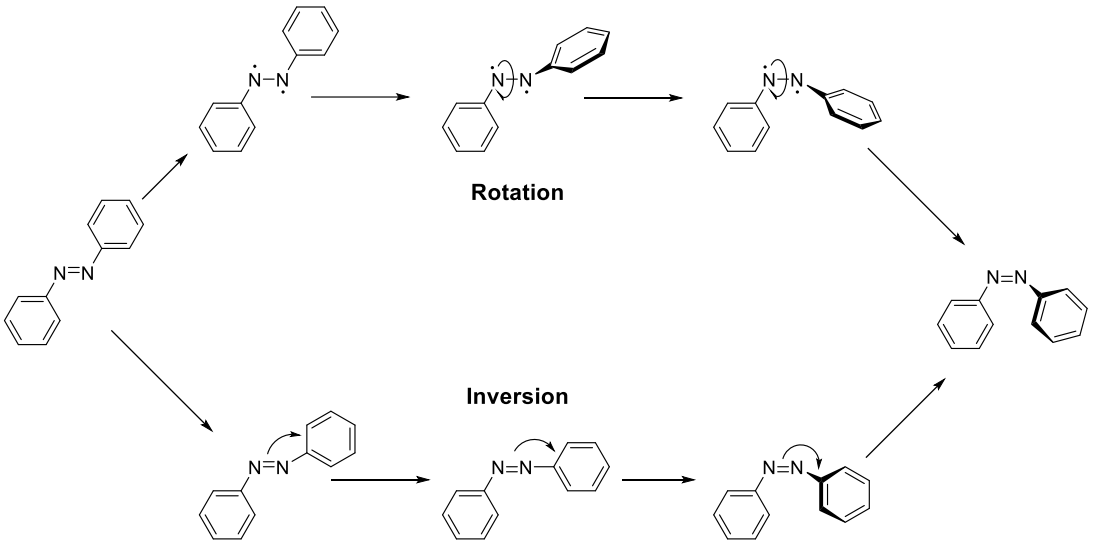


**Figure 4.3.** Two of the proposed mechanisms for the photoisomerisation of *trans* azobenzene to *cis* azobenzene.

### 4.1.2 Azobenzenes in supramolecular architectures

Azobenzenes have been incorporated into the design of a wide range of supramolecular structures, including coordination cages, supramolecular polymers and gels.[30-32] As discussed earlier, the ability of azobenzenes to undergo a geometric shift in response to light means that they can be used to modulate the physical and chemical properties of a substance. Harada and co-workers have reported azobenzene containing polymer system that can be switched between a solution and gel state through the use of light.[33] The system contains two polymers, one containing azobenzene side chain and the other cyclodextrin side chains. In the resting *trans* state the azobenzene acts as a guest for the cyclodextrin moiety, residing in the cavity where it is presumably held in place by hydrophobic interactions. Irradiation of the system by UV light switches generates a PSS where 88 % of the azobenzenes are in the *cis* conformation. The *cis* isomer is more polar than the *trans* isomer which promotes host-guest dissociation due to the weakening of the hydrophobic effect. A drastic decrease of the association constant between the two polymers was measured upon photoswitching to the *cis* conformation, dropping from 1100 $M^{-1}$ to 4 $M^{-1}$. As a consequence the polymers were unable

to cross-link and instead behaved as independent chains, resulting in a gel-sol transition. The reverse could be promoted by reforming the *trans* isomer through irradiation with visible light. A sol-gel transition was observed within two minutes of irradiation.[33]

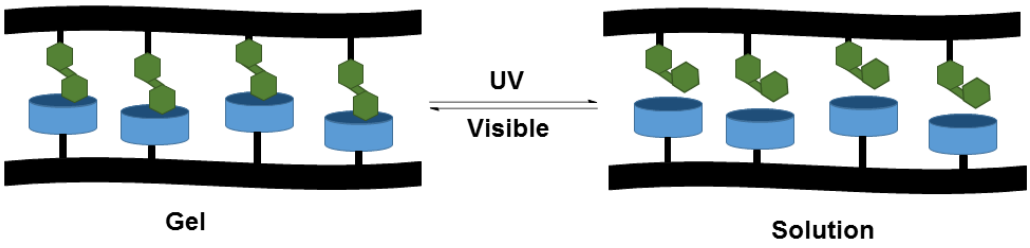


**Figure 4.4.** Azobenzene (green) and cyclodextrin (blue) appended polymers capable or switching undergoing a reversible sol-gel transition upon azobenzene *cis-trans* isomerisation.[33]

Incorporation of an azobenzene group within the framework of a cage or metallocycle can often inhibit its ability to photoswitch.[34, 35] In order to photoisomerise a large change in the geometry of the azobenzene must occur. Movement of the azobenzene group can be constrained within the rigid framework of a metallocycle. A decrease in the quantum yield of photoisomerisation results under these conditions.[36] Nabeshima and coworkers have reported a titanium based metallocycle base upon azobenzene containing ligands (Figure 4.5).[36] Incorporation of the ligands into the metallocycle completely switched off the photoisomerisation ability of the azobenzene groups. To eliminate the possibility that the switching was inhibited by the titanium metal an acyclic variant was synthesised. In this example the titanium was only bound at one end, giving the azobenzenes greater conformational flexibility. Under irradiation by UV light a *trans* to *cis* isomerisation was observed by $^{1}$H-NMR spectroscopy. This conclusively proved that the inhibition of photoswitching was due to the rigidity of the metallocycle.

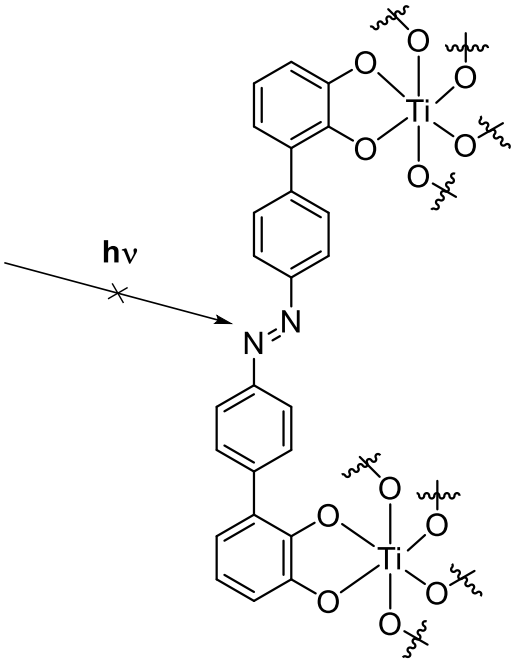


**Figure 4.5.** Nabeshima's tris azobenzene containing titanium metallocycle capable of completely inhibiting the photoswitching behaviour.[36]

Azobenzene photoswitching may still occur provided sufficient flexibility is present in the metallocycle or metallo-cage. However, the presence of labile coordination bonds within the construct means that disassembly or a structural transformation of the architecture can occur during this process.[37, 38] Liu and co-workers have reported a $Pd_2L_4$ cage containing azobenzene groups integral to the cage framework (Figure 4.6).[37] Irradiation with 365 nm light caused the azobenzenes to switch from the *trans* to *cis* conformation. This process resulted in the complete disassembly of the cage, with the only species detected in solution being the *cis* isomer of the free ligand. The *cis* isomer was unable to adopt the necessary geometry to facilitate the formation of the cage. Irradiation of the sample with visible light reformed the *trans* isomer and the cage was observed to spontaneously reform. The system could be cycled between these states many times, providing a convenient method of controlling cage assembly with the use of light.

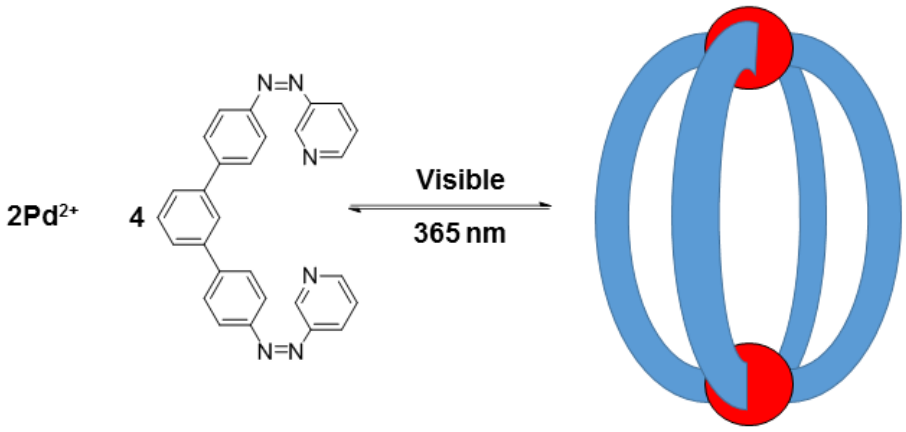


**Figure 4.6.** $Pd_2L_4$ cage reported by Liu and co-workers containing azobenzene groups embedded with the structural framework.[37]

It is apparent that construction of a metallo-cage embedded with photoswitchable groups capable of undergoing photoisomerisation is a considerable challenge. This is compounded by the observation that photoswitching often disrupts the structural integrity of these architectures. One of the rare examples where these processes do not occur has been reported by Clever and co-workers.[23] A $Pd_2L_4$ cage utilising DTE functionalised ligands was found to retain the ligands ability to photoswitch upon incorporation into the cage framework. What was even more unusual was that the cage retained the same structural composition throughout the photoswitching process. The cage could be switched between an open and closed form through irradiation with an appropriate form of light (Figure 4.7). Clever's $Pd_2L_4$ cage shares a very similar structure to Liu's $Pd_2L_4$ (Figure 4.6). Clever's cage did not disassemble upon photoswitching, unlike Liu's cage. The small molecular motion that occurs upon photoswitching of a DTE unit results in a very small geometric change of the cage. This change is not sufficient to perturb the composition of the cage. In contrast, photoisomerisation of an azobenzene is associated with a dramatic change in shape. In Liu's example, the change in geometry of the ligands was too severe and resulted in complete disassembly.

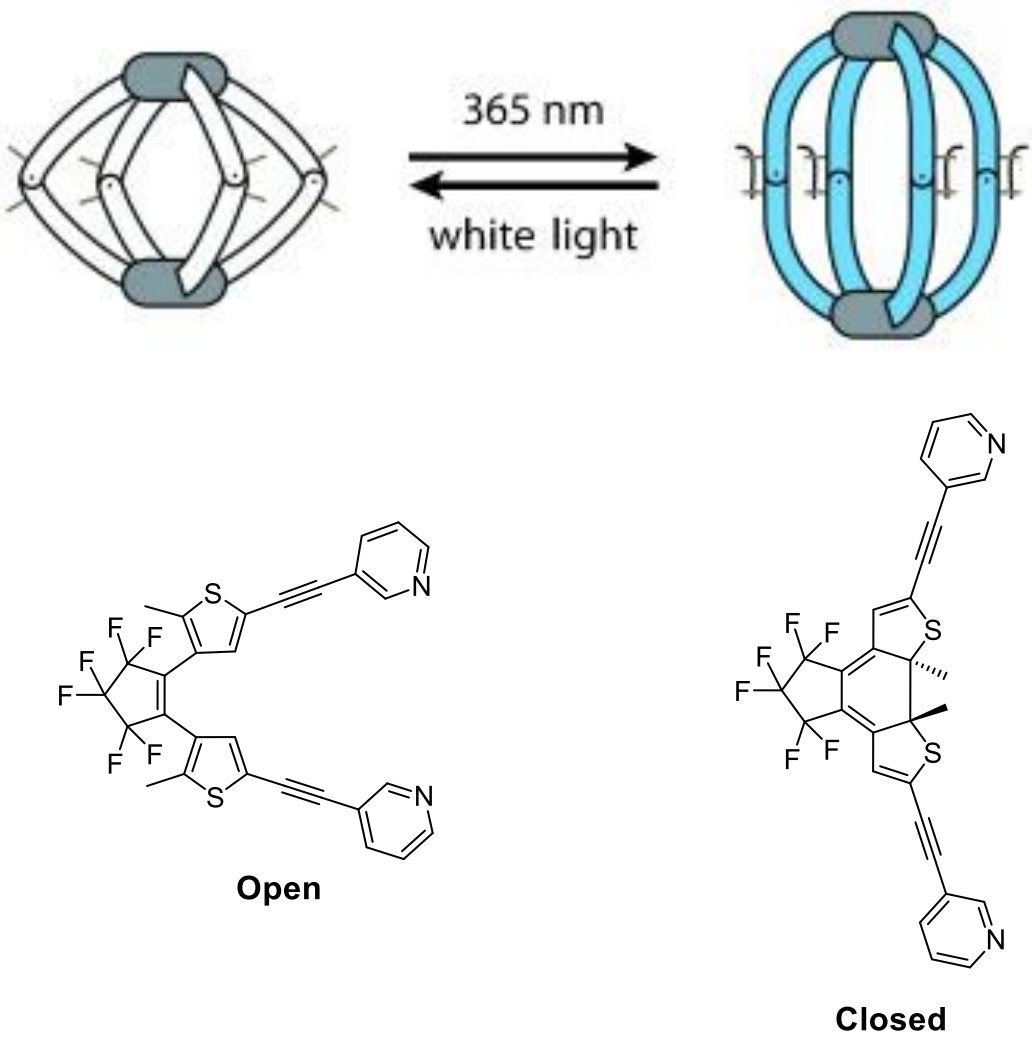


**Figure 4.7.** Clever's $Pd_2L_4$ DTE functionalised cage, able to photoisomerise between an open and closed form.[23]

To the authors knowledge, the only other example of a structurally robust photoswitchable metallo-cage has been reported by the Hardie group.[39] The azobenzene appended CTG ligand **L1** used throughout this thesis was self-assembled with iridium phenylpyridine tecton **M1** (Figure 4.8). Unlike the free ligands, a powerful light source was necessary to facilitate photoswitching of the cage, suggesting that inclusion of the azobenzenes into the cage framework inhibits photoswitching due to geometric constraints. The $M_3L_2$ metallo-cryptophane only underwent photoswitching upon irradiation with a 355 nm Nd:YAG laser. A decrease in the *trans* to *cis* quantum yield further corroborates this observation. The broad nature of the $^1$H-NMR spectra obtained suggests that a complex mixture of species was present in solution containing differing quantities of *cis* and *trans* azobenzene groups. Importantly, no changes were observed in the mass spectrum which still showed a large peak for the $M_3L_2^{3+}$ species. This suggests that the cage

remains intact during the photoisomerisation process. Irradiation with light at 450 nm reformed the all *trans* conformation of the metallo-cage.

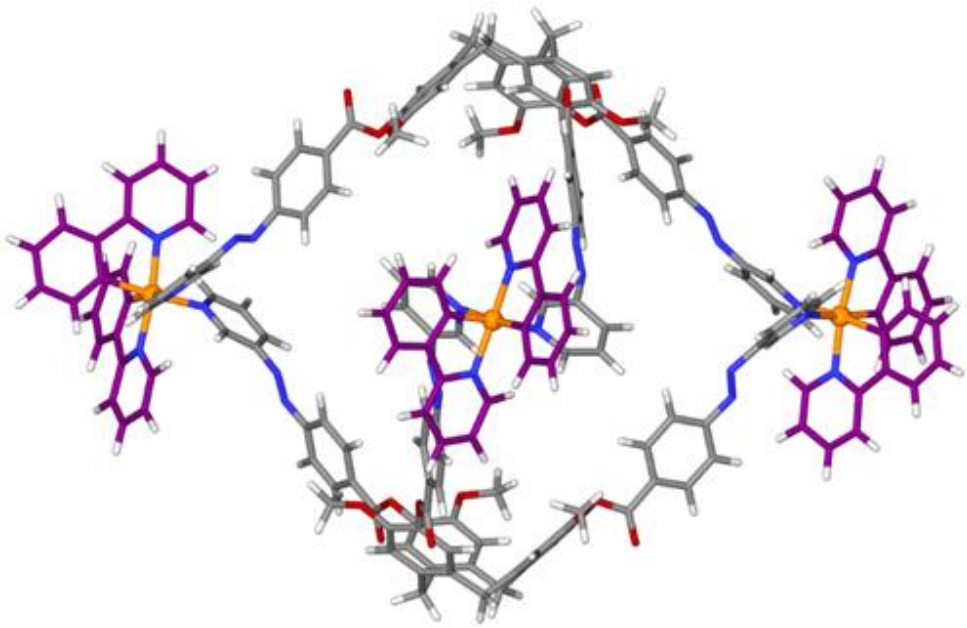

**Figure 4.8.** Molecular model of the azobenzene appended iridium-cryptophane reported by the Hardie group. The metallo-cage is capable of reversible *trans* to *cis* photoisomerisation.

The above examples by Clever and Hardie remain the only examples of a metallo-cage bearing structurally integral photoswitchable groups that remains intact during the photoisomerisation process. The remainder of this chapter will discuss the photoisomerisation behaviour of the novel azobenzene appended ligands CTG ligands and the palladium cages constructed from them.

## 4.2 Photoisomerisation studies of azobenzene appended CTG based ligands

Before the photophysical behaviour of the $Pd_3L_2$ cryptophanes was investigated it was necessary to determine the behaviour of the free ligands. The behaviour of **L1** has already been reported by the Hardie group. The substitution of the methoxy group for an ethoxy or propoxy group may affect the ability of the azobenzenes to photoisomerise. The behaviour of **L2** and **L3** was investigated with UV/visible spectroscopy. A 30 μM solution of the ligands in chloroform was prepared and an initial UV/vis spectrum was acquired (Figure 4.9). Each spectra consisted of two broad absorption bands with a weak n-π* band and a much stronger π-π* band centred. The presence of differing alkoxy groups does not affect the absorption spectra in any

considerable fashion. All ligands have a π-π* band with a maxima at approximately 325 nm and a n- π* band located at 450 nm.

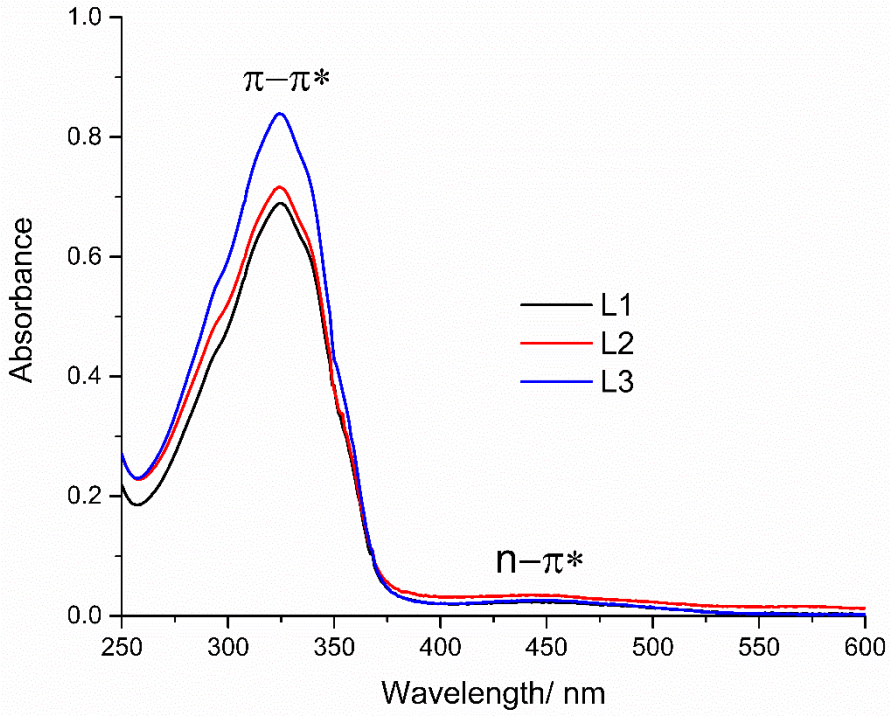


**Figure 4.9.** UV/visible spectra of **L1**, **L2** and **L3** showing the π-π* and n-π* azobenzene absorption bands.

The ligand solutions were then irradiated with a 30 W 365 nm lamp for 20 seconds and a UV/vis spectra was acquired (Figure 4.10, Figure 4.11 and Figure 4.12). This process was repeated until no further changes were observed in the spectra, confirming that the solution had reached the PSS. In total it took approximately 60 seconds for the system to reach the PSS.

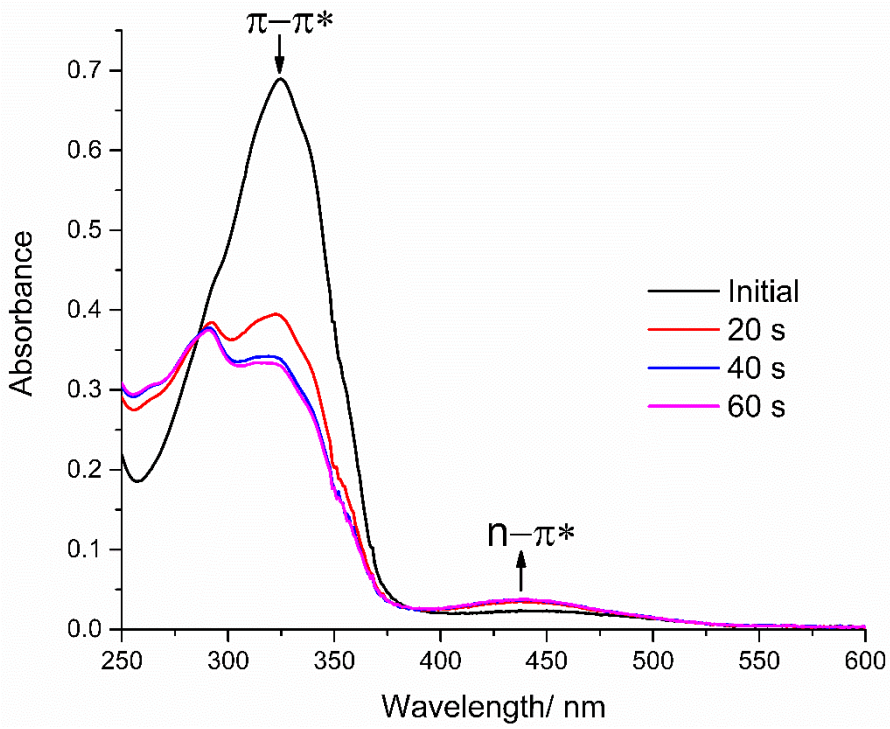


**Figure 4.10.** UV/visible spectrum of **L1** (30 μM, $CHCl_3$) upon irradiation with 365 nm light.

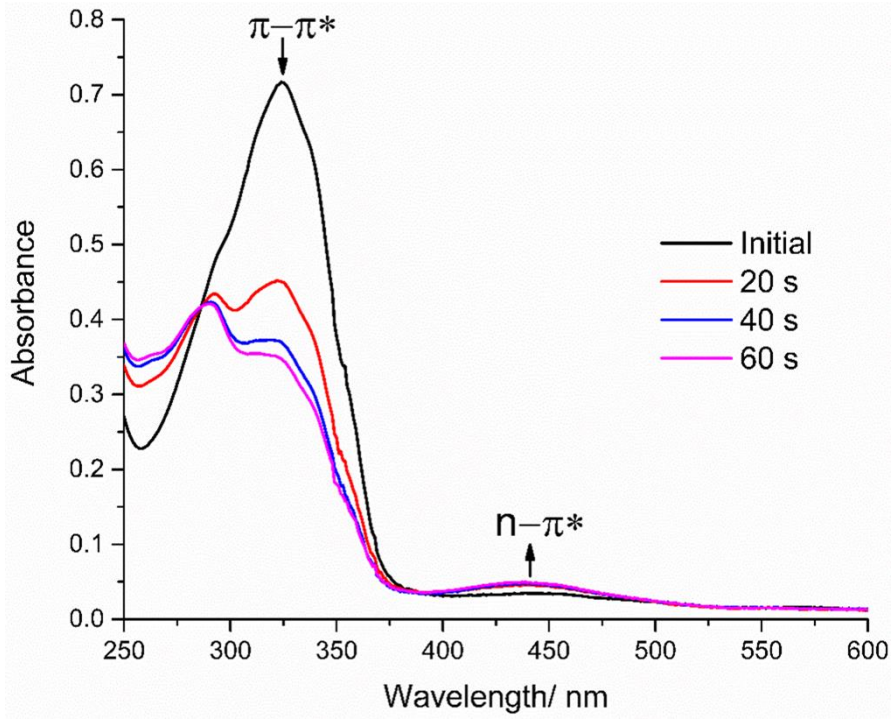


**Figure 4.11.** UV/visible spectrum of **L2** (30 μM, $CHCl_3$) upon irradiation with 365 nm light.

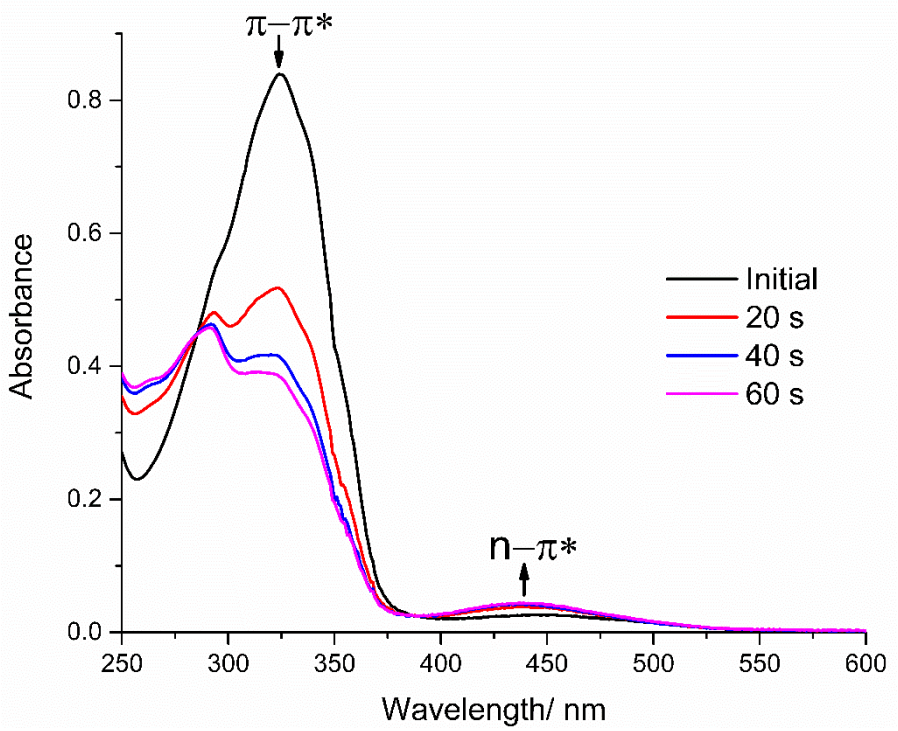


**Figure 4.12.** UV/visible spectrum of **L3** (30 μM, $CHCl_3$) upon irradiation with 365 nm light.

The presence of three azobenzene groups per molecule means that several possible isomers may be present at the PSS. Each azobenzene on the ligand can either be in the *trans* or *cis* conformation. In total four possible permutations exist, these being *EEE*, *EEZ*, *EZZ* and *ZZZ*. At the PSS it is likely that a mixture of all possible permutations are present. $^1$H-NMR has been used to confirm that this is the case for **L1**.[39] Due to the similarities between the ligands it is reasonable to conclude that this will be the case for each of them. This complicates the procedure for calculating quantum yields of photoisomerisation. Instead, a rough value of the *trans-cis* ratio could be calculated by considering the relative decrease in intensity of the π-π* band at the PSS (Equation 4.1). It should be noted that this calculation assumes that the *cis* isomer has zero absorption at approximately 325 nm which is unlikely. Therefore, more *cis* isomer is likely to be present than suggested from these calculations.

$$Conversion = \frac{A_0 - A_{PSS}}{A_0}$$

**Equation 4.1.** Calculation to determine the conversion of *trans* isomer to *cis* isomer. $A_0$ and $A_{PSS}$ are measured at the maxima of the π-π* transition.

**Table 4.1.** Percentage conversion of azobenzene groups in ligands **L1**, **L2** and **L3** upon irradiation with 365 nm light.

| Ligand | $\lambda_{max}$/ nm | Conversion (*trans*→*cis*) |
|---|---|---|
| **L1 (OMe)** | 325 | 52% |
| **L2 (OEt)** | 324 | 52% |
| **L3 (OPr)** | 324 | 54% |

It can be seen from Table 4.1 that the conversion of *trans* to *cis* isomer is almost identical across all ligands tested. The similarity of the UV/vis spectra and switching behaviour of the ligands implies that the alkoxy substituent has negligible impact on the photoswitching ability of the azobenzene groups. The conversion ratios for **L1** have been reported previously.[38] The conversion of *trans*→*cis* was reported to be 50% upon irradiation with 330 nm for 15 minutes. This is in good agreement with the values obtained for **L1** and corroborates the conversion values obtained for **L2** and **L3**.

The azobenzene in **L1**-**L3** possess electron withdrawing ester and pyridyl groups at either end. Of the three classes of azobenzenes discussed previously, these ligands would be classified as azobenzene derivatives. This is corroborated by the wide spacing between the π-π* and n-π* transitions in the UV/visible spectra. It would be expected that the *cis* isomers of these ligands would be relatively stable possessing a thermal half-life of several days. To determine this, a sample of **L1** was switched into the *cis* PSS using a 365 nm lamp and placed in the dark at 298K. At regular intervals a UV/visible spectrum was acquired. Over time an increase in the π-π* band was observed as more of the *cis* isomer thermally relaxed to the *trans* isomer. The spectra changed slowly, after 18 hours of monitoring under half of the *cis* isomer had reverted back to the *trans* isomer. By monitoring the increase of the π-π* band with respect to time it was possible to determine a thermal half-life for **L1** of approximately 40 hours. This lies within the predicted values for this class of azobenzenes.[5]

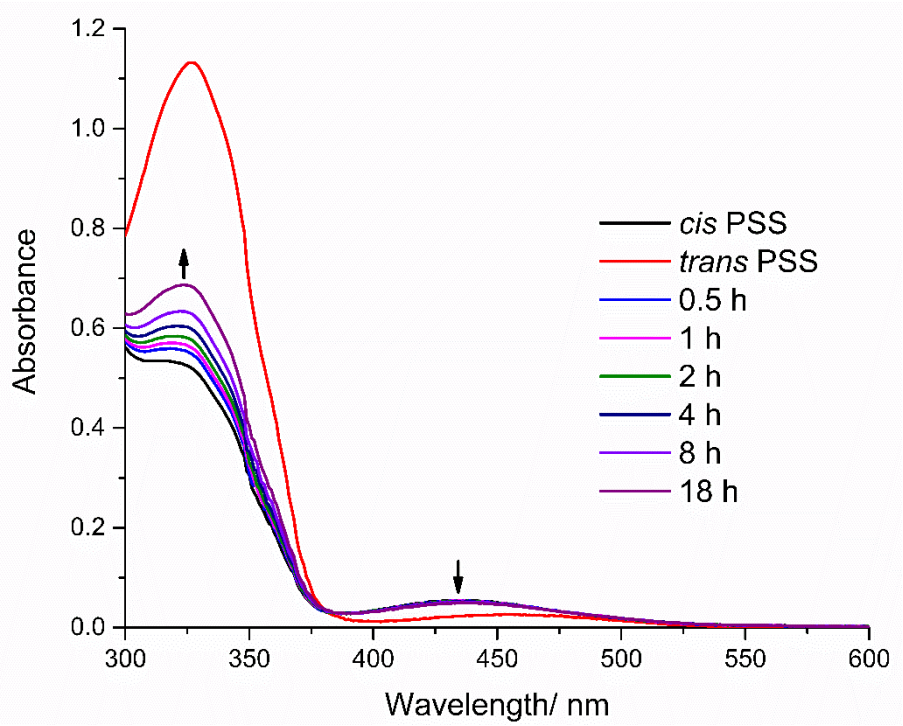


**Figure 4.13.** UV/visible spectra (30 μM, DMSO) of the thermal relaxation of *cis* **L1** to *trans* **L1** at 298 K.

Attempts to perform $^{1}$H-NMR studies on the switching behaviour of the ligands proved unsuccessful. No photoswitching was observed upon irradiation of samples at concentrations appropriate for $^{1}$H-NMR. It is probable that the 30 W light source used did not provide sufficient power to switch the azobenzene solution, which was too strongly absorbing and prevented efficient penetration of the light through the bulk solution. This is not completely unexpected as most photoisomerisation studies are performed with high power xenon lamps, presumably to enable efficient photoswitching of high concentration solutions. It has been shown that it is possible to switch concentrated solutions of **L1** using a Nd:YAG laser where weaker light sources had proved ineffective.[39]

## 4.3 Photoisomerisation studies of Pd(II) metallo-cryptophanes

Photoisomerisation studies of the metallo-cryptophanes focused upon the palladium metallo-cryptophanes **C19**, **C20** and **C21**. There are a number of reasons for this. First and foremost is that the cages were soluble in DMSO which was a solvent cut-off of 262 nm below which the solvent will absorb the majority of incoming light. This is in contrast to the nitromethane the rhodium and iridium cages were soluble in, which has a solvent cut-off of 380 nm. As the relevant excitation band is below this wavelength this would not be a

suitable solvent for UV/vis studies. Furthermore, irradiation of nitromethane with high powered laser light can result in solvent decomposition and explosion. This is an obvious safety concern and studies were not conducted in this solvent. Although a number of rhodium and iridium cages were soluble in tetrachloroethane, the presence of significant quantities of self-assembled impurities in these solvents would lead to challenging analysis of the photoswitched products.

To probe the photophysical behaviour of the palladium cryptophanes a 30 µM solution of **C19** in DMSO was prepared. An initial UV/visible spectrum was acquired of cage **C19** after which the cage was irradiated with 365 nm light from a 30 W lamp for increasing amounts of time (Figure 4.14). As before, the intensity of the π-π* absorption band decreased whilst the n-π* band increased slightly, indicative of the formation of a *cis* rich state. Overall the process took three times longer to reach the PSS than the free ligand. This is not unexpected as the geometric constraints placed upon the azobenzene by virtue of existing in a cage would be expected to inhibit photoswitching. Despite the apparent successful photoisomerisation of the cage a concerning feature was present in the UV/visible spectra. The initial spectrum obtained exhibited a likeness to the spectrum obtained for the free ligand **L1**. Upon complexation of the ligand with the palladium new MLCT bands from the palladium and pyridyl groups would be expected to appear in the spectrum.

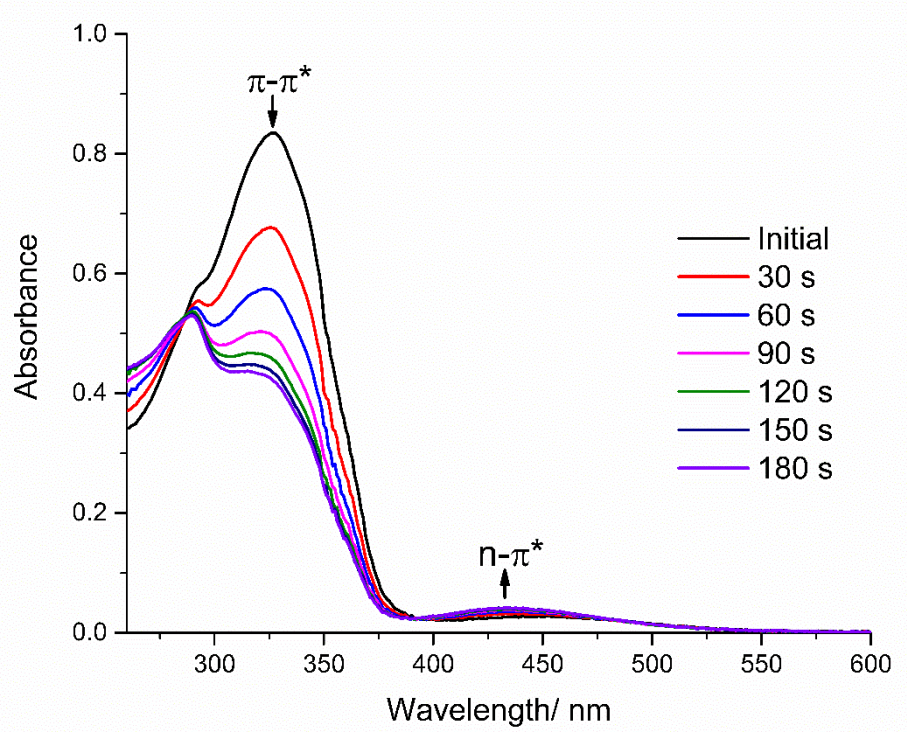


**Figure 4.14.** UV/visible spectrum (30 µM, DMSO) of **C19** upon irradiation with a 365 nm 30 W lamp for specified amounts of time.

For this reason a $^{1}$H-NMR of the 30 µM sample was acquired over 2048 scans and revealed that an unexpected phenomenon was occurring. The only peaks present in the NMR spectrum were of unreacted ligand and metal tecton (Figure 4.15). Due to the labile nature of the coordination bond all steps in the self-assembly process are reversible. This reversibility means that at very low concentrations of cage the backwards reactions can dominate due to Le Chatelier's principle. Concentration dependant disassembly behaviour has been observed in palladium cryptophanes previously.[40] Schaly and coworkers have shown that a nitrile appended palladium cryptophane begins to detect disassembled cage components below approximately 200 µM when monitored by $^{1}$H-NMR in DCM.[40] UV/visible spectra of the sample could be obtained by decreasing the path length from 10 mm to 1 mm and increasing the concentration to 300 µM. Acquisition of a $^{1}$H-NMR of the sample at 300 µM revealed that partial cage disassembly was occurring, with significant quantities of free ligand and metal tecton present in solution. Therefore, UV/visible spectroscopy was not a viable tool for studying the palladium cryptophanes and was not pursued further.

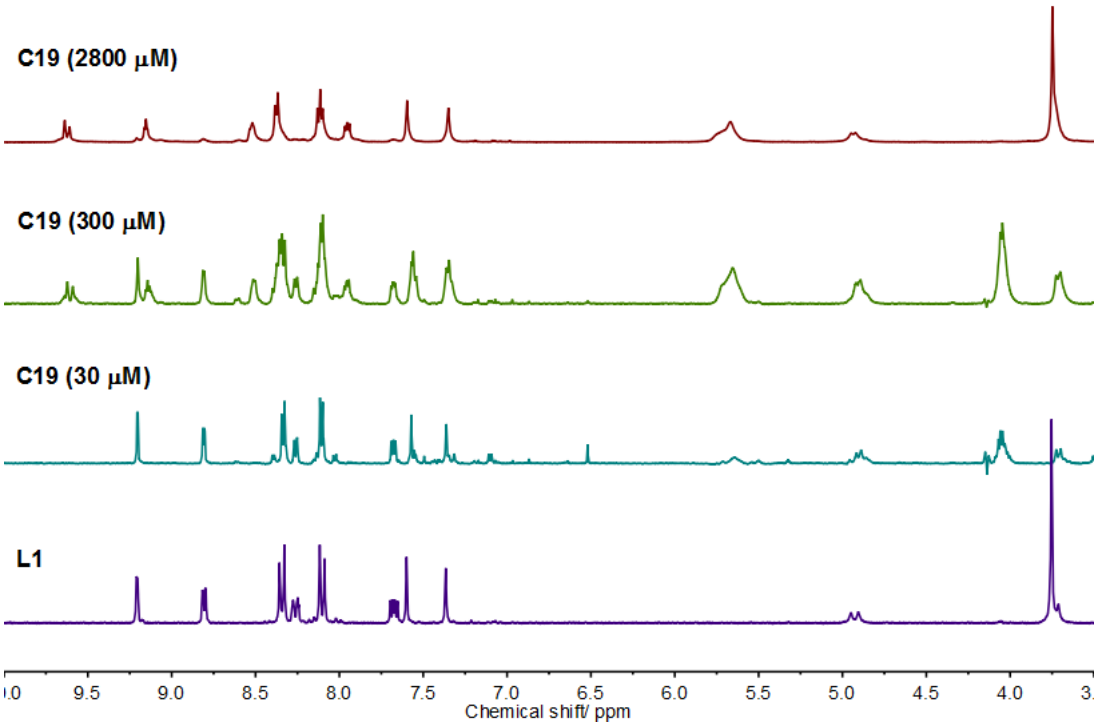


**Figure 4.15.** $^{1}$H-NMR (500 MHz, $d_6$-DMSO) of cage **C19** following dilution, compared to $^{1}$H-NMR (300 MHz, $d_6$-DMSO) of the free ligand **L1**.

At higher concentrations, $^{1}$H-NMR could be used to study the photoswitching behaviour of the cage. A standard NMR sample was prepared containing 5.7 mg of cage dissolved in $d_6$-DMSO to form a 2.8 mM solution. However, as observed with the free ligands, no changes in the $^{1}$H-NMR spectrum of the

cage was observed even after several hours of irradiation with a 30 W 365 nm light source. The highly absorbing nature of the azobenzene groups necessitate the use of a more powerful light source. Work within the Hardie group has shown that iridium azobenzene cryptophanes required laser light in order to effectively switch them.[41] This phenomenon has also been reported by Miyasaka where a high power laser light source is required to switch geometrically constrained azobenzenes.[42] For this reason a 355 nm Nd:YAG laser was employed to switch the cage. For all switching experiments discussed herein the laser was set to deliver 20 mJ of energy per pulse with a pulse rate of 10 Hz.

A standard NMR sample was prepared containing 5.7 mg of cage dissolved in $d_6$-DMSO to form a 2.8 mM solution. The sample was irradiated using the laser light for one minute. Analysis of the solution by $^1$H-NMR showed no evidence of photoswitching. No changes were observed upon further irradiation by the laser. This was unexpected as a comparable concentration of iridium metallo-cryptophane was reported to switch readily under similar conditions, reaching the PSS state after only 200 seconds. The only difference between the systems is the use of metal and the solvent. The iridium system contained the iridium phenylpyridine tecton **M1** and was dissolved in DCM,[39] whereas the palladium system employed palladium ethylenediamine tectons and was dissolved in DMSO. Iridium phenylpyridines are frequently used in photophysical applications due to the accessibility of the triplet excited state allowing them access to rich photochemistry. Overlap between excited states on the iridium and azobenzene could have a deactivating effect on both through FRET, examples of this occurring have been reported in the literature.[43, 44] The palladium centre meanwhile is much less photoactive and would not be expected to interfere with the azobenzene switching to the same degree. It is surprising therefore that the iridium cryptophane can switch more readily than a palladium analogue.

The differences in the ease of photoisomerisation between the two metallo-cryptophanes could be a consequence of the choice of solvent. In general non-viscous solvents promote photoswitching through a rotation mechanism, whereas viscous solvents favour an inversion mechanism.[5] DCM, the solvent used for the iridium cage studies, is a non-viscous solvent and would theoretically favour a rotation mechanism. Conversely, the solvent used in the palladium cage studies is DMSO, as a highly viscous DMSO promotes an inversion mechanism. More steric strain would be expected if a cage were to isomerise through an inversion mechanism than a rotational mechanism as

the length of the ligand 'arms' would increase in size considerably. Although a large change in shape would be associated with an rotation mechanism, the length of the ligand arms would remain constant. In addition, a rotational mechanism has more degrees of freedom than an inversion mechanism so could more effectively limit steric strain formed during isomerisation.

Dilution of the sample to 0.6 mM and irradiation with 355 nm light from a laser was sufficient to promote photoswitching of cage **C19** (Figure 4.16). In total the sample was irradiated for 1200 s and a $^{1}$H-NMR spectrum was acquired. Further irradiation caused a black precipitate to form, presumably due to decomposition of the sample. As the sample is isomerised into a *cis* rich state, the NMR resonances broaden considerably. This is not unexpected as it is likely that a large number of isomers are present in solution after photoswitching. Each cage contains a total of six azobenzene groups, any combination of which can isomerise to the *cis* conformation. Assuming all isomers are stable then a total of 12 possible isomers of the intact cage are possible. Unfortunately, due to the broad nature of the resonances no meaningful conclusions can be reached regarding the nature of the PSS. In particular it is not possible to determine what the conversion of *trans*→*cis* isomer is in the PSS and whether incorporation into a cage has inhibited the azobenzenes ability to photoswitch.

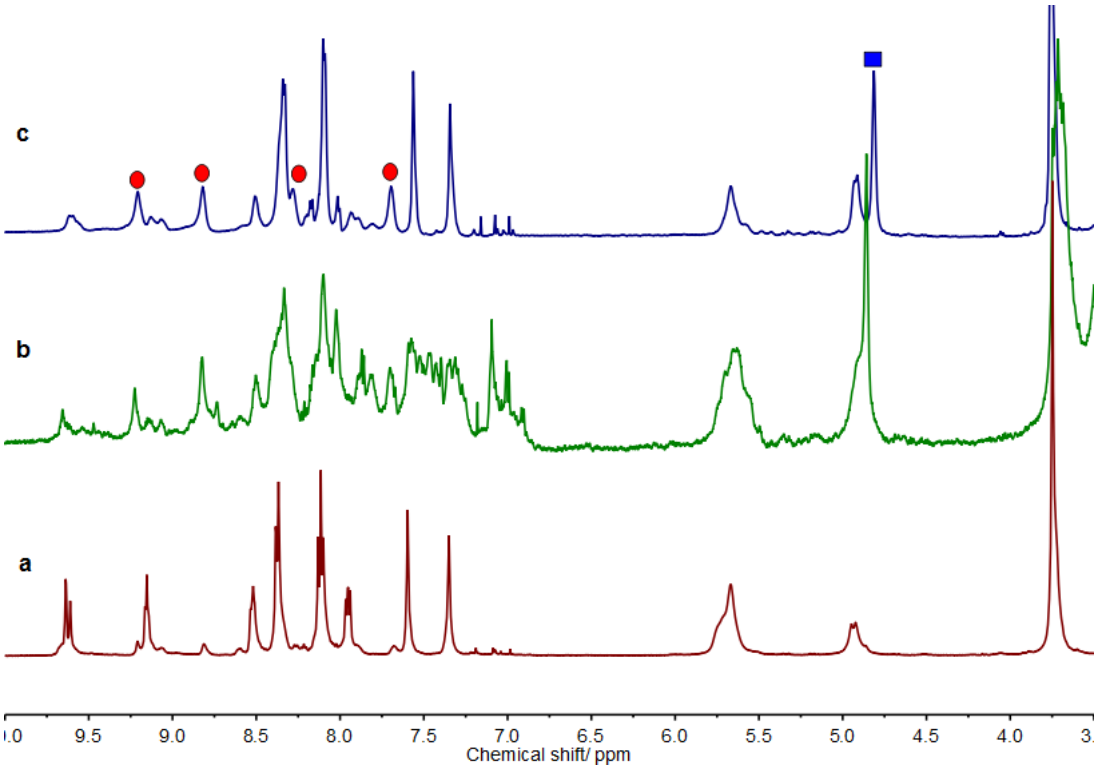


**Figure 4.16. a)** $^{1}$H-NMR (500 MHz, $d_6$-DMSO) of cage **C19**; **b)** upon illumination with a 355 nm Nd:YAG laser (20 mJ, 10 Hz, 1200 s); **c)** Re-irradiation with 450 nm Xe lamp (1 hour). **L1** (red) and $Pd(en)_2(NO_3)_2$ (blue) peaks are shown.

Upon irradiating the *cis* rich state with 450 nm light from a xenon lamp, the structure regains many of its original features. This is indicative of the re-emergence of the *trans* rich state and subsequent reformation of the all *trans* **C19**. The major difference between the original spectrum and the spectrum post-photoswitching back to the *trans* state is the increase of resonances arising from the free ligand as well as a large singlet at 4.81 ppm. This peak can be assigned as $Pd(en)_2(NO_3)_2$. This species can form when an ethylenediamine ligand is lost from one palladium centre and complexes to another palladium (Scheme 4.1). Isomerisation of the cage into the *cis* isomer may facilitate the loss of the ethylenediamine group from one of the palladium centres. The free ethylenediamine can then complex to another palladium and effectively sequester it from further reaction, disrupting the stoichiometry of the reaction. This observation explains why the system cannot completely revert back to its original state post-photoswitching and significant quantities of free ligand can be detected as the reaction stoichiometry has been disrupted.

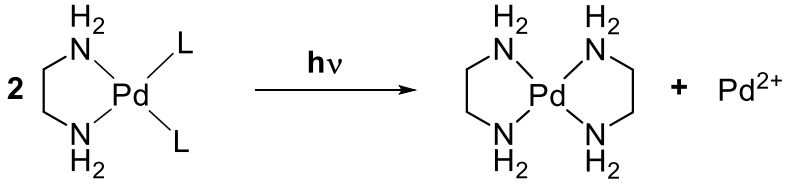


**Scheme 4.1.** Decomposition of palladium tecton, promoted by the photoswitching of cage **C19** into the *cis* rich state.

Ethylenediamine is a common *cis* protecting group used in supramolecular chemistry and there are few examples where it is displaced during a reaction. One notable example from the Hardie group has reported this occurring.[45] A 4-pyridyl functionalised CTG ligand was found to form metastable $M_3L_2$ metallo-cryptophanes. Over time the ethylenediamine was lost and the structure rearranged into a $Pd_6L_8$ stella octangula type structure. The loss of the ethylenediamine was attributed to a strong driving force towards the $M_6L_8$ structure that was sufficient to overcome the dissociation barrier from the kinetic centre. In the case of **C19** there is no evidence to suggest that a large discrete cage forms following the loss of the ethylenediamine. Instead, the loss of the protecting group is likely to be driven by the process of *trans*→*cis* photoswitching resulting in considerable strain around the palladium centre, facilitating the dissociation of the ethylenediamine.

In order to determine the distribution of species present at the PSS, small-angle X-ray scattering (SAXS) and ion-mobility mass spectrometry (IM-MS) were used. These experiments were carried out on a grant awarded by the

Royce Institute and the University of Liverpool. It was envisioned that SAXS would provide a convenient method of measuring the size of the particles in solution. The difference in size distribution between a *trans* rich and *cis* rich state would enable estimation of the number of species present. The studies were performed in DMSO. Unfortunately, the studies were hampered by the solvent which absorbed the incoming X-ray beam very effectively. Due to this, the scattering by the cage was incredibly weak and no meaningful data could be extracted from it. Synchrotron radiation may alleviate this problem.

More success was had using the IM-MS instrument. IM-MS measures the time taken for a species to diffuse along a drift tube against the flow of a carrier gas. Species with a larger radius of diffusion take longer to flow across the tube. At the end of the tube the mass of the species is measured. This compounds to be distinguished based upon their mass and volume. A mass spectrum was obtained of the *trans* rich state which displayed a large peak relating to the $[M_3L_2]^{6+}$ species. The time taken for this species to diffuse along the drift tube was measured and was revealed to exhibit a bell-shaped distribution. This is expected as the all *trans* system will exhibit a large degree of size homogeneity between cages. Upon photoswitching however, this homogeneity is broken as more *cis* isomer is formed. If a range of species bearing varying degrees of *cis* isomer are present at the PSS then the bell curve would be expected to broaden to reflect the increase in different sized species in solution. Alternatively, if the PSS contains only the original *trans* cage and a single *cis* isomer a new sharp peak would be expected close to the original one. This technique is becoming more popular in supramolecular chemistry as more groups are using it to distinguish between different sized species in a self-assembled system.[46-48] A number of excellent reviews have been written on the subject.[49, 50]

A sample of the cage was switched to a *cis* rich state using a 355 nm laser and the IM-MS spectrum was recorded. Small changes were detected in the drift times for the $[M_3L_2]^{6+}$ peak in the *trans* and *cis* rich states. Due to the relatively small size in the changes it is difficult to conclusively determine whether the change is due to photoswitching of the cage species, or due to experimental error. Analysis of all the fragmentation peaks such as $[M_3L]^{3+}$ and $[M_2L_2]^{2+}$ revealed no change in the size distribution between the *trans* and *cis* rich state. This was unexpected as there are several examples where IM-MS has been used to determine the change in shape associated with photoswitching. In most of these examples the switching of the azobenzene group is associated with a large change in the size of the molecule. Molecular

modelling of the iridium azobenzene cage suggests the change in the size of an all *trans* cage and an all *cis* cage is approximately 2 Å when measured between the two CTG bowls.[39] It should be noted that this is an extreme where all 6 azobenzenes have been switched. The PSS state likely contains a mixture of isomers bearing fewer *cis* azobenzenes where the difference in size will be less pronounced. This change in shape is also associated with a flattening of the cage into a more ellipsoidal shape. It is possible that the cage possesses sufficient flexibility that the differences between these two states is negligible when compared to the thermal fluctuations in the size of the cage and therefore cannot be detected by IM-MS. It is also possible that the cage disassembles upon switching into a *cis* rich state, although the observation of large species in the *cis* rich state by $^{1}$H-NMR evidence contradicts this.

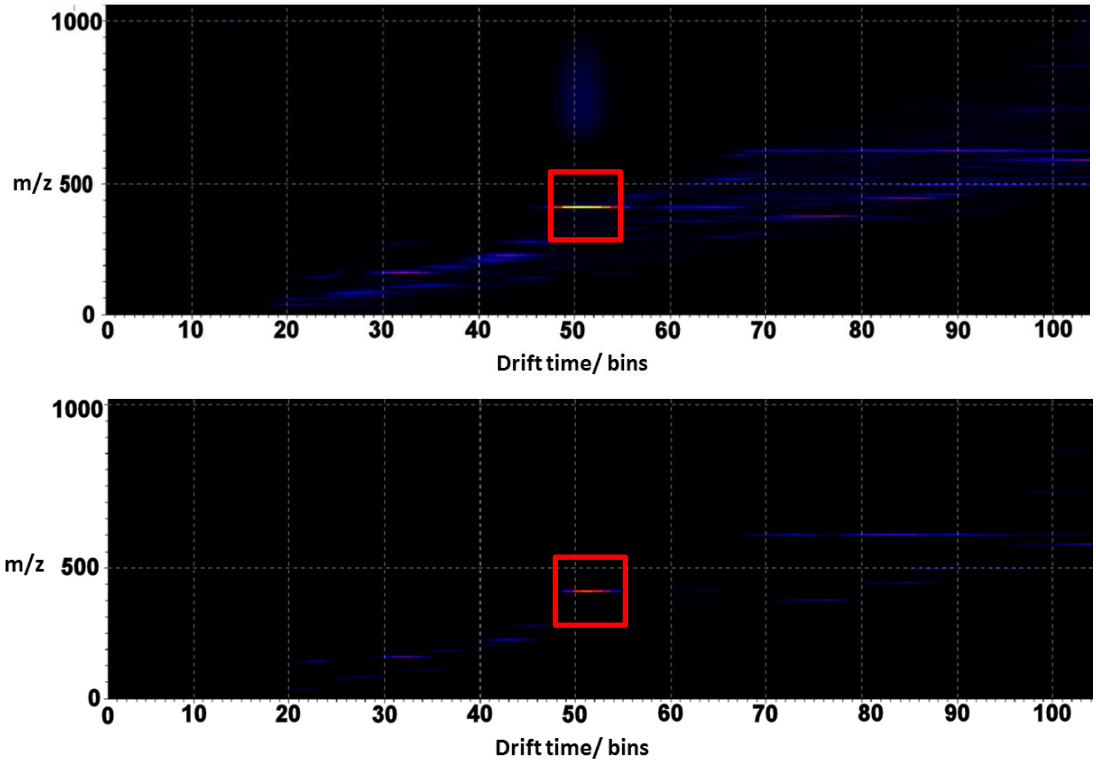


**Figure 4.17.** Drift plot of cage **C19** in *trans* rich state (top) and *cis* rich state (bottom). Peak highlighted in red corresponds to the $[M_3L_2]^{6+}$ peak.

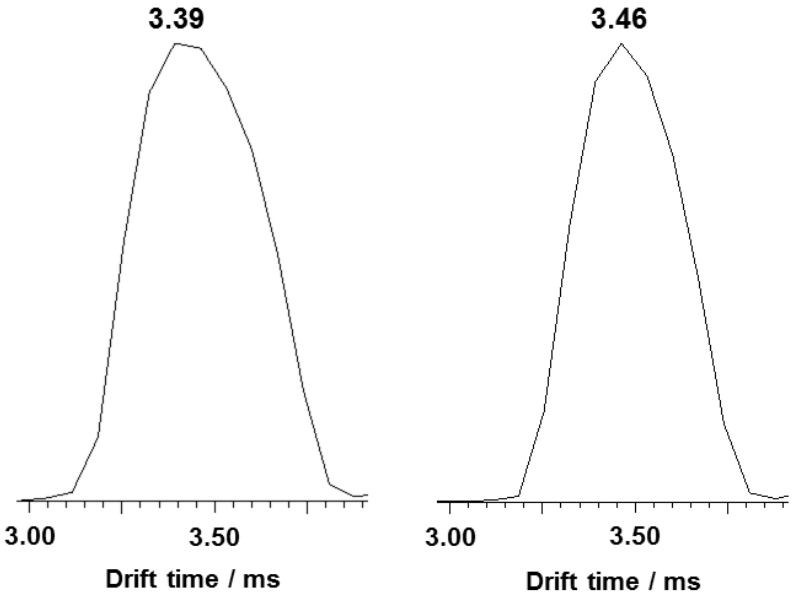


**Figure 4.18.** Drift time of $[M_3L_2]^{6+}$ peak for *trans* rich state (left) and *cis* rich state (right).

## 4.4 Conclusions

The photoswitching behaviour of the ligands **L1**, **L2** and **L3** has been investigated using UV/visible spectroscopy. The substitution of the upper rim alkoxy groups has negligible impact on the photoswitching potential of these ligands. The thermodynamically stable *trans* state could be switched to a *cis* rich state by irradiating with 365 nm light. The PSS state contained approximately 50% *cis* isomer. This shows that the substitution of the upper rim with varying lengths of alkoxy groups does not significantly affect the photoswitching behaviour of the azobenzene groups. The *cis* isomer of **L1** was found to have relatively high thermal stability, with a thermal half-life of approximately 40 hours.

Attempts to study the photophysical behaviour of palladium cage **C19** have been hampered by disassembly of the construct at low concentrations. UV/visible studies have not been possible and instead the samples were monitored using $^1$H-NMR. A 355 nm Nd:YAG laser was used to switch the cage into a *cis* rich state. Due to the extremely broad nature of the NMR resonances in this state, extracting information regarding the PSS has been challenging. The broad nature of the spectra does suggest the PSS consists of multiple isomers. IM-MS was used to probe the size distribution present at the PSS. Small differences of the drift-times for the $[M_3L_2]^{6+}$ peak were

detected, yet it is not clear whether this is a consequence of photoswitching or an experimental error.

**C19** could be reverted back to a *trans* rich state by irradiating with 450 nm light from a monochromated xenon lamp. When monitored by $^{1}$H-NMR the spectrum was found to regain many of the features present in the original spectrum. In addition, peaks corresponding to free ligand and $Pd(en)_2(NO_3)_2$ were found to form. The *cis* isomer of **C19** promotes loss of the ethylenediamine protecting ligand. The disruption of the ligand:metal stoichiometry ratio accounts for the fatigue resistance of the system and explains why the $^{1}$H-NMR spectrum does not revert to the same as the spectrum obtained pre-photoswitching.

## 4.5 Future work

Both the ligands and cage **C19** have been shown to photoisomerise upon irradiation with appropriate wavelengths of light. However, dissociation of the ethylenediamine protecting group from the palladium centre during the photoisomerisation process severely reduces the fatigue resistance of these compounds. The use of a stronger bound protecting group may increase the fatigue resistance of these systems. A NHC palladium tecton is likely to be a good candidate for this role as the strong C-Pd are unlikely to dissociate (Figure 4.19). A potential issue with this approach however is that the strong C-Pd bond will *trans* labilise bonds the ligand when assembled into a metallo-cryptophane. This may facilitate the disassembly of the cage at even higher concentrations which is an undesirable feature.

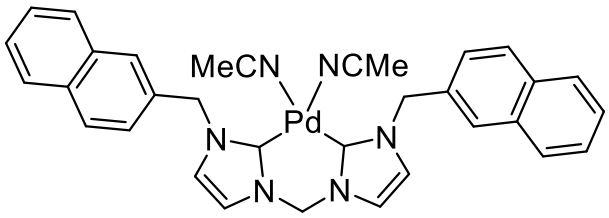


**Figure 4.19.** Structure of proposed NHC protected palladium tecton designed to resist photodegradation.

Another potential reason for the poor fatigue resistance of these cages is the use of a Nd:YAG laser. The high intensity of this light source may increase the likelihood of photodegradation occurring. Moreover, only a small area of the whole sample will be illuminated, this could feasibly lead to thermal decomposition in addition. A high wattage xenon lamp fitted with a filter for the correct wavelength would be a more appropriate for these applications.

UV/visible spectroscopy is a useful technique for studying azobenzenes, yet was not suitable in this instance due to the disassembly of the cages at low concentrations. To circumvent this problem, deposition of these cages into thin films may allow the UV/visible studies to take place. This would enable an estimation of the ratio of the *trans* to *cis* isomer present at the PSS. In addition, the study of cage complexes that have not been studied due to safety concerns associated with the use of nitromethane as a solvent would be made possible in thin films.

## 4.6 Experimental

### General Remarks

All reagents were purchased from commercial suppliers and without further purification. Where stated reactions were carried out under an inert atmosphere of nitrogen using a dual vacuum/ nitrogen manifold and standard Schlenk techniques. Dry solvent was obtained by passing through a column of activated alumina.

### Instrumentation

$^{1}H$ and $^{13}C$ NMR were performed on a Bruker 500-CP 500 MHz spectrometer and referenced to residual solvent peaks. Where appropriate NMR assignments were confirmed using 2-D NMR techniques acquired on a Jeol ECA 600ii 600 MHz spectrometer, techniques include COSY, TOCSY, HSQC, HMBC, NOESY, ROESY and DOSY.

IM-MS were performed on a Bruker Synapt G2-Si Imaging mass spectrometer. UV/visible spectra were recorded on an Agilent Cary 100 UV/Vis spectrophotometer.

SAXS measurement were performed on a Bruker Nanostar system at a concentration of 400 μM in DMSO.

*Trans*→*cis* isomerisation studies of the free ligand were performed using a 30 W 365 nm lamp.

*Cis*→*trans* isomerisation studies of the metallo-cryptophanes were carried out using a 75 W xenon lamp equipped with a tuneable PowerArc monochromator. The use of the monochromator filtered out much of the energy with <1 mW of energy being delivered to the sample.

*Trans*→*cis* isomerisation studies of the metallo-cryptophanes were carried out using a Continuum Powerlite 8010 355 nm Nd:YAG laser. The natural frequency of the laser (10 Hz) was used without interference and each pulse was set to deliver 20 mJ of energy.

### 4.6.1 UV studies of free ligands

*Trans*→*cis* isomerisations were performed by preparing a 30 μM of the appropriate ligand in chloroform and an initial UV/visible spectrum was recorded. The sample was irradiated with a 365 nm 30 W lamp for 120 seconds to promote the *trans*→*cis* isomerisation. A further UV/visible spectrum was then recorded for comparison.

*Cis*→*trans* isomerisations were performed thermally. A 30 μM sample of the ligand was dissolved in DMSO and irradiated with a 30 W 365 nm lamp for 120 s to generate the PSS. The samples were placed in the UV/visible spectrometer fitted with an internal heating block heated to 323 K. A UV/visible spectrum was recorded every 30 minutes for comparison.

### 4.6.2 $^{1}$H-NMR studies of C19

*Trans*→*cis* isomerisation was performed by preparing a sample of **C19** in $d_6$-DMSO (0.6 mM, 0.7 mL). An initial spectrum was recorded. The sample was irradiated with a 355 nm Nd:YAG laser (20 mJ, 10 Hz) for 1200 s to generate the *cis* rich state. A $^{1}$H-NMR spectrum was recorded for comparison.

*Cis*→*trans* isomerisation was performed by irradiating the *cis* rich sample at 450 nm using a 75 W xenon lamp equipped with a tuneable power arc monochromator for 60 minutes to generate the *trans* rich state. A $^{1}$H-NMR spectrum was recorded for comparison.

## References


1. M. Zhu and H. Zhou, *Org. Biomol. Chem.*, 2018, **16**, 8434-8445.
2. A. Natansohn and P. Rochon, *Chem. Rev.*, 2002, **102**, 4139-4176.
3. K. G. Yager and C. J. Barrett, *J. Photochem. Photobiol. A*, 2006, **182**, 250-261.
4. M. Natali and S. Giordani, *Chem. Soc. Rev.*, 2012, **41**, 4010-4029.
5. H. M. D. Bandara and S. C. Burdette, *Chem. Soc. Rev.*, 2012, **41**, 1809-1825.
6. G. S. Hartley, *Nature*, 1937, **140**, 281-281.
7. H. Rau and E. Lueddecke, *J. Am. Chem. Soc.*, 1982, **104**, 1616-1620.
8. M. Baroncini, J. Groppi, S. Corra, S. Silvi and A. Credi, *Adv. Opt. Mater.*, 2019, **7**, 1900392.
9. S. Crespi, N. A. Simeth and B. König, *Nat. Rev. Chem.*, 2019, **3**, 133-146.
10. X. Tong, M. Pelletier, A. Lasia and Y. Zhao, *Angew. Chem. Int. Ed.*, 2008, **47**, 3596-3599.
11. J. Henzl, M. Mehlhorn, H. Gawronski, K.-H. Rieder and K. Morgenstern, *Angew. Chem. Int. Ed.*, 2006, **45**, 603-606.
12. R. Turanský, M. Konôpka, N. L. Doltsinis, I. Štich and D. Marx, *Phys. Chem. Chem. Phys.*, 2010, **12**, 13922-13932.
13. T. Fujino, S. Y. Arzhantsev and T. Tahara, *J. Phys. Chem. A*, 2001, **105**, 8123-8129.
14. C.-W. Chang, Y.-C. Lu, T.-T. Wang and E. W.-G. Diau, *J. Am. Chem. Soc.*, 2004, **126**, 10109-10118.
15. P. Hamm, S. M. Ohline and W. Zinth, *J. Chem. Phys.*, 1997, **106**, 519-529.
16. G. Zimmerman, L.-Y. Chow and U.-J. Paik, *J. Am. Chem. Soc.*, 1958, **80**, 3528-3531.
17. P. Bortolus and S. Monti, *J. Phys. Chem.*, 1979, **83**, 648-652.
18. A. P. Demchenko, V. I. Tomin and P.-T. Chou, *Chem. Rev.*, 2017, **117**, 13353-13381.
19. L. Wang, W. Xu, C. Yi and X. Wang, *J. Mol. Graph. Model*, 2009, **27**, 792-796.
20. C. R. Crecca and A. E. Roitberg, *J. Phys. Chem. A*, 2006, **110**, 8188-8203.
21. I. K. Lednev, T. Q. Ye, P. Matousek, M. Towrie, P. Foggi, F. V. R. Neuwahl, S. Umapathy, R. E. Hester and J. N. Moore, *Chem. Phys. Lett.*, 1998, **290**, 68-74.
22. I. Conti, M. Garavelli and G. Orlandi, *J. Am. Chem. Soc.*, 2008, **130**, 5216-5230.
23. M. Han, R. Michel, B. He, Y.-S. Chen, D. Stalke, M. John and G. H. Clever, *Angew. Chem. Int. Ed.*, 2013, **52**, 1319-1323.
24. R. Siewertsen, J. B. Schönborn, B. Hartke, F. Renth and F. Temps, *Phys. Chem. Chem. Phys.*, 2011, **13**, 1054-1063.
25. J. S. Zhu, J. M. Larach, R. J. Tombari, P. W. Gingrich, S. R. Bode, J. R. Tuck, H. T. Warren, J.-H. Son, W. C. Duim, J. C. Fettinger, M. J. Haddadin, D. J. Tantillo, M. J. Kurth and D. E. Olson, *Org. Lett.*, 2019, **21**, 8765-8770.
26. D. Larsen, P. M. Bjerre and S. R. Beeren, *Chem. Commun.*, 2019, **55**, 15037-15040.

27. J. Dokić, M. Gothe, J. Wirth, M. V. Peters, J. Schwarz, S. Hecht and P. Saalfrank, *J. Phys. Chem. A*, 2009, **113**, 6763-6773.
28. A. Cembran, F. Bernardi, M. Garavelli, L. Gagliardi and G. Orlandi, *J. Am. Chem. Soc.*, 2004, **126**, 3234-3243.
29. D. Gegiou, K. A. Muszkat and E. Fischer, *J. Am. Chem. Soc.*, 1968, **90**, 12-18.
30. Y. Liu, C. Yu, H. Jin, B. Jiang, X. Zhu, Y. Zhou, Z. Lu and D. Yan, *J. Am. Chem. Soc.*, 2013, **135**, 4765-4770.
31. Y.-L. Zhao and J. F. Stoddart, *Langmuir*, 2009, **25**, 8442-8446.
32. T. Murase, S. Sato and M. Fujita, *Angew. Chem. Int. Ed.*, 2007, **46**, 5133-5136.
33. S. Tamesue, Y. Takashima, H. Yamaguchi, S. Shinkai and A. Harada, *Angew. Chem. Int. Ed.*, 2010, **49**, 7461-7464.
34. S. Venkataramani, U. Jana, M. Dommaschk, F. D. Sönnichsen, F. Tuczek and R. Herges, *Science*, 2011, **331**, 445-448.
35. H.-S. Tang, N. Zhu and V. W.-W. Yam, *Organometallics*, 2007, **26**, 22-25.
36. M. Yamamura, Y. Okazaki and T. Nabeshima, *Chem. Commun.*, 2012, **48**, 5724-5726.
37. S. Fu, Q. Luo, M. Zang, J. Tian, Z. Zhang, M. Zeng, Y. Ji, J. Xu and J. Liu, *Mater. Chem. Front.*, 2019, **3**, 1238-1243.
38. M. Han, Y. Luo, B. Damaschke, L. Gómez, X. Ribas, A. Jose, P. Peretzki, M. Seibt and G. H. Clever, *Angew. Chem. Int. Ed.*, 2016, **55**, 445-449.
39. S. Oldknow, D. R. Martir, V. E. Pritchard, M. A. Blitz, Colin W. G. Fishwick, E. Zysman-Colman and M. J. Hardie, *Chem. Sci.*, 2018, **9**, 8150-8159.
40. A. Schaly, M. Meyer, Chambron, Jean-Claude, M. Jean, N. Vanthuyne, E. Aubert, E. Espinosa, N. Zorn and E. Leize-Wagner, *Eur. J. Inorg. Chem.*, 2019, **2019**, 2691-2706.
41. S. Oldknow, PhD thesis, University of Leeds, 2018.
42. K. Uchida, S. Yamaguchi, H. Yamada, M. Akazawa, T. Katayama, Y. Ishibashi and H. Miyasaka, *Chem. Commun.*, 2009, DOI: 10.1039/B908303K, 4420-4422.
43. S. Monti, E. Gardini, P. Bortolus and E. Amouyal, *Chem. Phys. Lett.*, 1981, **77**, 115-119.
44. A. Raman, G. Augustine, N. Ayyadurai and S. Easwaramoorthi, *New J. Chem.*, 2018, **42**, 9300-9305.
45. J. J. Henkelis, C. J. Carruthers, S. E. Chambers, R. Clowes, A. I. Cooper, J. Fisher and M. J. Hardie, *J. Am. Chem. Soc.*, 2014, **136**, 14393-14396.
46. J. Ujma, M. De Cecco, O. Chepelin, H. Levene, C. Moffat, S. J. Pike, P. J. Lusby and P. E. Barran, *Chem. Commun.*, 2012, **48**, 4423-4425.
47. E. S. Baker, J. E. Bushnell, S. R. Wecksler, M. D. Lim, M. J. Manard, N. F. Dupuis, P. C. Ford and M. T. Bowers, *J. Am. Chem. Soc.*, 2005, **127**, 18222-18228.
48. I. Czerwinska, A. Kulesza, C. Choi, F. Chirot, A.-L. Simon, J. Far, C. Kune, E. de Pauw and P. Dugourd, *Phys. Chem. Chem. Phys.*, 2016, **18**, 32331-32336.
49. E. Kalenius, M. Groessl and K. Rissanen, *Nat. Rev. Chem.*, 2019, **3**, 4-14.

50. E. R. Brocker, S. E. Anderson, B. H. Northrop, P. J. Stang and M. T. Bowers, *J. Am. Chem. Soc.*, 2010, **132**, 13486-13494.

# Chapter 5

# Host-Guest Behaviour of Photoswitchable Metallo-Cryptophanes

## 5.1 Introduction

The birth of supramolecular chemistry began with the discovery that crown ethers are capable of recognising and binding sodium metal cations (Figure 5.1).[1, 2] Since then, host-guest chemistry has remained as one of the fundamental tenets of supramolecular chemistry. The chemistry of a host-guest system is dictated by weak, labile intermolecular interactions such as hydrogen bonding, hydrophobic, π-π and electrostatic interactions. Supramolecular research is the field of chemistry that is concerned with the study of these interactions and for this reason host-guest systems remain an area of research that is unique to the field of supramolecular chemistry.

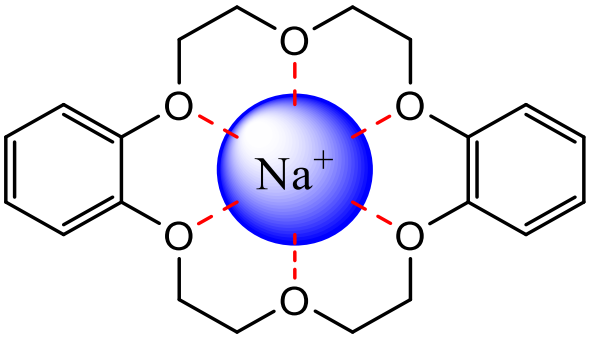


**Figure 5.1.** Pedersen discovered that crown ethers are capable of binding alkali metal cations *via* electrostatic interactions (red).[2]

The plethora of applications for these systems span a wide range of fields, with uses being discovered in molecular sensing and recognition,[3-5] catalysis displaying non-standard stereo and regioselectivity[6-9] and the separation of pollutants or fine chemicals from complex mixtures.[10-13] This chapter describes the host-guest behaviour of the photoswitchable metallo-cryptophanes discussed in previous chapters and attempts to answer whether the binding affinities of these systems can be modulated with the use of light.

### 5.1.1 Guest Encapsulation by CTV Derivatives

As a cavitand type molecule CTV possess a shallow hydrophobic cavity. This cavity has been utilised in the past to bind a wide range of hydrophobic moieties including carboranes to fullerenes.[14-17] The nature of the binding between CTV and guests of this type is often a hydrophobic interaction

between the CTV bowl and the non-polar guest.[18] In order to improve the binding efficiency and to impart additional functionality to the system, the CTV core is often functionalised. An excellent example of this was reported by Mendoza *et al*. where a CTG based receptor was designed to bind fullerene molecules in solution.[19] In order to increase the binding efficiency anthracene groups were attached to the CTG which were themselves functionalised in the 9,10-positions with sulfur containing heterocycles (Figure 5.2).

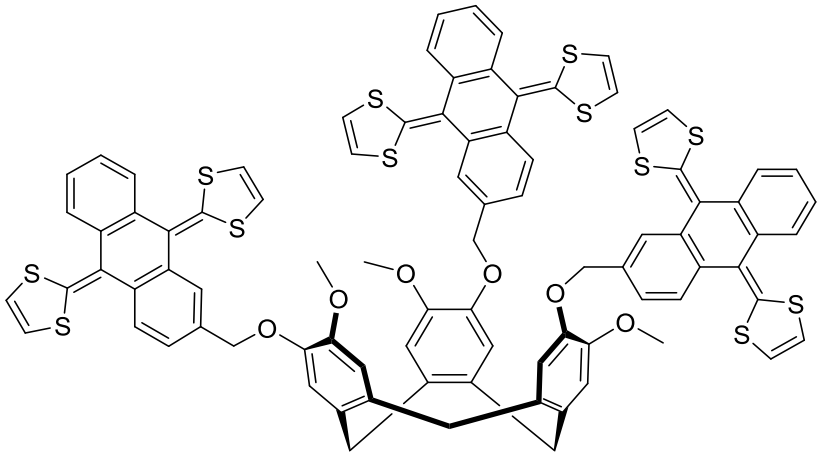

**Figure 5.2.** Structure of exTTF functionalised CTG receptor designed to bind to fullerene guests.[19]

The anthracene groups allowed for extensive π-π interactions with the fullerene guests whereas the sulfur containing groups increased the π electron density within the anthracene groups, permitting stronger interactions between them and the electron deficient fullerene guests. The culmination of these efforts to synthesise a fullerene receptor was realised with the host molecule capable of forming very stable complexes with $C_{60}$ and $C_{70}$ displaying a log$K_a$ of 5.3 and 6.3 respectively.[19]

Whilst functionalisation of the CTV core remains an attractive method for developing host molecules an alternative method is to connect two CTV cores together to produce a cryptophane. A benefit that cryptophanes possess over non-cage like hosts is that the internal cavity is separated from the bulk solvent, presenting a chemical environment that can be tuned to be vastly different to its surroundings, allowing for even stronger guest binding.[20] Dutasta *et al.* have used organic cryptophanes as a host for xenon in both organic and aqueous solvents (Figure 5.3). Despite the only interaction present between the cryptophane and xenon being weak van der Waals interactions, binding constants of 6900 $M^{-1}$ in water and 10000 $M^{-1}$ in organic solvents were obtained.[21, 22] This highlights the potential of cryptophanes as host molecules.

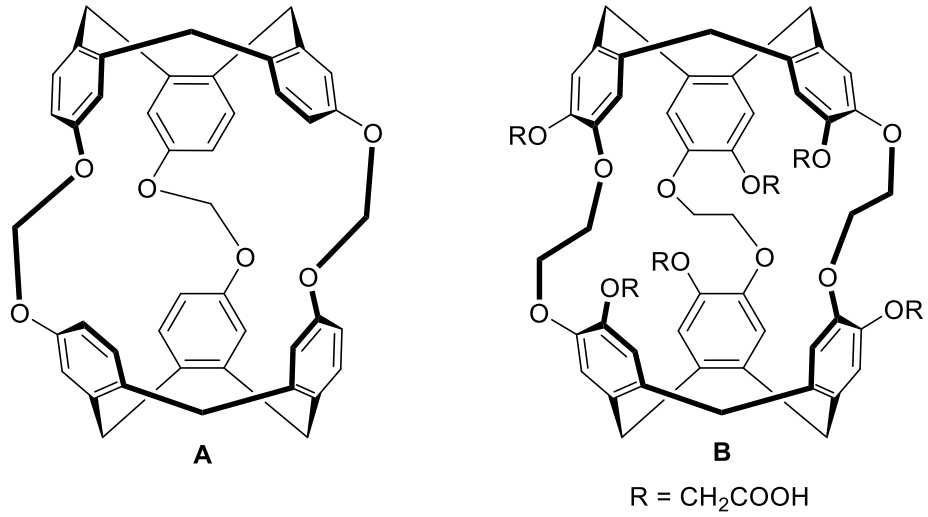


**Figure 5.3.** Structure of organic soluble cryptophane (**A**)[21] and water soluble cryptophane (**B**)[22] hosts capable of xenon binding.

In addition to the class of cryptophanes consisting of purely organic components, cryptophanes containing transition metal elements have been studied. The presence of the transition metal elements have often been used to impart specific functionality to a system. Chiu and co-workers report a cryptophane capable of binding fullerenes in both the solution and solid phase. The cryptophane consists of two CTV units connected by six long alkyl chains comprised of between 10–12 methylene groups.[11] There was a correlation between alkyl chain length and the size of fullerene preferentially bound. The smaller cage consisting of 10 methylene spacers was able to almost exclusively bind $C_{70}$ from a commercial fullerene blend, whereas the cages consisting of 11 and 12 methylene spacers bound the larger fullerene species $C_{76}$/$C_{78}$ and $C_{80}$ respectively.[11] Such a system allows for the separation of higher order fullerenes which traditionally require many cycles of repetitive HPLC in order to obtain. This illustrates the importance of matching the size of the cavity with that of the guest when developing a molecular host, small differences in shape can vastly alter the species that is preferentially bound.[11] Unsurprisingly the cryptophane was only soluble in non-polar organic solvents. Subsequent functionalisation of the arene faces on the CTV bowl with ruthenium cyclopentadienyl adducts increased the solubility of the host-guest system and allowed the dissipation of the host containing the fullerene in aqueous mixtures of alcohols (Figure 5.4).[23] $C_{60}$ is almost completely insoluble in polar solvents such as water and alcohols,[24] the potential to dissolve the fullerene in aqueous solvents expands the potential applications of such systems. Using ruthenium cyclopentadienyl moieties to solubilise cryptophanes was developed by Holman *et al*. and several excellent uses of the approach have been published by the group.[25-27] A good example is the

solubilisation of the cryptophane host **A** (Figure 5.3) which still retains the ability to bind xenon in aqueous solvents.[28]

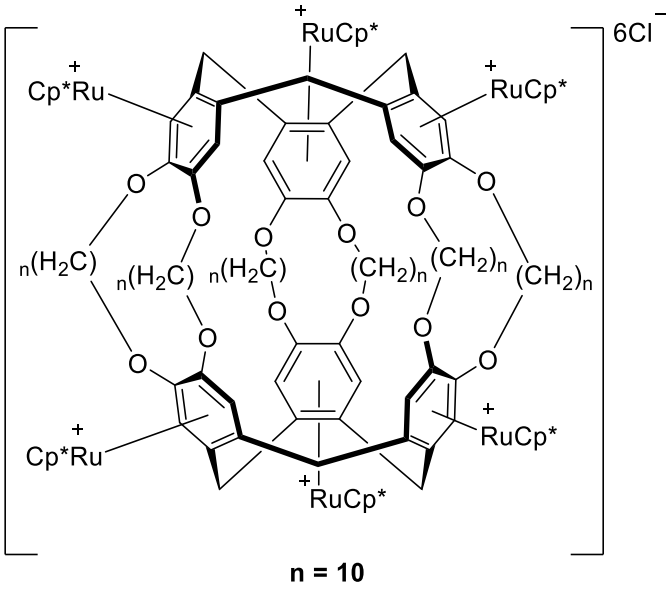


**Figure 5.4.** $[(\eta^5\text{-Cp}^*)\text{Ru}]^+$ coordinated to the arene faces of the CTV bowl improve aqueous solubility of fullerene cryptophane host.[28]

The Hardie group has published several examples of cryptophane systems exhibiting host-guest behaviour.[29-33] One of the first examples utilised a disulfide lined cryptophane that has the smallest cavity reported for a cryptophane at approximately 40 Å (Figure 5.5). Rebek's rule of packing dictates that the greatest binding efficiencies are obtained when the ratio of guest volume to the volume of the host cavity is 0.55.[34] A single molecule of methane has an estimated volume of 28 Å. This is close to the ideal size of guest for the cryptophane and indeed the cryptophane was shown to be capable of binding methane in organic solvents.[29]

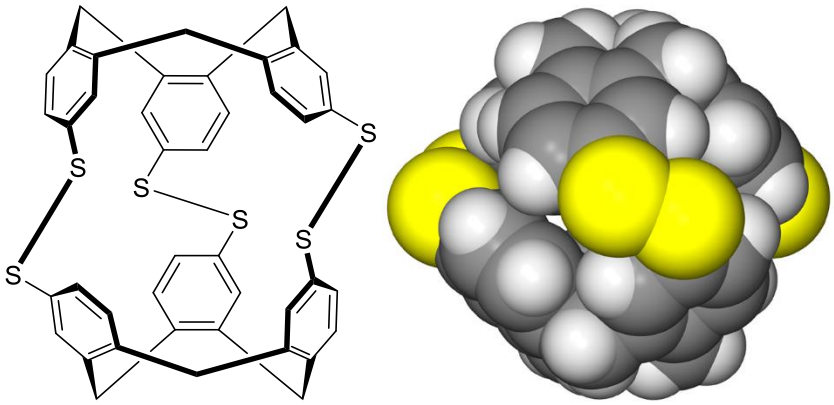

**Figure 5.5.** Structure of disulfide linked cryptophane (left) capable of binding methane in solution. SCXRD structure (right) highlights the small size of the internal cavity.[29]

More recent examples of guest binding from the Hardie group have focused upon systems employing metallo-cryptophanes. Henkelis *et al*. has shown that a palladium metallo-cryptophane made from 4-pyridyl functionalised CTG can bind iodine.[30] Crystals of the complex are capable of taking up iodine in the solid-state. Interestingly there are no obvious channels between the cavities in the solid-state meaning that the iodine molecules must diffuse through the crystal lattice, taking advantage of the small degree of molecular motion still present in the crystal and the ease of polarising the electron cloud of iodine. The presence of iodine within the crystal lattice was determined using single crystal X-ray diffraction (Figure 5.6).

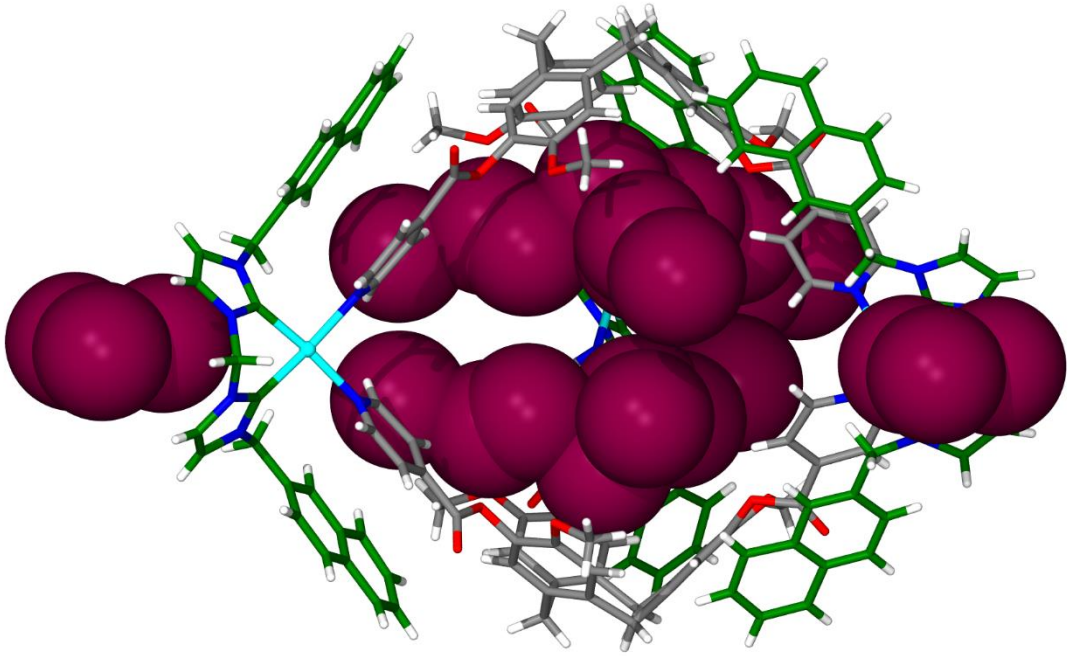

**Figure 5.6.** SCXRD structure of $Pd_3L_2$ cryptophane displaying the uptake of $I_2$ in the solid state.[30]

Metallo-cryptophanes synthesised with metal cations employing non-anionic ligands results in a cationic cage species. This improves the ability to bind anionic species as this results in favourable electrostatic interactions between cage and guest. Cookson *et al.* has reported the binding of anionic surfactant molecules sodium octyl-, decyl-, and tetradecyl sulfate (SOS, SDS, STS) within a $Pd_6L_8$ stella-octangula cage framework. The surfactant molecules were found to reside within the cage framework in a 1:2 HG ratio (Figure 5.7). ROESY NMR was used to elucidate the nature of the interaction by detecting which parts of the cage and surfactant molecules were held together close in space. Through space couplings were observed between the negatively charged surfactant head group and the protons close to the palladium cationic

centres. This shows that electrostatic interactions are a contributing factor to the binding of the surfactant molecules within the cage framework.

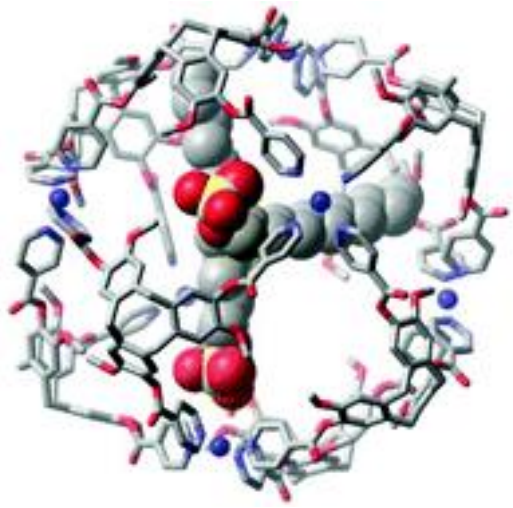

**Figure 5.7.** Molecular model of palladium stella-octangula cage with two surfactant guest molecules residing inside.

### 5.1.2 Photoswitchable Host-Guest Systems

There are numerous examples of metallo-supramolecular systems bearing photoresponsive groups that are able to change shape in response to light.[35] However most of these examples bear pendant photoswitchable groups which are not integral to the framework of the system and reside either *exo* or *endo* to the cage cavity. However, such systems are still capable of modulating the binding affinities of guests with the use of light.

An elegant example of this principle has been reported by Rebek and co-workers.[36] A cavitand was synthesised bearing an azobenzene group attached to the framework (Figure 5.8). The cavitand was shown to bind guest molecules such as 1-chloroadamantane or 2-andamantanone. Adamantanes bearing hydrogen bonding groups were found to bind an order of magnitude stronger within the cavity due to hydrogen bonding interactions with the amide groups on the rim of the bowl. It was envisioned that switching of the azobenzene group from *trans* to *cis* would result in ejection of the guest as the azobenzene moved to occupy the cavity. However this phenomenon was only observed when R = $^{t}$Bu and not when R = H. The $^{t}$Bu group was able to interact with the arene rings of the cavitand, forming favourable CH-π interactions and as a result would move to fill the cavity upon photoswitching.[36] In contrast, the absence of this group meant such favourable interactions could not form so the *cis* form had no driving force to occupy the cavity and as a result would not eject a bound guest molecule. The $^{t}$Bu variant was capable of completely

ejecting any bound guest molecule. This highlights the significance of intramolecular interactions and the filling of a cavities volume when designing a functional molecular host.

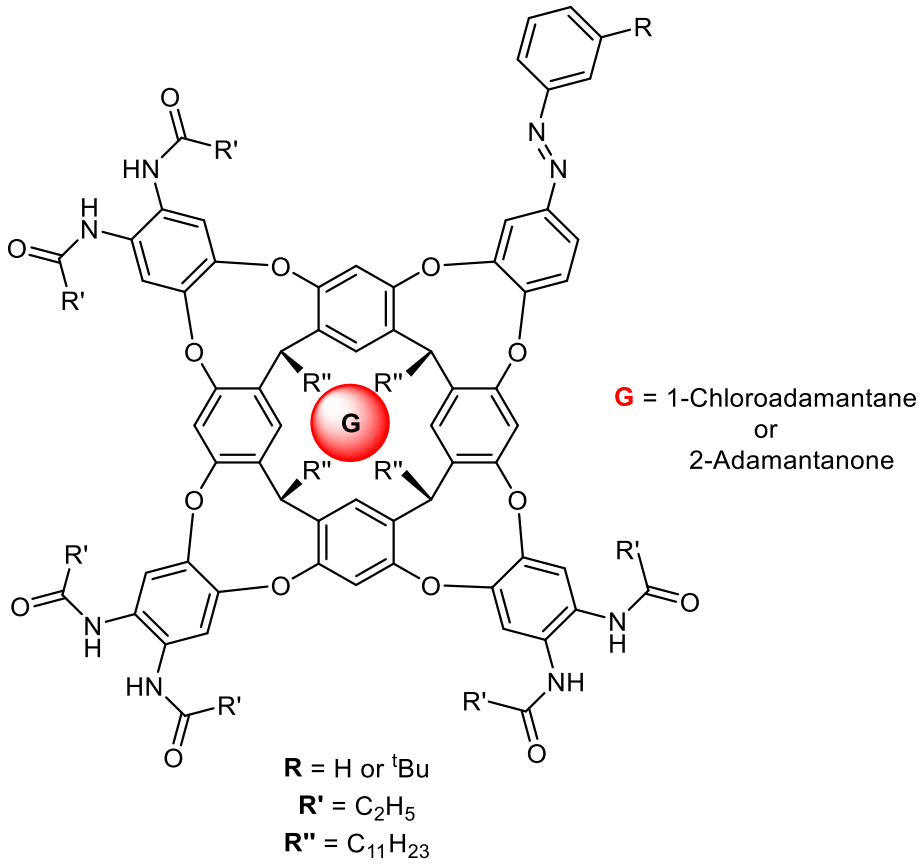


**Figure 5.8.** Example of a photoswitchable host system reported by Rebek and co-workers where an adamantane guest is ejected following the *trans* to *cis* photoswitching of an azobenzene group.[36]

Several organic hosts containing photoswitchable groups have been reported which have the ability to change the binding affinities of guests by photoisomerisation of these moieties.[37, 38] The Houk group have reported a carcerand which can interconvert to a hemicarcerand photochemically.[39] This was achieved by functionalising a hemicarcerand with two anthracene groups (Figure 5.9). Irradiation with 350 nm light caused the photodimerisation of these molecules which reacted to join the top and bottom of the carcerand, effectively closing it off. The reverse reaction could be promoted by irradiation at 254 nm, which split the anthracene dimer, opening the cage and reforming the hemicarcerand. The group synthesised a gated container molecule which could be opened or closed with the irradiation of an appropriate wavelength of light. Moreover, the open hemicarcerand form was shown to uptake 1,4-dimethoxybenzene in diphenylether solution. No evidence of guest uptake was observed for either open or closed species in chloroform. However, after guest uptake in diphenyl ether had occurred the cage could be closed by

irradiation with light and re-dissolved in chloroform. The host-guest species was stable under these conditions for several weeks. The dimerisation of the anthracene groups decreases the size of the cage portals and thus raises the activation energy of decomplexation, making the host-guest species stable. Upon opening of the cage portals with 254 nm light the guest was immediately decomplexed and replaced with the solvent chloroform.[39]

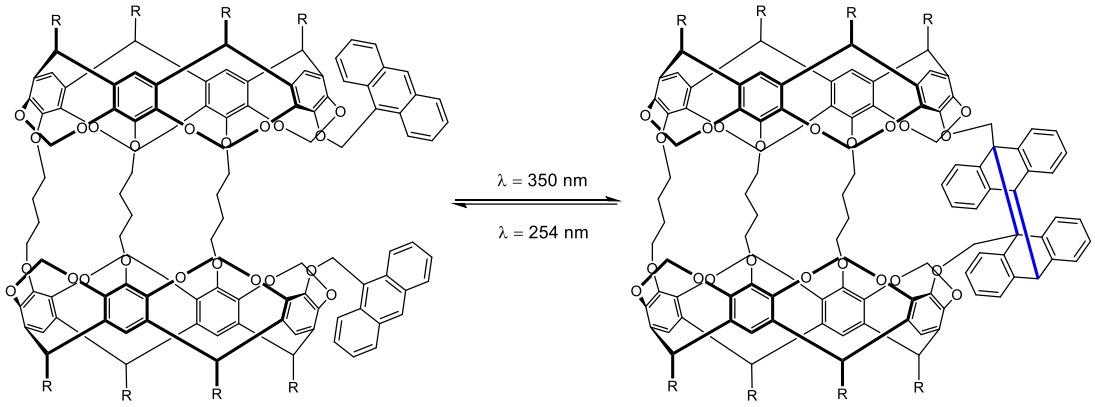


**Figure 5.9.** Structure of Houk's gated container molecule, capable of uptake and release of 1,4-dimethoxybenzene in solution.[39]

One of the only examples of a photoswitchable metallo-cage where the photoswitches themselves are embedded within the framework of the cage has been reported by Clever *et al*.[40] Their approach was to use dithienylethene (DTE) units in banana shaped ligands which would self-assemble in the presence of $Pd^{2+}$ cations to form a $Pd_2L_4$ type cage. The 'open' or 'closed' cage could be formed by photoswitching the ligand to it's appropriate state and then assembling with palladium cations. Conversely, the cage could be assembled first and subsequent photoswitching of the entire cage would result conversion to the 'open' or 'closed' form depending on the wavelength of light used.[40] Unusually for systems made up of labile coordination bonds the entire cage remained intact during this process. What is often observed for such systems is a rearrangement into a different cage species or total dissolution of the cage framework.[41] The switching of a DTE unit only results in a small change in shape, as such the difference between an 'open' and 'closed' cage is very subtle. Nevertheless the cage was found to associate with a $B_{12}F_{12}^{2-}$ guest two orders of magnitude stronger in the open conformation compared to the closed conformation. The reason for this is unclear, one possible explanation being that the open cage has greater structural flexibility and the presence of the guest results in an induced fit, with more favourable interactions between host and guest. However, Van't Hoff analysis reveals that the process is entropically driven. The displacement of high energy solvent from the internal void is likely to be the main driving force

for the encapsulation, with the induced fit between host and guest serving to form an even stronger interaction between the pair.[40]

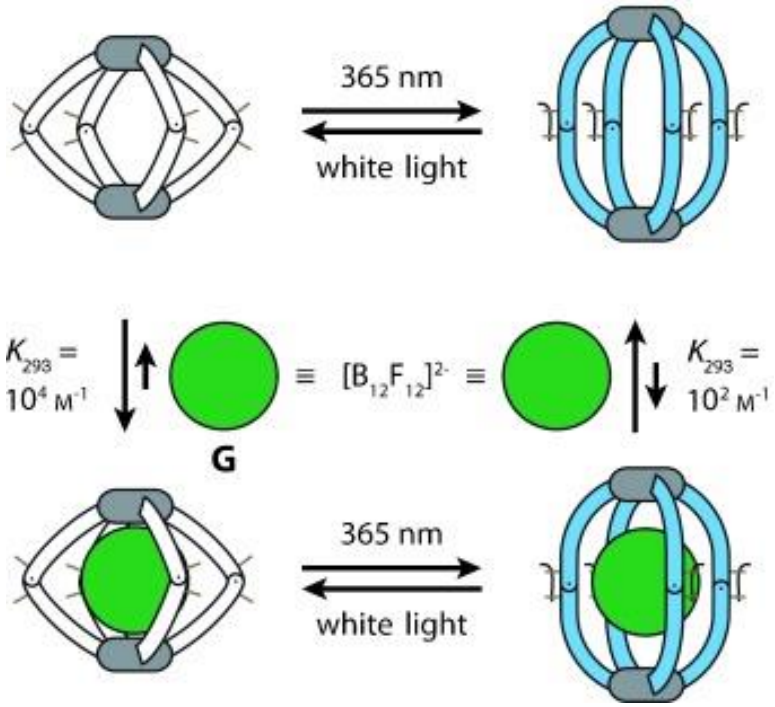


**Figure 5.10.** $Pd_2L_4$ Metallo-cage reported by Clever *et al*. photoswitching of the dithienylethene group results in uptake or release of a $B_{12}F_{12}^{2-}$ guest.[40]

This cage remains the most sophisticated example of guest binding control in a metallo-cage with the use of light.

## 5.2 Palladium Azobenzene Cryptophanes as Host Molecules

In order to ascertain the host-guest behaviour of the metallo-cryptophanes discussed in the previous Chapters, a range of guests were screened to evaluate their behaviour in the presence of the hosts. $^1$H-NMR spectroscopy was used to detect if any change in the chemical shifts of the host or guest could be observed when the two species were combined. Particular focus was given to the palladium cryptophanes as host molecules, due to the stability of the hosts in DMSO. The high solubilising potential of DMSO allowed for a wider range of guest species to be screened. The guests screened included $C_{60}$, $C_{70}$ $Cs_2B_{12}F_{12}$, sodium alkyl sulfates, haloalkanes and napthalamide derivatives. Of these candidates no interactions were observed for the large spherical non-polar guests, namely the fullerenes and the caesium dodecarborate. This is unusual as CTV based derivatives have a well-documented ability to encapsulate such species.[14, 42] However, strong evidence has been obtained that the sodium alkyl sulfates as well as a

napthalamide derivative all interact with the palladium cryptophane in solution. The remainer of this Chapter will discuss the nature of these interactions and the behaviour of the host-guest complex in further detail.

### 5.2.1 Interactions Between Palladium Cryptophanes and Napthalamide Derivatives

The first guest that was selected for host-guest studies was a functionalised napthalamide (**G1**) (Figure 5.11). The structure of **G1** contains a number of useful features which encourage its use as a guest molecule. The first such feature is the presence of both polar and non-polar domains. This could be used to good effect as the metallo-host contains both polar and non-polar regions and it can be envisaged how the like for like matching of these domains could lead to a strong host-guest complex through electrostatic forces and hydrophobic interactions respectively. Secondly, the presence of an extensive π cloud could result in π-π stacking interactions with the numerous arene rings present on the host. In addition, the molecule has a distinctive UV/vis spectrum and it is fluorescent. Both of these properties permit the use of a UV/vis or fluorescence titration experiments as a second method to corroborate the results obtained from the $^{1}$H-NMR titration. This was indeed the initial plan, however for reasons discussed in the previous Chapter, subsequent studies have shown that the metallo-cryptophanes are unstable at concentrations suitable for UV/vis and fluorescence spectroscopic techniques and as a result, the experiments were impossible to perform.

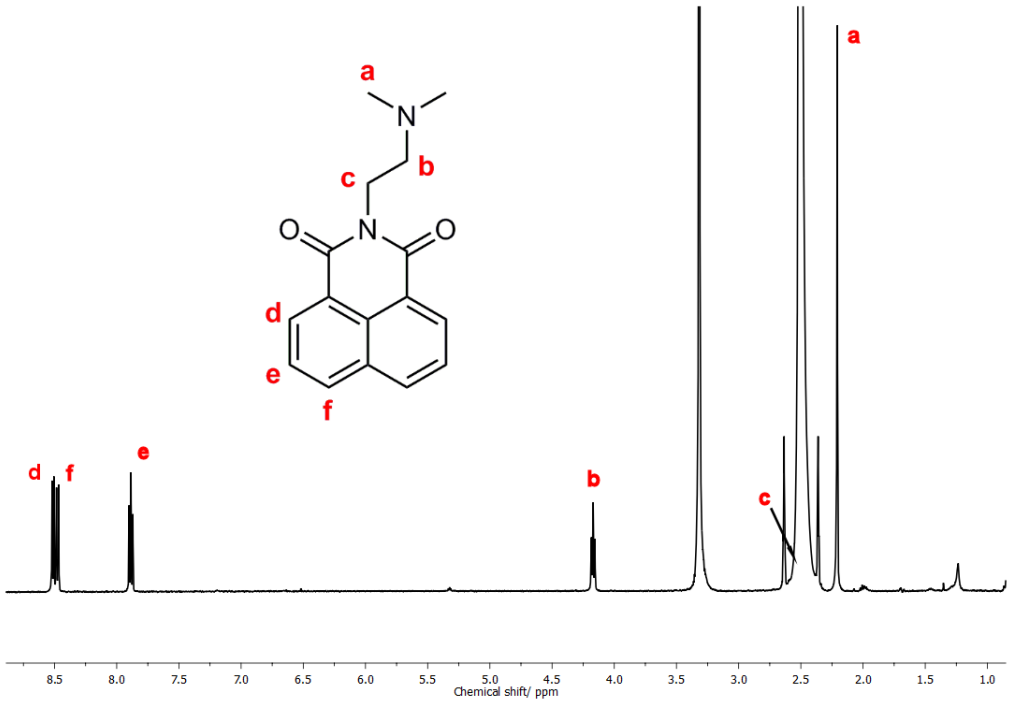


**Figure 5.11.** $^{1}$H-NMR (500 MHz, $d_6$-DMSO) of **G1**, the molecule contains a number of desirable features, beneficial for its use as a guest molecule for CTV based hosts.

$^{1}$H-NMR spectroscopy remained a viable tool to determine the binding efficiencies of the system. The initial titration experiment was performed using **G1** and the palladium metallo-cage **C19**. The changes in the $^{1}$H-NMR resonances were most pronounced for the protons found on **G1**, namely protons Ha, Hb and Hc. This implies that the alkyl chain of the guest was interacting strongly with the host. Unfortunately the signal for proton Hc was obscured by solvent and host peaks during the titration whereas the Ha signal shifted downfield during the titration and resided under the residual solvent peak. For this reason the only peak that significantly shifted and could be monitored during the entirety of the experiment was Hb. As the proton signals originating from the guest were to be monitored during the titration, keeping the concentration of this species constant during the process would simplify analysis as it would eliminate interactions originating from guest self-association from convoluting the binding isotherm. This procedure was initially attempted with a concentration of the host ranging from 0.06 – 1.4 mM. The results from this experiment can be seen in Figure 5.12 and definite shifts derived from association of the guest to the host were observed.

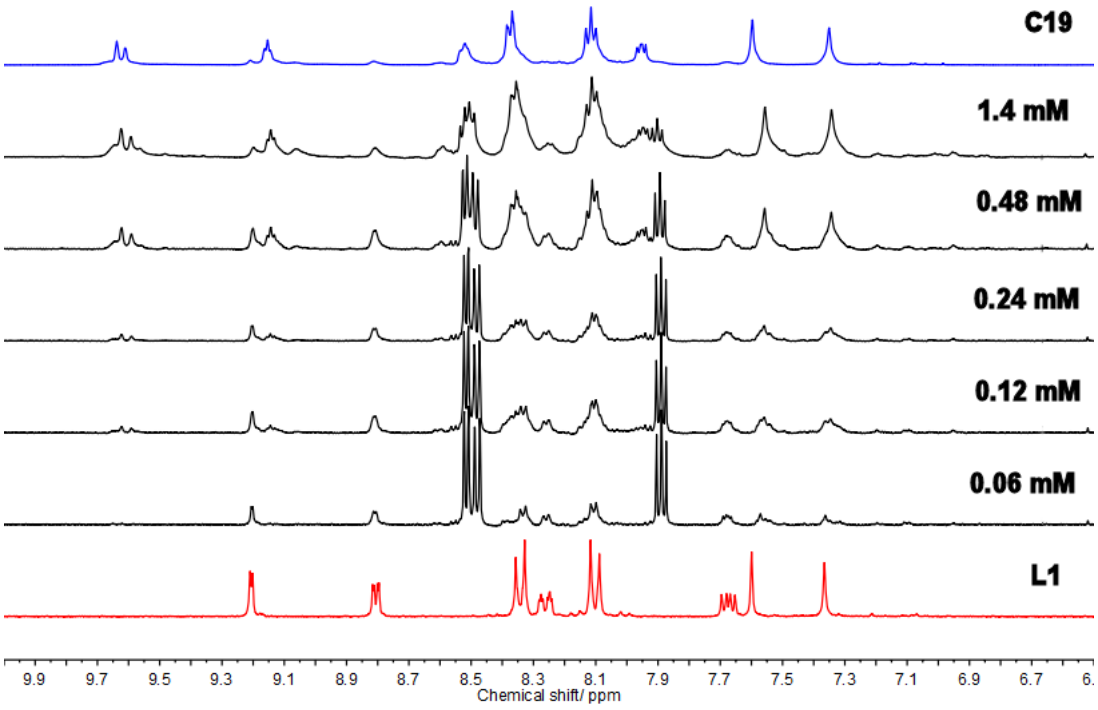


**Figure 5.12.** Stacked $^{1}$H-NMR (500 MHz, $d_6$-DMSO) of **G1** and **C19** titration experiment where [**G1**] is constant at 0.24 mM and [**H**] is decreasing from 1.4 – 0.06 mM (**black**). Degradation of host at low concentrations is evident when compared to fully formed host (**blue**) and **L1** (**red**).

The interaction is fast relative to the NMR timescale as the individual peaks for free **G1** and **G1@C19** cannot be resolved and instead a single coalesced signal was observed. Whilst the results do seem to indicate that guest binding is occurring, closer analysis of the aromatic region reveals that dissociation of the cage is beginning to occur at the lower end of the concentration range. Extrapolating reliable binding constants from binding isotherms is highly dependent upon accurate measurements of host and guest concentrations and unfortunately the data obtained from this experiment cannot be reliably used. Repeating this same experiment at a concentration high enough to completely remove the possibility of host dissociation would be prohibitive in terms of the amount of material required. Therefore a different approach was sought after.

Whilst not desirable to vary the concentration of the species being monitored in a $^{1}$H-NMR titration, the practicalities of this particular experiment necessitated this approach. However, the behaviour of the guest under varying conditions must first be determined. A self-titration of the guest was performed where the concentration of the guest was varied over the range to be used in the guest binding experiment (Figure 5.13). This revealed that the guest does self-associate in DMSO solution, most notable were the upfield

shifts signals corresponding to the protons on the naphthalene groups. This phenomenon has been reported before by similar molecules in the literature and has been attributed to π-π stacking of these groups in solution.[43] This presents a problem as fitting a binding isotherm in a 1:1 HG system for example requires the simultaneous determination of three variables; the chemical shift of the free guest, the chemical shift of the HG complex and the equilibrium constant *Ka*. Usually the chemical shift of the free guest is known as it can be determined experimentally. This simplifies the equation as only two unknown variables need to be solved. However, in the case of this system the signals of the free guest change with respect to the concentration and as the concentration of the guest is being varied the value of free guest cannot be ascertained experimentally. To further compound the issue two further values must be added to the equation to fit the curve, the chemical shift of the 2**G1** complex as well as the equilibrium constant this process *Ka(2G)*. This significantly increases the complexity of the system and makes obtaining reliable binding constants more difficult, albeit not impossible.

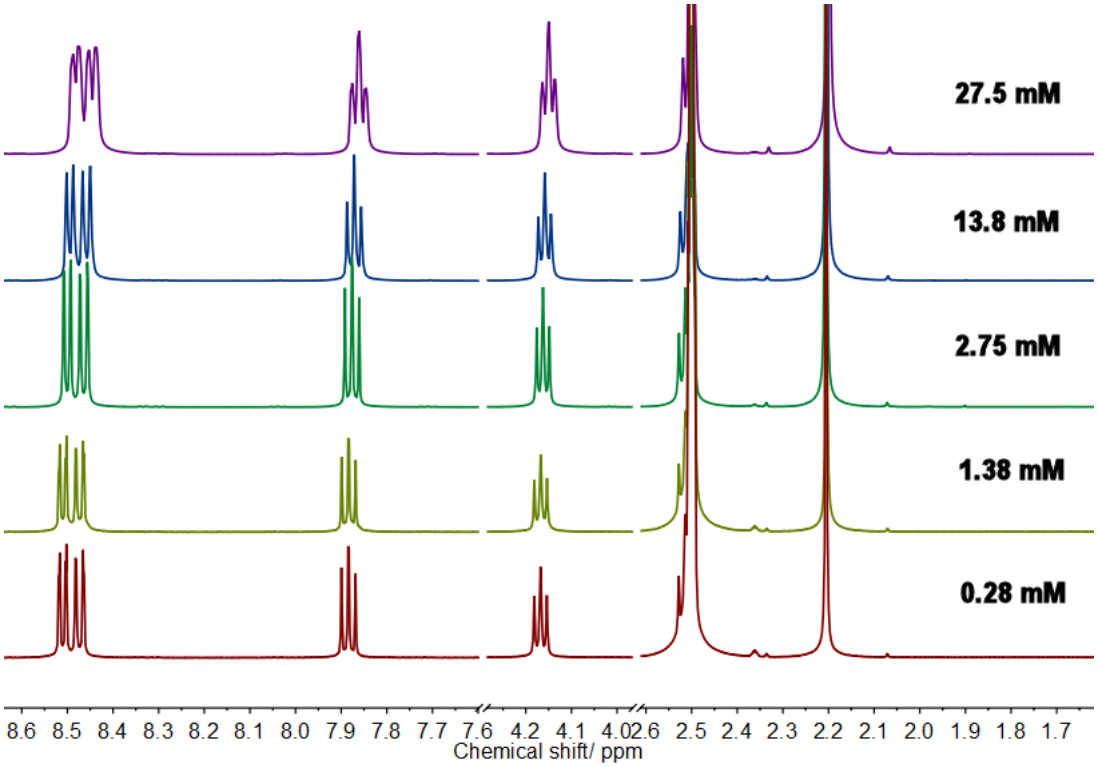


**Figure 5.13.** Self-titration of **G1** monitored by $^{1}$H-NMR, subtle shifts of the proton environments are observed.

The behaviour of **G1** in DMSO has been established and the behaviour of **G1** in the presence of host could now be probed. Another $^{1}$H-NMR titration experiment was performed but as mentioned previously the host concentration was fixed at 2.75 mM whilst the concentration of **G1** was varied over a range of 0.28 mM – 27.5 mM. The results can be seen in Figure 5.14

and once again shifts are observed for the peaks corresponding to **G1**. It is important to note that these shifts are substantially different to those noted for the self-titration of **G1** and therefore not purely a consequence of the change in guest concentration. This same experiment was then repeated with the other $Pd_3L_2$ cages where L = **L2** or **L3** respectively. The results are displayed in Figure 5.15 and Figure 5.16.

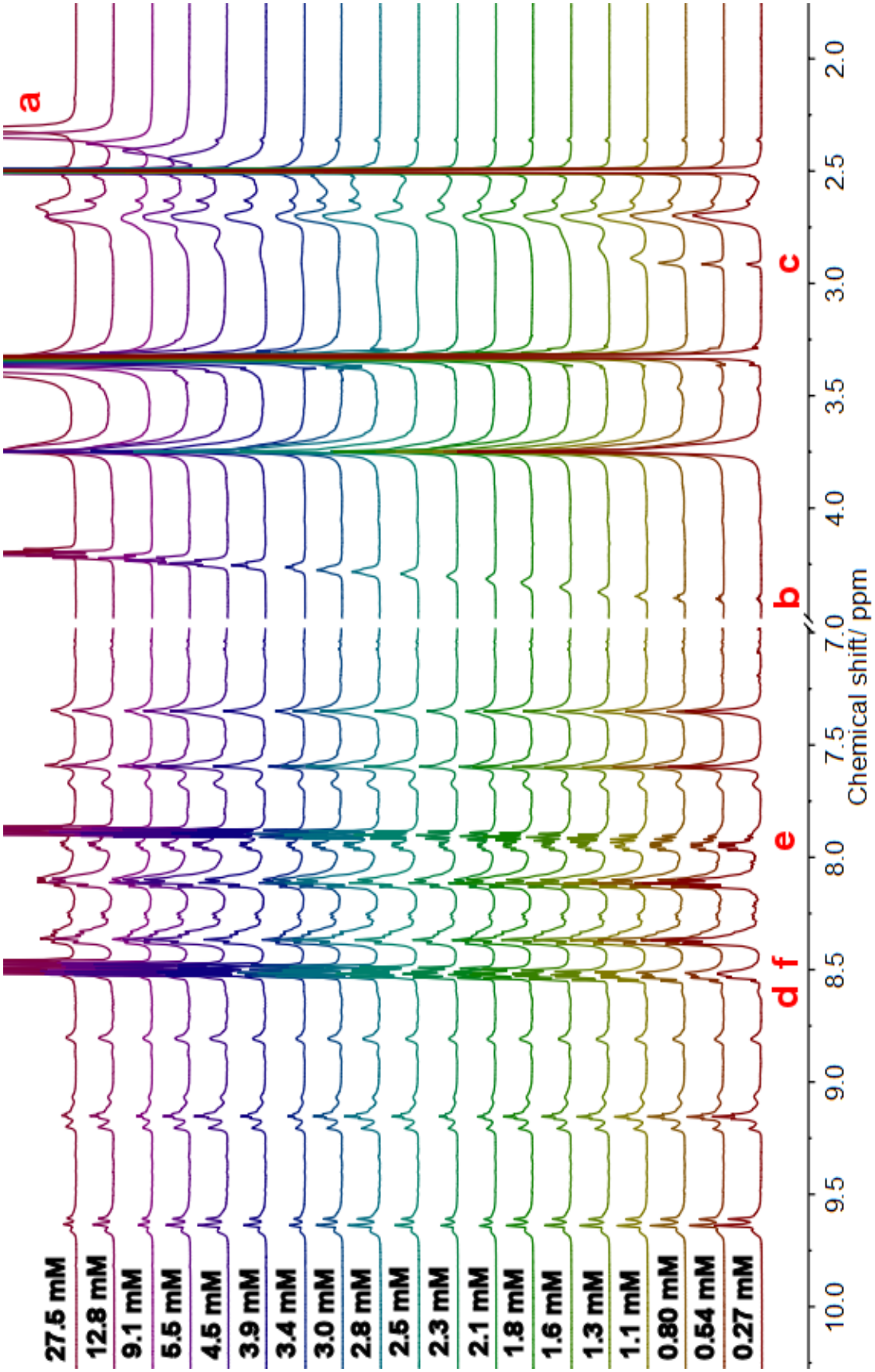


**Figure 5.14.** $^{1}$H-NMR (500 MHz, $d_6$-DMSO) titration of **G1** and **C19** where host concentration is constant (2.75 mM) and guest concentration is varied.

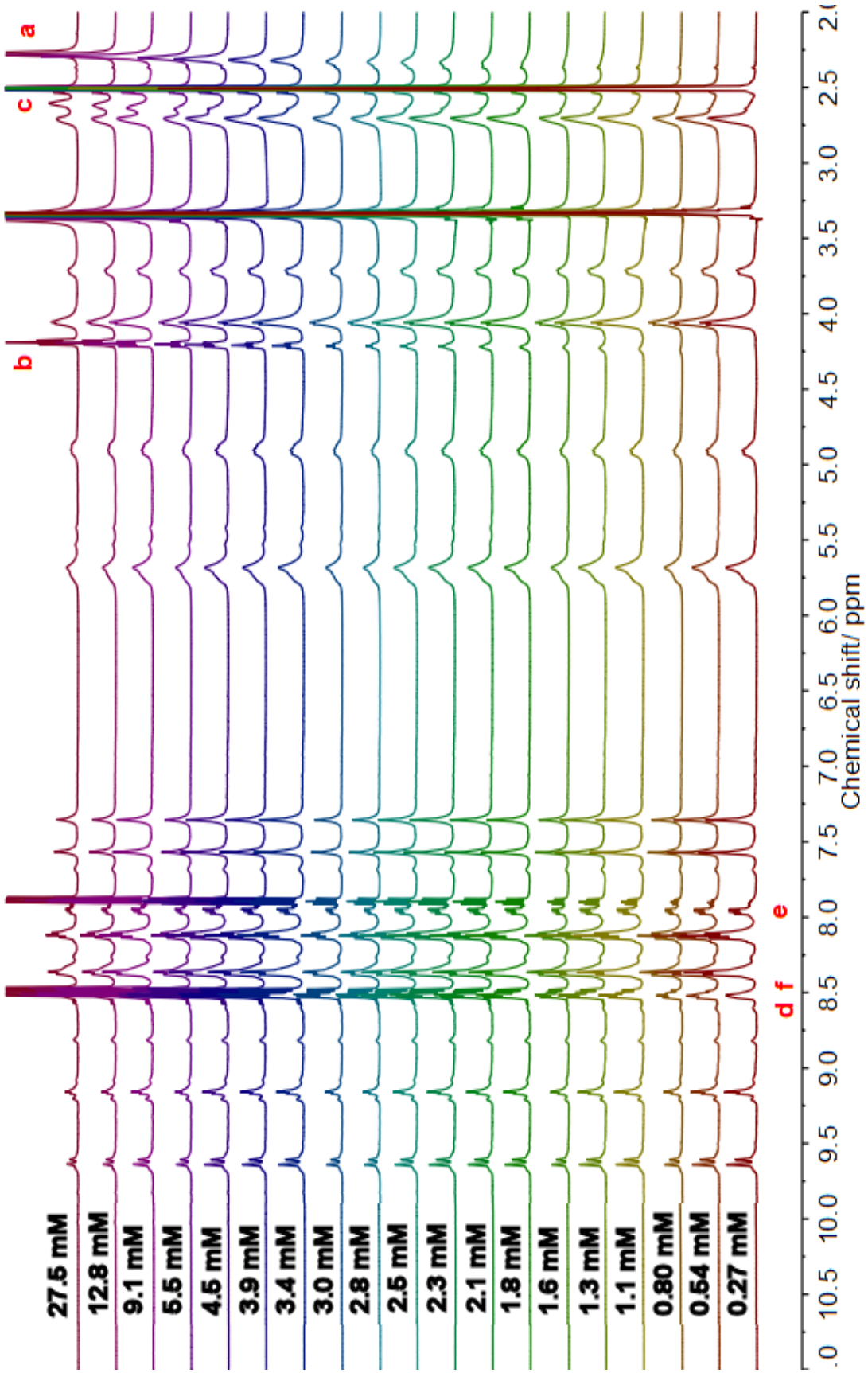


**Figure 5.15.** $^{1}$H-NMR (500 MHz, $d_6$-DMSO) titration of **G1** and **C20** where host concentration is constant (2.75 mM) and guest concentration is varied.

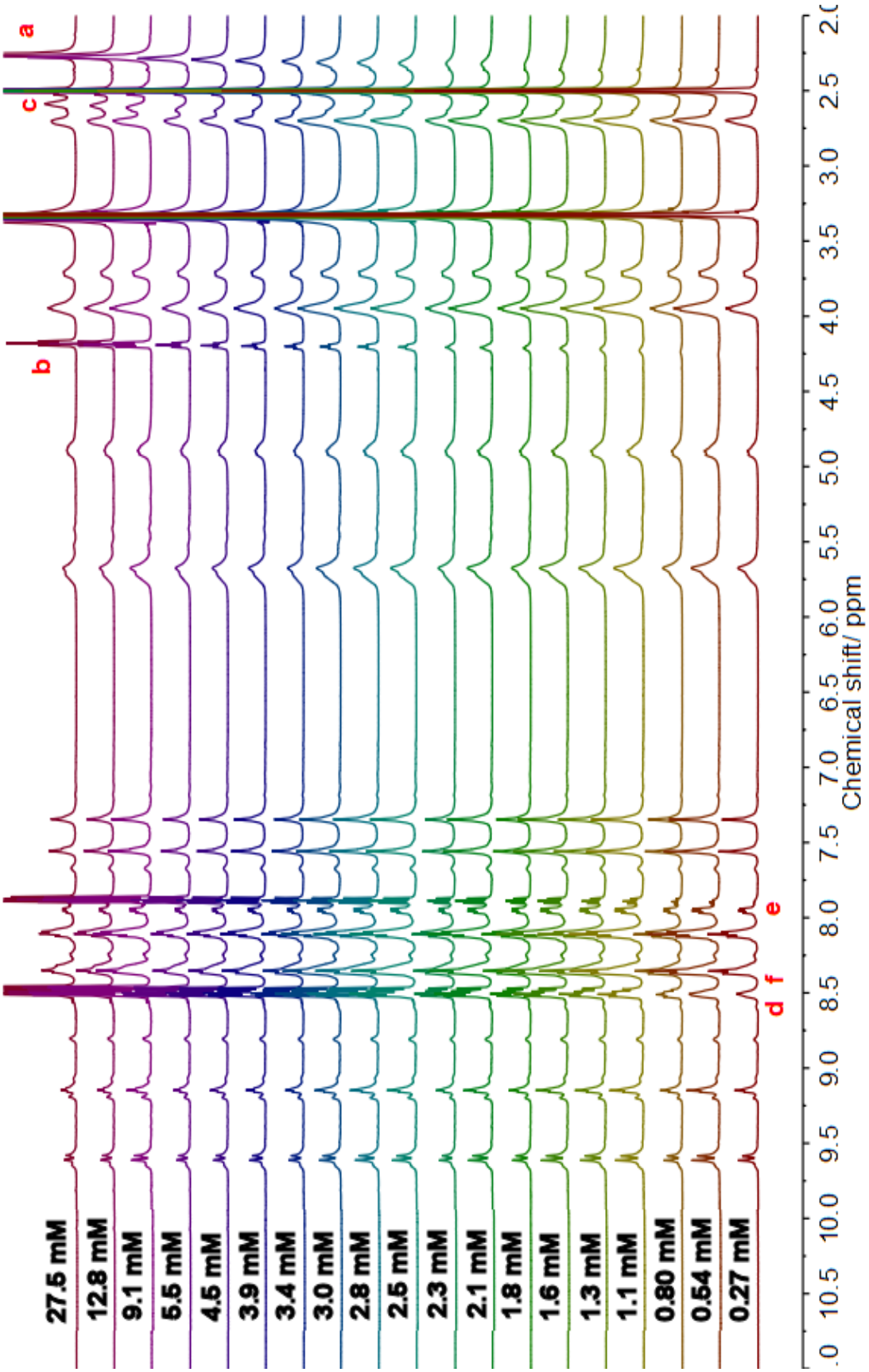


**Figure 5.16.** $^{1}$H-NMR (500 MHz, $d_6$-DMSO) titration of **G1** and **C21** where host concentration is constant (2.75 mM) and guest concentration is varied.

What is immediately apparent is that the use of different ligands alters the dynamics of the host-guest system. In the case where **L1** has been used the system is in fast exchange on the NMR timescale, this is evident as the signal from Hb on **G1** is a clear triplet at the high and low concentration regimes with only a slight broadening at intermediate concentrations.[44] Cages comprised of **L2** and **L3** on the other hand alter the dynamics of the system such that the system is exchanging at a slower rate, approximately in the intermediate exchange region on the NMR timescale (Figure 5.17). When viewing the same proton signal Hb, the expected triplet is only observed at high concentrations of **G1,** where it exists mostly unbound in solution. As the concentration drops the signal broadens out until at very low concentrations, when nearly all of **G1** will be in exchange with a host, the signal broadens out to such a degree it becomes indistinguishable from the baseline. The inclusion of a large ethoxy or propoxy moiety on **L2** and **L3** means that the cage windows will be smaller than for **L1**, which only bears smaller methoxy groups. The smaller cage windows may result in a larger kinetic barrier to encapsulation and de-encapsulation, slowing down the process which has the effect of broadening the NMR signals.[44] The effect of the size of portals between the exterior and interior of a cage and the kinetics of host-guest system is well documented and several examples to support this hypothesis can be found in the literature.[45]

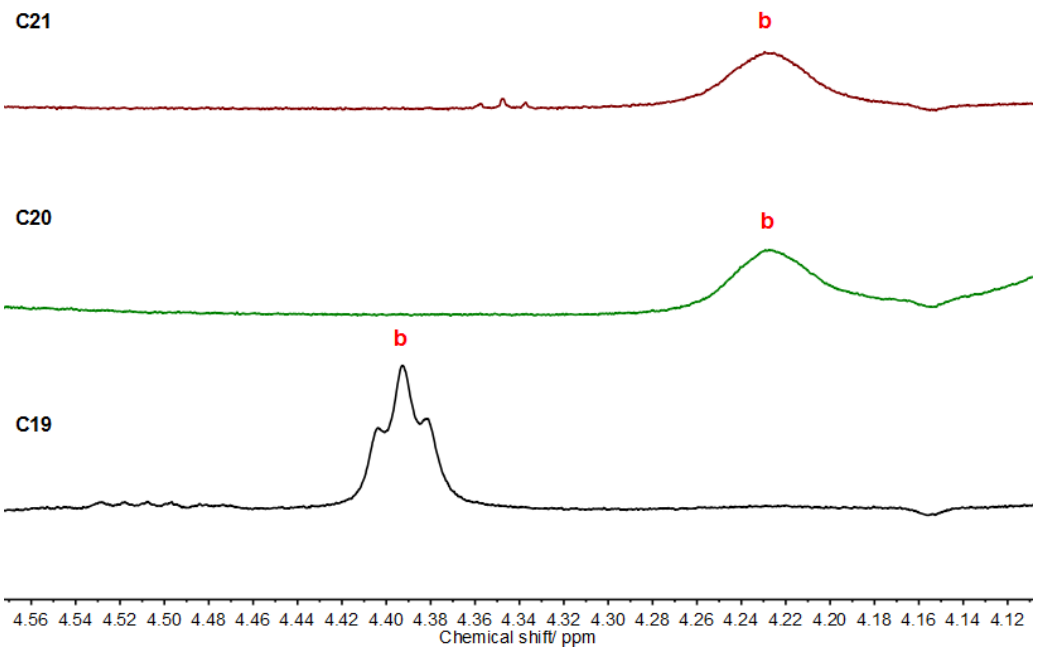


**Figure 5.17.** Comparison between the interaction of **G1** (1.0 M) and cages **C19**, **C20** and **C21** (2.75 M) displaying the faster interaction between **C19** than **C20** and **C21**.

Determining the stoichiometry of a host-guest interaction is pivotal to extracting reliable binding constants from titration data. The usual method to achieve this would be to perform a Job's plot, however this is unsuitable for this system for a number of reasons. First and foremost, as the cage is unstable at concentrations below approximately 0.2 mM all measurements would have to be taken above this concentration. As multiple measurements are required well above this concentration the material cost quickly becomes prohibitive. Moreover, the Job's plot method is considered unreliable for supramolecular systems where multiple stoichiometries of the HG system may exist.[46] As the relative size difference between the host and guest is large, it is highly likely that a stoichiometry greater than a 1:1 HG ratio could theoretically be achieved.

As a consequence the stoichiometry of the system was determined by modelling the binding isotherms as a HG, $HG_2$ and $HG_3$ system using the HypNMR software package.[55] As it has already been confirmed that guest self-association occurs all of the models included a guest dimerisation factor $G_2$. If a model fitted the experimental data well and contained reasonable values for the association constants and chemical shifts it was deemed reliable.

As mentioned previously many guest peaks did not move during the titration or became obscured by the host and solvent peaks. For this reason it was only possible to follow the signal arising from Hb on **G1**. A plot of the chemical shift of Hb vs the concentration of **G1** in the presence of the three different hosts revealed a set of binding isotherms (Figure 5.18).

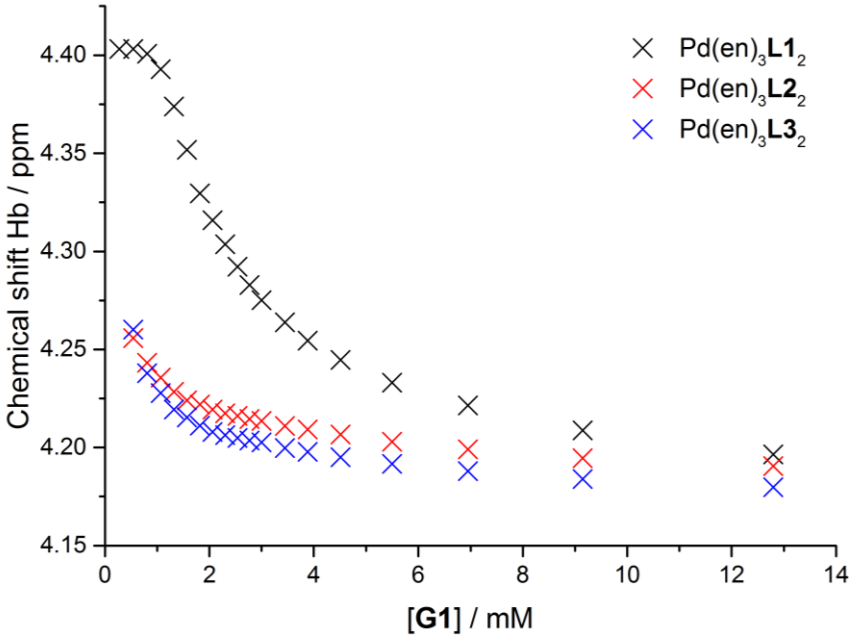


**Figure 5.18.** Plots of the chemical shift of Hb on **G1** vs the concentration of **G1** in the presence of $Pd_3$**Lx**$_2$ cages (**Lx** = **L1**, **L2** or **L3**) ([**H**] = 2.75 mM).

All attempts at fitting these binding isotherms to a HG, $HG_2$ or $HG_3$ system regrettably failed. The NMR data obtained does strongly suggest however that **G1** is binding within the cavity of **C19**-**C21**. In order to provide further evidence that this is indeed occurring a DOSY NMR was acquired of a mixed solution of **C19** and **G1** (Figure 5.19). The diffusion constant for **G1** and **C19** were very similar to each other, despite the vast difference in size between them. This is unexpected and again suggests that a host-guest complex is formed between these two species.

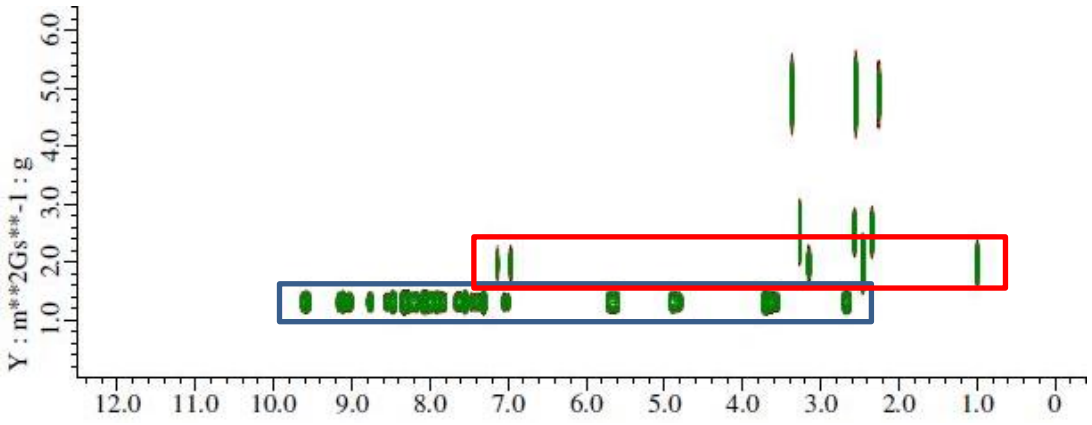


**Figure 5.19.** $^1$H DOSY-NMR (600 MHz, $d_6$-DMSO) of **C19** (blue) and **G1** (red) showing the similar diffusion constant.

### 5.2.2. Encapsulation of Sodium Alkyl Sulfates in Palladium Metallo-Cryptophanes

Despite not yielding any quantitative data on the equilibrium constants the study with **G1** has yielded some interesting insights into the system. Perhaps most notably the likely CH-π interactions suggest that the presence of methyl and methylene groups in a guest may improve the likelihood of a host-guest interaction occurring with this class of host molecules. For this reason, and due to the fact that CTVs have shown an ability to bind them before,[31] sodium alkyl sulfates were examined to determine whether any host-guest interaction took place. Sodium octyl sulfate (SOS) was chosen as the candidate for these tests. The linear shape of this guest molecule means that it should easily pass through the cage portals into the interior. The large amount of methylene groups present on this molecule were envisioned to interact with the multiple arene rings on the host in a CH-π fashion. Whereas the negatively charged sulfate head group has the potential to electrostatically interact with the positively charged palladium centres. The structure of SOS is shown below (Figure 5.20) along with the $^1$H-NMR spectrum in $d_6$-DMSO.

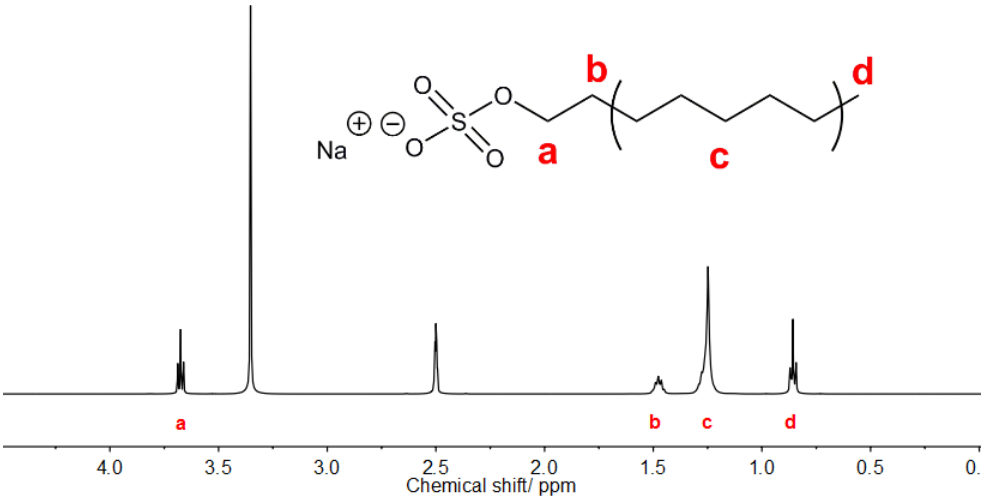


**Figure 5.20.** $^1$H-NMR (500 MHz, $d_6$-DMSO) of SOS at 298 K

As the concentration of the guest molecule was to be varied during the course of the experiment a self-titration of the SOS was performed to determine whether any self-association occurred and if this resulted in changes in the NMR spectrum. The results can be seen in Figure 5.21. Although subtle, definite shifts do occur during the titration, most notably for the signal arising from proton $H_a$. This is not surprising as SOS is a surfactant molecule and is capable of forming micelles. Fortunately however, all of the concentrations tested were below the critical micelle concentration (CMC) of SOS in water which has a value of 0.11 $M^{-1}$.[47] The experiments are performed in DMSO

which usually has the effect of causing the cmc to be larger than when measured in water.[48] This is due to the more effective solvation of the sodium cations by DMSO which inhibits favourable electrostatic interactions on the micelle surface.[48] For the related molecule sodium dodecyl sulfate (SDS) the cmc is 8 mM in water, but goes up to 30 mM in DMSO.[49] This implies that although aggregation is occurring in solution at the concentrations tested no large micelle like structures are forming which would complicate the analysis of the binding isotherms.

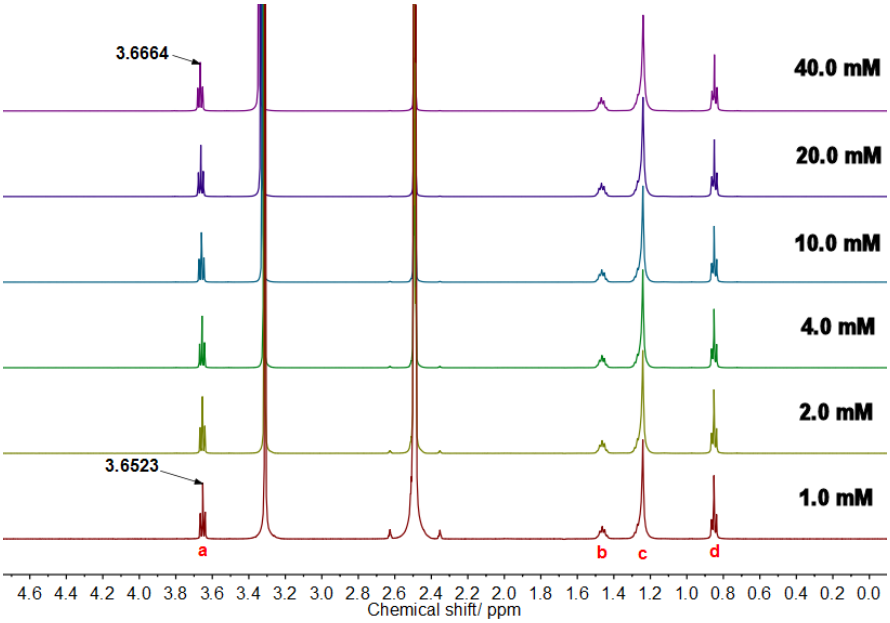


**Figure 5.21.** $^{1}$H-NMR (500 Hz, $d_6$-DMSO) of SOS over a concentration range of 1.0 mM – 40 mM.

Now that the solution state behaviour of SOS in DMSO is understood, a $^{1}$H-NMR titration experiment can be performed in the presence of a host molecule. Once again the initial experiment focused upon the host molecule **C19**. The experiment was performed identical to before where the host concentration is kept constant at 3.85 mM. Aliquots of a stock solution containing 3.85 mM of host and a large excess of guest were added in portions to the NMR tube so that the guest concentration was varied between 1.0 mM – 40.0 mM (Figure 5.22). Definite upfield shifts of all the proton environments on the SOS molecule were detected when the [H]:[G] ratio was large. The interaction was occurring fast relative to the NMR timescale as no resolvable peaks were observed for unbound and bound guest. When more SOS was added and the [H]:[G] ratio became smaller, the shifts began to revert back to the approximate values of the unbound SOS molecule as a greater ratio of unbound guest was present in solution at any given moment. The same experiment was repeated with cages **C20** (Figure 5.23) and **C21** (Figure 5.24), with all systems behaving in a similar fashion.

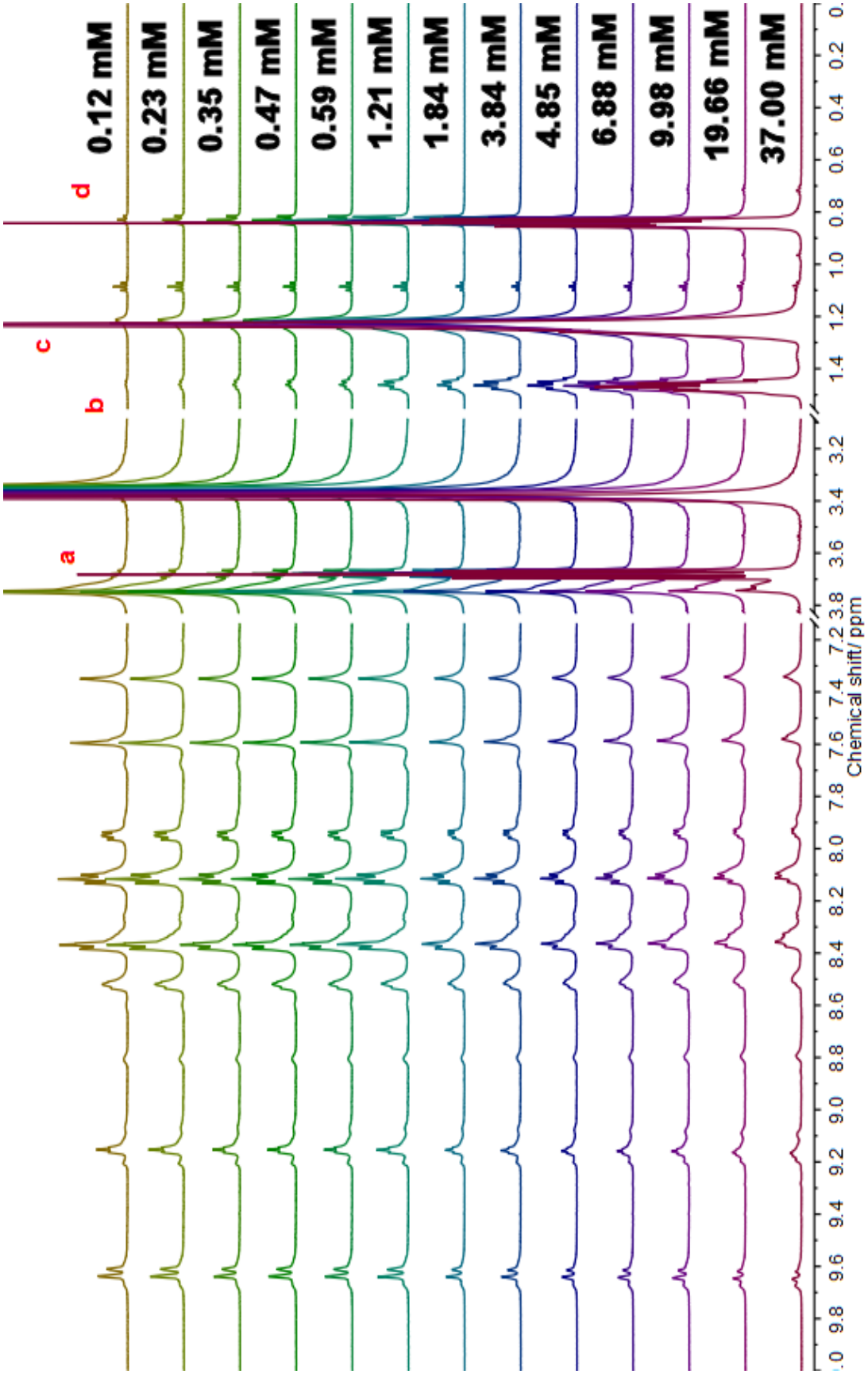


**Figure 5.22.** $^{1}$H-NMR (500 MHz, $d_6$-DMSO) of **C19** (3.85 mM) in the presence of varying concentrations of SOS.

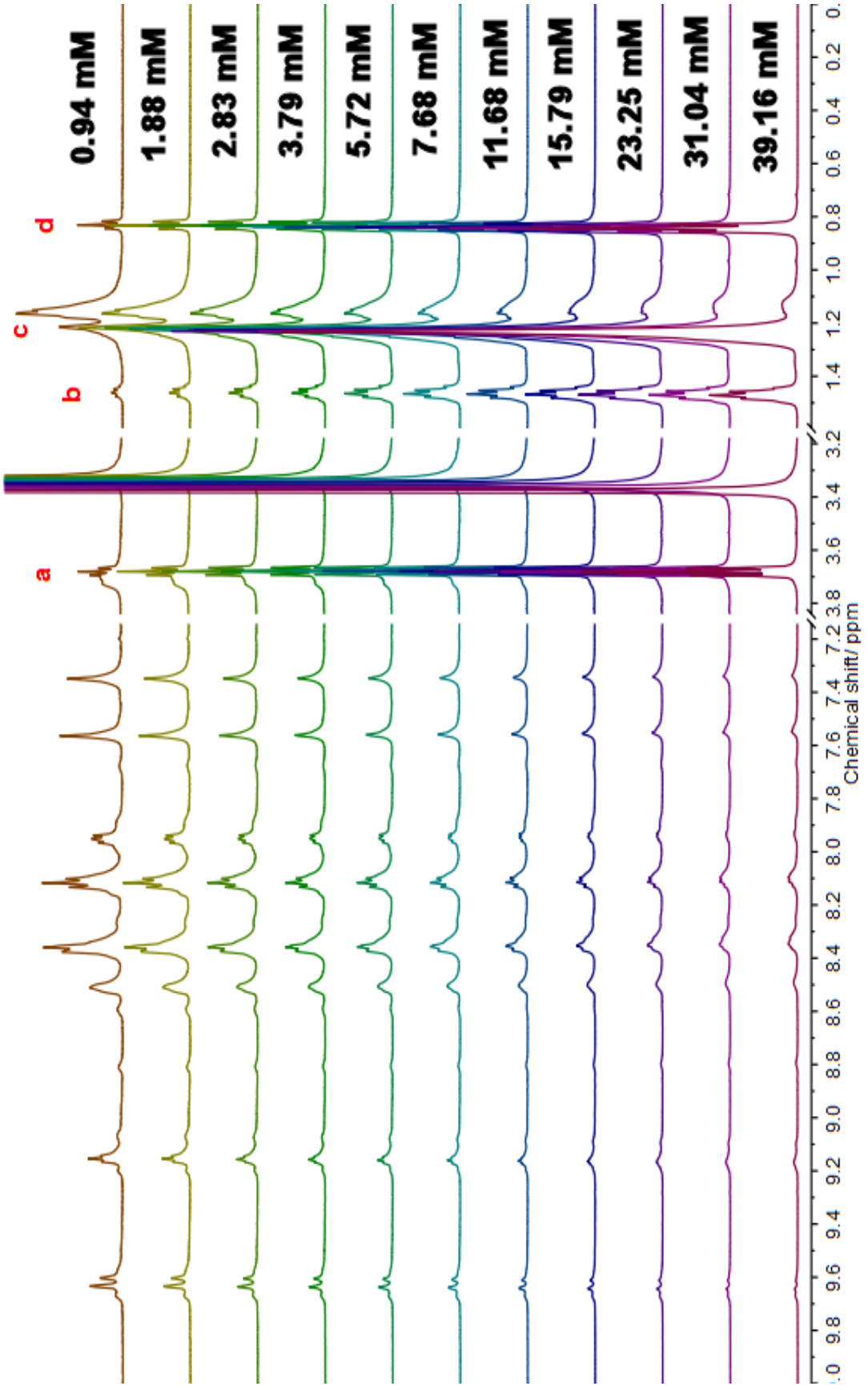


**Figure 5.23.** $^{1}$H-NMR (500 MHz, $d_6$-DMSO) of **C20** (3.85 mM) in the presence of varying concentrations of SOS.

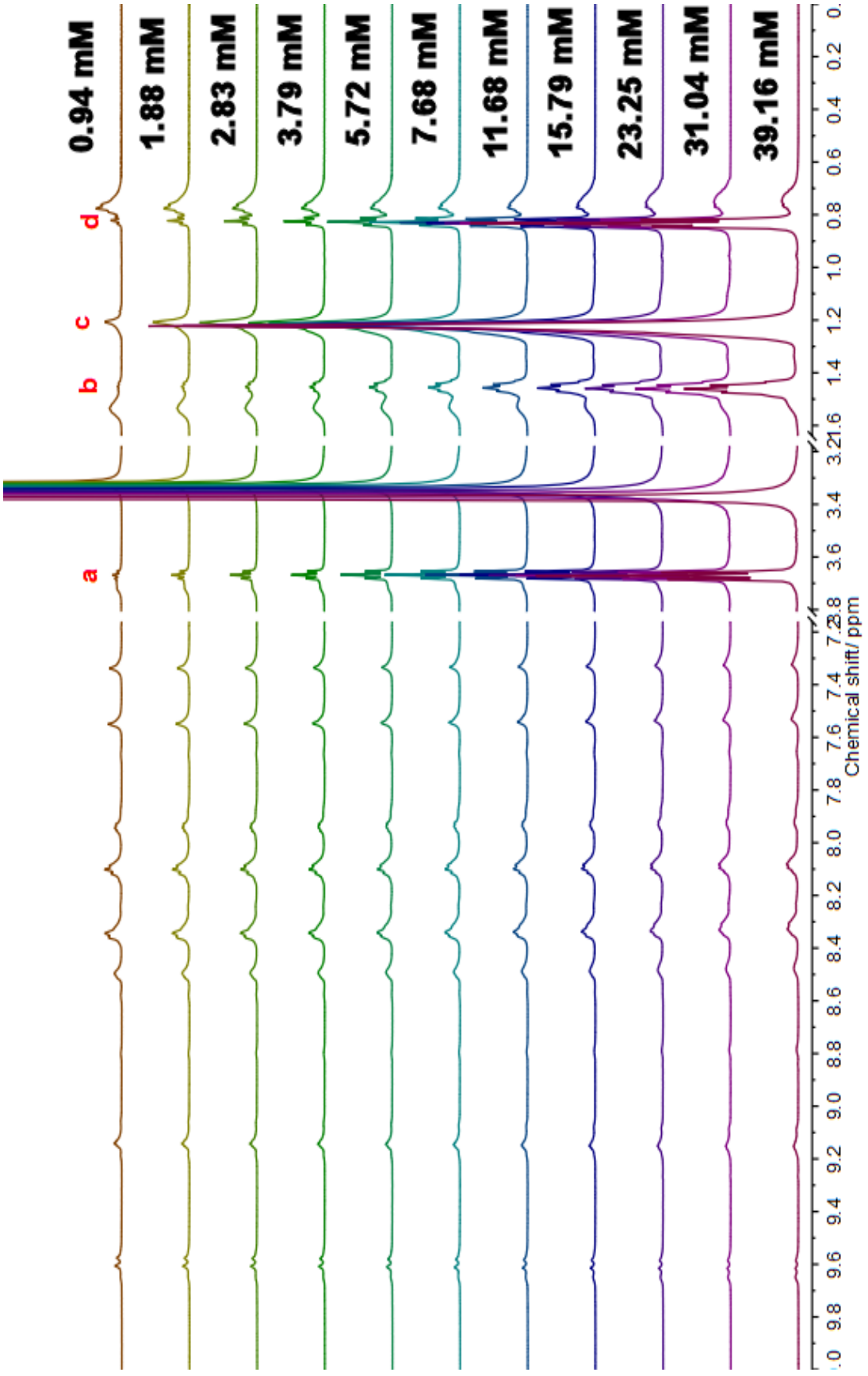


**Figure 5.24.** $^{1}$H-NMR (500 MHz, $d_6$-DMSO) of **C21** (3.85 mM) in the presence of varying concentrations of SOS.

In order to probe the nature of the interaction further, a NOESY spectrum of all three systems was acquired to distinguish which parts of the host and guest were in close proximity during the encapsulation. The only system which yielded positive results employed **C21** as the host molecule (Figure 5.25). Through space couplings were observed between the methylene protons on SOS, Hc, and the phenyl ring of the azo group found on the host architecture, Hx and Hy. The absence of couplings between the anionic head group of SOS and the pyridyl group near the palladium centre suggests the interaction between host and guest is not driven by electrostatic interactions. It is unlikely that this interaction would occur on the exterior on the cage as the guest molecule would likely be outcompeted by solvent molecules. Instead, association occurring within the cage and subsequent expulsion of solvent molecules from the cavity is a more likely explanation. Furthermore, the lack of couplings between the charged groups on the host and guest also suggests the interaction is occurring within the cage. The most likely intermolecular interaction to occur on the periphery of the cage would be between these groups, its absence implies encapsulation of the guest within the cavity and a combination of hydrophobic interactions, expulsion of high energy solvent molecules and CH-π interactions being the driving force.

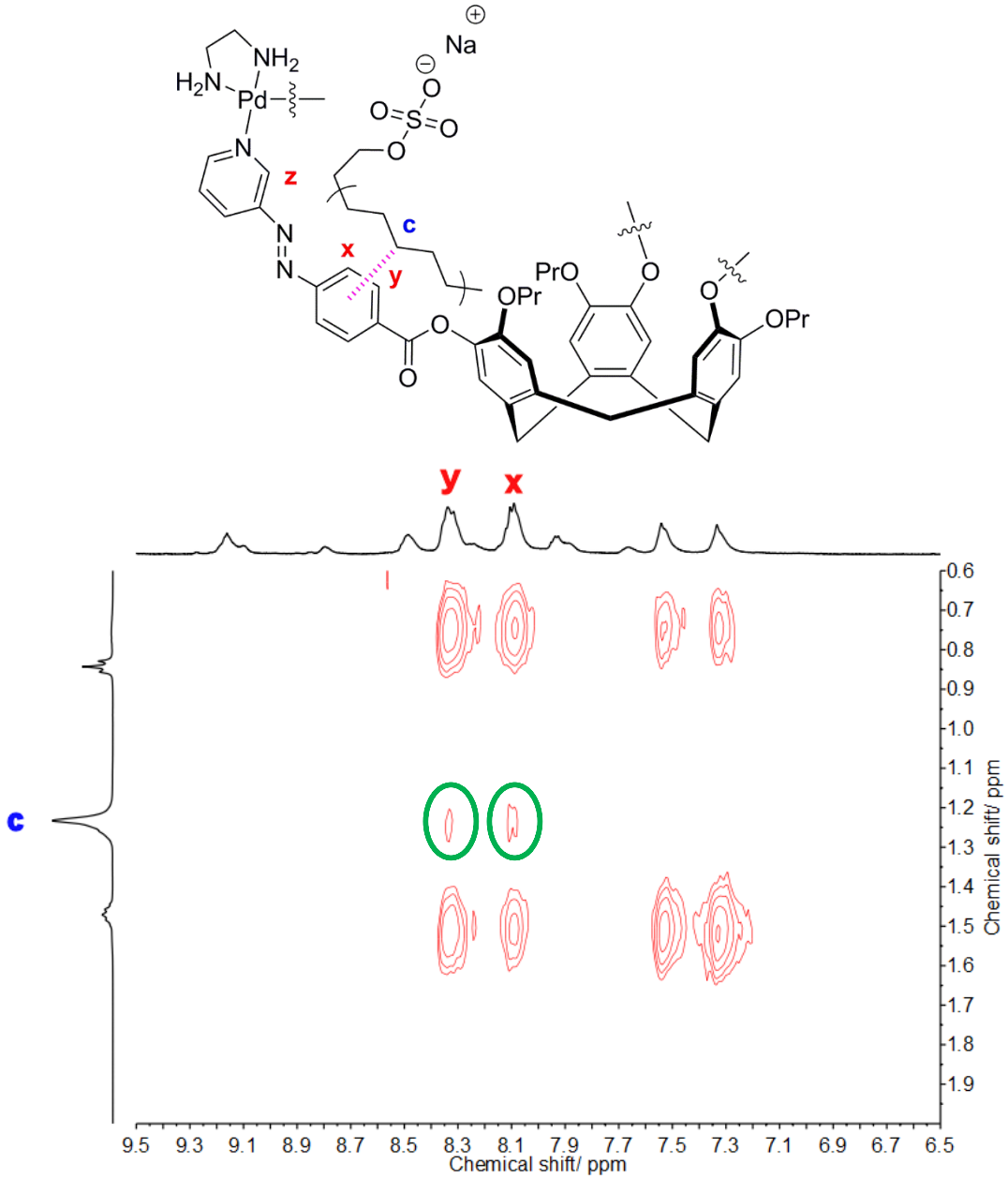


**Figure 5.25.** $^{1}$H-$^{1}$H NOESY spectrum (500 MHz, $d_6$-DMSO) of **C21** displaying couplings between host and guest circled in green.

The concentration of SOS vs the chemical shift of proton Hd found on the SOS guest molecule was plotted for each system using different host molecules, the results are shown in Figure 5.26 and reveal a set of un-remarkable binding isotherms. Similar isotherms could be obtained by plotting the signals from protons Ha and Hb on the SOS, as well as from proton Hz on the metallo-cryptophanes.

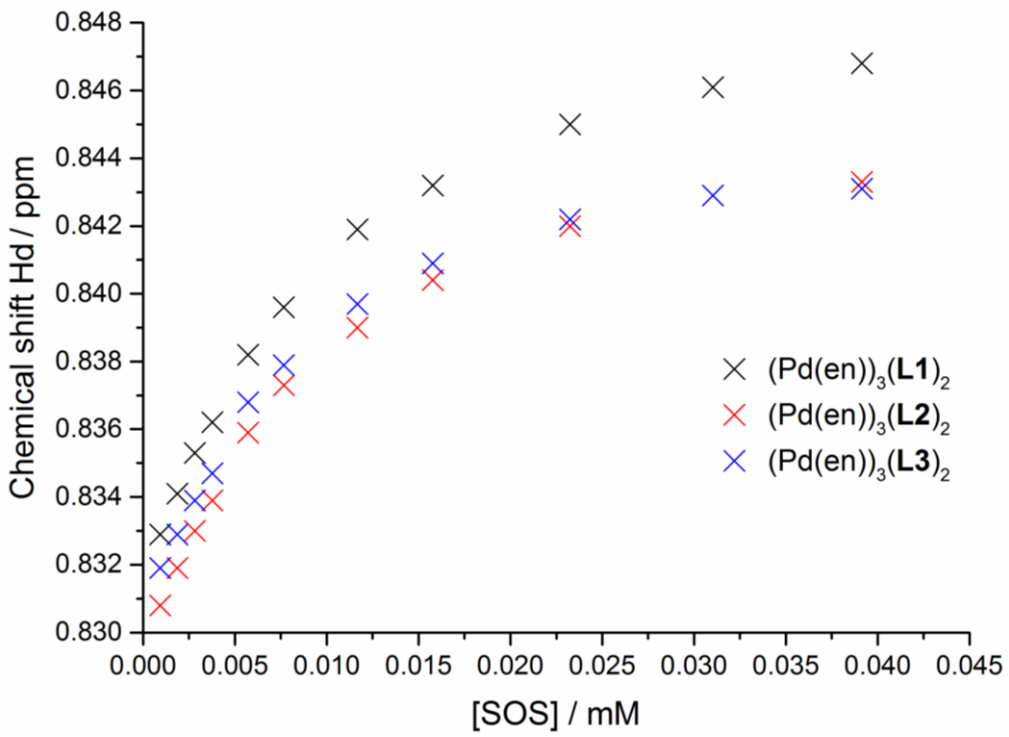


**Figure 5.26.** Binding isotherms derived from the chemical shift proton environment Hd on SOS plotted against the [SOS] for cages **C19**, **C20** and **C21**.

The binding isotherms were much simpler than those obtained when **G1** was used as the guest. Once again, attempts to fit were then performed by Dr. Richard Ansell using the HypNMR08 software. Initial attempts focused upon fitting the data obtained for the system containing **C19** and SOS. The fittings were attempted using the chemical shift data for peaks Ha, Hb and Hd on the SOS guest in addition to the *ortho* pyridyl peak Hz residing on the metallo-cryptophanes. A range of binding stoichiometries were tested including HG, H2G and H3G and a guest self-association factor (G2) was both included and excluded from the fitting model in each case. All attempts to model the system at a host guest stoichiometry greater than 1:1 failed. Reasonable binding constants could be obtained when the system was modelled as a 1:1 system when the guest self-association parameter was both included and excluded. However, examination of the calculated binding isotherms revealed a poor fit to the experimental data for the signal from proton Ha on the SOS molecule when a guest self-association parameter was not factored in. This is expected as the self-titration of the SOS guest confirmed that self-association does occur in solution, albeit weakly. Ha is the signal that changes the most during this process and explains why this factor in particular was not modelled well when G2 was not factored in. For these reasons all fits not including the guest self-association factor were deemed unreliable.

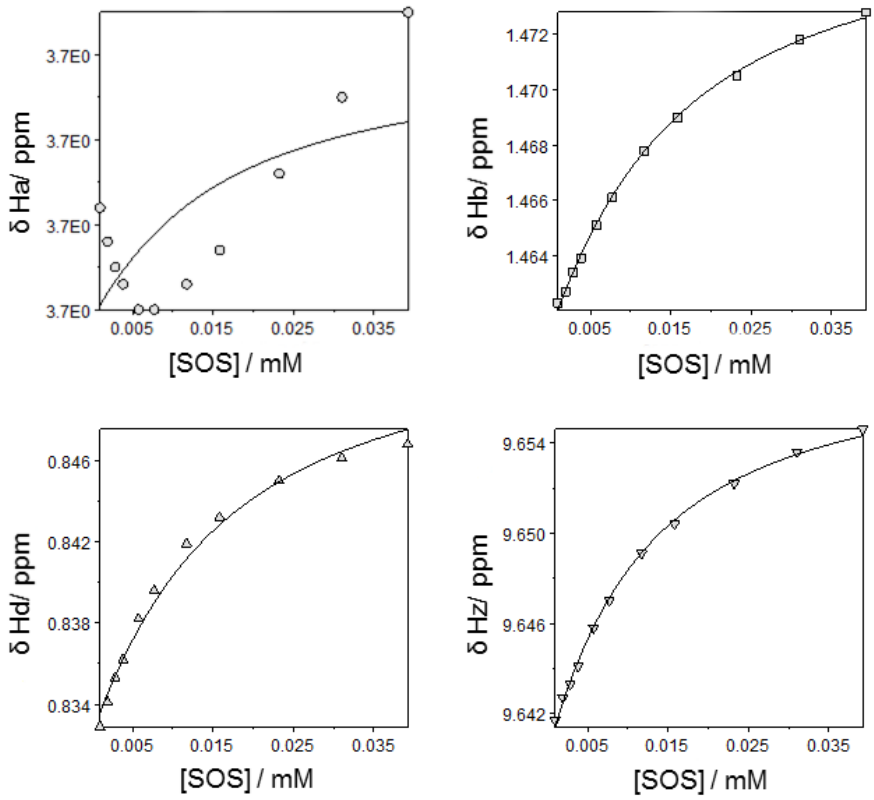


**Figure 5.27.** Fitting of the binding isotherms using HypNMR for a 1:1 HG ratio of **C19** and SOS with no guest self-association factor.

When the G2 factor was included fittings could be obtained that matched the experimental binding isotherms very closely (Figure 5.28). In addition, all of the predicted chemical shift data for the HG and G2 species agreed well with experimentally determined results (Table 5.1). The results shown in Table 5.1 are the calculated chemical shift values for all species present in the mixture of **C19** and SOS using the HypNMR software. Importantly, none of the predicted shifts have unreasonable values and also either increase or decrease in value as expected. For these reasons the fits were deemed to be reliable.

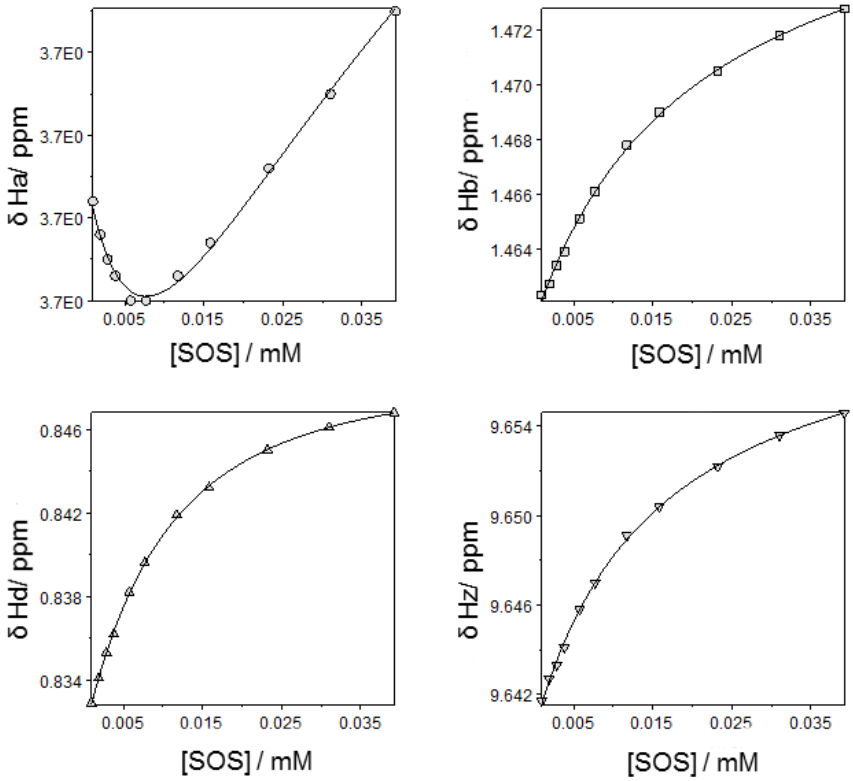


**Figure 5.28.** Fitting of the binding isotherms using HypNMR for a 1:1 HG ratio of **C19** and SOS, including a SOS dimerisation factor.

**Table 5.1.** Table containing the predicted chemical shifts of the species present in a system containing **C19** and SOS.

| | G | H | G2 | HG |
|---|---|---|---|---|
| **δ Ha / ppm** | 3.6548(4) | - | 3.7048(4) | 3.7709(4) |
| **δ Hb / ppm** | 1.4709(2) | - | 1.4827(2) | 1.4252(2) |
| **δ Hd / ppm** | 0.8644(2) | - | 0.8429(2) | 0.7063(2) |
| **δ Hz / ppm** | - | 9.6404(2) | - | 9.6642(2) |

Attempts to fit the experimental binding isotherms for the remaining palladium cryptophanes as the host molecule were successful. The palladium cryptophanes **C19**, **C20** (Figure 5.29) and **C21** (Figure 5.30) were all found to bind one molecule of SOS in DMSO, with weak SOS dimerisation also occurring in solution.

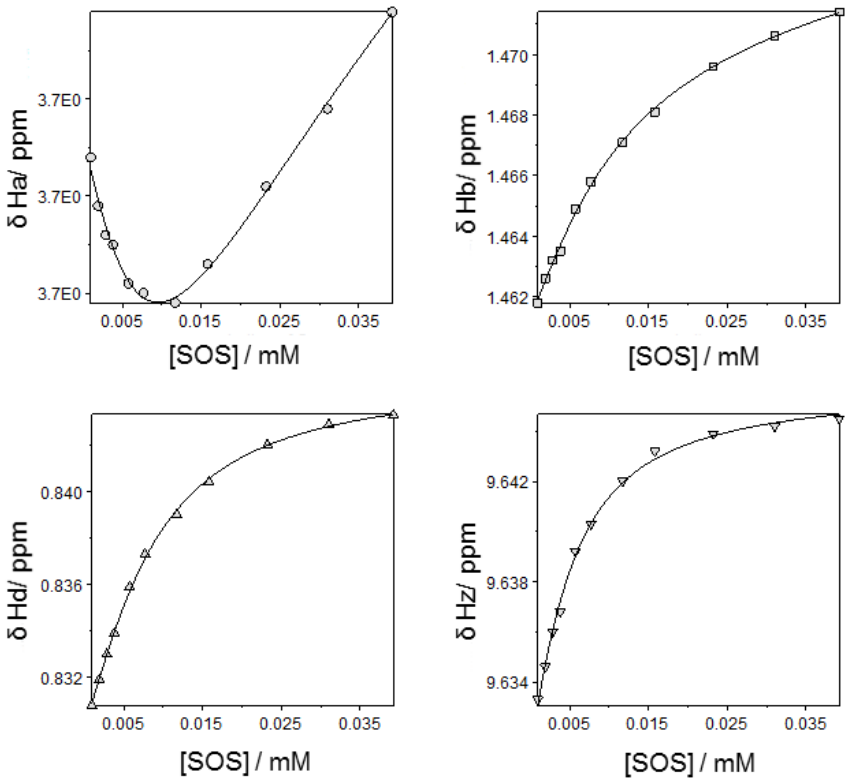


**Figure 5.29.** Fitting of the binding isotherms using HypNMR for a 1:1 HG ratio of **C20** and SOS, including a SOS dimerisation factor.

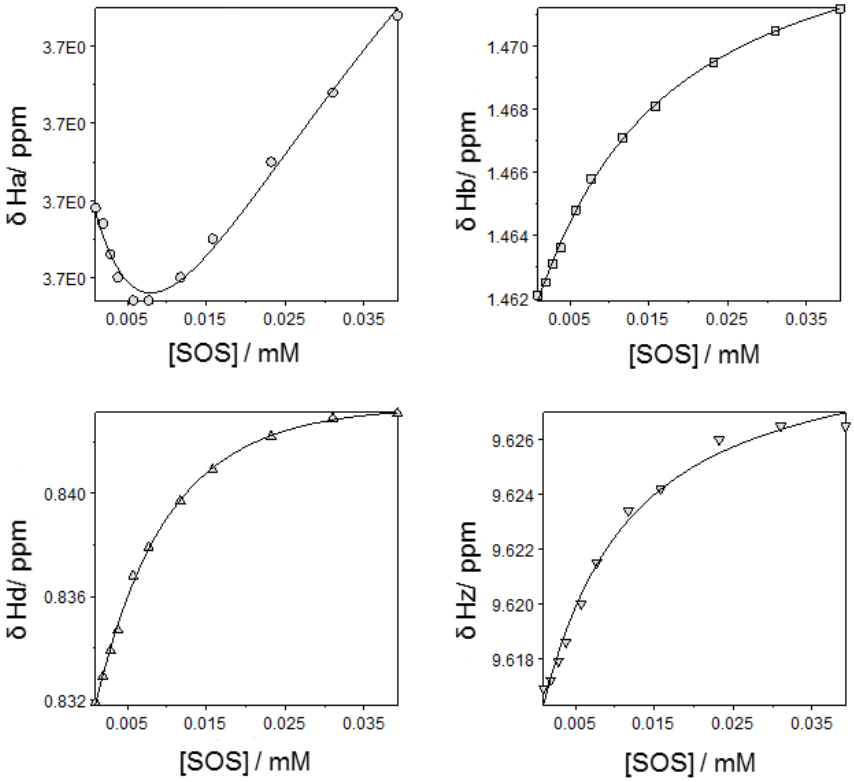


**Figure 5.30.** Fitting of the binding isotherms using HypNMR for a 1:1 HG ratio of **C21** and SOS, including a SOS dimerisation factor.

The successful fitting of the binding isotherms allowed extraction of the binding constants for the host-guest interactions and the guest self-association in all systems (Table 5.2). The SOS self-association values obtained independently for each system were very similar, the values for systems containing **C20** and **C21** were within experimental error. This further enhanced the validity of the model.

**Table 5.2.** Binding constants calculated for host guests systems containing palladium cryptophanes and SOS.

| | **C19** | **C20** | **C21** |
|---|---|---|---|
| $K_{aG2}$ / $M^{-1}$ | 16.2 ± 1.6 | 5.1 ± 3.3 | 9.1 ± 5.5 |
| $K_{aHG}$ / $M^{-1}$ | 68.6 ± 1.9 | 299.0 ± 9.2 | 115.9 ± 6.9 |

The binding of the sodium alkyl sulphates by the palladium cages is considerably weaker than other reported systems. A stella octangula cage reported by the Hardie group bound SOS in DMSO with a $K_a$ of 1 x $10^6$ $M^{-1}$.[31] In this example a 1:2 H:G complex was formed due to the large size of the cage. Whereas a curcubit[7]uril based receptor reported by Yu and coworkers bound SOS in water with a $K_a$ of 2.4 x $10^4$ $M^{-1}$ forming a 1:1 H:G complex.[50] Due to the fact that the association constant of the latter example was performed in water it is plausible that it may have a smaller or greater binding constant depending upon whether hydrophobic interactions or electrostatic interactions are the driving force for encapsulation. In both of these cases it is likely that the guests occupied a greater percentage of the internal cavity than in the examples using **C19**-**C21**. Evidence suggests that a 1:1 H:G complex is formed, this is unlikely to be sufficient to occupy 55% of the internal cavity that is required to achieve optimal binding.[34]

No trend was observed between the length of the alkoxy chain on the ligand and the strength of the SOS binding. However both **C20** and **C21** were found to bind the guest more strongly than **C19**. This implies that the length of the alkoxy chain does have an effect upon the strength of guest binding. The relationship between this is complicated. To improve the binding of guests the alkoxy chains should be long enough so that they are able to partially enclose the interior of the cage. This would make the interior environment more distinct from the bulk solution. However, if the chains are too long and obscure the entrances to the cage to a sufficient degree the host-guest potential would be worsened as they block the passage of guests from the bulk to the interior. It is possible that such a relationship is observed in Table 5.2. **C20** has ethoxy

chains on the upper rim of the CTG bowl in contrast to methoxy (**C19**) and propoxy (**C21**). This may be the ideal length to encourage guest binding without obscuring the cage entrances as **C20** has the highest binding constant, followed by **C21** and lastly **C19**. Further evidence to support this hypothesis was gathered from the NOESY data obtained for identical concentrations of each cage and SOS. The only example where cross-coupling between the cage and SOS was observed was for cage **C21**. This is unusual as the strongest cross-coupling would be expected for cage **C20** which has the highest $K_a$. An explanation may be that the due to the smaller cage windows of cage **C21** each SOS exchanges slower between the bulk solution and the interior of the cage. The slower dynamics would facilitate the detection of the cross-coupling interactions, despite the fact that fewer SOS molecules reside within the host **C21** compared to **C20** at any given moment.

## 5.3 Conclusion

The host-guest behaviour of the palladium metallo-cryptophane series has been investigated. No evidence was obtained for interactions between fullerenes and carboranes and the CTG containing metallo-cryptophanes. This is unusual as CTG has a well-documented ability to encapsulate globular non-polar guests.[30, 33, 42] Instead, strong evidence was obtained for the encapsulation of sodium alkyl sulfates and napthlamide derivatives. In both cases the alkyl chains were observed to interact with the cage through NOESY NMR data, suggesting that these regions are important in the binding of these species within the cage. CH-π interactions have been observed to form between the arene rings on the CTV core and guests in previous examples in the literature and may play an integral role in the examples described in this Chapter.

The binding of the sodium alkyl sulfates within the cage was effectively modelled by Dr Richard Ansell using HypNMR. This provided reliable association constants for the interactions between the host and guest in the range of 68.6 – 299.0 $M^{-1}$. These interactions are relatively weak and may be a result of the large size of the cage windows, resulting in inefficient shielding of the internal environment from the bulk solvent.

The binding isotherms obtained from the $^1$H-NMR titration data of the napthalamide derivative **G1** and the palladium cryptophanes could not be modelled using the HypNMR software. This, along with the shape of the

binding isotherms provides substantive evidence that the host and guest are interacting in a ratio greater than 1:1. The small size of the guest comparted to the internal cavity further reinforces this notion. The substantial shifts during the $^{1}$H-NMR titration of the peaks arising from **G1** suggest that the association constant between the palladium cages and **G1** is greater than that for the sodium alkyl sulfates.

## 5.4 Future Work

Evidence has been obtained for the encapsulation of a napthalamide guest and sodium alkyl sulfates. This proves that these azobenzene appended CTG based metallo-cryptophanes are capable of acting as host molecules for a range of species. It would be desirable to investigate the scope of the host-guest chemistry further. In particular interest would be the biologically relevant napthalamide derivative shown in Figure 5.31. This gold complex has been shown to possess anticancer properties and is structurally similar to the napthalamide guest **G1** used in the studies described in this chapter.[51, 52] The inclusion of therapeutic molecules within host-assemblies is an incredibly active area of research as it may provide novel mechanisms with which to achieve targeted drug delivery.[53]

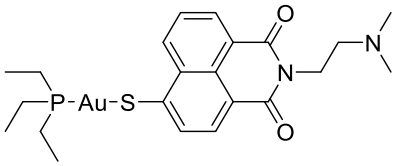


**Figure 5.31.** Gold napthalamide complex shown to possess anticancer properties.[51, 52]

Unfortunately, it was not possible to measure how the host-guest potential of the cage compounds varied upon photoswitching. This was due to the cage breakdown which often occurred upon irradiation with light. The relatively small changes in the chemical shifts of the guests upon encapsulation would also make it difficult to determine whether photoswitching the cage had affected the binding dynamics. The use of NHC appended palladium tectons has been shown to stabilise metallo-cryptophanes.[30] Incorporating this tecton into a cage as shown in Figure 5.32 may increase the photo-fatigue resistance of these cages and enable efficient photoswitching. In addition, the use of such a tecton would reduce the size of the cage windows, which may improve the guest binding potential of these cages.

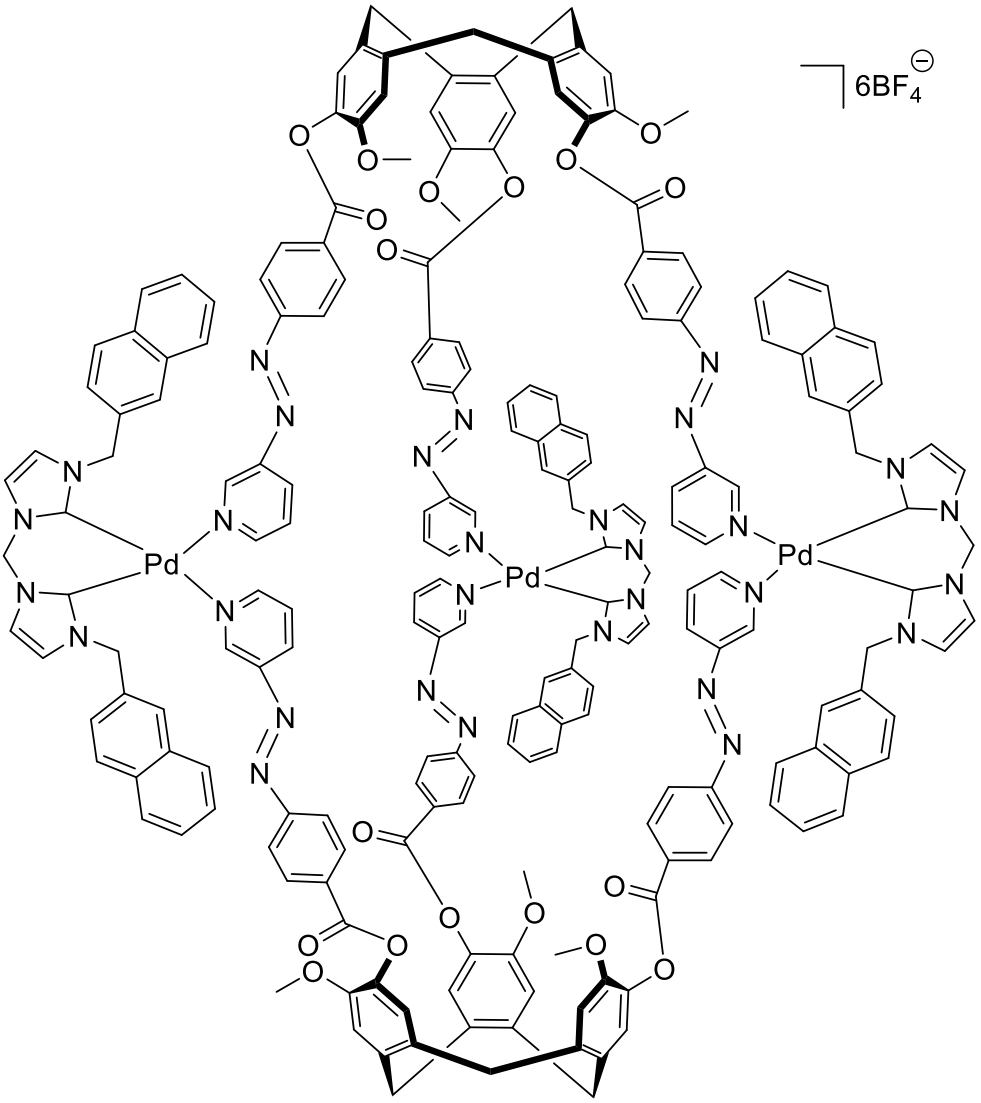


**Figure 5.32.** Palladium NHC appended azobenzene metallo-cryptophane. The extra stability afforded by the *bis*-NHC may be sufficient to increase the photo-fatigue resistance of this class of cages.

## 5.5 Experimental

### General Remarks

All reagents were purchased from commercial suppliers and used without further purification. Where stated, reactions were carried out under an inert atmosphere of nitrogen using a dual vacuum/ nitrogen manifold and standard Schlenk techniques. Dry solvent was obtained by passing through a column of activated alumina.

### Instrumentation

$^{1}$H and $^{13}$C NMR were performed on a Bruker 500-CP 500 MHz spectrometer and referenced to residual solvent peaks. Where appropriate NMR assignments were confirmed using 2-D NMR techniques acquired on a Jeol ECA 600ii 600 MHz spectrometer, techniques include COSY, TOCSY, HSQC, HMBC, NOESY, ROESY and DOSY.

Electrospray mass spectra were performed on a Bruker micro-TOFQ mass spectrometer.

### Preparation of compounds

2-[2-(Dimethylamino)ethyl]-1H-benzoisoquinoline-1,3(2H)-dione[54] (**G1**)

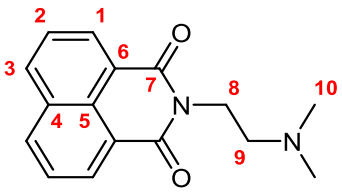


1,8-Napthalic anhydride (1.00 g, 5.04 mmol) was dispersed in ethanol (30 mL). *N,N*-Dimethylenediamine (0.58 mL, 5.31 mmol) was added and the mixture heated to reflux overnight resulting in an orange solution. The volume was reduced and the flask left in the freezer overnight. Colourless crystals grew which were collected by vacuum filtration and washed with ice-cold diethyl ether to yield the product as a colourless microcrystalline solid (0.38 g, 1.42 mmol, 28 %). Spectroscopic data is consistent with literature values.[54]

**$^{1}$H-NMR** ($CDCl_3$, 400 MHz): 8.58 (d, 2H, *J* = 7.2 Hz, **H$^{1}$**), 8.19 (d, 2H, *J* = 8.1 Hz, **H$^{3}$**), 7.73 (t, 2H, *J* = 7.7 Hz, **H$^{2}$**), 4.33 (t, 2H, *J* = 7.0 Hz, **H$^{9}$**), 2.65 (t, 2H, *J* = 7.2 Hz, **H$^{8}$**), 2.35 (s, 6H, **H$^{10}$**). **$^{13}$C-NMR** ($d_6$-DMSO, 125 MHz): . **ESI-MS** (+ve): $[M+H]^+$ m/z = 269.1297 calcd 269.1285.

**$^1$H-NMR titration procedure**

All $^1$H-NMR titrations were performed using the standard method detailed below. The example given is for the titration between **C19** and SOS. Concentrations differed between different systems although the general method remained constant. Binding isotherms were plotted using HypNMR2008.[55] All NMRs were acquired at 300 K.

A stock solution of **C19** was prepared in $d_6$-DMSO (3.85 mM, 2mL). 0.55 mL of the stock was transferred to an NMR tube and an initial $^1$H-NMR was acquired. SOS (19.7 mg, 84.8 μmol) was dissolved in 1 mL of the stock solution of **C19**. Aliquots of the solution containing SOS were added to the NMR tube incrementally such that the H:G ratio varied between 1:0.1 and 1:10. At each interval the NMR tube was mixed with a vortex mixer and equilibrated for 5 minutes before acquisition of the $^1$H-NMR spectrum.

## References


1. C. J. Pedersen, *Nobel Lecture*, 1988, **27**, 1021-1027.
2. C. J. Pedersen, *J. Am. Chem. Soc.*, 1967, **89**, 7017-7036.
3. N. Busschaert, C. Caltagirone, W. Van Rossom and P. A. Gale, *Chem. Rev.*, 2015, **115**, 8038-8155.
4. X. Su and I. Aprahamian, *Chem. Soc. Rev*, 2014, **43**, 1963-1981.
5. J. Li, D. Yim, W.-D. Jang and J. Yoon, *Chem. Soc. Rev*, 2017, **46**, 2437-2458.
6. L. S. Kaanumalle and V. Ramamurthy, *Chem. Comm.*, 2007, 1062-1064.
7. J. Chen and J. Rebek, *Org. Lett.*, 2002, **4**, 327-329.
8. Y. Nishioka, T. Yamaguchi, M. Yoshizawa and M. Fujita, *J. Am. Chem. Soc.*, 2007, **129**, 7000-7001.
9. M. Yoshizawa, Y. Takeyama, T. Kusukawa and M. Fujita, *Angew. Chem. Int. Ed.*, 2002, **41**, 1347-1349.
10. D. Dai, Z. Li, J. Yang, C. Wang, J.-R. Wu, Y. Wang, D. Zhang and Y.-W. Yang, *J. Am. Chem. Soc.*, 2019, **141**, 4756-4763.
11. K.-S. Liu, M.-J. Li, C.-C. Lai and S.-H. Chiu, *Chem. Eur. J.*, 2016, **22**, 17468-17476.
12. A. Alsbaiee, B. J. Smith, L. Xiao, Y. Ling, D. E. Helbling and W. R. Dichtel, *Nature*, 2015, **529**, 190.
13. Z. Jia, J. Pan, C. Tian and D. Yuan, *RSC Adv.*, 2018, **8**, 36812-36818.
14. J. W. Steed, P. C. Junk, J. L. Atwood, M. J. Barnes, C. L. Raston and R. S. Burkhalter, *J. Am. Chem. Soc.*, 1994, **116**, 10346-10347.
15. R. J. Blanch, M. Williams, G. D. Fallon, M. G. Gardiner, R. Kaddour and C. L. Raston, *Angew. Chem. Int. Ed.*, 1997, **36**, 504-506.
16. D. Felder, B. Heinrich, D. Guillon, J.-F. Nicoud and J.-F. Nierengarten, *Chem. Eur. J.*, 2000, **6**, 3501-3507.
17. F. Yang, Q. Chen, Q.-Y. Cheng, C.-G. Yan and B.-H. Han, *J. Org. Chem.*, 2012, **77**, 971-976.
18. M. J. Hardie, *Chem. Soc. Rev.*, 2010, **39**, 516-527.
19. E. Huerta, H. Isla, E. M. Pérez, C. Bo, N. Martín and J. d. Mendoza, *J. Am. Chem. Soc.*, 2010, **132**, 5351-5353.
20. Ł. Szyszka, P. Cmoch, A. Butkiewicz, M. A. Potopnyk and S. Jarosz, *Org. Lett.*, 2019, **21**, 6523-6528.
21. H. A. Fogarty, P. Berthault, T. Brotin, G. Huber, H. Desvaux and J.-P. Dutasta, *J. Am. Chem. Soc.*, 2007, **129**, 10332-10333.
22. G. Huber, T. Brotin, L. Dubois, H. Desvaux, J.-P. Dutasta and P. Berthault, *J. Am. Chem. Soc.*, 2006, **128**, 6239-6246.
23. T.-H. Wong, J.-C. Chang, C.-C. Lai, Y.-H. Liu, S.-M. Peng and S.-H. Chiu, *J. Org. Chem.*, 2014, **79**, 3581-3586.
24. R. S. Ruoff, D. S. Tse, R. Malhotra and D. C. Lorents, *J. Phys. Chem.*, 1993, **97**, 3379-3383.
25. R. M. Fairchild and K. T. Holman, *Organometallics*, 2007, **26**, 3049-3053.
26. K. T. Holman, M. M. Halihan, S. S. Jurisson, J. L. Atwood, R. S. Burkhalter, A. R. Mitchell and J. W. Steed, *J. Am. Chem. Soc.*, 1996, **118**, 9567-9576.

27. R. M. Fairchild and K. T. Holman, *J. Am. Chem. Soc.*, 2005, **127**, 16364-16365.
28. R. M. Fairchild, A. I. Joseph, K. T. Holman, H. A. Fogarty, T. Brotin, J.-P. Dutasta, C. Boutin, G. Huber and P. Berthault, *J. Am. Chem. Soc.*, 2010, **132**, 15505-15507.
29. M. A. Little, J. Donkin, J. Fisher, M. A. Halcrow, J. Loder and M. J. Hardie, *Angew. Chem. Int. Ed.*, 2012, **51**, 764-766.
30. J. J. Henkelis, C. J. Carruthers, S. E. Chambers, R. Clowes, A. I. Cooper, J. Fisher and M. J. Hardie, *J. Am. Chem. Soc.*, 2014, **136**, 14393-14396.
31. N. J. Cookson, J. J. Henkelis, R. J. Ansell, C. W. G. Fishwick, M. J. Hardie and J. Fisher, *Dalton Trans.*, 2014, **43**, 5657-5661.
32. C. J. Sumby and M. J. Hardie, *Angew. Chem. Int. Ed.*, 2005, **44**, 6395-6399.
33. C. Carruthers, J. Fisher, L. P. Harding and M. J. Hardie, *Dalton Trans.*, 2010, **39**, 355-357.
34. S. Mecozzi and J. Rebek, Julius, *Chem. Eur. J.*, 1998, **4**, 1016-1022.
35. R. Rojanathanes, T. Tuntulani, W. Bhanthumnavin and M. Sukwattanasinitt, *Org. Lett.*, 2005, **7**, 3401-3404.
36. O. B. Berryman, A. C. Sather and J. Rebek Jr, *Chem. Comm.*, 2011, **47**, 656-658.
37. G. Moncelsi and P. Ballester, *ChemPhotoChem.*, 2019, **3**, 304-317.
38. T.-T.-T. Nguyen, D. Türp, D. Wang, B. Nölscher, F. Laquai and K. Müllen, *J. Am. Chem. Soc.*, 2011, **133**, 11194-11204.
39. H. Wang, F. Liu, R. C. Helgeson and K. N. Houk, *Angew. Chem. Int. Ed.*, 2013, **52**, 655-659.
40. M. Han, R. Michel, B. He, Y.-S. Chen, D. Stalke, M. John and G. H. Clever, *Angew. Chem. Int. Ed.*, 2013, **52**, 1319-1323.
41. J. R. Nilsson, M. C. O'Sullivan, S. Li, H. L. Anderson and J. Andréasson, *Chem. Comm.*, 2015, **51**, 847-850.
42. R. Ahmad and M. J. Hardie, *CrystEngComm*, 2002, **4**, 227-231.
43. X. Cao, L. Meng, Z. Li, Y. Mao, H. Lan, L. Chen, Y. Fan and T. Yi, *Langmuir*, 2014, **30**, 11753-11760.
44. M. P. Williamson, *Prog. Nucl. Mag. Res. Sp.*, 2013, **73**, 1-16.
45. T. K. Ronson, W. Meng and J. R. Nitschke, *J. Am. Chem. Soc.*, 2017, **139**, 9698-9707.
46. P. Thordarson, *Chem. Soc. Rev*, 2011, **40**, 1305-1323.
47. T. Orville and W. James, *Molecular Interactions*, John Wiley and Sons, Ltd, 1981.
48. S. A. Markarian, L. R. Harutyunyan and R. S. Harutyunyan, *J. Solution Chem.*, 2005, **34**, 361-368.
49. N. J. Cookson, PhD Thesis, University of Leeds, 2016.
50. J.-S. Yu, F.-G. Wu, Y. Zhou, Y.-Z. Zheng and Z.-W. Yu, *Phys. Chem. Chem. Phys.*, 2012, **14**, 8506-8510.
51. I. Ott, X. Qian, Y. Xu, D. H. W. Vlecken, I. J. Marques, D. Kubutat, J. Will, W. S. Sheldrick, P. Jesse, A. Prokop and C. P. Bagowski, *J. Med. Chem.*, 2009, **52**, 763-770.
52. C. P. Bagowski, Y. You, H. Scheffler, D. H. Vlecken, D. J. Schmitz and I. Ott, *Dalton Trans.*, 2009, 10799-10805.
53. X. Ma and Y. Zhao, *Chem. Rev.*, 2015, **115**, 7794-7839.

54. D. D. Young, C. M. Connelly, C. Grohmann and A. Deiters, *J. Am. Chem. Soc.*, 2010, **132**, 7976-7981.
55. C. Frassineti, S. Ghelli, P. Gans, A. Sabatini, M. S. Moruzzi and A. Vacca, *Anal. Biochem.*, 1995, **231**, 374-382.

# Chapter 6
# Larger Supramolecular Assemblies of Azobenzene CTG Ligands

## 6.1 Introduction

The previous Chapters in this thesis have discussed the behaviour and synthesis of supramolecular metallo-cages of the general formula $M_3L_2$. Metallo-cryptophanes however are not the sole species that these azobenzene containing CTG ligands are able to access. Subtle changes to the bonding angle of ligand to metal and the protection or deprotection of the metal group allows access to larger more complex supramolecular arrays. This Chapter focuses on the synthesis, characterisation and behaviour of a massive $Pd_6L_8$ stella octangula assembly. The photoswitching properties and potential host-guest applications will also be discussed.

### 6.1.1 Expansion of the metallo-cage library

The preorganised pyramidal nature of CTG ligands results in a natural tendency to form $M_3L_2$ type capsules upon reaction with metal cations. There are however numerous examples in the literature of when these ligands do not behave as expected, and instead self-assemble into a wide array of different architectures. The stoichiometries of these architectures range from the smallest, $M_2L_2$,[1-3] to $M_6L_8$[4-6] and up to even larger $M_{12}L_8$ assemblies.[7] Even architectures sharing the same stoichiometry can have topologies that are vastly different from one another.[8-10] For example an $Ag_4L_4$ (L=tris(4-pyridylmethylamino)CTG) cage previously synthesised by Hardie and coworkers adopted a tetrahedral arrangement whereby the silver ions acted as the corners of a tetrahedron and the ligands were situated on the faces, coordinating to three silver centres respectively.[10] An $Ag_4L_4$ cage was still obtained if the ligand was changed to a 2-quinoline derivative of CTG which adopted the same general structure but with distinct differences.[8] Instead each ligand only coordinated to two silver centres, with the third ‘free’ arm found to reside in the hydrophobic cavity of an adjacent ligand in a motif known as a ‘molecular handshake’.[8] A wholly different $M_4L_4$ architecture can be obtained if tris(3-pyridylphenylcarboxy)CTG self-assembles in the presence of

palladium(II) cations to form a topologically complex cubic like structure known as a Solomon's cube (Figure 6.1).[9]

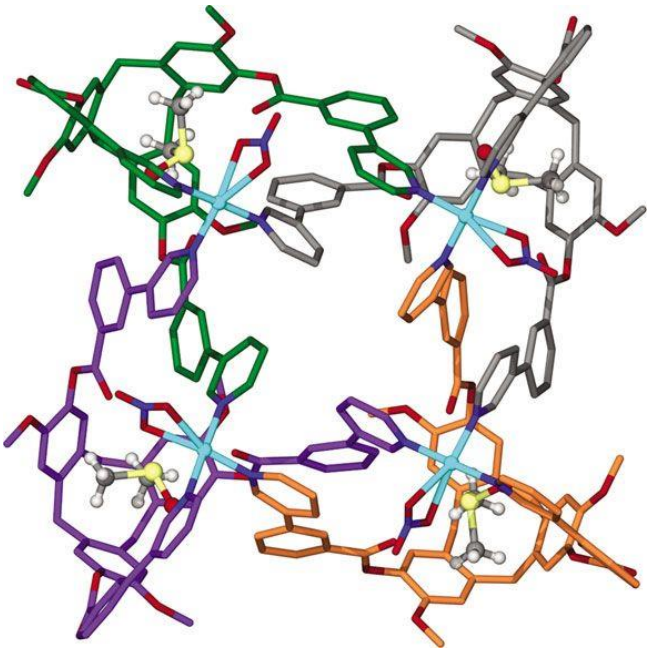

**Figure 6.1.** X-ray crystal structure of $Pd_4L_4$ topologically complex Solomon's cube, each ligand is represented by a different colour.[9]

These examples demonstrate that the chemistry of CTG derivatives is not limited to the metallo-cryptophane motif and indeed a plethora of other complicated and intricate architectures are obtainable.[11, 12] As is often the case in supramolecular chemistry, factors such as solvent,[13] counterion[14] and ligand rigidity[15] can subtlety influence the reaction to produce unexpected products, many of which cannot be predicted using our current understanding.[16]

The size of the internal cavity in coordination cages is pivotal in governing what substrates can potentially be bound within the cage. The more complementary the fit of a substrate into a cavity, the tighter it will be bound.[17] Enzymes found in nature provide excellent examples of this principle in action. The binding sites on these proteins are so intricately designed so that the desired substrate fits tightly within the cavity, thus achieving maximal binding efficiency. It has been calculated by Rebek and Mecozzi that in order to achieve maximal binding efficiency of a non-polar molecule, the guest must occupy 55% of the internal volume of the host.[17] As most coordination cages are mainly composed of non-polar $sp^2$ aromatic carbon environments they have a preference to bind similarly non-polar guests, therefore the rule of 55% holds true in most cases.

This general rule of packing efficiency dictates what guests can potentially bind within a host. Larger cages can not only bind larger guest molecules but are also capable of binding multiple guest molecules at once.[18, 19] Host-guest complexes which possess high stoichiometry are desirable if the purpose of the cage is to catalyse intermolecular reactions.[20] In this case, coenclathration of multiple substrates can vastly increase the rate of reaction.[21, 22] The preorganization of substrates within a cavity can also lead to regio and stereoselective control of even the most challenging reactions.[23, 24]

Fujita has shown that the use of a $Pd_6L_4$ cage can effectively control the regioselectivity of the reaction between *ortho*-quinone and a substituted toluene (Figure 6.2).[25] Upon irradiation a benzylic and semiquinone radicals are generated. The semiquinone radical is delocalised over the entire molecule so that recombination of the radical centres can lead to a large number of possible products. If the reaction is performed in the bulk solution unsurprisingly a complex mixture of products is obtained. However, in the presence of the cage the O-coupled 1,4 adduct is obtained exclusively. The specific product is not observed when the reaction is performed in the bulk solution. Such selectivity of a radical reaction is remarkable and is normally reserved only for enzymatic reactions.[25]

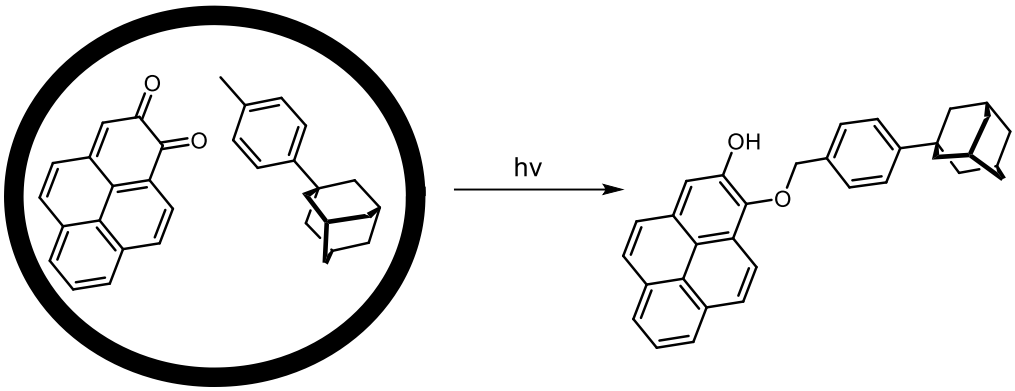


**Figure 6.2.** Regioselective control of the photochemical radical reaction between *ortho*-quinone and a substituted toluene leading to a single isomer in the presence of a $Pd_6L_4$ cage.[25]

The applications of larger metallo-cages are not limited to the catalysis of small organic molecules. It has been shown that these cages are capable of controlling the size and shape of inorganic nanoparticles.[26] The ability of selectively form nanoparticles of specific size and shapes could lead to new applications of these materials. Fujita has demonstrated that a huge $Pd_{12}L_{24}$ cage is obtained upon the mixing of $Pd(NO_3)_2$ with a bent *bis*-pyridyl ligand (Figure 6.3). The interior of the cage was decorated with glucose units capable of reversibly binding silanols. This feature was utilised in the sol-gel

condensation of tetramethoxysilane to form silica nanoparticles exclusively within the cage. Even more remarkable was the fact that the nanoparticles had a polydispersity of <1.01, indicating that all nanoparticles were almost exactly the same size. The ligands were easily modified to make the cage volume larger or smaller and in all cases the size of the nanoparticles changed to match the volume of the cage.[26]

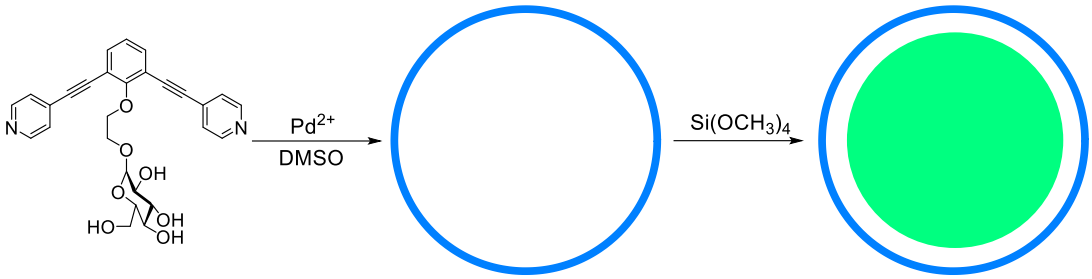


**Figure 6.3.** Synthesis of $Pd_{12}L_{24}$ cage (blue) capable of templating the formation of monodisperse silica nanoparticles (green).[26]

Stang *et al*. has recently described the fabrication of a large $M_{12}L_{24}$ metallo-cage which is able to mimic the activity of the green fluorescent protein (GFP) commonly used by biologists as a fluorescence marker in live cells.[27] The chromophore of the GFP is based upon the tetraphenylethylene unit (TPE). When the chromophore is in the bulk solution it is only weakly emissive, however confinement within the cavity of the GFP results in the unit becoming intensely fluorescent. The effect of confinement sterically restrains the chromophore such that it cannot undergo non-radiative decay *via* geometric distortion. Stang took inspiration from nature and designed the ligand so that upon self-assembly the TPE units would reside inside the metallo-cage and be similarly sterically restricted. The large cage allowed 24 TPE units to reside within the cavity, effectively restricting any geometric distortion. The effect of confinement and the high local concentration of chromophores within the microenvironment resulted in strong fluorescence from the nanosphere. Such biomimetic materials may have many potential applications ranging from bioimaging agents to LED fabrication.[27]

Examples of metallo-supramolecular architectures larger than a metallo-cryptophane have previously been described in the Hardie group. *Tris*(4-pyridylmethylamino)cyclotriguaiacylene and *tris*(4-pyridylmethyl) cyclotriguaiacylene were found to self-assemble with palladium(II) nitrate to form a $Pd_3L_4$ type structure. These species were found to adopt an open bowl type structure (Figure 6.4). In the solid state these bowls were found to weakly hydrogen bond to form an assembly more akin to a capsule. The bowls were found to form host-guest interactions with the DMSO solution where the

methyl groups of the DMSO would be directed towards the CTG cavities. The result is a hydrophobic interaction between bowl and solvent.

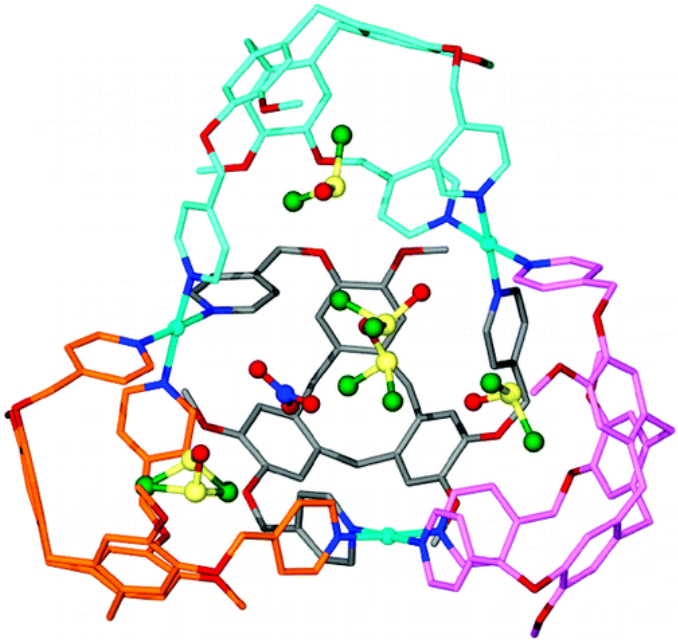

**Figure 6.4.** X-ray structure $Pd_3L_4$ cage synthesised by Hardie and co-workers displaying host-guest interactions with DMSO molecules.[6]

A larger assembly can be formed if the ligands are made more rigid by replacing the ether/amine linkages with ester groups. For example *tris*(isonicotinoyl)cyclotriguaiacylene self-assembles with palladium(II) nitrate to form a $Pd_6L_8$ structure resembling the first stellation of an octahedron (Figure 6.5).[5] The increased rigidity means that this ligand is not flexible enough to form the $Pd_3L_4$ type structure and as a result forms a larger $Pd_6L_8$ structure. This structure is referred to as a stella octangula throughout the remainder of this thesis. In this architecture, the palladium cations occupy the vertices of an octahedron. The CTG ligands then occupy the faces of an octahedron, with the CTG bowl protruding outwards, giving the general appearance of a stellated octahedron. The increased rigidity means that this ligand is not flexible enough to form the $Pd_3L_4$ type structure and as a result forms a larger stella octangula structure.

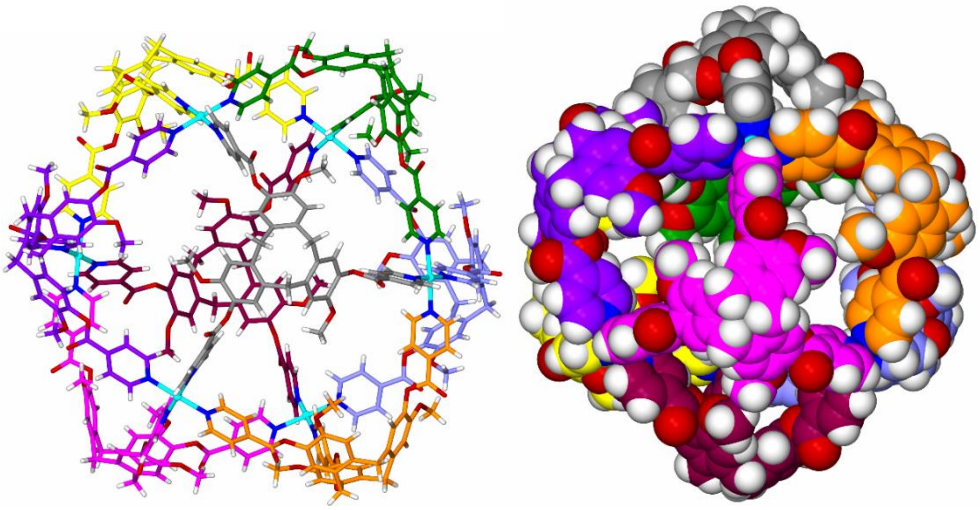

**Figure 6.5.** X-ray crystal structure of $Pd_6L_8$ stella octangula structure synthesised by Hardie and co-workers shown in ball and stick (left) and space filling (right) representations.[5]

The X-ray crystal structure shows that the assembly has a diameter of 3.1 nm and possesses a large internal cavity suitable for the binding of guests. Long linear guests such as sodium alkyl sulphates bind within the cage in a 1:2 H:G ratio. The nonpolar alkyl chains form hydrophobic interactions with the CTG cores whereas the charged sulphate head groups interact electrostatically with the palladium cations.[28] Subsequent studies have shown that the small size of the windows of the cage prevent binding of larger species such as *o*-carborane or fullerenes.

Further studies have shown that the stella octangula array can be obtained by reacting 'naked' palladium with a range of different ligands (Figure 6.6).[6] Some of these ligands have had their binding 'arm' extended with the addition of a phenyl group. The has the effect of increasing the size of the cage windows. The larger windows may allow for the diffusion of larger guests into the internal cavity, increasing the wealth of host guest chemistry as a consequence.

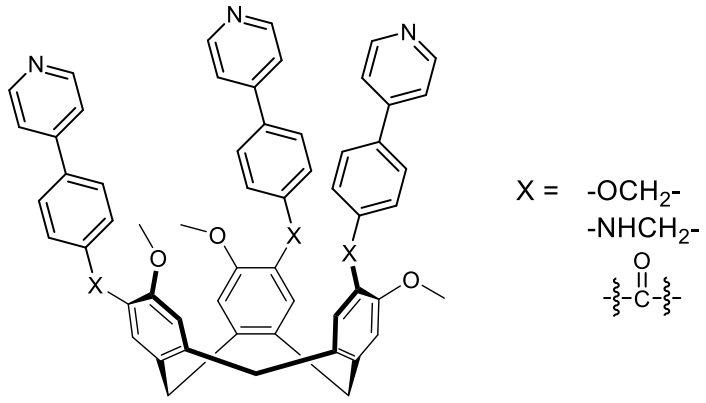


**Figure 6.6.** Structure of extended ligands capable of forming stella octangula structure with naked palladium.[6]

If the stella octangula cage can be synthesised using the azobenzene containing ligands discussed previously then this new cage may possess a number of potential advantages over previous ones. Firstly the cage windows will be further expanded, allowing a greater variety of guests to enter the cavity. Secondly the inclusion of azobenzenes into the cage framework may allow for structural modulation with the use of light. Stimulated guest uptake and release may be achieved using this method.

## 6.2 Synthesis of stella octangula azobenzene cage

In order to synthesise the stella octangula cage some alterations of the ligand and metal tecton were required. Initially it was envisioned that the cage could be synthesised in a similar manner to that previously reported by Ronson *et al*.[5] Simply reacting 'naked' palladium in the form of $Pd(NO_3)_2$ or $[Pd(MeCN)_4]2BF_4$ with ligands **L1** – **L3** would, in theory, react to furnish the stella octangula cage. However it quickly became apparent that the desired stella octangula cage is not isolated using this method. If this reaction is attempted the lack of obvious features in the $^1$H-NMR spectrum is immediately apparent. A large, broad and unassignable hump is observed in the aromatic region (Figure 6.7) in stark contrast to the sharp, well resolved peaks for ligands **L1 – L3**. This suggests that a complex mixture of oligomeric complexes may have formed instead of the stella octangula cage.

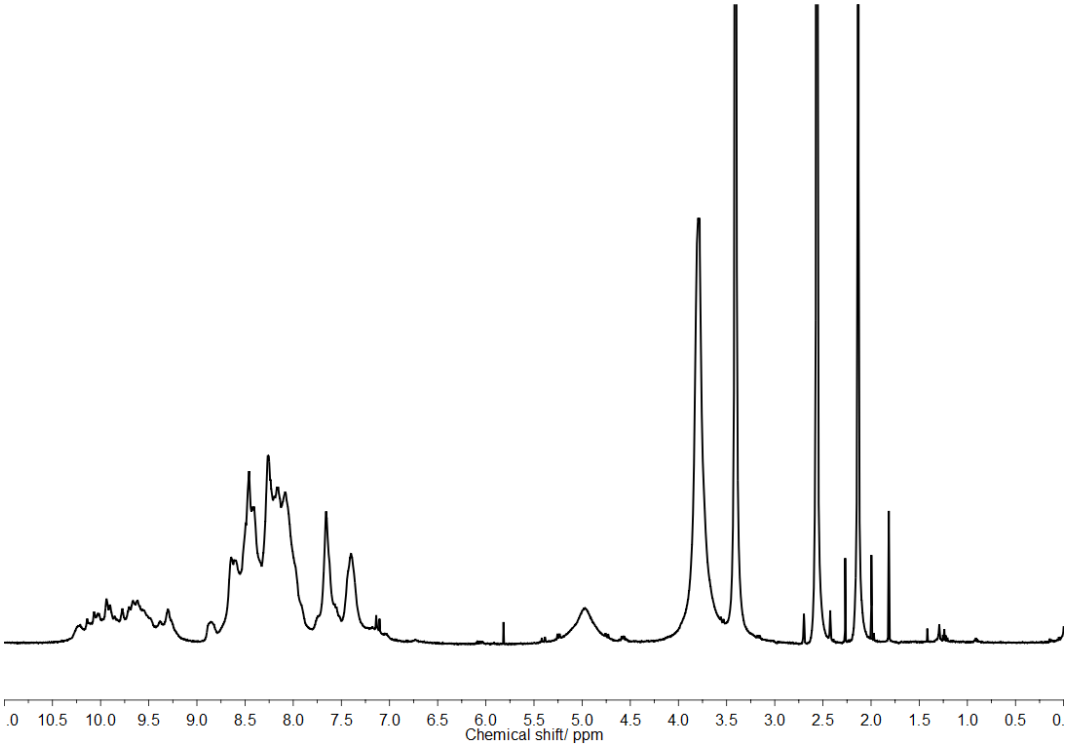


**Figure 6.7.** $^1$H-NMR (500 MHz, $d_6$-DMSO) of **L1** and $Pd(MeCN)_4.2BF_4$ in a 2:3 stoichiometry.

By taking into consideration the location of the nitrogen on the pyridyl moieties of ligands **L1** – **L3** it is possible to rationalise why this complex does not form. Molecular panelling provides a useful tool in predicting the outcome of reactions under the control of self-assembly. Several examples of large coordination cages rationally designed using this approach have been reported.[29, 30] In the case of the stella octangula complex the tripodal ligands act as panels on the face of an octahedron whereas the palladium cations are located on the vertices. Ligands **L1** – **L3** have the pyridyl nitrogen metal binding group located in the 3-position. If the ligand is treated as one of the faces of an octahedron the metal binding groups are found on the edges of the triangle, slightly away from the vertices (Figure 6.8). When the ligand is tessellated onto an octahedron it is not possible to overlap the metal binding groups (red) with the metal centres represented as the vertices. The stella octangula structure therefore cannot be obtained without significant distortion of the ligand, corresponding to a large enthalpic penalty.

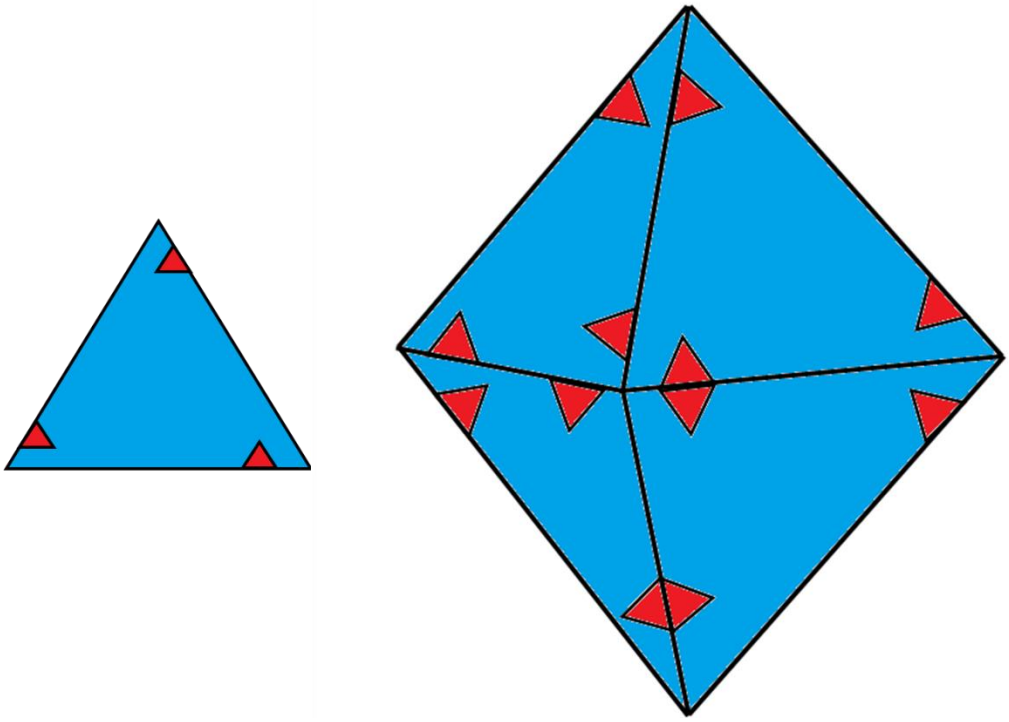

**Figure 6.8.** Molecular panelling of ligands **L1** – **L3** tessellated onto an octahedron showing the ligands are not sufficiently preorganised to form stella-octangula structure.

A ligand, previously reported by Dr Samuel Oldknow, was synthesised.[31] This new ligand **L4** was similar to **L1** with only a subtle change to the location of the metal binding group. The pyridyl group at the end of the azobenzene arm was changed so that it now resided in the 4 position (Scheme 6.1). **L4** possess poor solubility in all solvents and is only appreciably soluble in DMSO. Study

into the self-assembly of this ligand has been curtailed by this property as it was assumed that coordination cage formation would be inhibited by the coordinating nature of the solvent. However, recent work has shown that palladium, unlike iridium and rhodium is capable of self-assembling with this class of ligands in DMSO to furnish metallo-cryptophanes. The $^{1}$H-NMR spectrum of **L4** contained unusual features. There are twice as many resonances for the azobenzene groups than expected (Figure 6.9). Integrating the $^{1}$H-NMR spectrum of all the peaks due to the azobenzene arms and the CTG arene rings reveals that is the expected 4:1 ratio between these groups. Multiple attempts to purify the ligand through column chromatography made no effect on the additional peaks. It is possible that the additional peaks are due to a rotamer or dimeric host-guest interaction in solution. A $^{1}$H-NMR experiment was performed where the concentration of **L4** was incrementally decreased and a spectrum was acquired at each concentration. The integrals of the additional resonances did not decrease as expected, implying that the additional peaks are likely due to restricted rotation in the molecule. VT NMR of **L4** showed that the peaks did not move considerably upon heating the sample up to 80 °C. It is possible that 80 °C is not sufficiently high enough to enable free rotation to occur. Despite this, each of the main resonances could be fully assigned.

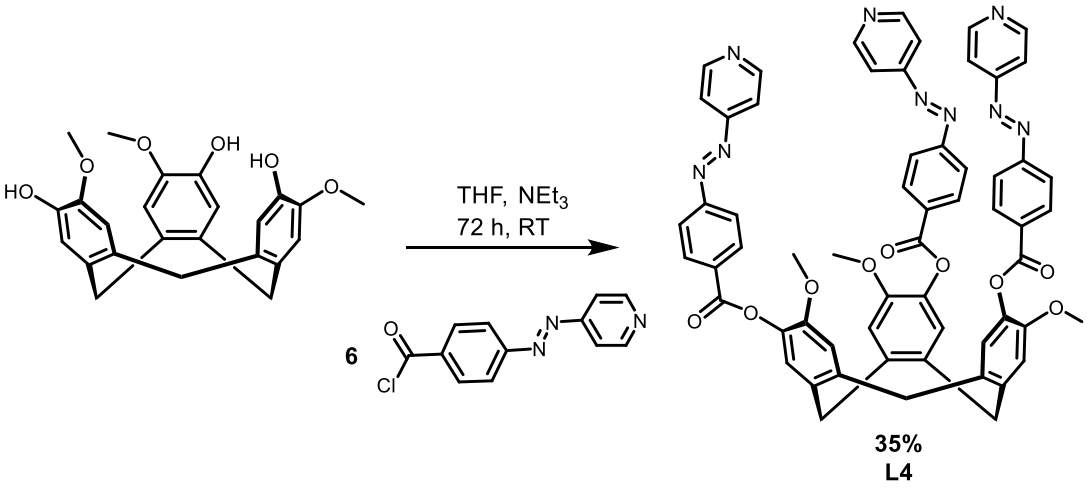


**Scheme 6.1.** Synthesis of ligand **L4** first reported by Dr Samuel Oldknow.[31]

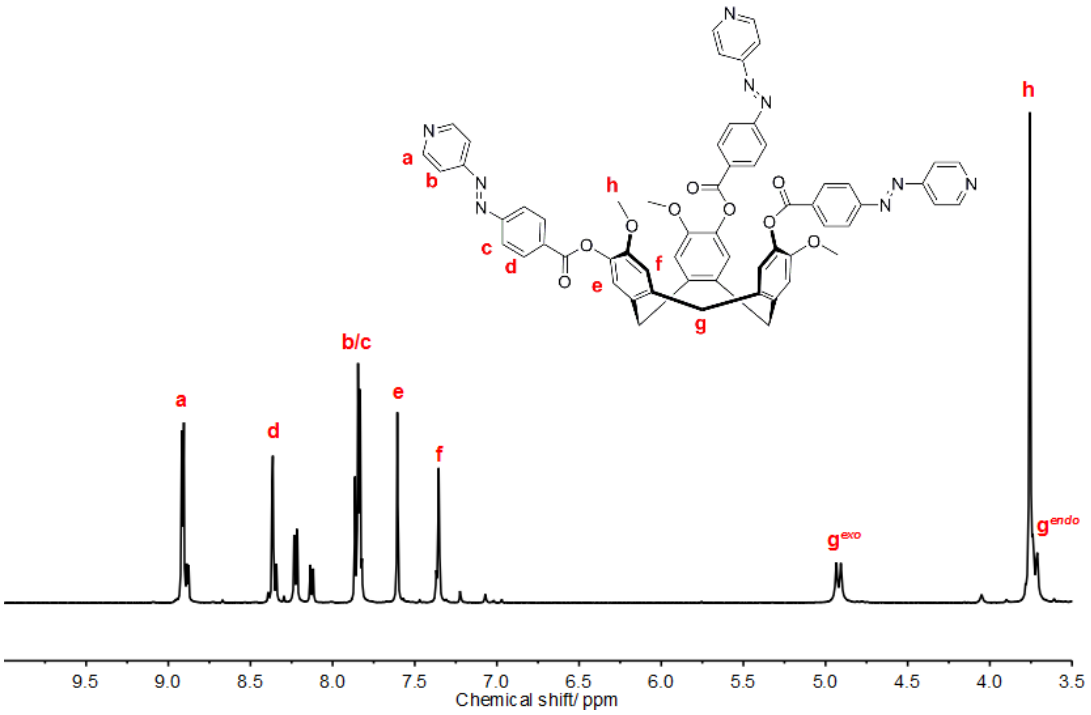


**Figure 6.9.** $^{1}$H-NMR (500 MHz, $d_6$-DMSO) of **L4**.

This slight change in the position of the pyridyl group has profound effects on the self-assembly behaviour of the ligand. Once again if the new ligand **L4** is treated as a 'panel' for the face of an octahedron it becomes apparent that the metal binding groups (red) have shifted to the vertices of the triangle. If this shape is tessellated onto an octahedron then four metal binding groups meet at each vertex (Figure 6.10).

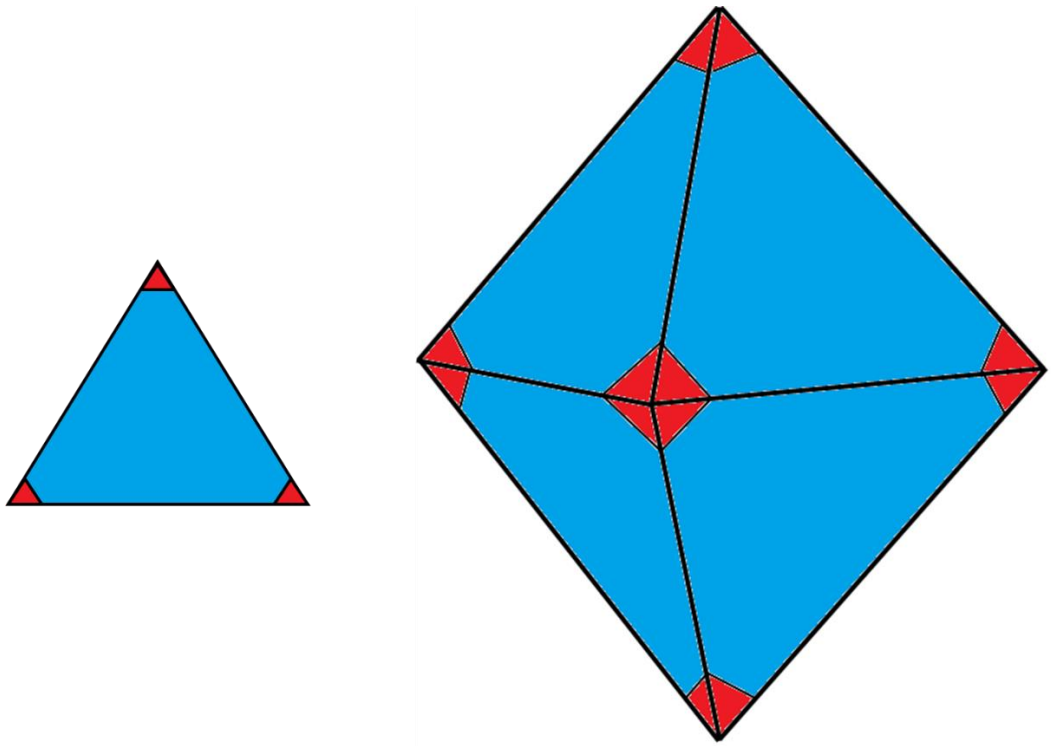

**Figure 6.10.** Molecular panelling of ligands **L4** tessellated onto an octahedron showing that a stella octangula structure is accessible from this ligand.

A square planar metal such as palladium should theoretically be able to form a stella octangula structure with **L4**. To test this hypothesis **L4** was dissolved in deuterated DMSO and a solution of $[Pd(MeCN)_4]2BF_4$ in deuterated DMSO was added in an 8:6 ratio (Scheme 6.2).

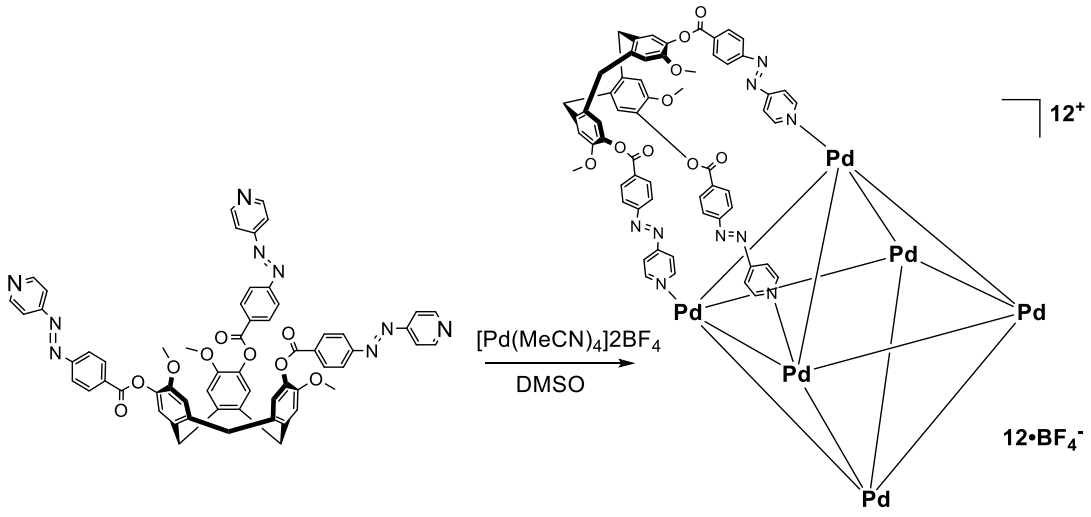


**Scheme 6.2.** Synthesis of $Pd_6$**L4**$_8$ stella octangula structure.

Changes were immediately seen in the $^1$H-NMR spectrum (Figure 6.11). The protons *ortho* to the pyridyl nitrogen were shifted downfield, suggesting complexation to the palladium centre has occurred. All of the peaks were also considerably broadened as is often the case upon formation of a large metallo-

supramolecular species. Due to the broad overlapping nature of the peaks it was not possible to fully assign the $^{1}$H-NMR spectrum. Interestingly however, the total number of peaks in the spectrum did not increase upon addition of the palladium salt from that of the pure ligand spectra. The complex that has formed has therefore retained the original symmetry of the ligand, $C_{3v}$, which can rule out the possibility of oligomer formation which would possess a much more complex NMR spectrum due to a decrease in the symmetry. Unlike previously reported stella octangula structures the spectra did not sharpen upon standing for a month.[32] The sharpening of the spectra has been attributed to the chiral self-sorting of the ligands to form cages consisting of a single enantiomer of the ligand, reducing the number of diastereomers in solution. $^{1}$H-NMR spectra which do not sharpen over time have been observed for a stella octangula cage formed from a 4-pyridyl appended propyl CTG ligand and palladium(II) cations.[4] This was attributed to an inability of the ligand to chirally self-sort into enantiopure cages. It is likely the case that the azobenzene appended CTG ligand **L4** is unable to chirally self-sort in solution.

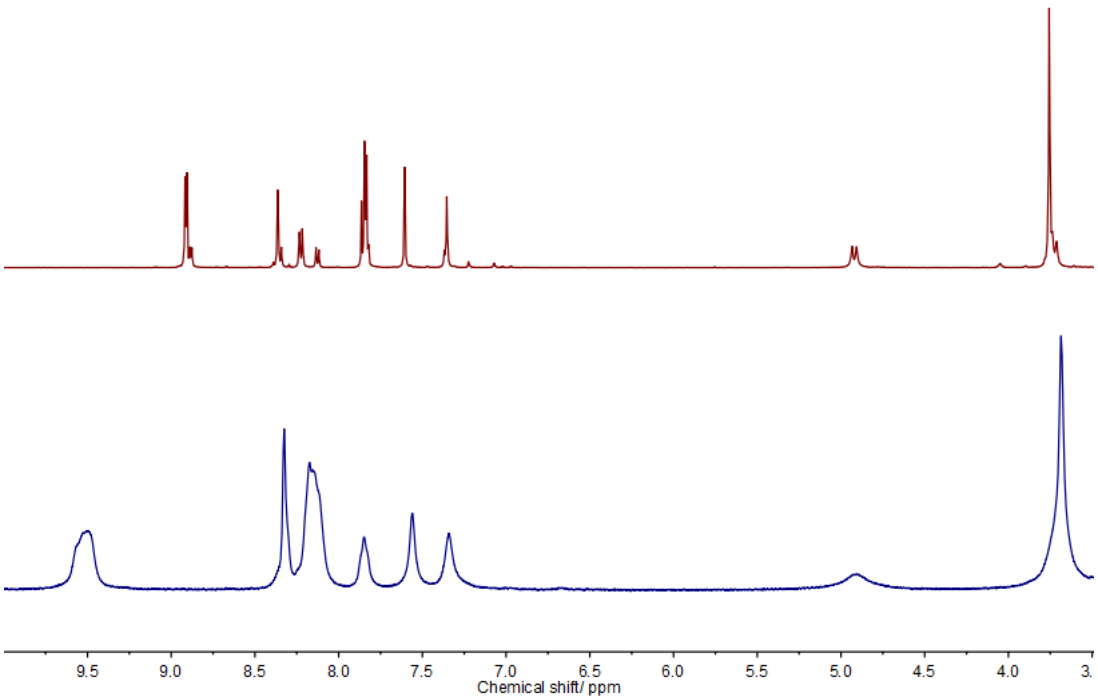


**Figure 6.11.** $^{1}$H-NMR (500 MHz, $d_6$-DMSO) of **L4** (red) and after immediately after addition of 0.75 equivalents of $[Pd(MeCN)_4]2BF_4$ (blue).

Routine analysis of the species by 2D NMR proved challenging and provided the first evidence that a large supramolecular species had been formed. Spectra acquired using a standard COSY experiment were found to have peaks that were missing in the 2D yet present in the 1D spectra. Specifically the missing peaks were assigned to the *exo* and *endo* protons on the CTG

bowl. Large molecules tumble slower in solution than small molecules and this leads to a faster relaxation in transverse magnetisation ($T_2$).[33] If the $T_2$ relaxation is too fast then the molecule, or parts of it, will be invisible to NMR techniques that rely upon the information obtained from the $T_2$ relaxation to produce a spectra. This explains why parts of the spectrum which were visible in a 1D $^1$H-NMR experiment which relies upon longitudinal relaxation ($T_1$) were subsequently invisible in a 2D experiment such as COSY or HSQC. In order to obtain a satisfactory spectrum the sample had to be heated up to 60 $^\circ$C which increased the rate of tumbling of the molecule in solution and decreased the rate $T_2$ relaxation such that all proton environments could be observed in the 2D spectrum, albeit weakly. COSY and HSQC spectra were acquired in this manner (Figure 6.12).

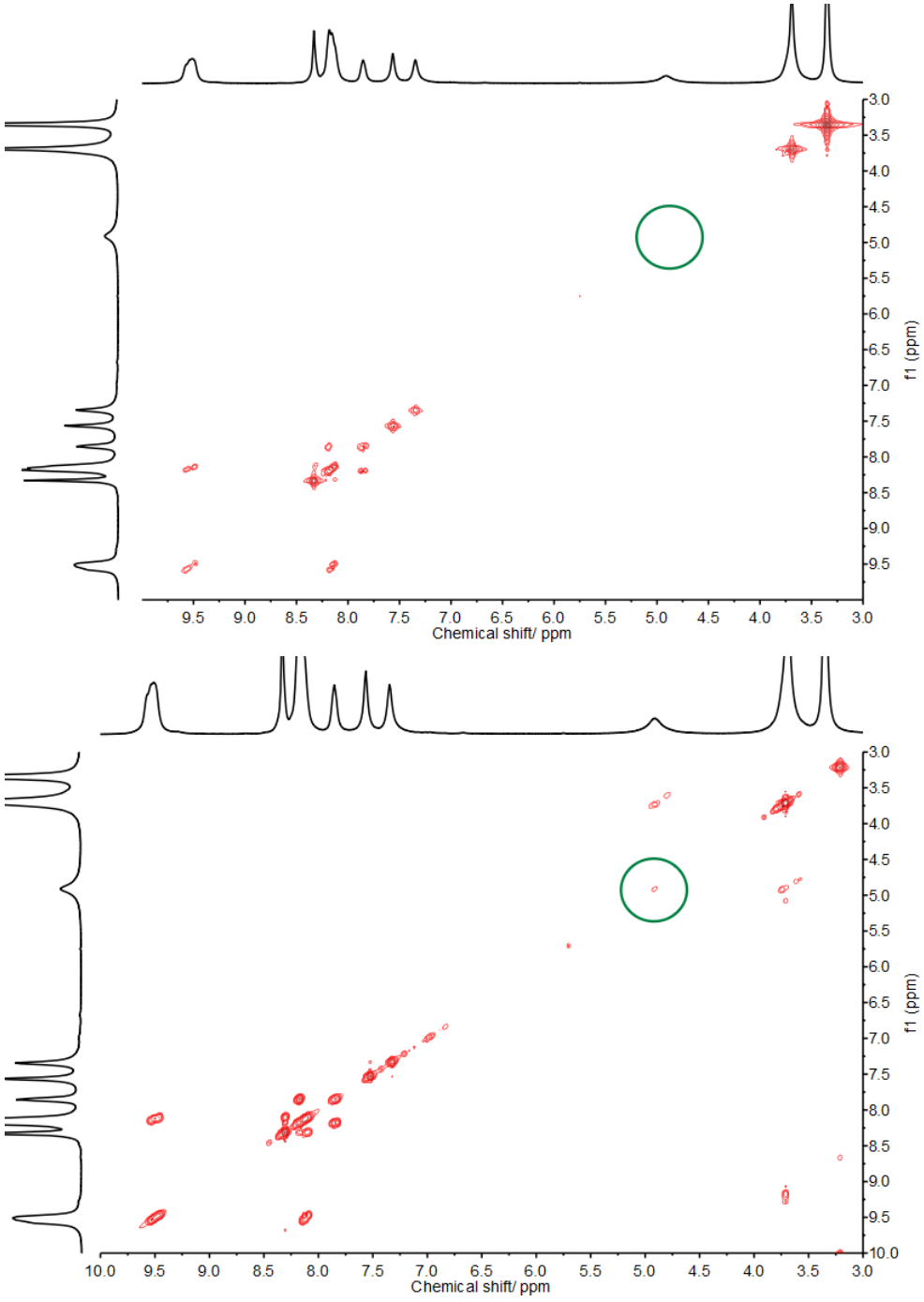


**Figure 6.12.** $^{1}$H-$^{1}$H COSY NMR (600 MHz, $d_6$-DMSO) of **C22** at room temperature (top) and 60 °C (bottom). Cross coupling peak highlighted in green only visible at elevated temperatures.

The difficulty experienced in obtaining routine 2D spectra strongly hints at the presence of a very large species in solution. DOSY NMR was utilised to gather further evidence that there was only a single species in solution (Figure 6.13) and to estimate the hydrodynamic radius of the species using the Stokes-Einstein equation (Equation 6.1). The spectra revealed that only a single species was present in solution and moreover it had a very slow rate of diffusion of 0.80 $m^2$/ Gs. Imputing this diffusion constant into the Stokes-

Einstein equation yielded a hydrodynamic radius of 12.5 Å and a molecular weight of 8140 g/ mol when calculated through the GNAT programme. Excluding anions the mass of the stella octangula cage is 8927 g/ mol.

$$D = \frac{RT}{N_A}\frac{1}{6\pi\eta r}$$

**Equation 6.1.** Stokes-Einstein equation to estimate hydrodynamic radius of particle in solution from diffusion constant. D = diffusion constant, R = ideal gas constant, T = temperature, $N_A$ = Avogadro constant, η = solvent viscosity, r = hydrodynamic radius.

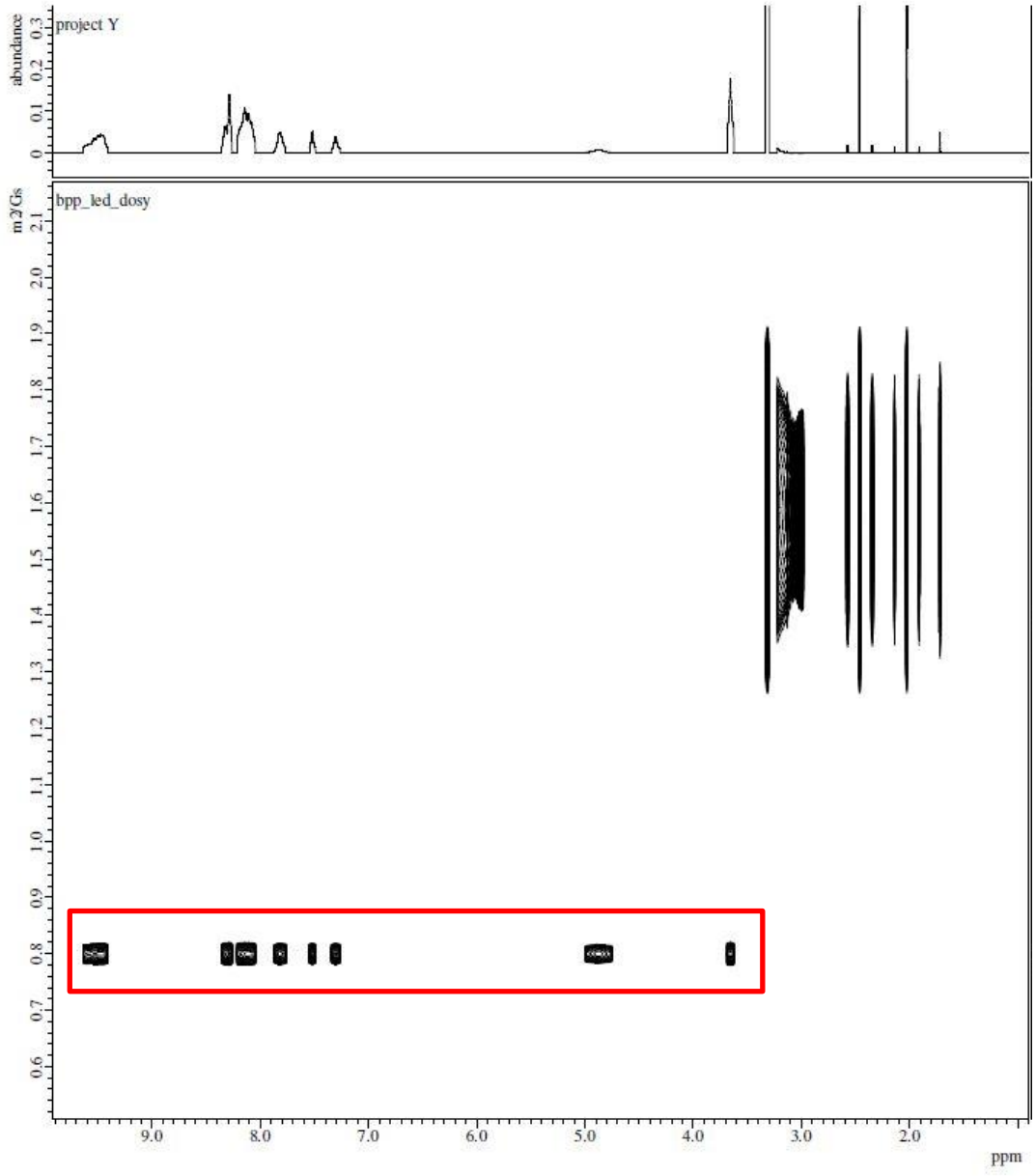


**Figure 6.13.** DOSY-NMR (500 MHz, $d_6$-DMSO) of $[Pd_6\mathbf{L4}_8]12BF_4$ cage showing a single large species in solution.

The large size of the species as calculated from this experiment explains why the 2D-NMR experiments were difficult to perform under standard conditions. In addition, it also provides growing evidence that a $Pd_6$**L4**$_8$ stella octangula cage has been synthesised.

Solution state studies have so far suggested at the formation of a large symmetrical species existing in solution, likely to be the stella octangula cage. In order to unequivocally determine that this is the correct structure attempts were made to collect the mass spectra of the complex. The mass spectrum (Figure 6.14) showed a mixture of peaks relating to different fragments and charge states of a stella octangula species. This indicated that the complex was fragmenting either during ionisation or due to competitive complexation of the palladium by the acetonitrile eluent. Similar dissociative behaviour has been observed for numerous metallo-cages in the gas phase utilising similar azobenzene appended CTG ligands.[31]

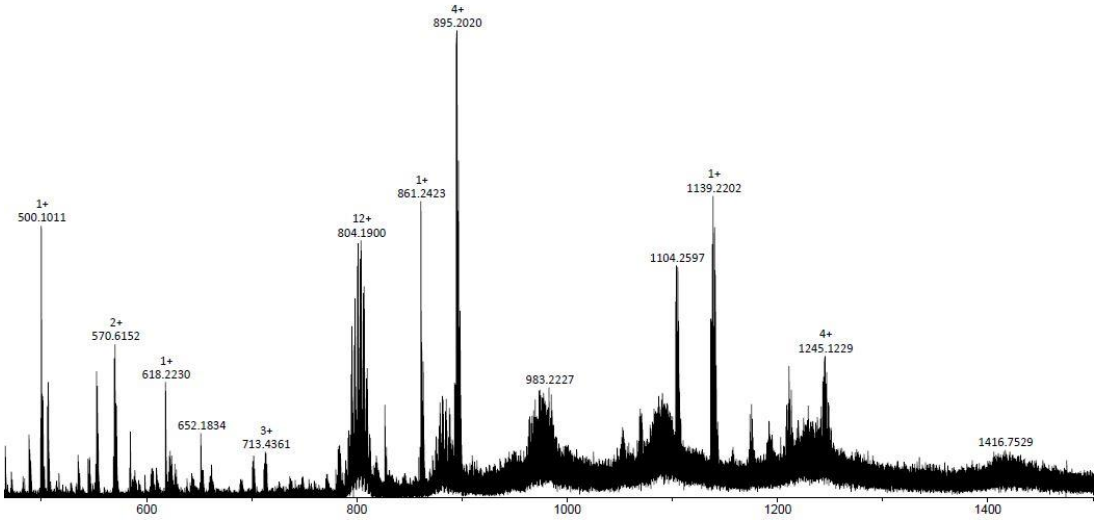


**Figure 6.14.** ESI-MS of $Pd_6$**L4**$_8$ showing a multitude of different species detected.

Closer analysis revealed the presence of a cluster of 12+ charge peaks centred on 804.1900 m/z. Each set of peaks in the cluster was separated by a distance of approximately 3 m/z and each displayed a distinctive isotope pattern of a six palladium species (Figure 6.15). All of the peaks in the cluster are too large to correspond to the $[Pd_6$**L4**$_8]^{12+}$ species which would have a calculated m/z of 744.18. It is possible that the cage is acting as a host to a varying amount of species in the gas phase, explaining the larger than expected m/z. The reaction was performed in DMSO which has been shown to act as a guest through CH-π interactions in other CTG based assemblies.[6] If one DMSO is assumed to interact with each CTG bowl in the assembly then eight DMSO molecules would be expected to complex with the $[Pd_6$**L4**$_8]^{12+}$

assembly in the mass spectrometer. This species would display a m/z of 795.1832 and indeed this is the lowest significant peak found in the cluster centred on 804.1900 (Figure 6.15). Additional methanol or acetonitrile adducts can account for the regular spacing of peaks at approximately 3 m/z apart.

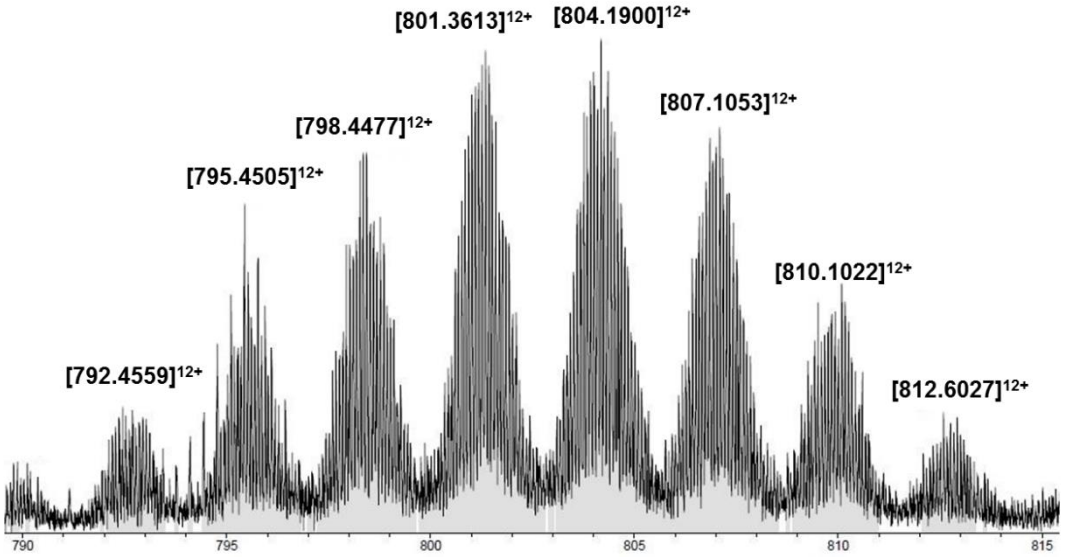


**Figure 6.15.** Zoomed in section of Figure 6.14 showing 12+ peaks of possible $[Pd_6L_8]^{12+}$ detected with varying amounts of solvent molecules.

Single crystals suitable of the stella octangula cage could be grown from vapour diffusion of ethyl acetate into a saturated solution of the cage in DMSO. The dark red block-like crystals took approximately a week to grow. The crystals adopted the shape of an octahedron (Figure 6.16). Single crystal X-ray diffraction analysis was attempted in-house yet showed extremely poor resolution, no peaks were detected past a resolution limit of 3.5 Å. The resolution could be improved marginally, up to 3 Å, by collecting the data using a synchrotron X-ray source at Diamond Light Source. Due to the extremely poor resolution the data could not be solved using traditional chemical methods. The poor resolution is not unexpected as the cage is approaching the size domain of small proteins which routinely diffract poorly. Moreover, the large internal cavity of the cage means that there will be large amounts of disordered solvent within the crystal lattice, further reducing the quality of diffraction. Fujita has described similarly large cages which could not be solved using traditional chemical crystallographic techniques. Instead, the use of methods commonly reserved for protein crystallography facilitated the solution of these structures. Attempts are ongoing to solve the structure using

protein crystallographic methods in collaboration with Dr Briony Yorke at the University of Bradford.

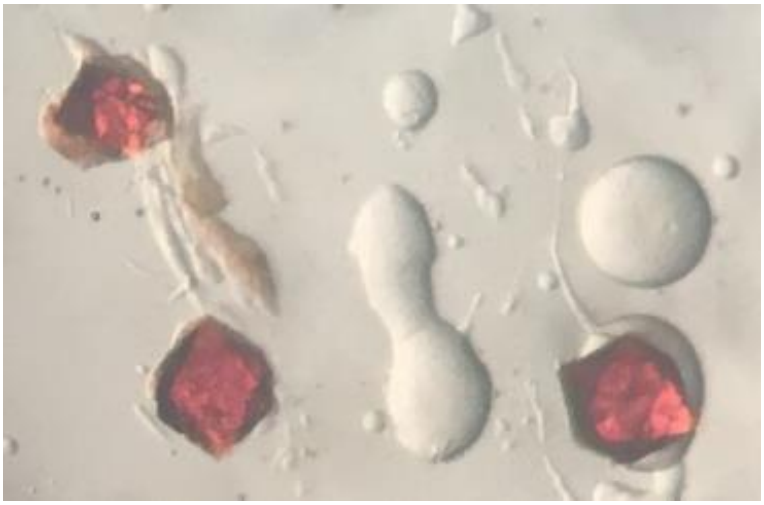

**Figure 6.16.** Appearance of the crystals of $[Pd_6L_8]12BF_4$ displaying the distinctive shape of an octahedron.

Although a structure solution has not been obtained from these experiments, a unit cell has been obtained that is consistent with a large stella octangula structure. The unit cell dimensions are a = 42.17 Å, b = 41.52 Å, c = 40.66 Å, α = 61.5°, β = 56.9°, γ = 59.7°. This is a similar sized unit cell as was obtained for a $Pd_6L_8$ stella octangula cage using the ligand shown in Figure 6.6 (where X = -(C=O)-).[34] Similarly, this X-ray data could not be solved but convincing evidence of the cages formation was acquired through mass spectrometry. In this example a face centred unit cell where a = 51.56 Å. If the unit cell for $Pd_6$**L4**$_8$ is transformed into a face centred cubic cell then the unit cell parameter a = 59.4 Å. This is slightly larger than the cell parameter for the previous extended ligand and is consistent with the slightly larger size of **L4** due to the azo group. The stella octangula cage consisting of 4-pyridyl appended CTG ligands can crystallise in a tetragonal or monoclinic space group.[5]

## 6.3 Photoisomerisation studies of stella octangula azo-cage

### 6.3.1 Photoisomerisation of the free ligand

The photoswitching behaviour of **L4** was determined using the same techniques as used for ligands **L1**-**L3** described in chapter 4. A 30 μM solution of **L4** in DMSO was prepared and an initial UV/visible spectrum was recorded (Figure 6.17). Comparison of the spectra of **L1** and **L4** shows that moving the pyridyl group from the 3 position to the 4 position has a considerable influence on the photophysical behaviour. The π-π* and transition shifts to a shorter

wavelength, increasing the gap between the π-π* and n-π* bands, centred on 320 nm and 450 nm respectively. In contrast to ligands **L1**-**L3**, **L4** required a 306 nm light source to promote the formation of a *cis* rich state, with 365 nm proving ineffective. This is likely due to the shift of the π-π* absorption band towards 306 nm. It took significantly longer for **L4** to reach its PSS compared to **L1**-**L3**. In total **L4** took 15 minutes of irradiation to reach the PSS compared to 1 minute for **L1**-**L3**.

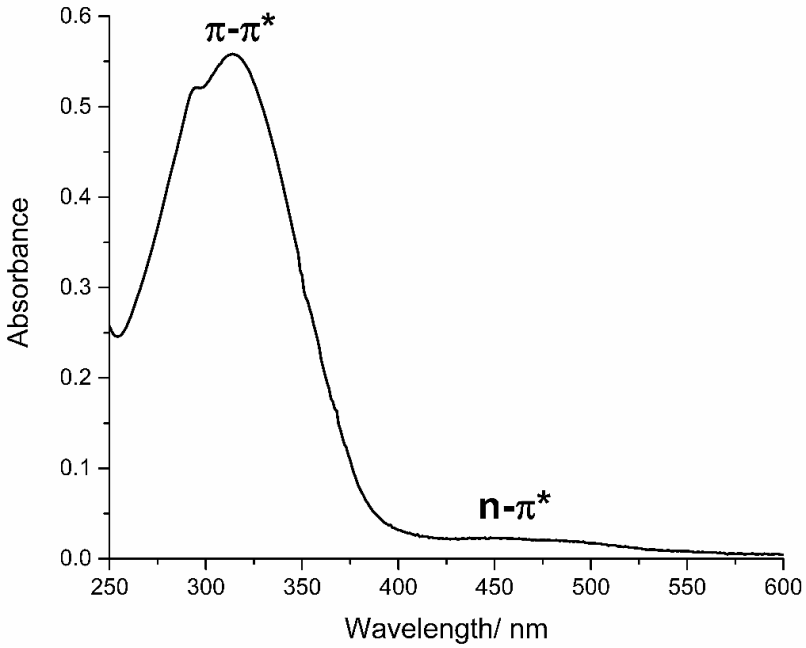


**Figure 6.17.** UV/visible spectrum (30 μM, $CHCl_3$) of **L4**.

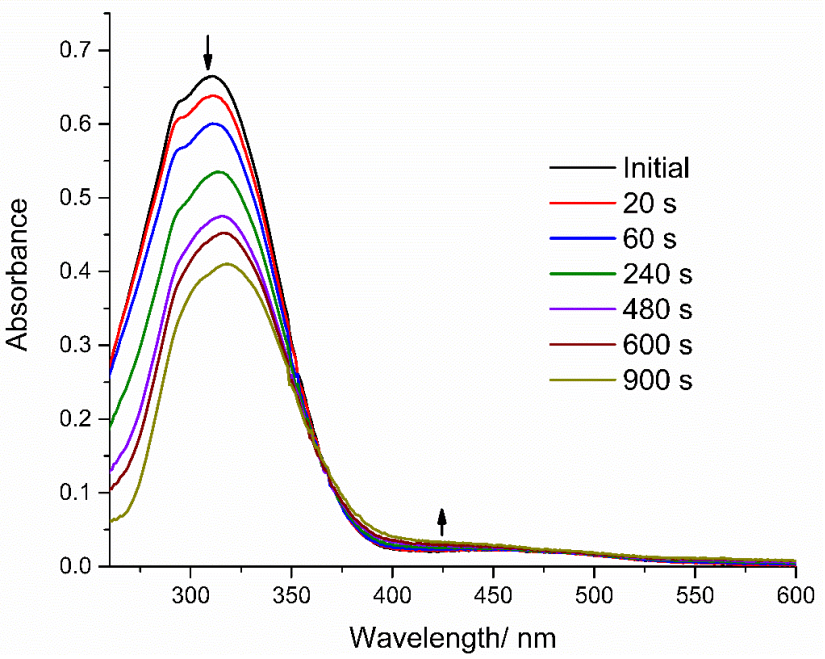


**Figure 6.18.** Timecourse UV/visible spectrum (30 μM, DMSO) of **L4** upon irradiation with a 30 W 306 nm lamp.

### 6.4.2 Photoisomerisation of the cage assembly

The $Pd_6$**L4**$_8$ cage contains 24 azobenzene groups embedded within the structural framework of the cage. It therefore may exhibit photoisomerisable properties which could enable the use of this cage as a host for the dynamic uptake and release of guest molecules using light. As detailed in chapter 4, studying the photoisomerisable character of the palladium cryptophanes was made considerably more challenging due to the disassembly of the construct at low concentrations. This precluded the use of UV/visible spectroscopy as a method for monitoring the cages. It was necessary therefore to determine the concentration at which the stella octangula cage begins to dissociate. A series of concentrations were prepared and an $^1$H-NMR spectrum was acquired for each sample. The stella octangula cage was considerably more stable than the metallo-cryptophanes. No cage dissociation was detected even at concentrations as low as 70 μM, over three times lower than the concentration limit for the palladium cages which had a value of over 300 μM. This implies that **C22** is more stable than its metallo-cryptophane counterparts. The highly absorbing nature of the cages due to the presence of multiple azobezene groups meant this concentration was still not sufficiently low to enable acquisition of a UV/visible spectrum.

Attempts were made to synthesise a platinum analogue of the stella octangula cage. The greater kinetic inertness of platinum should stabilise the complex at lower concentrations, enabling UV measurements to take place. Eight equivalents of **L4** were mixed with six equivalents of tetrakis(propionitrile) platinum(II) triflate. The reaction was monitored over the course of several days which showed that the stella octangula cage began to form. Unfortunately, the reaction would not go to completion and free ligand and metal tecton were present in the $^1$H-NMR even after several weeks in solution. Furthermore, the platinum complex slowly decomposed in air causing a black precipitate to form in solution. This is not unexpected as platinum complexes routinely require long reaction times to fully self-assemble. Heneklis reports that attempts to make a platinum variant of the stella octangula cage derived from 4-pyridyl appended CTG also failed with the reaction unable to go to completion.[32]

$^1$H-NMR spectroscopy was used to determine what processes occur upon irradiation of **C22** with UV light. A 30 W 306 nm light provided insufficient power to switch the cage. This behaviour was observed for cage **C19** and as before, a 355 nm Nd:YAG laser was used to promote the formation of the *cis* rich state. A 100 μM sample in DMSO was prepared and irradiated for 15

minutes. A $^{1}$H-NMR was acquired and revealed the presence of free ligand peaks in the spectrum (Figure 6.19). This implies that the *cis* isomer is not capable of forming the $M_6L_8$ structure and the cage spontaneously disassembles under these conditions. Cage disassembly following photoisomerisation of an azobenzene group has been reported by Liu and co-workers.[35] It was envisioned that reverting the ligand back to the *trans* state would reform the cage. The sample was heated to 80 °C to revert the ligands back to the *trans* resting state. However, over time a black precipitate began to form, likely due to the decomposition of the palladium cations. A sample of **C22** in the *trans* conformation can be heated to 80 °C indefinitely without decomposition occurring. It is probable that isomerisation of the ligand into a *cis* isomer destabilises the palladium cations, as they can no longer form the stable $M_6L_8$ structure. This makes them more susceptible to decomposition at elevated temperatures. After 24 hours at this temperature a $^{1}$H-NMR was recorded and revealed that mostly free ligand in the resting *trans* state was present in the sample. No evidence of the $M_6L_8$ cage could be observed. It appears that photoswitching **C22** into a *cis* rich states causes the disassembly of the cage to occur. Unfortunately the palladium is then destabilised in this state and rapidly decomposes, causing the cage disassembly process to be irreversible.

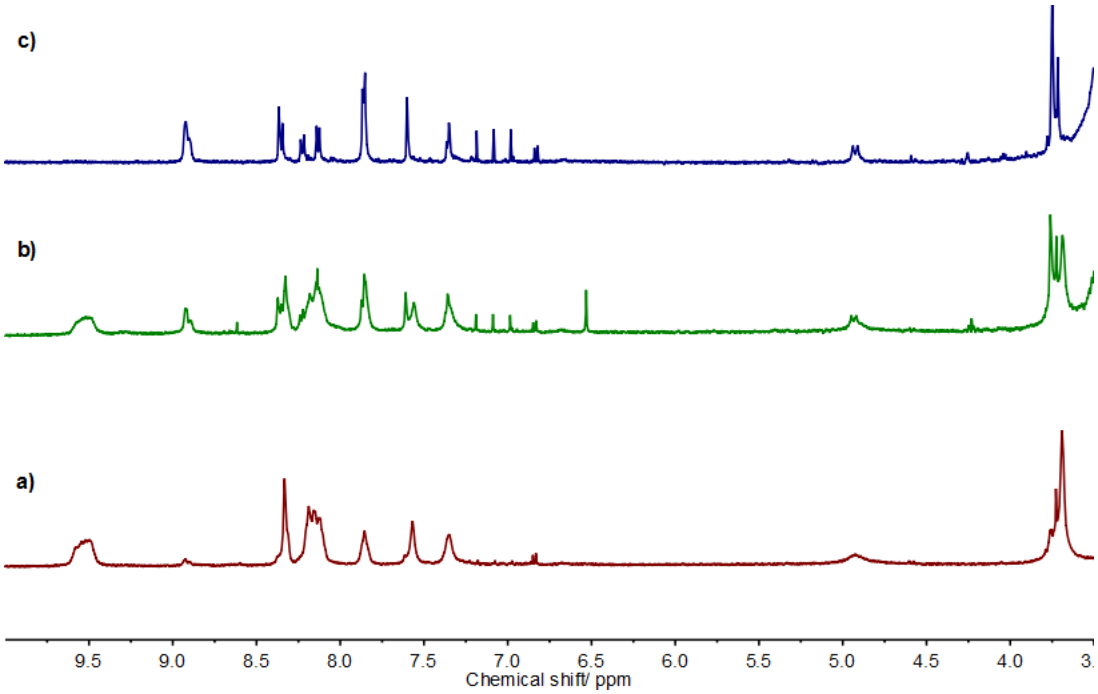


**Figure 6.19.** $^{1}$H-NMR (500 MHz, $d_6$-DMSO) of **a) C22** before photoswitching, **b)** after irradiation with 355 nm laser light for 15 mins, **c)** after heating to 80 °C for 24 hours.

SAXS studies were attempted on samples of the *trans* rich and *cis* rich states to determine if there were differences in the size of the cages between the samples. Unfortunately DMSO proved to be a poor solvent for the SAXS measurements, absorbing most of the incoming X-rays and resulting in a very weak scattering pattern. Unfortunately the scattering was too weak to extract meaningful data on size composition.

IM-MS was employed as a method to determine the size distribution of the cages in the resting *trans* state and a *cis* rich state. An IM-MS spectrum was acquired of a sample of **C22** in the resting *trans* state. A sample was then irradiated with a 355 nm Nd:YAG laser for 15 minutes and a second IM-MS spectrum was acquired. A drift plot of the was prepared and in both cases the $M_6L_8$ species could be identified in a range of charge states, from 12+ to 8+ (Figure 6.20). Each peak in the *cis* rich state had a slightly longer drift time than in the *trans* rich state. This is further confirmed by comparing the drift times for a number of these charged states (Figure 6.21). The *cis* rich states consistently have longer drift times than their *trans* analogue, yet the shape of the curves is not radically different, suggesting that a large change in the size distribution has not occurred. As the change in the drift times is relatively small it is not possible to determine whether the change is due to experimental error or the formation of a small amount of *cis* isomer. The small change in the drift times, as well as the NMR evidence acquired of the *cis* rich state suggests that photoswitching the sample into a *cis* rich state results in the disassembly of the stella octangula species. It is likely therefore that only the all *trans* cage is observed in the IM-MS as the *cis* isomer is unstable and rapidly disassembles.

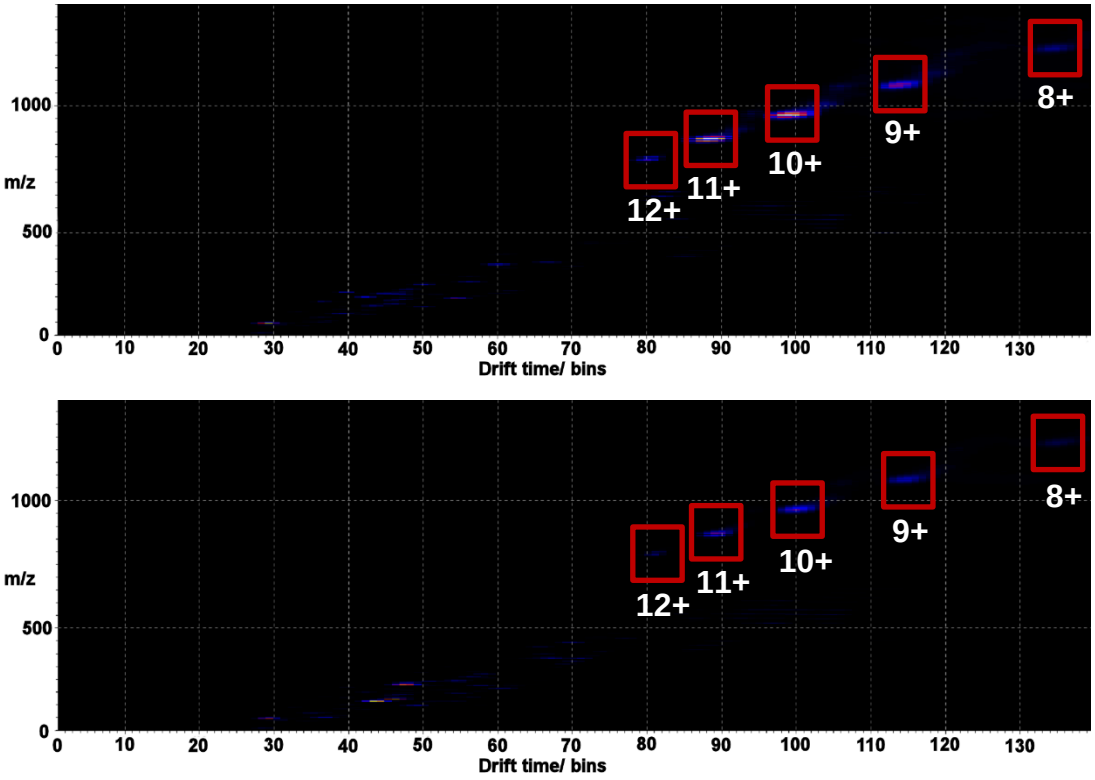


**Figure 6.20.** Drift plot of **C22** in resting *trans* state (top) and *cis* rich state (bottom). Peaks highlighted correspond to $[Pd_6\mathbf{L4}_8]^x$, where x is the charge labelled on the peak.

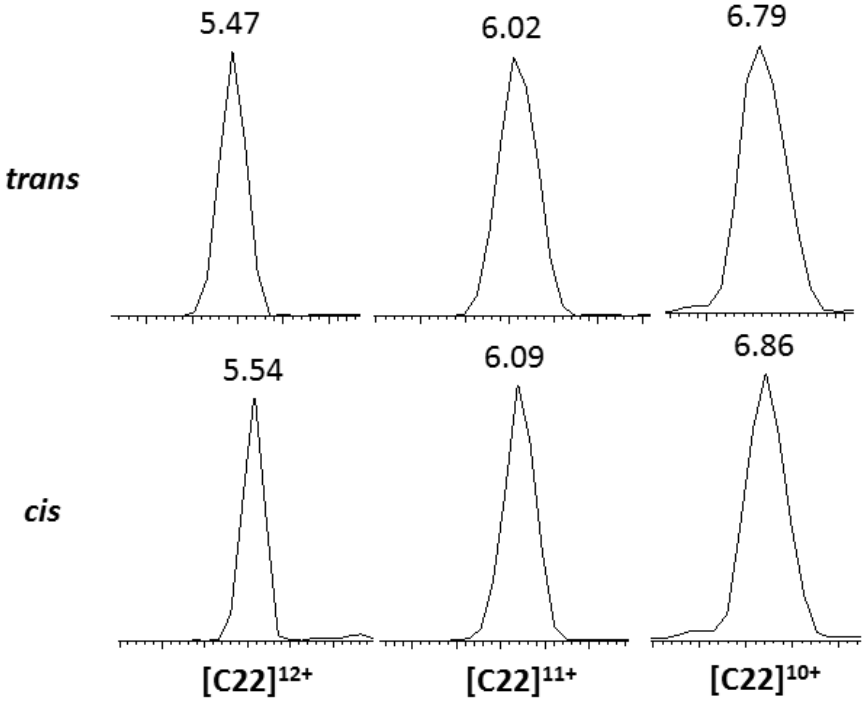


**Figure 6.21.** Drift times of $[Pd_6\mathbf{L4}_8]^{12+}$ (left), $[Pd_6\mathbf{L4}_8]^{11+}$ (middle) and $[Pd_6\mathbf{L4}_8]^{10+}$ (right) in a *trans* and *cis* rich state.

## 6.4 Conclusion

Compelling evidence has been obtained suggesting that a $[Pd_6\mathbf{L4}_8]12BF_4$ cage has been successfully synthesised. However, it is not possible to unequivocally assign the data as the proposed structure. NMR evidence strongly supports that an extremely large highly symmetrical and discrete product is formed in solution upon mixing of tetrakis(acetonitrile) palladium(II)tetrafluoroborate with **L4**. Mass spectral evidence has been obtained which displays the presence of a large 12+ species. The m/z is too large to correspond to $[Pd_6\mathbf{L4}_8]$ however, due to the large internal cavity of this species it is probable that this species will form adducts with large numbers of guests in the gas phase and could account for this discrepancy. SCXRD studies are ongoing, the structure has not been solved due to the extremely poor resolution. Preliminary results reveal that the palladium ions are arranged in an octahedron with reasonable Pd-Pd separations within the crystal lattice.

Attempts to determine the photoswitching behaviour of the complex have been challenging. The ligand has been shown to photoisomerise with relatively poor efficiency into the *cis* rich state with approximately 40% conversion to the *cis* isomer. This is lower than the conversion for the other ligands tested in this thesis (**L1**-**L3**) and the switching process also take 15 times longer. Photoswitching of **C22** to the *cis* isomer results in the subsequent disassembly of the cage. The palladium then spontaneously decomposes preventing reformation of the cage by reverting the ligands back to the resting *trans* state. **C22** is one of the largest cages reported composed of CTV based ligands. It therefore holds great potential as a molecular host for larger guests such as higher order fullerenes.

## 6.5 Future work

The photoswitching behaviour of **C22** has not been fully assessed due to issues arising from the decomposition of the cage at elevated temperatures post-photoswitching. It may be possible to revert the cage back to the *trans* state using a 450 nm light source. Doing so will negate the use of heat in the experiment and allow reversible photoswitching of **C22**. Unfortunately, due to equipment limitations this was not feasible at the time of writing.

The host-guest behaviour of this cage has not been explored. Due to the large size of the internal cavity, large globular non-polar guests are ideally suited to bind. Higher order fullerenes possess the necessary characteristics to potentially bind with the host. Such a system may have interesting applications in the separation of higher order fullerenes, currently a tedious and expensive task requiring multiple rounds of HPLC.

The X-ray crystal structure has not been solved due to the extremely poor resolution of the data. This is probably due to high levels of disordered solvent within the crystal lattice. Attempting to solve this structure using protein crystallographic methods may yield positive results as the supramolecular architecture described arguably shares more in common with protein crystals than standard small molecule crystals. Attempts are ongoing to solve the crystal structure using these methods in collaboration with Dr Briony Yorke at the University of Bradford.

## 6.6 Experimental

### General Remarks

All reagents were purchased from commercial suppliers and without further purification. Where stated reactions were carried out under an inert atmosphere of nitrogen using a dual vacuum/ nitrogen manifold and standard Schlenk techniques. Dry solvent was obtained by passing through a column of activated alumina.

### Instrumentation

$^{1}H$ and $^{13}C$ NMR were performed on a Bruker 500-CP 500 MHz spectrometer and referenced to residual solvent peaks. Where appropriate NMR assignments were confirmed using 2-D NMR techniques acquired on a Jeol ECA 600ii 600 MHz spectrometer, techniques include COSY, HSQC, HMBC, NOESY, ROESY and DOSY.

ESI-MS were performed on a Bruker micro-TOFQ mass spectrometer. IM-MS were performed on a Bruker Synapt G2-Si Imaging mass spectrometer.

UV/visible spectra were recorded on an Agilent Cary 100 UV/Vis spectrophotometer.

SAXS measurement were performed on a Bruker Nanostar system at a concentration of 100 μM in DMSO.

*Trans*→*cis* isomerisation studies of the free ligand were performed using a 30 W 365 nm lamp.

*Trans*→*cis* isomerisation studies of the metallo-cryptophanes were carried out using a Continuum Powerlite 8010 355 nm Nd:YAG laser. The natural frequency of the laser (10 Hz) was used without interference and each pulse was set to deliver 20 mJ of energy.

## Preparation of compounds

### 4-(4-sodiumbenzoateazo)pyridine (6.1)

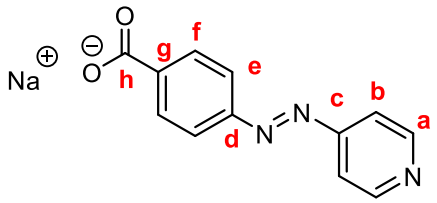


Methyl-4-nitrosobenzoate (2.78 g, 16.6 mmol) and 4-aminopyridine (2.92 g, 31.0 mmol) were dissolved in an aqueous NaOH solution (3% w/v, 300 mL) and heated to reflux overnight during which the solution turned a deep red colour. The solution was then cooled in an ice bath resulting the formation of an orange precipitate. The solid was filtered and washed with acetone then ether to yield the product as an orange microcrystalline powder (3.54 g, 15.6 mmol, 94%). Data is consistent with literature values.[31]

**$^{1}$H-NMR** (500 MHz, $d_6$-DMSO): 8.82 (d, 2H, *J* = 6.0 Hz, **H$^{a}$**), 8.04 (d, 2H, *J* = 8.6 Hz, **H$^{f}$**), 7.85 (d, 2H, *J* = 8.6 Hz, **H$^{e}$**), 7.75 (d, 2H, *J* = 6.0 Hz, **H$^{b}$**). **$^{13}$C-NMR** (126 MHz, $d_6$-DMSO): 167.8 (**C$^{h}$**), 156.8 (**C$^{c}$**), 151.8 (**C$^{g}$**), 151.5 (**C$^{a}$**), 145.2 (**C$^{d}$**), 130.0 (**C$^{f}$**), 122.2 (**C$^{e}$**), 116.0 (**C$^{b}$**). **ESI-MS** ($ES^-$): m/z 475.1120 $[2M+Na]^-$ calcd (475.11).

### 4-(4-benzoyl chlorideazo)pyridine (6.2)

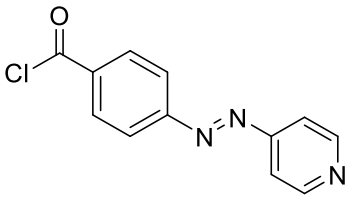


4-(4-benzoic acidazo)pyridine (369 mg, 1.48 mmol) was dissolved in thionyl chloride (5 mL) under $N_2$ and heated at 70 °C overnight forming a red solution. The thionyl chloride was removed under high vacuum leaving a red residue which was used without further purification (quantitative).

**(±)-2,7,12-Trimethoxy-3,8,13-*tris*(4-pyridyl-4-azophenylcarboxy)-10,15-dihydro-5H-tribenzo[a,d,g] cyclononatriene (L4)**

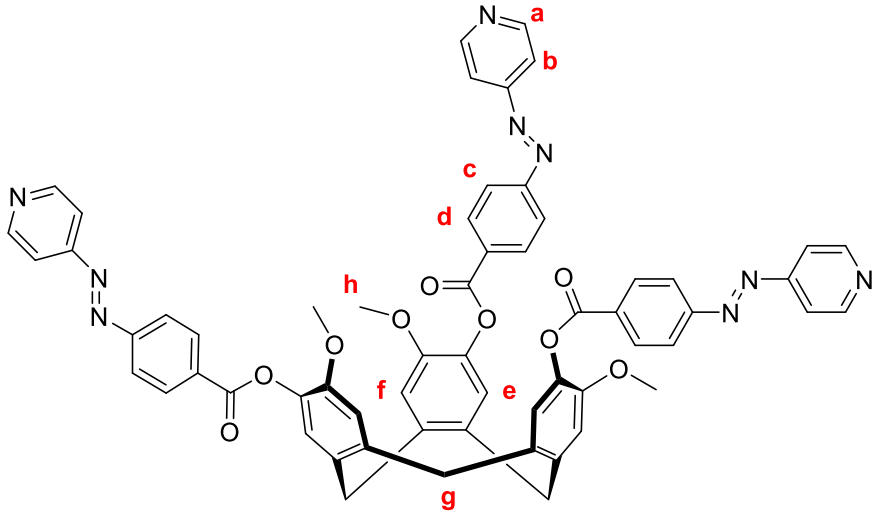


CTG (100mg, 0.24 mmol) was dissolved in anhydrous THF (30 mL) under $N_2$, anhydrous triethylamine (3 mL) was added and stirred for 30 minutes. The solution was transferred to a flask containing **6.2** (363 mg, 1.48 mmol) and stirred at room temperature for three days. The suspension was filtered and the solid was collected. Subsequent sonication in methanol (150 mL) and column chromatography on silica (5% MeOH/ DCM) yielded the product as a light yellow powder (86 mg, 0.083 mmol, 35%).

**$^1$H-NMR** (400 MHz, $d_6$-DMSO): 8.90 (m, 6H, **H$^a$**), 8.36-8.13 (m, 12H, **H$^{c/d}$**) 7.84 (m, 6H, **H$^b$**) 7.60 (s, 3H, **H$^e$**) 7.35 (s, 3H, **H$^f$**), 4.92 (d, 3H, *J* = 10.6 Hz, **H$^{g\text{-}exo}$**) 3.76 (s, 9H, **H$^h$**), 3.73 (d, 3H, *J* = 10.1 Hz, **H$^{g\text{-}endo}$**) **$^{13}$C-NMR** (126 MHz, $d_6$-DMSO): 162.4, 156.3, 151.9, 151.7, 150.7, 149.2, 138.9, 137.7, 134.7, 132.8, 131.9, 129.7, 118.6, 116.2, 56.3, 35.0. **ESI-MS** ($ES^+$): m/z 1140.2234 $[M+Na+2MeCN]^+$ calcd (1140.38).

**$[Pd_6(L4)_8]•12BF_4$ (C22)**

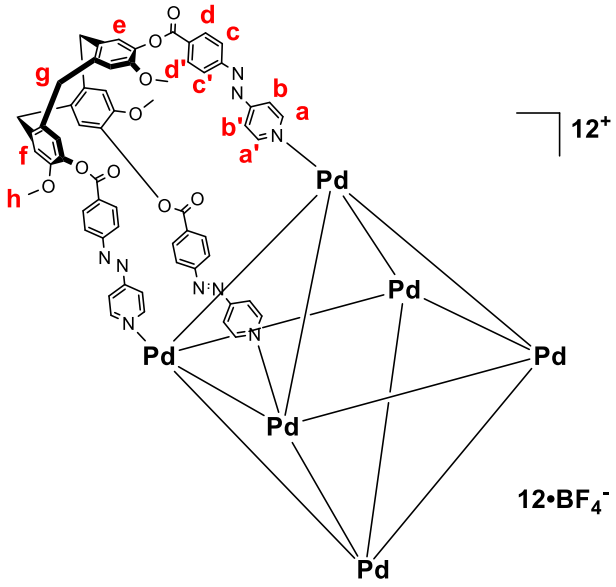


**L4** (4 mg, 3.76 µmol) was dissolved with heating in $d_6$-DMSO (0.4 mL). Tetrakis(acetonitrile)palladium(II) tetrafluoroborate (1.3 mg, 2,82 µmol) was dissolved in $d_6$-DMSO (0.3 mL) and added dropwise to the solution of **L4**. The stella octangula complex immediately formed in quantitative yield.

**$^1$H-NMR** (500 MHz, $d_6$-DMSO): 9.51 (bs, 6H, **$H^{a/a'}$**) 8.33 (bs, 3H, **Ar-H**), 8.19 (bs, 9H, **$H^{b/b'}$**, **Ar-H**), 7.86 (bs, 3H, **Ar-H**), 7.57 (bs, 3H, **$H^{e}$**), 7.35 (bs, 3H, **$H^{f}$**), 4.92 (bs, 3H, **$H^{g\text{-}exo}$**), 3.69 (bs, 12H, **$H^{h}$**,**$H^{g\text{-}endo}$**).

### 6.7.1 $^1$H-NMR photoswitching studies of C22

*Trans*→*cis* isomerisation was performed by preparing a sample of **C22** in $d_6$-DMSO (100 µM, 0.7 mL). An initial spectrum was recorded. The sample was irradiated with a 355 nm Nd:YAG laser (20 mJ, 10 Hz) for 900 s to generate the *cis* rich state. A $^1$H-NMR spectrum was recorded for comparison.

## References


1. J. J. Henkelis and M. J. Hardie, *Cryst. Eng. Comm.*, 2014, **16**, 8138-8146.
2. M. A. Little, M. A. Halcrow, L. P. Harding and M. J. Hardie, *Inorg. Chem.*, 2010, **49**, 9486-9496.
3. J. J. Henkelis, S. A. Barnett, L. P. Harding and M. J. Hardie, *Inorg. Chem.*, 2012, **51**, 10657-10674.
4. J. J. Henkelis, J. Fisher, S. L. Warriner and M. J. Hardie, *Chem. Eur. J.*, 2014, **20**, 4117-4125.
5. T. K. Ronson, J. Fisher, L. P. Harding and M. J. Hardie, *Angew. Chem. Int. Ed.*, 2007, **46**, 9086-9088.
6. T. K. Ronson, C. Carruthers, J. Fisher, T. Brotin, L. P. Harding, P. J. Rizkallah and M. J. Hardie, *Inorg. Chem.*, 2010, **49**, 675-685.
7. J. M. Fowler, F. L. Thorp-Greenwood, S. L. Warriner, C. E. Willans and M. J. Hardie, *Chem. Commun.*, 2016, **52**, 8699-8702.
8. C. Carruthers, T. K. Ronson, C. J. Sumby, A. Westcott, L. P. Harding, T. J. Prior, P. Rizkallah and M. J. Hardie, *Chem. Eur. J.*, 2008, **14**, 10286-10296.
9. T. K. Ronson, J. Fisher, L. P. Harding, P. J. Rizkallah, J. E. Warren and M. J. Hardie, *Nat. Chem.*, 2009, **1**, 212.
10. C. J. Sumby, J. Fisher, T. J. Prior and M. J. Hardie, *Chemistry – A European Journal*, 2006, **12**, 2945-2959.
11. M. J. Hardie, *Chem. Soc. Rev.*, 2010, **39**, 516-527.
12. M. J. Hardie, *Isr. J. Chem.*, 2011, **51**, 807-816.
13. C.-P. Li and M. Du, *Chem. Commun.*, 2011, **47**, 5958-5972.
14. P. J. Stang and B. Olenyuk, *Acc. Chem. Res.*, 1997, **30**, 502-518.
15. P. J. Steel, *Acc. Chem. Res.*, 2005, **38**, 243-250.
16. R. W. Saalfrank, H. Maid and A. Scheurer, *Angew. Chem. Int. Ed.*, 2008, **47**, 8794-8824.
17. S. Mecozzi and J. Rebek, *Chem. Eur. J.*, 1998, **4**, 1016-1022.
18. S.-Y. Yu, T. Kusukawa, K. Biradha and M. Fujita, *J. Am. Chem. Soc.*, 2000, **122**, 2665-2666.
19. S. Sato, J. Iida, K. Suzuki, M. Kawano, T. Ozeki and M. Fujita, *Science*, 2006, **313**, 1273-1276.
20. M. J. Wiester, P. A. Ulmann and C. A. Mirkin, *Angew. Chem. Int. Ed.*, 2011, **50**, 114-137.
21. R. Gramage-Doria, J. Hessels, S. H. A. M. Leenders, O. Tröppner, M. Dürr, I. Ivanović-Burmazović and J. N. H. Reek, *Angew. Chem. Int. Ed.*, 2014, **53**, 13380-13384.
22. S. H. A. M. Leenders, M. Dürr, I. Ivanović-Burmazović and J. N. H. Reek, *Adv. Synth. Catal.*, 2016, **358**, 1509-1518.
23. N. Takeda, K. Umemoto, K. Yamaguchi and M. Fujita, *Nature*, 1999, **398**, 794-796.
24. F. Yu, D. Poole III, S. Mathew, N. Yan, J. Hessels, N. Orth, I. Ivanović-Burmazović and J. N. H. Reek, *Angew. Chem. Int. Ed.*, 2018, **57**, 11247-11251.
25. T. Yamaguchi and M. Fujita, *Angew. Chem. Int. Ed.*, 2008, **47**, 2067-2069.

26. K. Suzuki, S. Sato and M. Fujita, *Nat. Chem.*, 2009, **2**, 25.
27. X. Yan, P. Wei, Y. Liu, M. Wang, C. Chen, J. Zhao, G. Li, M. L. Saha, Z. Zhou, Z. An, X. Li and P. J. Stang, *J. Am. Chem. Soc.*, 2019, **141**, 9673-9679.
28. N. J. Cookson, J. J. Henkelis, R. J. Ansell, C. W. G. Fishwick, M. J. Hardie and J. Fisher, *Dalton Trans.*, 2014, **43**, 5657-5661.
29. M. Fujita, K. Umemoto, M. Yoshizawa, N. Fujita, T. Kusukawa and K. Biradha, *Chem. Commun.*, 2001, DOI: 10.1039/B008684N, 509-518.
30. N. K. Al-Rasbi, I. S. Tidmarsh, S. P. Argent, H. Adams, L. P. Harding and M. D. Ward, *J. Am. Chem. Soc.*, 2008, **130**, 11641-11649.
31. S. Oldknow, D. R. Martir, V. E. Pritchard, M. A. Blitz, Colin W. G. Fishwick, E. Zysman-Colman and M. J. Hardie, *Chem. Sci.*, 2018, **9**, 8150-8159.
32. J. Henkelis, PhD thesis, University of Leeds, 2014.
33. M. P. Foster, C. A. McElroy and C. D. Amero, *Biochemistry.*, 2007, **46**, 331-340.
34. T. K. Ronson and M. J. Hardie, unpublished work.
35. S. Fu, Q. Luo, M. Zang, J. Tian, Z. Zhang, M. Zeng, Y. Ji, J. Xu and J. Liu, *Mater. Chem. Front.*, 2019, **3**, 1238-1243.